ASME
SETTING THE STANDARD
1880 2005

Transactions of the ASME, Journal of Applied Mechanics (ISSN 0021-8936) is published bimonthly (Jan., Mar., May, July, Sept., Nov.) by The American Society of Mechanical Engineers, Three Park Avenue, New York, NY 10016. Periodicals postage paid at New York, NY and additional mailing offices. POSTMASTER: Send address changes to Transactions of the ASME, Journal of Applied Mechanics, c/o THE AMERICAN SOCIETY OF MECHANICAL ENGINEERS, 22 Law Drive, Box 2300, Fairfield, NJ 07007-2300. **CHANGES OF ADDRESS** must be received at Society headquarters seven weeks before they are to be effective. Please send old label and new address.

Journal of Applied Mechanics

Published Bimonthly by ASME

VOLUME 73 • NUMBER 1 • JANUARY 2006

Special Issue on Thermal Science and Engineering With Emphasis on Porous Media

FOREWORD

TECHNICAL PAPERS

(**Contents continued on inside back cover**)

This journal is printed on acid-free paper, which exceeds the ANSI Z39.48-1992 specification for permanence of paper and library materials. ♾™
♻ 85% recycled content, including 10% post-consumer fibers.

ADDITIONAL TECHNICAL PAPERS

TECHNICAL BRIEFS

ANNOUNCEMENTS AND SPECIAL NOTES

The ASME Journal of Applied Mechanics is abstracted and indexed in the following:

Alloys Index, Aluminum Industry Abstracts, Applied Science & Technology Index, Ceramic Abstracts, Chemical Abstracts, Civil Engineering Abstracts, Compendex (The electronic equivalent of Engineering Index), Computer & Information Systems Abstracts, Corrosion Abstracts, Current Contents, EEA (Earthquake Engineering Abstracts Database), Electronics & Communications Abstracts Journal, Engineered Materials Abstracts, Engineering Index, Environmental Engineering Abstracts, Environmental Science and Pollution Management, Fluidex, Fuel & Energy Abstracts, GeoRef, Geotechnical Abstracts, INSPEC, International Aerospace Abstracts, Journal of Ferrocement, Materials Science Citation Index, Mechanical Engineering Abstracts, METADEX (The electronic equivalent of Metals Abstracts and Alloys Index), Metals Abstracts, Nonferrous Metals Alert, Polymers Ceramics Composites Alert, Referativnyi Zhurnal, Science Citation Index, SciSearch (Electronic equivalent of Science Citation Index), Shock and Vibration Digest, Solid State and Superconductivity Abstracts, Steels Alert, Zentralblatt MATH

Journal of Applied Mechanics

Foreword

Thermal Science and Engineering With Emphasis on Porous Media

This special issue of JAM brings together 16 selected papers from the First Conference on Thermal Engineering held in Beirut on May 31–June 4, 2004. I would like to express my gratitude to the Editor of JAM, Professor McMeeking, for dedicating a special issue of this prestigious journal to selected papers of the inaugural conference on Thermal Engineering.

It has always been the tradition for scientists from the Middle East and the Gulf region, as well as North Africa, to conduct their graduate studies abroad, particularly in North America and Europe. Governments in the region are committed to improving undergraduate education, but until recently it has been the norm not to focus so much on graduate education. Building research capability in institutions of higher learning and attracting highly motivated staff to advance the research agenda were not among the top priorities. But, higher education in this part of the world has started to change thanks to the foresight of the leaders in the region. However, the fact remains that highly-skilled scientists and engineers from the Middle East, the Gulf region, and North Africa sought and are still seeking work abroad in academic and research institutions.

Well-defined venues dedicated to contacts between the academics and researchers in the institutions of higher learning in the region and their counterparts abroad are almost nonexistent. The purpose of starting a biannual international conference to be rotated around the Middle East, Gulf, and North African region countries is to meet this need and provide a well-structured platform to boost research activity and productivity in the region as well as providing a point of contact and networking. Establishing a recurring platform which will serve as a focal point for the gathering of scientists and engineers from the region working abroad, in particular in Europe, North America and other countries of the industrial world, and their colleagues in the countries of the region was deemed essential. Thermal Engineering was selected as an umbrella title for the Conference series because of its encompassing meaning and because this research area is of great importance to the region. Topics related to environment, energy, petroleum and construction are examples of thermal engineering crucial to the economic development and well being of the countries in the region.

Discounting the recent unfortunate events in Lebanon, the country was poised to emerge from its long period of arrested development at the time the decision was made to hold the first Conference on Thermal Engineering in Beirut on May 31–June 4, 2004. Lebanon had come out of a long civil war and the long and arduous process of rebuilding the country had started. Beirut had experienced an explosive growth and rebuilding activity during the last ten years with billions of dollars in investment, and had regained some of its past glory and glitter worthy of its nickname "Paris of the East" of the 1950s and 1960s before the civil war. It was felt that the opportunity to start this exercise in Beirut, to be rotated later to elsewhere, could not be passed up.

The Conference is the brainchild of Professor Ziad Saghir of Ryerson University in Toronto, Canada. Professor Saghir's commitment and tireless efforts, not to mention his organizational skills, lay at the very foundations of the success of the Conference. The encouragement, help, and personal day-to-day involvement of Professor George Nasr from the Lebanese University in Beirut was also crucial and played a major role in this success story. The Conference has been very successful beyond our best expectations. The success of the Conference would not have been achieved without the support of the Lebanese and Canadian governments. The support provided by both governments is gratefully acknowledged. The Lebanese government was enormously supportive of the enterprise and the Canadian Embassy in Beirut was instrumental in making it a success. A large audience of scientists attended the meeting in the beautiful spring weather of Beirut and enjoyed the excellent Lebanese hospitality. The next Conference on Thermal Engineering is scheduled to be held in the United Arab Emirates at Al-Ain on January 3–6, 2006. At the time of this writing all indications are the success of the first Conference on Thermal Engineering will be duplicated and perhaps even eclipsed.

The common theme tying together more than half the contributions in this collection of selected papers is flow in porous medium and in particular thermal issues in porous media. A number of papers in this group are related to issues directly relevant to the oil industry starting with the review article on the Soret effect. Fluid flow through porous media is encountered in many different branches of science and engineering, ranging from agricultural, chemical, civil and petroleum engineering, to food and soil sciences. Scientists, engineers, and politicians recognize the economic importance of enhancing oil recovery techniques, in addition to their growing concerns about pollution and the quality of the water obtained from the ground. Over the past decades, flow through porous media has been extensively studied experimentally and theoretically as it is at the very heart of various industrial processes central to energy production and to environmental issues.

It is only appropriate to open the lineup of the 16 selected papers in this special issue with two pace-setting review articles by well-known experts Jean K. Platten, who reviews the latest in Soret effect research, and Georgy Lebon et al., who summarize thermodynamic theories in use and explore the foundations of a unified extended thermodynamic theory.

The name "Soret effect" is usually attributed to mass separation induced by temperature gradients. The effect was discovered in 1879 by the Swiss scientist Charles Soret who noticed that a salt solution contained in a tube with the two ends at different temperatures did not remain uniform in composition. The salt was more concentrated near the cold end than near the hot end of the tube. Charles Soret concluded that a flux of salt was generated by a temperature gradient resulting, in steady state conditions, in a concentration gradient. Although the German C. Ludwig described the same phenomenon several years before in 1856 in a short communication, the phenomenon bears his name because Soret studied the effect rather in detail and formulated the fundamental equations describing the phenomenon. The Soret effect plays an important role in the operation of solar ponds, biological

systems, and the microstructure of the world's oceans. In biological systems mass transport across biological membranes induced by small thermal gradients in living matter is an important factor. One of the challenges in optimizing exploitation of oil reservoirs is a good knowledge of the fluid physics in crude oil reservoirs. Today, the modeling methods are based on pressure-temperature equilibrium diagrams and on gravity segregation of the different components of crude oil. However, improved models which more accurately predict the concentrations of the different components are necessary. The concentration distribution of the different components in hydrocarbon mixtures is mainly driven by phase separation and diffusion, and the Soret effect plays an important role.

The aim of the second review paper by Georgy Lebon, Thomas Desaive, and Pierre Dauby is to convince the reader that the extended irreversible thermodynamics (EIT) theory provides a valuable tool for studying a large variety of macroscopic processes. The underlying principles which hold together the edifice of classical irreversible thermodynamics (CIT) are reviewed and familiar laws such as Fourier's and Fick's are derived from the framework of CIT as well as the Dufour and Soret effects. However, all field equations derived using the framework of CIT are parabolic implying that any disturbance anywhere in the system is felt instantaneously at all other points which is a violation of the fundamental principle of causality. Furthermore CIT is a linear theory which holds only in the vicinity of equilibrium. These shortcomings at the very foundations of CIT prompted the proposition of other formalisms aimed at removing them. Extended irreversible thermodynamics (EIT) provides a unified description of a large body of physical processes and remedies the shortcomings of CIT. The formalism is based on the assumption that fluxes of heat, mass, and momentum are also state variables as well as mass, momentum, and temperature. The open problem in EIT is to develop the evolution equations for the fluxes. The authors accomplish this by neglecting the terms which are second order and higher. The field equations are hyperbolic in EIT thereby removing the objection raised in CIT due to the violation of the causality principle.

The next group of seven papers in this special edition cover issues related to porous media flow and thermal management.

Transport phenomena in heterogeneous porous media are a challenging research topic. Charles-Guobing Jiang, M. Ziad Saghir, and M. Kawaji investigate numerically thermal diffusion phenomena in a laterally heated heterogeneous porous cavity filled with a binary mixture of methane and n-butane. The modeling of the Soret effect in porous media is based on nonequilibrium thermodynamics. The investigation of the Soret effect in a heterogeneous porous medium is important in itself, but the work gains more in significance as the Soret coefficient, the ratio of the thermal diffusion coefficient to molecular diffusion coefficient, is not kept constant but calculated at each point of the computational grid as a function of the temperature, pressure, and the composition of the fluid mixture. The phenomenon of natural convection, induced by two separate sources of buoyancy, through porous media has been recently studied extensively due to its importance in many natural and industrial problems. In double diffusive convection, the solutal field results from the imposition of solutal boundary conditions on the system. In Soret induced convection, solutal gradients are due to the thermal diffusion in a binary mixture, initially homogeneous. In both cases, the dynamics of heat and mass transfer can be very different from those driven by the temperature field alone.

In the next paper A. Bahloul et al. report an extensive analytical and numerical study of natural convection of a binary fluid induced by double diffusivity and Soret effect in a saturated vertical porous annulus. Both cases of buoyancy opposing and helping the motion are addressed. Uniform heat fluxes are applied to the vertical walls while the horizontal walls are impermeable and adiabatic. Solutal gradients are assumed to be induced either by the imposition of constant gradients of concentration on the vertical walls (double diffusive convection) or by the Soret effect.

D. B. Ingham et al. develop new mathematical and numerical techniques to deal with porous materials which undergo several orders of magnitude changes in their Darcy numbers. Flow through a composite channel that has undergone a vertical fracture is considered. The vertical connecting channel is also composed of a composite material. In the case of composite channels with fractures in geological applications order of magnitude changes in the Darcy number result in very large changes in the pressure in the vicinity of the interfaces between these materials, thus posing a challenge for numerical algorithms. Geological configurations involving discontinuities in channel height with sections of the channel composed of several layers of different porous materials occur in oil reservoirs and groundwater flows. The influence of these discontinuities on the fluid flow through regions of different permeability is nothing short of drastic.

Many industrial and environmental problems involve flow in fractured porous media, like oil production, nuclear waste storage, and groundwater pollution. The computation of the full permeability tensor in fractured heterogeneous media as well as other parameters such as the mass exchange coefficient presents a challenge. The paper by Moussa Kfoury et al. addresses the use of homogenization methods to estimate constitutive parameters like permeability and fracture/matrix exchange coefficient at large scale in fractured heterogeneous media. The inspiration for this paper came from the groundbreaking work of Barenblatt, Zheltov, and Kochina, "Basic Concepts in the Theory of Seepage of Homogeneous Liquids in Fissured Rocks" published in 1960 (the first reference in the paper), which blazed the path for several investigations since then along these lines.

Porous media are utilized in many industrial and natural processes as an effective means for the transport and storage of heat energy. Examples include heaters, dryers, cooling units, exchangers, and biological tissue. Most of the studies on packed beds involve the flow of the fluid phase through a fixed solid bed, and a few only deal with moving beds. Experimental investigations of heat transport in moving packed beds are usually difficult to carry out due to limited access to the inside of the packed bed, and to operating conditions that very often are not ideal for experimentation such as high temperature and pressure. Numerical modeling is used as a complementary, and sometimes as the sole, means to gain a better understanding of the phenomena taking place in packed beds and in particular in moving packed beds. Redhouane Henda and Daniel Falcioni study numerically the thermal performance of the preheater, essentially a tube-and-shell heat exchanger in the nickel carbonyl process. After leaving the preheater, the pellets enter a cold-wall reaction zone where coatings of nickel are deposited onto the pellets. Inefficiencies in heat transfer in the preheater greatly affect nickel deposition rate because of sensitivity of the diffusion controlled process to pellet temperature. Both one and two equation volume averaging models may be used to investigate transport phenomena in porous media. Averaging over a representative elementary volume containing both the fluid and solid phases yields the one-equation model, and averaging separately over each of the phases in the same representative volume results in a separate energy equation for each individual phase referred to as the two-equation model. The one-equation model is valid when the temperature difference between the solid and fluid phases is negligible, and is useful for comparison with experimental data as temperature measurements in a packed bed do not distinguish between solid and fluid phase temperatures. The two-equation model is used when thermal exchange between the two phases is not effective, and allows for a better understanding of the interactions between the two phases. The authors show that there is no appreciable difference between the two models under the investigated conditions. Further, they show that adopting a constant temperature at the preheater wall, that is directing the flue gas perpendicular to the preheater tube and decreasing the pellet velocity in the packing bed, improves

the thermal efficiency throughout the preheater greatly, and the difference in temperature from pellet to pellet at the preheater outlet is reduced from ~120 °C to ~55 °C.

MHD mixed convection for the buoyancy opposing flow in porous media has not yet been adequately addressed in the literature. Rebhi A. Damseh investigates the MHD-mixed convection heat transfer problem from a vertical surface embedded in a porous media. The effect of transverse magnetic field and radiation heat transfer are examined. Both types of mixed convection heat transfer problem, that is the buoyancy aiding flow and the buoyancy opposing flow, are investigated. In the former case increasing the magnetic field number will decrease the velocity inside the boundary layer, and at the same time the temperature increases; the effect of the magnetic field in this case is to decrease the heat transfer rates. Increasing radiation-conduction parameter will decrease local Nusselt numbers for both buoyancy aiding and opposing flows. The effect of increasing porosity is to increase and decrease the local Nusselt number for the buoyancy aiding and opposing flow, respectively. The effect of increasing magnetic field parameter is found to decrease the local Nusselt number.

Worldwide increase in energy cost and energy consumption requires more effective use of energy. Hence, ways of decreasing energy losses have never been more important. Second law based methods are well suited to analyze the overall energy performance in order to identify optimization criteria. It is well known that heat transfer rates are enhanced when and wherever porous materials are used. Although porous substrates generate a high pressure drop, they remain a good passive technique for heat transfer enhancement. Nadia Allouache and Salah Chikh search for an optimum solution, a compromise between hydrodynamics and thermal performance. A second law analysis based on the evaluation of entropy generation due to both fluid friction and heat transfer is developed and applied to laminar forced convection flow in a double pipe heat exchanger with a porous medium of variable thickness in the annular gap attached to the inner pipe. The minimization of the rate of entropy generation, due to fluid friction and heat transfer, depends on the porous layer thickness, its permeability, the inlet temperature difference between the two fluids, and the effective thermal conductivity of the porous substrate. An increase in the effective thermal conductivity of the porous medium seems to be thermodynamically advantageous. Rather surprisingly, the fully porous annular gap yields the best results in terms of the rate of total entropy generation.

The contribution by Konstantin Kostarev, Antonio Viviani, and Andrew Zuev presents an experimental study of thermo- and soluto-capillary Marangoni convection around a gas bubble in an inhomogeneous fluid with a vertical thermal or surfactant concentration gradient. It is well known that Marangoni convection may be driven by surface tension gradients due either to thermocapillary or soluto-capillary effects. The former has received considerable attention as temperature differences are very common in liquid systems. However, the soluto-capillary convection has not been adequately studied. Bubble migration in a liquid may be caused by either type of Marangoni convection. Convection caused by surface tension gradients due to concentration inhomogeneities, for instance, of dissolved surfactant along the free liquid/gas interface, attracts considerable interest because of its importance in manufacturing technologies. In microgravity when gravity-induced mechanisms of motion are absent or reduced Marangoni convection is the main driving mechanism determining the behavior of gas inclusions in many manufacturing processes. Among these are composite and foamy materials, formation and solidification of alloys, degassing of liquid substances in glasses, ceramics, crystals, and metals. The influence of the adsorbed insoluble surfactant layer at the bubble/drop interface on the thermocapillary convection is well established experimentally in the literature. The surfactant, transported by the convective flow to the trailing pole of the bubble, establishes surfactant concentration-induced Marangoni stresses opposing those caused by the thermal gradient. As a result, the motion driven by thermocapillary forces is slowed down drastically due to the presence of the surfactant. However, the convective motion generated by the external concentration gradient of surfactant dissolved in the surrounding fluid has not been studied. The influence of the diffusive and convective mass transfer mechanisms are determined by the characteristic times of surfactant and heat diffusion. The former are two or three orders of magnitude longer than those of heat diffusion.

The next three contributions address issues related to natural convection. The manufacturing of advanced materials is greatly facilitated in a microgravity environment as buoyancy-induced convection is suppressed or greatly reduced in magnitude. But small vibrations existing on space platforms can totally or substantially alter the fluid behavior under microgravity, thus leading to undesirable semiconductor and protein crystal properties. Thus, there is a need to understand and control the effects of vibrations on fluid systems relevant to material processing aboard space platforms including the g-jitter effects. Many studies have been conducted on fluid-induced vibrations of solid structures. However, the reverse situation of vibration-induced fluid motion, in a closed container full of liquid, has not yet been fully explored. Samer Hassan et al. investigate theoretically and experimentally the effect of small vibrations on the motion of a solid particle suspended in a fluid cell. An inviscid model is developed to predict the vibration-induced motion of the solid particle suspended by a thin wire in the water-filled rectangular cell which vibrates horizontally. The inviscid fluid assumption is valid when the inertial forces are more important than the viscous force, which is equivalent to a very thin boundary layer compared to the particle radius. The validity of this assumption is supported by good agreement between the model predictions and the experimentally measured amplitudes for steel particles in water at different cell vibration amplitudes and frequencies. Both their model and experimental data show the existence of a resonance frequency. At low frequencies the amplitude of the vibratory motion of the particle is linearly proportional to the amplitude of the fluid motion in the cell. At higher cell vibration frequencies well above the resonance frequency, both the model and experiments indicate that the particle amplitude becomes constant and independent of the wire length.

Shari J. Kimmel-Klotzkin and Fadi P. Deek consider a difficult problem—that of computing the time evolution of a rotating turbulent convective flow generated by a buoyancy source of finite size at a relatively high Rayleigh number. The large eddy simulation (LES) with the Smagorinsky subgrid scale model is used. For large-scale geophysical flows, the Coriolis effect due to the rotation of the Earth becomes an important influence in the evolution of the flow. However, the Smagorinsky model is not consistent with a non-inertial reference frame and thus is not the optimal choice for this type of flow. Global oceanic circulation simulations are very important in the study of climatic change. Buoyancy effects due to gravitational forcing can drive large-scale oceanic circulations. Natural phenomena that cause buoyancy driven circulations in the ocean include evaporation, extreme weather conditions such as storms, freezing at the surface, and heating through the ocean floor as a result of megaplumes. Numerical simulations of turbulent convection under the influence of rotation will help understand mixing in oceanic flows. Direct numerical simulation (DNS) techniques can accurately model rotating convective flows and give an "exact" solution to the governing equations but are limited to relatively low Reynolds numbers due to insufficient computational resources, as they may require hundreds of hours of CPU time and tens of millions of grid points even for a flow field bordering on the turbulent regime. By using a large eddy simulation (LES), which involves modeling the small scales and resolving only the large scales, a similar computation could be performed in less than 100 hours of CPU time using a number of grid points less than an order of magnitude smaller. The results demonstrate that LES can be used to qualitatively model large scale rotating flows. The resulting flow structure is in good agreement

with the limited available DNS simulations and experimental results. The results also demonstrate that the qualitative behavior of vortices which form under the source depend on the geometry of the flow. An eddy viscosity model is inadequate to accurately model the transition to turbulence between the convective plume and the quiescent ambient fluid, and it is suggested that other types of subgrid modeling should be used in future studies.

Low Prandtl number fluids present a challenge in heat transfer studies. They generate very strong diffusive thermal effects which should be taken into account in numerical modeling. Thus boundary layer approach is not suitable and extended computational domains need to be employed for accurate numerical solutions. The common thread for the next two papers is low Prandtl number fluids.

Mahfoud Djezzar and Michel Daguenet investigate the influence of the slope angle on the natural steady convection in an annulus between two elliptic confocal ducts. A primitive function formulation of the finite volume method is used. The effect of the inclination on the Nusselt number is examined for low Prandtl number fluids and for various Rayleigh numbers. Many cooling and heating devices used in engineering applications such as solar collectors, electronic equipment, certain types of nuclear reactors, and electric transformers can be modeled as vertical parallel plate channels. The focus of most studies in the literature is on air and water as working fluids. However, low Prandtl number fluids employed in the thermal design of core reactors behave differently than air and water. Liquid metals are of great engineering interest due to their unique heat transfer capabilities. In nuclear power plants, if the pump cooling system fails, the hot reactor core would cool off by natural convection with liquid metal as the heat transfer medium. These fluids possess low or very low Prandtl numbers of the order 10^{-2}. They present very strong diffusive thermal effects which should be taken into account in numerical modeling. For this reason the boundary layer approach is not suitable and extended computational domains need to be employed to generate accurate numerical solutions. Antonio Campo, Oronzio Manca, and Biagio Morrone present a numerical investigation of the natural convection of a low Prandtl number fluid in vertical parallel plate channels in the Rayleigh number range 10^3-10^6 and for channel aspect ratios 5, 10, and 15.

Heat and mass transfer from a rotating disk has led to important fluid dynamics studies since von Karman introduced his much celebrated similarity transformation. However, studies with non-Newtonian fluids are relatively few and new. Available literature is restricted to shear rate-dependent viscosity fluids and heat transfer studies have been favored more than mass transfer. Rashaida et al. consider mass transfer from a rotating disk to a Bingham fluid with applications to slurries and suspensions which exhibit yield stresses.

It may be appropriate to close this special edition with another paper related to petroleum management issues. A topic of importance to crude oil transportation as well as other fluids is investigated by Mohand Kessal and Rachid Bennacer who model the effect of dissolved gases on liquid transients in pipelines. In order to improve the reliability and the performance of hydraulic systems it is important to be able to predict the onset and the degree of cavitation during transient flow. Transient cavitation without dissolved gas release is well covered in the literature. But available studies with gas release are not as extensive. A mathematical model which describes homogeneous transient two-phase flow in a pipeline which takes into account gas release is presented. Cavity volume formation, during transients in a homogeneous gas-liquid mixture flow, is modeled and numerically simulated by taking into account the effect of the degassing.

In closing, I would like to express my appreciation to the anonymous reviewers and the authors. Liz Montana, Editorial Assistant of JAM, deserves special thanks.

Dennis A. Siginer
Guest Editor
Wichita State University
e-mail: dennis.siginer@wichita.edu

The Soret Effect: A Review of Recent Experimental Results

Jean K. Platten
University of Mons-Hainaut,
Place du Parc, 20,
Mons 7000, Belgium

In the first part of the paper, we recall what the Soret effect is, together with its applications in science and industry. We emphasize the need to have a reliable data base for the Soret coefficient. Next we review the different techniques to measure the Soret coefficient (elementary Soret cell, beam deflection technique, thermal diffusion forced Rayleigh scattering technique, convective coupling and, in particular, the onset of convection in horizontal layers and the thermogravitational method). Results are provided for several systems, with both negative and positive Soret coefficients, and comparison between several laboratories are made for the same systems. We end with "benchmark" values of the Soret coefficient for some organic liquid mixtures of interest in the oil industry and to which all future new techniques should refer before gaining confidence. We conclude that correct values of the Soret coefficient can be obtained in earth conditions and we deny the need to go to microgravity. [DOI: 10.1115/1.1992517]

1 Introduction

The Swiss scientist Charles Soret discovered, in 1879, [1] that a salt solution contained in a tube with the two ends at different temperatures did not remain uniform in composition: The salt was more concentrated near the cold end than near the hot end of the tube. He concluded that a flux of salt was generated by a temperature gradient resulting, in steady-state conditions, in a concentration gradient. Although the German Ludwig [2] described the same phenomenon several years before in a one-page report, the name "Soret effect" is usually attributed to mass separation induced by temperature gradients because Soret studied the effect rather in details, formulated equations and finally wrote 3 or 4 papers on the subject [1,3,4]. Today one writes for the x component of the mass flux of the reference chemical compound in a binary mixture

$$\mathbf{J_x} = -\rho \mathbf{D}\frac{\partial \mathbf{c}}{\partial \mathbf{x}} - \rho \mathbf{D_T c_0}(\mathbf{1}-\mathbf{c_0})\frac{\partial \mathbf{T}}{\partial \mathbf{x}} \tag{1}$$

The first term in the r.h.s. of Eq. (1) is Fick's law of diffusion, with c the mass fraction of the reference component and D the molecular (or isothermal) diffusion coefficient; the second term describes the Soret effect (or thermodiffusion effect), proportional to the temperature gradient $\partial T/\partial x$, with D_T the thermodiffusion coefficient. Since the effect does not exist in pure fluids one usually writes $c_0(1-c_0)$ factor of D_T. But as a matter of fact, D_T remains concentration dependant, exactly as D. Thus the second term in the r.h.s. of Eq. (1) describes mass separation due to a temperature gradient, whereas the first describes homogenization by normal diffusion. The two terms are thus of opposite sign, and when they are of equal intensity, we are in steady-state conditions $J_x=0$ implying

$$\frac{\partial \mathbf{c}}{\partial \mathbf{x}} = -\frac{\mathbf{D_T}}{\mathbf{D}}\mathbf{c_0}(\mathbf{1}-\mathbf{c_0})\frac{\partial \mathbf{T}}{\partial \mathbf{x}} \tag{2}$$

and the Soret coefficient is defined as

$$\mathbf{S_T} = \frac{\mathbf{D_T}}{\mathbf{D}} \tag{3}$$

The Soret coefficient may be positive or negative depending on the sign of D_T or on the sense of migration of the reference component (to the cold or to the hot). In absolute value an order of magnitude for usual organic mixtures or aqueous solutions is $|S_T| \sim 10^{-3}-10^{-2}$ K^{-1}.

According to Eq. (2), for a mixture containing 50 wt % of each component ($c_0=1/2$; $1-c_0=1/2$) and for a temperature difference ΔT of 4 K between hot and cold parts of the system, the difference in mass fraction Δc numerically will be equal to the Soret coefficient. Typically, Δc is of the order of 1%, sometimes smaller. But even if the separation remains small, the Soret effect has a lot of implications. Let us cite the operation of solar ponds [5], the microstructure of the ocean [6] since in both cases we have salty water and temperature gradients, and perhaps convection in stars [7]. The role of the Soret effect also has been evoked in biological systems, namely mass transport across biological membranes induced by small thermal gradients in living matter where thermodiffusion could assume a sizable magnitude for an ensemble of cells with the dimension of an organ or a tumor [8]. Another important application of the Soret effect is in natural hydrocarbon reservoirs [9,10]. One of the challenges in optimizing exploitation of oil reservoirs is a perfect knowledge of the fluid physics in crude oil reservoirs. Today, the modeling methods are based on pressure-temperature equilibrium diagrams and on gravity segregation of the different components of crude oil. However, improved models which more accurately predict the concentrations of the different components are necessary. The concentration distribution of the different components in hydrocarbon mixtures is mainly driven by phase separation and diffusion. One of the objectives in the oil industry is the prediction, as precisely as possible, of the gas-oil-contact in an oil reservoir. In order to achieve this goal, the local composition must be known. One of the reasons of a local compositional variation is molecular segregation in the gravitational field. Aside this important "force," the geothermal gradient (a few degrees per 100 meters) may also induce local variations in composition due to the thermodiffusion effect. In order to prove the implication of the Soret effect in crude oils, experiments in packed thermogravitational columns were undertaken by the group of Costesèque [11–14] on two samples of different origin: Alwijn and Oseberg, two oil fields in the North Sea. In packed thermogravitational columns we have two concentric cylinders kept at two different temperatures thanks to a flow of thermoregulated water. The space between the two

Contributed by the Applied Mechanics Division of ASME for publication in the JOURNAL OF APPLIED MECHANICS. Manuscript received August 13, 2004; final manuscript received April 17, 2005. Assoc. Editor: D. Siginer. Discussion on the paper should be addressed to the Editor, Prof. Robert M. McMeeking, Journal of Applied Mechanics, Department of Mechanical and Environmental Engineering, University of California—Santa Barbara, Santa Barbara, CA 93106-5070, and will be accepted until four months after final publication in the paper itself in the ASME JOURNAL OF APPLIED MECHANICS.

cylinders is filled with a porous medium, e.g., zirconium oxide spheres of given diameter. Next the porous medium is saturated by the mixture. The component that goes to the cold (resp. to the hot) cylinder under the effect of thermodiffusion is next advected to the bottom (resp. to the top) under the action of buoyancy. Thus a vertical concentration gradient for each component is built due to the interplay between Soret effect and convection. Samples are removed from two reservoirs at the top and at the bottom and analyzed. Even a simple inspection by eyes shows that the bottom sample is dark brown, whereas the top sample is almost clear indicating that the components belonging to the light fraction diffuse to the hot and are advected to the top; on the contrary the components of the heavy fraction diffuse to the cold cylinder. They also did a fine analysis by gas chromatography, analyzing the different isomers as, e.g., for hydrocarbons containing 8 carbon atoms: *n*-octane, 2-methylheptane, 3-methylheptane, 4-methylheptane, 2-2 dimethylhexane, 3-3 dimethylhexane, 2-3 dimethylhexane, 2-4 dimethylhexane, etc. They extended the analysis to all the isomers of ethyltoluene, trimethylbenzene, dimethylbutane, dimethylpentane, to meta-, ortho-, and paraxylene, and many more. In total 58 components were identified in the light fraction and analyzed. The same was done for the heavy fraction. By "analyzed" we mean that top and bottom concentrations (or mass fractions) of each component was determined. But in fundamental science, we need more than this. We need to quantify the Soret effect by "numbers." In Europe, there is a project initiated by the EGRT (European Group of Research in Thermodiffusion) with the aim to study a ternary system composed of dodecane (hereafter called C12), isobutylbenzene (IBB), and 1,2,3,4-tetrahydronaphtalene (THN). Results are in progress and all the 3 binaries were already investigated by 5 independent and different labs and results published [15]. But for ternary systems, there is no consent on the way to write the two independent fluxes, i.e., equations analogue to Eq. (1) and on the definition of the two independent Soret coefficients. Even in binaries, the measurement of the Soret coefficient defined by Eq. (3) remains delicate. Therefore, the paper is devoted to a summary of recent results that seem to us very safe, in contradistinction to the large discrepancies that are sometime observed in the literature, see [16] for an example, including recent microgravity determinations of S_T [17].

2 Some Different Techniques to Measure the Soret Coefficient

Arbitrarily we divide the different techniques into two groups: The first group supposes convectionless systems and Eqs. (1) and (2) apply; they are the correct working equations for the determination of the Soret coefficient. The second group of techniques uses convective coupling. We will mainly focus on this second group, simply because we made extensive use of these techniques. By the way these techniques will be different depending on the sign of the Soret coefficient we want to measure.

2.1 Convectionless Systems.

2.1.1 The Standard Soret Cell. A standard Soret cell (see Fig. 1) consists of two horizontal rigid plane plates, made of a good heat conducting material, e.g., copper or stainless steel. The plates are maintained at different temperatures by thermostatic circulating water in order to create a vertical temperature gradient in a parallelepipedic working space (there are of course lateral walls made of a poor heat conductivity material in order to minimize the heat exchange with the surroundings). The system usually is heated from above in order to avoid free convection. Between the plates a regular gap a is maintained by a brace made of, e.g., PVC into which small holes are managed (at least one, sometimes several in order to follow the kinetics of the separation). In each hole a watertight device is managed where curved hypodermic needles

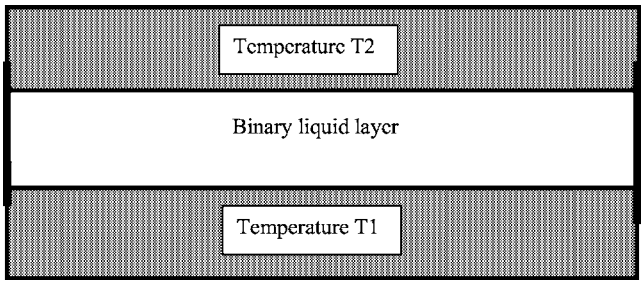

Fig. 1 Sketch of an elementary Soret cell

are inserted in order to remove very small liquid samples close to the isothermal horizontal boundaries. The samples are analyzed with a high resolution refractometer ($n \pm 0.00001$) or densimeter ($\rho \pm 0.000001$ gr/cm^3) in order to get the concentration difference Δc between the top and bottom removed samples after comparison with calibration curves. Next the use of Eq. (2) rewritten as

$$\Delta \mathbf{c} = -\mathbf{S_T c_0}(\mathbf{1}-\mathbf{c_0})\Delta \mathbf{T} \tag{4}$$

gives S_T. Instead of considering ΔT as the temperature difference between the two bounding plates (or between the two thermostatic baths) it is much better to measure the local value of T (e.g., by thermocouples) at the exact location of the removed sample. Cells with 6 holes along the longer side are of common use [18] and at different times samples are removed in order to follow the time evolution of $\Delta c/\Delta T$ given by

$$\frac{\Delta \mathbf{c(t)}}{\Delta \mathbf{T}} = -\mathbf{S_T c_0}(\mathbf{1}-\mathbf{c_0})\left[\mathbf{1}-\frac{\mathbf{8}}{\pi^2}\sum_{\mathbf{n\ odd}}\frac{\mathbf{e}^{-\mathbf{n}^2}\frac{\mathbf{t}}{\theta}}{\mathbf{n}^2}\right] \tag{5}$$

where θ is the relaxation time defined by

$$\theta = \frac{\mathbf{a}^2}{\pi^2 \mathbf{D}} \tag{6}$$

Thus by considering the few first terms into the Fourier expansion (5), e.g., the first 5 terms, and by a curve fitting procedure to the experimental points $\Delta c(t)/\Delta T$, it is possible to get simultaneously $S_T = D_T/D$ (from the value of the separation at the steady state) and D (knowing the gap a between the two bounding plates). Thus as a byproduct, the thermodiffusion coefficient D_T is also determined.

2.1.2 The Beam Deflection Technique. The same type of cell as described in Sec. 2.1.1 is also used in the beam deflection technique [19–21], the main difference being that two opposite lateral walls are made of glass of good optical quality. The way to measure the mass fraction gradient is, however, totally different. Indeed in absence of any gradient, a laser beam perpendicular to one of the lateral glass wall will cross the liquid layer horizontally and hit the beam detection unit BDU at point A (Fig. 2). Due to the existence of vertical temperature and concentration gradients, a resulting index of refraction gradient will be created according

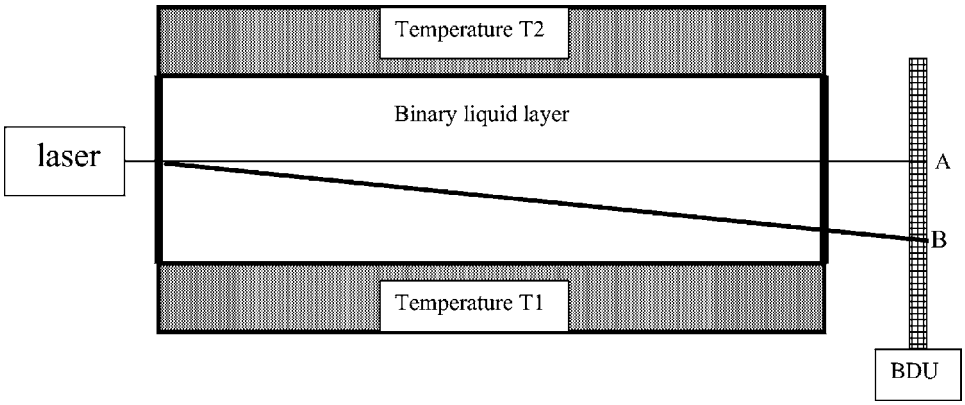

Fig. 2 Sketch of an elementary Soret cell using the beam deflection technique

to

$$\text{grad } \mathbf{n} = \frac{\partial \mathbf{n}}{\partial \mathbf{T}} \text{grad } \mathbf{T} + \frac{\partial \mathbf{n}}{\partial \mathbf{c}} \text{grad } \mathbf{c} \tag{7}$$

In such a situation the laser beam, traveling in an index of refraction field, will not propagate horizontally, but will be deflected and hit the BDU at position B. The distance AB is a measure the deflection of the beam from which the index of refraction gradient may be deduced. Clearly two calibration curves are needed $\partial n/\partial T$ and $\partial n/\partial c$; finally (since the temperature gradient is known), the mass fraction gradient is deduced and produces the value of the Soret coefficient at the steady state. In addition one can make use of the very different relaxation times for the establishment of the temperature gradient and of the concentration gradient: Typically there are two orders of magnitude difference between both relaxation times since in liquids the diffusion coefficient is much smaller than the thermal diffusivity. Thus there is a quick process, the establishment of the temperature gradient just after the thermostatic baths are switched on, corresponding to a first fast variation of the index of refraction and a first deflection of the beam, followed by the slow process, the establishment of the concentration gradient. If one follows the kinetics of the second deviation of the beam, we have access to the diffusion relaxation time, thus to D and subsequently to D_T. Alternatively once the steady state is reached, one could switch off the two thermostatic baths: The temperature gradient is destroyed rather quickly, but the concentration gradient will take a longer time to disappear. Once again by following the time dependence of the deflection angle that has to return to zero, we may have the isothermal diffusion coefficient D.

2.1.3 The Thermal Diffusion Forced Rayleigh Scattering Technique (TDFRS). In the TDFRS technique [22], light is used to create the temperature gradient, instead of "boundary conditions." A first laser beam is split into two beams of equal intensity. The two beams emerging from the beamsplitter are focused by a lens in the sample containing the liquid mixture (Fig. 3(*a*)). At the intersection of the two laser beams, interference fringes are created (Fig. 3(*b*)) and by putting some chemically inert dye in the mixture a temperature grating is impressed, the temperature being higher (typically of 100 μK) in the fringe of high light intensity. And this periodic temperature field induces via the Soret effect a periodic concentration field. Both the temperature grating and the concentration grating create an index of refraction grating which is itself read out by a second laser by Bragg diffraction. The technique requires also two contrast factors $\partial n/\partial T$ and $\partial n/\partial c$ but will not work in the vicinity of a maximum of index of refraction as it is the case of some water-alcohol rich (90 wt %) systems. But this is also true for any technique that uses the index of refraction as a way to analyze the concentration gradient. In the TDFRS technique, the characteristic length is the fringes spacing, i.e., $\sim$10 μm. Therefore, the temperature gradient is of the order of 1 K/cm, as in more classical techniques where the gradient is imposed by circulating water baths. A clear advantage of the TDFRS technique is the small relaxation time: Since the characteristic length is 1 μm, the characteristic diffusion time will be of the order of 1–10 milliseconds, instead of several hours with cells of $\sim$1 cm size. However, in the TDFRS technique the experiment must be repeated many times (e.g., 5000) and the results are averaged. The possible role of convection has been discussed in [22] showing that correct results are obtained by this technique.

2.2 Convective Coupling. In all convective coupling techniques, the idea is to study the modification of the velocity field (the pattern, the amplitude or the onset of convection in certain circumstances) under the effect of thermodiffusion. Therefore, the important parameter is the solutal contribution to the buoyancy force $\delta\rho.g$. We need an equation of state for the density and ignoring nonlinear terms we take

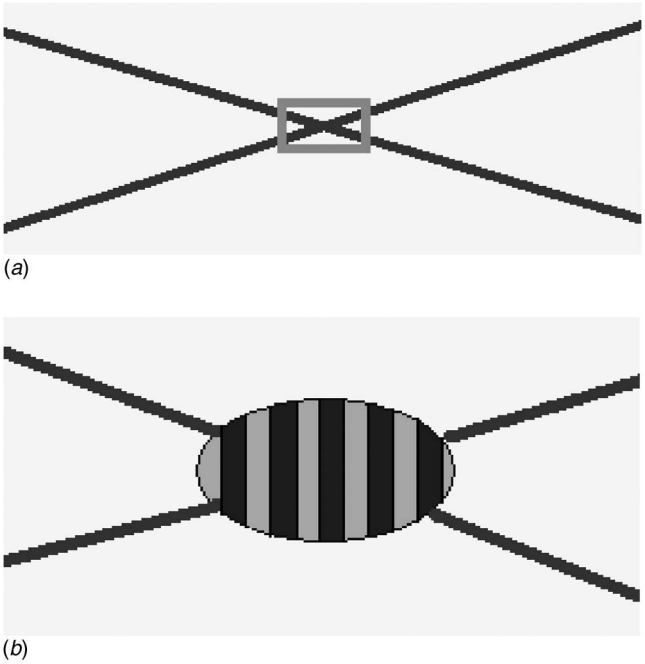

Fig. 3 Crossing of the beams in the sample (*a*) and zoom on the fringes (*b*) in the TDFRS technique

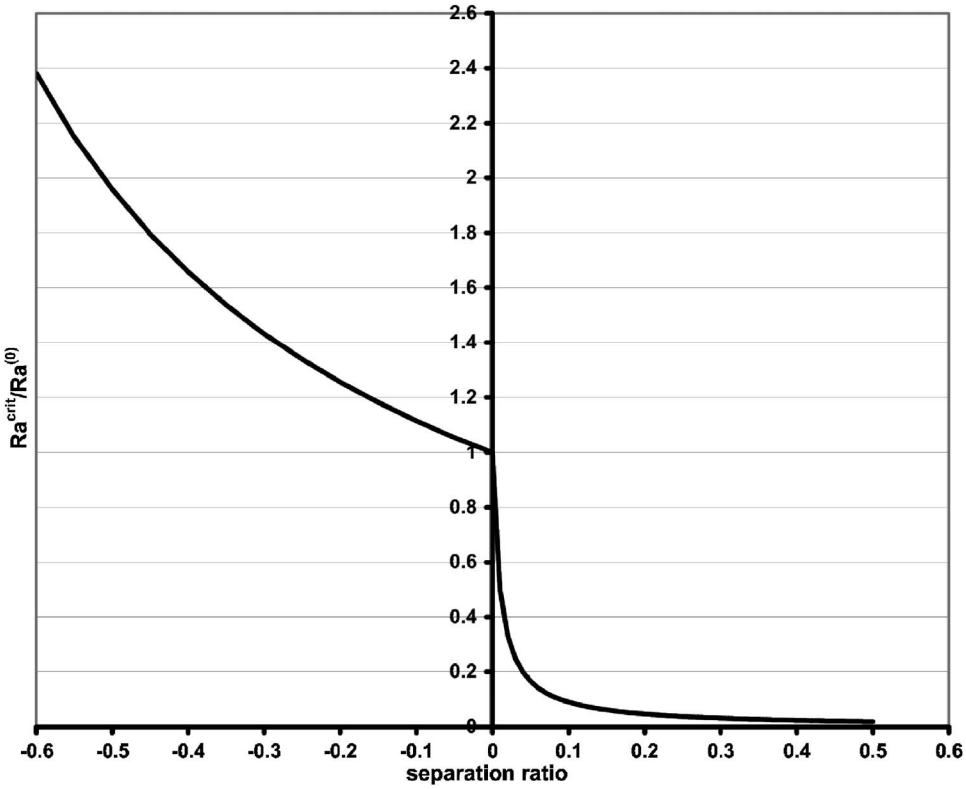

Fig. 4 Variation of the critical Rayleigh number in the Rayleigh-Benard configuration as a function of the separation ratio

$$\rho = \rho_0[\mathbf{1} - \alpha(\mathbf{T} - \mathbf{T_0}) + \beta(\mathbf{c} - \mathbf{c_0})] \quad \alpha > \mathbf{0};\ \beta > \mathbf{0} \tag{8}$$

where α is the thermal expansion coefficient and β the mass expansion coefficient. They are both defined positively, because we decide (arbitrarily) that c represents the mass fraction of the heavier component. Of course the opposite choice could equally be made without affecting the physical results. T_0 and c_0 are reference temperature and mass fraction (mean values). As written before, the important parameter is the solutal contribution to the buoyancy, but relative to the thermal contribution. This parameter is called the "separation ratio" Ψ and, using Eq. (4) can be written as

$$\Psi = \frac{\beta \Delta \mathbf{c}}{-\alpha \Delta \mathbf{T}} = \frac{\beta}{\alpha} \mathbf{S_T c_0 (1 - c_0)} \tag{9}$$

2.2.1 Rayleigh-Benard Configuration. In the classical Rayleigh-Benard configuration, the monocomponent horizontal liquid layer is heated from below, inducing a potentially unstable density gradient: Convection sets in provided the Rayleigh number overcomes some critical value $Ra^{(0)}$ with a numerical value depending on boundary conditions ($27\pi^4/4$ or 1708 or…). We shall not enter here into the details of this well known hydrodynamic stability problem [23]. For a binary liquid layer in the presence of the Soret effect, two cases must be considered depending on the sign of the separation ratio. If Ψ is positive, thermal and solutal contribution to the buoyancy are of the same sign and since the thermal contribution is destabilizing (we heat from below) so is the concentration gradient; in other words the denser component migrates to the cold upper boundary, and this is a destabilizing process; the onset of convection will appear for a temperature difference (or a Rayleigh number) much smaller than that for a pure fluid system. If Ψ is negative, thermal and solutal contributions are of opposite sign and since the thermal contribution is destabilizing, the concentration gradient is stabilizing: the denser component migrates to the hot lower boundary and the onset of convection is delayed to a temperature difference (or Rayleigh number) much greater than that for a pure fluid system. This is what Fig. 4 shows, but one recognizes immediately that the two curves for negative and positive separation ratio are quite different: They correspond to a different mode of instability. When Ψ is negative, we have an inverted Hopf bifurcation and instability arises as oscillations of increasing amplitude. The linear hydrodynamic stability theory gives the variation of the critical Rayleigh number as a function of the separation ratio see, e.g., [24] for a small review

$$\frac{\mathbf{Ra}^{\mathrm{crit}}}{\mathbf{Ra}^{(0)}} - \mathbf{1} = \mathbf{1.15} \frac{-\Psi}{\mathbf{1} + \Psi + \dfrac{\mathbf{1}}{\mathbf{Pr}}} \tag{10}$$

and the Hopf frequency as well

$$\omega = \mathbf{1.43} \frac{\mathbf{3}\pi^3}{\mathbf{2}} \sqrt{\frac{-\Psi}{\mathbf{1} + \Psi + \dfrac{\mathbf{1}}{\mathbf{Pr}}}} \tag{11}$$

In these two last equations, Pr is the Prandtl number $\mathrm{Pr} = \upsilon/\kappa$ where υ is the kinematic viscosity and κ the thermal diffusivity $\kappa = \lambda/\rho C$ (λ: thermal conductivity and C mass specific heat). Thus an indirect way, but nevertheless a not less precise way to determine a Soret coefficient, is to measure the critical Rayleigh number and the associated Hopf frequency. Therefore, we need to detect the onset of free convection as precisely as possible, together with a time record of the velocity each 2 s in order to deduce the Hopf frequency. This is achieved by Laser Doppler Velocimetry and with equipment specially dedicated to measure extremely low velocities, down to 5–10 μm/s. In Fig. 5 we show an example of the oscillatory onset of free convection that was recently obtained [25]. The experimental conditions are the fol-

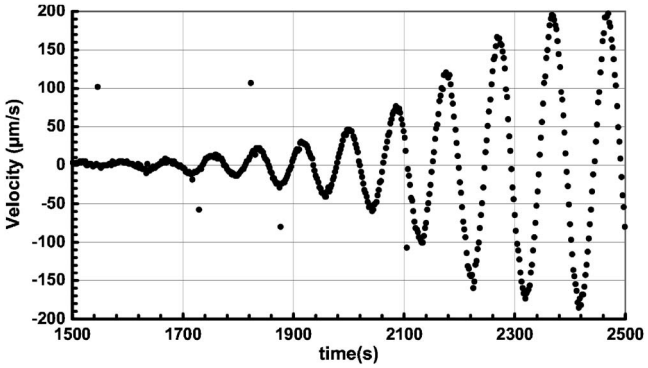

Fig. 5 Oscillatory onset of convection at ΔT=1.84 °C in the system water (90 wt %)–isopropanol (10 wt %). Mean temperature: 21 °C.

lowing: The working fluid is a mixture of water (90 wt %) –isopropanol (10 wt %) in a parallelepipedic container of large lateral extension compared to the fluid thickness (4.75 mm) and comparable to Fig. 1, except that we heat from below; the temperatures of the lower and upper bounding plates is thermoregulated and the difference ΔT increased very slowly (mean value: 21 °C). After each temperature increase, we wait five times the relaxation time, i.e., in the present case 8 h. Near the critical point, ΔT is increased by steps of 0.1 °C for a rough determination of the critical Rayleigh number and by steps of 0.01 °C for a precise determination; below ΔT=1.84 °C we have the rest stat, even after 8 h. When ΔT is increased up to ΔT=1.84 °C, convection sets in; however, we have to wait 1700 s after the last increase of ΔT before to record for the first time measurable velocity amplitudes. In Fig. 5 an experimental point is taken each 2 s. Thus from Fig. 5 we have two informations: The critical temperature difference for the onset of free convection from which the critical Rayleigh number may be computed provided we have accurate values of the viscosity and of the expansion coefficient, but this is usually not a problem (see later), and the Hopf frequency from the Fourier transform of the time signal $V(t)$ for small times, say between 1700 s $< t <$ 2300 s; for $t >$ 2300 s, when the amplitude of the velocity increases such that the nonlinear terms cannot be ignored in the theory, there is a gradual change in the frequency (or in the period); the final frequency, corresponding to nonlinear traveling waves differs from the Hopf frequency by one order of magnitude. Having the critical Rayleigh number and the Hopf frequency, we make use of Eqs. (10) and (11) to deduce the separation ratio Ψ and next S_T, having the two expansion coefficients α and β (and once again this is not a problem, see later). If the two values do agree within say a few %, then we may have confidence in the technique. Moreover having two values for S_T, we take their mean to compare with other values found in the literature. This comparison exercise has been made for several systems in [24]. The water (90 wt %)–isopropanol (10 wt %) system is spectacular because of its large Soret coefficient (and thus Hopf frequency) and that is why we did choose this system for showing Fig. 5 as an example, but this system is not popular (besides ourselves, only one other lab did investigate this system). Therefore, for a comparison between several labs the system water (92 wt %)–ethanol (8 wt %) at 25 °C is more appropriate. Table 1 gives a comparison between four different labs that use different techniques and clearly the use of the onset of convection in a Rayleigh-Benard experiment produces results in complete agreement with other techniques.

Since the onset of free convection seems a convenient way to measure negative Soret coefficients, we may think about using it for positive values. There are two reasons why this will not work. First, the bifurcation is forward and "normal;" thus we lose the possibility given by the Hopf frequency to have an additional experimental value of the Soret coefficient in the same experimental session. But moreover as shown by Fig. 4 there is a drastic drop in the critical Rayleigh number and Eq. (10) cannot be used because the instability mode is different. The variation of the critical Rayleigh number for positive values of the separation ratio is of the type

Table 1 Comparison of the Soret coefficient of the system water (92 wt %)–ethanol (8 wt %) obtained in different laboratories

From Rayleigh-Benard experiments [18]	Kolodner [13]	Zhang [14]	Bou-Ali et al. [20]
$-7.08\ 10^{-3}\ K^{-1}$	$-7.13\ 10^{-3}\ K^{-1}$	$-7.30\ 10^{-3}\ K^{-1}$	$-7.05\ 10^{-3}\ K^{-1}$

$$\mathbf{Ra}^{\mathrm{crit}} = \mathbf{Ra}^{0}\frac{\mathbf{1}}{\mathbf{1}+\Psi(\mathbf{Le}+\mathbf{1})} \tag{12}$$

where Le is the Lewis number defined by $\mathrm{Le}=\kappa/D$. Since in liquids the thermal diffusivity κ is two orders of magnitude larger than the mass diffusivity D, Le $\sim$ 100 and even for the modest value Ψ = +0.2 (the solutal contribution to the buoyancy force is only 20% of the thermal contribution), there is a typical decrease of a factor 20 in the Rayleigh number, thus in the temperature difference needed to promote convection. For a layer of a few mm thick (say 4 mm) the critical temperature difference for pure water is of the order of 2 °C, a convenient value that can be measured accurately using commercial thermostatic baths. The addition of alcohol (such that S_T becomes positive) lowers the temperature difference by a factor 20 down to 0.1 °C. In other words we totally lose accuracy. Therefore, for positive Soret coefficients the onset of free convection is not the appropriate way to measure a Soret coefficient unless the temperature of each bounding plate is controlled at the 0.001 °C level, which was not the case in our experiments. Consequently we use another strategy: The thermogravitational process.

2.2.2 The Thermogravitational Process. A thermogravitational column usually consists of two vertical concentric cylinders at two different temperatures in such a way to create a horizontal temperature gradient. For reasons explained later, we prefer the use of parallelepipedic columns made of two rigid vertical copper plates A (see Fig. 6 and [27]) maintained at two different temperatures by circulating water in circular cavities B managed in each plate (only shown for the left plate in Fig. 6). The gap between the two plates is fixed and imposed by spacers C and D. In the upper spacer D there are two small holes for the filling of the column and for air to escape during the filling. Along the column height 5 sampling taps allow to remove with a syringe small quantities (1 and 2 ml) of the liquid, next analyzed to find their composition. Indeed, since the temperature gradient is horizontal, under the action of the Soret effect one of the components goes to the left (or to the cold plate) and the other to the right (the hot plate). The component that thermodiffuses to the cold is advected to the bottom, and the one that goes to the hot is advected to the top of the cell. Thus the combined effect of thermodiffusion and convection finally creates a vertical mass fraction gradient, resolved by the sampling process. Finally in order to close the space available to the liquid we need front and back windows. We used windows made of glass of good optical quality in order to have optical access in the column. Using once again LDV, we may follow the time evolution of the velocity amplitude. Combined to the vertical mass fraction gradient, we have two informations related to the Soret coefficient from two separate experiments (that usually are made at different times).

The removed samples at the five sampling positions are ana-

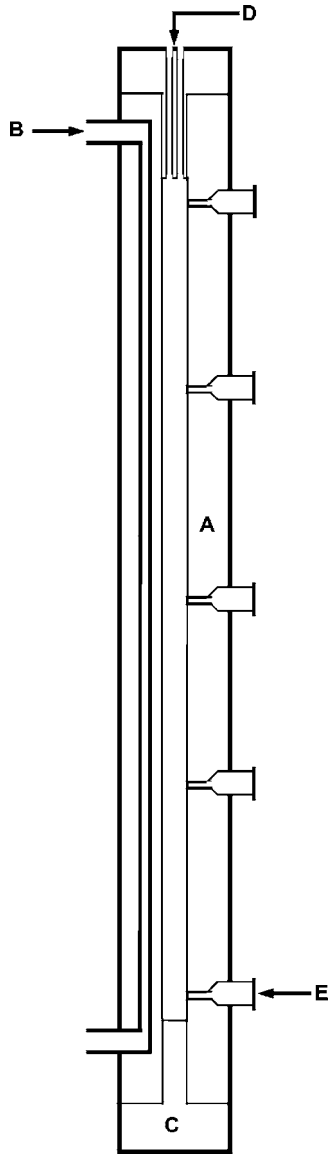

Fig. 6 Sketch of the thermogravitational column

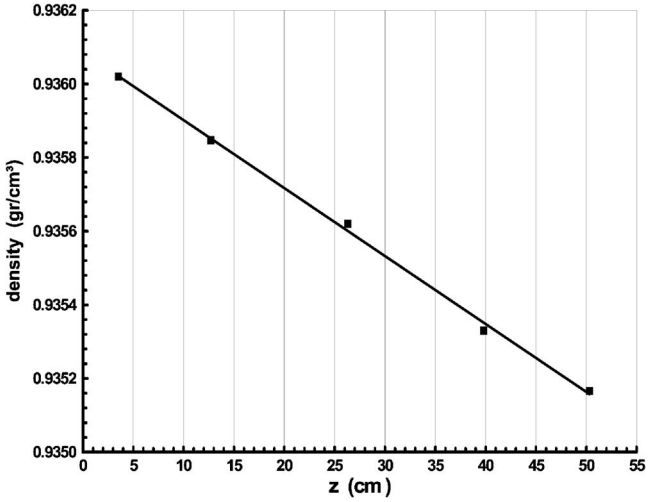

Fig. 7 Density profile in the thermogravitational column in the system water (60.88 wt %)–ethanol (39.12 wt %). T_{cold}=20 °C; T_{hot}=25 °C.

lyzed by measuring their density (the index of refraction could equally work well) using the quartz U-tube vibrating densimeter manufactured by Paar (DMA5000) having a resolution of 10^{-6} gr/cm^3. Figure 7 shows a vertical mass fraction profile for the system water (60.88 wt %)–ethanol (39.12 wt %), a system that has been investigated by several labs. The linearity of the profile seems perfect. Of course we have to transform density into mass fraction. To this end we prepared 13 samples around 60.88 wt % of water, namely between 58 and 64 wt %, by steps of 0.5 wt % taking for each prepared sample the density, Fig. 8. This is our calibration curve giving also the mass expansion coefficient β needed in the separation ratio, the relevant parameter when measuring velocity amplitudes. Combining Figs. 7 and 8, we have the mass fraction profile, in particular the mass fraction difference between the top and the bottom of the column. We need of course a correct working equation giving the thermodiffusive coefficients from the knowledge of this mass fraction difference. This equation is derived from the Furry-Jones-Onsager theory, modified by Majumdar for concentrated solutions [28–31]. Since this theory is more than half a century old, we do not feel the necessity to explain it here. Let us simply stress that the equations can be simplified when the gap between the two lateral walls of the column is "large," in practice for most of organic liquid mixtures, larger than 1 mm, but this is actually the case. The working equation then reads:

$$\Delta \mathbf{c} = \mathbf{c}_{\text{bottom}} - \mathbf{c}_{\text{top}} = 504 \frac{\nu}{\alpha \mathbf{g}} \mathbf{D_T} \mathbf{c_0} (\mathbf{1} - \mathbf{c_0}) \frac{\mathbf{H}}{\mathbf{e}^4} \tag{13}$$

where υ is the kinematic viscosity (the dynamic viscosity is measured for each system that we investigated by a falling ball Höppler viscosimeter, instead of trying to interpolate between values found in tables), H the height of the column (H=530 mm), e the gap (e=1.58 mm), and α the thermal expansion coefficient. This last parameter is determined by measuring the density of the initial sample at different temperatures as shown in Fig. 9 between 21 and 24°C, since the mean working temperature was 22.5°C (T_{cold}=20°C; T_{hot}=25°C). Let us mention that due to the simplifications made in the theory for "large gap," the temperature difference ΔT between the two walls no longer appears in Eq. (13); this is of course not true for the "small gap," theory for which Δc is an increasing function of ΔT. We now do possess all the necessary information to deduce from Eq. (13) the thermodiffusion coefficient D_T. But what we search is the Soret coefficient $S_T = D_T/D$. Therefore, we have to find in a supplementary and independent experiment the value of the isothermal diffusion coefficient D. This is achieved by the open ended tube technique [32], see Fig. 10. A small tube containing say the solute and the solvent is immersed at time t=0 in a container of very large volume compared to that of the tube and containing only the solvent. The system is of course at constant temperature by a circulating water flow and is covered to avoid evaporation. The solute diffuses outside of the tube and is not supposed to change the composition of the bulk because of its large volume. Instead of having pure solvent in the bulk and solvent+solute in the tube, the method works equally well with a mixture of two components in the bulk and in the tube, having, however, different mass fractions differing only by a few wt % around the initial mass fraction of the mixture for which we seek D_T and D (one should take care that the mixture in the tube has a density slightly higher than in the bulk to avoid free convection currents). The diffusion of the more concentrated component in the tube obeys Fick's law of diffusion

$$\frac{\partial \mathbf{c}}{\partial \mathbf{t}} = \mathbf{D} \frac{\partial^2 \mathbf{c}}{\partial \mathbf{z}^2} \tag{14}$$

Subjected initial and boundary conditions ($c=c_0$ $\forall z$ at t=0; $\partial c/\partial z$=0 at z=0 and $c=c_\infty$ at $z=L$ for $t>0$, where c_∞ is the con-

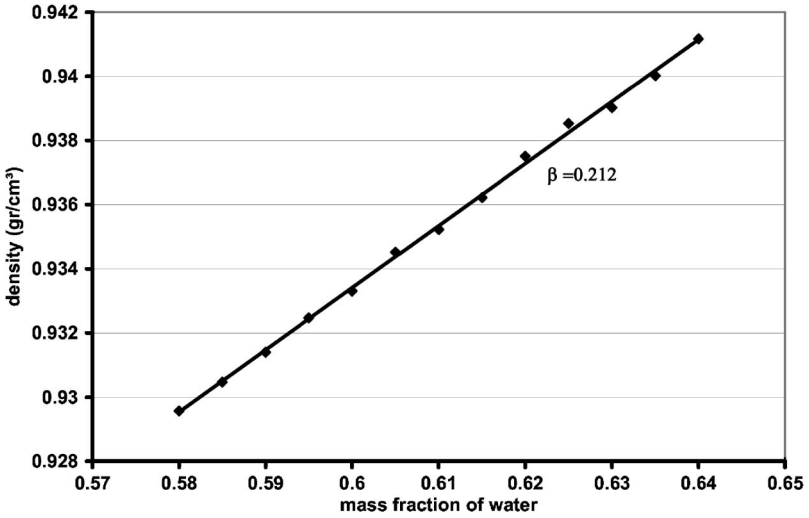

Fig. 8 Mass expansion coefficient in the system water (60.88 wt %) –ethanol (39.12 wt %)

centration of the bulk supposed to be of "infinite" volume and, therefore, of constant composition), the solution of Eq. (14) is

$$\mathbf{c(z,t)} - \mathbf{c}_\infty = \frac{4}{\pi}(\mathbf{c_0} - \mathbf{c}_\infty)\sum_{\mathbf{n}=0}^{\infty} \frac{\sin\left[\left(\mathbf{n}+\frac{1}{2}\right)\pi\frac{\mathbf{z}}{\mathbf{L}}\right]}{2\mathbf{n}+1} \mathbf{e}^{-(\mathbf{n}+1/2)^2(\pi^2/\mathbf{L}^2)\mathbf{Dt}} \tag{15}$$

After a sufficiently long time (depending of course on $\mathbf{D}/\mathbf{L}^2$), typically 24–48 h, the leading term $n=0$ in the Fourier expansion is far sufficient to describe the time evolution of the average tube concentration $\langle \mathbf{c(t)} \rangle = 1/\mathbf{L}\int_0^{\mathbf{L}} \mathbf{c(z,t)dz}$ and its decay is exponential. Thus the working equation for deducing D is

$$\ln\left(\frac{\pi^2(\langle \mathbf{c(t)} \rangle - \mathbf{c}_\infty)}{8(\mathbf{c_0} - \mathbf{c}_\infty)}\right) = -\frac{\pi^2}{4\mathbf{L}^2}\mathbf{Dt} \tag{16}$$

Figure 11 shows the result from which D is obtained, knowing the tube length L (~3 cm). In fact this result is not based on the time evolution of c in a single tube. Instead, we have several containers (3 or 4), and holders each containing 6–8 tubes. At time zero, all the holders are each immersed in a different container. At a given time, 2 tubes are removed from two different containers, mixed (in order to attenuate experimental fluctuations) and analyzed by densitometry for their mass fraction c.

We thus have a first way to measure a positive Soret coefficient: From a first experiment in thermogravitational column we get D_T. From a second experiment (the open ended tube) we get D, and next we calculate the ratio D_T/D. But there is another alternative: The modification of the velocity amplitude followed by laser Doppler velocimetry. Indeed in the same column the heavier component migrates to the cold wall (since $S_T>0$) and the lighter component to the hot wall. Thus the solutal effect adds to the thermal effect to increase the horizontal density gradient and the buoyancy force. Since the amplitude of the vertical velocity component V_a is proportional to the horizontal density gradient

$$\mathbf{V_a} \div \mathbf{g}\frac{\partial \rho}{\partial \mathbf{x}} \div -\alpha\frac{\partial \mathbf{T}}{\partial \mathbf{x}} + \beta\frac{\partial \mathbf{c}}{\partial \mathbf{x}} \div -\alpha\frac{\partial \mathbf{T}}{\partial \mathbf{x}}(\mathbf{1}+\Psi) \tag{17}$$

it is increased by a factor $(1+\Psi)$ with respect to the thermal effect only. Thus the enhancement of the velocity amplitude is a measure of the separation ratio Ψ, from which S_T is deduced knowing the thermal and mass expansion coefficient given in Figs. 8 and 9. The establishment of the horizontal temperature gradient $\partial T/\partial x$ is a quick process whereas that of the mass fraction gradient $\partial c/\partial x$ is a slow process. But the most important point is that this horizontal mass fraction gradient will almost be destroyed by convection since the component that goes to the cold (resp. to the hot) will be advected to the bottom (resp. to the top), creating a vertical mass fraction gradient $\partial c/\partial z$. In steady-state conditions, the horizontal gradient will not affect the buoyancy force. In other words, the increase in the velocity amplitude is only transitory in time: There is an overshoot phenomenon, nothing more, but this is sufficient to deduce Ψ. Figure 12 shows the time evolution for pure ethanol when at time $t=0$ the thermostats are switched on. Very quickly after 1000 s, the steady state is reached with a velocity amplitude close to 1500 μm/s. There are large fluctuations in the steady value of the velocity; they can be explained as follows: The gap

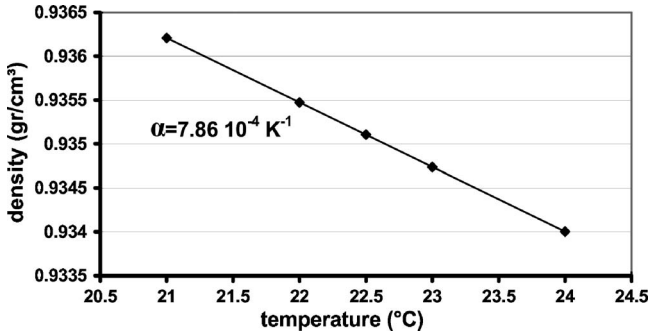

Fig. 9 Thermal expansion coefficient in the system water (60.88 wt %)–ethanol (39.12 wt %)

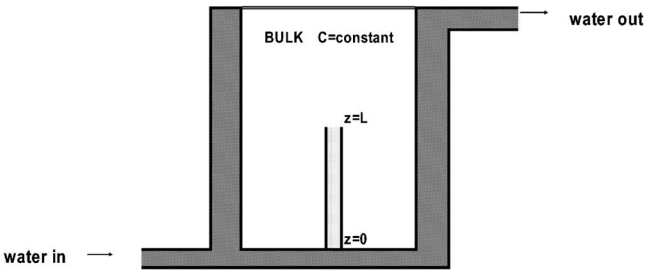

Fig. 10 Sketch of the open ended tube (OET) technique for measuring the isothermal diffusion coefficient

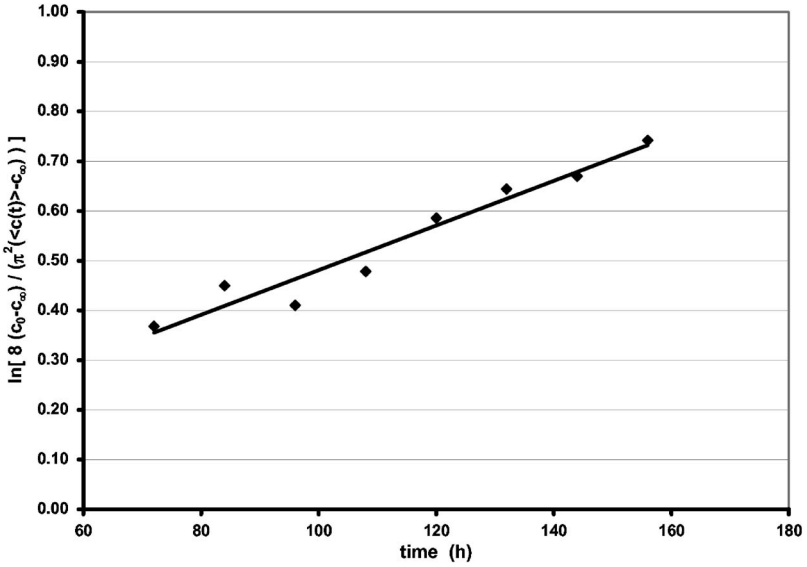

Fig. 11 Time variation of the logarithm of the mean tube concentration in the OET

between the two walls is ~1.6 mm; the raising column is, therefore, 800 μm thick and the velocity raises from zero at the wall to its maximum amplitude in 400 μm. The size of the optical probe in LDV is 90 μm which is not very small compared to the numbers given above. We understand that inside the optical probe there are velocity gradients responsible for the fluctuations. Nevertheless an averaging process for $t > 2000$ s gives the velocity amplitude which can be compared with theoretical predictions, an easy task for a pure substance. Comparison is excellent. For a binary mixture, the time evolution of the velocity amplitude is quite different as shown in Fig. 13 for a mixture of water (50 wt %) and ethanol (50 wt %). A steady-state value is obtained after 4000 s, a time larger than for a pure component. There are still fluctuations due to velocity gradients in the optical probe as explained before. The steady-state value, a little bit less than 300 μm/s is already reached (due to the thermal effect only) after 500 s, a time comparable to that necessary to reach the steady value in a one component system; but in the present case, the velocity continues to increases up to a value close to 380 μm/s, and next drops to the steady value. In order to find with precision the maximum value, excluding fluctuations, we use all the points between $t=800$ s and $t=2000$ s, fitted by a cubical polynomial from which by simple derivation we find the maximum value of the velocity in the least square sense. The relative difference between the maximum velocity and the steady value is a measure of the separation ratio, see Eq. (18), that we call Ψ_{exp}, an "experimental" value, not the real one.

$$\frac{\mathbf{V_a^{max}} - \mathbf{V_a^{steady\ st.}}}{\mathbf{V_a^{steady\ st.}}} = \Psi_{\text{exp}} \quad \Psi = \Psi_{\text{exp}} \times \tau(\mathbf{H/e}, \mathbf{Sc}, \mathbf{Gr}) \qquad (18)$$

In fact in order to find the real value, the experimental value has to be multiplied by a τ corrective factor which accounts for the non-infinite height of the cell. This correction factor τ (greater than one) tends to 1 when H (or better H/e) goes to infinity. Indeed a parcel of fluid raising along the hot wall and coming from the bottom could not have enough time to reach its concentration equilibrium value at the measuring point (the middle of the column) if the column is not high enough. Thus the main parameter in this correction factor is the aspect ratio H/e, but also the relaxation time for diffusion linked to D (or to the Schmidt number Sc in a nondimensional analysis) and the velocity amplitude (or the Grashof number Gr). But we believe that in this review paper this is too much details and interested readers should refer to the original paper [27] for tables of τ values or to [25] for an empirical

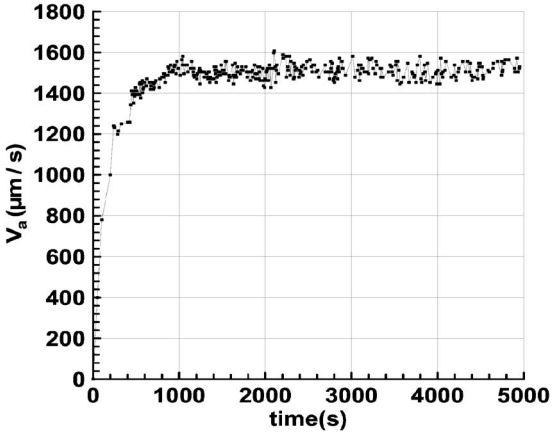

Fig. 12 Time variation of the velocity amplitude in pure ethanol

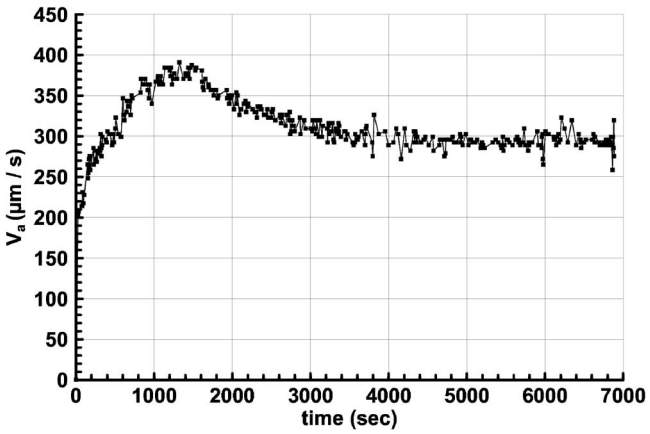

Fig. 13 Time variation of the velocity amplitude in the system water (50 %)–ethanol (50 %)

Table 2 Results for the Soret coefficient based on the overshoot phenomenon in the velocity field observed in thermogravitational columns for the system water (60.88 wt %) – ethanol (39.12 wt %)

Run	V_a^{max} (μm/s)	$V_a^{steady\ st.}$ (μm/s)	Ψ	S_T (10^{-3} K^{-1})
1	228	196	0.193	3.00
2	239	202	0.216	3.36
3	235	200	0.207	3.21
4	234	196	0.229	3.56
		mean value	0.211	3.28
		standard deviation	0.15	0.24
		standard deviation	7%	7%

equation. The experiment is not easy due to the small gap between the walls (1.58 mm) and the difficulty to enter with the laser beam parallel to the wall. In Fig. 13 we have shown the best result that we have for water (50 wt %) – ethanol (50 wt %). Usually the same experiment is repeated four times for each investigated system in order to estimate mean values and standard deviations as well. Table 2 shows the results obtained during the 4 runs for the system water (60.88 wt %) – ethanol (39.12 wt %), a system investigated by many authors.

A standard deviation of 7% is the best that we could obtain with 4 runs using the overshoot phenomenon in the velocity field, Fig. 13. We compare in Table 3 the two methods: Column 1 gives the value of D_T obtained in a first experiment by the 5 samplings along the column height, the analysis of the removed samples and the use of the Furry-Jones-Onsager theory, Eq. (13). Let us note that this value is also the average of several runs. Column 2 is the value of the isothermal diffusion coefficient D by the open ended tube technique and column 3 gives S_T as the ratio of col.1 by col.2. Column 4 reproduces the value of Table 2 for S_T, measuring by LDV the overshoot in the velocity field. The difference between the two values is only 3.4%, and we consider that the mean value of S_T=3.23 10^{-3} K^{-1} is in some sense the "true" value using convective coupling.

The comparison with other labs is made in [27] with a lot of details, but we give it here for convenience in Table 4. The agreement is simply perfect.

3 The Fontainebleau Benchmark

In view of the different techniques exposed in Sec. 2 and of the results on some water-alcohol mixtures, it seems quite natural to believe that accurate values of the Soret coefficient can be obtained in earth conditions. The E.G.R.T. (European Group of Research in Thermodiffusion) has initiated a project with the aim to provide accurate values for the Soret coefficient for some organic mixtures. During a workshop held at the "Ecole des Mines, Fontainebleau (France)", five European research groups decided to provide a benchmark value for the Soret coefficient for specified mixtures ("The Fontainebleau benchmark"). The participating laboratories are from the universities of Bayreuth, Bilbao, Mons, and Toulouse, and from the Max Planck Institute for Polymer Research in Mainz. The different techniques were already evoked in Sec. 2. Bayreuth and Mainz use the TDFRS technique that allows the simultaneous and independent determination of D, D_T, and S_T. Bilbao uses the convective coupling in annular thermogravitational columns and by a 2-point sampling process, determines from the mass fraction difference between top and bottom of the column, the thermal diffusion coefficient D_T. Mons in a first experiment determines the time dependent velocity amplitude in a vertical parallelepipedic column (obtained by laser Doppler velocimetry LDV), next uses the five-point sampling process, and finally, in isothermal conditions, the open-ended tube technique to obtain D. In Toulouse, annular thermogravitational columns are also used, but the space between the two cylinders is filled with a porous medium, characterized by its porosity ε and permeability k (packed columns). The Lorenz-Emery theory [33] (a remake of the Fury-Jones-Onsager theory that replaces the Navier-Stokes equation by Darcy's law) is used to deduce D_T. Thus in order to avoid systematic errors, a number of different techniques were employed. In view of a future comparison of these earth results with forthcoming space experiments [34] the five labs have chosen to investigate the mixtures which will fly on the ISS (International Space Station): The three binary mixtures that may be composed with dodecane (C12), isobutylbenzene (IBB), and 1,2,3,4 tetrahydronaphtalene (THN) at a mean temperature of 25 °C and 50 wt % in each component. These components have been chosen, as they are representative of a hydrocarbon reservoir mixture, containing (at least when the ternary mixture will be investigated in a next step) an alkane (C12), a one-ring component (IBB) and a two-ring component (THN) [35]. After two years of individual investigations, comparisons between the results produced by each laboratory have been completed and the results published in a common paper accompanied by five individual papers originating from each lab [15,36–40]. The aim of these papers was to propose benchmark values (see Table 5) to which all future techniques should refer. It is our opinion that each new technique, including microgravity experiments, should reproduce these values before gaining confidence.

Table 4 Comparison of the Soret coefficient of the system water (60.88 wt %) – ethanol (39.12 wt %) obtained in different laboratories

Convective coupling [21]	Kolodner [13]	Zhang et al. [14]	Bou-Ali et al. [20]	Köhler and Möller [24]
3.23× 10^{-3} K^{-1}	3.32× 10^{-3} K^{-1}	3.21× 10^{-3} K^{-1}	3.22× 10^{-3} K^{-1}	3.25× 10^{-3} K^{-1}

4 Conclusion

Clearly there is no universal technique that works for measuring the Soret coefficient of any binary mixture. Each technique has its own limitation. As an example, techniques that rely on the variation of index of refraction n with composition c (beam deflection, TDFRS, or simply the analysis of local composition of removed samples based on the measurement of n) will not work near a maximum of n, or at best will be very inaccurate. Also one has to take care of undesired convection currents if the working equations used for deducing S_T from measured quantities are derived for systems at rest. Normally today researchers should be aware of the stability diagram of binary liquid layers initially at

Table 3 Comparison of results for the Soret coefficient based on the overshoot phenomenon in the velocity field and on the vertical mass fraction profile in thermogravitational columns for the system water (60.88 wt %) – ethanol(39.12 wt %)

D_T(10^{-12} m^2 K^{-1}/s) from TGC	D(10^{-10} m^2–s) from OET	S_T(10^{-3} K^{-1}) =col1/col2	S_T(10^{-3} K^{-1}) from LDV	deviation %	$\langle S_T\rangle$(10^{-3} K^{-1}) mean value
1.37	4.32	3.17	3.28	3.4	3.23

Table 5 The Fontainebleau benchmark values for the Soret coefficient of 3 organic liquid mixtures. Initial mass fraction: 50 wt %–50 wt %. C12: dodecane. IBB: isobutylbenzene. THN: tetrahydronaphtalene

Values of S_T in units 10^{-3} K^{-1}						
Mixture	Mons [28]	Bilbao [29]	Bayreuth [30]	Mainz [31]	Toulouse [32]	Proposed benchmark value [9]
THN-C12	9.98	8.73	9.45	9.52	9.31	9.5 ±0.5
THN-IBB	3.14	3.03	3.46	3.55	3.10	3.3 ±0.3
IBB-C12	3.69	3.96	3.95	3.95		3.9 ±0.1

rest, modified by the Soret effect, including instability of systems heated from above, thought to be stable before 1970: This is the well-known double diffusive convective instability. Also horizontal (lateral) temperature gradients should be avoided in well conducted experiments. Therefore, high resolution laser Doppler velocimetry able to detect velocities down to a few μm/s, should reveal the presence, or not, of these convective currents. Alternatively the LDV technique can be used to catch as carefully as possible the onset of free convection in order to measure the variation of the critical Rayleigh number under the influence of negative separation ratio, from which S_T is deduced. More generally modification of the buoyancy forces due to the Soret effect (at least if density is sensitive to the local composition) will profoundly affect the velocity amplitude. Therefore, measurement of the velocity field is an indirect, but nevertheless not less precise way to have access to the separation ratio. Once again the limitation is due to the sensitivity of the density to compositional variation: Even if the components are quite different in their chemical nature and structure, when their densities are almost equal, buoyancy will not sufficiently change to induce measurable variations of some velocity components. But one has to remain optimistic: All these apparent difficulties are exceptional. And in order to prove that accurate values of the Soret coefficient can be obtained in earth conditions, five European labs decided to investigate independently the same systems, i.e., same chemical compounds from the same batch with the same purity, same composition, and same temperature. After two years of individual work, the comparison of results produced by the different labs showed that this benchmark campaign was a success: The highest difference from the mean was only 7% for one particular system. Therefore, we were able to propose benchmark values and we deny the need sometimes expressed [17] to go to microgravity for measuring Soret coefficients, at least for usual organic mixtures near room temperature. The conclusion could be different for less usual systems like molten salts or metals at higher temperatures.

Before ending this review paper, we should like to mention a recent complementary review by Wiegand [41]. In that paper, the author mainly focused on the optical techniques (rather than on convective coupling) to investigate the thermal diffusion process not only in liquid mixtures, but also in polymer solutions and colloïdal suspensions.

References

[1] Soret, Ch., 1979, "Sur l'état d'équilibre que prend au point de vue de sa concentration une dissolution saline primitivement homohéne dont deux parties sont portées à des températures différentes," Arch. Sci. Phys. Nat., **2**, pp. 48–61.

[2] Ludwig, C., 1856, "Diffusion zwischen ungleich erwwärmten orten gleich zusammengestzter lösungen," Sitz. Ber. Akad. Wiss. Wien Math-Naturw. Kl., **20**, p. 539.

[3] Soret, Ch., 1880, "Influence de la température sur la distribution des sels dans leurs solutions," Acad. Sci., Paris, C. R., **91**(5), pp. 289–291.

[4] Soret, Ch., 1881, "Sur l'état d'équilibre que prend au point de vue de sa concentration une dissolution saline primitivement homohéne dont deux parties sont portées à des températures différentes," Ann. Chim. Phys., **22**, pp. 293–297.

[5] Weinberger, W., 1964, "The Physics of the Solar Pond," Sol. Energy, **8**, pp. 45–56.

[6] Gregg, M., 1973, "The Microstructure of the Ocean," Sci. Am., **228**, pp. 65–77.

[7] Spiegel, E. A., 1972, "Convection in Stars-II: Special Effects," Annu. Rev. Astron. Astrophys., **10**, pp. 261–304.

[8] Bonner, F. J., and Sundelöf, L. O., 1984, "Thermal Diffusion as a Mechanism for Biological Transport," Z. Naturforsch. C, **39**, pp. 656–661.

[9] Montel, F., 1994, "Importance de la thermodiffusion en exploitation et production pétrolières," Entropie, **184–185**, pp. 86–93.

[10] Montel, F., 1998, "La place de la thermodynamique dans une modélisation des répartitions des espéces d'hydrocarbures dans les réservoirs pétroliers: Incidence sur les problémes de production," Entropie, **214**, pp. 7–9.

[11] Costeséque, P., El Maâtaoui, M., and Riviere, E., 1994, "Enrichissements sélectif d'dydrocarbures dans les huiles minérales naturelles par diffusion thermogravitationnelle en milieu poreaux et cas des isoméres paraffiniques," Entropie, **184–185**, pp. 94–100.

[12] Costesèque, P., and El Maâtaoui, M., 1994, "Sur la différenciation des hydrocarbures dans les fluids pétroliers par diffusion thermogravitationelle en milieu poreaux en présence d'un contact biphasique huile-eau," Entropie, **184–185**, pp. 101–107.

[13] Costesèque, P., El Maâtaoui, M., and Garrigues, J. C., 1996, "Essai d'analyse des relations entre la mobilité thermodiffusionnelle et les propriétés moléculaires intrinséques des espéces, par la méthode des réseaux de neurones artificiels, dans la cas de mélanges complexes ségrégués par diffusion thermogravitationnelle en milieu poreaux (huiles de gisement)," Entropie, **198–199**, pp. 15–24.

[14] Costesèque, P., Fargue, D., and Jamet, Ph., 2002, "Thermodiffusion in Porous Media and Its Consequences," *Thermal Nonequilibrium Phenomena in Fluid Mixtures* (Lecture Notes in Physics), Springer-Verlag, **584**, pp. 389–427.

[15] Platten, J. K., Bou-Ali, M. M., Costesèque, P., Dutrieux, J. F., Köhler, W. Leppla, C., Wiegand, S., and Wittko, G., 2003, "Benchmark Values for the Soret, Thermal Diffusion and Diffusion Coefficients of Three Binary Organic Liquid Mixtures," Philos. Mag., **83**(17-18), pp. 1965–1971.

[16] Legros, J. C., Goemare, P., and Platten, J. K., 1985, "Soret Coefficient and the Two-Compnoent Benard Convection in the Benzene-Methanol System," Phys. Rev. A, **32**, pp. 1903–1905.

[17] Van Vaerenbergh, S., and Legros, J. Cl., 1998, "Soret Coefficients of Organic Solutions Measured in the Microgravity SCM Experiment and by the Flow and Benard Cells," J. Phys. Chem., **102**, pp. 4426–4431.

[18] Costesèque, P., Pollak, T., Platten, J. K., and Marcoux, M., 2004, "Transient-State Method for Coupled Evaluation of Soret and Fick Coefficients, and Related Tortuosity Factors, Using Free and Porous Packed Thermodiffusion Cells: Application to CuSO4 Aqueous Solution (0.25 M)," Eur. Biophys. J., **15**(3), pp. 249–253.

[19] Kolodner, P., Williams, H., and Moe, C., 1998, "Optical Measurement of the Soret Coefficient of Ethanol/Water Solutions," J. Chem. Phys., **88**(1), pp. 6512–6524.

[20] Zhang, K. J., Briggs, M. E., Gammond, R. W., and Sengers, J. V., 1996, "Optical Measurement of the Soret Coefficient and the Diffusion Coefficient of Liquid Mixtures," J. Chem. Phys., **104**, pp. 6881–6892.

[21] Giglio, M., and Vendramini, A., 1975, "Thermal Diffusion Near a Consolute Critical Point," Phys. Rev. Lett., **34**, pp. 561–564.

[22] Wiegand, S., and Köhler, W., 2002, "Measureemt of Transport Coefficients by an Optical Grating Technique," *Thermal Nonequilibrium Phenomena in Fluid Mixtures* (Lecture Notes in Physics), W. Köhler and S. Wiegand, eds., Springer-Verlag, **584**, pp. 189–210.

[23] Chandrasekhar, S., 1961, *Hydrodynamic and Hydromagnetic Stability*, Oxford University Press, Oxford, UK.

[24] Platten, J. K., Dutrieux, J. F., and Chavepeyer, G., 2002, "Soret Effect and Free Convection: A Way to Measure Soret Coefficients," *Thermal Nonequilibrium Phenomena in Fluid Mixtures* (Lecture Notes in Physics), W. Köhler and S. Wiegand, eds., Springer–Verlag, **584**, pp. 313–333.

[25] Dutrieux, J. F., 2002, "Contribution à la métrologie du coefficient Soret," Ph.D Thesis, University of Mons, Mons, Belgium.

[26] Bou-Ali, M. M., Ecenarro, O., Madariaga, J. A., Santamaria, C., and Valencia, J. J., 1999, "Influence of the Grashof Number on the Stability of the Thermogravitational Effect in Liquid Mixtures With Negative Thermal Diffusion Factors," Entropie, **218-219**, pp. 5–7.

[27] Dutrieux, J. F., Platten, J. K., Chavepeyer, G., and Bou-Ali, M. M., 2002, "On the Measurement of Positive Soret Coefficients," J. Phys. Chem. B, **106**, pp. 6104–6114.

[28] Furry, W. H., Jones, R. C., and Onsager, L., 1939, "On the Theory of Isotope Separation by Thermal Diffusion," Phys. Rev., **55**, pp. 1083–1095.

[29] Jones, R. C., and Furry, W. H., 1946, "The Separation of Isotopes by Thermal Diffusion," Rev. Mod. Phys., **18**(2), pp. 151–224.

[30] Majumdar, S. D., 1951, "The Theory of the Separation of Isotope by Thermal Diffusion," Phys. Rev., **81**(5), pp. 844–848.

[31] Chavepeyer, G., and Platten, J. K., 1996, "Simulation numérique 2D de la séparation dans une colonne de thermogravitation et comparaison avec la théorie de Furry-Jones-Onsager-Majumdar," Entropie, **198-199**, pp. 25–29.

[32] Wakeham, W. A. Nagashima, A., and Sengers, J. V., 1991, "Measurement of the Transport Properties of Fluids," *Experimental Thermodynamics*, Vol. III, Blackwell Scientific Publications, Oxford, UK, Chap. 9.

[33] Lorenz, M., and Emery, A. H., 1995, "The Packed Thermal Diffusion Column," Chem. Phys., **11**, pp. 16–23.
[34] Legros, J. C., Montel, F., Shapiro, A., Caltagirone, J. P., Galieno, G., Agip, De Gieter, P., Dubois, F., Borthaire, L., Istasse, E., and Van Vaerenbergh, S., 2002, *Proceedings of the Fifth International Meeting on Thermodiffusion*, A. Shapiro, ed., University of Denmark, Aug. Lyngby.
[35] Costesèque, P., and Loubet, J. C., 1998, "Influence des concentrations relatives sur la diffusion thermogravitationnelle en milieu poreaux des constituants d'un mélange ternaire d'hydrocarbures (Systéme Dodécane-Isobutylbenzéne-Tétraline)," Entropie, **214**, pp. 53–59.
[36] Platten, J. K., Bou-Ali, M. M., and Dutrieux, J. F., 2003, "Precise Determination of the Soret, Thermodiffusion and Isothermal Diffusion Coefficients of Binary Mixtures of Docecane, Isobutylbenzene and 1,2,3,4-Tetrahydronaphtalene (Contribution of the University of Mons to the Benchmark Test)," Philos. Mag., **83**(17-18), pp. 2001–2010.
[37] Bou-Ali, M. M., Valencia, J. J., Madariaga, J. A., Santamaria, C., Ecenarro, O., and Dutrieux, J. F., 2003, "Determination of the Thermodiffusion Coefficient in Three Binary Orfanic Liquid Mixtures by the Thermogravitational Method (Contribution of the Universitad del País Basco, Bilbao, to the Benchmark Test)," Philos. Mag., **83**(17-18), pp. 2011–2015.
[38] Wittko, G., and Köhler, W., 2003, "Precise Determination of the Soret, Thermal Diffusion and Mass Diffusion Coefficients of Binary Mixtures of Dodecane, Isobutylbanzene and 1,2,3,4-Tetrahydronaphtalene by a Holographic Grating Technique," Philos. Mag., **83**(17-18), pp. 1973–1987.
[39] Leppla, C., and Wiegand, S., 2003, "Investigation of the Soret Effect in Binary Liquid Mixtures by Thermal-Diffusion-Forced Rayleigh Scattering (Contribution to the Benchmark Test)," Philos. Mag., **83**(17-18), pp. 1989–1999.
[40] Costesèque, P., and Loubet, J. C., 2003, "Measuring the Soret Coefficient of Binary Hydrocarbon Mixtures in Packed Thermogravitational Columns (Contribution of Toulouse University tot he Benchmark Test)," Philos. Mag., **83**(17-18), pp. 2017–2022.
[41] Wiegand, S., 2004, "Thermal Diffusion in Liquid Mixtures and Polymer Solutions," J. Phys.: Condens. Matter, **16**, pp. R357–R379.

A Unified Extended Thermodynamic Description of Diffusion, Thermo-Diffusion, Suspensions, and Porous Media

Georgy Lebon[1]
e-mail: g.lebon@ulg.ac.be

Thomas Desaive
e-mail: t.desaive@ulg.ac.be

Pierre Dauby
e-mail: pc.dauby@ulg.ac.be

Department of Astrophysics, Geophysics, and Oceanography,
Liège University,
17 Allée du 6 Août,
4000 Liège, Belgium

It is shown that extended irreversible thermodynamics (EIT) provides a unified description of a great variety of processes, including matter diffusion, thermo-diffusion, suspensions, and fluid flows in porous media. This is achieved by enlarging the set of classical variables, as mass, momentum and temperature by the corresponding fluxes of mass, momentum and heat. For simplicity, we consider only Newtonian fluids and restrict ourselves to a linear analysis: quadratic and higher order terms in the fluxes are neglected. In the case of diffusion in a binary mixture, the extra flux variable is the diffusion flux of one the constituents, say the solute. In thermo-diffusion, one adds the heat flux to the set of variables. The main result of the present approach is that the traditional equations of Fick, Fourier, Soret, and Dufour are replaced by time-evolution equations for the matter and heat fluxes, such generalizations are useful in high-frequency processes. It is also shown that the analysis can be easily extended to the study of particle suspensions in fluids and to flows in porous media, when such systems can be viewed as binary mixtures with a solid and a fluid component. [DOI: 10.1115/1.2131087]

1 Introduction

Nonequilibrium thermodynamics presents several faces; even though thermostatics, the science of equilibrium, is a unique and universal theory, this is not so with thermodynamics, whose purpose is the study of nonequilibrium processes. Actually, one can distinguish at least four main schools in thermodynamics: classical irreversible thermodynamics (CIT), rational thermodynamics (RT), extended irreversible thermodynamics (EIT), and GENERIC (general equation for nonequilibrium reversible irreversible coupling). Rational thermodynamics is a rather formal and sophisticated theory; it has known some success in the past, but now it is practically forgotten if one excepts a cluster of irreducible adherents. GENERIC is a rather recent formalism based on a Hamiltonian formulation of continuum thermomechanics, there remain indiscretions of youth still to be solved, and this is why we shall not examine it further in the present paper.

Our purpose is to present a unified description of several processes, including diffusion, thermo-diffusion, suspensions, and porous media in the framework of EIT. However, for pedagogical reasons, we shall preliminarily recall the main ingredients of CIT and apply it to the problem of thermo-diffusion in binary mixtures. Although CIT has been applied with success to a wide variety of phenomena, it suffers from some shortcomings that will be analyzed in the forthcoming. These deficiencies have been eliminated in EIT, which is a formalism that has met a growing interest during the last two decades and which will constitute the main part of this work.

The paper will run as follows: after briefly recalling the basic tenets of CIT in Sec. 2, we discuss in Sec. 3.1 the foundations underlying EIT. Applications to successive problems as thermo-diffusion, suspensions, and porous media are treated in Secs. 3.2–3.4. Since diffusion is a particular case of thermo-diffusion, we shall not devote special attention to this kind of process. General conclusions and an evaluation of the respective merits of CIT and EIT are found in Sec. 4.

2 Classical Irreversible Thermodynamics

2.1 General Considerations. Thermostatics is the science describing homogeneous systems at equilibrium. To cover more general and more realistic situations as nonhomogeneous systems undergoing dissipation, one needs new formalisms, presently known under the name of thermodynamic theories of irreversible processes. The first and simplest approach of nonequilibrium is provided by CIT, which has been developed by Onsager (Nobel Prize in chemistry 1968) [1], Prigogine (Nobel Prize in chemistry 1977) [2], Meixner [3], DeGroot and Mazur [4], among others. The basic assumption of CIT is the *local equilibrium hypothesis*. Accordingly, the local and instantaneous relations between thermal and mechanical properties of a material system are the same as for a uniform body in equilibrium. As a consequence the set of state variables are the same as in equilibrium at the condition to express them locally, which means that they depend explicitly on time t and position in space $\mathbf{x}$. Another consequence is that all the relations established in thermostatics, such Gibbs, Gibbs-Duhem, etc., relations remain valid when formulated locally. This is important as it allows us to calculate explicitly the rate of entropy production σ, defined through the time evolution equation of entropy

$$\rho \dot{s} = -\nabla \cdot \mathbf{J}^s + \sigma. \tag{1}$$

In virtue of the second principle of thermodynamics, σ is a positive definite quantity. The other quantities introduced in (1) are: the mass density ρ, the specific entropy s, and the entropy flux vector $\mathbf{J}$, the entropy production term σ is referred per unit volume while an upper dot denotes the material time derivative $\mathrm{d}/\mathrm{d}t = \partial/\partial t + \mathbf{v}\cdot\nabla$. It is shown [1–4] that σ takes the form of a bilinear relation in so-called thermodynamic fluxes $\mathbf{J}^\alpha$ and forces $\mathbf{X}^\alpha$:

[1]To whom correspondence should be addressed.

Contributed by the Applied Mechanics Division of ASME for publication in the JOURNAL OF APPLIED MECHANICS. Manuscript received May 18, 2004; final manuscript received October 5, 2005. Review conducted by B. A. Younis. Discussion on the paper should be addressed to the Editor, Prof. Robert M. McMeeking, Journal of Applied Mechanics, Department of Mechanical and Environmental Engineering, University of California - Santa Barbara, Santa Barbara, CA 93106-5070, and will be accepted until four months after final publication in the paper itself in the ASME JOURNAL OF APPLIED MECHANICS.

$$\sigma = \sum_{\alpha} \mathbf{J}^{\alpha}\mathbf{X}^{\alpha}. \tag{2}$$

These fluxes and forces are related by linear laws

$$\mathbf{J}^{\alpha} = \sum_{\beta} L^{\alpha\beta}\mathbf{X}^{\beta}, \tag{3}$$

indifferently called phenomenological or constitutive equations, $L^{\alpha\beta}$ are the phenomenological coefficients relating the processes α and β. These coefficients satisfy the celebrated Onsager-Casimir reciprocity relations [1,4]

$$L^{\alpha\beta} = \pm L^{\beta\alpha}, \tag{4}$$

while the coefficients with the same indices are positive ($L^{\alpha\alpha} > 0$) in order to satisfy the positiveness of σ. Let us now illustrate these general considerations with the example of thermo-diffusion.

2.2 Thermo-Diffusion in a Binary Mixture. For simplicity, the analysis is restricted to a binary mixture formed by a solute (1) and a solvent (2), both constituents are in motion and are assumed to be incompressible Newtonian fluids. In virtue of the local equilibrium hypothesis, the basic thermodynamic variables are the same as in equilibrium, i.e., ρ, the total mass density $\rho_1+\rho_2$, c $(=\rho_1/\rho)$ the mass concentration of one of the components, say the solute, and the specific internal energy u (or the temperature T). Of course, this set of variables must be complemented by the kinetic variable, the barycentric velocity $\mathbf{v}$ defined by $\mathbf{v}=(\rho_1\mathbf{v}_1+\rho_2\mathbf{v}_2)/\rho$. The thermodynamic variables obey the following Gibbs relation, written in rate form as

$$\dot{s} = T^{-1}\dot{u} + T^{-1}p(1/\rho)^{\cdot} - T^{-1}\mu\dot{c}, \tag{5}$$

wherein p designates the pressure and $\mu=\mu_1-\mu_2$ the difference of the chemical potentials. To calculate the rate of entropy production, we need the expressions of the evolution equations of the variables c and u, the mass density remains constant because of incompressibility $(\nabla\cdot\mathbf{v}=0)$; they take the form

$$\rho\dot{c} = -\nabla\cdot\mathbf{J}, \tag{6}$$

$$\rho\dot{u} = -\nabla\cdot\mathbf{q} + \tau:(\nabla\mathbf{v})^{\mathrm{sym}}, \tag{7}$$

wherein $\mathbf{J}=\rho_1(\mathbf{v}_1-\mathbf{v})$ is the diffusion flux of the solute and $\boldsymbol{\tau}$ the viscous symmetric stress tensor, superscript *sym* means the symmetric part of the corresponding tensor. By introducing (6) and (7) in the Gibbs equation (5) and by comparing with the balance Eq. (1) for s, we are able to derive the explicit expressions for the entropy flux $\mathbf{J}^s$ and the entropy production σ:

$$\mathbf{J}^s = (\mathbf{q}-\mu\mathbf{J})/T, \tag{8}$$

$$\sigma = \mathbf{q}\cdot\nabla T^{-1} - \mathbf{J}\cdot\nabla(\mu/T) + T^{-1}\tau:(\nabla\mathbf{v})^{\mathrm{sym}}, \tag{9}$$

the latter expression appearing as a bilinear relation in the fluxes $\mathbf{q}$, $\mathbf{J}$, $\boldsymbol{\tau}$, and their conjugated forces ∇T^{-1}, $\nabla(\mu/T)$, $(\nabla\mathbf{v})^{\mathrm{sym}}$. Introducing a new heat flux

$$\mathbf{q}' = \mathbf{q} - (h_1-h_2)\mathbf{J}, \tag{10}$$

where h_k $(=u_k+p/\rho_k)$ is the specific enthalpy of constituent k and making use of the result

$$T\nabla(T^{-1}\mu_k) = -h_k T^{-1}\nabla T + (\nabla\mu_k)_T, \tag{11}$$

where subscript T refers to a quantity evaluated at constant temperature, it is found that (9) takes the form

$$T\sigma = -\mathbf{q}'\cdot\frac{\nabla T}{T} - \mu_{11}\mathbf{J}\cdot\frac{\nabla c}{c} + \tau:(\nabla\mathbf{v})^{\mathrm{sym}}, \tag{12}$$

with $\mu_{11}=\partial\mu_1/\partial c$. Invoking *Curie's principle* [4], which forbids coupling between fluxes and forces of different tensorial orders, expression (12) suggests the following flux-force relations:

$$\mathbf{q}' = -\lambda\nabla T - \frac{\rho\mu_{11}T}{c}D_F\nabla c, \tag{13}$$

$$\mathbf{J} = -\rho D_T\nabla T - \rho D\nabla c, \tag{14}$$

$$\tau = \eta(\nabla\mathbf{v})^{\mathrm{sym}}, \tag{15}$$

wherein we have introduced the usual transport coefficients; namely, the coefficient of diffusion D, the Dufour coefficient D_F, the thermal diffusion coefficient D_T, and the dynamic shear viscosity η. Positivity of σ implies that $\lambda>0$, $D>0$, $\eta>0$, whereas from Onsager's reciprocity property, it is deduced that

$$D_F = D_T. \tag{16}$$

This equality was first established by Stefan at the end of the 19th century and widely confirmed theoretically and experimentally during the 20th century. The results (13) and (14) reflect the well-known properties of Dufour and Soret effects and can be directly generalized to the case of a n-component mixture. In absence of coupling, (13) and (14) reduce to the classical laws of Fourier and Fick respectively:

$$\mathbf{q} = -\lambda\nabla T \text{ (Fourier)}, \quad \mathbf{J} = -\rho D\nabla c \text{ (Fick)}. \tag{17}$$

2.3 Shortcomings of CIT. Despite its successes, CIT presents several shortcomings that are now briefly discussed. First of all, it should be realized that CIT is in contradiction with the principle of causality demanding that an effect be perceived after the application of a cause. In CIT, the field equations take the form of a set of parabolic partial differential equations with the consequence that any perturbation will be felt instantaneously and everywhere inside the system. Indeed going back to Fourier's (or Fick's) law, it is directly seen that any temperature (or concentration) gradient gives rise instantaneously to a heat (or mass) flux throughout the whole system, from which follows that cause and effect are simultaneous, in opposition with causality requirement.

Second, CIT is a linear theory in fluxes and forces. Therefore, it is only applicable in the close vicinity of equilibrium and cannot be generalized to nonlinear situations as polymers, non-Newtonian fluids, or shock waves. Third, the validity of the Onsager relations has been acridly contested mainly by the RT school, indeed there is no explicit demonstration of the validity of the reciprocity relations at the macroscopic level; the only pseudodemonstration that is available rests on pure microscopic considerations and has also been the subject of severe criticisms. These are the main reasons that have prompted people to propose other formalisms. EIT, which is one of them, will be presented in the next section.

3 Extended Irreversible Thermodynamics (EIT)

3.1 Generalities. The basic idea in EIT is to extend the space of state variables by including the dissipative fluxes among the set of variables. Denoting by $\mathbf{C}$ the ensemble of classical variables and by $\mathbf{F}$ the flux variables, the space of state variables will be formed by the union of $\mathbf{C}$ and $\mathbf{F}$:

$$\mathbf{V} = \mathbf{C}\cup\mathbf{F}. \tag{18}$$

In addition, it is postulated that there exists a nonequilibrium entropy that is a function of the whole set of variables [i.e., $s=s(\mathbf{V})$], it is worthwhile to stress that by doing so, we go beyond the local equilibrium hypothesis of CIT which implied that $s=s(\mathbf{C})$. To fulfil the requirement placed by second law of thermodynamics, it is admitted that the rate of entropy production σ is never negative: $\sigma\geqslant 0$.

The behavior in the course of time and in space of the classical variables $\mathbf{C}$ is well known as it is governed by the classical balance equations of mass, momentum and energy. The open problem in EIT is to derive the time evolution equations for the flux variables $\mathbf{F}$: several approaches have been proposed [5,6] that are

either inspired by the method followed in CIT to obtain the phenomenological relations or by more general and sophisticated procedures as utilized in rational thermodynamics. Here, for the sake of uniformity, we have decided in favor of the technique used in CIT. Of course, these evolution equations for the flux variables cannot take any arbitrary form as they are subject to the restrictions placed by the second law and the general axioms of thermomechanics.

3.2 Thermo-diffusion in Binary Mixtures. As in Sec. 2, we shall consider diffusion in a mixture of two incompressible Newtonian fluids subject to a temperature gradient. The space of basic variables is formed by the union of the space **C** of classical variables (mass concentration c of one of the constituents, internal energy u (or temperature T), plus eventually the barycentric velocity $\mathbf{v}$) and the space **F** of the flux variables, here the flux of diffusion $\mathbf{J}$ and the heat flux $\mathbf{q}'$. The corresponding Gibbs equation will take the form

$$\dot{s} = T^{-1}\dot{u} - T^{-1}\mu\dot{c} + \frac{\alpha}{\rho T}\mathbf{J}\cdot\dot{\mathbf{J}} + \frac{\beta}{\rho T}\mathbf{q}'\cdot\dot{\mathbf{q}}' \tag{19}$$

wherein, for simplicity, it has been assumed that $\partial s/\partial \mathbf{J} = (\alpha/\rho T)\mathbf{J}$, $\partial s/\partial \mathbf{q}' = (\beta/\rho T)\mathbf{q}'$ where α and β are unknown phenomenological coefficients allowed to depend on c and T, coupling and nonlinear terms in the fluxes are neglected. To calculate the entropy flux and the entropy production, we follow the same procedure as in Sec. 2. We substitute the evolution equations of c and u in the above Gibbs relation and compare with the general evolution equation (1) of s, it is then found that the entropy flux is still given by its classical expression (8), while the entropy production reads as

$$T\sigma = -\mathbf{J}\cdot\left(\frac{\mu_{11}}{c}\nabla c + \alpha\dot{\mathbf{J}}\right) - \mathbf{q}'\cdot\left(\frac{\nabla T}{T} + \beta\dot{\mathbf{q}}'\right) + \tau:(\nabla\mathbf{v})^{\mathrm{sym}}. \tag{20}$$

It is interesting to observe that the above relation is a bilinear expression in generalized fluxes and forces, the latter being the quantities appearing between brackets. Assuming linear flux-forces relations, one recovers at once Newton's law (15) between the stress and the symmetric velocity gradient tensors plus the missing evolution equations of $\mathbf{q}'$ and $\mathbf{J}$, that can be given the form

$$\dot{\mathbf{J}} + \frac{1}{\alpha\rho\Delta}\mathbf{J} = -\frac{\mu_{11}}{\alpha c}\nabla c + \frac{\xi}{\alpha}\mathbf{q}', \tag{21}$$

$$\dot{\mathbf{q}}' + \frac{1}{\beta T\Lambda}\mathbf{q}' = -\frac{1}{\beta T}\nabla T + \frac{\gamma}{\beta}\mathbf{J}, \tag{22}$$

wherein Λ, γ, Δ, and ξ are four supplementary phenomenological coefficients. In the case of time-independent processes, expressions (21) and (22) reduce to Dufour and Soret relations (13) and (14). This comparison is interesting as it allows us to identify the supplementary unknown coefficients introduced in (21) and (22). It is easily found that

$$\Lambda = \lambda - \frac{\rho T\mu_{11}}{c}\frac{D_F D_T}{D}, \quad \gamma = \frac{\mu_{11}}{c\Lambda}\frac{D_F}{D},$$
$$\Delta = \frac{c}{\mu_{11}}D - T\frac{D_F D_T}{\lambda}, \quad \xi = \frac{D_T}{\lambda\Delta}. \tag{23}$$

The two remaining coefficients α and β are related to the relaxation times τ_J and τ_q corresponding to the heat and mass fluxes respectively; indeed, referring to (21) and (22) these relaxation times are given, respectively, by

$$\tau_J = \alpha\rho\Delta, \quad \tau_q = \beta T\Lambda. \tag{24}$$

If these relaxation times can be determined either theoretically or experimentally, the above relations provide a direct means to evaluate α and β.

It should also be observed that within a more general context, expressions (21) and (22) may contain extra contributions of the form $\nabla\times\mathbf{J}$ and $\nabla\times\mathbf{q}$, which do not contribute to the entropy production and represent so-called "gyroscopic" or "lift" forces.

In absence of coupling between thermal and matter transports, Eqs. (21) and (22) take the form of Cattaneo relations [7]:

$$\tau_J\dot{\mathbf{J}} + \mathbf{J} = -\rho D\nabla c, \tag{25}$$

$$\tau_q\dot{\mathbf{q}} + \mathbf{q} = -\lambda\nabla T, \tag{26}$$

which play an important role in high-frequency phenomena. It is true that the relaxation times τ_J and τ_q are generally very small in ordinary fluids and in homogeneous materials (of the order of the time between two successive collisions in gases) and are therefore negligible in a great majority of applications. For polymer solutions and nonhomogeneous materials as organic tissues they can be relatively large of the order of 1 to 100 sec. Equations of the form (21) and (22) or (25) and (26) are also useful in the description of suspensions and porous media, as briefly described in the forthcoming.

3.3 Suspensions. In the case of *suspensions* of solid rigid particles in a fluid at uniform temperature, a good choice for the extra flux variable is the particle diffusion flux $\mathbf{J} = \rho c(1-c)(\mathbf{v}_p - \mathbf{v}_f)$ where c is the particle's mass fraction and indices p and f refer to the particles and the fluid, respectively. By following the same procedure as above, it has been shown that $\mathbf{J}$ obeys a time-evolution equation of the form [8]

$$\dot{\mathbf{J}} + \frac{\mathbf{J}}{\tau_J} = -\omega\nabla\mu + \chi\nabla\cdot\tau + \varsigma\nabla\cdot\tau^* + O(\mathbf{J}\cdot\mathbf{J}), \tag{27}$$

where ω, χ, ς are phenomenological coefficients, the second-order tensors $\boldsymbol{\tau}$ and $\boldsymbol{\tau}^*$ designate two viscous stress tensors; the first is related to the global convective motion and the second one to the relative motion of the particles and are given [8] by the following constitutive relations:

$$\tau = \eta[\nabla(\mathbf{v} + \chi\mathbf{J})]^{\mathrm{sym}}, \tag{28}$$

$$\tau^* = \eta^*[\nabla(\varsigma\mathbf{J})]^{\mathrm{sym}}, \tag{29}$$

with η and η^* two positive viscosity coefficients. Equation (28) is a generalization of Newton's law in presence of suspensions whereas (29) is typical of systems with suspensions. When nonlinear effects are taken into consideration, expression (27) becomes much more complicated [8] and the physical interpretation of the various phenomenological coefficients is a tedious task. To clarify their meaning, EIT is of no help and one must address to other theories like the kinetic theory or the internal variable theory [9]. In the case that coefficients χ and ς vanish, evolution equation (27) boils down to Cattaneo relation (25).

3.4 Porous Media. It is not unusual to model fluid motion through porous media as a binary system whose respective components are the fluid and the solid porous matrix, the latter being generally assumed to be rigid and at rest, so that its velocity $\mathbf{v}_s = 0$. As a flux variable, it is then rather natural to select the fluid diffusion flux $\mathbf{J} = \rho_f(\mathbf{v}_f - \mathbf{v})$. Following the same procedure as in the previous sections, it is easily shown [10] that $\mathbf{J}$ obeys an evolution equation of the form

$$\dot{\mathbf{J}} = -\frac{\rho D}{\tau_J}\nabla c - \frac{1}{\tau_J}\mathbf{J}, \tag{30}$$

where D is a diffusion coefficient and τ_J a relaxation time, nonlinear terms and thermal effects have been omitted. From the defi-

nition of **J** and making use of the momentum equation

$$\rho\dot{\mathbf{v}} = -\nabla p + \nabla\cdot\tau + \rho\mathbf{F}, \tag{31}$$

with τ the viscous stress tensor and **F** the body force per unit mass, expression (30) will read as

$$\dot{\rho}_f(\mathbf{v}_f-\mathbf{v}_f)+\rho_f\dot{\mathbf{v}}_f-\frac{\rho_f}{\rho}(-\nabla p+\nabla\cdot\tau+\rho\mathbf{F}) = -\frac{\rho D}{\tau_J}\nabla c-\frac{\rho_f}{\tau_J}(\mathbf{v}_f-\mathbf{v}). \tag{32}$$

Introducing Newton's law and the result $\mathbf{v}_f-\mathbf{v}=(\rho_s/\rho)\mathbf{v}_f$ in (32) leads to

$$\rho_f\dot{\mathbf{v}}_f = -\frac{\rho_f}{\rho}\nabla p-\frac{\rho_f}{\rho}\eta\nabla^2\mathbf{v}+\rho_f\mathbf{F}-\frac{\rho_s\rho_f}{\rho\tau_J}\mathbf{v}_f, \tag{33}$$

where η is the dynamic viscosity of the fluid and where the term involving the diffusion coefficient has been omitted as it is generally negligible. Let us now introduce the permeability K of the porous medium and the effective viscosity η_{eff} defined respectively as

$$K=\frac{\tau_J\phi\eta}{\rho_s},\quad \eta_{\text{eff}}=\frac{\rho_f\eta}{\rho\phi}, \tag{34}$$

where ϕ designates the porosity of the medium; i.e., the ratio of the volume occupied by the fluid and the total volume. With this notation, Eq. (33) reads as

$$\rho\dot{\mathbf{v}}_f = -\nabla p-\frac{\eta}{K}\mathbf{u}+\eta_{\text{eff}}\nabla^2\mathbf{u}+\rho\mathbf{F}, \tag{35}$$

wherein $\mathbf{u}=\phi\mathbf{v}_f$ is the seepage velocity. In absence of body forces and under stationary conditions, one recovers the Brinkman relation

$$-\nabla p-\frac{\eta}{K}\mathbf{u}+\eta_{\text{eff}}\nabla^2\mathbf{u}=0. \tag{36}$$

It is clear that (36) reduces to Navier-Stokes equation for $K\to\infty$ and to Darcy's relation

$$\nabla p = -\frac{\eta}{K}\mathbf{u} \tag{37}$$

for $K/L^2\ll 1$, where L is a reference length scale. It follows from the above considerations that Darcy and Brinkman relations are particular cases of the evolution equation for the diffusion flux. Darcy's law is generally selected when the volume of the solid particles is larger than the volume occupied by the fluid; otherwise, Brinkman's law is preferred. It is also interesting to recall that τ_J is of the order of the collision time between particles; i.e., 10^{-8} to 10^{-13} s. Identification (34) indicates that the permeability K will be of the same of order of magnitude, and this is indeed confirmed by experimental observations.

4 Conclusions

The aim of this paper is to convince the reader that extended irreversible thermodynamics (EIT) provides a valuable tool for studying a large variety of macroscopic processes. In the present work, four different situations have been analyzed: diffusion in binary systems, thermo-diffusion, suspensions, and flows through porous media. The central role played by the diffusion flux has been emphasized, it has in particular been shown that most of the relevant results in (thermo)diffusion, suspensions and porous media are derivable from one single relation: the time evolution equation of the mass flux. Such results attest of the simplicity and the universality of EIT.

When comparing EIT with CIT, the classical theory of irreversible processes [1–4], the following statements are worth pointing out.

(i) The phenomenological relations obtained in CIT (for instance, the Soret and Dufour expressions), are in EIT replaced by evolution equations for the mass and heat fluxes. EIT may be considered as a natural extension of CIT that is recovered when the relaxation times are going to zero.

(ii) In CIT, the differential field equations are parabolic, whereas they are hyperbolic in EIT. The consequence is that the application of an arbitrary disturbance will result in a signal propagating at infinite velocity in CIT but at finite velocity in EIT. This is important because, in contrast with CIT, EIT is in full agreement with the principle of causality requiring that any effect will be felt after the application of the cause; in CIT, cause and effect are simultaneous.

(iii) Because of the axiom of local equilibrium, the range of applications of CIT is restricted to linear and local processes, strictly speaking CIT is applicable to situations close to equilibrium. Such a constraint is not applicable to EIT, which encompasses nonlinear and nonlocal processes as it eliminates the local equilibrium hypothesis.

(iv) It can be argued that one shortcoming of EIT is the presence of a rather large number of phenomenological coefficients. However as shown in Sec. 3.2, such a difficulty can be circumvented by comparing with experimental data and/or other theories, such as kinetic theory or statistical mechanics.

To summarize, it can be claimed that that main characteristics of EIT are simplicity and universality. The basic idea is to enlarge the space of variables by including the fluxes; the latter are well defined as they are the dissipative parts of the fluxes appearing in the classical balance equations. In some problems involving strong nonlocality, it may be necessary to introduce higher-order fluxes like the flux of the fluxes [5], but this does not generate fundamental difficulties. Universality of EIT has been proved though the large amount of applications treated during the two last decades and for which the present analysis provides only a restricted partial sample.

Acknowledgment

Support from ESA through PRODEX VII and CIMEX II projects is acknowledged.

Nomenclature

D = diffusion coefficient, $m^2\ s^{-1}$
D_F = Dufour diffusion coefficient, $m^2\ s^{-1}\ K^{-1}$
D_T = Soret or thermal diffusion coefficient, $m^2\ s^{-1}\ K^{-1}$
$\mathbf{J}$ = diffusion flux, $kg\ m^{-2}\ s^{-1}$
$\mathbf{J}^s$ = entropy flux, $W\ m^{-2}\ s^{-1}$
K = permeability, m^2
T = temperature, K
c = mass concentration
h = specific enthalpy, $J\ kg^{-1}$
p = pressure, $N\ m^{-2}$
$\mathbf{q}$ = heat flux, $W\ m^{-2}$
s = specific entropy, $J\ kg^{-1}\ K^{-1}$
u = specific internal energy, $J.\ kg^{-1}$
$\mathbf{u}$ = seepage velocity, $m\ s^{-1}$
$\mathbf{v}$ = velocity field, $m\ s^{-1}$

Greek symbols

Λ = phenomenological coefficient
$\alpha, \beta, \Delta, \gamma, \zeta$ = phenomenological coefficients
φ = porosity
η = viscosity coefficient, $N\ s\ m^{-2}$
λ = heat conductivity, $W\ m^{-1}\ K^{-1}$
μ = chemical potential, $J\ kg^{-1}$
ξ = phenomenological coefficient

ρ = mass density, kg m^{-3}
ς = phenomenological coefficient
σ = rate of entropy production per unit volume, W K^{-1} m^{-3}
$\boldsymbol{\tau}$ = stress tensor, N m^{-2}
τ_j, τ_q = relaxation times, s
χ, ω = phenomenological coefficients

Subscripts

eff = effective
f = fluid
s = solid

Superscripts

$\dot{}$ (upper dot) = time derivative
sym = symmetric part of a tensor

References

[1] Onsager, L., 1931, "Reciprocal Relations in Irreversible Thermodynamics," Phys. Rev., **37**, pp. 405–426.
[2] Prigogine, I., 1961, *Introduction to Thermodynamics of Irreversible Processes*, Interscience, New York.
[3] Meixner, J., 1943, "Zur Thermodynamik der Irreversiblen Prozessen in Gases mit Chemisch Reagierenden, Dissozierenden und Anregbaren Komponenten," Ann. Phys., **43**, p. 244.
[4] de Groot, S. R., and Mazur, P., 1962, *Non-equilibrium Thermodynamics*, North-Holland, Amsterdam.
[5] Jou, D., Casas-Vazquez, J., and Lebon, G., 2001, *Extended Irreversible Thermodynamics*, 3rd ed., Springer, Berlin.
[6] Muller, I., and Ruggeri, T., 1998, *Rational Extended Thermodynamics*, Springer, New York.
[7] Cattaneo, C., 1948, "Sur une Forme de l'Équation de la Chaleur Éliminant le Paradoxe d'une Propagation Instantanée," Acad. Sci., Paris, C. R., **247**, pp. 431–433.
[8] Lebon, G., Depireux, N., and Lhuillier, D., 2002, "A Non-equilibrium Thermodynamic Formulation of Suspensions of Rigid Particles in Moving Fluids," in: S. Dost, H. Struchtrup, and I. Dincer, eds., *Progress in Transport Phenomena*, Elsevier, Paris, pp. 423–428.
[9] Lhuillier, D., 2001, "Internal Variables and the Non-equilibrium Thermodynamics of Colloidal Suspensions," J. Non-Newtonian Fluid Mech., **96**, pp. 19–30.
[10] Desaive, T., 2002, "Thermo-convection dans les Milieux Poreux: Stabilité et Dynamique Non-linéaire," PhD thesis, Liège University.

Charles-Guobing Jiang
e-mail: charlesguobing.jiang@utoronto.ca

M. Ziad Saghir
e-mail: zsaghir@Ryerson.ca

Department of Mechanical Engineering,
Ryerson University,
Gerrard Street,
Toronto M5B 2E8, Canada

M. Kawaji
Department of Chemical Engineering
and Applied Chemistry,
University of Toronto,
College Street,
Toronto M5S 3E5, Canada
e-mail: kawaji@ecf.utoronto.ca

Numerical Analysis of Thermal-Solutal Convection in Heterogeneous Porous Media

Thermal diffusion, or Soret effect, in porous media is mathematically modeled with the Firoozabadi model based on non-equilibrium thermodynamics. The Soret effect in a binary mixture is investigated in a vertical cavity with heterogeneous permeability, where natural convection can occur. The thermo solutal convection with heterogeneous permeability was studied in terms of flow pattern, concentration distribution, component separation ratio, and Soret coefficient distribution. A consistent analysis was conducted and it is concluded that the Soret coefficient of thermal diffusion in porous media strongly depends on the heterogeneity of permeability. [DOI: 10.1115/1.1992515]

1 Introduction

During a thermal diffusion process, a composition gradient will be built up in a previously uniform mixture when a temperature gradient is applied. This thermal diffusion effect is named the Ludwig–Soret effect, or Soret effect [1], and the ratio of the thermal diffusion coefficient to the molecular diffusion coefficient is known as the Soret coefficient. Researchers [2–4] have contributed to theoretical developments related to the calculation of the molecular, thermal and pressure diffusion coefficients. Among them, Shukla and Firoozabadi [2], Riley and Firoozabadi [5] and Ghorayeb et al. [6–8], using the irreversible thermodynamics theory, were able to extend the theoretical simulation of the Soret effect based on De Groot's non-equilibrium thermodynamics [9] to multicomponent systems. The significant advantage of this approach is that the Soret coefficient is calculated at each point of the cavity grid as a function of temperature, pressure, and compositions of the system. Compared with other theoretical approaches, such as Rutherford and Roof [10], the theoretical prediction of this approach is much closer to experimental data, especially for non-ideal mixtures, such as hydrocarbon mixtures [11].

The transport phenomenon in porous media is an important research topic and intensive studies have been continuously conducted on it. The complicated and heterogeneous properties of porous media bring challenges to researchers, who are interested in different characters of the transport phenomena in porous media. There are a large number of published papers studying the effect of heterogeneity in porous media. Ingham [12] discussed the viscosity effect on Darcy Law from a mathematical approach, and Storesletten [13] investigated the impact of heterogeneous permeability of porous media on convection flow and detailed the convection flow characteristics with respect to different permeability ratios. Saghir and Islam [14] studied the effect of convection in a dual-permeability and dual-porosity porous cavity.

However, all these papers are focused on the fluid mechanics issues and no thermal diffusion has been taken into account, even if mass diffusion process was considered in some papers. In parallel, there are a few research papers contributing to thermal diffusion with convection flow in porous media. Jacqmin [15] concluded the convection effect on mass transfer would be balanced by the compositional variation through a perturbation analysis. Riley and Firoozabadi [5] studied the Soret effect on natural convection in a rectangular reservoir with homogeneous permeability. Benano-Melly et al. [16] examined the Soret effect in binary mixtures with lateral heating. They assumed a constant Soret coefficient in their entire numerical analysis. Their numerical results indicate a multiple convection roll flow pattern depending on the Soret coefficient value and their experimentally measured thermal diffusion coefficient was used in their numerical model. Jiang et al. [17] analyzed the permeability effect on the thermal diffusion process and showed that there existed an optimum permeability in porous media providing maximum separation ratio in a combined thermal diffusion and convection process, which is consistent with the results reported by many researchers. But in each case, the homogeneous permeability was assumed. Ingham and Pop [18,19] have conducted extensive research on the transport phenomena in porous media, Nield and Bejan [20] contributed to convection investigation in porous media significantly, and Vafai [21] provided a comprehensive handbook for researchers in a porous media field.

This work investigates numerically the thermal diffusion phenomena in a heterogeneous porous cavity, which is laterally heated and filled with a binary mixture of methane and n-butane. The thermal diffusion process, as well as the concentration distribution and the separation ratio due to a temperature gradient and natural convection flow, were investigated. In the analysis, the streamlines of flow in heterogeneous porous media, the concentration distribution over the entire cavity, and the vertical distributions of the Soret coefficient along the center of the porous medium cavity have been analyzed to study the Soret effect in a heterogeneous porous medium. The separation ratio has also been used as a variable to investigate the effect of the Soret effect on convection flow as the permeability ratio of the porous medium varies. All results show consistent phenomena, and with the separation ratio, the effect of the convection flow on thermal diffusion has been clearly presented [22,23]. The significant point in this paper is that not only the Soret effect is investigated in a heterogeneous porous medium but also the Soret coefficient has not been fixed as constant in the computational domain but rather calculated at each point of the grid as a function of the temperature, pressure and the composition of the fluid mixture.

Contributed by the Applied Mechanics Division of ASME for publication in the JOURNAL OF APPLIED MECHANICS. Manuscript received June 15, 2004; final manuscript received April 25, 2005. Assoc. Editor: D. Siginer. Discussion on the paper should be addressed to the Editor, Prof. Robert M. McMeeking, Journal of Applied Mechanics, Department of Mechanical and Environmental Engineering, University of California—Santa Barbara, Santa Barbara, CA 93106-5070, and will be accepted until four months after final publication in the paper itself in the ASME JOURNAL OF APPLIED MECHANICS.

2 System Modeling

In a binary mixture, the diffusion mass flux of component 1 is formed based on three driving forces, the composition gradient, the temperature gradient, and the pressure gradient, and can be written in the following formula:

$$\mathbf{J}_1 = -\rho(D_m \nabla x_1 + D_T \nabla T + D_P \nabla P), \tag{1}$$

where ρ is the mass density of the fluid mixture, kg/m^3; x_1 is the mole fraction of the specified component 1 in the binary mixture, nondimensional; T is temperature, K; P is pressure, N/m^2; and D_m, D_T, and D_p are the molecular, thermal, and pressure diffusion coefficients in m^2/s, m^2/s/K, and m^3 s/kg, respectively; and $\mathbf{J}_1$ is the mass flux of the solute, methane, in kg/m^2/s.

The ratio between thermal diffusion coefficient and the molecule diffusion coefficient is called Soret coefficient

$$S_t = \frac{D_T}{D_m x_1 (1 - x_1)} \tag{2}$$

Based on non-equilibrium thermodynamics theory, the Soret coefficient can be described in the following formula:

$$S_t = \frac{Q_2^* - Q_1^*}{T x_1 \dfrac{\partial \mu_1}{\partial x_1}} \tag{3}$$

where T is temperature, K, x_1 is the mole fraction of component 1, μ_1 is the molar chemical potential of component 1, J/mol, Q_i^* is the net heat transport of component i, J/mol, $i=1,2$.

In the Firoozabadi model, the net heat transport is modeled as:

$$Q_i^* = \frac{U_i}{\tau_i} - \left(\sum_{j=1}^{n} \frac{x_j U_j}{\tau_j} \right) \frac{V_i}{\sum_{j=1}^{n} x_j V_j}, \quad i = 1,2; n = 2 \tag{4}$$

where U_i is the molar internal energy of component i, J/mol V_i is the molar volume of component i, m^3/mol, x_j is the mole fraction, and τ_i is the ratio of the energy of viscous flow and the energy of vaporization. For hydrocarbon components, the value of τ_i is set to be constant 4.0 [2]

In Haase's model, the net heat transport is interpolated with the molar enthalpy in a mass conserved system. With this assumption, the net heat transport is expressed in the following format:

$$Q_2^* - Q_1^* = \left(\frac{M_1}{M} H_2 - \frac{M_2}{M} H_1 \right) \tag{5}$$

where H_i is the partial molar enthalpy of component i, J/mol and M_i is the molecule weight of component i, M is the molecule weight of the mixture, $M = x_1 M_1 + x_2 M_2$.

In the Kempers model, the net heat transport is described with molar volume and enthalpy

$$Q_2^* - Q_1^* = \left(\frac{V_1}{V} H_2 - \frac{V_2}{V} H_1 \right) \tag{6}$$

where V_i is the partial molar volume of component i, m^3/mol and V is the molar volume of the mixture, $v = x_1 V_1 + x_2 V_2$.

The Firoozabadi model has shown good performance in predicting Soret coefficient in hydrocarbon mixtures [2], and it is applied in this paper for the numerical simulation of thermal diffusion in a rectangular porous cavity.

A porous cavity of height H and width L is shown in Fig. 1 with specified boundary conditions. The upper part and lower part are assigned different values of permeability, κ_1 and κ_2, respectively, with κ_2 set to be 10 md (1 md$=9.87\times10^{-15}$ m^2) and κ_1 varying over a wide range. The parameters in the model are given in Table 1. The thermal diffusion phenomenon in this heterogeneous porous medium is modeled with the following mathematical equations.

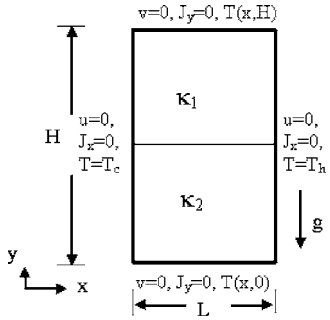

Fig. 1 Two-dimensional porous media domain and boundary conditions

The continuity equations are given below:

$$\frac{\partial \rho}{\partial t} + \nabla \cdot (\rho \mathbf{V}) = 0 \tag{7}$$

$$\frac{\partial (\rho x_1)}{\partial t} + \nabla \cdot (\rho x_1 \mathbf{V}) = -\nabla \cdot \mathbf{J}_1 \tag{8}$$

where ρ is the mass density of the fluid mixture, kg/m^3; t is time, s; $\mathbf{V} = u\mathbf{i} + v\mathbf{j}$ is the velocity vector, and u and v are the horizontal and vertical velocity components, m/s; x_1 is the mole fraction of the specified component 1, methane, in the binary mixture, nondimensional; and $\mathbf{J}_1$ is the mass flux of the solute, as shown in Eq. (1).

The momentum conservation equation is simplified by using Darcy's Law in porous media

$$\mathbf{V} = -\frac{\kappa}{\phi \mu} (\nabla P + \rho \mathbf{g}) \tag{9}$$

where $\mathbf{g}$ is the gravitational acceleration vector, m/s^2; κ, μ, and ϕ are the permeability, the dynamic viscosity, and the porosity, respectively. The unit of κ is m^2, the unit of μ is Pa/s, and ϕ is nondimensional.

Practically, the momentum equation used in the numerical simulation is obtained by substituting Eq. (9) into the mass conservation equation given by Eq. (7), and solving for pressure.

The energy conservation equation is expressed as follows:

$$\frac{\partial [(\rho C_p)_e T]}{\partial t} + \mathbf{V} \cdot \nabla [(\rho C_p)_f T] = k_e \nabla^2 T \tag{10}$$

where $(\rho C_p)_f$ is the volumetric heat capacity of fluid mixture, J/m^3/K; $k_e = \phi k_f + (1-\phi) k_p$ is the effective thermal conductivity of the system, W/m/K; and $(\rho C_p)_e = \phi (\rho C_p)_f + (1-\phi)(\rho C_p)_p$ is the effective volumetric heat capacity of the system, J/m^3/K.

The two lateral walls of the cavity have constant temperatures, $T_h = 344$ K and $T_c = 334$ K, respectively. All the walls are assumed rigid. At initial point, the binary mixture inside the cavity consists of 20% methane (CH_4) and 80% n-butane (nC_4H_{10}) uniformly, maintained under a pressure of 11.14 MPa and a linear temperature distribution in x direction with $T_c = 334$ K and $T_h = 344$ K. The result was obtained when the system reaches steady state in a time process. The Peng–Robinson equation of state [24] is applied to calculate the density of mixture, as well as other fluid properties. The flow is considered to be compressible, and the properties of the liquid, such as the density and viscosity, are functions of the temperature, pressure and the fluid mixture composition. The calculation of viscosity is referred to the model introduced by Herning and Zipperer [25], and the estimation of molecule diffusion coefficient D_m is based on the model proposed by Taylor [26].

Table 1 Parameters of the physical model

Width L of the cavity	0.5 m
Height H of the cavity	5.0 m
Characteristic Length, $L_c=\sqrt{L^2+H^2}$	5.025 m
Fluid mixture composition	$CH_4(20\%)+nC_4H_{10}(80\%)$
Fluid specific heat, $(Cp)_f$	2746.42 J/kg/K
Fluid thermal conductivity, k_f	0.095 J/m/s/K
Porosity, ϕ	0.20
Permeability, κ_2	10^{-3}, 0.1, 1, 10, 100, 10^4 md
Specific heat of porous medium, $(Cp)_p$	1840.0 J/kg/K
Thermal conductivity of porous medium, k_p	1.0 J/m/s/K
Density of porous medium, ρ_p	2050.0 kg/m^3
Reference temperature, T_0	339 K
Lateral wall temperature difference, T_h-T_c	10°C
Reference pressure, P_0	11.14 MPa

3 Results and Discussion

In the vertical porous cavity, the permeability of the lower part is set to be 10 md and kept constant, however, the permeability of the upper part is varied from 0.001 to 10000 md. The permeability ratios chosen in this study are 0.001/10, 0.1/10, 1/10, 10/10, 100/10, and 10,000/10, which cover a wide range.

The streamlines in the cavity for each heterogeneous permeability case corresponding to a different permeability ratio are shown in Figs. 2(*a*)–2(*f*). It is noticed that when the permeability ratios are 0.001/10 and 0.1/10, there is no streamline in the upper part of the cavity compared to the well developed convection flow in the lower part of the cavity. This is due to the lower permeability in the upper part. Actually, there is convection flow in the upper part in both cases. However, the flow is so weak compared to the flow in the lower part that it is negligible as shown in Figs. 2(*a*) and 2(*b*). In Fig. 2(*c*), the streamlines appear in the upper part with a permeability ratio 1/10. The convection flow in the upper part is not as strong as in the lower part. However, the effect on thermal diffusion is significant, which is discussed later.

With the permeability ratio equal to 10/10, convection is developed in the whole cavity as shown in Fig. 2(*d*). When the permeability in the upper part increases to 100 and 10,000 md, the flow in the upper part dominates. Noticeably, the convection in the lower part still maintains the formal pattern except for the interface area as shown in Figs. 2(*e*) and 2(*f*).

From the streamlines of the convection pattern for different permeability ratio cases, the heterogeneity of porous medium can be said to have a strong effect on convection pattern.

It is significant that when the value of permeability in the upper part of the cavity is smaller than the value of permeability at the lower part, convection in the lower part dominates, and this can be observed from the flow in the interface area when κ_1 varies from 0.001 to 0.1 md, and then to 1 md. When κ_1 is larger than κ_2, the convection flow at the upper part dominates and the flow pattern of the lower part is distorted at the interface area.

In Figs. 3(*a*)–3(*f*), the mole fraction distribution, usually called concentration distribution in literatures, inside the porous cavity is shown corresponding to the given permeability ratio. For all cases, the concentration distribution can be divided into two regions, the upper part and the lower part. According to different values of the permeability in the upper part, the concentration distribution varies drastically, however, in the lower part, the concentration distribution keeps the same pattern approximately. This behavior is consistent with the convection flow patterns, as shown in Figs. 2(*a*)–2(*f*). When the permeability is 0.001 or 0.1 md in the upper part, the concentration distribution in the upper part is given by vertical lines, which are generated for a thermal diffusion process with negligible convection flow. However, when the permeability is 1 md in the upper part, the concentration distribution lines tilt to about 45 deg, which is caused by the effect of convection flow as shown in Fig. 2(*c*). With 10 md permeability, the same as the lower part, the concentration distribution shows flat lines and the separation ratio reaches the maximum value, which was discussed in detail in Ref. [27]. As the value of upper permeability becomes larger, 100 and 10,000 md, than the value in the lower part, the strong convection flow in the upper part disturbs

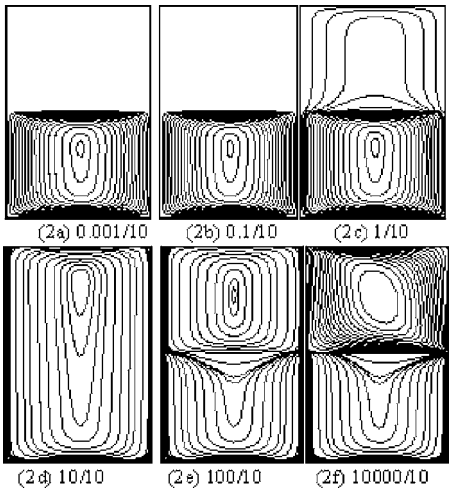

Fig. 2 Convection streamlines in the heterogeneous porous cavity

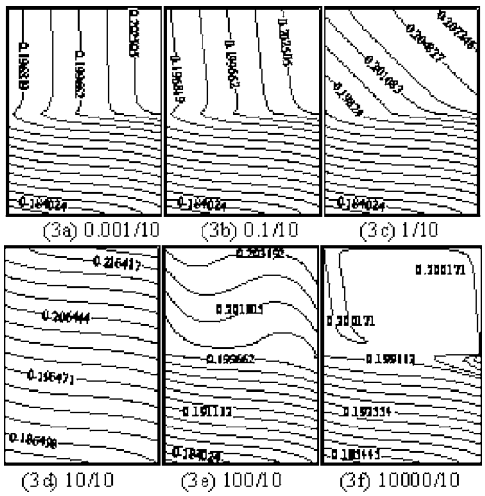

Fig. 3 Mole fraction of component 1 distribution in the heterogeneous porous cavity

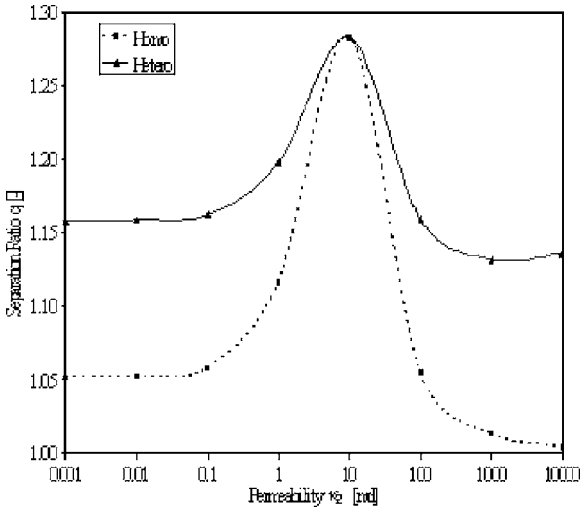

Fig. 4 Component separation ratio in the heterogeneous porous cavity

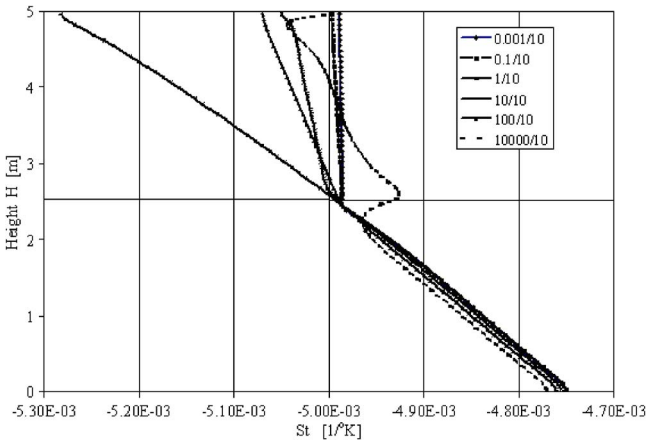

Fig. 5 Vertical soret coefficient distribution in the center of the cavity

the separation of components in the binary mixture. When the permeability of the upper part is 10,000 md, the strong convection flow in the upper part mixes up the whole upper part. However, the lower part is still identifiable with well established separation.

The concentration distribution in the lower part of the cavity does not change much with different permeability values in the upper part. However, from the concentration distribution at the interface area, one can observe that the lower part dominates when κ_1 is smaller than κ_2, as shown in Figs. 3(*a*)–3(*c*), and the upper part dominates when κ_1 is larger than κ_2, as shown in Figs. 3(*e*) and 3(*f*).

The separation ratio is defined as

$$q = \frac{x_h/(1-x_h)}{x_c/(1-x_c)} \tag{11}$$

where x_h and x_c are the maximum and minimum methane mole fraction at the hot and cold walls, respectively.

The variation of separation ratio, q, with different permeability in the upper part of the heterogeneous porous medium, is shown in Fig. 4, and compared to the separation ratio for the homogeneous case, for which the whole cavity is specified to have the same permeability.

The two curves meet at the 10 md point, which should happen as both are with identical specifications. It is important to point out that the separation ratio in heterogeneous porous media is always higher than that in the homogeneous porous media due to the heterogeneous condition of the problem. The higher separation ratio in heterogeneous porous media is of physical and practical interest in the research on thermal diffusion.

In heterogeneous porous media, the Soret coefficient, S_t, will be affected by the region-dependent convection flow. In order to investigate this effect, the Soret coefficient distribution along the central vertical line in the porous cavity is shown in Fig. 5. Corresponding to different values of permeability in the upper part of the cavity, the Soret coefficient changes dramatically in the upper part of the centerline and the effect of convection flow can be identified clearly. When the value of permeability is 0.001 md, the Soret coefficient distribution in the upper part is a vertical line, corresponding to very weak convection flow in the upper part. Similar behavior can be seen with 0.1 md permeability in the upper part. At 1 md permeability, the Soret coefficient distribution tilts in accordance with noticeable convection flow in the upper part. With 10 md permeability in the upper part, the Soret coefficient distribution reaches the maximum variation. When the permeability in the upper part increases to 100 md, the Soret coefficient distribution returns back close to a vertical line with slight distortion at the interface due to stronger convection flow in the upper part. With the permeability of 10,000 md in the upper part, the Soret coefficient distribution in the upper part along the centerline changes its pattern completely, which is the result of strong convection flow. Although the Soret coefficient in the upper part varies dramatically for different permeability values, the Soret coefficient distribution in the lower part remains the same with slight changes. Therefore, the thermal diffusion in the lower part of the heterogeneous porous cavity has been preserved and the relatively larger separation ratio shown in Fig. 4 is mainly due to the thermal diffusion in the lower part of the cavity, or the heterogeneity of the porous media.

Observing the Soret coefficient distribution near the interface, where the effect of difference in permeability appears, one can conclude that the Soret coefficient distribution in the lower part of the cavity does not change when κ_1 is smaller than κ_2, and varies slightly when κ_1 is larger than κ_2. This observation is consistent with both the convection flow pattern shown in Fig. 2, and the concentration distribution shown in Fig. 3.

4 Conclusions

The significance of heterogeneous porous media on thermal diffusion, or the Soret effect, in a vertical porous medium was investigated with specified permeability ratios 0.001/10, 0.1/10, 1/10, 10/10, 100/10, and 10,000/10. The Soret effect varies drastically in the upper part of the porous cavity in accordance with the variation in permeability. But the Soret effect in the lower part of the porous cavity, where a fixed permeability is specified, is preserved, even with the strong convection flow existing in the upper part, which ruins any Soret effect and mixes the components up in the upper part of the porous cavity. A significantly higher separation ratio is obtained compared to the homogeneous permeability case. The effect of the Soret coefficient given in this paper is consistent with the effect of permeability ratio in a heterogeneous porous cavity on the predicted convection pattern, concentration distribution, and separation ratio variation.

Acknowledgment

The authors acknowledge the full support of the center for research and space technology (CRESTech), the Canada Space Agency, and the National Science and Engineering Council (NSERC).

References

[1] Soret, C., 1880, "Influence de la Temperature sur la Distribution des Sels dans Leurs Solutions," Acad. Sci., Paris, C. R., **91**, pp. 289–291.

[2] Shukla, K., and Firoozabadi, A., 1998, "A New Model of Thermal Diffusion Coefficients in Binary Hydrocarbon Mixtures," Ind. Eng. Chem. Res., **37**, pp. 3331–3342.
[3] Bird, R. B., and Stewart, W. E., 2002, *Transport Phenomena*, Wiley, New York.
[4] Dougherty, E. L., and Drickamer, H. G., 1955, "Thermal Diffusion and Molecular Motion in Liquids," J. Phys. Chem., **59**, pp. 443–449.
[5] Riley, M. F., and Firoozabadi, A., 1998, "Compositional Variation in Hydrocarbon Reservoirs With Natural Convection and Diffusion," AIChE J., **44**, pp. 452–464.
[6] Firoozabadi, A., Ghorayeb, K., and Shukla, K., 2000, "Theoretical Model of Thermal Diffusion Factors in Multicomponent Mixtures," AIChE J., **46**, pp. 892–900.
[7] Ghorayeb, K., and Firoozabadi, A., 2001, "Features of Convection and Diffusion in Porous Media for Binary Systems," J. Can. Pet. Technol., **40**, pp. 21–28.
[8] Ghorayeb, K., and Firoozabadi, A., 2000, "Molecular, Pressure and Thermal Diffusion in Nonideal Multicomponent Mixtures," AIChE J., **46**, pp. 883–891.
[9] De Groot, S. R., 1984, *Non-Equilibrium Thermodynamics*, North-Holland, Amsterdam.
[10] Rutherford, W. M., and Roof, J. G., 1959, "Thermal Diffusion in Methane n-Butane Mixture in the Critical Region," J. Phys. Chem., **63**, pp. 1506–1511.
[11] Faruque, D., Chacha, M., Saghir, M. Z., and Ghorayeb, K., 2002, "Compositional Variation Considering Diffusion and Convection for Binary Mixture in Porous Media," J. Porous Media, **7**(2), pp. 1–17.
[12] Ingham, D. B., 2003, "Basic Equations for Laminar Flows through Porous Media, Current Issues on Heat and Mass Transfer in Porous Media," *Proc. of the NATO Advanced Study Institute on Porous Media*, Neptun-Olimp, Black Sea, Romania, pp. 1–10.
[13] Storesletten, L., 2003, "Anisotropy Effects on Convective Flow in Porous Media: Part I and Part II, Current Issues on Heat and Mass Transfer in Porous Media," *Proc. of the NATO Advanced Study Institute on Porous Media*, Neptun-Olimp, Black Sea, Romania, pp. 529–546.
[14] Saghir, M. Z., and Islam, M. R., 1999, "Double Diffusive Convection in Dual-Permeability, Dual-Porosity Porous Media," Int. J. Heat Mass Transfer, **42**, pp. 437–454.
[15] Jacqmin, D. J., 1990, "Interaction of Natural Convection and Gravity Segregation in Oil/Gas Reservoirs," SPE Reservoir Eval. Eng., **289**, pp. 233–238.
[16] Benano-Melly, L. B., Caltagirone, J. P., Faissat, B., Montel, F., and Costeseque, P., 2001, "Modelling Soret Coefficient Measurement Experiments in Porous Media Considering Thermal and Solutal Convection," Int. J. Heat Mass Transfer, **44**, pp. 1285–1297.
[17] Jiang, C. G., Saghir, M. Z., Kawaji, M., and Ghorayeb, K., 2003, "Permeability Effects in a Vertical Porous Cavity With Soret Contribution, Current Issues on Heat and Mass Transfer in Porous Media," *Proc. of the NATO Advanced Study Institute on Porous Media*, Neptun-Olimp, Black Sea, Romania, pp. 187–197.
[18] Ingham, D. B., and Pop, I., (eds.), 2002, *Transport Phenomena in Porous Media*, Pergamon, Oxford, Vol. II.
[19] Pop, I., and Ingham, D. B., 2001, *Convective Heat Transfer: Mathematical and Computational Modeling of Viscous fluids and Porous Media*, Pergamon, Oxford.
[20] Nield, D. A., and Bejan, A., 1999, *Convection in Porous Media*, 2nd ed., Springer, New York.
[21] Vafai, K., (ed.), 2000, *Handbook of Porous Media*, Marce Dekker, New York.
[22] Chacha, M., Faruque, D., Saghir, M. Z., and Legros, J. C., 2002, "Thermodiffusion in Binary Mixture in the Presence of g-jitter," Int. J. Therm. Sci., **41**, pp. 899–911.
[23] Jiang, C. G., Saghir, M. Z., Kawaji, M., and Ghorayeb, K., 2004, "Contribution of the Thermal and Molecular Diffusion to Convection in a Vertical Porous Cavity," *NATO ASI Series*, Kluwer, Dordrecht, Vol. ASI978745, pp. 1–13.
[24] Peng, D. Y., and Robinson, D. B., 1976, "A New Two-Constant Equation of State," Ind. Eng. Chem. Fundam., **15**, pp. 59–64.
[25] Herning, F., and Zipperer, L., 1936, "Calculation of the Viscosity of Technical Gas Mixtures From the Viscosity of Individual Gases," Gas u. Wasserfach, **79**, 69.
[26] Taylor, R., and Krishna, R., 1993, *Multicomponent Mass Transfer*, Wiley, New York.
[27] Jiang, C. G., Saghir, M. Z., Kawaji, M., and Ghorayeb, K., 2004, "Two-Dimensional Numerical Simulation of Thermo-Gravitational Convection in a Vertical Porous Column Filled With a Binary Fluid Mixture," Int. J. Therm. Sci., **43**, pp. 1057–1065.

A. Bahloul

M. A. Yahiaoui

P. Vasseur

École Polytechnique,
C. P. 6079, Succ. "Centre Ville" Montréal,
Montreal, QC H3C 3A7,
Canada

R. Bennacer

H. Beji

LEEVAM,
Rue d'Eragny,
Neuville sur Oise,
Cergy-Pontoise Cedex,
France

Natural Convection of a Two-Component Fluid in Porous Media Bounded by Tall Concentric Vertical Cylinders

This paper reports an analytical and numerical study of the behavior of a binary mixture saturating a vertical annular porous medium. Uniform heat fluxes are applied to the vertical walls while the horizontal walls are impermeable and adiabatic. Solutal gradients are assumed to be induced either by the imposition of constant gradients of concentration on the vertical walls (double diffusive convection, $a=0$) or by the Soret effect ($a=1$). Governing parameters of the problem under study are the thermal Rayleigh R_T, buoyancy ratio φ, Lewis number Le, aspect ratio A, constant a, and curvature η. An analytical solution, valid for tall enclosures ($A \gg 1$), is derived on the basis of the parallel flow approximation. In the range of the governing parameters considered in this study, a good agreement is found between the analytical predictions and the numerical results obtained by solving the full governing equations. For large Rayleigh numbers ($R_T \gg 1$), an approximate solution valid in the limit of the boundary layer regime is obtained. [DOI: 10.1115/1.1993666]

1 Introduction

The phenomenon of natural convection, induced by two sources of buoyancy, through porous media has been recently studied extensively due to its importance in many natural and industrial problems (see for instance [1–3]). Available studies on this phenomenon can be classified into two types of problems in regard to the solutal contribution to the total buoyancy force induced by the thermal and solutal gradients. In the first type of problem, called double diffusive convection, the solutal field results from the imposition of given solutal boundary conditions on the system. In the second type of problem, called Soret induced convection, the solutal gradients are due to the thermal diffusion in a binary mixture, initially homogeneous. In both cases, the dynamic of heat and mass transfer can be very different from those driven by the temperature field alone.

A review of the literature concerning natural convection due to combined buoyancy forces indicates that most of the existing studies on this topic are concerned with the case of a vertical cavity subject to horizontal temperature and concentration gradients. Thus, analytical and numerical results have been reported for this configuration for both double diffusive convection [4,5], and Soret induced convection [6–8]. A few studies have also been concerned with the case of columns [9] and vertical annulus [10]. The results obtained in these investigations show that, depending on the governing parameters of the problem and in particular on the solutal to thermal buoyancy ratio φ, various modes of convection are possible. In particular, the flows driven by opposing thermal and solutal buoyancy forces ($\varphi<0$) were observed to be considerably more complex than those driven by aiding buoyancy forces ($\varphi>0$). For instance a purely diffusive state is possible for the special situation where the buoyancy forces induced by the thermal and solutal effects are opposing each other and of equal intensity ($\varphi=-1$). The onset of convection was investigated in [11–14] for the case of double diffusive convection and in [7,15] for Soret induced convection. The existence of oscillating flows, in the case of opposing fluxes of heat and mass ($\varphi<0$), was demonstrated numerically in [5,16] among others. The ranges in parametric values necessary to make convection oscillatory were investigated by these authors. Also for opposing forces, the existence of multiple solutions has been demonstrated analytically in [17]. The transition between aiding and opposing double-diffusive flows in a vertical porous cavity has been investigated numerically and analytically in [18]. It was demonstrated that two types of solutions exist in which thermal and solutal buoyancy forces oppose each other and are of comparable intensity. Also, an analytical solution was developed in [19] for boundary layer flows in a vertical layer, induced by opposing buoyancy forces. It was shown that the resulting boundary layer regimes are extremely different from those found in the previous studies for the case of aiding buoyancy forces.

This paper reports an analytical and numerical study of natural convection through a binary fluid saturating a vertical porous annulus. Both problems of double diffusive and Soret induced convection are investigated. In the present study, both case of opposing ($\varphi<0$) and aiding ($\varphi>0$) buoyancy forces are considered. An outline of the paper is as follows. The mathematical formulation is given in Sec. 2. Section 3 describes the numerical method used to solve the problem. The analytical approach for steady state solution is presented and discussed in Sec. 4. The concluding remarks are reported in Sec. 5.

2 Problem Statement

The flow configuration under study is a two-dimensional vertical cylindrical annular cavity of height H' and width $L'=(r'_o)-r'_i$ filled with a homogeneous fluid-saturated porous medium. The geometry of the physical system is shown in Fig. 1. r' and z' are the cylindrical polar coordinates. Neumann boundary conditions are applied, for both temperature (q'_i, and $q'_o=q'_i r'_i/r'_o$), and concentration (j'_i and $j'_o=j'_i r'_i/r'_o$), on the vertical walls of the annular layer. All the boundaries are impermeable. The sub-

Contributed by the Applied Mechanics Division of ASME for publication in the JOURNAL OF APPLIED MECHANICS. Manuscript received September 30, 2004; final manuscript received May 12, 2005. Assoc. Editor: D. Siginer. Discussion on the paper should be addressed to the Editor, Prof. Robert M. McMeeking, Journal of Applied Mechanics, Department of Mechanical and Environmental Engineering, University of California-Santa Barbara, Santa Barbara, CA 93106-5070, and will be accepted until four months after final publication in the paper itself in the ASME JOURNAL OF APPLIED MECHANICS.

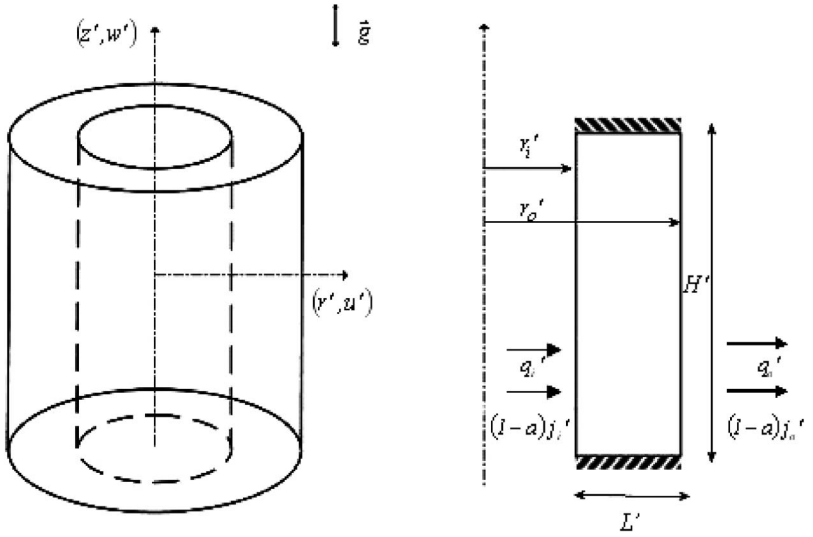

Fig. 1 Schematic diagram of the physical model and coordinate system

scripts i and o refer to the inner and outer cylinder, respectively. The porous medium is considered to be isotropic and in local thermal and compositional equilibrium with the fluid. The effect due to viscous dissipation and porous medium inertial are assumed to be negligible. The binary fluid saturating the cavity is assumed to be Newtonian and to satisfy the Boussinesq approximation. The density variation upon temperature and concentration is described by the state equation

$$\rho = \rho_0[1 - \beta'_T](T' - T'_0) - \beta_N(N - N_0) \tag{1}$$

where ρ_0 is the fluid mixture density at temperature $T' = T'_0$ and mass fraction $N = N_0$, and β'_T and β_N are the thermal and concentration expansion coefficients, respectively. The mass fraction of the denser component of the mixture, N_0, is assumed to be initially uniform. The phenomenological equations relating the fluxes of heat $\vec{Q}'$ and matter $\vec{J}'$ to the thermal and solute gradients present in a binary fluid mixture are given by (see for instance, [20]):

$$\vec{Q}' = -k \nabla T' \tag{2}$$

$$\vec{J}'(1-a) = -\rho D \nabla N - a\rho D' N(1-N) \nabla T' \tag{3}$$

where a is a real number, the significance of which will be discussed in the following text, k and D are the thermal conductivity and the mass diffusivity of species through the fluid saturated porous medium. D' is the thermal diffusion coefficient.

In the foregoing analysis, the stream function formulation is introduced in the mathematical model. In order to satisfy the continuity equation, the stream function Ψ' is defined such that

$$u' = \frac{1}{r'}\frac{\partial \Psi'}{\partial z'}, \quad w' = -\frac{1}{r'}\frac{\partial \Psi'}{\partial r'} \tag{4}$$

where u' and w' are the velocity components.

The dimensionless variables (primed quantities are dimensional) are defined as follows:

$$\begin{gathered}(r,z) = (r',z')/L' \quad (u,w) = (u',w')/L'/\alpha \\ t = t'\alpha/L'^2\sigma \quad \varepsilon = \phi/\sigma \\ T = (T' - T'_0)/\Delta T' \quad \Delta T' = qL'/k \\ \Psi = \Psi'/L'\alpha \quad C = N/\Delta N\end{gathered} \tag{5}$$

where $\Delta N = -j'/\rho_0 D$ for double diffusive convection and $\Delta N = N_0(1-N_0)\Delta T' D'/D$ for Soret driven convection; α is the thermal diffusivity, $\sigma = (\rho_0 C)_p/(\rho_0 C)_f$ is the heat capacity ratio, and ϕ the porosity of the porous medium.

In terms of the above definitions, the dimensionless governing equations are given by

$$\nabla^2 \Psi - \frac{2}{r}\frac{\partial \Psi}{\partial r} = -rR_T\left(\frac{\partial T}{\partial r} + \varphi\frac{\partial C}{\partial r}\right) \tag{6}$$

$$\frac{\partial T}{\partial t} + u\frac{\partial T}{\partial r} + w\frac{\partial T}{\partial z} = \nabla^2 T \tag{7}$$

$$\varepsilon\frac{\partial C}{\partial t} + u\frac{\partial C}{\partial r} + w\frac{\partial C}{\partial z} = \frac{1}{Le}(\nabla^2 C - a\nabla^2 T) \tag{8}$$

where

$$\nabla^2 = \frac{1}{r}\frac{\partial}{\partial r}\left(r\frac{\partial}{\partial r}\right) + \frac{\partial^2}{\partial z^2}$$

The corresponding dimensionless boundary conditions are

$$r = r_i = \frac{\eta}{1-\eta} \quad \Psi = 0 \quad \frac{\partial T}{\partial r} = -1; \quad \frac{\partial C}{\partial r} = (a-1) + a\frac{\partial T}{\partial r} \tag{9}$$

$$r = r_o = \frac{1}{1-\eta} \quad \Psi = 0 \quad \frac{\partial T}{\partial r} = -\eta; \quad \frac{\partial C}{\partial r} = (a-\eta) + a\frac{\partial T}{\partial r} \tag{10}$$

$$z = \pm A/2 \quad \Psi = 0 \quad \frac{\partial T}{\partial z} = \frac{\partial C}{\partial z} = 0 \tag{11}$$

From the above equations it is seen that the present problem is governed by the thermal Rayleigh number R_T, the buoyancy ratio φ, the Lewis number Le, the curvature parameter η, the constant a, the normalized porosity ε, and the cavity aspect ratio A. These parameters are given by

$$R_T = \frac{g\,K\,\beta_T \Delta T' L'}{\alpha\nu} \quad \varphi = \frac{\beta_N \Delta N}{\beta'_T \Delta T'} \quad \mathrm{Le} = \frac{\alpha}{D} \tag{12}$$

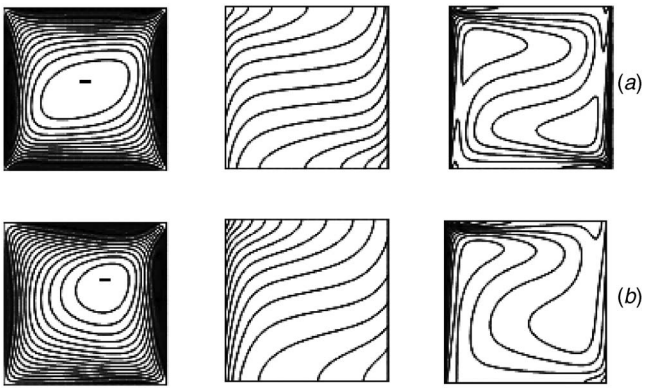

Fig. 2 Contour lines of stream function (left), temperature (center), and concentration (right) for R_T=50, φ=−0.8, *Le*=10, *a*=1, and *A*=1 ; (a) η=1 ; (b) η=0.1

$$\varepsilon = \frac{\phi}{\sigma} \quad \eta = \frac{r'_i}{r'_o} \quad A = \frac{H'}{L'}$$

The heat and solute transports can be expressed in terms of the Nusselt and Sherwood numbers defined, respectively, as

$$\mathrm{Nu} = \frac{1}{r_i \ln \eta} \frac{1}{\Delta T} \quad \mathrm{Sh} = \frac{1}{r_i \ln \eta} \frac{1}{\Delta C} \tag{13}$$

where $\Delta T = T(r_i,0) - T(r_o,0)$ and $\Delta C = C(r_i,0) - C(r_o,0)$ are the temperature and concentration differences, evaluated at $z=0$.

In the above equations the case $a=0$ corresponds to double diffusive convection for which the solutal buoyancy forces in the porous layer are induced by the imposition of constant mass fluxes j'_i and j'_o on the vertical boundaries. On the other hand, the case $a=1$ corresponds to the case of a binary fluid subject to the Soret effect. For this situation the boundary conditions on concentration result from the fact that the solid boundaries are assumed impermeable ($\vec{J}'=0$) such that $(\partial C/\partial r - \partial T/\partial r)=0$.

3 Numerical Solution

The numerical solution of governing equations (6)–(8), with specified boundary conditions Eqs. (9)–(11) is obtained using the SIMPLER algorithm proposed by Patankar [21]. The control volume formulation used in the algorithm ensures continuity of the convective and diffusive fluxes as well as overall momentum and energy conservation. The mesh size required for sufficient numerical accuracy depends mainly on the thermal and solutal Rayleigh numbers and the aspect ratio of the porous layer. Numerical tests, using various mesh sizes, were done for the same conditions in order to determine the best compromise between accuracy of the results and computer time. Besides the usual control, the accuracy of computations was estimated using the energy and mass fraction conservation within the system.

Typical numerical results are presented in Figs. 2(*a*) and 2(*b*) for the case R_T=50, φ=−0.8, Le=10, a=1 (Soret driven convection), A=1, and for η=1, η=0.1, respectively. In the present investigation, only the case of ε=1 is considered. The flow pattern, isotherms, and isoconcentrates obtained for η=1 (square cavity), Fig. 2(*a*), are similar to those reported in the literature by numerous investigations while studying the thermally driven convection of a binary fluid in a rectangular cavity. A clockwise rotating cell fills up the entire cavity with hydrodynamic, thermal, and solutal boundary layers along the vertical boundaries of the enclosure. Because of the relatively high Le considered here the concentration boundary layers are observed to be sharper than the thermal boundary layers. Also, it is noticed that the temperature in the core region varies almost linearly in the vertical direction and is nearly constant in the horizontal direction. The concentration field in the region is observed to be almost uniform.

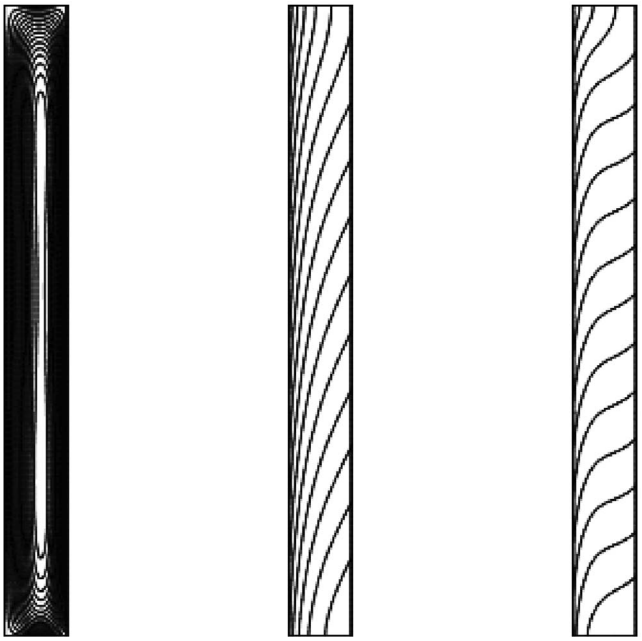

Fig. 3 Contour lines of stream function (left), temperature (center), and concentration (right) for R_T=50, φ=−0.8, *Le*=10, *a*=1, η=0.1, and *A*=10

Decreasing the curvature η from 1 to 0.1 yields the results depicted in Fig. 2(*b*). As expected, the effect of η is to destroy the centrosymmetric properties of the rectangular cavity case. Hence a shift of the isotherms toward the inner heated vertical wall is clearly observed in Fig. 2(*b*), resulting in a significant asymmetry of the temperature and concentration fields in the core of the annulus. A noticeable change in the flow patterns, as compared to those in the rectangular cavity, is also observed. The effect of decreasing η is to shift the core of the convective cell from the center of the cavity (η=1) toward the bottom edge of the cooled wall.

Figure 3 illustrates typical numerical results obtained for a tall enclosure ($A \gg 1$) namely for R_T=50, φ=−0.8, Le=10, a=1, A=10, and η=0.1. The results clearly illustrate the fact that for this situation the flow in the core region, i.e., except in regions close to the upper and lower boundaries, can be considered as parallel. Also it is observed that the temperature and concentration are linearly stratified in the vertical direction. The analytical solution, developed in the following section, will rely on those observations.

Numerical tests have been performed to determine the minimum aspect ratio above which the flow can be assumed to be parallel. In the range of the parameters considered in this investigation it was found that the numerical results can be considered independent of the aspect ratio when $A \geqslant 8$. For this reason most of the numerical results reported here were obtained for A=8 with typically 60×180 mesh points.

4 Analytical Solution

In this section an analytical model, for steady state flows within a slender enclosure is proposed. Thus, in the limit $A \gg 1$, the parallel flow approximation (see for instance [22,23]) leads to the following approximations

$$\Psi(r,z)=\Psi(r)\quad T(r,z)=C_T z+\theta_T(r)\quad C(r,z)=C_S z+\theta_S(r) \tag{14}$$

Using the above approximations, together with the boundary conditions, Eqs. (6)–(8) are reduced to a set of ordinary differential equations

$$\frac{d^2\Psi}{dr^2}-\frac{1}{r}\frac{d\Psi}{dr}-\Lambda\Psi=\Gamma \tag{15}$$

$$\frac{d\theta_T}{dr}=-\frac{1}{r}[C_T\Psi+r_i] \tag{16}$$

$$\frac{d\theta_s}{dr}=-\frac{1}{r}[(\mathrm{Le}C_S+aC_T)\Psi+r_i] \tag{17}$$

The solution of above equation being function of the parameter Λ and Γ defined as

$$\Lambda=R_T[C_T+\varphi(\mathrm{Le}C_S+aC_T)]\quad \Gamma=-R_T r_i(1+\varphi) \tag{18}$$

With the approximations involved in Eq. (14) it is not possible to apply the boundary conditions in the z direction, Eq. (11). However, it can be easily demonstrated [4] that the heat and species transport across a transversal section, at any z, are given by

$$\int_{r_i}^{r_o}\frac{\partial T}{\partial z}dr-\int_{r_i}^{r_o}wTdr=0$$

$$\int_{r_i}^{r_o}\frac{\partial C}{\partial z}dr+a\int_{r_i}^{r_o}\frac{\partial T}{\partial z}dr-Le\int_{r_i}^{r_o}wC\,dr=0 \tag{19}$$

The solution of the above set of equations depends on the parameter Λ. According to the values of R_T,φ,Le, and a this parameter can be greater or smaller than zero. The two situations will be now discussed.

4.1 Case of $\Lambda\geqslant 0$. For this situation the parameter $\Omega^2=\Lambda$ is introduced, such that Ω is a real value. The solution of the set of equations (15)–(17) satisfying the boundary conditions in the r direction, Eqs. (9) and (10), yields

$$\psi(r)=-r_i\Psi_0\frac{1+f(r)}{1+f(\xi)} \tag{20}$$

$$\theta_T(r)=C_T r_i\Psi_0\frac{\ln r+g(r)}{1+f(\xi)}-r_i\ln r \tag{21}$$

$$\theta_S(r)=(\mathrm{Le}\ C_S+aC_T)r_i\Psi_0\frac{\ln r+g(r)}{1+f(\xi)}-r_i\ln r \tag{22}$$

where

$$f(r)=r[C_1I_1(\Omega r)+C_2K_1(\Omega r)]$$

$$g(r)=C_1I_0(\Omega r)+C_2K_0(\Omega r)$$

$$\Psi_0=\frac{\Gamma}{r_i\Omega^2}[1+f(\xi)]\quad \xi=\frac{1+\eta}{2(1-\eta)} \tag{23}$$

$$C_1=\frac{1}{r_i r_o}\frac{r_oK_1(\Omega r_o)-r_iK_1(\Omega r_i)}{I_1(\Omega r_o)K_1(\Omega r_i)-I_1(\Omega r_i)K_1(\Omega r_o)}$$

$$C_2=-\frac{1}{r_i r_o}\frac{r_oI_1(\Omega r_o)-r_iI_1(\Omega r_i)}{I_1(\Omega r_o)K_1(\Omega r_i)-I_1(\Omega r_i)K_1(\Omega r_o)}$$

In the above equations I_n and K_n are the Bessel functions of the nth orders and $\Psi_c=-\Psi_0$ is the stream function value at the center of the cavity.

Substituting Eqs. (20)–(23) into Eq. (19) and performing the resulting integrals yields the values of C_T and C_S as

$$C_T=\frac{2b}{c}\frac{\Psi_0}{1+b\Psi_0^2}$$

$$C_S=\frac{2b}{c}\frac{Le\ \Psi_0+a\Psi_0(1-Leb\ \Psi_0^2)/(1+b\Psi_0^2)}{1+Leb\ \Psi_0^2} \tag{24}$$

where

$$b=\frac{r_i^2X_2}{\xi}\quad c=\frac{2X_2}{X_1}\quad X_1=\int_{r_i}^{r_o}\frac{1}{r}\frac{[1+f(r)]}{[1+f(\xi)]}dr\quad X_2=\int_{r_i}^{r_o}\frac{1}{r}\frac{[1+f(r)]^2}{[1+f(\xi)]^2}dr \tag{25}$$

To compute the value of Ω a transcendental equation is established by combining Eqs. (18) and (24)

$$b^2\mathrm{Le}^2\Psi_0^4+b(1+\mathrm{Le}^2)\Psi_0^2+\frac{2\ b\ R_T}{c\ \Omega^2}\{1+\varphi[\mathrm{Le}^2-a(1+\mathrm{Le})]\Psi_0$$
$$+(1+\varphi)b\ \mathrm{Le}^2\Psi_0^2\}+1=0 \tag{26}$$

The above equation can be solved numerically using the Newton-Raphson procedure. In this way the temperature and concentration gradients C_T and C_S can be obtained as function of $R_T,\varphi,\mathrm{Le},\eta$, and a.

From Eqs. (13), (14), (21), and (22) it is found that the Nusselt and Sherwood numbers are given by

$$\mathrm{Nu}=\frac{r_i\ln\eta(1+b\Psi_0^2)}{r_i\ln\eta+b(d+r_i\ln\eta)\Psi_0^2} \tag{27}$$

$$\mathrm{Sh}=\frac{r_i\ln\eta(1+b\ Le^2\Psi_0^2)}{r_i\ln\eta+b(d+r_i\ln\eta)Le^2\Psi_0^2+a\ b\ c(1+Le)\Psi_0/(1+b\Psi_0^2)} \tag{28}$$

where $d=r_iX_1^2/X_2$.

4.1.1 Boundary Layer Regime ($\Omega\gg 1$). The above equations can be considerably simplified for the boundary layer regime for which $\Omega\gg 1$. For this situation we have that $I_0(\Omega r)\approx e^{\Omega r}(1+1/8\Omega r+\cdots)/\sqrt{2\pi\Omega r}$, $I_1(\Omega r)\approx e^{\Omega r}(1-3/8\Omega r+\cdots)/\sqrt{2\pi\Omega r}$, $K_0(\Omega r)\approx\sqrt{\pi}e^{-\Omega r}(1-1/8\Omega r+\cdots)/\sqrt{2\Omega r}$ and $K_1(\Omega r)\approx\sqrt{\pi}e^{-\Omega r}(1+3/8\Omega r+\cdots)/\sqrt{2\Omega r}$. After a considerable amount of algebra, it is found that X_1 and X_2 are now given by

$$X_1=-[\ln\eta+(1-\eta^2)/\eta\Omega]\quad X_2=-[\ln\eta+3(1-\eta^2)/2\eta\Omega] \tag{29}$$

Also, it is found that Eq. (26) reduces to

$$\Psi_0^2=\frac{\Omega^2K_0}{2r_i^2K_1}(1\pm\sqrt{1-\zeta}) \tag{30}$$

where $\Psi_0=\Gamma/r_i\Omega^2$ and

$$K_0=[\mathrm{Le}^2+\varphi-a\varphi(1+Le)]\ln\eta\quad K_1=\mathrm{Le}^2(1+\varphi)\Omega\ln\eta$$

$$K_2=(1+\varphi)\Omega^2\quad \zeta=\frac{4K_1K_2}{\Omega^4K_0^2} \tag{31}$$

There again the value of Ω must be evaluated by solving numerically the above equation. However, upon assuming that $\zeta\to 0$ it is found that the solution of Eq. (30) is given by

$$\Omega=\left(\frac{\eta}{\alpha_0}\right)^{1/5}R_T^{2/5}(1+\varphi)^{2/5}\quad \psi_0^2=\frac{\alpha_0}{\eta\Omega} \tag{32}$$

where $\alpha_0=[\varphi+\mathrm{Le}^2-a\ \varphi(1+\mathrm{Le})]/(1+\varphi)\mathrm{Le}^2$ must be positive to obtain a real solution of Eq. (32), i.e.

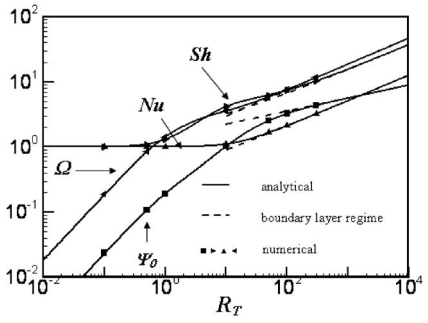

Fig. 4 Comparison between analytical and numerical solutions for the case $\varphi=1$, Le=10, and $\eta=0.3$. Effect of R_T on Ω, Ψ_0, Nu and Sh for $a=0$ (double diffusive convection)

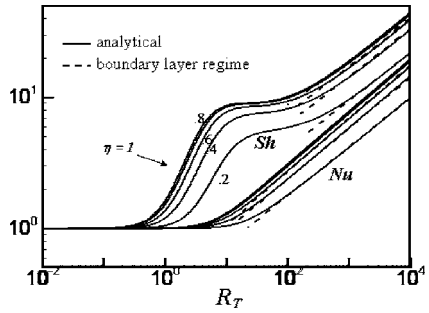

Fig. 5 Comparison between analytical and boundary layer solutions for the case $\varphi=0.01$, Le=10, $a=1$ and various values of η; effect of R_T on Nu and Sh

$$\varphi \leqslant \frac{\mathrm{Le}^2}{a(1+\mathrm{Le})-1} \tag{33}$$

which is an excellent approximation to the boundary layer regime ($\zeta \to 0$) and this for a wide range of the governing parameters.

From Eqs. (27)–(29) and (32), the Nusselt and Sherwood numbers are given by

$$\mathrm{Nu} = \frac{1-\alpha_0(3-Y)}{1+\alpha_0(1-4/Y)} \tag{34}$$

$$\mathrm{Sh} = \frac{1-\mathrm{Le}^2\alpha_0(3-Y)}{1+\mathrm{Le}^2\alpha_0(1-4/Y)+so} \tag{35}$$

where $Y=2\Omega G(\eta)$, $G(\eta)=\eta \ln \eta/(\eta^2-1)$ and $so=a(1+\mathrm{Le})(1-\eta)/\eta \ln \eta\, \mathrm{Nu}$. In the limit $Y \to \infty$, Eqs. (34) and (35) reduce to

$$\mathrm{Nu} = 2\alpha_1 G(\eta)\Omega + (1-4\alpha_1+4\alpha_1^2)\left(\sum_{i=1}^{n}(Y_1)^i\right) \tag{36}$$

$$\mathrm{Sh} = 2\alpha_2 G(\eta)\Omega + (1-4\alpha_2+4\alpha_2^2-\alpha_3)\left(1+\sum_{i=1}^{n}(Y_2)^i\right) \tag{37}$$

where $\alpha_1=\alpha_0/(1+\alpha_0)$, $\alpha_2=\alpha_0\mathrm{Le}^2/(1+so+\alpha_0\mathrm{Le}^2)$, $\alpha_3=\alpha_2 so/\alpha_0\mathrm{Le}^2$, $Y_1=4\alpha_1/Y$ and $Y_2=4\alpha_2/Y$.

For a rectangular cavity $\eta \to 1$ and $G(\eta) \to 1/2$ it is readily found that

$$\mathrm{Nu} = \alpha_1\Omega + (1-4\alpha_1+4\alpha_1^2)\left(\sum_{i=1}^{n}(Y_1)^i\right) \tag{38}$$

$$\mathrm{Sh} = \alpha_2\Omega + (1-4\alpha_2+4\alpha_2^2-\alpha_3)\left(1+\sum_{i=1}^{n}(Y_2)^i\right) \tag{39}$$

where $Y_1=4\alpha_1/\Omega$ and $Y_2=4\alpha_2/\Omega$.

Figure 4 exemplifies the effect of the thermal Rayleigh number R_T on ψ_0, Ω, the Nusselt number Nu, and the Sherwood number Sh for the case $\varphi=1$, Le=10, $\eta=0.3$, and $a=0$ (double diffusive convection). The analytical solution represented by solid lines, Eqs. (23)–(28), is seen to be in excellent agreement with the numerical solution of the full governing equations, depicted by closed symbols. Figure 4 shows that when the thermal Rayleigh number is small enough ($R_T \leqslant 1$) both the side-to-side heat and mass transfers are ruled by pure diffusion and Nu and Sh become of order one. Upon increasing the value of the thermal Rayleigh number both Nusselt and Sherwood numbers increase monotonously with R_T up to $R_T \geqslant 10^2$ where the boundary layer regime is reached. This situation will be discussed later on. The variation of ψ_0 and Ω, as predicted by the present theory, is also presented, for convenience, in the graph. It is noted that the inverse of Ω is a measure of the thickness of the boundary layers adjacent to the vertical walls of the cavity.

Figure 5 illustrates the effect of Rayleigh number R_T and curvature η on the Nusselt and Sherwood numbers, Nu and Sh, for the case $\varphi=0.01$, Le=10, and $a=1$. At very low Rayleigh numbers both the Nusselt and Sherwood numbers approach unity for all radius ratios η. This follows from the fact that Nu and Sh have been normalized with respect to the pure conduction value $r_i \ln \eta$. An increase in R_T is naturally always associated with the decrease of ΔT and ΔS. As indicated by Fig. 5, Nu and Sh depend on η. At a given R_T, both Nu and Sh are observed to increase as the value of η is made larger.

Equations (36) and (37) can be further reduced by considering two important extremes in which the present phenomena can exist, namely

4.1.2 Heat-Transfer-Driven Boundary Layer Flows. Heat-transfer-driven boundary layer flows, which are dominated by the buoyancy effect due to side heating such that the condition $|\varphi \ll 1|$ is satisfied, are now discussed. Under these circumstances, Eqs (36) and (37) in the limit $\mathrm{Le} \gg 1$, reduce to

$$\mathrm{Nu} = G(\eta)\Omega \quad \mathrm{Sh} = (1+2\mathrm{Nu}) \tag{40}$$

where $\Omega=\eta^{1/5}R_T^{2/5}(1+\varphi)^{2/5}$ and $G(\eta) \to 1/2$ when $\eta \to 1$.

The asymptotic behavior of the Nusselt and Sherwood numbers, as predicted by the above equations, is represented in Fig. 5 as dotted lines. It is observed that the start of the boundary layers depends upon η. The higher the radius ratio is, the larger the Rayleigh number required to reach the boundary layer.

On the other hand, in the limit $\mathrm{Le} \ll 1$, it is found that

$$\begin{aligned} \mathrm{Nu} &= 2G(\eta)\alpha_1\Omega + 1 - 4\alpha_1 + 4\alpha_1^2 \\ \mathrm{Sh} &= 2G(\eta)\alpha_2\Omega + 1 - 4\alpha_2^2 - \alpha_3 Le \end{aligned} \tag{41}$$

4.1.3 Mass-Transfer-Driven Boundary Layer Flows. Mass-transfer-driven boundary layer flows, where the buoyancy is caused primarily by concentration variation where the condition $|\varphi| \gg 1$ is satisfied. For this situation Eqs. (34) and (35) yield

For $\mathrm{Le} \gg 1$

$$\begin{aligned} \mathrm{Nu} &= 2G(\eta)\alpha_1\Omega + 1 - 4\alpha_1 + 4\alpha_1^2 \\ \mathrm{Sh} &= 2G(\eta)\alpha_2\Omega + 1 - 4\alpha_2 + 4\alpha_2^2 - \alpha_3 \end{aligned} \tag{42}$$

and for $\mathrm{Le} \ll 1$

$$\begin{aligned} \mathrm{Nu} &= 2G(\eta)\alpha_1\Omega + 1 \\ \mathrm{Sh} &= 2G(\eta)\alpha_2\Omega + 1 \end{aligned} \tag{43}$$

The above approximate solutions for $\mathrm{Le} \gg 1$, are more precise than predicted by [22] for $\eta \to 1$ especially when Ω is small. As an

example, for $R_T=100$, $\varphi=10^{-3}$, Le=10, $\eta=1$, and $a=0$, Eq. (40) gives a Sherwood number Sh=8.35 which is close to that predicted by the exact solution Eq. (28), namely Sh=8.37. On the other hand, for the same case the value of the Sherwood number predicted by [22] is Sh=6.31, the deviation of this result from the exact solution being about 25%. In addition, the above approximate solutions are valid for a large range of the Lewis number, Le, and buoyancy ratio φ, and this even when the two buoyancy forces are approximately equal. Available solutions in the literature ($\eta=1$) are only concerned with asymptotic situations such as the heat driven flows and the solute driven flows for which $\varphi \rightarrow 0$ and $\varphi \rightarrow \infty$ respectively.

4.2 Case of $\Lambda \leqslant 0$. For this situation the parameter $\omega^2=-\Lambda$ is considered. Thus, the solution for this situation is obtained by substituting $i\omega=\Omega$ into Eqs. (20) and (28). The resulting solution is very similar with the functions $I_0(i\omega r)$, $K_0(i\omega r)$, $I_1(i\omega r)$, and $K_1(i\omega r)$, merely replaced by the modified Bessel functions $J_0(i\omega r)$, $Y_0(i\omega r)$, $J_1(i\omega r)$, and $Y_1(i\omega r)$.

For instance the value of the stream function, Eq. (20), is now expressed by

$$\Psi(r) = -r_i \Psi_0 \frac{1+f(r)}{1+f(\xi)} \tag{44}$$

where

$$f(r) = r[C_1 J_1(\omega r) + C_2 Y_1(\omega r)]$$
$$\Psi_0 = \frac{\Gamma}{r_i \omega^2}[1+f(\xi)] \tag{45}$$

The transcendental equation (26) is then given by

$$b^2 \mathrm{Le}^2 \Psi_0^4 + b(1+\mathrm{Le}^2)\Psi_0^2 - \frac{2bR_T}{c\Omega^2}\{1+\varphi[\mathrm{Le}^2 - a(1+\mathrm{Le})]\Psi_0 + (1+\varphi)b\ \mathrm{Le}^2 \Psi_0^3\} + 1 = 0 \tag{46}$$

4.3 Effect of Buoyancy Ratio φ. The effect of buoyancy ratio φ on the stream function, temperature, and concentration contours is demonstrated in Fig. 6 for the case $R_T=50$, Le=10, $\eta=0.5$, $A=8$, $a=1$ and various values of φ. The flows direction in the graphs can be easily identified according to the distributions of temperature or solute. As a result of the thermal and solutal boundary conditions considered here, the direction of the flow induced by the thermal buoyancy forces is clockwise, whereas that imposed by the solutal buoyancy forces depends upon the sign of the concentration coefficient β_s in the state equation. Thus the direction of the solutal flow is clockwise for β_s (i.e., $\varphi>0$) and counterclockwise for β_s (i.e. $\varphi<0$).

Figure 6(*a*) shows the results obtained at $\varphi=0$ for which the effect of the concentration is nil such that the resulting clockwise circulation is completely governed by the temperature gradients. When the buoyancy ratio is increased above zero ($\varphi>0$), the mass species and thermal buoyancy forces are augmenting each other, and thus they accelerate the flow clockwise. This is the region of aiding flows. Figure 6(*b*) illustrates the results obtained for a large buoyancy ratio $\varphi=10$ for which the flow is dominated by the mass species buoyancy forces. The results indicate that a large portion of the fluid in the center of the annulus is stagnant because of the blocking effect of the vertical stratification of the density field. The boundary layer character of the flow pattern is noticed. When the buoyancy ratio is decreased below zero $\varphi<0$, the mass species and thermal buoyancy forces are counteracting each other and the resulting flow pattern evolutes from a thermal-dominated clockwise vortex (Fig. 6(*a*)) to a solutal-dominated counterclockwise circulation, as exemplified in Fig. 6(*c*) for the case $\varphi=-10$. As discussed in the following, for intermediate values of φ the transition between thermally and solutably dominate

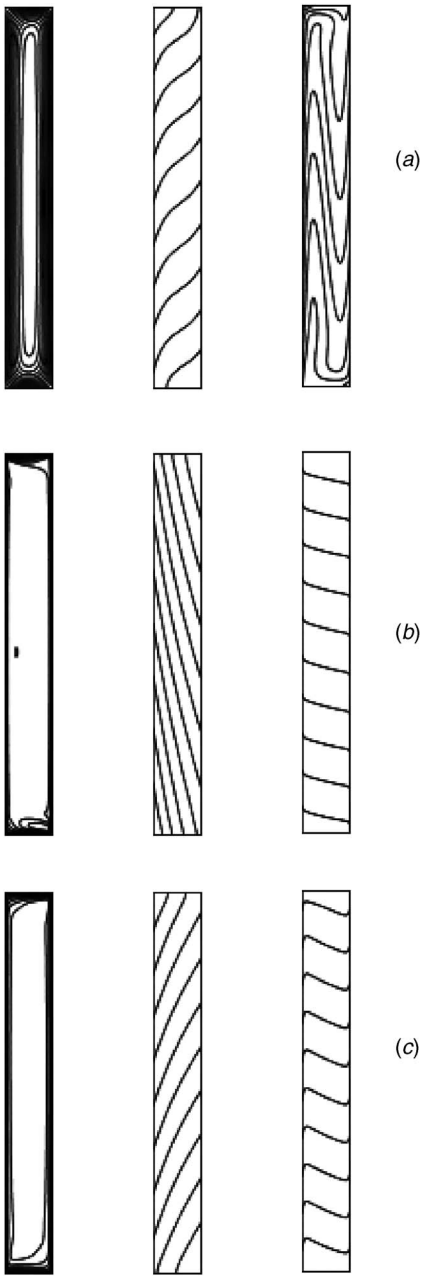

Fig. 6 Contour lines of stream function (left), temperature (center), and concentration (right) for $R_T=50$, Le=10, $\eta=0.5$, $a=1$, and $A=8$; (a) $\varphi=0$, (b) $\varphi=10$, and (c) $\varphi=-10$

flow is characterized by multicellular flow patterns in which thermal and mass species buoyancy forces dominate separate circulations within the enclosure.

The effect of the buoyancy ratio φ on Ψ_0 is illustrated in Fig. 7 for the case $R_T=50$, Le=10, $a=1$ and various values of curvature parameter, η. Here again an excellent agreement is observed between the analytical and the numerical results. The buoyancy ratio is varied in the range −9 to 9. This covers the spectrum from opposed but solutal-dominated flow $\varphi=-9$, to purely thermal-dominated flow ($\varphi=0$) to aided solutal-dominated flow $\varphi=9$. When φ is above zero the thermal and solutal buoyancy forces act in the same direction (aiding flow). The values of Ψ_0 are positive indicating a clockwise flow circulation. Increasing the buoyancy ratio from 0 to 9 the flow becomes more and more dominated by the mass species buoyant forces. When φ is below zero the ther-

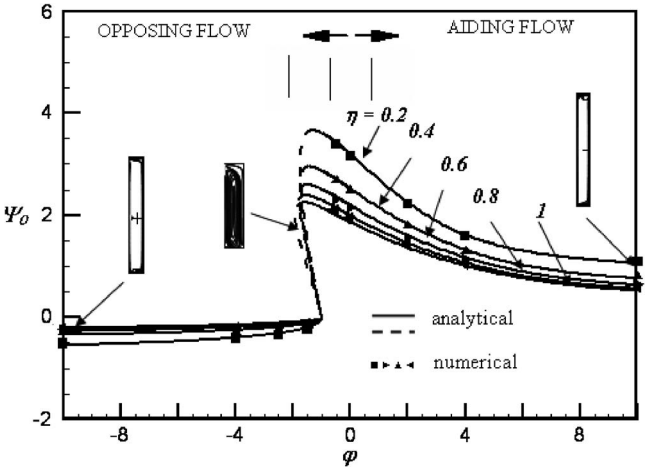

Fig. 7 Effect of the buoyancy ratio φ on the amplitude Ψ_0 for the case R_T=50, Le=10, a=1, and various values of η

mal and solutal buoyancy forces act now in opposing directions. In the range $-1 \leq \varphi \leq 0$ the thermal buoyancy forces are clearly dominating the flow such that Ψ_0 remains positive. As the value of φ is decreased below -1 the analytical model predicts the existence of three possible solutions for a given value of φ. Two solutions, represented by solid lines, correspond to unicellular flows. The flows, corresponding to the upper branches, are induced by the thermal buoyancy forces and thus circulate in the clockwise direction. For the lower branches the flows are driven by the solutal effects yielding a counterclockwise circulation. These two type unicellular flow branches are connected by dashed lines which correspond to flow patterns consisting in three vertical counterrotating cells. The range of φ, for which these multicellular flows patterns exist, depends slightly upon the value of η.

Numerical confirmation of the existence of multiple solutions is illustrated in Fig. 8 for the case R_T=50, Le=10, φ=−1.8, A=4, and a=1. The results obtained for the case of a rectangular cavity (η=1), Fig. 8(a), are first discussed. The first result (i) shows a

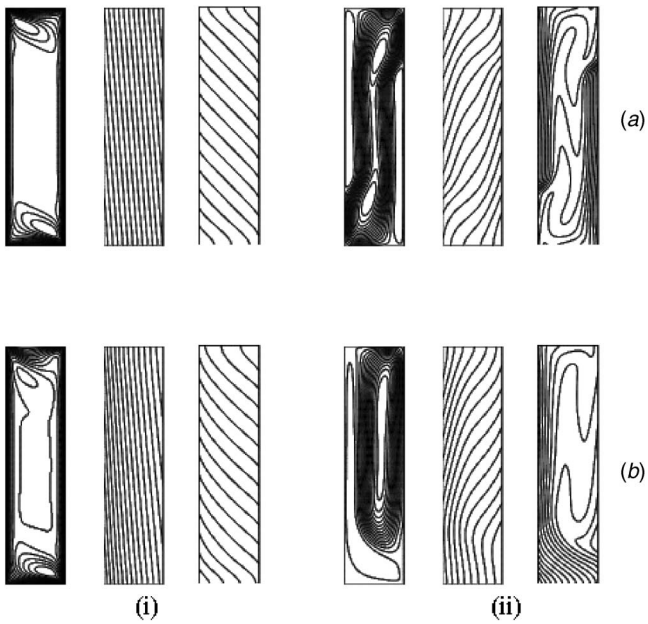

Fig. 8 Contour lines of stream function (left), temperature (center), and concentration (right) for R_T=50, Le=10, φ=−1.8, a=1, A=4, and (a) η=1 and (b) η=0.5

counterclockwise unicellular circulation corresponding to the lower solutal branch. This solution was obtained using, as initial conditions, the numerical results obtained for φ=−3, i.e., a strong counterclockwise flow dominated by the mass species buoyancy force. The second result (ii) indicates the existence of a large clockwise rotating cell in the core of the cavity, induced by the thermal buoyancy forces and two smaller cells, adjacent to the vertical walls, induced by the solutal buoyancy forces. This flow configuration was obtained numerically starting the numerical code with a perturbated flow consisting in two vertical symmetrical cells. It is noted that, for the parameters considered here, it has not been possible to obtain the third solution predicted by the analytical model namely the thermally dominated unicellular clockwise circulation. Also it is noted that the results presented here were obtained for cavity with an aspect ration A=4 for which the flow is not fully parallel. This is due to the fact that for higher values of A steady state flows are not possible in a range of φ that depends upon curvature parameter η.

The effect of η on these solutions is illustrated in Fig. 8(b) for η=0.5. Multiple solutions are also observed for this situation but, naturally, the symmetry of the flows patterns is destroyed. Thus, the multicellular flow pattern consists now in only two cells. The concentration-governed eddy occurring near the outer wall at η=1 vanishes at η=0.5 due to the increase of the thermal-dominated vortex.

5 Conclusion

In this paper a study of natural convection in a vertical porous annulus filled with a binary fluid is carried out. Both the case of double-diffusive convection (a=0) and Soret-driven convection (a=1) are considered. The influences of the major system parameters on the present phenomenon have been predicted in two different ways, using an analytical approach based on the parallel flow approximation and a numerical solution of the full governing equations. The summary of the major results is as follows.

(i) Under the thermal and solutal boundary conditions imposed on the vertical walls of the enclosure it has been demonstrated numerically that the flow in the core of the cavity is almost parallel provided that the aspect ratio A is large enough. Based on this fact, an approximate analytical solution, valid for flows ranging from pseudo-conduction to boundary layer regimes, has been derived. Although the resulting analytical model requires a numerical procedure to solve a transcendental equation, this is by far a much easier task than solving numerically the full set of governing equations.

(ii) The parallel flow model proposed in this study has been found to be quite accurate in predicting the flow structure and heat and mass transfers for a wide range of the governing parameters. Useful approximate expressions have been derived to describe the boundary layer regime. Simplified equations for Nu and Sh have been obtained for heat-driven and solute-driven flow regimes. For the case of opposing flow the existence of multiple solutions, for a given set of the governing parameters, has been demonstrated analytically and numerically.

Nomenclature

a = real number
A = aspect ratio of the cavity, H'/L'
C = dimensionless concentration, $(N-N_0)/\Delta N$
C_S = dimensionless concentration gradient in z direction
C_T = dimensionless temperature gradient in z direction
D = mass diffusivity of species, $m^2\ s^{-1}$
D' = thermal diffusion coefficient, $m^2\ s^{-1}\ K^{-1}$

g = gravitational acceleration, m s^{-2}
H' = height of enclosure, m
j' = solute flux per unit area, kg m^{-2} s^{-1}
k = thermal conductivity, W m^{-1} K^{-1}
K = permeability of porous medium, m^2
L' = enclosure width$=r'_o-r'_i$, m
Le = Lewis number, α/D
ΔN = characteristic concentration$=$ $aN_0(1-N_0)\nabla T'D'/D-(1-a)j'/\rho_0 D$
q' = constant heat flux per unit area, W m^{-2}
S' = concentration of the denser component, kg m^{-3}
S'_0 = initial mass fraction
t = dimensionless time, $t'\alpha/L'^2$
T = dimensionless temperature, $(T'-T'_0)/\Delta T'$
$\Delta T'$ = characteristic temperature, $q'L'/k$
u = dimensionless velocity in r direction, $u'L'/\alpha$
w = dimensionless velocity in z direction, $w'L'/\alpha$
r, z = cylindrical polar coordinates, $r'/L', z'/L'$

Greek Symbols

α = thermal diffusivity, m^2 s^{-1}
μ = dynamic viscosity of fluid, kg m^{-1} s^{-1}
ν = kinematic viscosity of fluid, m^2 s^{-1}
θ = dimensionless temperature field
ρ = density of fluid, kg m^{-3}
$(\rho C)_f$ = heat capacity of fluid
$(\rho C)_p$ = heat capacity of saturated porous medium, J m^{-3} K^{-1}
σ = heat capacity ratio, $(\rho C)_p/(\rho C)_f$
η = curvature parameter, r'_i/r'_o
Ψ = dimensionless function, $\Psi'/\alpha L'$
ϕ = porosity of the porous medium

Subscripts

i = inner cylinder
o = outer cylinder

Superscript

$'$ = dimensional variable

References

[1] Montel, F., 1994, "Importance de la Thermodiffusion en Exploration et Production Petrolières," Entropie, **184-185**, pp. 86–93.
[2] Alavyoon, F., Eklund, A., Bark, F. H., and Simonsson, D., 1991, "Theoretical and Experimental Studies of Free Convection and Stratification of Electrolyte in a Lead-acid Cell during Recharge," Electrochim. Acta, **14**, pp. 2153–2164.
[3] Trevisan, O. V., and Bejan, A., 1985, "Natural Convection with Combined Heat and Mass Transfer Buoyancy Effects in a Porous Medium," Int. J. Heat Mass Transfer, **28**, pp. 1597–1611.
[4] Trevisan, O. V., and Bejan, A., 1986, "Mass and Heat Transfer by Natural Convection in a Vertical Slot Filled with Porous Medium," Int. J. Heat Mass Transfer, **29**, pp. 403–415.
[5] Masuda, Y., Yoneya, M., Ikeshoji, T., Kimura, S., Alavyoon, F., Tsukada, T., and Hozawa, M., 2002, "Oscillatory Double-diffusive Convection in a Porous Enclosure due to Opposing Heat and Mass Fluxes on the Vertical Walls," Int. J. Heat Mass Transfer, **45**, pp. 1365–1369.
[6] Ouazazi, M. N., and Bois, P. A., 1994, "Convective Instability of a Fluid Mixture in a Porous Medium With Time-dependent Temperature Gradient," Eur. J. Mech. B/Fluids, **13**, pp. 275–278.
[7] Marcoux, M., and Charrier-Mojtabi, M., 1998, "Etude Paramétrique de la Thermogravitation en Milieu Poreux," C. R. Acad. Sci., Ser. IIb: Mec., Phys., Chim., Astron., **326**, pp. 539.
[8] Joly, F., Vasseur, P., and Labrosse, G., 2001, "Soret Instability in a Vertical Brinkman Porous Enclosure," Numer. Heat Transfer, Part A **39**, pp. 339–359.
[9] Lorenz, M., and Emery, A. H., 1959, "The Packed Thermal Diffusion Column," Chem. Eng. Sci. **11**, pp. 16–23.
[10] Marcoux, M., and Charrier-Mojtabi, M., 1999, "Diffusion Thermogravitationnelle Dans un Mélange Binaire Saturant un Espace Annulaire Poreux Vertical," Entropie, **218**, pp. 8–12.
[11] Mamou, M., Hasnaoui, M., Amahmid, A., and Vasseur, P., 1998, "Stability of Double-diffusive Convection in a Vertical Brinkman Pourous Enclosure," Int. Commun. Heat Mass Transfer, **25**, pp. 491–500.
[12] Mamou, M., Vasseur, P., and Bilgen, E., 1998, "A Galerkin Finite Element Study of the Onset of Double-diffusive Convection in an Inclined Pourous Enclosure," Int. J. Heat Mass Transfer, **41**, pp. 1513–1529.
[13] Mamou, M., Vasseur, P., and Bilgen, E., 1998, "Double Diffusive Convection Instability Problem in a Vertical Porous Enclosure," J. Fluid Mech., **368**, pp. 263–289.
[14] Marcoux, M., Karimi-Fard, M., and Charrier-Mojtabi, M., 1999, "Naissance de la Convection Thermosolutale dans une Cellule Rectangulaire Poreuse Soumise à des Flux de Chaleur," Int. J. Therm. Sci., **38**, pp. 258–266.
[15] Joly, F., Vasseur, P., and Labrosse, G., 2000, "Soret Driven Thermosolutal Convection in a Vertical Enclosure," Int. Commun. Heat Mass Transfer, **27**, pp. 755–764.
[16] Alavyoon, F., Masuda, Y., and Kimura, S., 1994, "On Natural Convection in Vertical Porous Enclosures due to Opposing Fluxes of Heat and Mass Prescribed at the Vertical Walls," Int. J. Heat Mass Transfer, **37**, pp. 195–206.
[17] Mamou, M., Vasseur, P., and Bilgen, E., 1995, "Multiple Solutions for Double-diffusive Convection in a Vertical Porous Enclosure," Int. J. Heat Mass Transfer, **38**, 1787–1798.
[18] Amahmid, A., Hasnaoui, M., Mamou, M. and Vasseur, P., 2000, "On the Transition between Aiding and Opposing Double Diffusive Flows in a Vertical Porous Matrix," Int. J. Porous. Media, **3**, pp. 123–137.
[19] Amahmid, A., Hasnaoui, M., Mamou, M., and Vasseur, P., 1999, "Boundary Layer Flows in Vertical Pourous Enclosures Induced by Opposing Buoyancy Forces," Int. J. Heat Mass Transfer, **42**, pp. 3599–3608.
[20] De Groot, S. R., and Mazur, P., 1962, *Non Equilibrium Thermodynamics*, North Holland, Amsterdam.
[21] Patankar, S. V., 1980, *Numerical Heat Transfer and Fluid Flow*," Hemisphere, New York.
[22] Alavyoon, F., 1993, "On Natural Convection in Vertical Porous Enclosures due to Prescribed Fluxes of Heat and Mass at the Vertical Boundaries," Int. J. Heat Mass Transfer, **36**, pp. 2479–2498.
[23] Mamou, M., Vasseur, P., Bilgen, E., and Gobin, D., 1995, "Double-diffusive Convection in an Inclined Slot Filled with Porous Medium," Eur. J. Mech. B/Fluids, **14**, pp. 629–652.

D. B. Ingham
A. K. Al-Hadhrami
L. Elliott

Department of Applied Mathematics,
University of Leeds,
Leeds LS2 9JT, UK

X. Wen
School of the Environment,
University of Leeds,
Leeds LS2 9JT, UK

Fluid Flows Through Some Geological Discontinuities

In this paper the fluid flow through some composite channels has been investigated in the physical parameter ranges appropriate to some flows in geological applications. In particular, we have considered the fluid flow through a composite channel that has undergone a vertical fracture. The vertical connecting channel is also composed of a composite material. In such physical situations, the materials undergo several orders of magnitude changes in their Darcy numbers. This results in very large changes in the pressure in the vicinity of the interfaces between these materials. Therefore it is necessary to develop mathematical and numerical techniques to deal with such situations and in this paper an approach is presented. [DOI: 10.1115/1.1991861]

1 Introduction

Fluid flow through porous media is encountered in many different branches of science and engineering, ranging from agricultural, chemical, civil, and petroleum engineering, to food and soil sciences, see Nield and Bejan [1] and Ingham and Pop [2,3]. In particular, the processes of such fluid flows have attracted the attention of scientists, engineers, and politicians who recognize the economical importance of enhancing oil recovery techniques, in addition to their growing concerns about pollution and water quality extracted from ground water flows. Over the past decades, flows through porous media have extensively been studied experimantally and theoretically. The one-dimensional problem studied by Darcy [4] has served as a starting point for numerous practical examples and it is a constant challenge for theoreticians. While the original conditions studied by Darcy are found in many practical situations, it is the existence of more general situations that are especially deserving of theoretical analysis as they usually represent situations in which experiments are difficult to perform.

The main focus of this paper is to consider numerical investigations of fluid flow through some geological configurations involving discontinuities in channel height and where different sections of the channel are composed of several different layers of different porous materials. The effects of these discontinuities on the fluid flow through the regions of different permeabilities is demonstrated by presenting for each situation both the streamline pattern and the change in the overall pressure. The discontinuities and the layered system channels are demonstrated since they are the typical physical phenomena that occur in oil reservoirs and groundwater flows. For example, oil is found underground, trapped in the interstices of porous rocks such as sandstone and limestone. An oil bearing stratum will have above it an impermeable rock, such as clay or shale, which prevents the oil from migrating upward. There will be a horizontal variation of the depth of the stratum due to an upward dome or an upward slant terminated by an impermeable fault, which prevents the oil from moving sideways, or a permeable fracture, which creates a cavity where the oil can flow through.

The governing equation for flows through geological structures is the Brinkman equation which has to be solved along with the continuity equation. If the Darcy number ($=k/H^2$, where k is the permeability of the porous media and H is a typical length scale) is of the order of unity or is infinite then it is fairly easy to obtain numerical solutions of these equations even in complex geometries. However, values of the permeability vary widely for natural materials and typical values of k, in units of m^2, are as follows: sand 1.8×10^{-10}, sandstone, 1.0×10^{-12}, limestone 4.5×10^{-14}, and shale 1.0×10^{-16}, see Scheidegger [5]. Thus if we take the characteristic length, in units of m, to be in the range $10^{-1}\leqslant H\leqslant10^{2}$ then for a channel filled with sandstone the Darcy number is in the range $10^{-16}\leqslant \mathrm{Da}\leqslant10^{-10}$. These are typical values of the Darcy number in geological situations.

2 Mathematical Model

The focus of this paper is to consider some of these real physical values of Da in solving flow through composite channels that incorporate the geological features of both faults and fractures. Unfortunately, on implementing very small values of Da in the nondimensional Brinkman equation then the numerical results of the discretized form of the Brinkman equation are found to converge extremely slowly. For example, the solution for flow in a channel with $H=1$ m which is filled with sandstone, where Da $=1.0\times10^{-12}$, takes approximately four weeks of CPU time (where all the CPU times stated in this paper are based on using a SUN workstation with an ULTRA 10 processor) to converge into a fully developed solution. This is because of the high resistance provided by the Darcy parameter, $\alpha=\Gamma/\mathrm{Da}$, in the Brinkman equation, and hence for a given nondimensional flux of fluid through the channel then extremely large values of the pressure gradient are required in order to balance the Darcy term, $\alpha\mathbf{v}$.

In addition, the presence of large velocity gradients close to the boundaries can also slow down the rate of convergence. In most of the previous investigations in this class of problems, both impermeable and no slip boundary conditions on the perimeter of the channels have been assumed and hence the conditions $u=v=w=0$, where u, v, and w are the velocity components in the Cartesian coordinate directions x, y, and z, respectively, have been implemented on the boundaries. However, in order to attempt to speed up the rate of convergence for very small values of the Darcy number, say $\mathrm{Da}\leqslant10^{-5}$, in this paper a set of boundary conditions that avoids the large velocity gradients on the boundary, while maintaining the same flow structure throughout the rest of the configuration, has been introduced. In particular, while we have retained the zero normal velocity on the boundary, rather than enforce the zero tangential velocity condition we have assumed that the normal gradient of the tangential velocity is zero on the boundary, as this would be the appropriate boundary condition for Darcy flow. Thus in the two-dimensional situation we have imposed $v=\partial u/\partial y=0$ on the upper and lower surfaces of horizontal channels, and $u=\partial v/\partial x=0$ on the sides of vertical

Contributed by the Applied Mechanics Division of ASME for publication in the JOURNAL OF APPLIED MECHANICS. Manuscript received May 24, 2004; final manuscript received May 6, 2005. Assoc. Editor: D. Siginer. Discussion on the paper should be addressed to the Editor, Prof. Robert M. McMeeking, Journal of Applied Mechanics, Department of Mechanical and Environmental Engineering, University of California - Santa Barbara, Santa Barbara, CA 93106-5070, and will be accepted until four months after final publication of the paper itself in the ASME JOURNAL OF APPLIED MECHANICS.

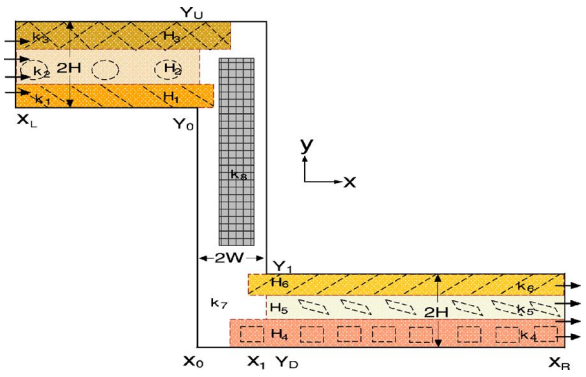

Fig. 1 A schematic diagram of the problem when fluid flows through a two-dimensional geometrical configuration consisting of inlet and outlet composite channels which are linked by a vertical channel

channels, which is linked with the horizontal channel. However, the extremely slow convergence rates at small values of permeability still prevail, increasing by only about 2% compared to when implementing the no slip boundary condition. This suggests that the large velocity gradients near solid surfaces are not the cause of the slow convergence and exactly what is the cause is more debatable.

Numerical accuracy is another factor that requires consideration. Since, when imposing a constant flux of fluid, the pressure gradient can change over several orders of magnitude as the Darcy number is modified, for example, from $\mathrm{Da}=10^{-2}$ to $\mathrm{Da}=10^{-16}$ then the pressure gradient changes from 10^2 to 10^{16}. Hence in such situations the convergence criteria must be based on the mass residual, rather than on the maximum difference between the velocity and the pressure values at successive iterations, since this latter condition assumes that both these physical quantities are of approximately the same order of magnitude. Likewise, it should be noted that when fixed pressure gradients are imposed, and the flux of fluid is allowed to adjust accordingly over such a range of values of the Darcy parameter, then for situations resulting in very small flow rates, a convergence criteria based on the mass residual will no longer be appropriate. This arises because the magnitude of the fluid velocity itself will be very small and hence the mass residual would be required to be even smaller in order to achieve accurate results.

The aim of this paper is to present a technique in order to accelerate the rate of convergence of the control volume method (CVM) for solving the Brinkman and continuity equations when implementing very small values of the Darcy number $\mathrm{Da}\lesssim 10^{-5}$ on various numerical investigations of flow through some geological discontinuities of the composite channel presented in Fig. 1. This figure corresponds to the flow through a two-dimensional geometrical configuration composed of inlet and outlet channels which are linked by a vertical channel. The upper and lower surfaces of the horizontal channels are assumed to be impermeable and the lengths of these channels to be sufficiently long for fully developed solutions to be reached. In addition, the vertical sides and the upper and lower ends of the vertical channel are taken to be closed and the length of the channel sufficient for the flow details throughout the majority of the channel to be independent of its length. Situations analogous to the present configuration can be found in oil reservoirs composed of several layers of sandstone or sand and impermeable shales in which faults and fractures are located, see Clennell [6] and Lesnic et al. [7].

3 Mathematical Formulation

The general steady Brinkman and continuity equations are given by

$$\mathcal{P}(\mathbf{V}\cdot\nabla)\mathbf{V} = -\nabla P + \tilde{\mu}\nabla^2\mathbf{V} - \frac{\mu_f}{k}\mathbf{V} \tag{1}$$

$$\nabla(\mathcal{P}\mathbf{V}) = 0 \tag{2}$$

We now introduce the following nondimensional variables:

$$\mathbf{V} = U_0\mathbf{v}, \quad P = \alpha^*\frac{\tilde{\mu}U_0}{H}p, \quad \mathbf{X} = H\mathbf{x}, \quad \mathcal{P} = \rho_0\rho, \quad Da_i = \frac{k_i}{H^2} \tag{3}$$

where $i=1,2,\ldots,$ represents the different materials within the structure, and ρ_0 and U_0 are the reference fluid density and velocity, respectively. On substituting these quantities into Eqs. (1) and (2), we obtain the following nondimensional steady Brinkman and continuity equations:

$$\rho\frac{\Gamma}{\alpha^*}(\mathbf{v}\cdot\nabla)\mathbf{v} = \frac{1}{\mathcal{R}}\left[-\nabla p + \frac{1}{\alpha^*}\nabla^2\mathbf{v} - \frac{\alpha_i}{\alpha^*}\mathbf{v}\right] \tag{4}$$

$$\nabla(\rho\mathbf{v}) = 0 \tag{5}$$

Thus it can be seen that at large values of α_i, i.e., small Darcy numbers, the dominant terms in Eq. (4) are the pressure gradient and the Darcy term $(\alpha_i/\alpha^*\mathbf{v})$, which are both O(1) in the region where $\alpha_i=\alpha^*$. In addition, the magnitudes of the inertia and diffusion terms are negligible in comparison with the magnitudes of these dominant terms. Hence the nondimensional Brinkman Eq. (4) reduces effectively to the Darcy equation for $\mathrm{Da}\ll 1$. Therefore, it has been found that the Brinkman equation, in the form given by Eq. (4), enables us to consider very small values of the Darcy number, together with much improved rates of convergence.

4 Approach to the Average Pressure Correction (APC)

When implementing the modified version of the Brinkman Eq. (4) for a composite channel where the ratio of the lowest permeability to the highest permeability of the different media is less than about 10^{-3} m^2, i.e., the ratio of the largest to the smallest Darcy parameter is $\gtrsim 10^3$, then difficulties arise in securing a converged numerical solution using the CVM. The presence of a low relative permeability, by several orders of magnitude relative to elsewhere in the channel, can result in a large and rapid pressure drop and hence a very slow convergence rate in the solution procedure. This slow convergence results from the global mass conservation being obtained from the local mass conservation through the pressure correction equation, see Al-Hadhrami et al. [8], which is not sensitive to changes in the fluid velocity caused by rapid changes in the permeability of the porous media. Hence, the iterative procedure requires many iterations to establish the large pressure gradients.

Based on the global mass conservation principle, Wen and Ingham [9] integrated the momentum equation for an approximate one-dimensional flow and derived a line average pressure correction from an average velocity correction. This pressure correction can significantly accelerate the rate of convergence of the iterative procedure when rapid changes are present due to changes in the physical properties within the solution domain. Next, Wen and Ingham [9] developed a procedure for dealing with the large pressure drops which are produced when fluid is forced to flow through a filter paper, again resulting in a significantly accelerated rate of convergence of the iterative scheme when the resistance from the filter is large.

In order to obtain convergent results for small permeability values in the present work, a similar procedure to that proposed by Wen and Ingham [9,10] is employed, but now related to a horizontal fluid flow across an arbitrary thick vertical porous media composed of two different Darcy parameters $\bar{\alpha}_1$ and $\bar{\alpha}_2$ rather than to a thin filter paper. The technique can also be generalized to situations when the porous media is composed of any number of

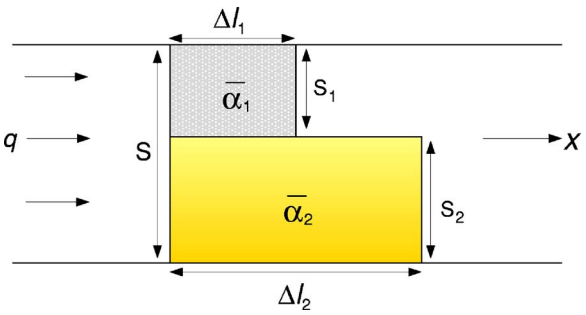

Fig. 2 The geometry of a horizontal fluid flow across an arbitrary vertical porous media composed of two Darcy parameters $\bar{\alpha}_1$ and $\bar{\alpha}_1$ of thicknesses Δl_1 and Δl_2, and cross-sectional areas S_1 and S_2, where $S_1+S_2=S$

Darcy parameters. Likewise, the same analysis is valid when there is a vertical fluid flow across a horizontal porous media, except for the change of the parameters which relate to the vertical flow, e.g., the fluid velocity and the mesh sizes.

In the porous media the momentum change in the x direction and the shear stress are both small compared with the resistance. Thus, the Brinkman Eq. (4) simplifies to the Darcy equation and the resistance is balanced by a large pressure drop in the x direction. Therefore, when there are two porous regions with Darcy parameters $\bar{\alpha}_1$ and $\bar{\alpha}_2$ and areas S_1 and S_2, where $S_1+S_2=S$ is the total cross-sectional area of the porous media as shown in Fig. 2, then the governing equations can be approximated by

$$\left(\frac{\Delta \bar{p}_1}{\Delta l_1}\right) = -\bar{\alpha}_1 \bar{u}_1 \tag{6}$$

$$\left(\frac{\Delta \bar{p}_2}{\Delta l_2}\right) = -\bar{\alpha}_2 \bar{u}_2 \tag{7}$$

where $\bar{\alpha}_1=\alpha_1/\alpha^*$, $\bar{\alpha}_2=\alpha_2/\alpha^*$, and α^* can be taken to be either α_1 or α_2, Δl_1 and Δl_2 are the thicknesses in the x direction of the porous regions $\bar{\alpha}_1$ and $\bar{\alpha}_2$, respectively, $\bar{u}_1$ and $\bar{u}_2$ are the average velocities, and $\bar{p}_1$ and $\bar{p}_2$ are the corresponding average pressures. If q^* and $\bar{u}^*$ are assumed to be the updated total flux of fluid and updated total average fluid velocity, respectively, in the x direction, and q' and $\bar{u}'$ the corrections of the total flux of fluid and total average velocity, respectively, then

$$q = q^* + q' \quad \text{and} \quad \bar{u} = \bar{u}^* + \bar{u}' \tag{8}$$

The total average velocity correction is obtained by using the global mass conservation principle, namely,

$$\int_S (\bar{u}^* + \bar{u}')dS = q \tag{9}$$

and this yields the total average velocity of fluid correction as

$$\bar{u}' = \frac{q - \int_S \bar{u}^* dS}{\int_S dS} \tag{10}$$

where q is the total specified flux of fluid in the x direction, which is given by

$$q = \int_S \bar{u} dS = \int_{S_1} \bar{u}_1 dS + \int_{S_2} \bar{u}_2 dS \tag{11}$$

Substituting $\bar{u}_1$ and $\bar{u}_2$ from Eqs. (6) and (7) into (11) results in

$$q = -\frac{1}{\bar{\alpha}_1}\int_{S_1} \frac{\Delta \bar{p}_1}{\Delta l_1} dS - \frac{1}{\bar{\alpha}_2}\int_{S_2} \frac{\Delta \bar{p}_2}{\Delta l_2} dS \tag{12}$$

If we let $\bar{p}_1'$ and $\bar{p}_2'$ be the average pressure corrections, and $\bar{p}_1^*$ and $\bar{p}_2^*$ be the updated values of the average pressure, then the correct average pressures for each of the regions are given by

$$\bar{p}_1 = \bar{p}_1^* + \bar{p}_1', \quad \bar{p}_2 = \bar{p}_2^* + \bar{p}_2' \tag{13}$$

Inserting the values of q and $\bar{p}_1$ and $\bar{p}_2$ from expressions (8) and (13) into Eq. (12) yields

$$q^* + q' = -\frac{1}{\bar{\alpha}_1}\int_{S_1} \left(\frac{\Delta \bar{p}_1^*}{\Delta l_1} + \frac{\Delta \bar{p}_1'}{\Delta l_1}\right) dS - \frac{1}{\bar{\alpha}_2}\int_{S_2} \left(\frac{\Delta \bar{p}_2^*}{\Delta l_2} + \frac{\Delta \bar{p}_2'}{\Delta l_2}\right) dS \tag{14}$$

The updated values of the flux of fluid q^* and pressures $\bar{p}_1^*$ and $\bar{p}_2^*$ satisfy Eq. (12), and hence combining Eqs. (12) and (14) results in the following:

$$q' = -\frac{1}{\bar{\alpha}_1}\int_{S_1} \frac{\Delta \bar{p}_1'}{\Delta l_1} dS - \frac{1}{\bar{\alpha}_2}\int_{S_2} \frac{\Delta \bar{p}_2'}{\Delta l_2} dS \tag{15}$$

Based upon the assumption that the average pressure on the rear faces of the two porous regions $\bar{\alpha}_1$ and $\bar{\alpha}_2$ are of approximately the same order of magnitude, and likewise on the front faces, then

$$\Delta \bar{p}_1' \simeq \Delta \bar{p}_2' \tag{16}$$

On substituting Eq. (16) into Eq. (15), we obtain

$$q' \simeq \left[-\frac{1}{\bar{\alpha}_1} S_1 - \frac{1}{\bar{\alpha}_2} S_2 \frac{\Delta l_1}{\Delta l_2}\right] \frac{\Delta \bar{p}_1'}{\Delta l_1} \tag{17}$$

When the pressure nodes are located on the two sides of the porous media, expression (17) can be modified to the form

$$\Delta \bar{p}_1' \simeq -\frac{\bar{\alpha}_1 \bar{\alpha}_2 q' \Delta l_1}{\left[\bar{\alpha}_2 S_1 + \bar{\alpha}_1 S_2 \frac{\Delta l_1}{\Delta l_2}\right]} \tag{18}$$

where $\Delta \bar{p}_1'$ is the difference between the pressure corrections on the two sides of the porous region $\bar{\alpha}_1$. Furthermore, if we let the average pressure correction in front of the porous media take the value of zero then we obtain the average pressure correction (APC) across the porous media as

$$\bar{p}_1' \simeq -\frac{\bar{\alpha}_1 \bar{\alpha}_2 q' \Delta l_1}{\left[\bar{\alpha}_2 S_1 + \bar{\alpha}_1 S_2 \frac{\Delta l_1}{\Delta l_2}\right]} \tag{19}$$

The value of the APC in Eq. (19) should then be added to the pressure in the domain downstream of the porous media such that the pressure in this region becomes

$$p = p^* + \alpha_p p' + \alpha_a \bar{p}_1' \tag{20}$$

where α_p is an under-relaxation factor that takes a value of about 0.4 or even less. The relaxation factor α_a takes a small value in order to avoid an overcorrection when the Darcy parameters are very large; for example, when the value of $(\bar{\alpha}_1 \bar{\alpha}_2 \Delta l_1)=10^{20}$, we set $\alpha_a=10^{-3}$ or less. The APC should be used in the CVM after each global iteration. In addition, although expression (19) is established as the additional pressure correction required from one side of the media to the other side, it should be subdivided and applied on a series of lines within the media, using different constants of proportionality for $\bar{\alpha}_1$ and $\bar{\alpha}_2$, with the number of lines applied depending on the thickness of the low permeable porous media. However, as mentioned above, the value on the last line after which this technique is not employed should be added to all the grid nodes located downstream of this line in order to maintain the same flux of fluid q. Further, it should be noted that the APC

formula (19) can be employed provided that the approximations assumed in establishing Eq. (16) are satisfied.

5 Numerical Investigations

The average pressure correction (APC) technique is employed on several geometrical configurations of the composite channel presented in Fig. 1. It should first be remembered that the linear Brinkman equation holds for flows at low Reynolds numbers, namely, $\mathcal{R} \lesssim 10$, in which the driving forces are balanced by both the viscous forces and the media resistance. In the present investigation of the configuration shown in Fig. 1, the horizontal inlet and outlet channels have dimensional distances $(X_0 - X_L) \gtrsim 3H$ and $(X_R - X_1) \gtrsim 4H$, and the vertical sides have dimensional distances $(Y_0 - Y_D) = (Y_U - Y_1) \gtrsim 5H$. These distances ensure that when $0 < \mathcal{R} \lesssim 1$ the fully developed solutions have been reached and the flow details throughout the majority of the vertical channel are independent of its length. Numerous geometrical configurations have been investigated but in order to illustrate the typical results obtained, in all the results presented in this paper, the dimensional width of the vertical channel is taken to be equal to half the width of the inlet and outlet channels, namely, H, and the outlet channel is offset from the inlet channel by a distance $5H$.

The small values of the Darcy numbers used in all the numerical investigations are $\mathrm{Da} = 10^{-10}$, $\mathrm{Da} = 10^{-12}$, and $\mathrm{Da} = 10^{-16}$, which represent the physical permeability values of the natural materials, sand, sandstone, and shale, respectively. All the numerical results presented in this paper are for $\rho = 1$, $\Gamma = 1$, $\mathcal{R} = 1$, $R_{\mathrm{mass}} = 10^{-4}$, the same nondimensional flux of fluid through the channel, namely, $q = 2$, and for mesh sizes $\Delta x = 0.1$ and $\Delta y = 0.05$, since the results obtained for any smaller mesh are graphically indistinguishable.

In the next section, the use of the APC technique to accelerate the rate of convergence of the CVM, enables us to perform several numerical investigations when implementing the above values of the Darcy numbers. These will generate a deeper understanding of the general flow processes in the composite channel shown in Fig. 1, and model some of the physical situations of the geological structures that are likely to be observed in the field. It should be noted that all the geometrical configurations and the physical values of Da considered for each numerical investigation have been carefully selected with the assistance from several geologists and other experts in the field, namely, staff at the Rock Deformation Research (rdr) Centre, University of Leeds (Leeds, UK). In addition, for the figures relating to each numerical investigation considered in this paper, the streamline pattern is presented at regular values of the streamfunction, namely, $\psi = 0.1, 0.2, 0.3, \ldots, 1.9$.

6 Results and Discussion

All the figures presented in this section relate to when the light shaded regions of the channel have $\mathrm{Da} = 10^{-16}$, shale, while elsewhere, $\mathrm{Da} = 10^{-10}$, sand. We first illustrate an investigation of a situation where the APC technique is employed in both the horizontal and vertical porous regions. This investigation is presented in Fig. 3, which shows the streamline pattern corresponding to flow perpendicular to vertical and horizontal barriers of shale, $\mathrm{Da} = 10^{-16}$, which are positioned in the horizontal and vertical sections, respectively, of the channels that are filled with sand, $\mathrm{Da} = 10^{-10}$. The nondimensional values associated with the vertical barriers and the horizontal barrier are height 2 and width 0.6 and height 0.6 and width 1.0, respectively. It is observed from Fig. 3 that as the fluid passes through the barriers then its velocity becomes more uniform, decreasing in the central region of the channel but increasing near the walls of the channel, as indicated by the widening of the streamlines across the barriers. However, since $Da = 10^{-10}$ elsewhere in the channel then the streamlines in these regions are observed to be contracting toward the axis of symmetry where the fluid velocity is increasing.

In addition, Fig. 4 shows the variation of the pressure along the axis of the three channels in Fig. 3, namely, (*a*) the inlet, (*b*) the vertical, and (*c*) the outlet, channels. Figure 4 illustrates the large drop of the pressure as the fluid crosses the low permeable barriers of shale $\mathrm{Da} = 10^{-16}$, which results in a very slow rate of convergence of the iteration procedure. However, the use of the APC technique across these barriers rapidly builds up the large pressure drop and hence improves the rate of convergence of the CVM. In particular, Fig. 5(*a*) shows the convergence history for the mass residual R_{mass} as a function of the number of iterations in the CVM both with and without the use of the APC technique in the configuration shown in Fig. 3, where in the barriers $\mathrm{Da} = 10^{-16}$, while elsewhere $\mathrm{Da} = 10^{-10}$. It is observed that without the use of the APC technique then with these small values of Da in which the ratio of the smallest to the largest Da is small, namely, 10^{-6}, the value of R_{mass} is not reduced and still remains at a value of about 1.0 even after 20,000 iterations. Hence, clearly in this case

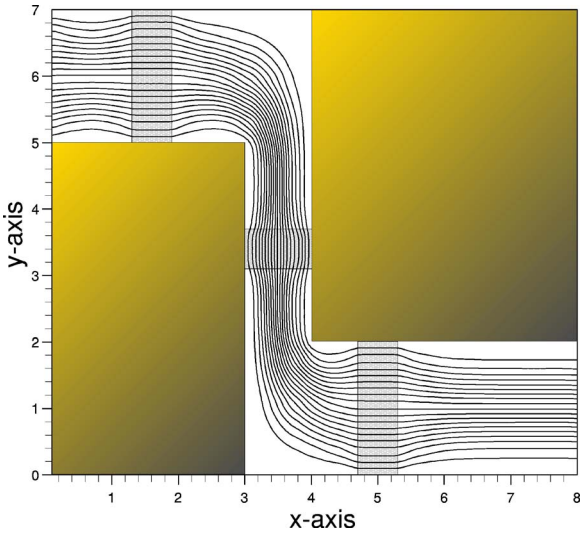

Fig. 3 The streamlines where the light shaded regions have $\mathrm{Da} = 10^{-16}$, shale, while elsewhere $\mathrm{Da} = 10^{-10}$, sand. The nondimensional values associated with the two vertical barriers, positioned in the regions $1.3 < x < 1.9$ and $4.7 < x < 5.3$, respectively, are height 2 and width 0.6, while the values associated with the horizontal barrier positioned in the region $3.1 < y < 3.7$ are height 0.6 and width 1.0

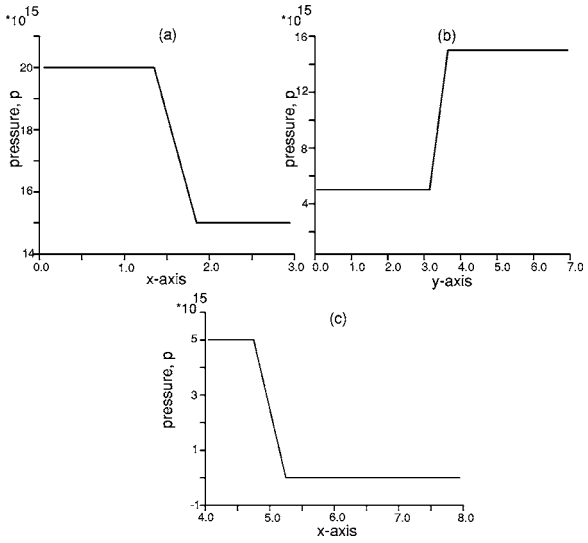

Fig. 4 The variation of the nondimensional fluid pressure along the axis of the three channels, namely, (*a*) the inlet, (*b*) the vertical, and (*c*) the outlet, channels, see Fig. 3

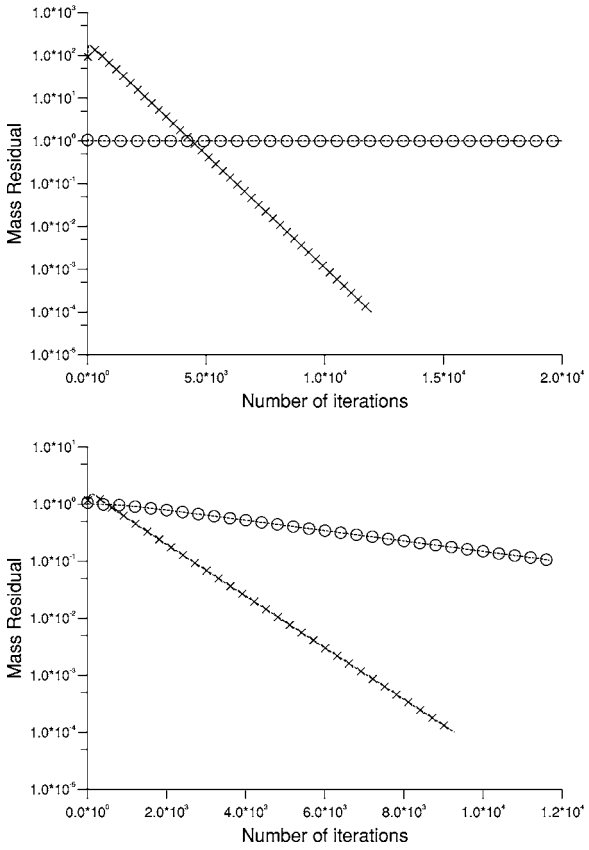

Fig. 5 The convergence history for the mass residual R_{mass} as a function of number of iterations in the CVM with the APC, (–×–), and without the APC, (-o-), for the configuration shown in Fig. 3, where in (a) the light shaded regions have Da=10^{-16}, while elsewhere Da=10^{-10}, and (b) the light shaded regions have Da=10^{-14}, while elsewhere Da=10^{-10}

we cannot expect that the value of R_{mass} will satisfy the convergence criterion within a reasonable number of iterations. However, when using the APC technique to correct the pressure drops across the barriers of shale Da=10^{-16}, we observe that the value of R_{mass} decreases rapidly as the number of iterations increases, such that after about 11,970 iterations $R_{mass}=1.0\times10^{-4}$. Furthermore, in order to illustrate a situation for the configuration shown in Fig. 3 where the value of R_{mass} decreases as the number of iterations increases, both with and without the use of the APC technique, then the ratio of the smallest to the largest Da has to be increased, say to 10^{-4}, i.e., now the barriers in Fig. 3 have Da $=10^{-14}$, while elsewhere Da=10^{-10}. The results obtained are presented in Fig. 5(*b*) where it is clearly observed that the APC technique rapidly builds up the pressure drops across the barriers of Da=10^{-14}, with R_{mass} decreasing rapidly as the number of iterations increases, such that after about 9280 iterations R_{mass} $=1.0\times10^{-4}$. While without employing the APC technique then it requires about 11,672 iterations for the value of R_{mass} to reach a value 1.0×10^{-1} and more than 44,867 iterations for it to reach 1.0×10^{-4}. Thus, we conclude that the rate of convergence of the CVM has been significantly improved by adopting the APC technique.

We next illustrate the use of the APC technique on various geometrical configurations of the composite channel shown in Fig. 1, where all the investigations are related to changes in the flow patterns that occur in the vertical channel which physically can be considered as a fault/fracture region. While the inlet and outlet channels are composed of two outer layers of shale *Da* $=10^{-16}$ of thickness 0.5 on their upper and lower impermeable

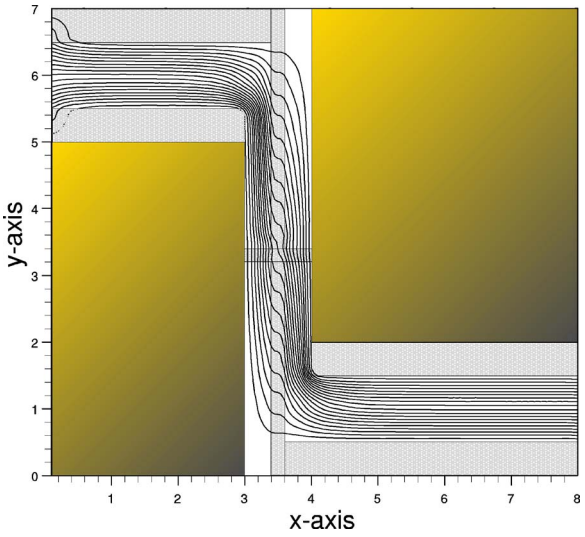

Fig. 6 The streamlines where the light shaded regions have Da=10^{-16}, shale, while elsewhere Da=10^{-10}, sand, and the nondimensional values associated with the vertical barrier positioned in the region 3.4<*x*<3.6 are height 7 and width 0.2

surfaces, together with an inner core of sand Da=10^{-10}, of height 1.0, since such a layered system is a more physically realistic representation of the geological structures in the field. In addition, in all the following investigations, we present situations where the horizontal layers from the inlet and outlet channels are linked with some barriers from the vertical channel, since such configurations incorporate physically the geological features of both faults and fractures.

Initially, we consider a geological situation where there exists some complete irregular restriction on the flow in the vertical fault region. This physical configuration is modeled in Fig. 6 by positioning a uniform vertical barrier of shale Da=10^{-16} of width 0.2, and height the same as that of the vertical channel so as to link with the upper and lower layers from the inlet and outlet channels, respectively. The streamline pattern presented in Fig. 6 shows that most of the fluid finds an easy passage through the gaps of sand Da=10^{-10} between the vertical barrier and the horizontal layers so as to flow across the barrier in an almost uniform manner.

As the contours of constant pressure across the layers in the inlet and outlet channels, apart from at their entrances and exits, are vertical and equally spaced, they are not presented in the present case, or for any of the other situations investigated in this paper. Furthermore, the APC technique is not required to be employed in either of the channels. However, since all the investigations in this paper relate to changes that occur in the vertical channel then the pressure contours in the vertical channel, which show much greater variations depending on the different structures, are presented in Fig. 7. Therefore, as shown in Fig. 7(*a*), there is a large increase in the overall pressure gradient across the central region of the vertical barrier of shale Da=10^{-16} in order to ensure the same flux of fluid through the channel. Although there are large horizontal pressure gradients across the vertical barrier Da=10^{-16}, the magnitude of the fluid velocity is much reduced compared to that in the regions of sand Da=10^{-10}. In addition, a relatively small vertical pressure gradient ensures a substantial flow is observed in the vertical direction either side of the barrier where sand is present. The situation presented in Fig. 6 shows the use of the APC technique across the barrier in the vertical channel where the technique rapidly builds up the pressure drop across the barrier. The APC formula (19) has been implemented with Da_1 $=Da_2=10^{-16}$, $S_1=7$, $S_2=0$, and $\Delta l_1=\Delta l_2=0.2$.

In the next investigation, the geological feature of flow being restricted by a barrier in the vertical direction, as presented in Fig.

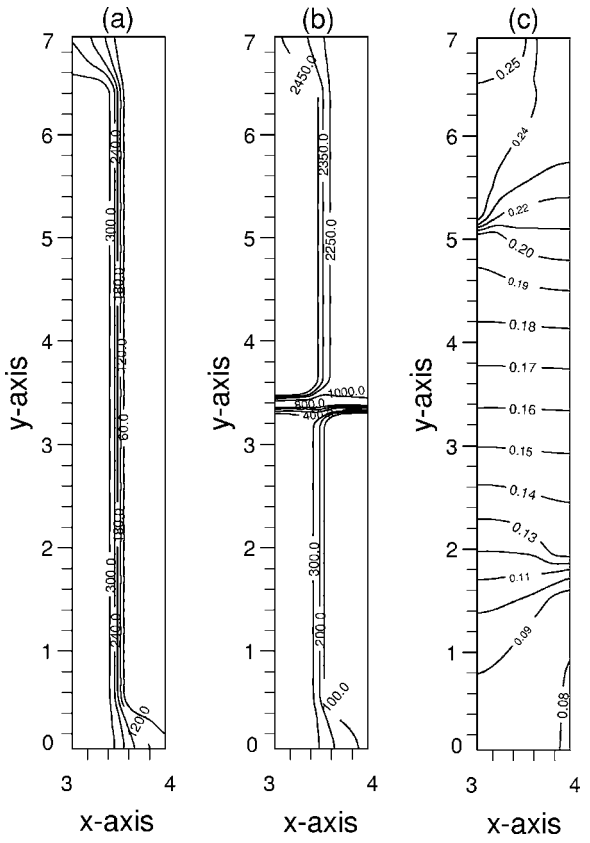

Fig. 7 The pressure contours in the vertical channels which correspond to: (a) Fig. 6, where there is a vertical barrier of height 7, width 0.2 and positioned in the region $3.4<x<3.4$, (b) Fig. 8, where there are vertical and horizontal barriers of heights 7 and 0.2, widths 0.2 and 1.0, respectively, and positioned in the region $3.4<x<3.4$ and $3.2<y<3.4$, respectively, and (c) Fig. 9, where there are two thin vertical barriers each of height 4.5, width 0.1, and at a distance 0.2 apart, and positioned in the region $3.3<x<3.4$ and $3.5<x<3.6$, respectively. All the barriers have $Da=10^{-16}$, shale, while elsewhere $Da=10^{-10}$, sand, and the values of the pressure presented are scaled by a factor 10^{12}.

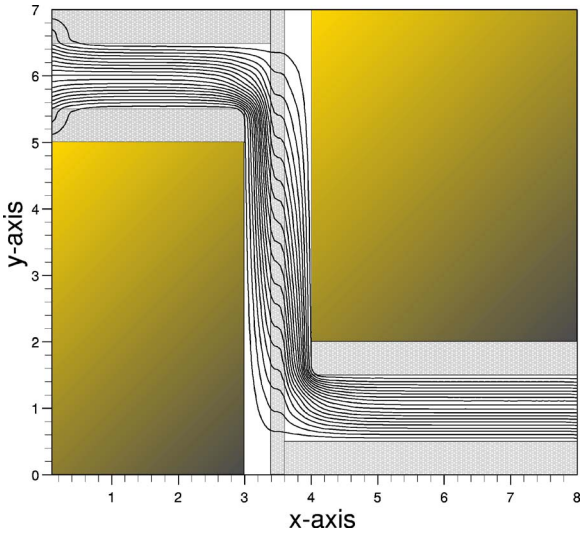

Fig. 8 The streamlines where the light shaded regions have $Da=10^{-16}$, shale, while elsewhere $Da=10^{-10}$, sand, and the nondimensional values associated with the vertical barrier, positioned in the region $3.4<x<3.6$, are height 7 and width 0.2, while the nondimensional values associated with the horizontal barrier, positioned in the region $3.2<y<3.4$, are height 1.0 and width 0.2

6, is incorporated with the presence of an additional irregular restricted region which can occur in the horizontal direction of the fault region. This physical situation is modeled similarly to that shown in Fig. 6, but with the presence of a uniform horizontal barrier of sand $Da=10^{-16}$, of height 0.2, and of width the same as that of the vertical channel, namely, 1.0. The idealized model, corresponding to both vertical and horizontal barriers in the fault/fracture region of the geological structure, is presented in Fig. 8. Clearly, the streamline pattern illustrated in Fig. 8 is similar to that presented in Fig. 6, except in the region where the horizontal and vertical barriers of shale $Da=10^{-16}$, intersect where it can be observed that the fluid velocity is forced to be almost uniform. Figure 7(*b*) shows that for the same flux of fluid much larger values of vertical and horizontal pressure gradients are required across the horizontal and vertical barriers, respectively. Although $Da=10^{-10}$ in the vertical direction either side of the barrier, a relatively small vertical pressure gradient ensures that fluid flows much easier in that direction compared to elsewhere. In addition, due to the presence of the horizontal barrier, the magnitude of the pressure contours above the horizontal barrier are approximately ten times greater than those in Fig. 7(*a*) at similar locations.

Figure 8 demonstrates a situation where the APC technique has successfully been employed across a combination of vertical and horizontal barriers. In particular, due to the large rapid pressure drops across these barriers then a very slow rate of convergence would have been achieved, and an excessively large number of iterations would have been required without the use of the APC technique. However, employing this technique has resulted in a quick buildup of the pressure drops across the barriers and hence enabled the global mass conservation to be satisfied extremely rapidly.

The following investigation is concerned with a physical situation where within the fault region there still exists a clear passage from the inlet channel to the outlet channel, but the cross-sectional area within which such a flow can occur is substantially reduced. In addition, other regions are present in which the fluid can easily flow, recirculating if necessary, provided that the fluid can pass through at least one, and probably more, region of low permeability. This physical configuration is modeled in Fig. 9 by connecting the horizontal layers from the inlet and outlet channels to two thin vertical barriers, which are of height 4.5, width 0.1, and at a distance 0.2 apart. Hence, we consider in Fig. 9 the fluid flow through a restricted central passageway within the vertical channel. The streamlines in this figure indicate that the fluid avoids the horizontal barriers that are present in the vertical channel and distributes itself almost uniformly between the two vertical barriers and between these barriers and the walls of the channel. Although both the vertical and horizontal barriers consist of the same low permeable porous material, namely, shale $Da=10^{-16}$, the thicknesses of the horizontal layers, namely, 0.5, are much greater than those of the vertical barriers, namely, 0.1. As a result of having these thin vertical barriers then the horizontal pressure gradients necessary to force the fluid from the entrance channel into the sand region to the right of the second vertical barrier, and from the sand region to the left of the first vertical barrier into the exit channel, are only of the same order of magnitude as the vertical pressure gradients necessary to ensure the flow through the restricted cross section. Hence the fluid flows relatively easily down the whole region of the vertical channel. This result is also confirmed from an inspection of Fig. 7(*c*), which shows almost uniform horizontal contours of constant pressure across the central region. In addition, although somewhat larger vertical pressure gradients exist across the horizontal barriers compared to across

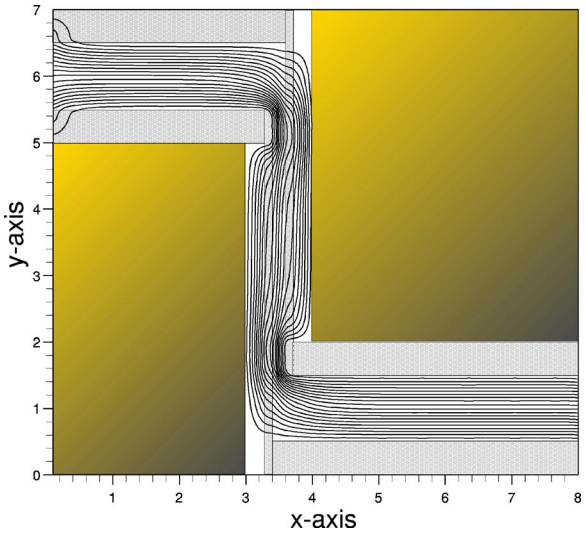

Fig. 9 The streamlines where the light shaded regions have Da=10^{-16}, shale, while elsewhere Da=10^{-10}, sand, and the nondimensional values associated with the two thin vertical barriers, positioned in the regions 3.3<*x*<3.4 and 3.5<*x*<3.6, respectively, are height 5.5, width 0.1, and at a distance 0.2 apart

the vertical barriers, there is no flow across the horizontal barriers as a result of their greater thickness compared with that of the vertical barriers.

Thus, the configuration in Fig. 9 illustrates a situation where the APC technique is employed across two vertical barriers. In particular, for the first barrier the APC formula (19) is implemented with $Da_1=10^{-16}$, $Da_2=10^{-10}$, $Da_3=10^{-16}$, $S_1=5.5$, $S_2=1.0$, $S_3=0.5$, and $\Delta l_1=\Delta l_2=\Delta l_3=0.1$, and similarly for the second barrier. Although, in this situation the resulting pressure field in Fig. 7(*c*) shows no rapid pressure drops, which indicates that the application of the APC technique may not be necessary. Unfortunately, this fact is only available once the problem has been solved. However, with the inclusion of the technique then the rate of convergence has been improved such that it has been found that by employing the technique, the CPU time is reduced from approximately two days to approximately one hour. Hence, it can be concluded from this investigation that the APC technique can still improve the rate of convergence even where the geometrical changes of the porous media do not result in rapid pressure drops.

In general, it has been found that the CPU time required for the solution of the Brinkman Eq. (4) in all the above numerical investigations when the APC technique is employed for these physically realistic values of Darcy numbers, namely, Da=10^{-16} and Da=10^{-10}, is approximately 3% of the CPU time consumed when solving Eq. (4) without using the APC technique. In addition, the convergence histories for the mass residual R_{mass} as a function of number of iterations, both with and without employing the APC technique, shows a similar behavior to that presented in Fig. 5(*a*), where without employing the APC technique in the CVM of these investigations then an excessively large number of iterations are required in order to satisfy the convergence criterion, while with the use of the APC technique the convergence criterion is satisfied within a reasonable number of iterations.

To summarize, it can be concluded from all the numerical investigations presented in this section that the APC technique can be effectively employed to all the situations that are related to a horizontal and vertical fluid flow across an arbitrary vertical and horizontal porous media, respectively, of any thickness and composed of any number of the Darcy numbers Da, see Figs. 3, 6, and 9. In addition, it can also be employed to situations where the fluid flows across regions of a combined vertical and horizontal porous media, see Fig. 8.

7 Conclusions

In this paper, some real physical values of the permeability k have been considered in solving fluid flow through composite channels that incorporate geological features of both faults and fractures.

A difficulty arises in securing a converged solution when the ratio of the lowest permeability to the highest permeability of the natural materials in different media is very small, namely, less than about 10^{-3}. This is due to large and rapid pressure drops as a result of the flow through the changing media. Therefore, the average pressure correction (APC) technique, which was developed by Wen and Ingham [10] for flow through a thin paper filter, has been extended in order to build up the large pressure drops that occur due to large variations in the permeability of the media within several geometrical configurations of the composite channels. Such configurations are related to horizontal or vertical flows across arbitrary thick vertical or horizontal porous media, respectively, composed of any number of Darcy parameters. Thus, the inclusion of the APC technique in the CVM has successfully led to a substantial enhancement in the rate of convergence of the iterative scheme.

In addition, the APC technique has been employed on several numerical investigations which have added a better understanding of the general flow processes that can occur in different geological structures of a composite channel. In all the investigations presented, it has been clearly demonstrated that the APC technique, which is based on global mass conservation, can rapidly build up the large pressure drop whenever employed and hence the global mass conservation is satisfied extremely rapidly. Furthermore, the examples relating to flows across both horizontal and vertical single barriers consisting of porous materials where the ratio of the values of Da differ by O(10^{-6}), see Sec. 6, can provide useful benchmark solutions for future researchers when developing codes for more complex situations.

On the other hand, most of the investigations presented in this paper are related to changes in the flow patterns that occur within a vertical channel, which has been considered as a fault/fracture region. The results obtained have established that a high pressure gradient in a particular direction, for example, across the barriers, does not neccessarily indicate large fluid velocities in that direction. Instead, it all depends on both the value of the permeability and the dimension of the porous medium, a feature which has been discussed in all the investigations.

References

[1] Nield, D. A., and Bejan, A., 1999, *Convection in Porous Media*, Springer-Verlag, NY, 2nd ed.
[2] Ingham, D. B., and Pop, I., 1998, *Transport Phenomena in Porous Media*, Vol. 1, Pergamon, Elsevier Science, Oxford.
[3] Ingham, D. B., and Pop, I., 2001, *Transport Phenomena in Porous Media*, Vol. 2, Pergamon, Elsevier Science, Oxford.
[4] Darcy, H. P. C., 1856, *Les Fontaines Publiques de la Ville de Dijon*, Victor Dalmont, Paris.
[5] Scheidegger, A. E., 1974, *The Physics of Flow through Porous Media*, University of Toronto Press, Toronto.
[6] Clennell, B., 1997, "Fluid Flow Transients in the Petrophysical Characterisation of Reservoir Rocks," Internal Report for the Rock Deformation Research, Dept. of Earth Sciences, University of Leeds.
[7] Lesnic, D., Elliott, L., Ingham, D. B., Clennell, B., and Knipe, R. J., 1998, An Inverse Problem to Determine the Piecewise Homogeneous Hydraulic Conductivity within Rocks, Faulting, Fault Sealing and Fluid Flow in Hydrocarbon Reservoirs, **147**, pp. 261–268.
[8] Al-Hadhrami, A. K., 2003, Flows Through Horizontal Channels of Porous Materials, Int. J. Energy Res., **27**, pp. 875–889.
[9] Wen, X., and Ingham, D. B., 1993, "A New Method for Accelerating the Rate of Convergence of the SIMPLE-like Algorithm," Int. J. Numer. Methods Fluids, **17**, pp. 385–400.
[10] Wen, X., and Ingham, D. B., 1994, "A New Method for Accelerating the Rate of Convergence of the SIMPLE-like Algorithm for Flow Through a Thin Filter," Int. J. Numer. Methods Fluids, **19**, pp. 889–903.

Moussa Kfoury
Institut Français du Pétrole,
1 et 4 avenue de Bois-Préau,
92852 Rueil-Malmaison Cedex,
France and Institut de Mécanique
de Fluides de Toulouse,
Allée Prof. C. Soula,
31400 Toulouse,
France
e-mail: kfoury_moussa@yahoo.fr

Rachid Ababou
Institut de Mécanique de Fluides de Toulouse,
Allée Prof. C. Soula,
31400 Toulouse,
France

Benoît Noetinger
Institut Français du Pétrole,
1 et 4 avenue de Bois-Préau,
92852 Rueil-Malmaison Cedex,
France

Michel Quintard
Institut de Mécanique de Fluides de Toulouse,
Allée Prof. C. Soula,
31400 Toulouse,
France

Upscaling Fractured Heterogeneous Media: Permeability and Mass Exchange Coefficient

In order to optimize oil recuperation, to secure waste storage, CO_2 *sequestration and describe more precisely many environmental problems in the underground, we need to improve some homogenization methods that calculate petrophysical parameters. In this paper, we discuss the upscaling of fluid transport equations in fractured heterogeneous media consisting of the fractures themselves and a heterogeneous porous matrix. Our goal is to estimate precisely the fluid flow parameters like permeability and fracture/matrix exchange coefficient at large scale. Two approaches are possible. The first approach consists in calculating the large-scale equivalent properties in one upscaling step, starting with a single continuum flow model at the local scale. The second approach is to perform upscaling in two sequential steps: first, calculate the equivalent properties at an intermediate scale called the "unit scale," and, second, average the flow equations up to the large scale. We have implemented the two approaches and applied them to randomly distributed fractured systems. The results allowed us to obtain valuable information in terms of sizes of representative elementary volume associated to a given fracture distribution.* [DOI: 10.1115/1.1991864]

Introduction

Many industrial and environmental problems involve flow in fractured porous media, like oil production, nuclear waste storage, and groundwater pollution. In this paper, we start from a fractured reservoir model as described by a geologist (Long et al. [1], Le Ravalec et al. [2]). We focus our study on the flow description at the scale of a grid-block in a numerical model (large scale). In this paper, we consider only characteristics associated with one-phase flow, such as the fracture permeability and fracture/matrix exchange coefficient.

We distinguish three scales illustrated in Fig. 1: (i) the local-scale characteristic of the fracture aperture; (ii) an intermediate scale called unit scale; and (iii) the large scale of the reservoir model also called a block scale. To describe the flow at the block scale, we have two main possible approaches. We present two approaches we have developed to identify large-scale parameters. The first approach consists of upscaling in one step (direct upscaling) from the local scale to the block scale and the second approach involves two stages (sequential upscaling) through the intermediate unit scale. We assume that the flow at the local scale is described by a simple Darcy-type equation. We also assume that the flow at the unit scale is described by a system of matrix-fracture equations according to the dual continuum model of Barenblatt and Zheltov [3]. This model was further developed by Warren and Root [4], and by many other contributors, e.g., Lough and Kamath [5] Quintard and Whitaker [6] In this paper, we use the general formulation developed theoretically by Quintard and Whitaker [6]

Contributed by the Applied Mechanics Division of ASME for publication in the JOURNAL OF APPLIED MECHANICS. Manuscript received June 15, 2004; final manuscript received May 8, 2005. Assoc. Editor: D. Siginer. Discussion on the paper should be addressed to the Editor, Prof. Robert M. McMeeking, Journal of Applied Mechanics, Department of Mechanical and Environmental Engineering, University of California - Santa Barbara, Santa Barbara, CA 93106-5070, and will be accepted until four months after final publication in the paper itself in the ASME JOURNAL OF APPLIED MECHANICS.

$$\phi_m c_m \frac{\partial}{\partial t}\{P_m\}^m = \nabla\left(\frac{1}{\mu}\mathbf{K}_{mm}\cdot\nabla\{P_m\}^m + \frac{1}{\mu}\mathbf{K}_{mf}\cdot\nabla\{P_f\}^f\right) - \frac{\alpha}{\mu}(\{P_m\}^m - \{P_f\}^f) \tag{1}$$

$$\phi_f c_f \frac{\partial}{\partial t}\{P_f\}^f = \nabla\left(\frac{1}{\mu}\mathbf{K}_{fm}\cdot\nabla\{P_m\}^m + \frac{1}{\mu}\mathbf{K}_{ff}\cdot\nabla\{P_f\}^f\right) - \frac{\alpha}{\mu}(\{P_f\}^f - \{P_m\}^m) \tag{2}$$

In this dual medium model, the first equation describes matrix flow, the second describes fracture flow, and the term with α models the fluid exchange between the matrix and fracture systems (Noetinger and Estébenet [7], Bourbiaux et al. [8]). Without going into details, let us emphasize that the upscaling from the unit scale to the block scale or the direct upscaling, may lead to (two) different classes of flow equations. If conditions are such that a single continuum model is valid, we only need to identify the equivalent permeability and the equivalent compressibility. But if a mechanical nonequilibrium model is required at the large scale, for instance in the form of a large-scale dual medium model similar to the one described by Eqs. (1) and (2), we need to identify a large-scale parameters that will be denoted by Kff^*, Kmm^*, α^*.

Direct Upscaling From the Local-Scale to the Block-Scale

By using the standard laboratory flow configuration, an imposed pressure drop and no flow boundaries called permeameter boundary conditions; we have developed an algorithm to calculate the full permeability tensor of heterogeneous anisotropic media or fractured systems [9]. For more details, by simulating a flow along the ox direction (resp. oy) for a square porous medium of dimension $L \times L$, the permeameter boundary conditions take this form

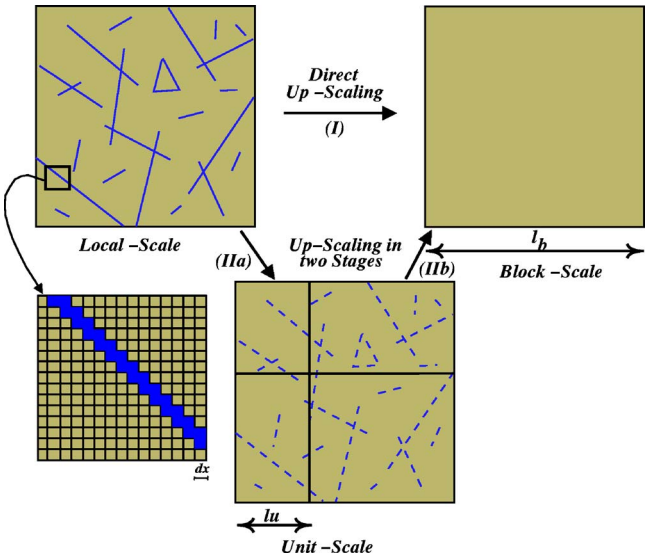

Fig. 1 Two different up-scaling paths: (I) Direct upscaling from the local-scale (*dx*) to the block-scale (L_b), and (II) Up-scaling in two stages passing through the intermediate unit-scale(l_u)

$$\begin{cases} \nabla p_{x,x} = \text{constant} \\ \displaystyle\int_{\Gamma_{yy}} \mathbf{n}\,.\,\mathbf{K}\,.\,\nabla p_{x,y=0,L} = 0 \end{cases} \quad \text{(Flow along the } ox \text{ direction)} \quad (3)$$

$$\begin{cases} \nabla p_{y,y} = \text{constant} \\ \displaystyle\int_{\Gamma_{xx}} \mathbf{n}\,.\,\mathbf{K}\,.\,\nabla p_{x=0,L,y} = 0 \end{cases} \quad \text{(Flow along the } oy \text{ direction)} \quad (4)$$

Where $p_{x,y=0,L}$ (resp. $p_{x=0,L,y}$) means the pressure calculated at the Γ_{yy} (resp. Γ_{xx}) faces for an imposed pressure gradient at the ox axis (resp. oy) quoted $\nabla p_{x,x}$ (resp. $\nabla p_{y,y}$). Where Γ_{yy} is perpendicular to the oy axis and Γ_{xx} is perpendicular to the ox axis (see Fig. 2). For a flow along the ox direction (resp. oy), the pressure on the impermeable edge will generate a transverse viscous force $\{\partial p/\partial y\}_x$ (resp. $\{\partial p/\partial x\}_y$) measurable numerically and experimentally. By measuring this additional information coupled to the fluxes measured on the ox, oy directions, we can calculate the full permeability tensor of the heterogeneous porous media

$$k_{xx} = \frac{q_{xx} - q_{yy}\dfrac{\delta x_y}{L}\left\{\dfrac{\partial p}{\partial y}\right\}_x}{1 - \left\{\dfrac{\partial p}{\partial x}\right\}_y \left\{\dfrac{\partial p}{\partial y}\right\}_x}; \quad k_{yy} = \frac{q_{yy} - q_{xx}\dfrac{\delta y_x}{L}\left\{\dfrac{\partial p}{\partial x}\right\}_y}{1 - \left\{\dfrac{\partial p}{\partial x}\right\}_y \left\{\dfrac{\partial p}{\partial y}\right\}_x} \quad (5)$$

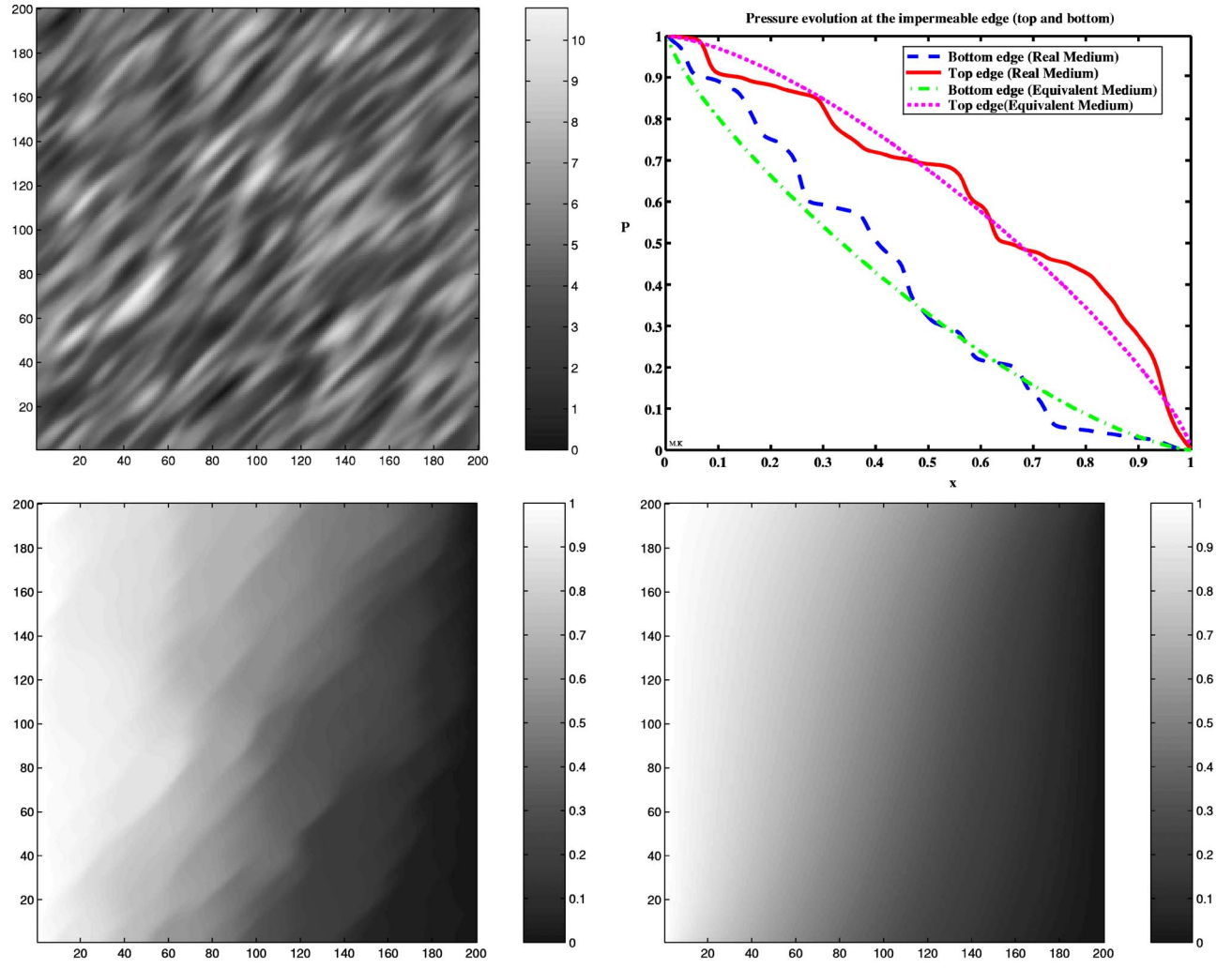

Fig. 2 This figure shows the faces quotation used in this paper for a square porous medium

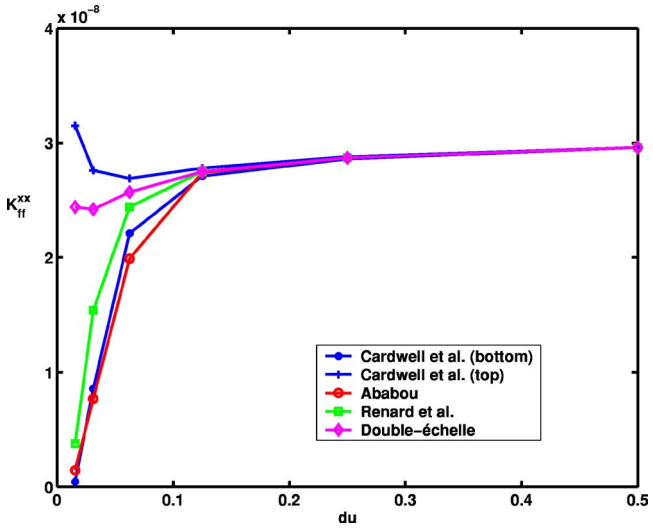

Fig. 3 Lognormal permeability map (Darcy) generated using FFTMA for 200×200 cells (at left) and the pressure (bar) evolution at the impermeable edges for a horizontal confined flow for the real medium and its anisotropic homogeneous equivalent (at right). At bottom, pressure maps for the real medium (at left) and its equivalent homogeneous medium (at right).

$$k_{xy} = -\left\{\frac{\partial p}{\partial x}\right\}_y k_{xx} + \frac{\delta x_y}{L} q_{yy}; \quad k_{yx} = -\left\{\frac{\partial p}{\partial y}\right\}_y k_{yy} + \frac{\delta y_x}{L} q_{xx} \quad (6)$$

Where δy_x (resp. δx_y) corresponds to the difference between the two flow barycentre at the outlet edge and the inlet edge of the sample for a flow imposed according to ox (respectively oy).

In Fig. 3 (top, left), we show a lognormal permeability map ($k_g = 121$ Darcy; $\sigma^2 = 2$) generated with the stochastic code FFTMA [2]. Locally, the permeability is isotropic (scalar), but its correlation function (or variogram) is anisotropic. Here, it has an orientation of 44.46° with respect to the horizontal axis. Also we present in the same figure (Fig. 3, top, right) the pressure variations at the impermeable edges for a horizontal confined flow for the real medium and its anisotropic homogeneous equivalent medium determined by using the method in Ref. [9] and shortly described in this paper. In addition, we show, respectively, the pressure maps for the real medium (Fig. 3, bottom, left) and its equivalent medium (Fig. 3, bottom, right). For these calculations, the effective permeability tensor for the researched equivalent medium provided by this method is

$$\mathbf{K} = \begin{pmatrix} 122.05 & 58.08 \\ 58.08 & 119.86 \end{pmatrix} \quad (7)$$

The eigenvalues of this tensor are: $k'_{xx} = 179.05$, $k'_{yy} = 62.86$. The principal axes have an orientation of 44.46° with respect to the direction of the imposed flow.

Also, we have developed a numerical solver based on a two-dimensional (2D) finite volume scheme with a five point stencil for the "closure problems" presented in Quintard and Whitaker [6] Landereau et al. [10] which give all the required permeability tensors and the matrix-fracture exchange coefficient at the different large scales (unit scale or block scale). The flow is described by a dual continuum model. In Fig. 4, we show a zoom of a fractured porous media studied in this paper. The volume fraction of the 26,538 fractures present in the medium is around 9%, and the ratio of fracture permeability to matrix permeability at local-scale is around 1000. At local scale, we build a fine grid with 2048×2048 cells. We then choose to partition the domain into units of different sizes, leading to several possible partitions (4×4 units, 8×8 units, 16×16 units, and 32×32 units). For each partition, we have calculated a map of the matrix-fracture exchange coefficient α and of the first principal component of the equivalent permeability tensor $\mathbf{K}_{EQ}^{XX}$, and we have plotted their histograms in Fig. 4. The histogram for α shows a classical normal shape for all unit-scale partition. The results for $\mathbf{K}_{EQ}^{XX}$ show a more complicated structure. For fine unit-scale partition, we observe a bimodal histogram with a group of low values corresponding to nonpercolating units. This bimodal structure disappears for unit size "sufficiently" large. This word "sufficiently" will be associated in the discussion at the end of this paper to the size of a representative elementary volume (REV), important notion for practical applications.

Sequential Upscaling in Two Stages Through the Intermediate Unit-Scale

Once the permeability and the matrix/fracture exchange coefficient distributions (maps) are known at the intermediate scale of the "units," further averaging is required to obtain the flow behavior at the block scale. We have formulated a dual continuum model at the block scale starting from the Barenblatt et al. [3] model at the unit scale. We have obtained two systems of dual continuum equations in the matrix and fractured regions for averaged pressure (P_m or P_f) and for pressure deviations ($\tilde{P}_m$ or $\tilde{P}_f$). Without going into details, the equivalent permeability for the fractured region is obtained by solving the closure problem described below

$$\tilde{p}_f = \mathbf{b}_f \cdot \nabla \mathrm{P}_f \quad (8)$$

$$0 = \nabla(\mathbf{K}_{ff} \cdot \nabla \mathbf{b}_f) + \nabla \cdot \mathbf{K}_{ff} \quad (9)$$

$$\mathbf{b}_f(x + l_i) = \mathbf{b}_f(x) \quad (10)$$

$$\{\mathbf{b}_f\} = 0 \quad (11)$$

$$\mathbf{K}_{ff}^* = \{\mathbf{K}_{ff}\} + \{\mathbf{K}_{ff} \cdot \nabla \mathbf{b}_f\} \quad (12)$$

which is reminiscent of classical equations obtained for diffusion problem with heterogeneous diffusion coefficients (Saez et al. [11], Bourgeat et al. [12] Quintard and Whitaker [13]). We applied those formulas to the permeability map obtained at the unit scale for each partition of the block (see Fig. 4). The equivalent permeability of the fracture network is presented in Fig. 5 as a function of the unit size l_u. Our upscaled permeability called the "double scale" is compared to that obtained by using the Cardwell and Parsons [14] technique, Ababou [15] approach, Renard et al. [16] method. These results will be discussed below.

The determination of a large-scale mass exchange coefficient from the mapped α is not a trivial matter. Our approach is based on direct numerical simulation of the dual medium model at the unit scale and interpretation of the resulting block-scale fields. We studied the case $K_m \ll \phi_f K_f$. We have shown by numerical simulations that, when the exchange coefficient is large enough, the fracture pressure diffusion flux is negligible compared to the exchange flux. More precisely, this occurs when $\mu\alpha l_u^2 / K_f \gg 1$. Our simulation tests show that the asymptotic upscaled exchange coefficient α is the harmonic mean of the local coefficient α^*. On the other hand, when the exchange coefficient is small enough, the fracture pressure gradient becomes negligible because there is a strong diffusion which tends to homogenize the fracture pressure in space. More precisely, this occurs when $\mu\alpha l_u^2 / K_f \ll 1$. Our simulation tests show that the asymptotic upscaled exchange coefficient α is the minimum of the local coefficient α. Similar results were obtained with a stochastic method presented in the paper by Kfoury et al. [17].

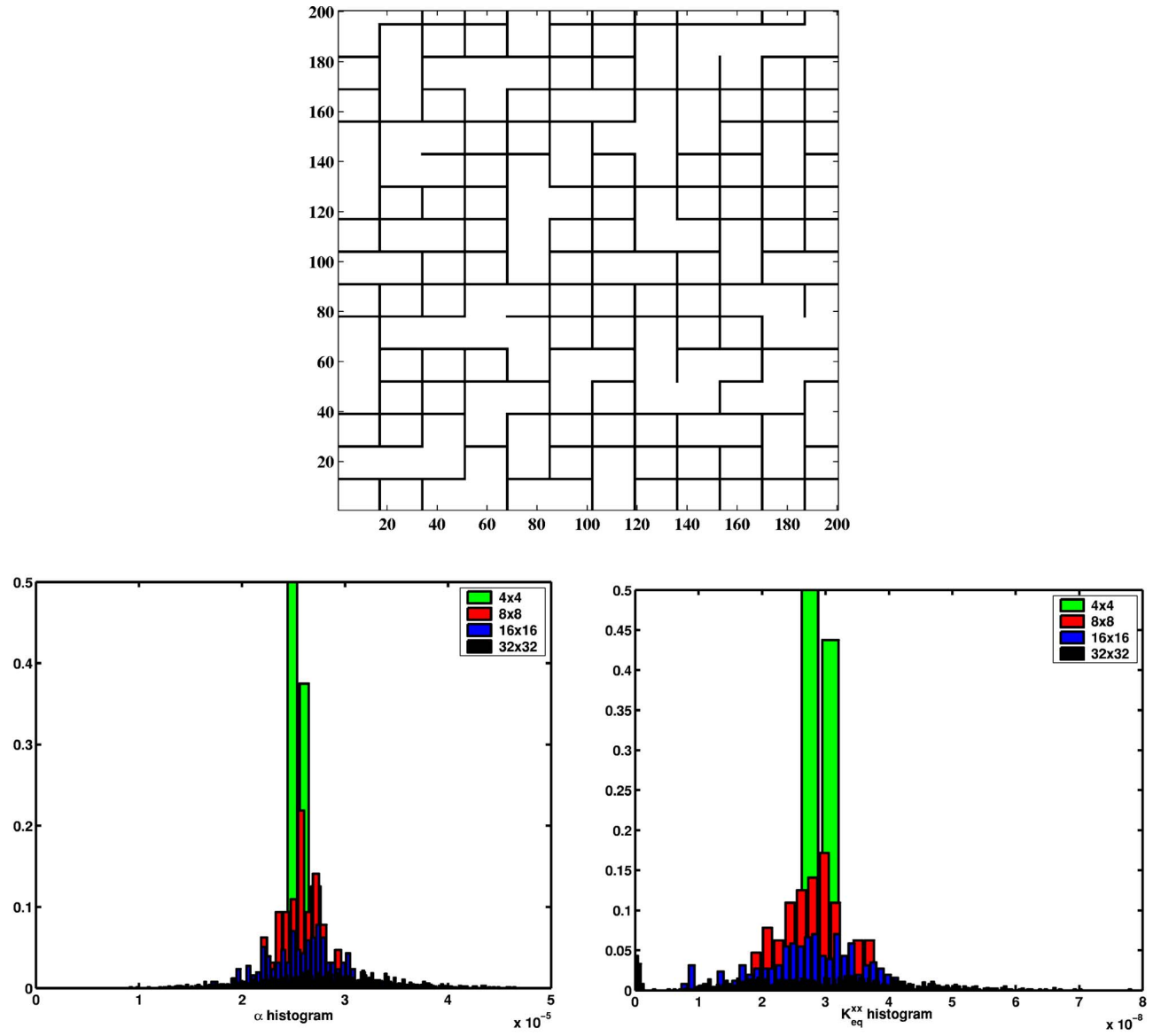

Fig. 4 Above: example of a fractured porous medium used in this work (200×200 cells). Below: histogram of matrix-fracture exchange coefficient α (left), and histogram of first component K^{XX}_{EQ} of equivalent permeability (right).

Representative Elementary Volume

While the choice of the block size by reservoir engineers is not in general truly determined by scientific considerations based on a detailed analysis of the lower-scale properties, it may be a safe engineering practice to have the block size a little bit larger than the spatial correlation length (or REV size) of the heterogeneous field under consideration within the grid block. The sequential upscaling technique presented in this paper offers some information about this important aspect. This is illustrated in Fig. 5. Results for $l_u \geqslant 1/8m$ are close to those obtained directly with a fine gridding of the Darcy-scale geometry. This result can also be confirmed by looking at the unit-scale repartition of K_{ff}. This is shown in Fig. 6 that represents the different values of K_{ff} as a function of ϕ_f, for each unit. We observe two populations, the one with a very low permeability being associated with nonpercolating fractures. We see that this nonpercolating cloud disappears for $l_u \geqslant 1/16m$, which is compatible with the REV size estimated from Fig. 5. The REV size can also be analyzed by looking at the distribution of α. Figure 7 represents the evolution of the arithmetic and harmonic mean of α, with respect to the unit-size l_u. We

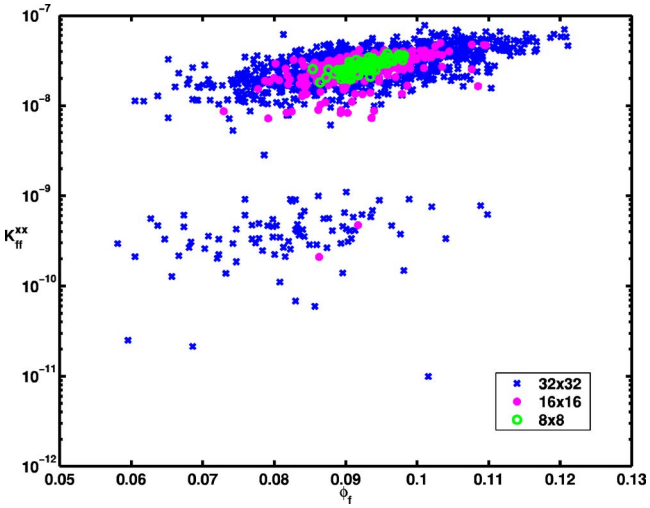

Fig. 5 First component of the equivalent permeability for a fracture network at the block-scale (k^{xx}_{ff},m^2)

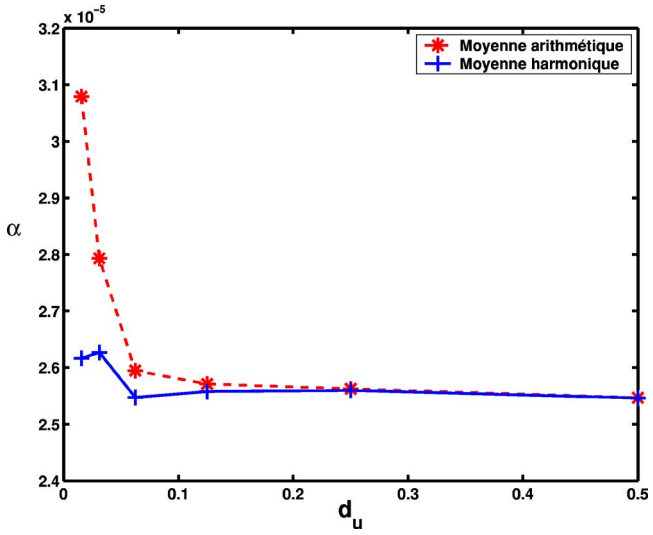

Fig. 6 Sequential upscaling: First component of fracture network permeability in each cell at the unit-scale for all partitions

remind the reader that these two values represent the two limiting behaviors of the system. We observe that the evolution of these two values is relatively small for $l_u \geqslant 1/8m$. This characteristic REV length scale is compatible with the estimate obtained from the analysis of the fracture permeability.

Conclusions

Direct and sequential approaches to upscaling flow properties in fractured heterogeneous porous media have been presented. Different methods to optimize the calculation of petrophysical parameters have been developed. We find that the idea of sequential upscaling in two steps is interesting in terms of computer effort (CPU time calculation) and of REV information.

Acknowledgment

M. Kfoury thanks the Université Libanaise and the Institut National Polytechnique de Toulouse for their support.

Nomenclature

$\mathbf{b}_f$ = Vector that map ∇P_f onto $\tilde{p}_f$ in the new double continuum model at the block-scale, m
c_f = Total compressibility in the fracture region, Pa^{-1}
c_m = Total compressibility in the matrix region, Pa^{-1}
K_g = Geometric average of the permeability distribution, Darcy

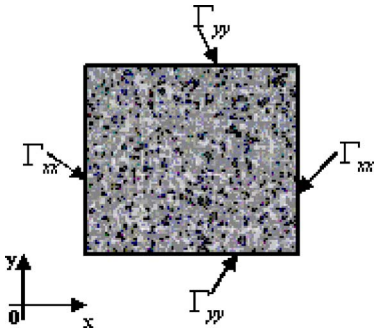

Fig. 7 Sequential upscaling: Arithmetic and harmonic values of exchange coefficient for each partition at the unit scale

$\mathbf{K}_f$ = Darcy scale permeability tensor in the fracture region, m^2; 1 Darcy $\approx 10^{-12}$ m^2
$\mathbf{K}_m$ = Darcy scale permeability tensor in the matrix region, m^2
$\mathbf{K}_{ff}$ = Fracture region, unit-scale permeability tensor in the two-equation model, m^2
$\mathbf{K}_{mm}$ = Matrix region, unit-scale permeability tensor in the two-equation model, m^2
$\mathbf{K}_{mf}=\mathbf{K}_{fm}$ = Unit-scale cross-effect permeability tensor in the two-equation model, m^2
$\mathbf{K}^*_{ff}$ = Fracture region, block-scale permeability tensor, m^2
$\mathbf{K}^*_{mm}$ = Matrix region, block-scale permeability tensor, m^2
l_u = Unit size, m
$\{P_f\}^f$ = Intrinsic macroscopic pressure for the fracture region, Pa
$\{P_m\}^m$ = Intrinsic macroscopic pressure for the matrix region, Pa
$\tilde{P}_f$ = Large-scale pressure deviation associated with the fracture region, Pa
P_f = Superficial regional average pressure for the fracture region, Pa
q = Flux, m^2
V_∞ = Large-scale averaging volume, m^3
V_f = Volume of the fractured region contained within V_∞, m^3
V_m = Volume of the matrix region contained within V_∞, m^3
α = Exchange coefficient at the unit scale
α^* = Exchange coefficient at the block scale
$\phi_f = V_f/V_\infty$ = Volume fraction of the fracture region contained in the averaging volume
$\phi_m = V_m/V_\infty$ = Volume fraction of the matrix region contained in the averaging volume
σ^2 = Variance of the permeability distribution
μ = dynamic viscosity, $\mathrm{N\,s/m}^2$

References

[1] Long, C. S., Wilson, J. S., and Witherspoon, P. A., 1982, "Porous Media Equivalents for Networks of Discontinuous Fractures," Water Resour. Res., **18**, pp. 645–658.
[2] Le Ravalec, M., Noetinger, B., and Hu, L. Y., 2000, "The FFT Moving Average (FFT-MA) Generator: An Efficient Numerical Method for Generating and Conditioning Gaussian Simulations," Math. Geol., **23**, pp. 701–723.
[3] Barenblatt, G. I., Zheltov, I. P., and Kochina, I. N, 1960, "Basic Concepts in the Theory of Seepage of Homogeneous Liquids in Fissured Rocks," J. Appl. Math., **24**, pp. 1286–1303.
[4] Warren, J. E. and Root, P. J., 1963, "The Behavior of Naturally Fractured Reservoirs," SPE J., pp. 245–255.
[5] Lough, M. F., and Kamath, J., 1996, "A New Method to Calculate the Effective Permeability of Grid Blocks Used in the simulation of Naturally Fractured Reservoirs," SPE J., pp. 493–499.
[6] Quintard, M., and Whitaker, S., 1996, "Transport in Chemically and Mechanically Heterogeneous Porous Media I: Theoretical Development of Region-Averaged Equations for Slightly Compressible Single-Phase Flow," Adv. Water Resour., **19**(1), pp. 29–47.
[7] Nœtinger, B, and Estébenet, T., 2000, "Up-Scaling of Fractured Media Using Continuous Time Random Walks Methods," Transp. Porous Media, **39**, pp. 315–337.
[8] Bourbiaux, B., Cacas, M. C., Sarda, S., and Sabathier, J. C., 1997, "A Fast and Efficient Methodology to Convert Fractured Reservoir Images into a Dual-Porosity Model," SPE paper no. 38907, pp. 671–676.
[9] Kfoury, M., 2005, "Changement d'Echelle Séquentiel pour des Milieux Fracturés Hétérogénes," Ph.D. thesis, **2162**, Institut National Polytechnique de Toulouse (http://ethesis.inp-toulouse.fr/archive/00000085/).
[10] Landereau, P., Noetinger, B., and Quintard, M., 2001, "Quasi-Steady Two-Equation Models for Diffusive Transport in Fractured Porous Media: Large-Scale Properties for Densely Fractured Systems," Adv. Water Resour., **24**(8), pp. 863–876.
[11] Saez, A. E., Otero, C. J., and Rusinek, I., 1989, "The Effective Homogeneous

Behavior of Heterogeneous Porous Media," Transp. Porous Media, **4**(3), pp. 213–238.
[12] Bourgeat, A., Quintard, M., and Whitaker, S., 1988, "Eléments de Comparaison entre la Méthode d'homogénéisation et la Prise de Moyenne avec Fermeture," C. R. Acad. Sci. Paris, **306**(2), pp. 463–466.
[13] Quintard, M., and Whitaker, S., 1987, "Ecoulements Monophasiques en Milieu Poreux: Effet des Hétérogénéités Locales," J. Mec. Theor. Appl., **6**, pp. 691–726.
[14] Cardwell, W. T., and Parsons, R. L., 1942, "Average Permeabilities of Heterogeneous Oil Sands," Trans. Am. Inst. Min., Metall. Pet. Eng., **160**, pp. 34–42.
[15] Ababou, R., 1996, "Random Porous Media Flow on Large 3-D Grids: Numerics, Performance, and Application to Homogenization," *IMA, Mathematics and Applications: Environmental Studies—Mathematical, Computational and Statistical Analysis*, edited by M. F. Wheelered., Springer, New York, Chap. 1, pp. 1–25.
[16] Renard, P., Genty, A., and Stauffer, F., 2001, "Laboratory Determination of the Full Permeability Tensor," J. Geophys. Res., **106**, pp. 443–452.
[17] Kfoury, M., Ababou, R., Noetinger, B., and Quintard, M., 2004, "Matrix Fracture Exchange in Fractured Porous Medium: Stochastic Upscaling," C. R. Méchanique, **332**, pp. 679–686.

Modeling of Heat Transfer in a Moving Packed Bed: Case of the Preheater in Nickel Carbonyl Process

Redhouane Henda[1]
School of Engineering,
Laurentian University,
Ramsey Lake Road,
Sudbury, ON P3E 2C6, Canada

Daniel J. Falcioni
Noranda/Falconbridge Ltd.,
MTG Extractive Metallurgy,
Falconbridge Technology Centre,
Falconbridge, ON P0M 1S0, Canada

Heat transfer in a two-dimensional moving packed bed consisting of pellets surrounded by a gaseous atmosphere is numerically investigated. The governing equations are formulated based on the volume averaging method. A two-equation model, representing the solid and gas phases separately, and a one-equation model, representing both the solid and gas phases, are considered. The models take the form of partial differential equations with a set of boundary conditions, some of which were determined experimentally, and design parameters in addition to the operating conditions. We examine and discuss the parameters in order to reduce temperature differences from pellet to pellet. The calculation results show that by adopting a constant temperature along the preheater outer wall and decreasing the velocity of the pellets in the preheater, the difference in temperature from pellet to pellet is reduced from ~120 °C to ~55 °C, and the thermal efficiency of the preheater is tremendously improved. [DOI: 10.1115/1.1991862]

Introduction

Porous media are utilized in many industrial processes as an effective means for the transport and storage of heat energy. Examples of industrial and practical applications include heaters, dryers, cooling units, exchangers, and biological tissue [1–5]. The study of heat transfer in processes based on packed beds is important for a better understanding of the operation of the process unit and its efficient design. Therefore, there has been a continuing interest in and a huge amount of literature exists on this subject (e.g., see [6–10]). Most of the studies on packed beds involve the flow of the fluid phase through a fixed solid bed, and a few only deal with moving beds. Experimental investigations of heat transport in moving packed beds are usually difficult to carry out due to limited access into the inside of the packed bed, and to operating conditions that very often are not ideal for experimentation, e.g., high temperature and pressure. Even when possible, experiments are generally carried out in small, cost-intensive setups, and the results are scaled up to the size of the real process. Numerical modeling is used as a complementary and sometimes as the sole means to gain a better understanding of the phenomena taking place in a packed bed.

A rigorous approach for investigating transport phenomena in porous media is through the use of the volume averaging technique [11–13]. The latter can be implemented by means of two approaches: The first one is via averaging over a representative elementary volume containing both the fluid and solid phases (referred to as the one-equation model), and the second one is via averaging separately over each of the phases, thus resulting in a separate energy equation for each individual phase (referred to as the two-equation model). The one-equation model is valid when the temperature difference between the solid and fluid phases is negligible, and is practical for comparison purposes with experimental data as temperature measurements in a packed bed do not distinguish between solid and fluid phase temperatures. The two-equation model is used when thermal exchange between the two phases is not effective [14], and allows for a better understanding of the interactions between the two phases. In the two-equation model the two energy equations, accounting for heat transfer in the solid and gas phases making up the bed, are coupled by a flux that depends on an energy exchange coefficient and the difference between the temperatures in the two phases.

In the present work, the thermal performance of the preheater in the industrial carbonyl process [15] (Fig. 1) is numerically investigated. The preheater is essentially a tube-and-shell heat exchanger, with the moving packed bed of nickel pellets in a stagnant carbon monoxide atmosphere composing the "tube" side, while hot flue gases make up the "shell" side. After leaving the preheater, the pellets enter a cold-wall reaction zone where coatings of nickel are deposited onto the pellets. Inefficiencies in heat transfer in the preheater can result in poor nickel decomposition later on in the reaction zone, for nickel deposition rate is very sensitive to pellet temperature as the process is diffusion controlled [16]. The primary goal of the work is to arrive at solving the issue of the large differences in temperature from pellet to pellet in the industrial preheater. A parametric study of several variables is conducted in order to analyze heat transfer in the preheater in an attempt to optimize the overall process. Both one-equation and two-equation models are used and the corresponding results are compared.

Matehmatical Modeling

Figure 2 depicts a detailed schematic diagram of the moving packed bed under consideration. Heat is transferred from the hot flue gases to the pellets by convective and conductive heat transport. The pellets are heated up from an entry temperature of 210 °C as they travel down the preheater. In establishing the model for anlyzing the problem at hand, the following assumptions are employed:

- The pellets are randomly distributed, i.e., bed porosity is assumed to be constant, and their mass flow rate is constant.

[1]To whom correspondence should be addressed.

Contributed by the Applied Mechanics Division of ASME for publication in the JOURNAL OF APPLIED MECHANICS. Manuscript received June 28, 2004; final manuscript received April 18, 2005. Assoc. Editor: O. M. O'Reilly. Discussion on the paper should be addressed to the Editor, Prof. Robert M. McMeeking, Journal of Applied Mechanics, Department of Mechanical and Environmental Engineering, University of California—Santa Barbara, Santa Barbara, CA 93106-5070, and will be accepted until four months after final publication of the paper itself in the ASME JOURNAL OF APPLIED MECHANICS.

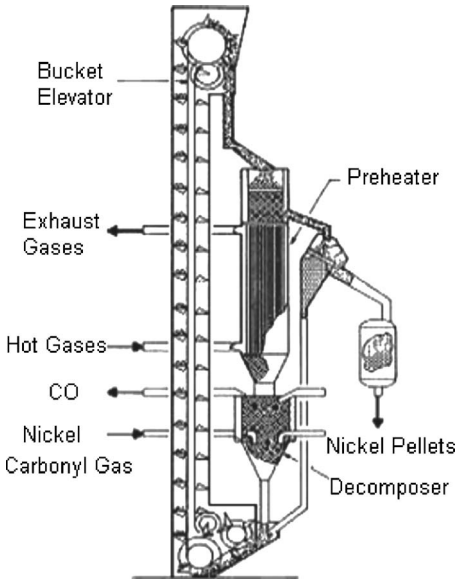

Fig. 1 Cross-sectional view of the industrial nickel carbonylation process [15]

- The fluid is stagnant, i.e., the corresponding convective term is ignored.
- Variation of thermal, physical and transport properties with temperature is negligible.
- Heat transfer is two-dimensional.

Based on these assumptions and the two-equation model, the energy equations written in cylindrical coordinates for the solid and fluid phases are

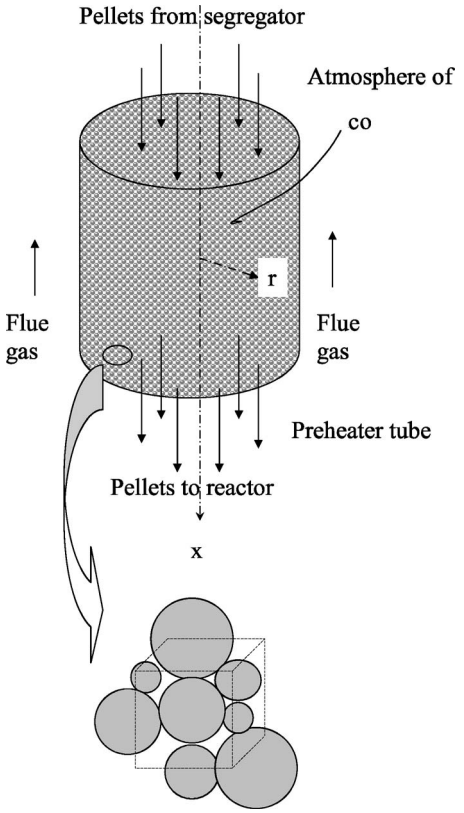

Fig. 2 Schematic diagram of the moving packed bed in the preheater

Solid phase

$$\rho_s C_{p_s}\frac{\partial T_s}{\partial t}+\rho_s C_{p_s} v_s\left(\frac{\partial T_s}{\partial x}\right)=k_s\left(\frac{1}{r}\frac{\partial}{\partial r}\left\{r\frac{\partial T_s}{\partial r}\right\}+\frac{\partial^2 T_s}{\partial x^2}\right)-\left(\frac{hA}{1-\varepsilon}\right)(T_s-T_f) \quad (1)$$

Fluid phase

$$\rho_f C_v\frac{\partial T_f}{\partial t}=k_f\left(\frac{1}{r}\frac{\partial}{\partial r}\left\{r\frac{\partial T_f}{\partial r}\right\}+\frac{\partial^2 T_f}{\partial x^2}\right)+\frac{hA}{\varepsilon}(T_s-T_f) \quad (2)$$

where k_s and k_f are the thermal conductivities of the solid and fluid phases, respectively, $T_s(\rho_s)$ and $T_f(\rho_f)$ are the solid and fluid temperatures (densities), respectively, Cp_s and C_v are the heat capacities of the solid and fluid phases, respectively, v_s is the linear velocity of the solid phase, h is the fluid-to-solid (or interstitial) heat transfer coefficient, A is the surface area per unit volume of solid, ε is the porosity of the packed bed, t is time, and x and r are the axial and radial coordinates, respectively. The specific surface area of the packed bed can be expressed in terms of ε and pellet diameter d_p as suggested by Dullien [17]

$$A=\frac{6(1-\varepsilon)}{d_p}. \quad (3)$$

Data on heat transfer coefficients in moving packed beds are quite scarce. However, recent studies have shown that, in general, transport coefficients in moving beds are similar in magnitude to those in a stopped bed [18,19]. In this wok, the interstitial heat transfer coefficient has been estimated from a correlation based on experimental findings of Wakao et al. [20] for a fluid flowing in a fixed bed. For the purpose of this study, the Reynolds number (Re), with magnitudes <50, has been defined relative to a pellet particle. Further details are given in the Appendix.

In order to make the problem more tractable, the energy equations have been non-dimensionalized. Written in dimensionless form, Eqs. (1) and (2) become

$$\frac{\partial T_s^*}{\partial t^*}+c_s\left(\frac{\partial T_s^*}{\partial x^*}\right)=d_s\left(\frac{1}{r^*}\frac{\partial}{\partial r^*}\left\{r^*\frac{\partial T_s^*}{\partial r^*}\right\}+\frac{\partial^2 T_s^*}{\partial x^{*2}}\right)-g_s(T_s^*-T_f^*) \quad (4)$$

$$\frac{\partial T_f^*}{\partial t^*}=d_f\left(\frac{1}{r^*}\frac{\partial}{\partial r^*}\left\{r^*\frac{\partial T_f^*}{\partial r^*}\right\}+\frac{\partial^2 T_f^*}{\partial x^{*2}}\right)+g_f(T_s^*-T_f^*) \quad (5)$$

with the following boundary and initial conditions for each phase:

Inlet: A Dirichlet type boundary condition is employed at the preheater inlet

$$T_s^*=T_f^*=T_{\text{inlet}}^*, \quad x^*=0. \quad (6)$$

Outlet: The preheater is long enough ($L/R=92$) so as to neglect the effect of the inlet, i.e.,

$$-\frac{\partial T_s^*}{\partial x^*}=-\frac{\partial T_f^*}{\partial x^*}=0, \quad x^*=1 \quad \text{(Danckwerts condition)}. \quad (7)$$

Centerline: A symmetry condition is adopted along the preheater centerline

$$\frac{\partial T_s^*}{\partial r^*}=\frac{\partial T_f^*}{\partial r^*}=0, \quad r^*=0. \quad (8)$$

Inner wall: A mixed type boundary condition is invoked at the preheater inner wall

$$-\frac{\partial T_s^*}{\partial r^*}=\frac{h_{sw}L}{k_s}(T_s^*-T_w^*)$$

Table 1 Properties and parameters considered in the investigation

Two-Equation Model											
ε	c_s	d_s	g_s	d_f	g_f	h	h_{fw}	h_{sw}	L	k_s	k_f
0.37	1.00	4.27×10^{-05}	0.47	7.68×10^{-4}	7.40×10^{3}	19.9	8.78	1.02×10^{4}	4.07	19.6	3.81×10^{-2}

One-Equation Model					
ε	c	d	h_w	L	$\langle k\rangle$
0.37	1.00	4.279×10^{-05}	171	4.07	12.4

$$-\frac{\partial T_f^*}{\partial r^*}=\frac{h_{fw}L}{k_f}(T_f^*-T_w^*)\quad r^*=R/L \tag{9}$$

where h_{sw} and h_{fw} are the solid-to-wall and fluid-to-wall heat transfer coefficients, respectively. The latter along with k_s have been estimated from correlations based on theoretical findings of previously performed studies. The correlations established by Dixon and Cresswell [21] were found to be suitable for use for the range of particle Reynolds numbers that were considered in the present work (see the Appendix).

Initial conditions

$$T_s^*=T_{so}^*,\quad T_f^*=T_{fo}^*,\quad t^*=0 \tag{10}$$

with

$$T_f^*=\frac{T_f}{T_{w\,\max}},\quad T_s^*=\frac{T_s}{T_{w\,\max}},\quad r^*=\frac{r}{L},\quad x^*=\frac{x}{L},\quad t^*=\frac{t}{t_o},$$

$$d_f=\frac{k_f t_o}{\rho_f C_v L^2},\quad g_f=\frac{hAt_o}{\rho_f C_v \varepsilon},\quad c_s=\frac{t_o v_s}{L},\quad d_s=\frac{k_s t_o}{\rho_s C_{p_s} L^2},$$

$$g_s=\frac{hAt_o}{\rho_s C_{p_s}(1-\varepsilon)}$$

where T_{so}^* and T_{fo}^* are the initial dimensionless solid and fluid temperatures, respectively, T_{inlet}^* is the dimensionless temperature of the solid and fluid before entering the preheater, L and R are the preheater tube length and radius, respectively, and t_o is the residence time of the pellets in the preheater. The maximum packed-bed wall temperature is $T_{w\,\max}$, and T_w^* is the dimensionless packed-bed wall temperature determined experimentally as a function of the distance along the preheater wall as follows:

$$T_w^*=0.2058x^*+0.7942. \tag{11}$$

Equation (11) has been obtained by measuring the temperature at different points on the outer side of the packed-bed wall, using a thermocouple whose accuracy is of the order of ±0.5%. Equation (11) has been used to compute the thermal behavior of the bed unless otherwise stated. The one-equation model, which does not distinguish between the solid and fluid phases and assumes a unified temperature T^* takes the form

$$\frac{\partial T^*}{\partial t^*}+c\left(\frac{\partial T^*}{\partial x^*}\right)=d\left(\frac{1}{r^*}\frac{\partial}{\partial r^*}\left\{r^*\frac{\partial T^*}{\partial r^*}\right\}+\frac{\partial^2 T^*}{\partial x^{*2}}\right) \tag{12}$$

with boundary and initial conditions

$$T^*=T_{\mathrm{inlet}}^*,\quad x^*=0 \tag{13}$$

$$-\frac{\partial T^*}{\partial x^*}=0,\quad x^*=1 \tag{14}$$

$$\frac{\partial T^*}{\partial r^*}=0,\quad r^*=0 \tag{15}$$

$$-\frac{\partial T^*}{\partial r^*}=\frac{h_w L}{\langle k\rangle}(T^*-T_w^*),\quad r^*=R/L \tag{16}$$

where h_w is the apparent wall heat transfer coefficient and was calculated from a correlation in Ref. [21] (see the Appendix).

$$T^*=T_o^*,\quad t^*=0 \tag{17}$$

and

$$c=\frac{(1-\varepsilon)\rho_s C_{p_s} t_o v}{\langle\rho C_p\rangle L},\quad d=\frac{\langle k\rangle t_o}{\langle\rho C_p\rangle L^2},$$

$$\langle k\rangle=(1-\varepsilon)k_s+\varepsilon k_f,\quad \langle\rho C_p\rangle=(1-\varepsilon)\rho_s C_{p_s}+\varepsilon\rho_f C_v$$

where $\langle k\rangle$ and $\langle\rho C_p\rangle$ are the average conductivity and heat capacity between the solid and fluid phases, respectively.

The set of Eqs. (4) and (5) with boundary and initial conditions (6)–(10), based on the two-equation model, constitute a complete set of equations for the moving bed as a function of the diffusion coefficients d_s and d_f, flow parameter c_s, interstitial convection parameters g_s and g_f, and preheater aspect ratio R/L. Similarly, for the one-equation model, Eq. (12) with boundary and initial conditions (13)–(17) constitute a complete set of equations for the moving bed as a function of the diffusion coefficient d, flow parameter c, and preheater aspect ratio R/L. An analytical solution for the coupled system of partial differential equations, corresponding to the two-equation model, may be difficult to find. Our initial attempt to analytically solve the one-equation model has so far proved to be a nontrivial one because of the nature of the boundary conditions. For their solution, both models with their proper boundary conditions have been implemented and numerically solved in Femlab environment [22]. Femlab (Stockholm, Sweden) provided for the discretization of the equations using a finite-element scheme, and for the iterative solution of the set of equations using an implicit ordinary differential equation (ODE) solver based on the method of lines.

Results and Discussion

Pellets with a d_{80} size (80% passing) of 9.2 mm have been used to carry out the numerical runs. The thermal and physical properties have been evaluated at the average temperature of the packed bed of 508 K, and some of the properties, such as ε and T_w, have been experimentally determined. Table 1 lists a range of solid and fluid phase properties along with other parameters that have been used in this work. These data correspond to the standard process operating conditions. In order to perform a parametric study of the preheater performance some of the parameters have been changed and their new values are given along with the corresponding numerical runs. The mesh, defined in terms of Δx^* and Δr^*, was refined and the integration time step Δt^* was decreased until the calculated temperatures have become independent of the discretisation parameters.

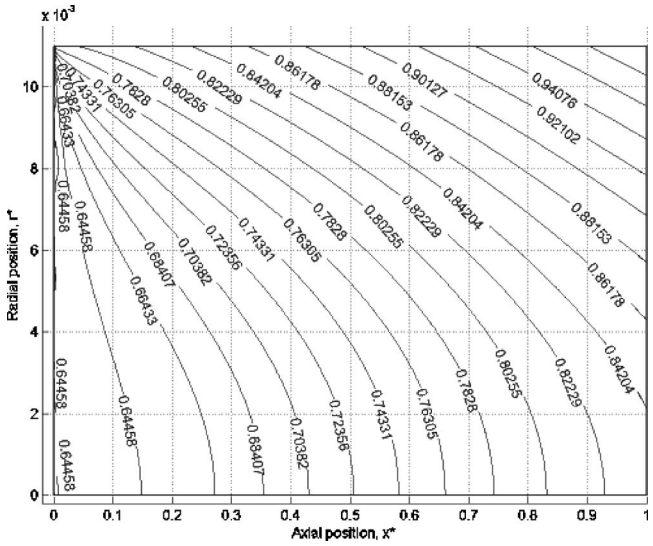

Fig. 3 Space distribution of the solid phase dimensionless temperature in the preheater under standard process conditions and at time $t^*=1$

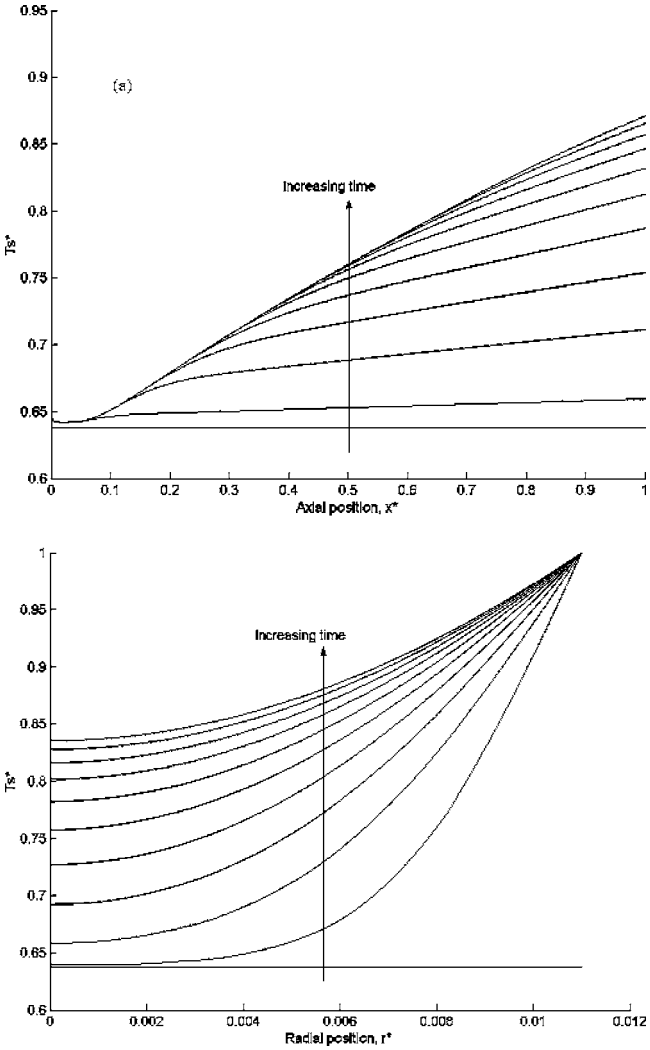

Fig. 4 Transient dimensionless temperature profiles of the solid phase along the preheater at position $r^*=0.005$ (*a*) and at the preheater outlet, $x^*=1$ (*b*). The curves correspond to the dimensionless time range 0–1 with an increment of 0.1.

Two-Equation Model. The space distribution of the solid phase temperature, under the standard process conditions and at $t^*=1$, is depicted in Fig. 3. It can be noticed that temperature gradients exist in both axial and radial directions of the preheater. The transient temperature behavior along the packed bed and at its outlet is shown in Figs. 4(*a*) and 4(*b*), respectively. The pellet temperature progressively reaches steady-state throughout the packed bed, as shown in Fig. 4(*a*), except near the bed outlet. The temperature of the pellets as they are about to leave the preheater is smallest near the preheater center and largest near its wall, as illustrated in Fig. 4(*b*). The relative temperature difference at $t^*=1$ is $\Delta T_s^* \sim 16\%$, which translates into a maximum absolute difference of $\Delta T_s \sim 120$ K between pellets near the center and at the wall of the preheater. The magnitude of ΔT_s^* at the preheater outlet reflects the degree of discrepancy in temperature from pellet to pellet as pellets are about to enter the cold-wall reaction zone. Reducing the temperature difference between pellets is crucial and is further investigated in the next section.

Figure 5 shows the temperature difference between the fluid and solid phases along the packed bed at $r^*=0.005$. Generally, the difference is quite small throughout the bed and does not exceed 2 K, except within a region close to the preheater wall (around $r^*=0.009$) and just after the inlet where the difference can reach $\sim$15 K. There is also a change in the sign of the temperature difference, corresponding to ~ -1.25 K, between the two phases just after the inlet. Although the genuine reason behind the sign change is not quite clear, it might be due to the abrupt change in temperature at the entrance.

One-Equation Model. Figure 6 depicts the space distribution of the temperature of the bed under the standard conditions and at $t^*=1$. The calculated temperature pattern is very similar to the pattern obtained using the two-equation model (see Fig. 3), both qualitatively and quantitatively. The concordance between the two models is expected at least from the findings of the two-equation model, viz., the difference between the temperature profiles of the solid and fluid phases is quite small as described in the previous section. The direct assumption associated with the one-equation model is that of local thermal equilibrium (LTE) whereby the temperature difference between the two phases is negligible [13,23–26]. In other studies, LTE has also been found to depend on process conditions such as the ratio k_s/k_f, Reynolds number, and convective transport [9,14,27]. Local thermal equilibrium is generally met for values of k_s/k_f ratio approaching unity, at low values of the Reynolds number, and when convective transport is not important. In the present study, while the condition on k_s/k_f ratio is not met, the latter two are.

In order to improve the preheater performance a parametric study has been conducted using the one-equation model. From the practical viewpoint the results obtained after the manipulation of two parameters, viz., c and T_w^*, are given in the following. Although increasing the magnitude of the parameter d leads to an improvement in the temperature pattern along the preheater, this parameter consists of terms that are essentially inherent properties of the packed bed (e.g., thermal conductivity, density, etc.).

Wall Temperature. Instead of the decreasing T_w^*, expressed by Eq. (11), as the flue gas flows upward along the outer wall of the preheater, a constant value of $T_w^*=1$ has been adopted throughout the preheater wall. The resulting space distribution of the temperature is shown in Fig. 7(*a*). There is a noticeable decrease in the radial temperature gradient at the preheater outlet where $\Delta T^* \sim 8\%$ or $\Delta T \sim 60$ K. A constant wall temperature can be materialized by altering the direction of the flue gas from parallel to perpendicular to the preheater, for instance by having the inlets of the flue gas on one side of the bed and the outlets on the opposite side.

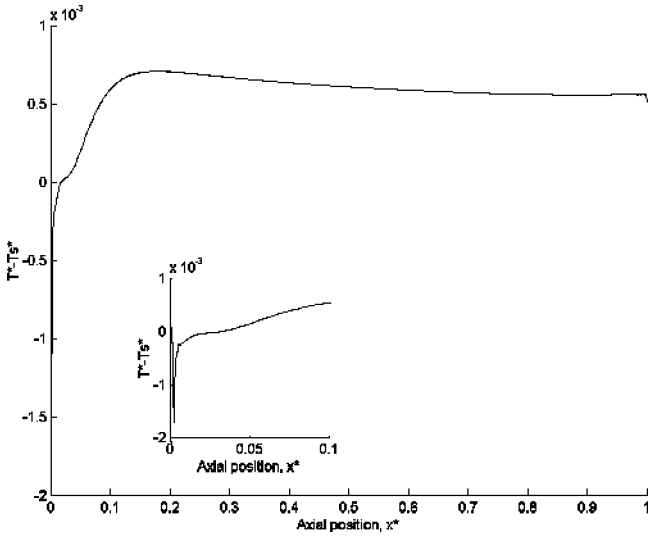

Fig. 5 Temperature difference between the fluid and solid phases along the preheater at position $r^*=0.005$ and time $t^*=1$. The figure in the inset is a "zoom-in" view of the region near the preheater inlet.

Momentum Term. A decrease in c results in a twofold improvement in the temperature pattern of the packed bed, as shown in Fig. 7(*b*) for $c=0.1$. The temperature difference drops at the preheater outlet, and heat transfer is fostered in the radial direction throughout the preheater. A small value of c is synonymous with a slow motion and/or large residence time of the pellets in the preheater. A viable solution would be to keep the mass flow rate constant, to maintain the same level of productivity of pellets, by increasing the cross-section of the preheater tube.

Finally, a combination of the previous two approaches yields the space distribution of the temperature of the packed bed illustrated in Fig. 7(*c*). As can be noticed from the comparison of the current results with those of Figs. 7(*a*) and 7(*b*), a drastic improvement in radial heat transfer throughout the preheater can be achieved, and about the same temperature difference at the outlet, $\Delta T \sim 55$ K, is reached as depicted in Fig. 8.

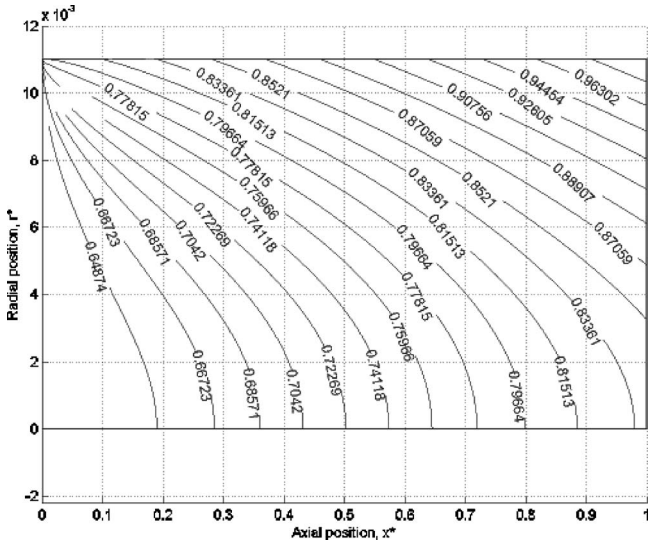

Fig. 6 Space distribution of the bed dimensionless temperature in the preheater under standard process conditions and at time $t^*=1$

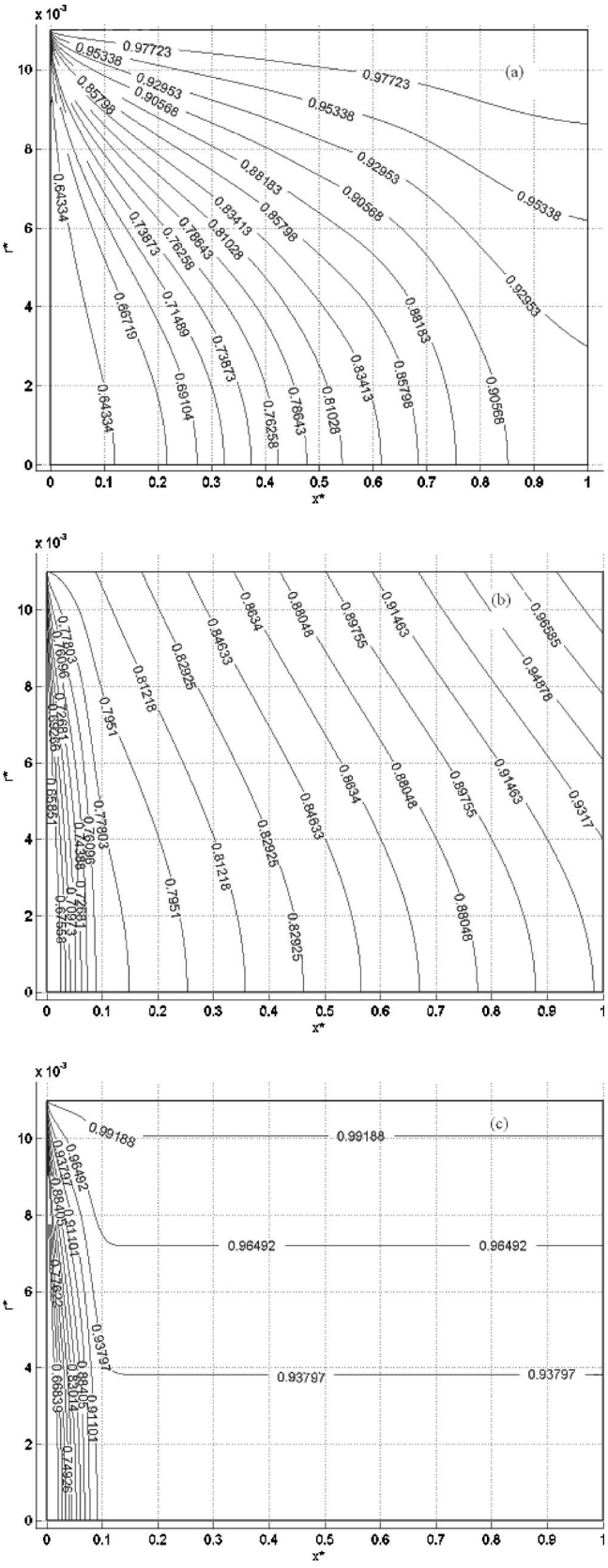

Fig. 7 Space distribution of the bed dimensionless temperature in the preheater at time $t^*=1$ and corresponding to $T_{wall}=1$ (*a*), $c=0.1$ (*b*), and to (*a*) and (*b*) combined (*c*).

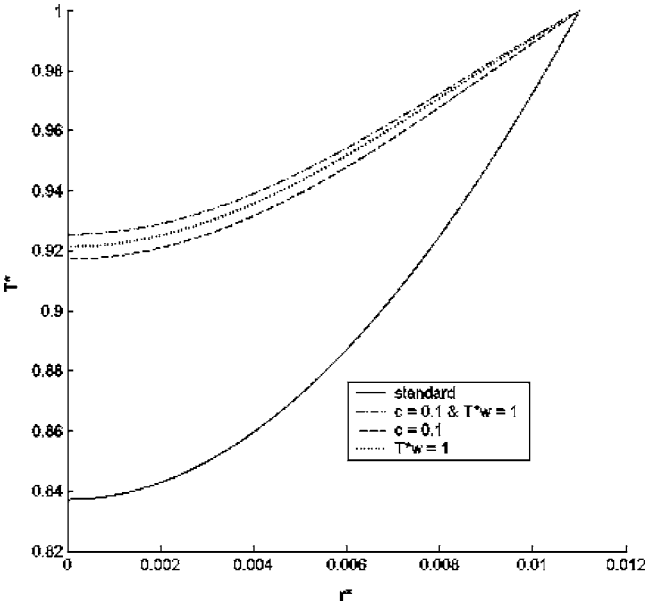

Fig. 8 Temperature profiles of the bed at the preheater outlet and at time $t^* = 1$. The corresponding conditions are indicated in the inset.

Conclusions

This paper describes the thermal performance of an industrial preheater consisting of a moving packed bed of nickel pellets. Both two- and one-equation models have been used to describe the transient thermal response of the preheater. The findings show that there is no appreciable difference between the two models under the investigated conditions. The calculation results show that by adopting a constant temperature at the preheater wall, e.g., by directing the flue gas perpendicular to the preheater tube and decreasing the pellet velocity in the packed bed, the thermal efficiency throughout the preheater is tremendously improved, and the difference in temperature from pellet to pellet at the preheater outlet is reduced from ~120 °C to ~55 °C.

Acknowledgment

Financial support from the Natural Sciences and Engineering Research Council (NSERC) and Laurentian University Research Fund is acknowledged and appreciated.

Nomenclature

A = area of nickel pellet surface per unit volume (m^{-1})
C_p, C_v = specific heat capacities (J kg^{-1} K^{-1})
c = dimensionless convection coefficient
d = dimensionless diffusivity
d_p = pellet diameter (m)
g = dimensionless interstitial heat transfer coefficient
h = effective interstitial heat transfer coefficient (W m^{-2} K^{-1})
k = thermal conductivity (W m^{-1} K^{-1})
L = preheater tube length (m)
P_r = Prandtl number ($\mu C_p/k_f$)
R = preheater tube radius (m)
R_e = Reynolds number, (vd_p/ν)
r = radial direction of preheater tube (m)
T = temperature (K)
T_{inlet} = inlet temperature (K)
T_{so}, T_{fo} = initial temperatures of solid, fluid (K)
$T_{w\,max}$ = maximum preheater wall temperature (K)
t = time (s)
t_o = residence time of pellets in preheater tube (s)
x = axial direction of preheater tube (m)

Greek symbols

v = linear velocity of the medium (m s^{-1})
Δ = increment/difference
ε = porosity of the packed bed
ρ = density of the medium (kg m^{-3})
μ = fluid dynamic viscosity (N s m^{-2})
ν = fluid kinematic viscosity (m^2 s^{-1})

Subscripts

f = fluid phase
p = particle
s = solid phase
w = preheater wall
sw, fw = solid-to-wall, fluid-to-wall

Superscripts

$*$ = dimensionless quantity

Other symbols

$\langle\ \rangle$ = volume average

Appendix

Two-Equation Model

The interstitial h, fluid-to-wall h_{fw}, and solid-to-wall h_{sw}, heat transfer coefficients have been obtained from the following correlations [20,21].

$$h = k_f(2 + 1.1P_r^{1/3}R_e^{0.6})/d_p$$

$$\frac{h_{fw}d_p}{k_f} = 0.6P_r^{1/3}R_e^{1/2}$$

$$\frac{h_{sw}d_p}{k_s} = 2.12$$

The thermal conductivity of the solid phase k_s is given by the following relationship [21]:

$$k_s = 2k_f(1-\varepsilon)^{0.5}\frac{1}{A}\left[\frac{AB}{A^2}\ln\left(\frac{k_p}{Bk_f}\right) - \frac{B+1}{2} - \frac{B-1}{A}\right]$$

with

$$A = 1 - \frac{k_f B}{k_p}$$

and

$$B = 1.25\left(\frac{1-\varepsilon}{\varepsilon}\right)^{10/9}$$

One-Equation Model

The apparent wall heat transfer coefficient h_w was calculated from the following correlation [21]:

$$\frac{h_w d_p}{k_f} = 4\beta\left(\frac{d_p}{R}\right) + \left(\frac{h_{fw}d_p}{k_f}\right)$$

where

$$\beta = \frac{\left(\frac{k_s}{k_f}\right)}{\left(\frac{8k_s}{AR^2h} + \frac{4 + \frac{h_{sw}R}{k_s}}{\frac{h_{sw}R}{k_s}}\right)}$$

References

[1] Tien, C. L., and Vafai, K., 1989, "Convective and Radiative Heat Transfer in Porous Media," Adv. Appl. Mech., **27**, pp. 225–281.

[2] Kuzay, T. M., Collins, J. T., Khounasry, A. M., and Morales, G., 1991, "Enhanced Heat Transfer with Metal-Wood-Filled Tubes," *Proc. of ASME/JSEM Thermal Engineering Conference*, Reno, NV, ASME, New York, pp. 145–151.

[3] Kuzay, T. M., 1992, "Cryogenic Cooling of X-ray Crystals Using a Porous Matrix," Rev. Sci. Instrum., **63**(1), pp. 468–472.

[4] Rosenfled, J. H., and North, M. T., 1995, "Porous Media Heat Exchangers for Cooling of High-Power Optical Components," Opt. Eng., **34**, pp. 335–341.

[5] Khaled, A.-R. A., and Vafai, K., 2003, "The Role of Porous Media in Modeling Flow and Heat Transfer in Biological Tissue," Int. J. Heat Mass Transfer, **46**, pp. 4989–5003.

[6] Schumann, T. E. W., 1929, "Heat Transfer: Liquid Flowing Through a Porous Prizm," J. Franklin Inst., **208**, pp. 405–416.

[7] Burch, D. M., Allen, R. W., and Peavy, B. A., 1976, "Transient Temperature Distribution within Porous Slabs Subjected to Sudden Transpiration Heating," ASME J. Heat Transfer, **98**, pp. 221–225.

[8] Whitaker, S., 1977, "Simultaneous Heat, Mass, and Momentum Transfer in Porous Media: A Theory of Drying," Adv. Heat Transfer, **13**, pp. 119–203.

[9] Vafai, K. and Sözen, M., 1990, "Analysis of Energy and Momentum Transport for Fluid Flow Through a Porous Bed," ASME J. Heat Transfer, **112**, pp. 690–699.

[10] Amiri, A., and Vafai, K., 1999, "Transient Analysis of Incompressible Flow through a Packed Bed," Int. J. Heat Mass Transfer, **41**, pp. 4259–4279.

[11] Vortmeyer, J., and Schaefer, R. J., 1974, "Equivalence of One- and Two-Phase Models for Heat Tarnsfer Processes in Packed Beds: One Dimensional Theory," Chem. Eng. Sci., **29**, pp. 485–491.

[12] Riaz, M., 1977, "Analytical Solutions for Single- and Two-Phase Models of Packed-Bed Thermal Storage Systems," ASME J. Heat Transfer, **99**, pp. 489–492.

[13] Whitaker, S., 1998, *The Method of Volume Averaging*, "Theory and Applications of Transport" in Porous Media Series, Kluwer Academic Publishers, Dordrecht, The Netherlands, Vol. 13.

[14] Lee, D.-Y., and Vafai, K., 1999, "Analytical Characterization and Conceptual Assessment of Solid and Fluid Temperature Differentials in Porous Media," Int. J. Heat Mass Transfer, **42**, pp. 423–435.

[15] Wiseman, L. G., Bale, R. A., Chapman, E. T., and Martin, B., 1988, "Inco's Copper Cliff Nickel Refinery," *Proc. Symposium on Metallurgy of Nickel and Cobalt*, edited by G. P. Tyroler and C. A. Landolt, The Metallurgical Society, Warrendale, PA, pp. 373–390.

[16] Tonneau, D., Auvert, G., and Pauleau, Y., 1989, "Deposition of Nickel Microstructures by CO_2 Laser-Assisted Decomposition of Nickel Tetracarbonyl," J. Appl. Phys., **66**(1), pp. 165–168.

[17] Dullien, F. A. L., 1979, *Porous Media Fluid Transport and Pore Structure*, Academic Press, NY.

[18] Crawshaw, J. P., Paterson, W. R., and Scott, D. M., 2000, "Gas Channelling and Heat Transfer in Moving Beds of Spherical Particles," Trans. Inst. Chem. Eng., Part A, **78**, pp. 465–472.

[19] Crawshaw, J. P., Paterson, W. R., and Scott, D. M., 1993, "Gas Residence Time Distribution Studies of Fixed, Moving and Frozen Beds of Spheres." Trans. Inst. Chem. Eng., Part A, **71**, pp. 643–648.

[20] Wakao, N., Kaguei, S., and Funazkri, T., 1979, "Effect of Fluid Dispersion Coefficients on Particle-to-Fluid Heat Transfer Coefficients in Packed Beds," Chem. Eng. Sci., **34**, pp. 325–336.

[21] Dixon, A. G., and Cresswell, D. L., 1979, "Theoretical Predictions of Effective Heat Transfer Parameters in Packed Beds," AIChE J., **25**, pp. 663–676.

[22] Femlab 2.3, Comsol AB, Stockholm, Sweden, 2003.

[23] Whitaker, S., 1991, "Improved Constraints for the Principle of Local Thermal Equilibrium," Ind. Eng. Chem. Res., **30**, pp. 983–997.

[24] Thorpe, G. R., and Whitaker, S., 1992, "Local Mass and Thermal Equilibrium in Ventilated Grain Bulks I: The Development of Heat and Mass Conservation Equations," J. Stored Prod. Res., **28**, pp. 15–27.

[25] Quintard, M., and Whitaker, S., 1993, *One and Two-Equation Models for Transient Diffusion Processes, in Advances in Heat Transfer*, Vol. 23, Academic Press, NY.

[26] Quintard, M., and Whitaker, S., 1995, "Local Thermal Equilibrium for Transient Heat Conduction: Theory and Comparison with Numerical Experiments," Int. J. Heat Mass Transfer, **38**, pp. 2779–2796.

[27] Sozen, M., Vafai, K., and Kennedy, L. A., 1991, "Analysis of Thermal Charging and Discharging for Sensible Heat and Latent Heat Storage Packed Beds," J. Thermophys. Heat Transfer, **5**, pp. 623–625.

Magnetohydrodynamics-Mixed Convection From Radiate Vertical Isothermal Surface Embedded in a Saturated Porous Media

Rebhi A. Damseh
Mechanical Engineering Department,
Alhuson University College,
Albalqa Applied University,
P. O. Box 50
Irbid 009612, Jordan
e-mail: rdamseh@yahoo.com

The magnetohydrodynamics-mixed convection heat transfer problem from a vertical surface embedded in a porous media is studied. The effects of transverse magnetic field and radiation heat transfer are examined. Both cases of the mixed convection heat transfer problem, namely: the buoyancy aiding flow and the buoyancy opposing flow are investigated. It is found that three dimensionless groups can describe the problem under consideration, the mixed convection parameter ζ, the radiation-conduction parameter R_d, and the magnetic field number Ha_x^2/Re_x. Different velocity profiles, temperature profiles, and the local Nusselt number variations are also drawn. [DOI: 10.1115/1.1991863]

Introduction

High-temperature plasmas, cooling of nuclear reactors, liquid metal fluids, magnetohydrodynamics (MHD) accelerators, and power generation systems are important applications for radiation heat transfer from a vertical wall to conductive gray fluids. The inclusion of radiation effect in the energy equation, however, leads to a highly nonlinear partial differential equation [1]. Hossain [2] studied the effects of viscous and Joule heating from vertical surfaces with variable wall temperature. Soundalgekar et al. [3] studied the radiation effects on free convection flow of a gas past a semi-infinite flat plate using the Cogley-Vincenti-Giles equilibrium model. Cogely et al. [4], Hossain and Takhar [5] analyzed the effect of radiation using the Rosseland diffusion approximation on the forced and natural convection flow of an optically dense fluid from vertical surfaces. Hossain et al. [6] studied the effect of radiation on natural convection heat transfer. Many problems of Darcian and non-Darcian mixed convection about a vertical plate and other types of geometries had been reported, as in Hsu and Cheng [7], Vafai and Tien [8], Minkowycz et al. [9], Nield [10], Lai and Kulacki [11], Hsieh et al. [12], Aldoss et al. [13], and Duwairi et al. [14].

However, many authors studied the effects of magnetic field on forced and natural convection heat transfer problems. Among those, Kafoussias [15] who studied the effect of magnetic field on free convection through a nonhomogenous porous medium over an isothermal cone. Gulab and Mishra [16] analyzed the unsteady magnetohydrodynamic porous medium. Raptis and Kafoussias [17] studied the effect of the magnetic field on the heat transfer problem along a vertical wall embedded in saturated porous medium. Takhar and Ram [18] studied the magnetohydrodynamic free convection flow of water at 4 °C through a porous medium. Aldoss et al. [19] studied the MHD mixed convection heat transfer problem from vertical surfaces embedded in saturated porous medium, finally, Duwairi and Damseh [20] analyzed the MHD natural convection heat transfer from radiate vertical surfaces with fluid suction or injection. The effects of thermal radiation and magnetic field on natural convection heat transfer from an inclined plate embedded in a variable porosity porous medium analyzed recently by Chamkha et al. [21].

On the other hand, few works are available in the literature on the subject of MHD mixed convection flow in porous media, and the MHD mixed convection for the buoyancy opposing flow had not been yet addressed.

In this work, the buoyancy aiding or opposing mixed convection heat transfer form vertical surfaces embedded in porous media with radiation-conduction interaction is studied. Both the transverse and induced magnetic field effects are included in the transformation.

Analysis

Consider a semifinite vertical isothermal plate with uniform surface temperature subjected to combined natural and forced convection as shown in Fig. 1. The fluid considered is a gray, emitting-absorbing but nonscattering medium. We also consider the influence of a transversely applied magnetic field on such flow. In the present paper, the variations in fluid properties are limited only to those density variations which affects the buoyancy term. The radiate heat flux in the x direction is considered negligible in comparison with that in the y direction. The physical coordinate x is measured from the leading in the stream wise direction and y is measured normal to the surface of the plate. These conditions do not lead to a similar solution of the laminar boundary-layer equations. Therefore, solutions of the governing equations are obtained utilizing a nonsimilar approach. Under boundary-layer approximations, the continuity, momentum, and energy equations are written as, Kaviany [22]

$$\frac{\partial u}{\partial x}+\frac{\partial v}{\partial y}=0 \tag{1}$$

$$\frac{\left(u\dfrac{\partial u}{\partial x}+v\dfrac{\partial u}{\partial y}\right)}{\varepsilon^2}+\frac{\nu}{K}(u-u_\infty)+\frac{K'}{\sqrt{K}}(u^2-u_\infty^2)+\frac{\sigma B_0^2}{\rho}(u-u_\infty)=\frac{\nu\dfrac{\partial^2 u}{\partial y^2}}{\varepsilon}\pm g\beta(T-T_\infty) \tag{2}$$

Contributed by the Applied Mechanics Division of ASME for publication in the American Society of Mechanical E. Manuscript received June 2, 2004; final manuscript received April 20, 2005. Assoc. Editor: D. Siginer. Discussion on the paper should be addressed to the Editor, Prof. Robert M. McMeeking, Journal of Applied Mechanics, Department of Mechanical and Environmental Engineering, University of California—Santa Barbara, Santa Barbara, CA 93106-5070, and will be accepted until four months after final publication in the paper itself in the ASME Journal of Applied Mechanics.

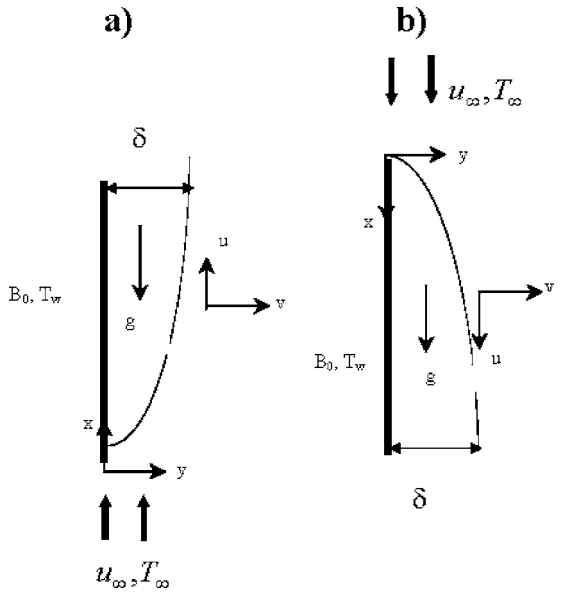

Fig. 1 Flow model and coordinate system

$$\rho c_p\left(u\frac{\partial T}{\partial x}+v\frac{\partial T}{\partial y}\right)-\sigma B_0^2u^2=k_{\text{eff}}\left(\frac{\partial^2 T}{\partial y^2}\right)+\frac{\partial}{\partial y}\left(\frac{16a}{3\alpha_R}T^3\frac{\partial T}{\partial y}\right) \quad (3)$$

Note that the momentum equation includes both the macroscopic and microscopic inertial forces with the effect of the damping shear stress near the isothermal wall being considered. Also the momentum equation includes a magnetic influence term. The second term on the right-hand side of the energy equation represents the radiation heat transfer effects of an optically thick fluid as described by Ali et al. [23], and the second term on the left-hand side represents the Joule heating effects. In the above system of partial differential equations a is the Stefan-Boltzmann constant and α_R is the Rosseland mean absorption coefficient. There is an interesting aspect involving magnetohydrodynamic effects in mixed convection boundary layers, that is the induced magnetic forces modify the free stream flow, and this in turn affects the external pressure gradient or the free stream velocity which is imposed in the boundary layer. Thus a complete boundary-layer solution would involve a magnetohydrodynamic solution for the inviscid free stream.

$$-\frac{1}{\rho}\frac{\partial p}{\partial x}=\pm g\beta(T-T_\infty)-\frac{\nu}{K}u_\infty-\frac{K'}{\sqrt{K}}u_\infty^2+\frac{\sigma B_0^2}{\rho}u_\infty \quad (4)$$

The boundary conditions for the problem under consideration are

$$y=0,\quad u=0,\quad v=0,\quad T=T_w$$
$$y\to\infty,\quad u=u_\infty,\quad T=T_\infty \quad (5)$$

In order to satisfy continuity equation, define $u=\partial\psi/\partial y$, $v=-\partial\psi/\partial x$, and introduce the following dimensionless variables:

$$\eta=(y/x)\text{Pe}_x^{1/2},\quad \zeta=\zeta(x) \quad (6)$$

$$\psi=\alpha_{\text{eff}}\text{Pe}_x^{1/2}f(\zeta,\eta),\quad \theta(\zeta,\eta)=\frac{T-T_\infty}{T_w-T_\infty} \quad (7)$$

Substitute Eqs (6) and (7) in the governing Eqs. (1) and (4), the momentum and energy equations can be written as

$$\frac{f'''}{\varepsilon}+\frac{(1/2)ff''}{\varepsilon^2}+\left[\frac{1}{K_1}+\frac{Ha_x^2}{\text{Re}_x}\right](1-f')+K_2(1-f'^2)\pm\zeta\theta=0 \quad (8)$$

$$\theta''+[\{(4/3R_d)[1+(\theta_w-1)\theta]^3\}\theta']'+(1/2)f\theta'+\frac{Ha_x^2}{Re_x}\text{Ec}(f')^2=0 \quad (9)$$

Where

$$\zeta(x)=\text{Ra}_x/\text{Pe}_x,\quad \text{Re}_x=u_\infty x/\upsilon,\quad \text{Ha}_x^2=\sigma B_0^2x^2/\rho\upsilon,$$
$$\text{Ec}=u_\infty^2/cp(T_w-T_\infty),\quad \text{Da}_x=K/x^2,\quad \text{Pr}=\upsilon/\alpha,$$
$$K_1=1/\text{Re}_xDa_x,\quad K_2=K'u_\infty/\upsilon,\quad \theta_w=T_w/T_\infty,$$
$$R_d=k_{\text{eff}}\alpha_R/4aT_\infty^3.$$
$$f'(\zeta,0)=0,\quad f(\zeta,0)=0,\quad \theta(\zeta,0)=1$$

and

$$f'(\zeta,\infty)=1,\quad \theta(\zeta,\infty)=0 \quad (10)$$

The primes denote partial differentiations with respect to η. In the above system of equations, the radiation-conduction parameter is absent from the MHD-mixed convection heat transfer problem when $1/R_d\to 0$. The plus and minus signs correspond to the buoyancy aiding and buoyancy opposing flows under consideration. In the above system of nonsimilarity equations, the effects of the magnetic field are included as a ratio of Hartman number to the Reynolds number. K_1 and K_2 will reflect the effect of Darcian and Forchheimere flows on the present problem. The physical quantities of interest are the velocity components u and v, the wall shear stress, and the local surface heat flux from the porous wall. They are given by

Table 1 Comparison between the $\text{Nu}_x/\sqrt{\text{Re}_x}$ calculated by the present method and that of Duwairi and Damseh [25], Oosthuizen and Hart [26]. The values of ζ and $\text{Nu}_x/\sqrt{\text{Pe}_x}$ presented in this study are multiplied by Pr and $\sqrt{\text{Pr}}$, respectively, to get the same definitions as in Oosthuizen and Hart.

Aiding						
ζ	Pr=0.7			Pr=7		
	Present method	Duwairi and Damseh	Oosthuizen and Hart	Present method	Duwairi and Damseh	Oosthuizen and Hart
0.1	0.31112	0.31120	0.32001	0.71220	0.71231	0.70804
0.5	0.36511	0.36501	0.35502	0.82012	0.82006	0.80500
1	0.39628	0.39745	0.40506	0.86515	0.86609	0.89603
Opposing						
ζ	Pr=0.1			Pr=7		
	Present method	Duwairi and Damseh	Oosthuizen and Hart	Present method	Duwairi and Damseh	Oosthuizen and Hart
0.01	0.15105	0.15020	0.14022	0.66084	0.66134	0.65031
0.05	0.14003	0.14035	0.13980	0.62108	0.62187	0.61010
0.1	0.10777	0.10867	0.11765	0.65033	0.65000	0.60024

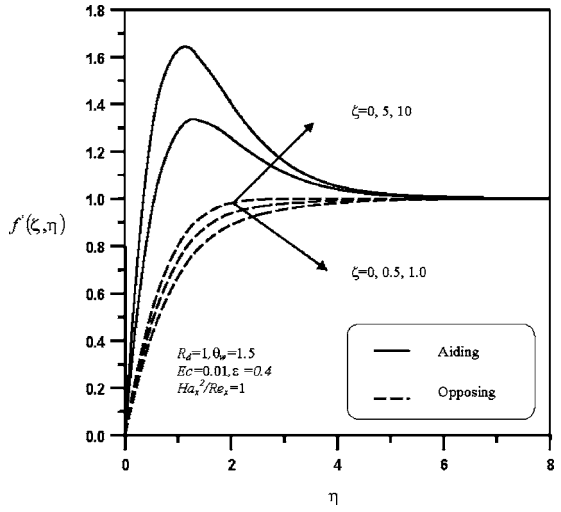

Fig. 2 Dimensionless velocity profiles for different ζ

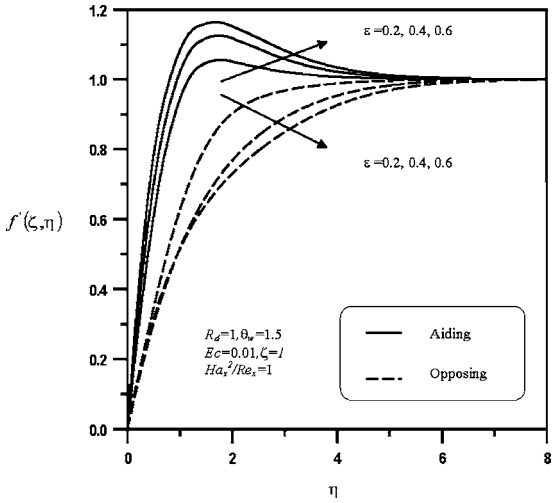

Fig. 4 Dimensionless velocity profiles for different ε

$$u = u_\infty f'(\zeta, \eta) \tag{11}$$

$$v = -\left(\frac{\alpha_{\text{eff}}}{x}\right)\text{Pe}_x^{1/2}\left\{(1/2)f(\zeta,\eta) + \zeta\frac{\partial f}{\partial \xi} - (1/2)\,\eta f'(\zeta,\eta)\right\} \tag{12}$$

$$Cf_x\text{Pr}^{-1}\text{Pe}_x^{1/2} = 2f''(\zeta,0) \tag{13}$$

$$\frac{\text{Nu}_x\text{Pe}_x^{-1/2}}{(1+(4/3R_d)\theta_w^3)} = -\,\theta'(\zeta,0) \tag{14}$$

Numerical Solution

The partial differential Eqs. (8) and (9) under boundary conditions (10) are solved numerically by using an implicit iterative tridiagonal finite-difference method, Cebeci and Bradshaw [24]. In this method, any quantity g at point (ζ_n, η_j) is written as g_j^n. Quantities at the midpoints of grid segments are approximated to second order as

$$g_j^{n-1/2} = \frac{1}{2}(g_j^n + g_j^{n-1}), \quad g_{j-1/2}^n = \frac{1}{2}(g_j^n + g_{j-1}^n) \tag{15}$$

The derivatives are approximated to second order as

$$\left(\frac{\partial g}{\partial \zeta}\right)_j^{n-1/2} = \Delta\zeta^{-1}(g_j^n - g_j^{n-1}), \quad (g')_{j-1/2}^n = \Delta\eta^{-1}(g_j^n - g_{j-1}^n) \tag{16}$$

Where g is any dependent variable, n and j are the node locations along ζ and η directions, respectively. First, the third-order partial differential equation is converted into a first-order one by substitutions of $f' = s$ and $s' = w$. The difference equations used to approximate the previous equations are obtained by averaging about the midpoint $(\zeta_n, \eta_{j-1/2})$ and those to approximate the resulting equations are obtained by averaging about $(\zeta_{n-1/2}, \eta_{j-1/2})$. At each line of constant ζ, a system of algebraic equations is obtained. With the nonlinear terms evaluated at the previous iteration, the algebraic equations are solved iteratively. The same process is repeated for the next value of ζ and the problem is solved line by line until the desired ζ value is reached. A convergence criterion based on the relative difference between the current and previous iterations is employed. When this difference reaches 10^{-5}, the solution is assumed to have converged and the iterative process is terminated.

The accuracy of the selected method is tested by comparing the results with those of Duwairi and Damseh [25] and the classical mixed-convection problem over a vertical isothermal impermeable plate for aiding and opposing flow [26,27]. Table 1 shows a

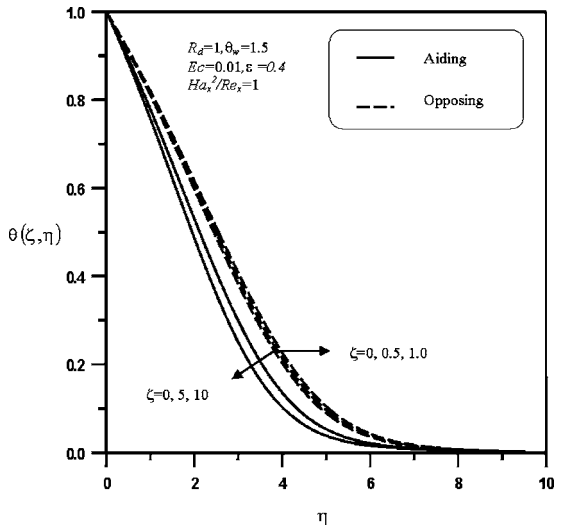

Fig. 3 Dimensionless temperature profiles for different ζ

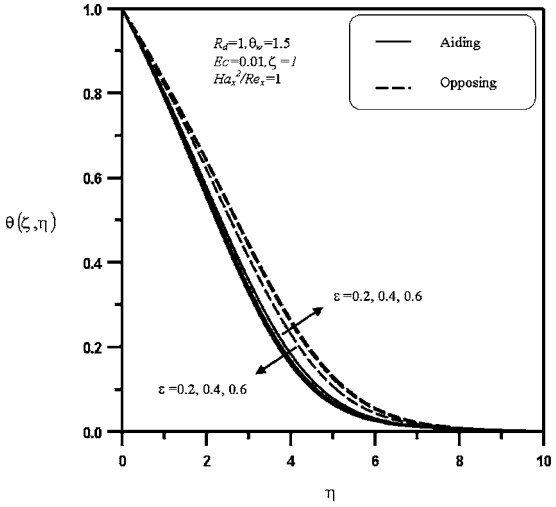

Fig. 5 Dimensionless temperature profiles for different ε

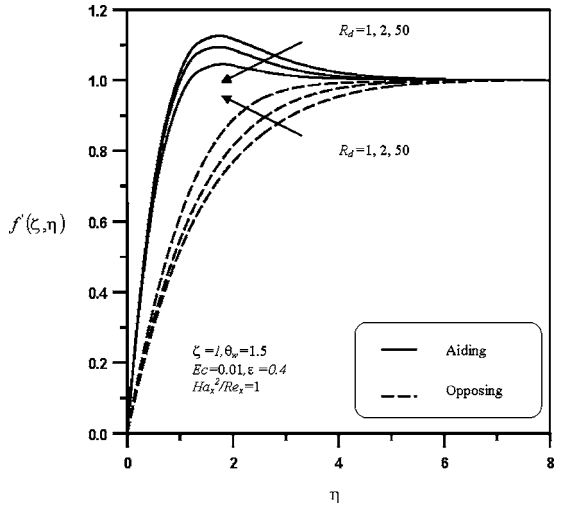

Fig. 6 Dimensionless velocity profiles for different R_d

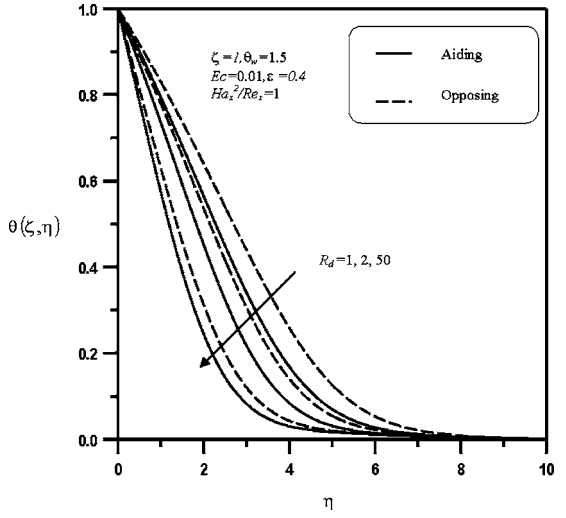

Fig. 7 Dimensionless temperature profiles for different R_d

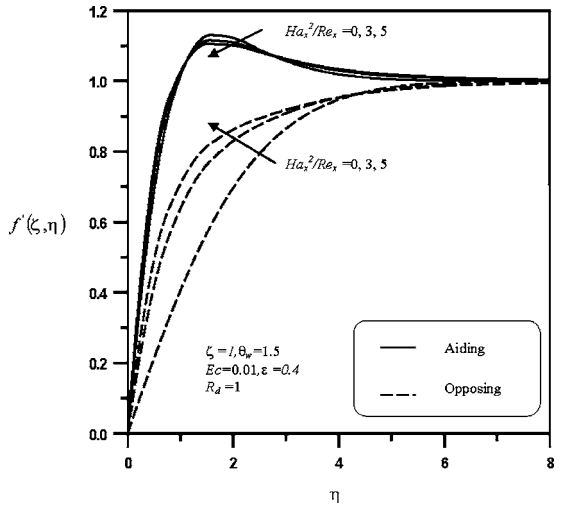

Fig. 8 Dimensionless velocity profiles for different Ha_x^2/Re_x

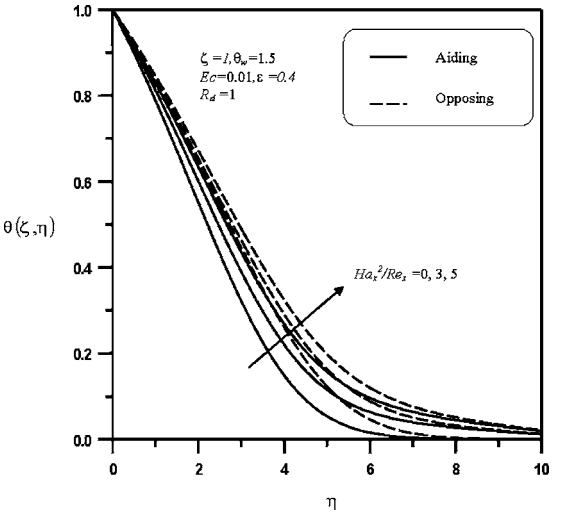

Fig. 9 Dimensionless temperature profiles for different Ha_x^2/Re_x

comparison between the Nusselt number at different mixed parameter ζ obtained by the presented numerical method and that of the mentioned references. The values of Ha_x^2/Re_x and Ec are assigned 0 to remove the effects of magnetic field. The radiation

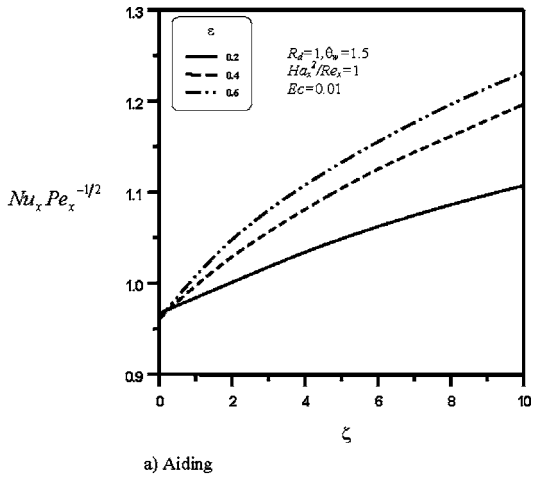

a) Aiding

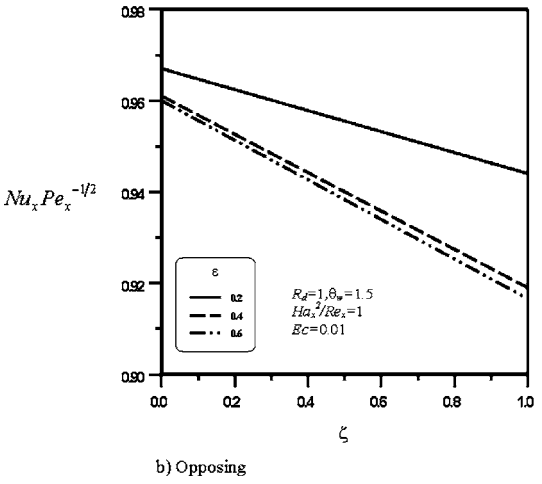

b) Opposing

Fig. 10 Local Nusselt number variations for different ε

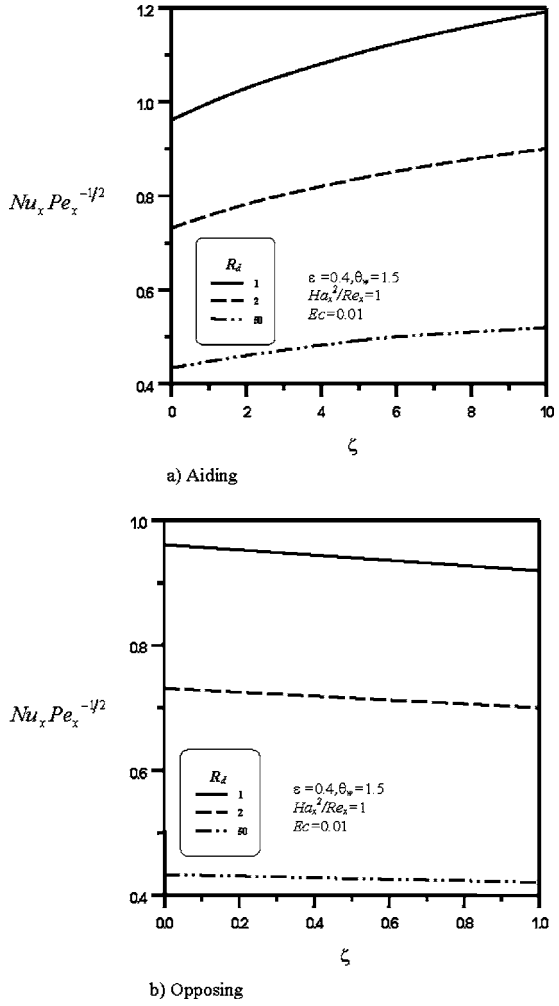

Fig. 11 Local Nusselt number variations for different R_d

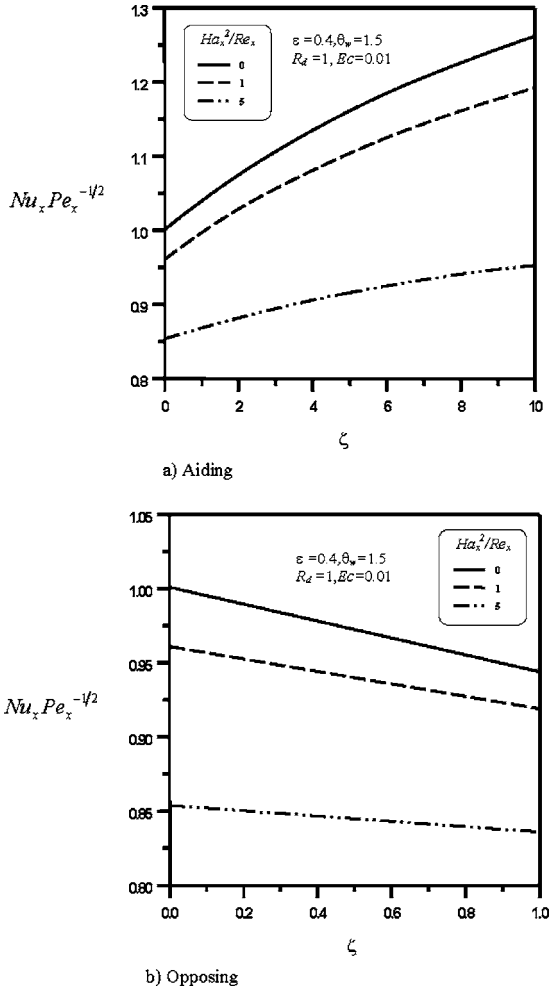

Fig. 12 Local Nusselt number variations for different Ha_x^2/Re_x

effect is absent when $R_d \to \infty$. Mathematically, to remove the effect of porous media the values of ε, K_1, and K_2 are assigned 1, ∞, and 0 respectively.

Results and Discussion

The MHD-mixed convection heat transfer problem with radiation heat transfer effects from isothermal wall embedded in saturated porous medium between fluid layers is analyzed. The buoyancy aiding and opposing flows have been studied. The results are drawn for selected values of $K_1=10$ and $K_2=2$ against dimensionless groups. Comparisons with previously published work were performed and the results were found to be in good agreements. It is hoped that this work will serve as a motivation for future experimental work which seems to be lacking at the present time.

The effects of the mixed parameter for the buoyancy aiding and opposing flows on both the velocity and temperature profiles are drawn on Figs. 2 and 3. For the buoyancy aiding flow, increasing the mixed parameter will increase the velocity inside the boundary layer due to favorable buoyancy effects and consequently increase the heat transfer rates form the porous wall. In contrast, increasing the mixed convection parameter for the buoyancy opposing flow has an opposing effect on both the velocity and temperature profiles. The effect of the porosity on the present problem as shown in Figs. 4 and 5 is to increase the velocity and broaden the temperature profile for the buoyancy aiding flow and to decrease the velocity and thicken the temperature profile for the buoyancy opposing flow. The effects of the radiation-conduction parameter on both the velocity and temperature profiles are drawn in Figs. 6 and 7 for the buoyancy aiding and opposing flows. Increasing this parameter will decrease the velocity and the heat transfer rates for the buoyancy aiding flow. For the buoyancy opposing flow, the effect of this parameter is to increase the velocity and to decrease the heat transfer rates from the porous wall.

The effects of the magnetic field on the mixed convection heat transfer problem under consideration are drawn in Figs. 8 and 9. It is shown that, for the aiding flow, increasing the magnetic field number will decrease the velocity inside the boundary layer and the heat transfer rates. For the buoyancy opposing flow, increasing the magnetic field effects will increase the velocity inside the boundary layer, and at the same time the temperature increases, the effect of the magnetic field on this case is to decrease the heat transfer rates for constant mixed parameters.

Figures 10–12 show the variations of the local Nusselt numbers against the mixed parameter for the buoyancy aiding and opposing flows for different values of porosity, radiation-conduction parameter, and magnetic field parameter. Increasing porosity will increase the local Nusselt numbers for aiding flow and decreases the local Nusselt for opposing flow. Increasing the radiation-conduction parameter will decrease local Nusselt numbers for the buoyancy aiding flow and buoyancy opposing flow. It is clear that increasing the mixed convection parameter will increase local Nusselt numbers for the buoyancy aiding flow and decreases local Nusselt numbers for the buoyancy opposing flow. Increasing the magnetic field effect is found to decrease the local Nusselt for both aiding and opposing flows.

Conclusions

The MHD-mixed convection heat transfer problem is analyzed for the buoyancy aiding or opposing flows with radiation heat transfer effects between the conductive gray fluid layers included in the governing equations. The effect of increasing porosity is found to increase the local Nusselt number for the buoyancy aiding flow and to decrease it for the buoyancy opposing flow. Increasing the radiation conduction parameter decreased the local Nusselt number for both aiding and opposing flows. The effect of increasing the magnetic field parameter is found to decrease the local Nusselt number.

Nomenclature

a = Stefan-Boltzmann constant
B_0 = magnetic field flux density, $\mathrm{Wb/m^2}$
Cf_x = local skin friction factor
c_p = specific heat capacity
Da_x = local Darcy number, K/x^2
f = dimensionless stream function
Ec = Eckert number, $u_\infty^2/cp(T_w-T_\infty)$
g = gravitational acceleration
Ha_x = Hartman number, $\sqrt{\sigma B_0^2 x^2/\rho\upsilon}$
K = permeability
K' = coefficient of Forchheimers equation
K_1 = parameter of the porous medium effect, $1/\mathrm{Re}_x Da_x$
K_2 = parameter of the inertial effect, $K'u_\infty/\upsilon$
k_{eff} = effective thermal conductivity
L = length of the plate
Nu_x = local Nusselt number, hx/k
$\bar{\mathrm{N}}\mathrm{u}$ = average Nusselt numbers, $\bar{h}L/k$
p = pressure
Pe_x = local Peclet number, $u_\infty x/\alpha$
Pr = Prandtl number, υ/α
$q_w(x)$ = local surface heat flux
Ra_x = local Rayleigh number, $Kg\beta(T_w-T_\infty)x/\upsilon\alpha$
Re_x = local Reynolds number, $u_\infty x/\upsilon$
R_d = radiation-conduction parameter, $k_{\mathrm{eff}}\alpha_R/4aT_\infty^3$
T = temperature
T_∞ = free stream temperature
T_w = wall temperature
u, v = velocity components in x and y directions
u_∞ = free stream velocity
x, y = axial and normal coordinates

Greek Symbols

α_{eff} = effective thermal diffusivity
α_R = rosseland mean absorption coefficient
δ = boundary layer thickness
ε = porosity
β = volumetric coefficient of thermal expansion, $-1/\rho(\partial\rho/\partial T)_p$
ζ = nonsimilarity parameter, $\mathrm{Ra}_x/\mathrm{Pe}_x$
η = pseudosimilarity variable
θ = dimensionless temperature
θ_w = ratio of surface temperature to the ambient temperature, T_w/T_∞
μ = dynamic viscosity
υ = kinematic viscosity
ρ = fluid density
σ = electrical conductivity
τ_w = local wall shear stress
ψ = dimensional stream function

References

[1] Kuo-Ann Yih, 2001, "Radiation Effect on Mixed Convection Over an Isothermal Wedge in Porous Media: The Entire Regime," Heat Transfer Eng., **22**, pp. 26–32.
[2] Hossain, M. A., 1992, "Viscous and Joule Heating Effects on MHD-Free Convection Flow With Variable Plate Temperature," Int. J. Heat Mass Transfer, **35** pp. 3485-3487.
[3] Soundalgekar, V. M., Takhar, H. S., and Vighnesam, N. V., 1988, "The Combined Free and Forced Convection Flow Past a Semi-Infinite Plate With Variable Surface Temperature," Nucl. Eng. Des., **110**, pp. 95–98.
[4] Cogley, A. C., Vincenti, W. G., and Giles, S. E., 1968, "Differential Approximation For Radiative in a Non-Gray Gas Near Equilibrium," AIAA J. **6**, pp. 95–98.
[5] Hossain, M. A., and Takhar, H. S., 1996, "Radiation Effect on Mixed Convection Along a Vertical Plate With Uniform Surface Temperature," Int. J. Heat Mass Transfer, **31**, pp. 243–248.
[6] Hossain, M. A., Alim, M. A., and Rees D. A., 1999, "The Effect of Radiation on Free Convection From a Porous Vertical Plate," Int. J. Heat Mass Transfer, **42**, pp. 181–191.
[7] Hsu, C. T., and Cheng, P., 1985, "The Brinkman Model For Natural Convection About A Semi-Infinite Vertical Plate in A Porous Medium," Int. J. Heat Mass Transfer, **28**, pp. 683–697.
[8] Vafai, K., and Tien, C. L., 1981, "Boundary and Inertia Effects on Flow and Heat Transfer in porous Media," Int. J. Heat Mass Transfer, **24**, pp. 195–203.
[9] Minkowycz, W. J., Cheng, P., and Chang, C. H., 1985, "Mixed Convection About a Nonisothermal Cylinder and Sphere in a Porous Medium," Numer. Heat Transfer, **8**, pp. 249–359.
[10] Nield, D. A., 1991, "The Limitation of The Brinkman-Forchheimer Equation in Modeling Flow in a Saturated Porous Medium and at Interface," Int. J. Heat Fluid Flow, **12**, pp. 296–272.
[11] Lai, F. C., and Kulacki, F. A., 1991, "Non-Darcy Mixed Convection Along a Vertical Wall in a Saturated Porous Medium," Int. J. Heat Mass Transfer, **113**, pp. 252–255.
[12] Hsieh, J. C., Chen, T. S., and Armaly, B. F.,1993, "Nonsimilarity Solutions For Mixed Convection From Vertical Surfaces in a Porous Medium-Variable Surface Temperature or Heat Flux," Int. J. Heat Mass Transfer, **36**, pp.1485–1493.
[13] Aldoss T. K., Chen T. S., and Armaly B. F.,1994, "Mixed Convection Over Nonisothermal Horizontal Surfaces in a Porous Medium," Int. J. Heat Mass Transfer, **25**, pp. 685–701.
[14] Duwairi, H. M., Aldoss, T. K., and Jarrah, M. A., 1997, "Nonsimilarity Solutions For Non-Darcy Mixed Convection From Horizontal Surfaces in a Porous Medium," Heat Mass Transfer, **33**, pp. 149–156.
[15] Kafoussias, N. G., 1992, "MHD Free Convection Flow Through a Nonhomogenous Porous Medium Over an Isothermal Cone Surface," Mech. Res. Commun., **19**, pp. 89–94.
[16] Gulab, R., and Mishra, 1977, "Unsteady Flow Through Magnetohydrodynamic Porous Media, Indian J. Pure Appl. Math., **8**, pp. 637–642.
[17] Raptis, A., and Kafoussias, N., 1982, "Heat Transfer in Flow Through Porous Medium Bounded by an Infinite Vertical Plate Under The Action of a Magnetic Field," Int. J. Energy Res., **6**, pp. 241–245.
[18] Takhar, H. S., and Ram, P. C.,1994, "Magnetohydrodynamic Free Convection Flow of Water at $4\,C^0$ Through a porous Wall," Int. Commun. Heat Mass Transfer, **21**, pp. 371–376.
[19] Aldoss, T. K., Al-Nimr, M. A., Jarrah, M. A., and A-Sha'er, B. J., 1995, "Magnetohydrodynamic Mixed Convection From a Vertical Plate Embedded in a Porous Medium," Numer. Heat Transfer, Part A, **28**, pp. 635–645.
[20] Duwairi, H. M., and Damseh, Rebhi A., 2003, "Magnetohydrodynamic Natural Convection Heat Transfer From Radiate Vertical Surfaces," Heat Mass Transfer, **40** (10), pp. 787–792.
[21] Chamkha, A. J., and Camille Issa, Khalil Khanafer, 2002, "Natural Convection From an Inclined Plate Embedded in a Variable Porosity Medium Due to Solar Radiation," Int. J. Therm. Sci., **41**, pp. 73–81.
[22] Kaviany, M., 1991, *Principles of Heat Transfer in Porous Media*, Springer-Verlag, New York.
[23] Ali, M. M., Chen, T. S., and Armaly, B. F., 1984, "Natural Convection Radiation Interaction in Boundary Layer Flow Over Horizontal Surfaces," AIAA J., **22**, pp. 1797–1803.
[24] Cebeci, T., and Bradshaw, P., 1984, *Physical and Computational Aspects of Convective Heat Transfer*, Springer, New York,
[25] Duwairi, H. M., and Rebhi, A. Damseh, 2004, "MHD-Buoyancy Aiding and Opposing Flows with Viscous Dissipation Effects From Radiate Vertical Surfaces" Can. J. Chem. Eng. (to be published).
[26] Oosthuizen, P. H., and Hart, R., 1973, "A Numerical Study of Laminar Combined Convective Flow Over Flat Plates," ASME J. Heat Transfer, **95**, pp. 60–63.
[27] Oosthuizen, P. H., and Naylor, D., 1999, *An Introduction to Convective Heat Transfer Analysis*, McGraw-Hill, New York.

Second Law Analysis in a Partly Porous Double Pipe Heat Exchanger

Nadia Allouache

Salah Chikh[1]

Faculte de Genie Mecanique
et Genie des Procedes
e-mail: salahchikh@yahoo.fr
Universite des Sciences et de la Technologie
Houari Boumediene,
B. P. 32,
El Alia, Bab Ezzouar 16111,
Algeria

A combination of the first and second laws of thermodynamics has been utilized in analyzing the performance of a double pipe heat exchanger with a porous medium attached over the inner pipe. The goal of this work is to find the best conditions that allow the lowest rate of entropy generation due to fluid friction and heat transfer with respect to the considered parameters. Results show that the minimization of the rate of entropy generation depends on the porous layer thickness, its permeability, the inlet temperature difference between the two fluids, and the effective thermal conductivity of the porous substrate. An increase in the effective thermal conductivity of the porous medium seems to be thermodynamically advantageous. Unexpectedly, the fully porous annular gap yields the best results in terms of the rate of total entropy generation.
[DOI: 10.1115/1.1991865]

1 Introduction

The increase in energy cost and energy consumption has required more effective use of energy. Hence, decreasing energy losses is getting more and more important. Presently, second law based methods are widely employed to analyze the overall energy performance in a unified way and hence to identify criteria for optimization. A thermodynamic basis to evaluate the merit of augmentation techniques by second law analysis has been proposed by Bejan [1,2].

The use of porous materials as an alternative technique to increase exchange area and to improve heat transfer is well established. Although porous substrates generate a high pressure drop, they remain a good passive technique for heat transfer augmentation. In order to find a compromise between hydrodynamics and thermal performances, a second law analysis based on evaluation of entropy generation due to both fluid friction and heat transfer seems very suited. In this context, several works have been carried out. Baytas [3] has studied the entropy generation in a tilted saturated porous cavity for laminar natural convection heat transfer. He found that the calculation of local entropy generation maps are feasible and can supply useful information for selection of a suitable angle inclination. The research of forced convection in a partly porous annular duct has also been conducted by Chikh et al. [4,5] and Bouhadef et al. [6]; they reported that, for well chosen conditions, heat transfer can be improved. Yet, only a few numbers of studies considered entropy generation in forced convective heat transfer with porous media. Demirel [7], Demirel and Kahraman [8,9] analyzed the volumetric entropy generation rate due to convection heat transfer and friction in a packed duct with uniform heating, a rectangular packed duct with asymmetric heating, and an annular packed bed. They showed that packing causes equipartition of entropy generation over the cross section of the bed.

The present paper reports a numerical calculation of entropy generation rate for laminar forced convection flow in a double pipe heat exchanger of inner and outer diameters d_i and d_e, respectively. The thickness of the inner pipe of good conducting material is assumed very weak and its thermal resistance is neglected in the present study. The hot fluid flows in the inner cylinder and the cold one in the annular gap. A porous substrate is attached to the inner cylinder and the outer cylinder is perfectly insulated, as sketched in Fig. 1. The effects of the porous layer thickness, its permeability, the inlet temperature difference between the two fluids, and the effective thermal conductivity are investigated.

2 Mathematical Formulation

A laminar boundary layer-type flow of incompressible fluid in a steady state is considered. In addition, the properties are assumed constant and the porous medium is considered homogeneous, isotropic, and is saturated with a fluid in local thermal equilibrium with the solid matrix. The case of prevailing convection in the streamwise direction is analyzed so that axial conduction is neglected. The flow is governed by the Navier-Stokes equations in the fluid region and is modeled by the Darcy-Brinkman-Forchheimer equation in the porous region.

The dimensionless governing equations are

$$\text{Continuity equation:}\quad \frac{\partial \mathrm{u}}{\partial \mathrm{x}}+\frac{1}{r}\frac{\partial(rv)}{\partial r}=0 \tag{1}$$

where u and v are the axial and radial dimensionless velocities, respectively.

Momentum equation

Inner cylinder

$$u\frac{\partial u}{\partial x}+v\frac{\partial u}{\partial r}=-R_\rho\frac{dp}{dx}+\frac{1}{\mathrm{Re}\,R_{\mathrm{vch}}}\left[\frac{1}{\mathrm{r}}\frac{\partial}{\partial r}\left(r\frac{\partial u}{\partial r}\right)\right] \tag{2}$$

Annular gap

Porous region

$$u\frac{\partial u}{\partial x}+v\frac{\partial u}{\partial r}=-\frac{dp}{dx}+\frac{1}{\mathrm{Re}\,R_v}\left[\frac{1}{r}\frac{\partial}{\partial r}\left(r\frac{\partial u}{\partial r}\right)\right]-\frac{u}{\mathrm{Re\,Da}}-\frac{\mathrm{CF}}{\mathrm{Re\,Da}}u^2 \tag{3}$$

[1]To whom correspondence should be addressed.

Contributed by the Applied Mechanics Division of ASME for publication in the JOURNAL OF APPLIED MECHANICS. Manuscript received June 22, 2004; final manuscript received April 27, 2005. Assoc. Editor: D. Siginer. Discussion on the paper should be addressed to the Editor, Prof. Robert M. McMeeking, Journal of Applied Mechanics, Department of Mechanical and Environmental Engineering, University of California - Santa Barbara, Santa Barbara, CA 93106-5070, and will be accepted until four months after final publication in the paper itself in the ASME JOURNAL OF APPLIED MECHANICS.

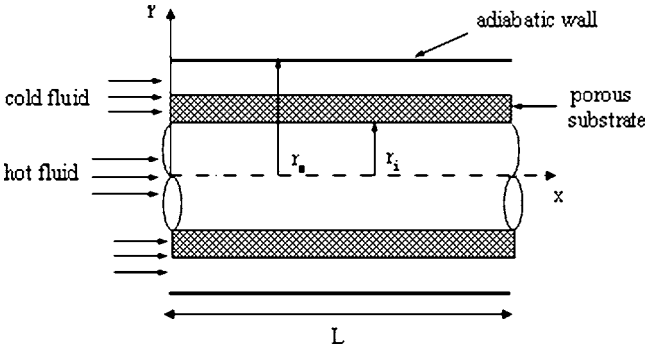

Fig. 1 Schematic of physical domain

Fluid region

$$u\frac{\partial u}{\partial x}+v\frac{\partial u}{\partial r}=-\frac{dp}{dx}+\frac{1}{\mathrm{Re}}\left[\frac{1}{r}\frac{\partial}{\partial r}\left(r\frac{\partial u}{\partial r}\right)\right] \tag{4}$$

The dimensionless parameters R_{vch}, R_ρ, and R_v represent the viscosity ratio (cold to hot), the density ratio (cold to hot), and the viscosity ratio (cold to effective viscosity), respectively.

Energy equation

Inner cylinder:
$$u\frac{\partial \theta}{\partial x}+v\frac{\partial \theta}{\partial r}=\frac{1}{\mathrm{Re\,Pr}\,R_\alpha}\left[\frac{1}{r}\frac{\partial}{\partial r}\left(r\frac{\partial \theta}{\partial r}\right)\right] \tag{5}$$

Annular gap

Porous region:
$$u\frac{\partial \theta}{\partial x}+v\frac{\partial \theta}{\partial r}=\frac{R_{ce}}{\mathrm{Re\,Pr}}\left[\frac{1}{r}\frac{\partial}{\partial r}\left(r\frac{\partial \theta}{\partial r}\right)\right] \tag{6}$$

Fluid region:
$$u\frac{\partial \theta}{\partial x}+v\frac{\partial \theta}{\partial r}=\frac{1}{\mathrm{Re\,Pr}}\left[\frac{1}{r}\frac{\partial}{\partial r}\left(r\frac{\partial \theta}{\partial r}\right)\right] \tag{7}$$

with R_α being the diffusivity ratio (cold to hot) and R_{ce} the thermal conductivity ratio (effective thermal conductivity to fluid thermal conductivity).

Local rate of entropy generation

$$\dot{S}_g=\dot{S}_{\Delta p}+\beta\dot{S}_{\Delta T} \tag{8}$$

where $\dot{S}_{\Delta p}$ is the part of entropy generation rate due to friction and is computed as in Bejan [1] by the following relationship:

$$\dot{S}_{\Delta P}=\left[2\left(\frac{\partial u}{\partial x}\right)^2+\left(\frac{\partial u}{\partial r}\right)^2\right] \tag{9}$$

$\beta\dot{S}_{\Delta T}$ is the part of entropy generation rate due to heat transfer.

$\dot{S}_{\Delta T}$ is the proportion of entropy generation rate due to temperature gradient and is given by

$$\dot{S}_{\Delta T}=\left[\left(\frac{\partial \theta}{\partial x}\right)^2+\left(\frac{\partial \theta}{\partial r}\right)^2\right] \tag{10}$$

and

$$\beta=\frac{k_j(T_{h_{\mathrm{in}}}-T_{c_{\mathrm{in}}})^2}{\mu_{\mathrm{j}}u_{\mathrm{c_{in}}}^{*2}[\theta(T_{h_{\mathrm{in}}}-T_{c_{\mathrm{in}}})+\mathrm{T}_{c_{\mathrm{in}}}]} \tag{11}$$

The subscript j in k_j and μ_j stands for h in the hot side and for c in the cold side. While in the porous region, j indicates the effective thermal conductivity in k_j.

The parameter β characterizes the fluid nature and depends on the hydrodynamics and the thermal inlet conditions.

The rate of entropy generation over the whole cross section, accounting for both porous and fluid regions, is calculated by integration

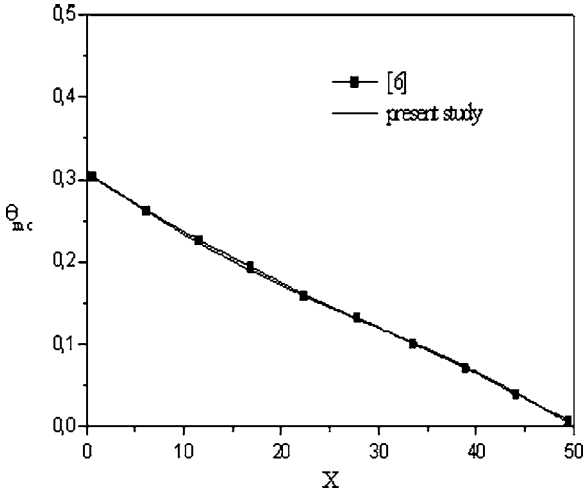

Fig. 2 Mean temperature along the heat exchanger (R_{ce}=1, cold side, e=0.6, Da=10^{-3})

$$S_g=\int_{r_i}^{r_e}\left\{\left[2\left(\frac{\partial u}{\partial x}\right)^2+\left(\frac{\partial u}{\partial r}\right)^2\right]+\beta\left[\left(\frac{\partial \theta}{\partial x}\right)^2+\left(\frac{\partial \theta}{\partial r}\right)^2\right]\right\}2\pi r\,dr \tag{12}$$

The Bejan number is defined as

$$\mathrm{Be}=\frac{\beta S_{\Delta T}}{S_g} \tag{13}$$

where $S_{\Delta T}$ is the rate of entropy generation over the cross section and due to temperature gradient. Be=1 is the limit at which the irreversibility due to heat transfer dominates and Be=0 is the opposite limit at which the irreversibility due to fluid friction is the prevailing effect.

The dimensionless quantities used in all the previous equations are defined as

$$p=\frac{p^*}{\rho_{\mathrm{c}}u_{c_{\mathrm{in}}}^*},\quad \mathrm{Re}=\frac{\rho_c u_{c_{\mathrm{in}}}^* D_h}{\mu_c},\quad \mathrm{Da}=\frac{K}{D_h^2},\quad \mathrm{Pr}=\frac{\mu_c c_{p_c}}{k_c},\quad \mathrm{R_{ce}}=\frac{k_e}{k_c},$$

$$R_\rho=\frac{\rho_c}{\rho_h},\quad R_{\mathrm{vch}}=\frac{\mu_c}{\mu_h},\quad R_v=\frac{\mu_c}{\mu_e},\quad R_\alpha=\frac{\alpha_c}{\alpha_h},\quad \mathrm{u}=\frac{u^*}{u_{c_{\mathrm{in}}}^*},$$

$$v=\frac{v^*}{v_{c_{\mathrm{in}}}^*},\quad \theta=\frac{T-T_{c_{\mathrm{in}}}}{T_{h_{\mathrm{in}}}-T_{c_{\mathrm{in}}}},\quad \mathrm{CF}=\rho_c\varepsilon F\frac{\sqrt{K}}{\mu_c}u_{c_{\mathrm{in}}}^*,\quad D_h=(d_e-d_i).$$

The subscripts c and h indicate, respectively, the cold fluid and the hot fluid, while the subscript e corresponds to effective values in the porous medium.

$u_{c_{\mathrm{in}}}^*$ and $v_{c_{\mathrm{in}}}^*$ are, respectively, the axial and radial inlet velocities of the cold fluid and the * designates the dimensional quantities.

2.1 Boundary Conditions. The boundary conditions necessary to complete the problem formulation are

Hydrodynamic conditions:

$$x=0\quad 0<r<r_i\quad u=u_{h_{\mathrm{in}}}$$

$$r_i<r<r_e\quad u=u_{c_{\mathrm{in}}}$$

$$r=0\quad \frac{\partial u}{\partial r}=0$$

$$r=r_i\quad u=0$$

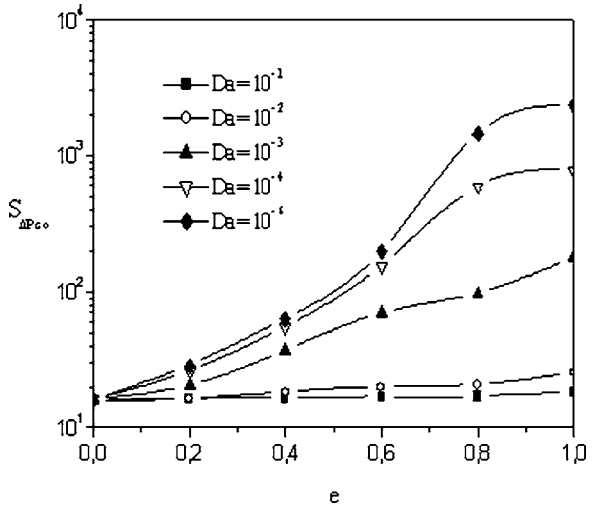

Fig. 3 Rate of entropy generation due to fluid friction at the exit of heat exchanger (R_{ce}=1, cold side)

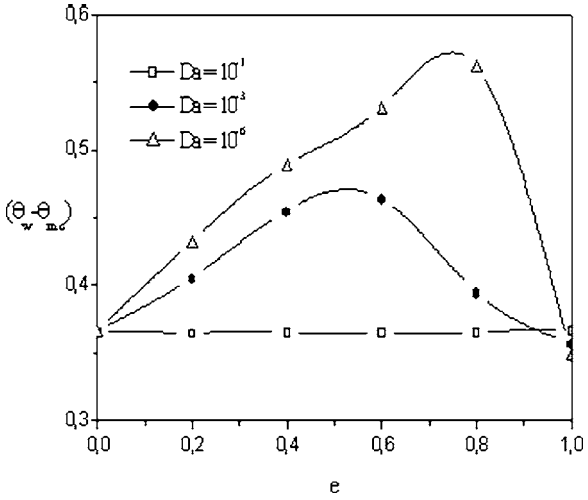

Fig. 5 Difference between the wall temperature and the mean temperature of the cold fluid

$$r = r_e \quad u = 0$$

Continuity at the porous-fluid interface:

$$r = r_i + e \begin{cases} u_c = u_p \\ R_v\left(\frac{\partial u_c}{\partial r}\right) = \left(\frac{\partial u_p}{\partial r}\right) \end{cases}$$

Thermal conditions

$$x = 0 \quad 0 < r < r_i \quad \theta = 1$$

$$r_i < r < r_e \quad \theta = 0$$

$$r = r_i \quad \left(\frac{\partial \theta_h}{\partial r}\right) = R_{ce}\left(\frac{\partial \theta_p}{\partial r}\right)$$

Porous-fluid interface

$$r = r_i + e \begin{cases} \theta_p = \theta_c \\ R_{ce}\left(\frac{\partial \theta_p}{\partial r}\right) = \left(\frac{\partial \theta_c}{\partial r}\right) \end{cases}$$

$$r = r_e \quad \frac{\partial \theta}{\partial r} = 0$$

3 Numerical Procedure

A numerical procedure based on the control volume method is used to solve the set of Eqs. (1)–(7) with the associated boundary conditions. The inertia term in Eq. (3) is linearized as suggested by Patankar [10].

The partial differential equations are discretized by means of upwind and central differencing schemes to treat the convection and diffusion terms. The obtained system of algebraic equations is then solved with a combination of a direct matrix inversion method (TDMA) and a marching procedure.

After several trial computations to test the code sensitivity, a uniform zonal grid with different step sizes in each region (porous and fluid) and a total number of nodes equal to 16,800 (48 $\times$ 350 in r and x, respectively) is utilized. The convergence criteria of the iterative process are met when the absolute value of relative error on the flow rate at each grid point is less than 10^{-3} and when the absolute error on the heat flux transferred between the two fluids over the entire heat exchanger is less than 10^{-3}.

The velocity and the temperature fields found with the computer code are compared with those found by Bouhadef et al. [6]. Figure 2 shows the comparison of the mean temperature in the cold side and illustrates the excellent agreement.

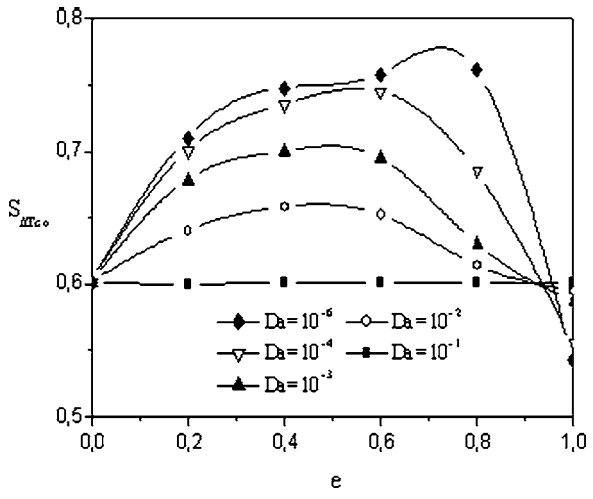

Fig. 4 Rate of entropy generation due to temperature gradient at the exit of heat exchanger (R_{ce}=1, cold side)

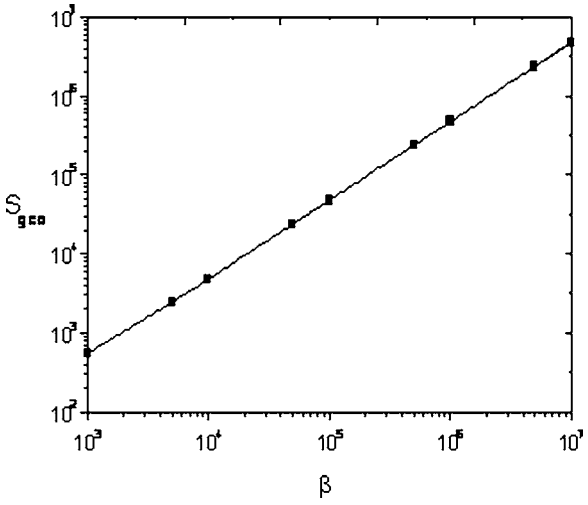

Fig. 6 Rate of total entropy generation as function of β parameter

Table 1 β parameter as function of ΔT_{in}

$(T_{h_{in}} - T_{c_{in}})$	5	10	20	30	40	50	60	70	80
β(water)$^*10^{-5}$	0.0757	0.2982	1.1573	2.5280	4.3670	7.4912	10.620	14.235	22.180
β(toluene)$^*10^{-5}$	0.0306	0.2556	0.9917	2.1663	3.6730	6.4906	9.2018	12.333	19.006
β(benzene)$^*10^{-5}$	0.0300	0.2411	0.9356	2.0608	3.5306	6.1238	8.6817	11.636	17.932

4 Results and Discussion

Computations are carried out for a diameter ratio equal to 2; the same fluid flowing in both ducts; the effective viscosity in the porous medium equals the fluid viscosity (Brinkman assumption); Prandtl number set equal to 4; the inertia coefficient in the porous medium CF equals 0.35, Reynolds number Re=500, and the dimensionless heat exchanger length equals 50.

The first set of figures is presented for porous materials with a small effective thermal conductivity, i.e., R_{ce} equals unity. Then follows the case of porous substrates with a high thermal conductivity in the last figures (Figs. 11 and 12).

Figure 3 illustrates the proportion of entropy generation rate due to fluid friction with respect to the porous layer thickness for different values of the Darcy number characterizing the permeability of the porous material. Obviously, increasing the porous layer thickness or decreasing its permeability leads to an increase in the rate of entropy generation. This is due to the significant macroscopic resistance [Darcy term in Eq. (3)] imposed by a weakly permeable porous material. On the other hand, the part of entropy generation rate due to temperature gradient is displayed in Fig. 4. It increases until a maximum value corresponding to a critical thickness of the porous layer that depends on the permeability. Above this critical thickness, the rate of entropy generation decreases and becomes even lower than the value obtained for the fluid case when the annular gap is filled above 95%. This may be explained by the difference between the wall temperature and the mean temperature of the cold fluid which has the same trend as reported in Fig. 5. A highly permeable porous substrate yields a higher heat transfer coefficient and thus a smaller convection resistance. Consequently, the rate of entropy generation is smaller for high values of the Darcy number. Moreover, since the porous material is not a good thermal conductor in this case of $R_{ce}=1$, then it may be considered more as an insulation material. For instance, the critical thickness may be seen in a similar manner as the critical thickness of insulation in conduction for a cylindrical geometry. Nevertheless, it should be pointed out that this critical thickness does not show when the porous layer acts as a good thermal conductor ($R_{ce}>1$).

The rate of total entropy generation highly depends on the parameter β. This latter, which is a function of fluid properties, varies significantly with an inlet temperature difference as reported in Table 1.

Figure 6 exhibits the linear dependency on the parameter β. Because of the importance of the parameter ΔT_{in} (inlet temperature difference between the hot and cold fluids) particularly on the rate of entropy generation due to heat transfer, it is interesting to investigate the influence on ΔT_{in}. Let us examine two cases. At moderate values of ΔT_{in} (between 10 °C and 20 °C) the irreversibility due to heat transfer prevails over $S_{\Delta p\ co}$ as illustrated in Fig. 7 in which the curves of $S_{g\ co}$ follow nearly the same trend as the curves of $S_{\Delta T\ co}$ in Fig. 4. However, the proportion of $S_{\Delta pco}$ becomes significant at high values of the porous layer thickness (over approximately 80%) and for a weak permeability ($Da=10^{-6}$). Then, the rate of entropy generation due to both fluid friction and heat transfer are significant. This result is confirmed in Fig. 8 by the values of Bejan number. For example, for a fully porous case with the Darcy number equaling 10^{-6}, Be=0.7 means that 70% of the rate of entropy generation is due to heat transfer and 30% due to fluid friction. For higher values of inlet temperature difference ($\Delta T_{in}>20$ °C), most of the irreversibility is due to heat transfer since the curves displayed in Fig. 9 present the same trend as the curves of $S_{\Delta T\ co}$.

The value of Be would then be in the upper limit (Be=1). Obviously, increasing the inlet temperature difference results in more irreversibility mainly due to heat transfer. Nevertheless, starting from a moderate value of ΔT_{in} approximately 15 °C the case of fully porous annulus seems to be a very promising case in terms of entropy generation rate. A reduction of 12% is obtained in comparison to the case without a porous material as shown in Fig. 10. This result is obtained for a thermal conductivity ratio equal to 1. Then, it is worth exploring the case of porous substrates with a higher effective thermal conductivity, i.e., $R_{ce}>1$.

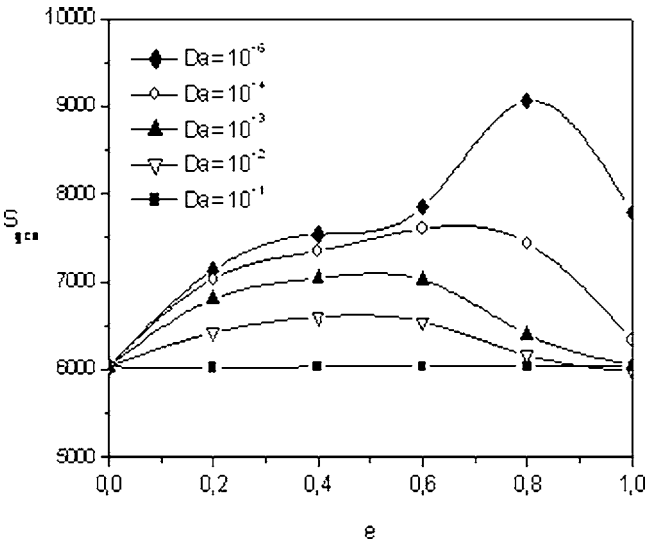

Fig. 7 Rate of total entropy generation at the exit of heat exchanger ($R_{ce}=1$, cold side, 10 °C$<\Delta T_{in}<$20 °C)

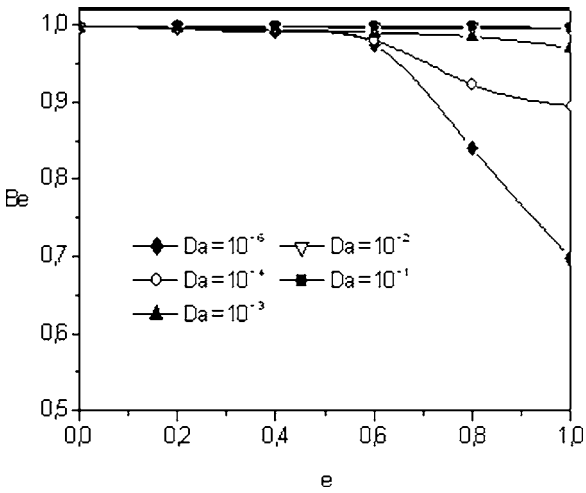

Fig. 8 Bejan number ($R_{ce}=1$, cold side, 10 °C$<\Delta T_{in}<$20 °C)

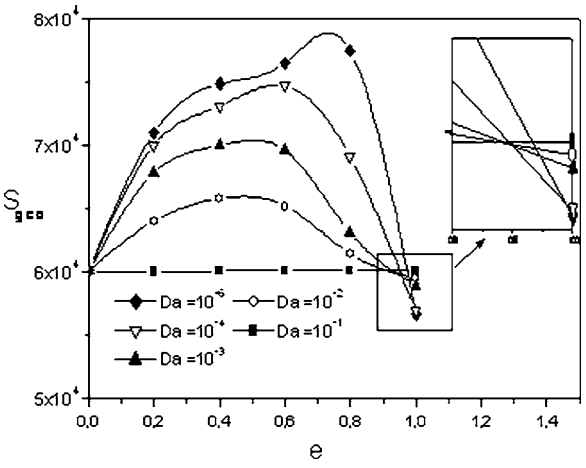

Fig. 9 Rate of total entropy generation at the exit of heat exchanger ($R_{ce}=1$, cold side, $\Delta T_{in} \geqslant 20\ ^{\circ}C$)

As illustrated in Fig. 11 for two values of Darcy (10^{-2} and 10^{-6}), when the porous matrix is a good thermal conductor ($R_{ce} \geqslant 5$), the heat transfer rate is improved and thus increasing the porous layer thickness is no longer a cause of entropy generation due to heat transfer but yields a substantial reduction of the total rate of entropy generation (the proportion due to heat transfer being the prevailing one).

For example, for a fully porous case with $Da=10^{-2}$ and $R_{ce}=10$ a reduction of 97% in the total rate of entropy generation is obtained. Furthermore, at a given thickness there is a critical value of the thermal conductivity ratio above which the total rate of entropy generation with the porous medium is lower than the one without the porous layer. This value depends on the parameter β, the permeability, and the thickness of the porous matrix. The case of $e=80\%$ is plotted in Fig. 12 for $\beta=10^5$. When $Da=10^{-6}$ the critical ratio is 2.5, but when $Da=10^{-2}$ this ratio is equal to 1.1. For lower values than this critical ratio, the total rate of entropy generation is higher than the one of the fluid case without the porous substrate. This is explained by the fact that in this situation the porous matrix constitutes a high resistance to heat transfer.

On the other hand, beyond this critical ratio, the reduction of the total rate of entropy generation is significant.

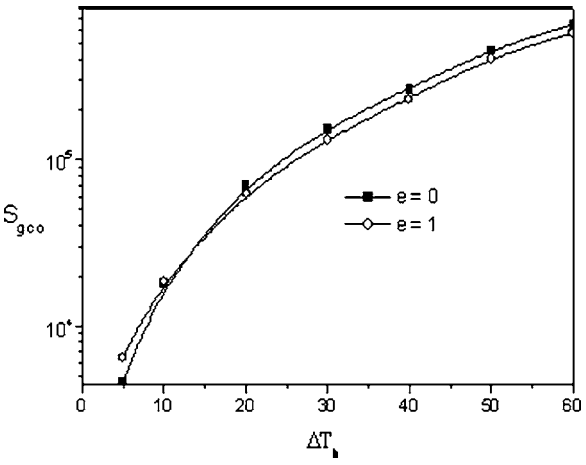

Fig. 10 Rate of total entropy generation at the exit of heat exchanger ($R_{ce}=1$, cold fluid, $Da=10^{-6}$, case of water)

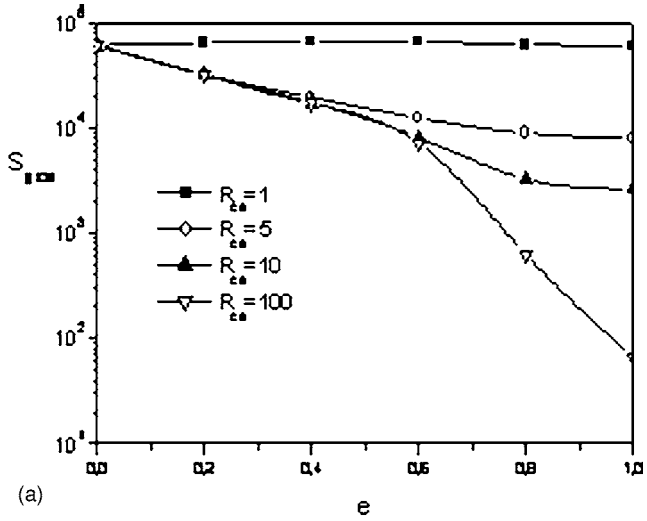

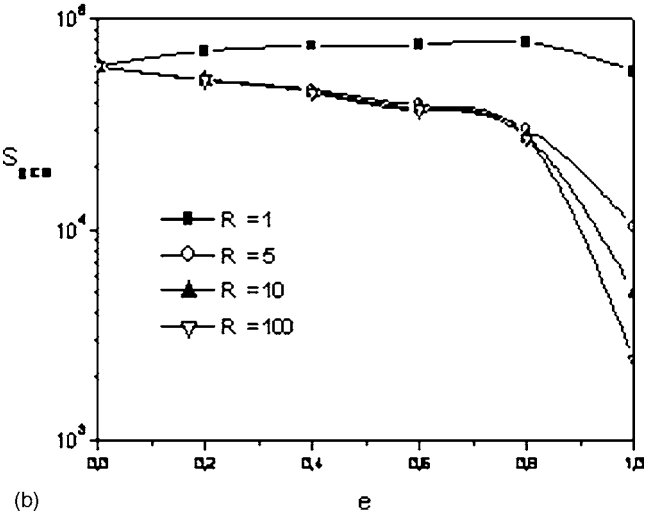

Fig. 11 (*a*) rate of total entropy generation at the exit of the heat exchanger (cold fluid, $\beta=10^5$, $Da=10^{-2}$). (*b*) Rate of total entropy generation at the exit of the heat exchanger (cold fluid, $\beta=10^5$, $Da=10^{-6}$).

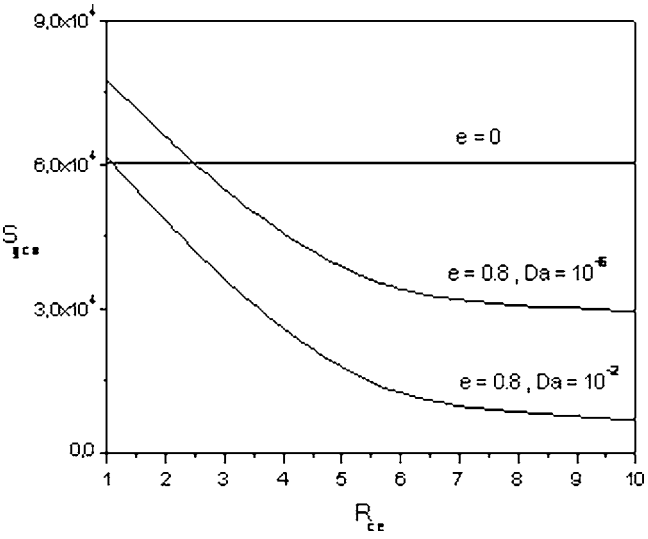

Fig. 12 Rate of total entropy generation as function of thermal conductivity ratio ($\beta=10^5$)

5 Conclusion

In this paper we presented a thermodynamic analysis in a double pipe heat exchanger with a porous medium in the annular gap attached to the inner cylinder. The aim of this work was to find the optimal conditions in order to reduce the rate of entropy generation. The numerical procedure is based on the control volume method and allowed to obtain the velocity and temperature fields and thus to compute the rate of entropy generation. The effects of the porous layer thickness, its permeability, the inlet temperature difference between the cold and hot fluids, and the thermal conductivity ratio are documented.

Results show that the rate of entropy generation due to heat transfer prevails over the one due to friction in most situations where ΔT_{in} is high. Whereas, in the case of small values of ΔT_{in}, irreversibility due to fluid friction becomes significant particularly for weakly permeable porous substrates. The properties of the porous material have a considerable impact on entropy generation. The predictions show that in the case of a small thermal conductivity ratio ($R_{\text{ce}}=1$), only cases of the fully porous annulus or the porous layer thickness over 95% are of interest. However, if the porous substrates have a high effective thermal conductivity ($R_{\text{ce}}>1$) then there exists a critical value of R_{ce} above which a substantial reduction of the rate of entropy generation is obtained even with a small thickness of the porous layer, and this is very promising in terms of irreversibility.

Nomenclature

- Be = Bejan number, $\text{Be}=\beta S_{\Delta T}/S_g$
- c_p = specific heat of the fluid (J/kg)
- CF = inertia coefficient, $CF=\rho_c \varepsilon F\sqrt{K}u^*_{c_{\text{in}}}/\mu_c$
- D_h = hydraulic diameter, $D_h=d_e-d_i$(m)
- Da = Darcy number, $\text{Da}=K/D_{\text{h}}^2$
- d_e = outer diameter (m)
- d_i = inner diameter (m)
- e = dimensionless porous layer thickness, $e=e^*/D_h$
- F = Forchheimer coefficient
- K = permeability of the porous substrate (m^2)
- k = thermal conductivity (W/m k)
- p = dimensionless pressure, $p=p^*/\rho_c u^*_{c_{\text{in}}}$
- Pr = Prandtl number, $\text{Pr}=\mu_c c_p/k_c$
- Re = Reynolds number, $\text{Re}=\rho_c u^*_{c_{\text{in}}} D_h/\mu_c$
- R_{ce} = thermal conductivity ratio, $R_{\text{ce}}=k_e/k_c$
- R_v = viscosity ratio, $R_v=\mu_c/\mu_e$
- R_{vch} = viscosity ratio, $R_{\text{vch}}=\mu_c/\mu_h$
- R_ρ = density ratio, $R_\rho=\rho_c/\rho_h$
- R_α = diffusivity ratio, $R_\alpha=\alpha_c/\alpha_h$
- r = dimensionless radial coordinate, $r=r^*/D_h$
- r_e = outer dimensionless radius, $r_e=r^*_e/D_h$
- r_i = inner dimensionless radius, $r_i=r^*_i/D_h$
- $\dot{S}$ = dimensionless rate of local entropy generation in Eqs. (8)–(10)
- S = dimensionless rate of entropy generation over the cross section, in Eq. (15)
- T = Temperature (K)
- u = dimensionless axial velocity, $u=u^*/u^*_{c_{\text{in}}}$
- v = dimensionless radial velocity, $v=v^*/v^*_{c_{\text{in}}}$
- x = dimensionless radial coordinate, x^*/D_h

Greek Symbols

- ΔT_{in} = inlet difference temperature
- ε = porosity
- ρ = density (kg/m^3)
- α = diffusivity (m^2/s)
- θ = dimensionless temperature, $\theta=(T-T_{c_{\text{in}}})/(T_{h_{\text{in}}}-T_{c_{\text{in}}})$
- μ = dynamic viscosity (kg/m s)

Subscripts

- c = cold
- e = effective
- g = total
- h = hot
- in = inlet
- m = mean
- o = exit
- p = porous
- Δp = due to fluid friction
- ΔT = due to temperature gradient

Superscript

- $*$ = dimensional quantities

References

[1] Bejan, A., 1994, "Entropy Generation Through Heat and Fluid Flow," Wiley, New York.

[2] Bejan, A., 2001, "Thermodynamic Optimization of Geometry in Engineering Flow Systems," Int. J. Energy Res. **1**(4), pp. 269–277.

[3] Baytas, A. C., 2000, "Entropy Generation for Natural Convection in an Inclined Porous Cavity," Int. J. Heat Mass Transfer, **43**(12), pp. 2089–2099.

[4] Chikh, S., Boumedien, A., Bouhadef, K., and Lauriat, G., 1995, "Analytical Solution of Non-Darcian Forced Convection in an Annular Duct Partially Filled with a Porous Medium," Int. J. Heat Mass Transfer, **38**(9), pp. 1543–1551.

[5] Chikh, S., Boumedien, A., Bouhadef, K., and Lauriat, G., 1995, "Non-Darcian Forced Convection Analysis in an Annulus Partially Filled with a Porous Material," Numer. Heat Transfer, Part A, **28**(6), pp. 707–722.

[6] Bouhadef, K., Chikh, S., Boumedien, A., and Lauriat, G., 1999, "Effect of Porous Substrate Addition on Heat Exchanger Efficiency," IMechE Conf. Trans., c565/021/99, pp. 13–19.

[7] Demirel, Y., 1995, "Thermodynamic Optimization of Convective Heat Transfer in a Packed Duct," Energy, **20**(10), pp. 959–967.

[8] Demirel, Y., and Kahraman, R., 1999, "Entropy Generation in Rectangular Packed Duct with Wall Heat Flux," Int. J. Heat Mass Transfer, **42**(13), pp. 2337–2344.

[9] Demirel, Y., and Kahraman, R., 2000, "Thermodynamic Analysis of Convective Heat Transfer in an Annular Packed Bed," Int. J. Heat Fluid Flow, **21**, pp. 442–448.

[10] Patankar, S. V., 1980, "Numerical Heat Transfer and Fluid Flow," McGraw-Hill, New York.

Konstantin Kostarev
Institute of Continuous
Media Mechanics UB RAS,
Acad Korelev Str. 1,
614013 Perm, Russia

Antonio Viviani
Dipartimento di Ingegneria
Aerospaziale e Meccanica,
Seconda Università di Napoli,
Via Roma 29, 81031 Aversa Italy
e-mail: Antonio.viviani@unina2.it

Andrew Zuev
Institute of Continuous
Media Mechanics UB RAS,
Acad Korelev Str. 1,
614013 Perm, Russia

Thermal and Concentrational Maragoni Convection at Liquid/Air Bubble Interface

The paper presents the experimental study of thermo- and solutocapillary Marangoni convection around a gas bubble in an inhomogeneous fluid with a vertical thermal or surfactant concentration gradient. The stationary bubble in the form of a short horizontal cylinder with a free lateral surface was placed into a vertically oriented thin liquid layer (Hele-Shaw cell). The evolution of thermal and concentration fields and fluid flows was studied applying the interferometric method. In contrast to a thermocapillary convection representing a stationary flow and stable temperature distribution, the periodic concentration disturbances around the bubble were observed in the solutocapillary case. The regularities of the discovered effect were revealed, and its interpretation was proposed. [DOI: 10.1115/1.1991866]

1 Introduction

It is well known that inhomogeneity of temperature or dissolved surfactant concentration along the free liquid/gas interface is responsible for the generation of tangential capillary stresses, directed toward the surface tension gradient [1]. These stresses, in turn, generate in the surrounding liquid a convective flow, known as the Marangoni convection, in the direction of the temperature or surfactant concentration decrease. The Marangoni convection around a gas bubble suspended in a liquid matrix was studied in 1959 by Young et al. [2] and after that has been the subject of a great number of investigations. A steady interest in this problem is caused by its considerable practical importance for multiphase system technologies, especially, in conditions where gravity-induced mechanisms of motion are absent or reduced, for instance, in microgravity. In this case, the Marangoni phenomenon is just to be the main factor determining the behavior of gas inclusions in many technological processes. Among these are preparation of composite and foamy materials, formation and solidification of alloys, and degassing of liquid substances in glasses, ceramics, crystals, and metals.

Until recently, the overwhelming majority of theoretical and experimental studies have been focused on thermocapillary-caused Marangoni convection since the temperature dependence is the most common reason of surface tension inhomogeneity. Therefore thermocapillary flows arising in a liquid around the bubble and causing its movement toward the temperature gradient (the so-called thermocapillary bubble migration) have been well investigated. The most detailed discussion of earlier studies in this field was given in reviews [3–6]. There is a great deal of papers [7–16] showing that in the case of upward vertical thermal gradient the arising flow is an axisymmetrical flux in the shape of a toroidal roll around the bubble. The liquid at the bubble surface is driven by the capillary forces to the lower bubble pole, and the liquid far from the bubble moves upward generating a return flow. More often the flow and the temperature field are steady. Then in any diametral plane the thermocapillary flow has the form of two vertical two-dimensional vortices located symmetrically about the bubble. Some authors point out [9,11,13–16] that when a critical value of the temperature gradient is exceeded (the Marangoni numbers are higher than 3×10^4 [13]), a periodic oscillatory thermocapillary flow occurs. The initially stable vortex and the temperature field are distorted and experience the weak oscillations. The oscillatory modes were observed either thermally by means of interferometry or hydrodynamically by tracer particles. This oscillatory flow is three dimensional, i.e., the vortices acquire the azimuthal velocity component as well [9]. At the same time, two-dimensional (2D) modeling of this 3D oscillatory phenomenon in microgravity [11] revealed no oscillations. Initiation of the oscillations is independent of gravity and thus of the buoyancy convection [15] and most likely is related to a trivial loss of stability of a laminar flow whenever the flow velocities become too large.

In contrast to thermocapillary, the solutocapillary convection has not been adequately studied. Experimentally, the establishment and sustention of the constant homogeneous concentration gradient is a more difficult task. Moreover, in the absence of adequate methods for measuring surfactant concentration at the free surface, it is impossible to determine precisely the local values of the surface tension. Most of the recent papers deal with studying the influence of the adsorbed insoluble surfactant layer at the bubble/drop interface on the thermocapillary convection [17–19]. It has been found that the surfactant, transported by the convective flow to the trailing pole of the bubble, establishes surfactant-induced Marangoni stresses opposing those caused by the thermal gradient. As a result, the thermocapilary-caused motion is slowed down drastically due to the presence of the surfactant. However, to our knowledge nobody has studied the convective motion, generated by the external concentration gradient of the surfactant dissolved in the surrounding fluid.

Evidently, due to the similarity of driving mechanisms, there exists a subsequent analogy between thermo- and solutocapillary phenomena. Thus, as in the case of thermocapillary bubble migration [20,21] we detected experimentally the appearance of solutocapillary migration—the bubble motion in the direction of the surfactant concentration growth [22,23]. However, in real conditions the effects observed in both cases appear to be not completely similar. The key difference is the degree of contribution made by the diffusion and convective mass transfer mechanisms, since the characteristic times of surfactant diffusion are two or three orders of magnitude longer than those of heat diffusion. Besides, there are some additional factors that influence the distribution of the surface tension, for example, surfactant adsorption at the interface. In this situation, it seems to be possible and en-

Contributed by the Applied Mechanics Division of ASME for publication in the JOURNAL OF APPLIED MECHANICS. Manuscript received June 24, 2004; final manuscript received April 18, 2005. Assoc. Editor: D. Siginer. Discussion on the paper should be addressed to the Editor, Prof. Robert M. McMeeking, Journal of Applied Mechanics, Department of Mechanical and Environmental Engineering, University of California - Santa Barbara, Santa Barbara, CA 93106-5070, and will be accepted until four months after final publication in the paper itself in the ASME JOURNAL OF APPLIED MECHANICS.

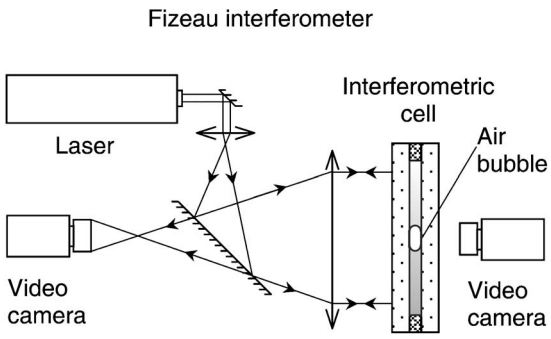

Fig. 1 Experimental setup

ergetically beneficial for a bubble to "extract" the surfactant from the surrounding solution and accumulate it on its own free surface reducing thus the surface tension. In the thermal case thermodynamic laws prohibit analogous heating of the bubble surface at the expense of fluid cooling.

As a result, the solutocapillary Marangoni convection differs from the thermocapillary one. Thus, the original solutocapillary phenomenon was found in our recent investigations of the air bubble behavior in a horizontal two-layer system of dissolvable fluids. In these experiments [24] a vertical concentration difference generating the solutocapillary Marangoni convection around the bubble was initiated between its upper and lower poles. In a similar thermal problem for a bubble placed in a fluid with a vertical thermal gradient, the initiated thermocapillary flow was stationary. In the solutal case it was found out that the convective flow had the oscillatory character since the concentration field around the bubble experienced strong periodic disturbances. The oscillations period and duration depended on the initial surfactant concentration difference, solution average concentration, and physico-chemical parameters, bubble dimensions. Thus, the period decreased distinctly with the concentration difference increase, whereas the time of oscillation continuance on the contrary grew.

Based on the available evidence it was speculated that such a mass transfer was caused by a regular ejection of the surfactant excess, accumulated on the bubble poles under the action of the capillary forces, into the surrounding medium. However, for the mentioned liquid layer geometry and orientation this hypothesis could not be proved by direct investigations of the concentration fields and convective flow velocities. Therefore the experiments were performed in a vertically oriented liquid layer with surfactant concentration stratification in order to visualize the concentration distributions and the structures of solutocapillary convective flows around the bubble. In the same experimental cuvette the thermocapillary Marangoni flow and temperature distribution around a bubble in a pure liquid with a vertical upward-directed thermal gradient were studied and the comparison between thermocapillary and solutocapillary cases was performed.

2 Experimental Technique

The test cuvette was a shallow $90\times40\times1.2$ mm rectangular cavity confined between two parallel semi-transparent mirror plates (the so-called Hele-Shaw cell) and set vertically on its narrow face. The experimental setup is shown schematically in Fig. 1. To investigate thermocapillary convection the cell was filled with pure isopropyl alcohol and heated from above by an electric heater located at the top of the cuvette. This allowed us to initiate in the liquid an upward thermal gradient. In a solutocapillary experiment, the cuvette was filled half-full with distilled water and then topped up with 50%–100 % water solution of isopropyl alcohol (by concentration we mean the mass fraction of the dissolved surfactant). Due to diffusion at the interface the fluids partially mixed forming in the central part of the cuvette a stable region with nearly linear vertical distribution of concentration.

An air bubble was injected with a medical syringe in the center of the region with a maximum temperature or concentration gradient. Due to a small cavity thickness the bubble appeared to be squeezed between the vertical cell walls taking the shape of a flat disk with a free lateral surface. Thus the bubble can be considered as a short horizontal cylinder, and a convection flow around the bubble—as a two-dimensional one. A special wire frame in the form of a small ring clamped between the cuvette walls was used to prevent the bubble from buoying under the action of the Archimedean force. The thickness of the wire was 0.3 mm, therefore the frame reduced the effective thickness of the cavity up to 0.6 mm, which appeared to be enough to keep the bubble motionless. On the other hand, owing to small dimensions of the frame the upper lateral surface of the bubble remained free and the development of the Marangoni convection occurred in the usual manner.

The experimental cuvette was used as a cell of the Fizeau laser interferometer operating both in reflected and transmitted light (see Fig. 1). Therefore the surfactant distribution was recorded as a system of isolines of the refraction index, which under isothermal conditions varies proportional to the solution concentration. An interval between two interference fringes corresponds to a variation of the surfactant concentration by a magnitude ranging from 0.28% to 0.31% because of the nonlinear character of the dependence of the refraction index on the solution concentration [25]. All solutocapillary experiments were carried out at the ambient temperature (20 ± 1) °C.

In thermocapillary experiments, the temperature dependence of the refraction index allowed us to visualize temperature distribution in the fluid. To fit the temperature difference to the number of interference fringes we performed additional thermocouple measurements. This allows us to take into account thermal expansion of the cuvette walls, which also contribute to the interference patterns.

3 Experimental Results

Typical interferograms of the temperature field around the bubble obtained from experiments on isopropyl alcohol heated from above are given in Fig. 2(*a*). The height of the bubble was 3.3 mm, and its width—7.6 mm. After some time required for diffusion heating of the fluid, a vertical, almost time invariable temperature stratification was established in the cuvette. At a distance from the bubble surface the isothermal lines of the undisturbed temperature field are horizontal, whereas in the immediate vicinity of the surface they are curved downward. This can be regarded as supporting evidence for generation of the stationary thermocapillary Marangoni flow.

Plots of temperature θ versus vertical coordinate z with the origin at the bubble center are constructed for this interference pattern in Fig. 2(*b*). Vertical dashed lines on the plot show the position of the bubble boundaries. Curve 1 describes temperature distribution at a distance from the bubble (along the section A-A, Fig. 2(*a*)), where it is not disturbed by a thermocapillary flow at the interface. Curve 2 corresponds to the temperature along the section B-B while in the liquid, and to the temperature at the surface at the level of the bubble. As it is evident from the comparison of the plots, the evolution of the capillary flow has an inessential effect on the character of the concentration field around the bubble and therefore there still exist appropriate conditions for the Marangoni convection. The value of the temperature gradient obtained in this experiment corresponds the thermal Marangoni number equal approximately to 7×10^3.

The solutocapillary situation appears to be different. The interferogram of the concentration field around the bubble obtained for isopropyl alcohol solutions is given in Fig. 3(*a*). The height of the bubble was 4 mm, width—7.7 mm. The alcohol concentration in the upper part of the cuvette was 50%, and in the lower part—0%

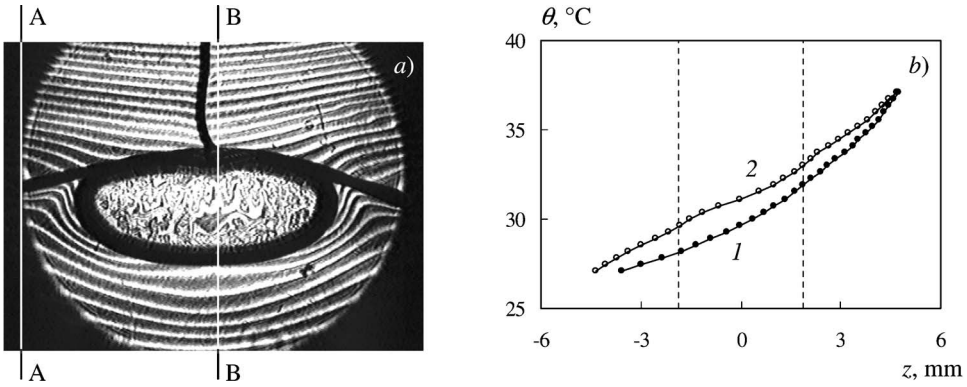

Fig. 2 Thermocapillary convection: (*a*) interference pattern; (*b*) temperature distribution far from (1) and near (2) the bubble. Temperature gradient 1.2 °C/mm.

(pure water). This generated in the cuvette a stationary vertical stratification of the surfactant concentration with a downward-directed gradient of the surface tension. Initially the isolines of the concentration field are horizontal. As in the thermal case, the tangential capillary forces initiate in a thin boundary fluid layer around the bubble a solutocapillary flow directed toward its lower pole. However, in contrast to thermocapillary motion, this flow deforms the concentration field much stronger curving its isolines around the bottom of the bubble.

Figure 3(*b*) demonstrates the concentration distribution at a distance from the bubble (line A-A) and along its diameter (line B-B). Concentration C of the undisturbed field monotonically increases with the height (curve 1), whereas the concentration distribution near the bubble is quite different (curve 2). It is readily seen that just under the bubble there appears a narrow zone with the maximum gradient of the surfactant concentration, whereas the concentration along the whole lateral surface of the bubble up to its upper pole remains practically unchanged. The corresponding flat section of the experimental curve 2 is denoted by long-dash line. Thus, in the solutocapillary case, unlike the thermocapillary one, the development of the capillary flow leads to generation of a thin near-surface layer around the bubble. In this layer, the surfactant concentration is found to be homogeneous and equal to the value of concentration at the bubble upper pole. For this reason, the distribution of the surface tension over the whole bubble surface becomes homogeneous and the solutocapillary flow ceases, this being the main difference from the thermocapillary flow, which is sustained by heat diffusion.

However, the achieved equilibrium in the liquid/bubble system is not final. During the Marangoni convection the capillary forces generate under the bubble a region of concentrated surfactant solution with the density lower than that of the surrounding liquid. The established stratification is unstable, and when the solutocapillary flow sustaining this concentration distribution vanishes, the equilibrium is disturbed. Under the action of the Archimedean forces the streams of the alcohol begin to buoy up near the lateral surfaces of the bubble. Due to fluid continuity, this motion is accompanied by a downward flow along the free bubble surface. The surfactant-concentrated fluid over the bubble, entailed by this flow, is carried to the upper pole of the bubble and after reaching the free surface is again transferred downward along the surface in the direction of surface tension growth.

Reestablishment of the surface tension difference triggers the capillary mechanism of mass transfer, and intensity of the surface motion abruptly increases, giving rise to a violent convection flow around the bubble in the form of two symmetric vortices (Fig. 4(*a*)). During evolution these vortices capture and mix more and more areas of the solution with higher surfactant concentration. As a result the average density of the solution within the vortex cell decreases, the cell shifts upward and at a certain moment cuts off the surfactant supply to the bubble surface. Once this happens, the convection motion ceases as fast as it has started.

Later, under the action of the gravity forces a nearly initial pattern of the vertical concentration stratification is gradually restored (Fig. 4(*b*)). Then, after a time, the whole process is repeated. Such oscillations of the fluid state occur with the period of about 1–2 min and may continue as long as there exists external stratification of the surfactant concentration. Figure 4(*c*) shows interference patterns observed 60 min after the beginning of oscillations. It is seen that the homogeneous concentration area above the bubble extends significantly due to mixing of the solution. However, the vertical concentration difference around the

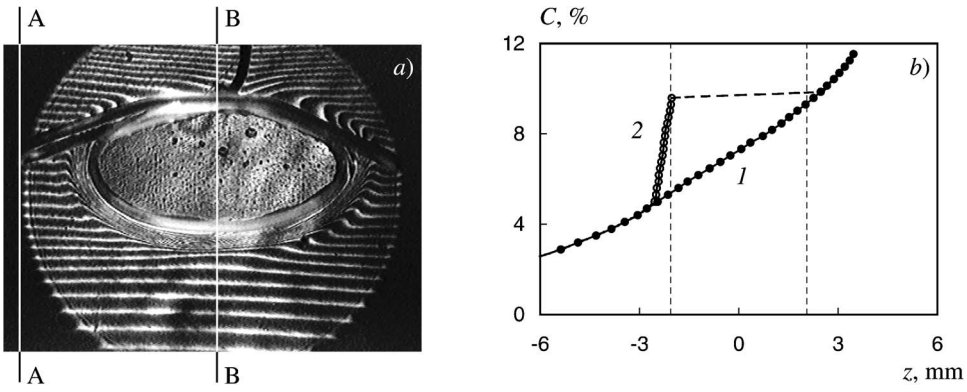

Fig. 3 Solutocapillary convection: (*a*) interference pattern; (*b*) concentration distribution far from (1) and near (2) the bubble. Concentration gradient 0.9 %/mm.

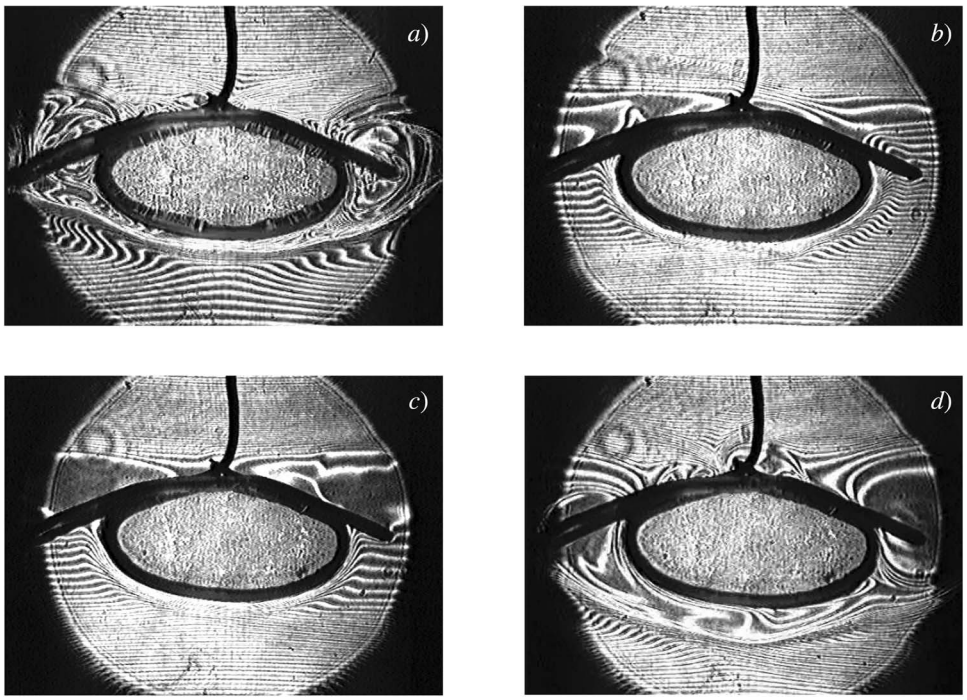

Fig. 4 Interferograms of concentration distribution: (*a*) *t*=0.2 min; (*b*) *t*=1.8 min; (*c*) *t*=60.0 min; (*d*) *t*=60.3 min. Initial concentration gradient 2.5 %/mm.

bubble still exist and thus the oscillatory convective flow is periodically resumed (Fig. 4(*d*)), though with less intensity and frequency.

4 Discussion

A key point in understanding the reasons for periodic initiation of solutocapillary motion is the fact that the difference of the surfactant concentration between the bubble poles measured at a distance from the bubble is similar to that in the zone of strong concentration heterogeneity under the bubble. Based on the results of the preliminary experiments [24] one would expect that adsorption essentially contributes to formation of the concentrated surfactant "cap" at the lower pole of the bubble. However the fact that there is no excess of the surfactant concentration in the cap over the maximum concentration of the surrounding solution suggests that the principal mechanism in the examined phenomenon is just the solutocapillary surface stresses rather than adsorption.

In its turn the action of these forces is determined by the external conditions (with respect to the bubble), in particular, by the concentration difference existing in the liquid. It is to be noted however, that the bubble itself affects its environment in the sense that a capillary flow initiates a large-scale flow of the gravitational nature. This type of the flow can change the structure of the concentration field at a rather long distance from the bubble and thus exert a back action on the capillary flow.

A continuous video recording of the interference picture allowed us to investigate the evolution of the concentration field around the bubble. Since the surfactant distribution changed periodically the measurements of its structure were made at the starting time of each cycle of the convection motion. The characteristic interference patterns, obtained 60 and 180 min after the beginning of the test are presented in Figs. 5(*a*) and 5(*b*) (the moment of time $t=0$ has been shown in Fig. 3(*a*)). The corresponding concentration distributions in the section A-A are shown in Fig. 6. It can be seen (curves 1, 2, 3), that the values of concentration far above and below the bubble are slowly equalized, and the averaged solution concentration in the operation zone of the cuvette increases due to the diffusion processes. In this zone—at the level of the bubble—a periodically arising convection flow gradually mixes the solution, forming convective vortices with clearly defined boundaries (see Fig. 4(*a*)). As a result, the concentration difference ΔC between the bubble poles decreases with time t. This relationship is given in Fig. 7. The graph demonstrates that first the concentration difference diminishes quite

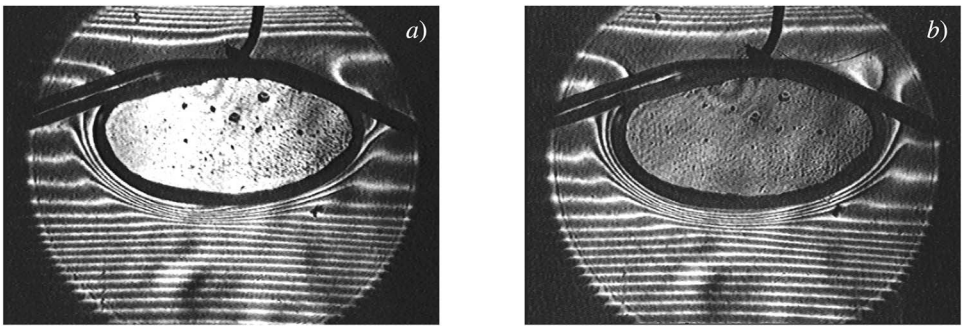

Fig. 5 Interferograms of concentration distribution: (*a*) *t*=60 min; (*b*) *t*=180 min

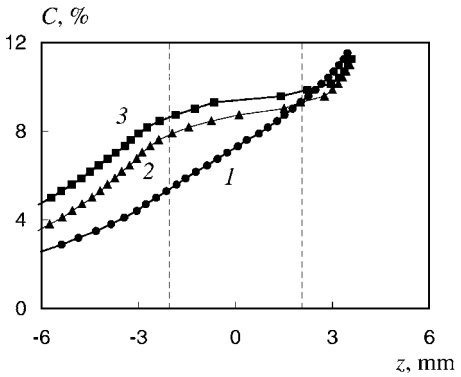

Fig. 6 Variation of concentration far from the bubble with vertical coordinate at time moments 0 min (1), 60 min (2) and 180 min (3)

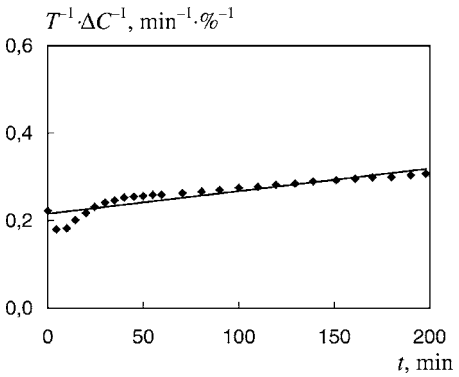

Fig. 9 Variation of oscillation frequency, referred to the concentration difference at bubble poles, with time

rapidly, but approximately after 60 min the decrease becomes much slower approaching some constant asymptotic value. The values of the concentration Marangoni number corresponding to these concentration differences are from 3.5×10^6 to 16.8×10^6.

The disturbance frequency of the concentration field has similar time dependence. Figure 8 shows the variation of the oscillation period T with time. The period, being first about 1 min, increases monotonically and also reaches the maximum within 60 min, after which it remains practically invariable. The coincidence of the characteristic times of the above relationships (Figs. 7 and 8) suggests that the oscillation frequency is defined by the concentration difference in the undisturbed solution. Therefore in Fig. 9 we have plotted on the ordinate axis the oscillation frequency normalized to the concentration difference between the upper and lower poles of the bubble.

It is seen that all experimental points are located on the straight line with the ordinate values increasing from 0.2 to 0.3 $\mathrm{min}^{-1}\ \%^{-1}$ within the whole time interval except the region at the very beginning, where the concentration gradient is determined by the initial conditions. An increase in this relationship with time may be caused by the growth of the average concentration of the solution whose general physical parameters (surface tension, dynamic viscosity, density) are nonlinearly concentration functions. The obtained result supports the view that despite the complicated nature of the considered phenomenon, these are just the solutocapillary Marangoni forces that are responsible for the origin of periodical convective fluid motion.

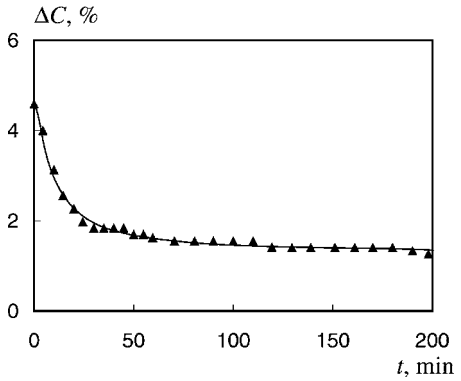

Fig. 7 Variation of concentration difference between bubble upper and lower poles with time

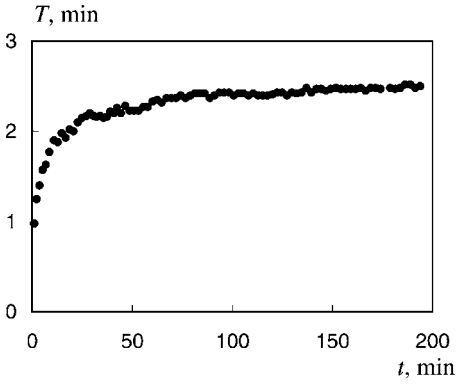

Fig. 8 Variation of concentration field oscillation period around the bubble with time

Acknowledgment

The work was supported by Russian Foundation for Basic Research under grant 03-01-00579.

Nomenclature

C = concentration
D = surfactant diffusion coefficient
Ma_C = concentration Marangoni number, $=(h^2/\eta D)\sigma_C\nabla C$
Ma_θ = thermal Marangoni number, $=(h^2/\eta\chi)\sigma_\theta\nabla\theta$
T = period of oscillations
d = bubble width
h = bubble height
t = time
z = vertical coordinate
∇C = concentration gradient, $=\partial C/\partial z$
$\nabla\theta$ = thermal gradient, $=\partial\theta/\partial z$
χ = fluid thermal diffusivity
η = fluid dynamic viscosity
θ = temperature
σ = surface tension
σ_C = concentration coefficient of surface tension, $=\partial\sigma/\partial C$
σ_θ = thermal coefficient of surface tension, $=\partial\sigma/\partial\theta$

References

[1] Levich, V. G., 1962, *Physicochemical Hydrodynamics*, Prentice-Hall, Englewood Clifs, NJ.
[2] Young, N. O., Goldstein, J. S., and Block, M. J., 1959, "The Motion of Bubbles in a Vertical Temperature Gradient," J. Fluid Mech., **6**, pp. 350–356.
[3] Wozniak, G., Siekman, J., and Srulijes, J., 1988, "Thermocapillary Bubble and Drop Dynamics Under Reduced Gravity—Survey and Prospects," Z. Flugwiss. Weltraumforsch., **12**, pp. 137–144.
[4] Subramanian, R. S., 1992, "The Motion of Bubbles and Drops in Reduced

Gravity," *Transport Processes in Drops, Bubbles and Particles*, Hemisphere Publ. Corp., NY, pp. 1–42.
[5] Subramanian, R. S., Balasubramaniam, R., and Wozniak, G., 2001, "Fluid Mechanics of Bubbles and Drops," *Physics of Fluids in Microgravity*, Gordon & Breach, Amsterdam, Chap. 6, pp. 149–177.
[6] Subramanian, R. S., and Balasubramaniam, R., 2001, *The Motion of Bubbles and Drops in Reduced Gravity*, Cambridge University Press, Cambridge, UK.
[7] Raake, D., Siekmann, J., and Chun, C.-H., 1989, "Temperature and Velocity Fields Due to Surface Tension Driven Flow," Exp. Fluids, **7**, pp. 164–172.
[8] Wozniak, K., Wozniak, G., and Rösgen, T., 1990, "Particle-Image-Velocimetry Applied to Thermocapillary Convection," Exp. Fluids, **10**, pp. 12–16.
[9] Chun, C.-H., Raake, D., and Hansmann, G., 1991, "Oscillating Convection Modes in the Surroundings of an Air Bubble Under a Horizontal Heated Wall," Exp. Fluids, **11**, pp. 359–367.
[10] Rashidnia, N., and Balasubramaniam, R., 1991, "Thermocapillary Migration of Liquid Droplets in a Temperature Gradient in a Density Matched System," Exp. Fluids, **11**, pp. 167–174.
[11] Kassemi, M., and Rashidnia, N., 2000, "Steady and Oscillatory Thermocapillary Convection Generated by a Bubble," Phys. Fluids, **12**, pp. 3133–3146.
[12] Arlabosse, P., Tadrist, L., Tadrist H., and Pantaloni, J., 2000, "Experimental Analysis of the Heat Transfer Induced by Thermocapillary Convection Around a Bubble," Heat Mass Transfer, **122**, pp. 66–73.
[13] Betz, J., and Straub, J., 2001, "Numerical and Experimental Study of the Heat Transfer and Fluid Flow by Thermocapillary Convection Around Gas Bubbles," Heat Mass Transfer, **37**, pp. 215–227.
[14] Wozniak, K., Balasubramaniam, R., Hadland, P. H., and Subramanian, R. S., 2001, "Temperature Fields in a Liquid Due to the Thermocapillary Motion of Bubbles and Drops," Exp. Fluids, **31**, pp. 84–89.
[15] Reynard, C., Santini, R., and Tadrist L., 2001, "Experimental Study of the Gravity Influence on the Periodic Thermocapillary Convection Around a Bubble," Heat Mass Transfer, **122**, pp. 66–73.
[16] Reynard, C., Santini, R., and Tadrist L., 2003, "Experimental Study of Fluid-Wall Heat Transfer Induced by Thermocapillary Convection: Influence of the Prandtl Number," C. R. Mec., **331**(3), pp. 237–244.
[17] Barton, K. D., and Subramanian, R. S., 1989, "The Migration of Liquid Drops in a Vertical Temperature Gradient," J. Colloid Interface Sci., **133**(1), pp. 211–222.
[18] Nallani, M., and Subramanian, R. S., 1993, "Migration of Methanol Drops in a Vertical Temperature Gradient in a Silicone Oil," J. Colloid Interface Sci., **157**(1), pp. 24–31.
[19] Chen, J., and Stebe, K., 1997, "Surfactant-Induced Retardation of the Thermocapillary Migration of a Droplet," J. Fluid Mech., **340**, pp. 35–59.
[20] Bratukhin, Yu. K., and Zuev, A. L., 1984, "Thermocapillary Drift of Air Bubbles in a Horizontal Hele-Shaw Cell," Fluid Dyn., **19**(3), pp. 393–397.
[21] Briskman, V. A., Bratukhin, Yu. K., Zuev, A. L., and Viviani, A., 2001, "On Terrestrial Modeling of Thermocapillary Migration of Gas Bubbles at Weak Buoyant Convection," AIAA Paper No. 2001-0763.
[22] Zuev, A. L., and Kostarev, K. G., 2004, "Experimental Observation of the Solutocapillary Migration of Air Bubbles in Inhomogeneous Liquid Solutions," Dokl. Phys., **49**(12), pp. 747–750.
[23] Bratukhin, Yu. K., Kostarev, K. G., Viviani A., and Zuev, A. L., 2005, "Experimental Study of Marangoni Bubble Migration in Normal Gravity," Exp. Fluids, **38**(5), pp. 594–605.
[24] Kostarev, K. G., Zuev, A. L., and Viviani, A., 2004, "Oscillatory Marangoni Convection Around the Air Bubble in a Vertical Surfactant Stratification," C. R. Mec., **332**(1), pp. 1–7.
[25] Verschueren, K., 1997, *Handbook of Environmental Data on Organic Chemicals*, Van Nostrand Rehinold Company, New York.

Samer Hassan
Department of Chemical Engineering
and Applied Chemistry,
University of Toronto,
Toronto, Ont. M5S 3E5, Canada

Tatyana P. Lyubimova
Professor
Institute of Continuous
Media Mechanics UB, RAS,
Perm, Russia

Dmitry V. Lyubimov
Professor
Theoretical Physics Department,
Perm State University,
Perm, Russia

Masahiro Kawaji[1]
Professor
Department of Chemical Engineering
and Applied Chemistry,
University of Toronto,
Toronto, Ont. M5S 3E5, Canada
e-mail: kawaji@ecf.utoronto.ca

Motion of a Sphere Suspended in a Vibrating Liquid-Filled Container

The effects of small vibrations on the motion of a solid particle suspended in a fluid cell were investigated theoretically and experimentally. An inviscid model was developed to predict the amplitude of a solid particle suspended by a thin wire in the fluid cell which was vibrated horizontally. Both the model and experimental data showed that the particle amplitude is linearly proportional to the cell amplitude, and the existence of a resonance frequency. At higher cell vibration frequencies well above the resonance frequency, both the model and experiments showed that the particle amplitude becomes constant and independent of the wire length. [DOI: 10.1115/1.1992516]

1 Introduction

Advanced materials can be produced under microgravity where gravity induced convection is suppressed, but many semiconductor and protein crystal experiments conducted in the past aboard the Space Shuttle and Mir Space Station have yielded unexpected results due to certain fluid behavior unique to the space environment. Small vibrations existing on the space platforms can totally alter the fluid behavior under microgravity which may lead to inferior crystal properties. Thus, there is a need to understand and control the effects of vibrations on fluid systems relevant to material processing aboard space platforms including the g-jitter effects. More specifically, the motion of a solid particle in fluid cells filled with liquids of different densities and viscosities, and subjected to random and forced vibrations need to be investigated over a wide range of experimental conditions.

To this end, a systematic series of theoretical and experimental investigations have been conducted to study the effects of controlled vibrations on the motion of a solid particle in a fluid cell, relevant to the fields of material processing, fluid physics, and protein crystal growth. Many studies have been conducted on flow-induced vibrations of solid structures. However, the reverse situation of vibration-induced fluid motion, in a closed container full of liquid, has not yet been fully explored and tackled by any physical experiment. Some theoretical and experimental studies exist on fluid flow in homogeneous and heterogeneous systems at high vibration frequencies, so those results would be utilized.

Stokes [1], Basset [2], and Boussinesq [3] derived the expressions for the hydrodynamic forces on a sphere, subjected to harmonic and arbitrary motion respectively, exerted by the surrounding fluid. They omitted the inertia terms (nonlinear terms) in all calculations in order to simplify the Navier-Stokes equations. The inertia terms were first included by Whitehead [4] who started from the undisturbed parallel flow at infinity, and showed that the first approximation using the perturbation technique cannot satisfy the boundary condition. Happel and Brenner [5] mentioned the next approximation also diverges at infinity. Those results are known as Whitehead's paradox. Oseen [6] linearized the nonlinear terms up to the first order and showed that the ratio of the inertial to the viscous terms cannot be neglected at large distances (1/Re) as assumed by Stokes for creeping flow no matter how small the particle diameter is. Later, Proudman and Pearson [7], showed the inaccuracy of Oseen' equations near the edge of the particle, and introduced solutions near and far from the body, and matched them asymptotically as described by Nayfeh [8].

Lighthill [9] was the first to investigate drag caused by periodic vibrations. He mentioned that below a critical frequency a quasi-steady state exists in the laminar boundary layer. Fuat Odar [10] dealt with the forces acting on a sphere accelerating in an otherwise quiet and viscous fluid, and stated that the general situations in which both the fluid and the body move are very difficult to study, since the motion of the fluid could be curved and unsteady.

Other important studies have been performed to determine the terminal velocities of a spherical particle in a vertically oscillating liquid. Among them were those published by Baird et al. [11], Ikeda [12], Jameson and Davidson [13], and Tunstall et al. [14]. An article by Molinier et al. [15] dealt with a study of the motion of a sphere in a column where there is a circulation of a viscous oil. An important reference that summarizes the works of the above authors and others is by Clift et al. [16] which included all the main studies up to 1978 on the motion of drops, bubbles and particles. It is an important reference for flows at low and high Reynolds numbers and calculating the drag force induced and the wall effects on the particle motion.

Ganiev et al. [17] and Kawaji et al. [18] studied the effect of vibrations on liquid-vapor or liquid-gas bubble systems in space. Friesen et al. [19] numerically predicted the linear relationship between the bubble amplitude and cell vibration amplitude, shown experimentally and theoretically for an inviscid liquid by Kawaji

[1]To whom correspondence should be addressed.

Contributed by the Applied Mechanics Division of ASME for publication in the JOURNAL OF APPLIED MECHANICS. Manuscript received August 6, 2004; final manuscript received May 19, 2005. Assoc. Editor: D. Siginer. Discussion on the paper should be addressed to the Editor, Prof. Robert M. McMeeking, Journal of Applied Mechanics, Department of Mechanical and Environmental Engineering, University of California—Santa Barbara, Santa Barbara, CA 93106-5070, and will be accepted until four months after final publication in the paper itself in the ASME JOURNAL OF APPLIED MECHANICS.

et al. [18]. Other relevant studies include that of Houghton [20] who analyzed the nonlinear drag (Newton's law) of free particles in a sinusoidal velocity field leading to the Mathieu equation, where he found that stable particle trajectories may occur in certain ranges of amplitude and frequency. Chelomey [21] performed some experiments on a solid particle immersed in a liquid-filled container and concluded that under certain conditions, nonuniform forces arise with zero-mean values acting on the particle. In the experiments by Chelomey [21], these forces lead to a paradoxical behavior of bodies in an oscillating liquid; bodies of greater density than the surrounding fluid can emerge at the top, whereas light bodies can move downwards against the force of gravity. Lyubimov et al. [22] dealt with the mean forces and torques acting on the bodies of different shapes, under some constraints of the vibration frequencies; they derived analytically the vibrational forces acting on the particle in a fluid subjected to a sinusoidal motion.

Recent protein crystal growth experiments conducted in our laboratory by Gamache [23] have shown that small vibrations can induce movements in crystals which in turn cause significant fluid motion around the growing crystal. This may explain the motion of protein crystals observed in space experiments performed by Chayen et al. [24] and others, and possibly caused by small vibrations called g-jitter on space platforms.

The objective of the present work was to theoretically and experimentally investigate the response of a solid particle in a fluid cell to vibrations of small amplitude and frequency less than 10 Hz. To conduct experiments with solid-liquid systems of different densities on the ground subjected to vibrations of low frequencies, the particle was attached to a wire and suspended in a closed fluid cell, so that no sedimentation by gravity would occur.

2 Experimental Apparatus

The experimental apparatus consisted of a test section, a PC-controlled linear translation stage, and a video camera/recording system as shown in Fig. 1. The test equipment had to be totally vibration free before starting, so all the equipment was mounted on a vibration-isolation table. The background vibration level in the range of 0.1 mg was considered to be acceptable (where 1 g is normal gravity). Each of the major components is described below in detail.

A computer-controlled translation stage was used to vibrate the fluid cell with sub-micron resolution and repeatability. It was controlled to move horizontally with a specified amplitude and frequency in a nearly sinusoidal manner. The test section was a liquid filled rectangular vessel (110 mm $\times$ 70 mm $\times$ 70 mm) made of smooth, polished acrylic plates. Six grooves were cut on the side walls to place flat inserts in order to adjust the width of the cell and to study the wall proximity effects on the particle motion. To study the effects of the wire diameter as well as wire length, thin platinum wires of different diameters (50, 75, 125, 175, and 250 μm) and length (40, 60, 70, and 80 mm) were used. The wires were made of platinum to avoid any anticipated corrosion in water and to minimize any galvanic effect.

Only spherical steel particles have been used in the experiments conducted so far leaving other particle shapes for a future study. The liquid used to fill the fluid cell was distilled water, which has relatively low viscosity ($\mu = 10^{-3}$ kg/m.s at 20°C and 1 atm), and may be considered as inviscid from a theoretical point of view. A color video camera (Hitachi D.S.P. VK C-370) with interchangeable lenses was used to capture the particle motion with sufficient magnification. The edge of the particle was captured at 30 frames per second. The shutter speed was set at $1/1000$ s^{-1} to obtain sharp images. The particle edges recorded in a video tape were analyzed 85 frames at a time using an image analysis program. For each run, 255 frames or particle edges captured over a period of 8.64 s were measured, and the data were entered into a spreadsheet to calculate the particle amplitude and frequency.

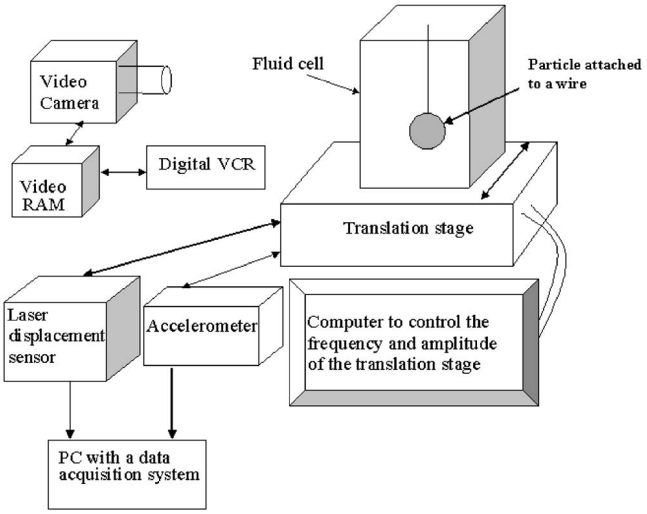

Fig. 1 Experimental setup

First, the cell vibration frequency was set at 0.1 Hz and the cell amplitude was changed from 0.5 to 10 mm over small increments. Then the vibration frequency was increased by 0.25 Hz up to 3 Hz, and the experiment was run again with the same amplitudes as before for 0.1 Hz. The procedure was then reversed such that at a fixed cell vibration amplitude of 0.5 mm, the cell frequency was increased from 0.1 to 3 Hz. After reaching 3 Hz, different amplitudes were imposed from 2 to 10 mm. The system was run for at least 5 min to allow the particle and fluid motions to become stabilized, before the particle images were recorded for at least 2 min on a digital video tape by means of a digital VCR (JVC Model AG-7355). It is important to note that the light source was placed far from the fluid cell to avoid any heating effect. The experiments were repeated at least 15 times for a given experimental condition.

The phase of the particle motion with respect to the vibrated cell motion was identified by fixing a rod with a sharp marker on the vibration isolation table, and vibrating the fluid cell while the particle edge and the marker position were recorded simultaneously. This way, the direction and speed of the cell motion could be detected in the video image with respect to the fixed marker rod. A pixel to μm conversion factor was obtained by lowering a platinum wire of known diameter to the bottom of the fluid cell and recording its image. Then by using the same image analysis program, the wire diameter in pixels was calculated and the conversion factor was computed.

3 Theoretical Analysis

The particle motion in an inviscid fluid and infinite cell under forced vibration was theoretically analysed as follows. Neglecting the effects of surface tension and heating, the Navier-Stokes equations for the fluid of density, ρ_L, surrounding a spherical particle are given by,

$$\frac{\partial \boldsymbol{v}}{\partial t} + (\boldsymbol{v} \cdot \nabla)\boldsymbol{v} = -\frac{\nabla p}{\rho_L} - \ddot{\boldsymbol{R}} + \boldsymbol{g} \tag{1}$$

where $\boldsymbol{v}$ is fluid velocity, p is the pressure, $\ddot{\boldsymbol{R}}$ is the particle acceleration, and $\boldsymbol{g}$ is the acceleration field. The velocity far away from the particle is

$$\boldsymbol{v}_\infty = -\dot{\boldsymbol{R}} + a\omega \cos \omega t \boldsymbol{i} \tag{2}$$

where a is the imposed vibration amplitude and ω is the angular frequency ($=2\pi f$). The velocity field is related to the velocity potential by

$$\boldsymbol{v} = \nabla \varphi \tag{3}$$

where $\Delta\varphi = 0$ for a potential field. (4)

Substituting (3) into (1) and (2) and integrating, we obtain

$$\frac{\partial\varphi}{\partial t} + \frac{1}{2}(\nabla\varphi)^2 = -\frac{p}{\rho_L} - \ddot{\boldsymbol{R}} \cdot \boldsymbol{r} + \boldsymbol{g} \cdot \boldsymbol{r} \tag{5}$$

$$\text{and } \varphi_\infty = -\dot{\boldsymbol{R}} \cdot \boldsymbol{r} + a\omega \cos \omega t \boldsymbol{i} \cdot \boldsymbol{r} \tag{6}$$

where $\boldsymbol{r}$ is the vector from the center of the particle to any point in the fluid cell, $\boldsymbol{i}$ is the direction of cell motion, and ϕ_∞ is the velocity potential at infinity. The harmonic solution of (5) is given by,

$$\varphi = a\omega \cos \omega t \boldsymbol{i} \cdot \boldsymbol{r} + C_1 \frac{\boldsymbol{i} \cdot \boldsymbol{r}}{r^3} - \dot{\boldsymbol{R}} \cdot \boldsymbol{r} + C_2 \frac{\dot{\boldsymbol{R}} \cdot \boldsymbol{r}}{r^3} \tag{7}$$

where C_1 and C_2 are determined by applying the kinematic constraints for an inviscid fluid on the surface of the sphere.

$$v_r = \nabla\varphi \cdot \boldsymbol{n} = 0 \tag{8}$$

where $\boldsymbol{n}$ is the outward normal from the sphere of radius R_0. Substituting (7) into (3) gives,

$$\vec{\boldsymbol{v}} = a\omega \cos \omega t \boldsymbol{i} + C_1 \frac{\boldsymbol{i}}{r^3} - 3C_1 \frac{(\boldsymbol{i} \cdot \boldsymbol{r})\boldsymbol{r}}{r^5} - \dot{\boldsymbol{R}} + C_2 \frac{\dot{\boldsymbol{R}}}{r^3} - 3C_2 \frac{(\dot{\boldsymbol{R}} \cdot \boldsymbol{r})\boldsymbol{r}}{r^3} \tag{9}$$

Using the condition (8) yields

$$v_r = a\omega \cos \omega t \boldsymbol{i} \cdot \boldsymbol{n} + C_1 \frac{\boldsymbol{i} \cdot \boldsymbol{n}}{R_0^3} - 3C_1 \frac{\boldsymbol{i} \cdot \boldsymbol{n}}{R_0^3} - \dot{\boldsymbol{R}} \cdot \boldsymbol{n} + C_2 \frac{\dot{\boldsymbol{R}} \cdot \boldsymbol{n}}{R_0^3} - 3C_2 \frac{\dot{\boldsymbol{R}} \cdot \boldsymbol{n}}{R_0^3} = 0 \tag{10}$$

where the constants C_1 and C_2 can be calculated and are given by

$$C_1 = \tfrac{1}{2} a\omega R_0^3 \cos \omega t \tag{11}$$

$$C_2 = -\tfrac{1}{2} R_0^3 \tag{12}$$

Hence, the fluid velocity $\vec{\boldsymbol{v}}$ is given by,

$$\boldsymbol{v} = a\omega \cos \omega t \left(1 + \frac{1}{2}\left(\frac{R_0}{r}\right)^3\right) - \frac{3}{2} a\omega R_0^3 \cos \omega t \frac{(\boldsymbol{i} \cdot \boldsymbol{r})\boldsymbol{r}}{r^5} - \dot{\boldsymbol{R}}\left(1 + \frac{1}{2}\left(\frac{R_0}{r}\right)^3\right) + \frac{3}{2} R_0^3 \frac{(\dot{\boldsymbol{R}} \cdot \boldsymbol{r})\boldsymbol{r}}{r^5} \tag{13}$$

The pressure p on the surface of the sphere is determined now from (5) as follows:

$$p = \tfrac{3}{2} \rho_L a\omega^2 R_0 \sin \omega t \boldsymbol{i} \cdot \boldsymbol{n} + \tfrac{1}{2} \rho_L R_0 \ddot{\boldsymbol{R}} \cdot \boldsymbol{n} + \rho_L R_0 \boldsymbol{g} \cdot \boldsymbol{n} \tag{14}$$

Thus, the total pressure force acting on the sphere is given by,

$$\boldsymbol{F}_p = -\oint p \vec{\boldsymbol{ds}} \tag{15}$$

Substituting (14) into (15) leads to,

$$\boldsymbol{F}_p = -\tfrac{3}{2} \rho_L a\omega^2 V \sin \omega t \boldsymbol{i} - \tfrac{1}{2} \rho_L V \ddot{\boldsymbol{R}} - \rho_L V \boldsymbol{g} \tag{16}$$

By performing a force balance on the particle of mass m, and radius R_0, suspended by a wire of length $(L - R_0)$ as shown in Fig. 2, we can write the equation of motion for the particle as,

$$m\ddot{\boldsymbol{R}} = -\oint p \boldsymbol{ds} + m\boldsymbol{g} + \boldsymbol{f} \tag{17}$$

where $\boldsymbol{f}$ is the wire tension.

Substituting (16) into (17) gives,

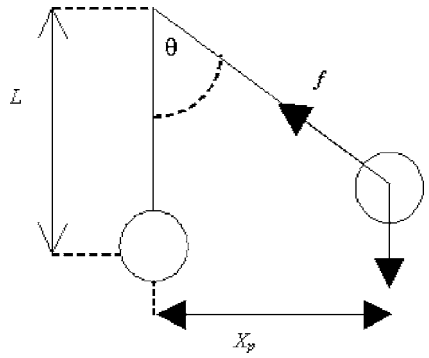

Fig. 2 Balance of forces acting on a particle of a mass *m* suspended by a wire of length *L*

$$m\ddot{\boldsymbol{R}} = -\tfrac{3}{2} \rho_L a\omega^2 V \sin \omega t \boldsymbol{i} - \tfrac{1}{2} \rho_L V \ddot{\boldsymbol{R}} + m\boldsymbol{g} + \boldsymbol{f} - \rho_L V \boldsymbol{g} \tag{18}$$

Since $\boldsymbol{R} = \boldsymbol{R}_p + a \sin \omega t \boldsymbol{i}$, (19)

substitution of (19) into (18) yields

$$\left[1 + \frac{1}{2}\frac{\rho_L}{\rho_S}\right] \ddot{\boldsymbol{R}}_p = \left(\frac{\rho_S - \rho_L}{\rho_S}\right)[a\omega^2 \sin \omega t \boldsymbol{i} + \boldsymbol{g}] + \frac{\boldsymbol{f}}{m} \tag{20}$$

The vertical component of (20) yields the wire tension as follows.

$$f = mg\left(\frac{\rho_S - \rho_L}{\rho_S}\right) \tag{21}$$

To determine the instantaneous displacement in the $\boldsymbol{i}$ direction, the horizontal component of (20) has to be calculated by assuming small amplitude of particle oscillations from the equilibrium position of the particle. Substituting the horizontal component of the force $\boldsymbol{f}$ from (21) into (20), the following differential equation for the horizontal displacement, X_p, of the particle with respect to the equilibrium position can be obtained.

$$\left[1 + \frac{\rho_L}{\rho_S}\right] \ddot{X}_p = \left(\frac{\rho_S - \rho_L}{\rho_S}\right)\left[a\omega^2 \sin \omega t - g\frac{X_p}{L}\right] \tag{22}$$

By solving Eq. (22) analytically, the particle amplitude is given by

$$A = \frac{a}{\dfrac{g}{L\omega^2} - \dfrac{2\rho_S + \rho_L}{2(\rho_S - \rho_L)}}, \tag{23}$$

In (23), we can see clearly that the denominator becomes zero for

$$\omega_{\text{res}} = \sqrt{\frac{2(\rho_S - \rho_L)}{2\rho_S + \rho_L}\left(\frac{g}{L}\right)} \tag{24}$$

which is the resonance frequency. At this frequency, ω_{res}, the particle amplitude would be theoretically infinite. Whether this prediction is valid or not can be tested by vibrating the cell at gradually increasing frequencies and measuring the particle amplitude. Beyond the resonance frequency, the denominator of (23) would become negative but finite indicating a phase shift between the particle and cell motions. Before the resonance, the particle and cell move in the same direction, but above the resonance frequency, they move in opposite directions. A further increase in the vibration frequency beyond the resonance frequency gives rise to a reduction in the particle amplitude and the following asymptotic particle amplitude, A_∞, as $\omega \to \infty$.

$$|A_\infty| = 2a\left(\frac{\rho_S - \rho_L}{2\rho_S + \rho_L}\right) \tag{25}$$

It is noted that Eq. (23) can be obtained by starting from the general form of the forces acting on a particle as shown in Mag-

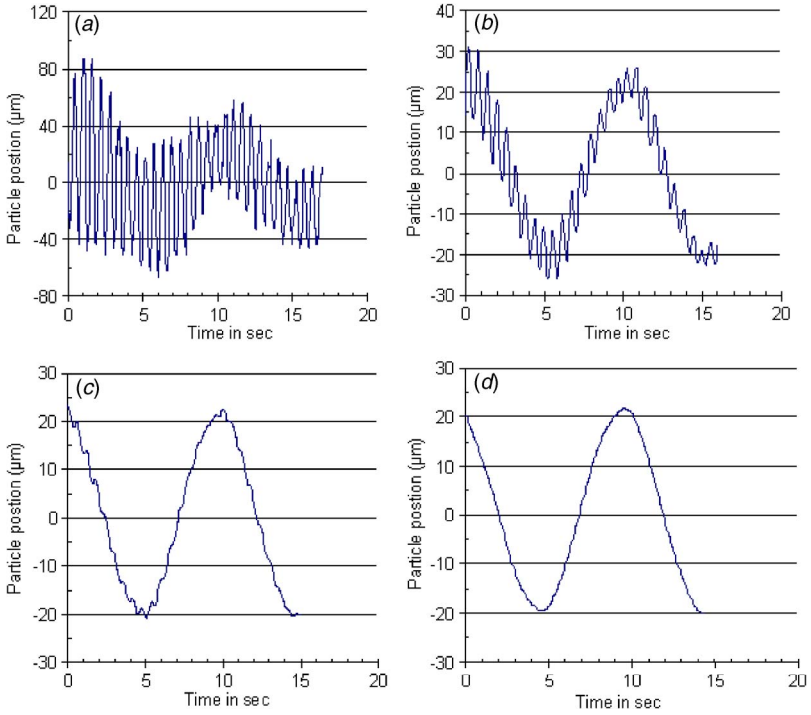

Fig. 3 Particle displacement from the mean position, (*a*) instantaneous data, (*b*) first-smoothed data, (*c*) second-smoothed data, and (*d*) third-smoothed data

naudet et al. [25] in their theoretical analysis of the bubble motion in inhomogeneous flows. The present analysis additionally reveals the expressions for the temporal and spatial fluid velocity and pressure fields around the oscillating particle, which were then used to predict the particle amplitude.

4 Results and Discussion

The steel particle response to the external vibration is shown in Figs. 3 and 4 for imposed cell amplitudes of 8, 4, 2, and 1 mm and a range of vibration frequencies from 0.1 to 3 Hz for the wire

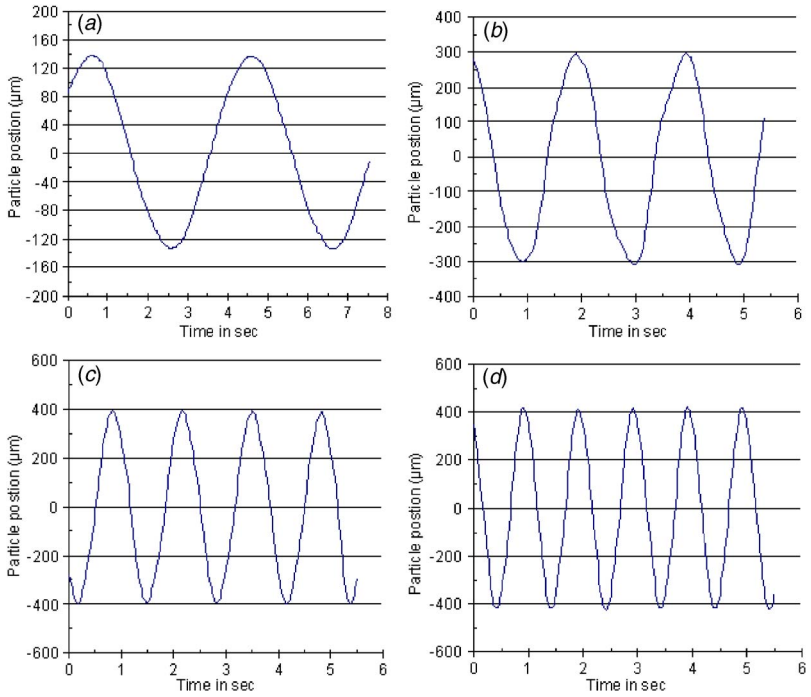

Fig. 4 Instantaneous particle displacement from the mean position, (*a*) *f* =0.25 Hz, *a*=8 mm; (*b*) *f*=0.5 Hz, *a*=4 mm; (*c*) *f*=0.75 Hz, *a*=2 mm; (*d*) *f*=1 Hz, *a*=1 mm

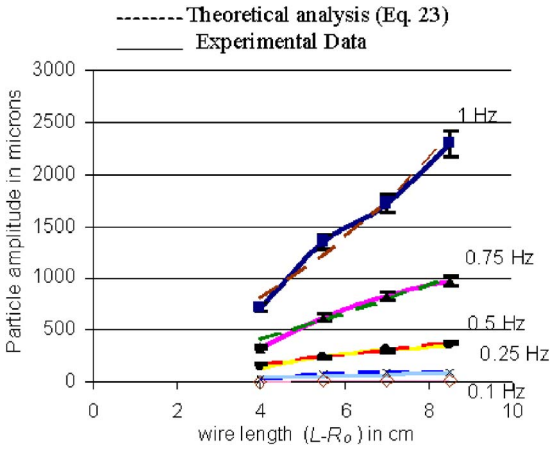

Fig. 5 Variation of particle amplitude with wire length ($L-R_0$) for cell vibration amplitude of 4.0 mm at different frequencies

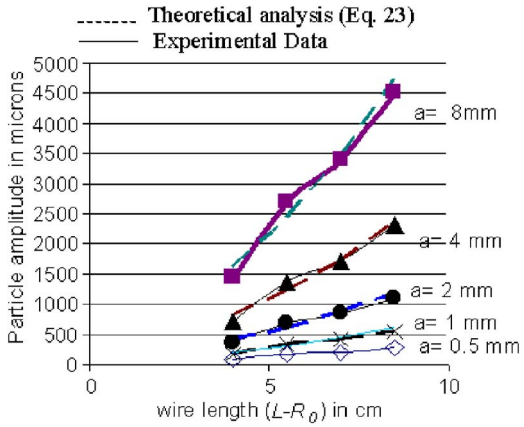

Fig. 6 Variation of particle amplitude with wire length ($L-R_0$) for cell vibration frequency of 1 Hz at different cell vibration amplitudes

length, $L=70$ mm. In Figs. 3(a)–3(d), the particle position data are presented for the case of the cell vibration frequency equal to 0.1 Hz and amplitude of 8 mm. Figure 3(a) shows the raw position data. Figure 3(b) shows the results of smoothing using a moving average calculation method, in which 30 consecutive points were averaged at any given time. Figure 3(c) shows the data obtained after applying the same smoothing operation to Fig. 3(b), while Fig. 3(d) shows the result after the third smoothing operation. From Figs. 4(a)–4(d), it is clear the particle followed a near sinusoidal motion for cell vibration frequencies above 0.25 Hz, but the effect of a pendulum motion was superimposed for frequencies less than 0.25 Hz.

For a cell vibration at 0.1 Hz shown in Fig. 3, the particle motion consisted of:

1- a simple pendulum motion with a period equal to that of a wire attached to a particle swinging under the force of gravity. The period of such motion depends on the wire length only and not the imposed vibration frequency.
2- Smoothed particle motion had a frequency equal to that of the imposed vibration.

The effect of the wire length on the particle amplitude was found to be large as shown in Fig. 5. If the wire length was increased, the particle amplitude would increase markedly for a given cell amplitude and frequency. Larger increases in the particle amplitude occurred at higher cell vibration frequencies (e.g., 0.75 and 1.0 Hz). The dashed lines correspond to the theoretical predictions given by Eq. (23), which are in good agreement with the data. As the wire length was increased, the particle amplitude increased nearly linearly mainly for frequencies less than 0.75 Hz. The error bars shown for some data points in Fig. 5 indicate the maximum and minimum values of the 15–20 measurements obtained for a given run. The deviations of the maximum and minimum values from the mean value remained within ±5% even in the worst case.

For a constant cell vibration frequency of 1.0 Hz shown in Fig. 6, the particle amplitude increases with the wire length and cell amplitude. Again, the inviscid model predictions are in good agreement with the experimental data. In Fig. 7, the wire diameter is shown to have a small effect on the particle amplitude. For wire diameters $\leqslant 125$ μm, it is clear that the particle amplitude remained constant but as the wire diameter was increased above 125 μm, the particle amplitude decreased only by a small amount as shown particularly for an imposed cell amplitude of 8 mm and a frequency of 1.0 Hz. This reduction in the particle amplitude is due to the drag force exerted on the wire. Thus, we can conclude that the use of a wire with a diameter less than 125 μm does not influence the particle motion in the present experiments due to a negligible drag force exerted on the wire.

Several experiments have been performed with different cell inserts to reduce the cell width and to see the effect of the ratio of the cell width to particle diameter. The results obtained for a steel particle in water (not shown here) indicated that the effect of the inserts is negligible for the cell width to particle diameter ratio greater than 3. To see the effect of the attractive force caused by vibration, it would be necessary to observe the particle moving in the fluid near the wall.

The particle amplitude increased linearly with the cell amplitude for a given frequency as shown in Fig. 8, and this increase is more clearly observed at high cell vibration frequencies; these results also agree well with the predictions of the present inviscid model described earlier. Figure 9 shows the variation of the particle amplitude with the cell vibration frequency for various cell amplitudes. It is noticed that for any cell amplitude, as the vibration frequency was increased, the particle amplitude increased and reached a maximum where the system is in a resonant state, and this resonance frequency was equal to 1.7 Hz for a steel particle in water. Above this resonance frequency, the particle amplitude started decreasing in magnitude markedly as the cell frequency was increased further.

The sign of the particle amplitude in Fig. 9 indicates the phase angle relation between the particle and the cell: Positive amplitudes mean the same direction for the cell and particle motions, while the negative amplitudes mean motions in opposite directions. The experimental results agreed well with the theoretical

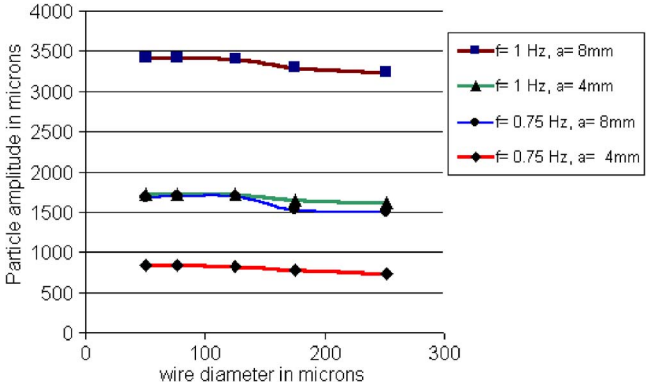

Fig. 7 Effect of wire diameter on the particle amplitude for wire length=7 cm and different cell vibration conditions

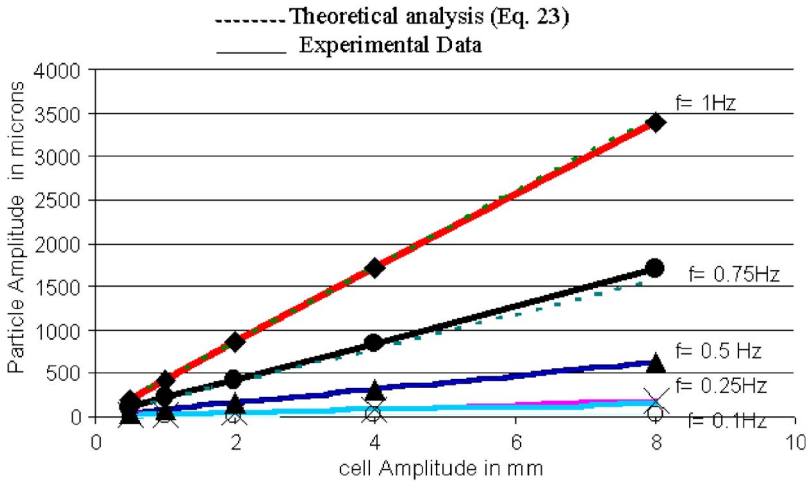

Fig. 8 Variation of particle amplitude with cell amplitude for different frequencies (water, wire length: 70 mm)

predictions for an inviscid fluid. In Fig. 9 an asymptotic line is indicated at 1.7 Hz where the particle amplitude reaches a maximum for a steel particle in water. Below this frequency, the particle and the cell moved in phase with each other; above that frequency, the particle moved in opposite phase with respect to the cell. This was experimentally confirmed for any cell amplitude, using a marker fixed in the laboratory frame of reference and comparing the relative motions of the cell and particle with respect to this marker.

An important theoretical prediction to check is the absence of the particle diameter effect on the amplitude and frequency of the particle motion. Table 1 presents the particle amplitude data obtained for two steel particle diameters of 12.7 and 9.53 mm attached separately to a wire of 70 mm length. The results showed no effect of the particle diameter and agreed with the theoretical prediction given by Eq. (23), provided the wire length, cell amplitude and frequency, and liquid and solid densities are kept constant. It is noted again that the values shown in Table 1 and Figs. 5–10 are the average values obtained from 15 to 20 experiments for a given experimental condition.

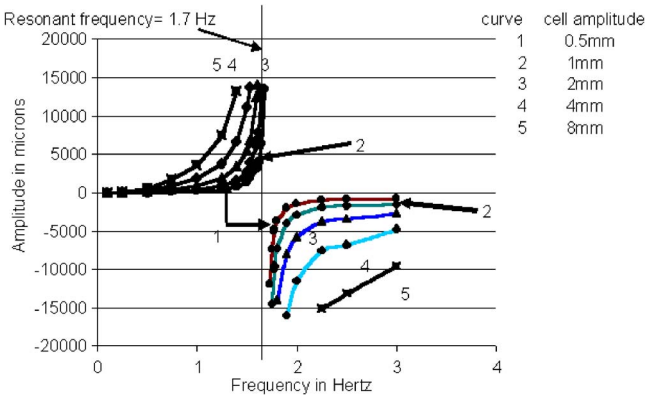

Fig. 9 Particle Amplitude versus frequency for different cell amplitude, L=70 mm

Finally, the present theory predicts an asymptotic particle amplitude independent of the vibration frequency and wire length at high cell vibration frequencies as given by Eq. (25). The experimental data obtained at high vibration frequencies, well above the resonance frequency, validate this prediction as shown in Fig. 10. The particle amplitude converges to a constant value for all vibration frequencies and is no longer dependent on the wire length as predicted. For a cell vibration amplitude of 1.0 mm shown in Fig. 10, the asymptotic particle amplitude was measured to be ~0.83 mm, which agrees well with the value predicted by Eq. (25) for a steel particle (ρ_S=7,830 kg/m^3) in water (ρ_L =997 kg/m^3). This indicates that for cell vibration frequencies well above the resonance frequency, the motion of a spherical particle suspended by a thin wire on the ground may correspond to the motion of a wire-free particle in a fluid cell under microgravity. This result establishes a firm basis on which the vibration-induced particle motion in microgravity could be studied under normal gravity on the ground.

5 Conclusions

A study of vibration-induced particle and fluid motion has been conducted theoretically and experimentally. A series of experi-

Table 1 Particle amplitude data for a spherical particle of different diameters.

Cell Vibration		Particle Amplitude (μm)		
Frequency (Hz)	Amplitude (mm)	12.7 mm particle	10.25 mm particle	Prediction by Eq. (23)
0.25	2.0	35	35	36.0
0.25	4.0	70	72	72.0
0.25	8.0	140	150	144.0
0.5	2.0	160	160	154.2
0.5	4.0	300	315	308.4
0.5	8.0	600	620	616.7
0.75	2.0	400	420	393.4
0.75	4.0	790	815	786.9
0.75	8.0	1580	1610	1573.7

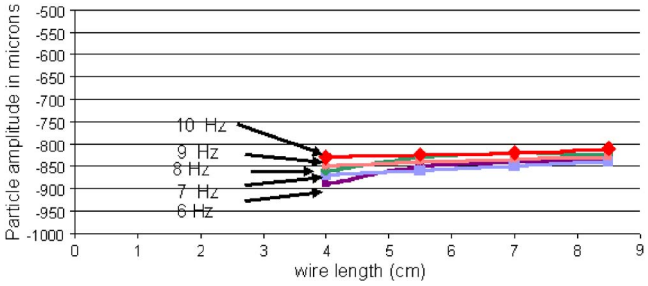

Fig. 10 Particle amplitude variation with wire length for different frequencies (steel ball, liquid: Water, cell amplitude: 1.0 mm)

ments were conducted using steel particles of different diameters in a water-filled rectangular container under different vibration conditions. An inviscid model of a particle suspended in a fluid cell by a thin wire was developed to predict the vibration-induced particle motion. The inviscid fluid assumption is valid when the inertial forces are more important than the viscous force, which is equivalent to a very thin boundary layer compared to the particle radius used as a characteristic length. The validity of this assumption was supported by good agreement obtained between the model predictions and the experimentally measured amplitudes for a steel particle in water at different cell vibration amplitudes and frequencies. In addition, the experimental results on the effects of the wire length on the particle amplitude, the resonance frequency and the phase shift agreed well with the predictions of the theoretical analysis. Finally, in accordance with the theoretical prediction, the experiments performed at high cell vibration frequencies showed that the particle amplitude is independent of the wire length possibly corresponding to the case of a wire-free particle motion in microgravity.

Acknowledgment

This work has been supported by the Microgravity Sciences Program of the Canadian Space Agency.

Nomenclature

a = cell vibration amplitude, m
A = particle amplitude in the cell frame of reference, m
f = vibration frequency, Hz
$\boldsymbol{f}$ = wire tension, N
$\boldsymbol{g}$ = gravitational acceleration, m/s^2
$\boldsymbol{i}$ = direction of cell motion
L = distance from the attachment point to the center of mass of the sphere, m
m = particle mass, kg
p = static pressure, N/m^2
$\boldsymbol{r}$ = fluid element position with respect to the particle, m
R_0 = particle radius, m
$\boldsymbol{R}$ = absolute position of the particle with respect to the inertial system, m
$\boldsymbol{R}_p$ = position of the particle with respect to the cell frame of reference, m
t = time, s
$\boldsymbol{v}_\infty$ = fluid velocity far away from the particle, m/s
$\boldsymbol{v}$ = fluid velocity relative to the particle, m/s
X_p = horizontal displacement of the particle with respect to the cell, m
ρ_S = particle density, kg/m^3
ρ_L = liquid density, kg/m^3
φ = velocity potential, m^2/s
ω = cell vibration frequency, rad/s
ω_{res} = resonance frequency $(=2\pi f)$, rad/s
θ = angle between the wire and the vertical, rad
μ = liquid viscosity kg/m.s

References

[1] Stokes, G. G., 1851, *Mathematical and Physical Papers*, Johnson Reprint Corp., New York, 3, pp. 25–35.
[2] Basset, A. B., 1888, *A Treatise on Hydrodynamics*, Deighton, Bell and Co Press, Cambridge, UK, 2, Chap. 21.
[3] Boussinesq, J. V., 1885, "Sur la Resistance qu'oppose un Liquide Indefeni au Repos, sans Pesanteur, au Mouvememt d'une Sphere Solide qu'il Mouille sur toute sa Surface," C. R. Seances de l' Acad., **100**, pp. 935–937.
[4] Whitehead, A. N., 1889, "Second Approximation to Viscous Fluid Motion. A Sphere Moving Steadily in a Straight Line," Q. J. Math., **23**, pp. 143–152.
[5] Happel, J., and Brenner, H., 1965, *Low Reynolds Number Hydrodynamics*, Prentice Hall Press, Englewood Cliffs, NJ.
[6] Oseen, C. W., 1910, "Uber die Stokes'sche Formel und Uber eine verwandte Aufgabe in der Hydrodynamik," Ark. Mat., Astron. Fys., **6**, pp. 29–45.
[7] Proudman, I., and Pearson, J. R. A., 1957, "Expansion at Small Reynolds Numbers for the Flow Past a Sphere and a Cylinder," J. Fluid Mech., **2**, pp. 237–262.
[8] Nayfeh, A. H., 1973, *Perturbation Methods*, Wiley, New York.
[9] Lighthill, M. J., 1954, "The Response of Laminar Skin Friction and Heat Transfer to Fluctuations in the Stream Velocity," Proc. R. Soc. London, Ser. A, **224**, pp. 1–23.
[10] Odar, F., 1963, "Forces on a Sphere Accelerating in a Viscous Fluid," J. Fluid Mech., **18**, pp. 302–314.
[11] Baird, M. H. I., Senior, M. G., and Thompson, R. J., 1967, "Terminal Velocities of Spherical Particles in a Vertically Oscillating Liquid," Chem. Eng. Sci., **22**, pp. 551–558.
[12] Ikeda, S., 1989, "Fall Velocity of Single Spheres in Vertically Oscillating Fluids," Fluid Dyn. Res., **5**, pp. 203–216.
[13] Jameson, G. J., and Davidson, J. F., 1966, "The Motion of a Bubble in a Vertically Oscillating Liquid: Theory for an Inviscid Liquid and Experimental Results," Chem. Eng. Sci., **21**, pp. 29–33.
[14] Tunstall, E. B., and Houghton, G., 1968, "Retardation of Falling Spheres by Hydrodynamic Oscillations," Chem. Eng. Sci., **23**, pp. 1067–1081.
[15] Molinier, J., Kuychoukov, G., and Angelino, H., 1971, "Etude du Mouvement d'une Sphere dans un Liquide pulse," Chem. Eng. Sci., **26**, pp. 1401–1412.
[16] Clift, R. J., Grace, R., and Weber, M. E., 1978, *Bubbles, Drops and Particles*, Academic Press, London.
[17] Ganiev, R. F., Okhotin, A. S., Lakiza, V. D., and Tsapenko, A. S., 1977, "Controlled Vibratory Displacement of Liquid and Gas in Conditions Close to Weightlessness," Dokl. Akad. Nauk SSSR, **233**, pp. 338–340.
[18] Kawaji, M., Ichikawa, N., Kariyasaki, A., and Tryggvason, B. V., 1999, "Large Bubble Motion in a Fluid Cell Under Microgravcity: ISCAP Experiments on the Effects of g-Jitter and Forced Vibration," J. of Japan Society of Microgravity Applications, **16**(4), pp. 245–254.
[19] Friesen, T. J., Takahira, H., Allegro, L., Yasuda, Y., and Kawaji, M., 2004, "Numerical Simulations of Bubble Motion in a Vibrated Cell Under Microgravity Using Level Set and VOF Algorithms," Ann. N.Y. Acad. Sci., **974**, pp. 288–305.
[20] Houghton, G., 1961, "The Behavior of Particles in a Sinusoidal Vector Field," Proc. R. Soc. London, Ser. A, **272**, pp. 33–43.
[21] Chelomey, V. N., 1983, "Paradoxes in Mechanics Caused by Vibrations," Dokl. Akad. Nauk SSSR, **270**, pp. 62–67.
[22] Lyubimov, D. V., Chereaonov, A. A., Lyubimova, T. P., and Roux, B., 2001, "Vibration Influence on the Dynamics of a Two-Phase System in Weightlessness Conditions," J. Phys. IV, **11**, pp. 83–90.
[23] Gamache, O., 2002, "Experimental Investigation of Marangoni Convection and Vibration Induced Crystal Motion During Protein Crystal Growth," M.A.Sc. Thesis, Dept. of Chemical Engineering & Applied Chemistry, University of Toronto.
[24] Chayen, N., Snell, E. H., Helliwell, J. R., Zagalsky, P. F., 1997, J. Cryst. Growth, **171**, pp. 219–225.
[25] Magnaudet, J., and Eames, I., 2000, "The Motion of High-Reynolds-Number Bubbles in Inhomogeneous Flows," Annu. Rev. Fluid Mech., **32**, pp. 659–708.

Large Eddy Simulation of Rotating Finite Source Convection

Shari J. Kimmel-Klotzkin
Visiting Research Scientist
New Jersey Institute of Technology,
Information Technology Program,
323 M. L. King Boulevard,
University Heights, Newark, NJ 07102-1982
e-mail: Sklotzkin@alumni.Rutgers.edu

Fadi P. Deek
College of Science and Liberal Arts,
New Jersey Institute of Technology,
323 M. L. King Boulevard,
University Heights, Newark, NJ 07102-1982
e-mail: fadi.deek@njit.edu

Numerical simulations of turbulent convection under the influence of rotation will help understand mixing in oceanic flows. Though direct numerical simulations (DNS) can accurately model rotating convective flows, this method is limited to small scale and low speed flows. A large eddy simulation (LES) with the Smagorinsky subgrid scale model is used to compute the time evolution of a rotating convection flow generated by a buoyancy source of finite size at a relatively high Rayleigh number. Large eddy simulations with eddy viscosity models have been used successfully for other rotating convective flows, so the Smagorinsky model is a reasonable starting point. These results demonstrate that a LES can be used to model larger scale rotating flows, and the resulting flow structure is in good agreement with DNS and experimental results. These results also demonstrate that the qualitative behavior of vorticies which form under the source depend on the geometry of the flow. For source diameters that are small compared to the size of the domain, the vortices propagate away from the source. On the other hand, if the ratio of source diameter to domain size is relatively large, the vortices are constrained beneath the source. Though the results are qualitatively similar to a direct numerical simulation (DNS) and other LES, in this simulation the flow remains laminar much longer than the DNS predicts. This particular flow is complicated by the turbulence transition between the convective plume and the quiescent ambient fluid, and an eddy viscosity model is inadequate to accurately model this type of flow. In addition, the Smagorinsky model is not consistent in a noninertial reference frame. Thus the Smagorinsky model is not the optimal choice for this type of flow. In particular, the estimation model has demonstrated better results for other types of rotating flows and is the recommended subgrid scale model for future work. [DOI: 10.1115/1.1991859]

1 Introduction

Convection or similar buoyancy effect due to gravitational forcing can drive large scale oceanic circulations, including thermohaline circulations. Natural phenomena that cause buoyancy driven circulations in the ocean include evaporation, extreme weather conditions such as storms, freezing at the surface, and heating through the ocean floor as a result of a megaplume event. Of particular relevance to this study is the process of surface water freezing, which causes a buoyancy driven flow due to increased salinity just below the ice because the colder water cannot hold as much dissolved salt [1–3].

Some of the current research in environmental turbulent convection focuses on deep water formation, which is thought to be related to major climatic events [4]. Deep water is very cold, fairly dense water, generally found in arctic regions. New deep water formed near the surface tends to sink by creating a chimney, which consists of a relatively homogeneous water column surrounded by more stratified water [5]. Only extreme conditions can cause sinking all the way to the ocean floor. Though such conditions are not common, they are most often found in the Greenland and Weddell Seas [6]. Initially, cooling simply deepens the mixed layer near the surface. When the mixed layer reaches a certain depth, a thermobaric instability occurs and the chimneys form.

Global oceanic circulation simulations are very important in the study of climatic change, but current models do not provide adequate long-term predictions [4] of the flow field. Using field studies and experiments to clarify the important physical processes will assist in the development of better numerical models that can be used on a larger scale. Localized simulations have had more success, such as a numerical model of turbulent line buoyant plumes which occur due to brine rejection when cracks in ice refreeze [7].

A direct numerical simulation (DNS) for an unstratified ambient fluid has been performed successfully [8]. However, these detailes require hundreds of hours of CPU time and 16 million grid point simulations even for a flow field bordering on the turbulent regime. DNS techniques give an "exact" solution to the governing equation but are limited to relatively low Reynolds number due to insufficient computational resources. By using a large eddy simulation (LES), which involves modeling the small scales and resolving only the large scales, a similar computation could be performed using half a million grid points and less than 100 hours of CPU time. The current study involves using a LES to simulate rotating turbulent convection with a finite source. Detailed quantitative comparisons between these computations and the DNS of [8] and the LES of [9] would validate the use of the Smagorinsky model for this type of flow.

2 Background

For large scale geophysical flows, the Coriolis effect due to the rotation of the earth becomes an important influence in the evolution of the flow. When significant rotation is added to turbulent Rayleigh-Bérnard convection, the cells orient radially as a result of the radial acceleration which increases with increasing radius. Higher rotation rates break up these rolls and very high rotation induces the formation of cyclonic and anticyclonic vortices. The

Contributed by the Applied Mechanics Division of ASME for publication in the JOURNAL OF APPLIED MECHANICS. Manuscript received May 17, 2004; final manuscript received May 16, 2005. Assoc. Editor: D. Siginer. Discussion on the paper should be addressed to the Editor, Prof. Robert M. McMeeking, Journal of Applied Mechanics, Department of Mechanical and Environmental Engineering, University of California - Santa Barbara, Santa Barbara, CA 93106-5070, and will be accepted until four months after final publication in the paper itself in the ASME JOURNAL OF APPLIED MECHANICS.

structure of high Rayleigh number turbulent convective flows under the influence of rotation has been previously investigated experimentally by Rossby [10], Boubnov and Golitsyn [11], Fernando et al. [12], Brickman and Kelly [13], and Maxworthy and Narimousa [14]. Field studies in arctic regions [15,16] examine the chimney structure and corroborate well with experimental results. Because of the very large scale of oceanic flows, simulation of a realistic geophysical flow field is still beyond the capabilities of current computational resources. However, recent smaller scale simulations have been able to obtain flow fields that agree well with experimental studies, including the DNS of Chan [8] and LES of Jones and Marshall [9], Lavelle and Baker [7], Julien et al. [17], and Cui and Street [18]. In addition, some LES studies of atmospheric flows have successfully used eddy viscosity methods [19].

The dimensionless parameters that define this type of flow are the Rayleigh number, the Prandtl number, and the Taylor number. The Rayleigh number, which represents the ratio of buoyancy forces to viscous forces, can be expressed in terms of the surface buoyancy flux

$$\mathrm{Ra}_f = \frac{B_o H^4}{\kappa^2 \nu} \tag{1}$$

where

$$B_o = \frac{\alpha g \kappa \frac{\partial T}{\partial z}}{\rho_o c_p} \tag{2}$$

which is the buoyancy flux of the fluid resulting from an imposed temperature gradient at the boundary. The Taylor number (Ta), which represents the ratio of rotational forces to viscous forces, and the Prandlt number (Pr), which gives the relative importance of the momentum diffusivity to the thermal diffusivity, are expressed as follows:

$$\mathrm{Ta} = \frac{4\Omega^2 H^4}{\nu^2} \tag{3}$$

and

$$\mathrm{Pr} = \nu/\kappa \tag{4}$$

The previous parameters are based on molecular quantities. However, this flow may be better described using parameters that do not depend on molecular quantities. For instance, a natural Rossby number Ro^* is defined as

$$\mathrm{Ro}^* = \frac{B_o^{1/2}}{f^{3/2} H} = \mathrm{Ra}_f^{1/2} \mathrm{Pr}^{-1} \mathrm{Ta}^{-3/4} \tag{5}$$

which is less than one when rotational effects are significant.

3 Numerical Methodology

The governing equations are the incompressible Navier-Stokes equations with the Boussinesq approximation plus the energy equation. The LES equations are obtained by applying spatial filtering to the governing equations. The spatial filtering is defined by the integral relation

$$\bar{f}(x) = \int f(x') G(x) dx' \tag{6}$$

where $G(x)$ is the Fourier cutoff filter and the overbar ($\bar{f}$) represents a filtered quantity. The filtered equations in nondimensional form are

$$\frac{\partial \bar{u}_j}{\partial x_j} = 0 \tag{7}$$

$$\frac{\partial \bar{u}_i}{\partial t} + \frac{\partial \bar{u}_i \bar{u}_j}{\partial x_j} + \sqrt{Ta}\ \mathrm{Pr}\ \bar{u}_j \varepsilon_{ij3} = -\frac{\partial P}{\partial x_i} + \mathrm{Pr} \frac{\partial^2 \bar{u}_i}{\partial x_j \partial x_j} - \frac{\partial}{\partial x_j} \tau_{ij} + \mathrm{Pr}\ \mathrm{Ra}_f \bar{T} \delta_{i3} \tag{8}$$

$$\frac{\partial \bar{T}}{\partial t} + \frac{\partial \bar{u}_j \bar{T}}{\partial x_j} = \frac{\partial^2 \bar{T}}{\partial x_j \partial x_j} + \frac{\partial}{\partial x_j} \tau_{\theta j} + F_T \tag{9}$$

where F_T is a nondimensional forcing term that is used to apply a buoyancy. The above equations are nondimensionalized using the characteristic length, time, and temperature scales H, H/κ^2, and $(B_o H)/(\alpha g \kappa)$, respectively.

The effects of the turbulent scales, or unresolved subgrid scales (SGS), removed by the filtering operation on the filtered (resolved) scales is accounted for by the following subgrid scale quantities:

$$\tau_{ij} = \overline{u_i u_j} - \bar{u}_i \bar{u}_j \tag{10}$$

$$\tau_{\theta j} = \overline{u_j T} - \bar{u}_i \bar{T} \tag{11}$$

These SGS stresses are modeled in terms of the resolved quantities.

Since the Smagorinsky model is relatively simple and similar eddy viscosity models have been successfully applied to oceanic convection [20], this subgrid scale model is a reasonable starting point for this study. The Smagorinsky model uses an eddy viscosity to define the subgrid scale stresses as

$$\tau_{ij} = -2\nu_T \bar{S}_{ij} + \frac{1}{3} \tau_{kk} \delta_{ij} \tag{12}$$

$$\tau_{\theta j} = \frac{\nu_T}{\mathrm{Pr}_T} \frac{\partial \bar{T}}{\partial x_j} \tag{13}$$

where $\mathrm{Pr}_T = 1$ and the resolved rate of strain tensor $\bar{S}_{ij}$ is defined as

$$S_{ij} = \frac{1}{2} \left(\frac{\partial \bar{u}_i}{\partial x_j} + \frac{\partial \bar{u}_j}{\partial x_i} \right) \tag{14}$$

For the Smagorinsky model, the eddy viscosity is defined as

$$\nu_T = \begin{cases} (C_s \Delta)^2 \left(2\bar{S}_{ij} - \dfrac{\mathrm{Ra}_f}{\mathrm{Pr}\,\mathrm{Pr}_T} \dfrac{\partial \bar{T}}{\partial x_i} \right)^{1/2} & \text{if} \left(2\bar{S}_{ij} - \dfrac{\mathrm{Ra}_f}{\mathrm{Pr}\,\mathrm{Pr}_T} \dfrac{\partial \bar{T}}{\partial x_i} \right) > 0 \\ 0 & \text{otherwise} \end{cases} \tag{15}$$

which includes a term to take into account mixing due to statically unstable conditions [21]. Several attempts at calculating an optimal value for C_s using theoretical methods [22,23] have produced values between 0.1 and 0.2. The present study uses $C_s = 0.21$ which is a typical value for turbulent convection [24]. The turbulent Prandlt number $\mathrm{Pr}_T \equiv \kappa_T/\nu_T = 1$, and Δ, a length scale determined by the mesh size, is usually defined as

$$\Delta = (\Delta x \Delta y \Delta z)^{1/3} \tag{16}$$

For wall bounded flows, the maximum Δz is often an order of magnitude greater than the minimum value due to the finer grid spacing near the wall. An alternative definition for Δ which would keep it constant throughout the domain is

$$\Delta = \Delta x = \Delta y \tag{17}$$

These equations are solved numerically using a pseudospectral code developed by Chan [8], and the Smagorinsky model was implemented exactly as in [24]. By performing the vertical derivatives in spectral space and using Legendre-Gauss-Lobatto collocation points, in which the grid points in the z direction are more finely spaced near the boundaries, the vertical derivatives can be computed almost exactly. Temporal advancement is accomplished using the Crank-Nicolson scheme for the viscous terms and the

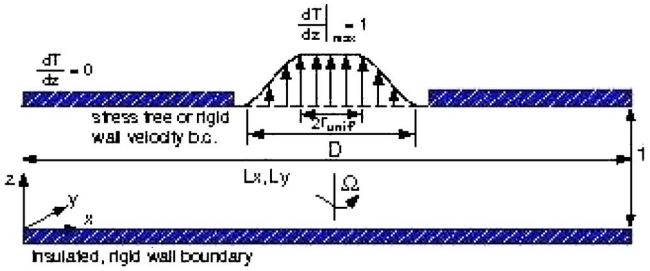

Fig. 1 Computational domain and boundary conditions for rotating finite source convection

Adams-Bashforth method for the advective terms and subgrid scale stresses.

4 Description of Flow

The current work uses the LES method to study thermal plumes and chimneys in a rotating reference frame. The three-dimensional rectangular domain with periodic boundary conditions in the horizontal directions and a no-slip, insulated bottom boundary is shown in Fig. 1. The depth of the domain H is defined to be 1. The horizontal dimensions, L_x and L_y are large enough so that the flow at the boundaries is not influenced by the developing plume during the time of the simulation. The top surface boundary conditions are stress free for the velocity and a circular heat source of radius D/2 centered on the surface for the temperature. The magnitude of the circular finite source varies from a maximum in the center to zero at the edge, and the rest of the boundary is insulated.

The buoyancy force on the surface can be treated either as a boundary condition or as a forcing function in the simulation distributed over a finite depth h_s [9]. The latter method is used in this study because it gives better agreement with DNS [25].

Though the DNS has a noslip top surface, this boundary condition is impractical for LES because the Smagorinsky model requires wall functions for proper behavior near a solid boundary. However, no wall function exists to impose proper behavior near the boundary for flow without a mean shear, so the eddy viscosity is not predicted properly very close to the wall [25].

The heat flux source is implemented by setting

$$F_T = \begin{cases} -2\frac{1-(1-z)/h_s}{h_s} & r < r_{\text{unif}} \\ \frac{1-(1-z)/h_s}{h_s}\frac{B_o}{\alpha g}\left\{1.0+\cos\left[\frac{\pi(r-r_{\text{unif}})}{\frac{D}{2}-r_{\text{unif}}}\right]\right\} & r < D/2 \text{ and } z \leqslant h_s \\ 0 & r > D/2 \text{ or } z > h_s \end{cases} \tag{18}$$

in Eq. (9). The forcing is applied over the top 6% of the domain and is scaled so that it would be equivalent to a concentrated heat flux of B_o applied on the upper surface as a boundary condition.

The development of a flow field due to a finite circular cooling source at the surface in the presence of rotation occurs in three stages. Initially, the flow is laminar natural convection. If the Rayleigh number is high enough, individual plumes start to develop from the mixed layer signifying the onset of turbulence. The flow behavior is convection dominated until the mixed layer reaches a critical depth. Then the rotation starts limiting the horizontal spreading of the plumes. Eventually the flow becomes quasi-two-dimensional and geostrophic in which the pressure forces balance the Coriolis force. For higher rotation rates and larger Rayleigh numbers, the flow becomes more three-dimensional and less geostrophic. For small D_x/L, the plume begins to spread when it hits the bottom, but for large D_x/L, the plume remains confined to the region below the source.

5 Results

Results for a convection-dominated case were promising when compared with DNS results [8] for $\text{Ra}_f = 10^7$ and $\text{Ta} = 10^6$. LES of a rotating finite source were computed with $\text{Ra}_f = 5\times10^{10}$ and $\text{Ta} = 3\times10^8$ for a large D/L_x of 1/2 and a small D/L_x of 1/5. Since the purpose of LES is to attempt to simulate more realistic flows, a relatively high Rayleigh number was chosen. However, the natural Rossby number [10], which is most representative of the type of flow (flow regime), and the D/L_x were chosen to enable comparison with the LES of Jones and Marshall [9], hereafter referred to as JM, and with the DNS of Chan [8]. JM is a prior numerical study with this type of domain and more recent studies have used their results for comparison. $\text{Ro}^* = 0.1$ for most of these simulations, which puts the flow in the transitional regime. The LES was initialized with zero temperature and velocity fields. A distributed source boundary condition and a free surface are applied at the upper surface, with an insulated no-slip bottom boundary, similar to the boundary conditions used by JM. All quantities are nondimensionalized by a characteristic length scale, H, temperature scale $B_o H/\alpha g\kappa$ and velocity scale κ/H.

5.1 Large D/L_x Case. The sensitivity of the computation to the grid spacing, eddy viscosity model, and surface heat flux was

Table 1 Parameters for LES simulations for $\text{Ro}^*=0.1$, $L_x=16$, and source radius=4. Note that the value of Δ is only relevant if the Smagorinsky model is being used.

	Ra_f	Ta	Ro^*	$B_{o\text{avg}}$	ν_T model	Δ	Grid
T1	5×10^{10}	3×10^8	0.1	0.42	Smagorinsky	Δ_x	$128\times128\times33$
T2	5×10^{10}	3×10^8	0.1	0.42	Smagorinsky	$(\Delta_x\Delta_y\Delta_z)^{1/3}$	$128\times128\times33$
T3	5×10^{10}	3×10^8	0.1	0.71	$\nu_T=25$		$128\times128\times33$
T3a	5×10^{10}	3×10^8	0.1	1.00	$\nu_T=25$		$128\times128\times33$
T4	5×10^{10}	3×10^8	0.1	1.00	Smagorinsky	$(\Delta_x\Delta_y\Delta_z)^{1/3}$	$128\times128\times33$
T5	5×10^{10}	3×10^8	0.1	1.00	Smagorinsky	$(\Delta_x\Delta_y\Delta_z)^{1/3}$	$128\times128\times23$
T6	5×10^{10}	0.0	∞	1.00	Smagorinsky	$(\Delta_x\Delta_y\Delta_z)^{1/3}$	$128\times128\times33$
T7	8×10^8	4×10^6	0.33	1.00	Smagorinsky	$(\Delta_x\Delta_y\Delta_z)^{1/3}$	$128\times128\times33$
T8	5×10^{10}	3×10^8	0.1	0.42	$\nu_T=25$		$128\times128\times33$
JM1	8×10^8	9.6×10^8	0.1	1.00	$\nu_h=5;\ \nu_v=0.2$		$128\times128\times20$
JM2	8×10^8	4×10^6	0.33	1.00	$\nu_h=5;\ \nu_v=0.2$		$128\times128\times20$
JM3	8×10^8	400	316	1.00	$\nu_h=5;\ \nu_v=0.2$		$128\times128\times20$

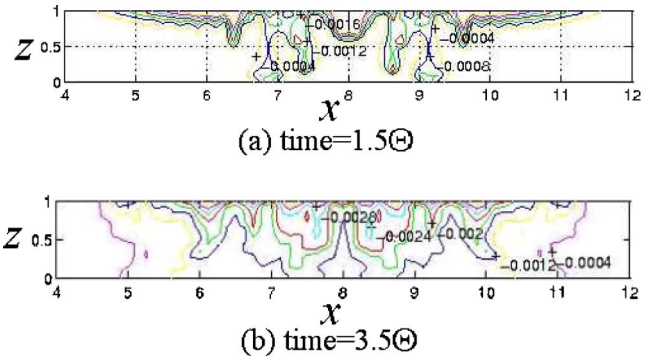

Fig. 2 Development of thermal plume for run T1 with $Ra_f=5\times10^{10}$, $Ta=3\times10^8$, $D/L_x=1/2$

studied, and these results were compared with the results of JM. JM performed an LES using finite differencing spacial discretization with a constant eddy viscosity which is 25 times larger in the horizontal direction than in the vertical. The parameters for the simulations of the current study as well as those from the relevant JM cases are shown in Table 1. Horizontally averaged velocity, $u_H=(\overline{u^2+v^2})^{1/2}/(B_oH)^{1/3}$, and reduced gravity g' vertical profiles are presented for all cases after two rotation periods. In the following discussion, unless otherwise specified, $Ro^*=0.1$.

As shown by temperature contours in a vertical slice through the center of the domain in Fig. 2, the plumes take about 1 1/2 rotations to reach the bottom boundary. This plume development is slower than in the results of JM in which it takes less than one rotation since the eddy viscosity in JM is significant even when the velocity is small. Though the horizontal velocity field through a horizontal cross section (Fig. 3) is qualitatively comparable, the vortices in JM are well developed within the first rotation. However, in this study, they are barely starting to appear after 1 1/2 rotations. This difference is likely due to the difference between the subgrid scale models and the computational methods. The current study uses very accurate finite differencing in the vertical direction while JM uses a finite difference which would have significant artificial viscosity. Also, the eddy viscosity for the Smagorinsky model becomes very small if the flow rate is very low and no significant velocity or temperature gradients exist. Since JM uses a constant viscosity, a large thermal diffusivity is present even in the absence of flow which would result in faster growing plumes. The major differences between the current study and JM are the magnitude and distribution of the heat flux, the grid spacing, and the eddy viscosity model. The following discussion of horizontally averaged vertical profiles show that the current study can reproduce the shape of the curves in JM but not the magnitude. The sensitivity of the results to these differences is examined in an attempt to see which of them, if any, can account for the discrepancies between the current study and JM.

The JM simulations had a constant buoyancy flux of $B_o=1.0$ over the entire source while the present simulation required a buoyancy flux which was tapered as shown in Fig. 1. This variable buoyancy flux is computed in Eq. (18) and is characterized by an average value $B_{o\text{avg}}$ computed by integrating B_o, over the source. With $B_{o\text{max}}=1.0$ and $r_{\text{unif}}=0.25$, $B_{o\text{avg}}=0.42$. To create a more uniform distribution of B_o, r_{unif} was increased to 0.75, which resulted in $B_{o\text{avg}}=0.71$. As a final test, the maximum B_o, the value in the r_{unif} region, was modified so that $B_{o\text{avg}}=1.0$ and the total buoyancy flux would be the same as JM. Using the constant eddy viscosity model (case T3a), the plume saturated the entire domain well before two rotations, so results for this buoyancy flux are presented with the Smagorinsky model. After two rotations, the horizontally averaged velocity and reduced gravity profiles for these three buoyancy fluxes are compared with the JM simulations as shown in Fig. 4. An increase in the buoyancy flux causes an

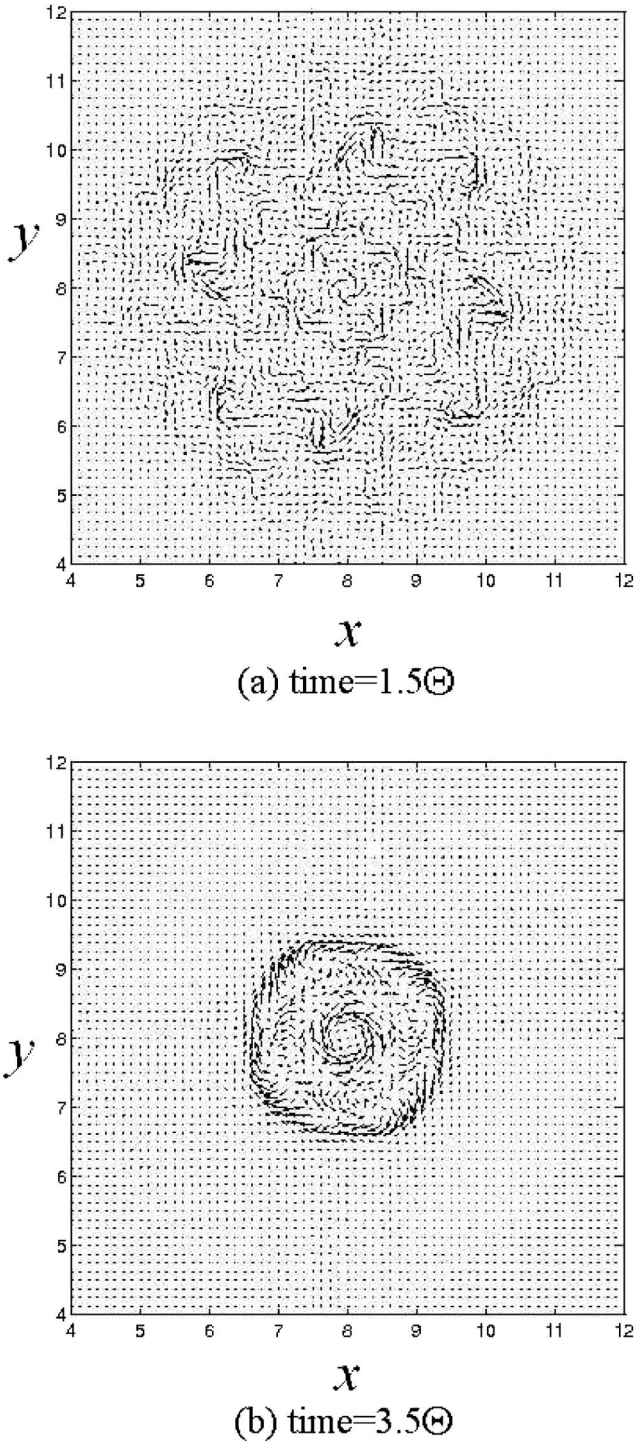

Fig. 3 Horizontal velocity field for run T1 with $Ra_f=5\times10^{10}$, $Ta=3\times10^8$, and $D/L_x=1/2$

increase in the velocity and reduced gravity vertical profiles slightly. The reduced gravity profile exhibits reasonable agreement with JM results, but the velocity is approximately a factor of 2 less than JM for a similar average buoyancy flux. On the other hand, the shape of the profile near the top and bottom demonstrate correct near wall behavior in the current study but not in JM.

Next, the effect of the eddy viscosity model is examined. As previously discussed, JM used a constant eddy viscosity in both space and time, which is 25 times larger in the horizontal direction than in the vertical direction. In an attempt to obtain a more accurate simulation, the Smagorinsky eddy viscosity model was

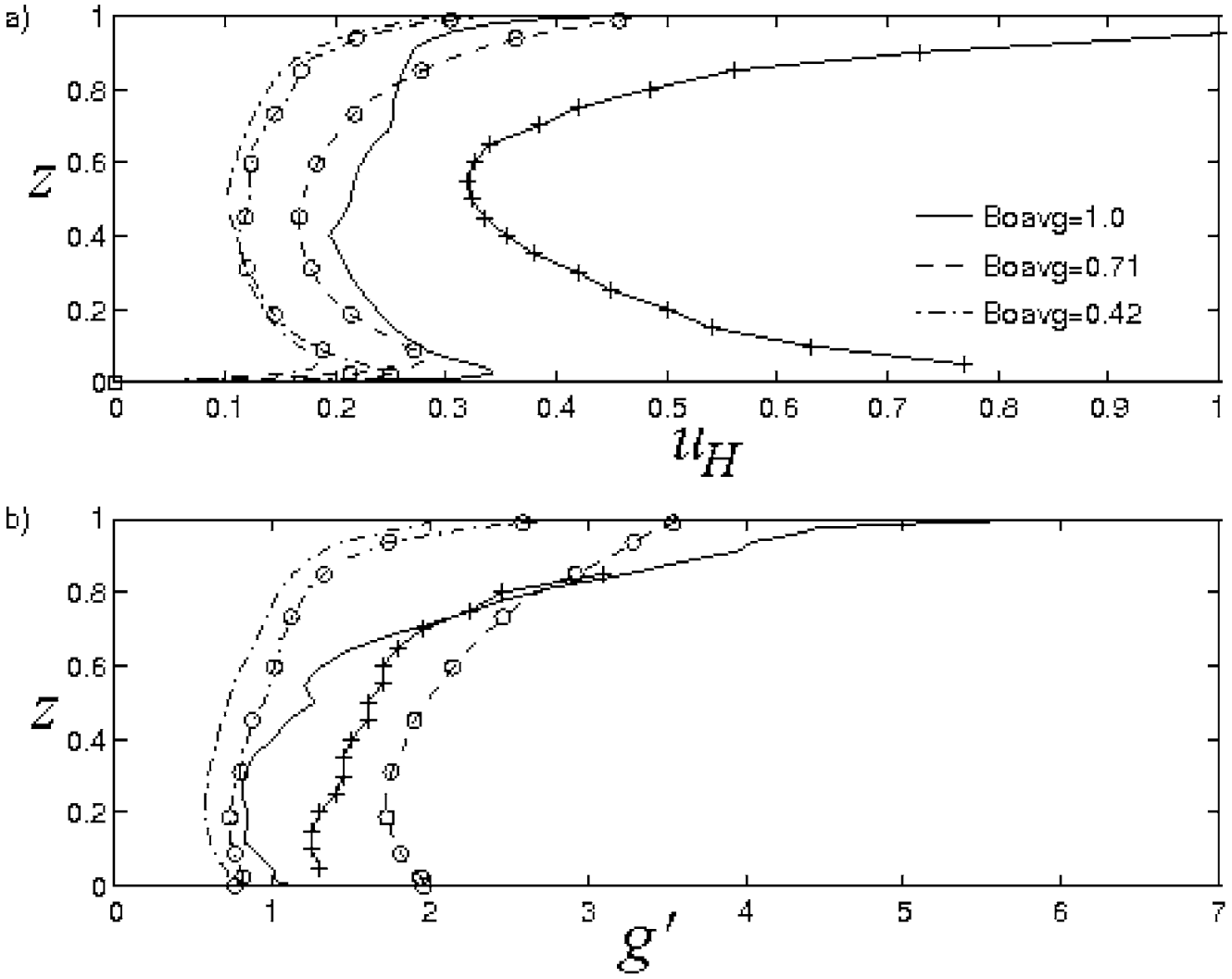

Fig. 4 Effect of varying average surface buoyancy flux for (a) u_H and (b) g'. No symbols: Smagorinsky model, runs T2, T4. Symbols: ν_T=constant; o: cases T8, T3; +: JM1.

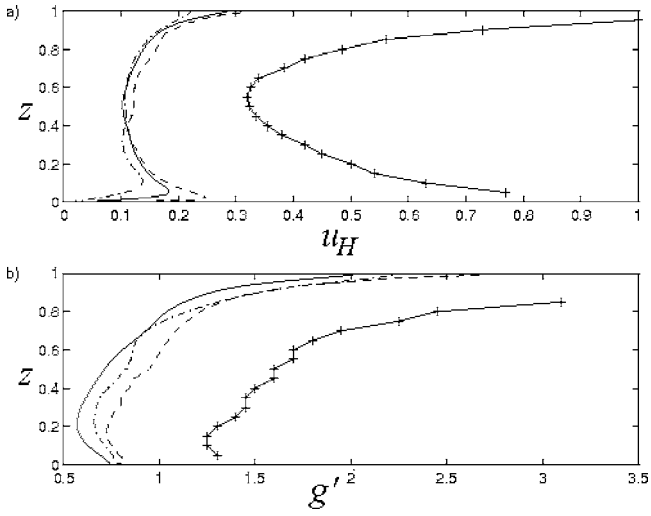

Fig. 5 Effect of varying eddy viscosity model for (a) u_H and (b) g'. No symbols: - T1;–T2; -. T8; Symbols: JM1.

chosen, which varies in both space and time to represent the changing conditions of the flow, including becoming zero when no flow is present. Three different eddy viscosity models were examined. One with a constant eddy viscosity equivalent to the vertical eddy viscosity in JM and the Smagorinsky model with two different values of the length scale Δ: one which varies in space (Eq. (16)), and one which is constant (Eq. (17)). The resulting horizontally averaged vertical profiles in Fig. 5 for each of these cases show that the simulation is not particularly sensitive to the eddy viscosity model. Although the shapes of the horizontal velocity and reduced gravity profiles are similar to JM, the velocity magnitudes are smaller by a factor of two.

To check if the finer vertical resolution of the current LES can explain the discrepancy, a simulation with only 23 grid points in the vertical direction is compared with JM, as shown in Fig. 6. These two Smagorinsky simulations give the same results for both resolutions indicating that the grid size does not account for the difference between the current LES and JM and that the LES is properly resolved.

Finally, the simulations using the Smagorinsky model at several natural Rossby numbers are shown in Fig. 7. The current results show a smaller boundary layer region at the no-slip bottom surface for a smaller Rossby number, which is not reproduced in JM. Even though the velocity profiles are approximately a factor of

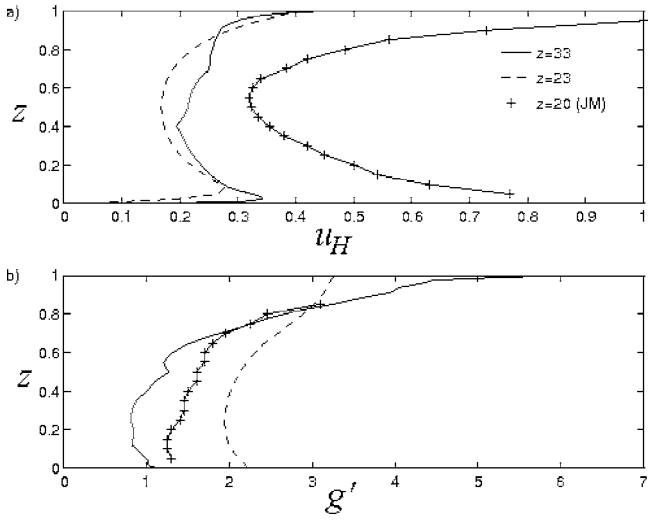

Fig. 6 Effect of vertical grid spacing for (a) u_H and (b) g'. No symbols: runs T4, T5; Symbols: JM1.

two less than JM, the shapes of the profiles and the significant decrease in magnitude with the addition of rotation are represented in both simulations.

5.2 Small D/L_x Case. Since the Smagorinsky model tries to reproduce more of the physics of the flow than a constant eddy viscosity model, perhaps a comparison with DNS data will be favorable. The relevant parameters of both simulations are presented in Table 2. The simulation presented in this section is similar to those of the previous section, except that the D/L_x parameter is significantly smaller to match the geometry of the DNS. As a result, changes in the flow due to the differences in the geometry

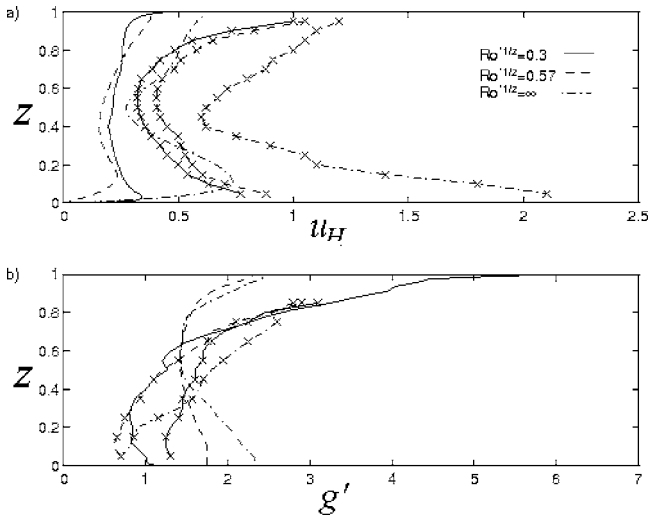

Fig. 7 Effect of varying Ro^* for (a) u_H and (b) g'. No symbols: runs T6, T7, T8; Symbols: JM1, JM2, JM3.

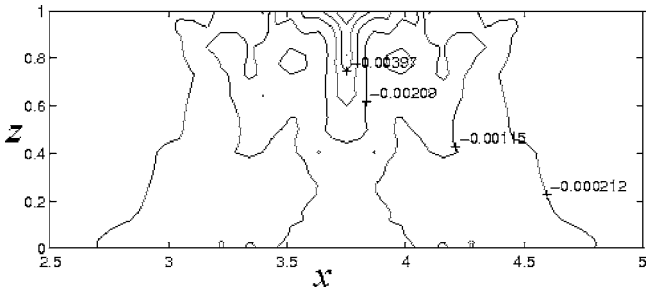

Fig. 8 Development of thermal plume for LES with $Ra_f=5\times10^{10}$, $Ta=3\times10^8$, and $D/L_x=1/5$ at time=3.5Θ

will also be discussed.

This simulation ran for 3 1/2 rotations. After 1 1/2 rotations, rotational effects had not yet become dominant, but, after 3 1/2 rotations, the LES results look more promising as shown in Figs. 8 and 9. The vertical temperature contours in Fig. 8 show that the plume has started spreading along the bottom. On the other hand, the plume in the DNS computation reached the bottom within 1 1/2 rotations as shown in Fig. 10. The horizontal flow field after 3 1/2 rotations in Fig. 9 is more similar to the DNS at 1.3 rotations, shown in Fig. 11, than at 3.3 rotations. Like the DNS, the LES shows vortices that separate from the region under the source and move outward which is consistent with observations [26]. The horizontal flow fields illustrate the major differences in the flow as a result of changing D/L_x. According to these simulations, the larger D/L_x of 0.5 contains a series of smaller vortices which stay confined underneath the source while the smaller D/L_x of 0.2 seems to have larger vortices which eventually split from the source and move outward. $D/L_x=0.4$ in both the experiments of Coates et al. [27] and the simulations of Cui and Street [18] is between the two values examined in the current simulations. Their results showed vortices underneath the source with a well-defined rim current at the edge of the source. However, they did not mention any observations of vortices propagating away from the source, and JM did not observe a well-defined rim current. It is possible that these differences in flow structure beneath the source depend on D/L_x. Brickman and Kelly [13] observed these differences in flow structure in their observations of the evolution of a rotating convective plume. First a tendril phase, which is convectively dominated, characterized by small, thin plumes. Second, they call the formation of the horizontal vortices the convecting vortex phase, similar to the horizontal vortex structure of the large D/L_x. Finally, the frontal instability phase occurs when larger scale frontal vortices form, similar to the small D/L_x case. Brickman and Kelly [13] perform experiments with one large D/L_x and one small D/L_x. Though any differences resulting from the different source sizes are not mentioned, pictures of the frontal instability phase are shown only for the small D/L_x case.

Though asymmetry due to random small-scale fluctuations is an important property of turbulent flows, the contours for both the large D/L_x and this case are very symmetric as shown in both the horizontal and vertical instantaneous profiles. In the DNS and in JM as well as most turbulence simulations, instantaneous profiles

Table 2 Parameters for simulations with $Ro^*=0.1$, $L_x=7.5$, source radius=0.75; LES uses the Smagorinsky model with $\Delta=(\Delta_x\Delta_y\Delta_z)^{(1/3)}$

	Ra_f	Ta	Rotation Period $=4\pi/\sqrt{Ta}$	Grid	Velocity boundary condition	Temperature boundary condition
LES	5×10^{10}	3×10^8	7.25×10^{-4}	$128\times128\times33$	Stress free	Insulated
DNS [4]	10^9	2.5×10^7	2.52×10^{-3}	$256\times256\times65$	No slip	$Dt/dz=-1$

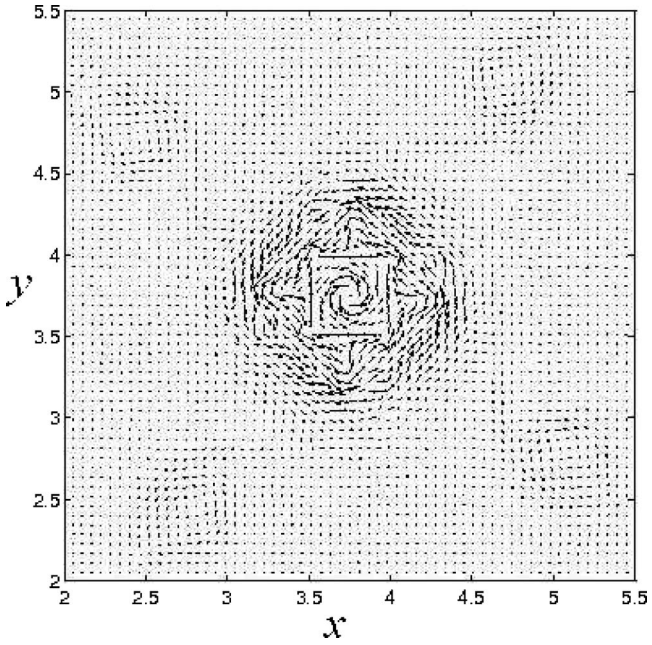

Fig. 9 Horizontal velocity field through the center of the domain for LES with $Ra_f=5\times10^{10}$, $Ta=3\times10^8$, and $D/L_x=1/5$ at time=3.5Θ

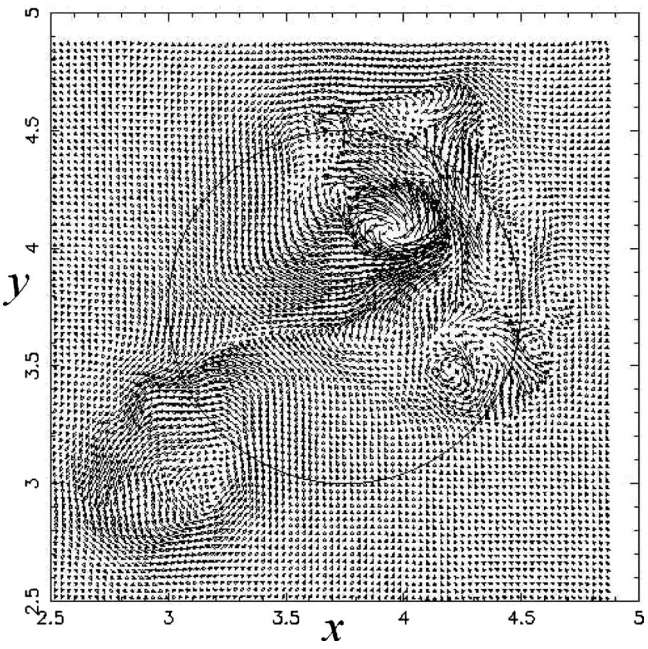

Fig. 11 Horizontal velocity field through the center of the domain for DNS with $Ra_f=10^9$, $Ta=2.5\times10^7$, and $D/L_x=1/5$ at time=3 1/2Θ ([4] Fig. 3.83b)

tend to be asymmetric and contain random small-scale fluctuations which are often due to random perturbations in the initial flow field. In this simulation, random perturbations in the initial flow field were damped out and did not influence the instantaneous flow.

Azimuthally averaged quantities for this flow also contain some favorable comparisons with the DNS. The reduced gravity, defined as

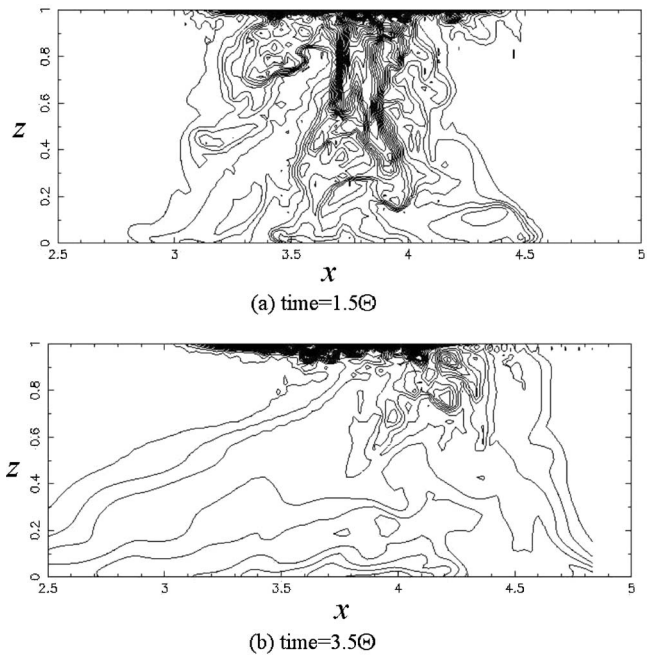

Fig. 10 Thermal plume for DNS with $Ra_f=10^9$, $Ta=2.5\times10^7$, and $D/L_x=1/5$ in the $Y=3.75$ plane ([4] Fig. 3.79)

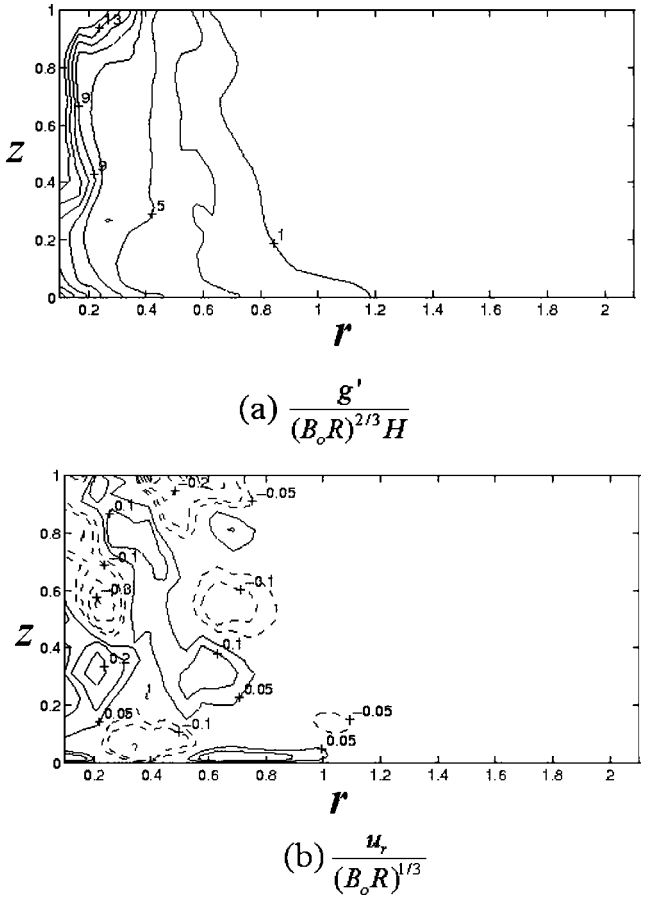

Fig. 12 Azimuthally averaged quantities for LES with $Ra_f=5\times10^{10}$, $Ta=3\times10^8$, and $D/L_x=1/5$ at time=3.5Θ

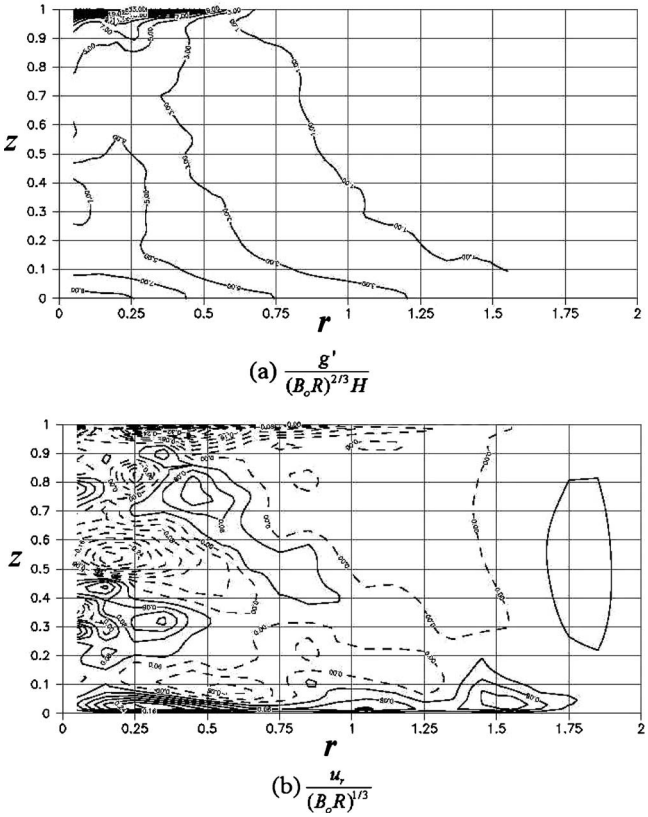

Fig. 13 Azimuthally averaged quantities for DNS with $Ra_f = 10^9$, $Ta = 2.5 \times 10^7$, and $D/L_x = 1/5$ at time=3 1/2Θ ([4] Fig. 3.94b)

$$g' = g\frac{\rho'}{\rho_o} \tag{19}$$

is nondimensionalized by the buoyancy flux as follows:

$$\frac{g'}{(B_o H)^{2/3}/H} = \frac{T}{B_o H/\alpha g \kappa}\mathrm{Ra}_f^{1/3}\mathrm{Pr}^{1/3} \tag{20}$$

Figure 12 shows that the plume in the LES has not developed as much as in the DNS shown in Fig. 13, but the plume in the LES has started spreading along the bottom, and the contours have the same general shape and magnitude as the DNS. The azimuthally averaged radial velocity is scaled relative to the buoyancy flux

$$\frac{u_r}{(B_o H)^{1/3}} = \frac{u_r}{\kappa/H}\mathrm{Ra}_f^{-1/3}\mathrm{Pr}^{1/3} \tag{21}$$

u_r qualitatively resembles the DNS results at time=3.3Θ but the magnitude is slightly larger. The LES results are more similar to the DNS at time=1.3Θ. These results emphasize that the development of the flow lags behind the DNS results. The delayed development may be a result of the different top boundary conditions (stress-free, distributed source for LES and no-slip, concentrated source for DNS) as well as limitations of the Smagorinsky model in a transitional flow.

6 Summary and Future Work

Though the LES results are qualitatively similar to the DNS, better quantitative agreement is desirable. The Smagorinsky model is unlikely to provide better agreement because of inherent shortcomings of the model, which include the inability to correctly predict transitional flows and incorrect behavior in a noninertial reference frame. In addition, the flow stayed very symmetric for the duration of the simulation which is not a physically correct result. This asymmetry may have occurred because the horizontal component of the rotation vector was neglected. Though this assumption is a common simplification, the presence of the horizontal component of the rotation vector increases the asymmetry of the flow [26]. These results do not yet agree with the DNS well enough to confidently apply this subgrid scale model to higher speed flows; they do give evidence that a proper subgrid scale model could give very reasonable results for high Rayleigh number flows.

Table 3 Limiting parameters for different methods used for studying rotating convection [10]

Method	Ra_f	Ta
Observations	$>10^{25}$	$>10^{14}$
Experiments	$<10^{20}$	$<10^{10}$
Turbulence simulations	$<10^{10}$	$<10^{8}$

The present simulations show that the horizontal vortical structure depends on the ratio of the source diameter to domain size (D/L_x). With a small D/L_x, vortices form under the source and propagate away; a larger D/L_x causes small (relative to the source diameter) vortices to remain under the source. These observations are consistent with other studies which also show the development of a rim current at intermediate values of D/L_x.

One effect of a subgrid scale model is to increase the turbulent energy in the large scales as a result of subgrid scale turbulence. In this flow the region of greatest subgrid scale fluctuations would be near the source. However, the Smagorinsky model predicts that the region with the largest gradients would have the most significant small-scale fluctuations. In this flow, the largest gradients are at the edges of the plume where the velocity is very small. As a result, the turbulent fluctuations do not propagate in the flow as they probably do in the DNS, which would help explain why the plume in this study develops more slowly. This shortcoming would be characteristic of eddy viscosity models in general, so a different type of subgrid scale model that could more accurately identify regions of large subgrid scale quantities would probably give better results.

For instance, the subgrid scale estimation model has been used successfully in both high Reynolds number flows [28], turbulent convection [29], and rotating turbulent convection [30] and does not require a wall function for correct near wall behavior in shear flows. In addition, the estimation subgrid scale model obeys transformation rules required for the subgrid scale stress tensor in a noninertial frame of reference [31], and the LES results agree well with DNS data for simple rotating turbulent flows [32]. Current work on this project involves applying the estimation subgrid scale model to rotating turbulent convection. Eventually, these methods should enable simulations of higher Rayleigh numbers. As shown in Table 3, the maximum Rayleigh number for numerical simulations is still far from that of a realistic geophysical flow.

In spite of inadequacies of the Smagorinsky model in transitional flows, the LES simulations were able to reproduce some of the qualitative features of the flow as well as demonstrating the effect of the D/L_x on the flow field. The development of the convective plume is similar to the DNS and experimental studies but much slower, which is probably due to a combination of the use of the distributed source boundary condition and the subgrid scale model. The computed velocities are closer to the DNS results than the velocities computed by JM and the near wall region behavior is more reasonable; in this instance, the Smagorinsky model is more accurate than the constant eddy viscosity model. Future work will focus on using LES methods to obtain reasonable simulations at higher Rayleigh number flows. In this way, a simulation with physically realistic parameters for geophysical flows can be developed.

Acknowledgment

The authors thank Dr. D. Chan for providing the numerical code used in the work and for allowing us to use his figures.

Nomenclature

All quantities have been nondimensionalized by length scale H (depth of the computational domain) and the velocity scale κ/H.

B_o = buoyancy flux
$B_{o\mathrm{avg}}$ = average buoyancy flux over the circular source
$B_{o\max}$ = maximum buoyancy flux in the circular source
c_p = specific gravity
C_S = Smagorinsky model constant
D = diameter of finite buoyancy source
f = period of rotation
$f(x)$ = unfiltered function
$\bar{f}(x)$ = filtered function (resolved on LES grid)
F_T = buoyancy forcing term
g = acceleration due to gravity
$G(x)$ = filter function
g' = reduced gravity
H = depth of computational domain
h_s = depth to which buoyancy flux is applied
L_x, L_y = horizontal size of computational domain
P = pressure
Pr = Prandtl number
Pr_T = turbulent Prandtl number
r = radial distance from source center in horizontal plane
Ra_f = Rayleigh number defined based on buoyancy flux
Ro^* = natural Rossby number
r_{unif} = radius of uniform region in the buoyancy source
S_{ij} = rate of strain tensor
T = temperature
Ta = Taylor number
u_H = horizontally averaged velocity
u_i = component of velocity
x,y,z = coordinate directions in physical space
α = volumetric thermal expansion coefficient
δ_{ij} = kronecker delta
Δ = factor in Smagorinsky model which depends on the mesh size
Δx, Δy, Δz = grid cell sizes in the x, y, and z directions
ε_{ijk} = alternating unit tensor
Θ = period of rotation
κ = thermal diffusivity
ν = molecular diffusivity
ν_h = constant eddy viscosity in the horizontal direction (used in [5])
ν_T = eddy viscosity for present study
ν_v = constant eddy viscosity in the vertical direction (used in [5])
ρ_o = density of ambient fluid
ρ = local fluid density
Ω = rotation rate of frame of reference
τ_{ij} = subgrid scale stress tensor
$\tau_{\theta j}$ = subgrid scale heat transfer

References

[1] Gascard, J. C., and Clarke, R. A., 1983, "The Formation of Labrador Sea Water. Part II: Mesoscale and Smaller Scale Processes," J. Phys. Oceanogr., **13**, pp. 1779–1797.
[2] Schott, F., Visbeck, M., and Fischer, J., 1993, "Observations of Vertical Currents and Convection in the Central Greenland Sea During the Winter of 1988/89," J. Geophys. Res., [Atmos.], **98**, pp. 14,401–14,421.
[3] Rhien, M., 1996, "Convection in the Greenland Sea, 1982–1993," J. Geophys. Res., [Atmos.], **101**, pp. 18,183–18,192.
[4] Toggweiler, J. R., 1994, "The Ocean's Overturning Circulation," Phys. Today, **47**, pp. 45–50.
[5] Gascard, J. C., 1991, "Open Ocean and Deep Water Formation Revisited in the Mediterranean, Labrador, Greenland and Weddell Seas," *Deep Convection and Deep Water Formation in the Oceans*, P. C. Chu and J. C. Gascard, eds., Elsevier Oceanography Series, Amsterdam, Vol., **57**, pp. 157–182.
[6] Gill, A. E., 1982, *Atmosphere-Ocean Dynamics*, Academic Press, San Diego, CA.
[7] Lavelle, J. W., and Baker, E. T., 1994, "A Numerical Study of Local Convection in the Benthic Ocean Induced by Episodic Hydrothermal Discharges," J. Geophys. Res., [Atmos.], **99**, pp. 16,065–16,080.
[8] Chan, D. C., 1996, "Effects of Rotation on Turbulent Convection: Direct Numerical Simulation Using Parallel Processors," Ph.D. thesis, University of Southern California.
[9] Jones, H., and Marshall, J., 1993, "Convection with Rotation in a Neutral Ocean: A Study of Open-Ocean Deep Convection," J. Phys. Oceanogr., **23**, pp. 1009–1039.
[10] Rossby, H. T., 1969, "A Study of Bénard Convection With and Without Rotation," J. Fluid Mech., **36**, pp 309–335.
[11] Boubnov, B. M., and Golitsyn G. S., 1990, "Temperature and Velocity Field Regimes of Convective Motions in a Rotating Plane Fluid Layer." J. Fluid Mech., **219**, pp. 215–239.
[12] Fernando, H. J. S., Chen, R. R., and Boyer, D. L., 1991, "Effects of Rotation on Convective Turbulence," J. Fluid Mech., **228**, pp. 513–547.
[13] Brickman, D., and Kelly, D. E., 1993, "Development of Convection in a Rotating Fluid: Scales and Patterns of Motion," Dyn. Atmos. Oceans, **19**, pp. 389–405.
[14] Maxworthy, T., and Narimousa, S., 1994, "Unsteady, Turbulent Convection into a Homogeneous Rotating Fluid, with Oceanographic Applications," J. Phys. Oceanogr., **24**, pp. 865–887.
[15] Scott, J. C., and Killworth, P. D., 1991, "Upper Ocean Structures in the Southwestern Iceland Sea—A Preliminary Report," *Deep Convection and Deep Water Formation in the Oceans*, P. C. Chu and J. C. Gascard, eds., Elsevier Oceanography Series, Amsterdam, pp. 87–106.
[16] Johannessen, O. M., Sandven, S., and Johannessen, J. A., 1991, "Eddy-Related Winter Convection in the Boreas Basin," *Deep Convection and Deep Water Formation in the Oceans*, P. C. Chu and J. C. Gascard, eds., Elsevier Oceanography Series, Amsterdam, pp. 87–106.
[17] Julien, K., Legg, S., McWilliams, J., and Werne, J., 1996, "Rapidly Rotating Turbulent Rayleigh-Bénard Convection," J. Fluid Mech., **322**, pp. 243–273.
[18] Cui, A., and Street, R. L., 2001, "Large Eddy Simulation of Turbulent Rotating Convective Flow Development," J. Fluid Mech., **447**, pp 53–84.
[19] Peltier, L. J., and Wyngaard, J. C., 1995, "Structure-Function Parameters in the Convective Boundary Layer from Large-Eddy Simulation," J. Atmos. Sci., **52**, pp. 3641–3660.
[20] Noh, Y., and Hyoung, J. K., 1999, "Simulations of Temperature and Turbulence Structure of the Oceanic Boundary Layer with the Improved Near-Surface Process," J. Geophys. Res., [Atmos.], **104**, pp. 15,621–15,634.
[21] Mason, P. J., 1994, "Large-Eddy Simulation of the Convective Atmospheric Boundary Layer," J. Atmos. Sci., **46**, pp. 1492–1516.
[22] Deardorff, J. W., 1971, "On the Magnitude of the Subgrid Scale Eddy Coefficient," J. Comput. Phys., **7**, pp. 120–133.
[23] Lilly, D. K., 1966, "On the Application of the Eddy Viscosity Concept in the Inertial Subrange of Turbulence," NCAR Manuscript No. 123, National Center for Atmospheric Research, Boulder, CO..
[24] Eidson, T. M., 1985, "Numerical Simulation of the Turbulent Rayleigh-Bénard Problem," J. Fluid Mech., **158**, pp 245–268.
[25] Kimmel, S. J., 1998, "Large Eddy Simulation of Turbulent Convection," Ph.D. thesis, University of Southern California.
[26] Denbo, D. W., and Skyllingstad, E. D., 1996, "An Ocean Large-Eddy Simulation Model with Applications to Deep Convection in the Greenland Sea," J. Geophys. Res., [Atmos.], **101**, pp. 1095–1110.
[27] Coates, M. J., Ivey, G. N., and Taylor, R. J., 1995, "Unsteady Turbulent Convection into a Rotating Linearly Stratified Fluid: Modeling Deep Ocean Convection," J. Phys. Oceanogr., **25**, pp. 3032–3050.
[28] Domaradzki, J. A., and Saiki, E. M., 1997, "A Subgrid-Scale Model Based on the Estimation of Unresolved Scales of Turbulence," Phys. Fluids, **9**, pp. 2148–2164.
[29] Kimmel, S. J., and Domaradzki, J. A., 2000, "Large Eddy Simulations of Rayleigh-Bénard Convection Using Subgrid Scale Estimation Model," Phys. Fluids, **12**, pp. 169–184.
[30] Kimmel, S. J., and Domaradzki, J. A., 2001, "Large Eddy Simulation of Rotating Turbulent Convection Using the Subgrid Scale Estimation Model," *DNS/LES—Progress and Challenges, Proceedings of the Third AFOSR International Conference on Direct Numerical Simulation and Large Eddy Simulation*, C. Liu, L. Sakall, and T. Beutner, eds., Greyden Press, Arlington, TX, pp. 351–358.
[31] Horiuti, K., 2001, "Transformation Properties of Subgrid-Scale Models in a Frame of Reference Undergoing Rotation," Modern Simulations S. 123.
[32] Domaradzki, J. A., Loh, K. C., and Yee, P. P., 2002, "Large Eddy Simulations Using the Subgrid-Scale Estimation Model and Truncated Navier-Stokes Dynamics," Theor. Comput. Fluid Dyn., **15**, pp 421–450.

Mahfoud Djezzar
e-mail: mdjezzar@caramail.com

Michel Daguenet

Département de Physique,
Faculté des Sciences,
University Mentouri Constantine,
Route Aïn El Bey 25000,
Constantine 25000, Algeria

Natural Steady Convection in a Space Annulus Between Two Elliptic Confocal Ducts: Influence of the Slope Angle

The authors express the Boussinesq equations of the laminar thermal and natural convection, in the case of permanent and bidimensional flow, in an annular space between two confocal elliptic cylinders. The latter is oriented at an arbitrary angle α with respect to the gravity force, using the elliptic coordinates system. A new calculation code using the finite volumes with the primitive functions (velocity-pressure formulation) is proposed. The Prandtl number is fixed at 0.7 (case of the air) with varying the Rayleigh number. The effect of the system inclination is examined. [DOI: 10.1115/1.2041656]

1 Introduction

Heat transfer by natural convection, in an annular space delimited by two concentric or eccentric horizontal cylinders, was the subject of many theoretical and experimental studies because of their importance in many engineering applications.

The majority of these studies are related to cylinders, whose cross sections are circular, and whose walls are maintained at constant temperatures. Mack and Bishop [1] made a study in an annular space ranging between two horizontal concentric cylinders. They employed a power series truncated at the third power of the Rayleigh number to represent the stream function and temperature variables. Their results pertain to radius ratios from 1.15 to 4.15, Prandtl numbers between 0.02 and 6.10^6 and Rayleigh numbers less than or equal to 3000.

The work of Kuehn and Goldstein [2] can be referred to as a comprehensive review for concentric cases. They compared the obtained experimental and numerical results using a method with finite differences. They discuss the influence of the Prandtl number and the ratio of the diameters for a Rayleigh number of about 10^4. The experimental and analytical studies for the eccentric cases include the work of Kuehn and Goldstein [3], Guj and Stella [4].

Comparatively, fewer publications were found for natural convection in non-circular domain, e.g., the elliptic domain considered in this study. Lee and Lee [5] attempted to formulate the free convection problem in terms of elliptical coordinates for the symmetrical cases of oblate and prolate elliptical annuli and have performed experiments for this geometry. Schreiber and Shingh [6] treated the same case numerically by using the method of the spectral development in series, to reduce the partial derivative equations with three systems of differential equations of the second order. Elshamy et al. [7] studied numerically the case in the horizontal confocal elliptical annulus and developed some practical correlations for the average Nusselt number. Chmaissem et al. [8] simulated the case of natural convection in an annular space: having a horizontal axis bounded by circular and elliptical isothermal cylinders. They used a calculation code for the original finite element method that utilizes Cartesian coordinates, vorticity, stream function, and triangular elements (P1) associated with an iterative technique to solve the matrix system. Cheng and Chao [9] employed the body-fitted coordinate transformation method to generate a non-staggered curvilinear coordinate system and performed numerical study for some horizontal eccentric elliptical annuli.

In the numerical simulation of natural convection in elliptical space annuli, finite difference, finite volume, and finite element methods were usually used with the vorticity-stream function formulation. For example, the work of Guj and Stella [10] was conducted by the finite difference method, Shreiber and Singh [6] and Chmaissem et al. [8] used the finite element method, Elshamy et al. [7] and Cheng and Chao [9] used the finite volume method, and in the study of Zhu et al. [11] the natural convective heat transfer was simulated using the differential quadrature method.

In this work we use a new calculation code with the finite volumes [12–14] which uses the elliptic coordinates and the primitive functions (velocity-pressure formulation), associated with the traditional SIMPLER algorithm [12,14], in order to resolve our system of equations. The grid is made of 130×60 nodes.

2 Problem Formulation and Basic Equations

Let us consider an annular space, filled with a Newtonian fluid, and located between two confocal elliptic cylinders of horizontal axes. Figure 1 represents a cross section of the system. Both internal and external walls are maintained, respectively, at the temperatures $T1$ and $T2$ with $T1 > T2$. The physical properties of the fluid are constant, apart from the density ρ whose variations are at the origin of the natural convection. Viscous dissipation is neglected, just as the radiation (emissive properties of the two walls being neglected). We admit that the problem is bidimensional, permanent, and laminar.

The laminar natural convection equations within the framework of the Boussinesq approximation are written in vectorial form

– Continuity equation:

$$\text{div } \mathbf{V} = 0 \tag{1}$$

– Momentum equation:

$$(\mathbf{V} \cdot \mathbf{grad})\mathbf{V} = \frac{\rho}{\rho_0}\mathbf{g} + \frac{\nabla \pi}{\rho_0} \tag{2}$$

– Heat equation:

Contributed by the Applied Mechanics Division of ASME for publication in the JOURNAL OF APPLIED MECHANICS. Manuscript received June 30, 2004; final manuscript received June 14, 2005. Assoc. Editor: D. Siginer. Discussion on the paper should be addressed to the Editor, Prof. Robert M. McMeeking, Journal of Applied Mechanics, Department of Mechanical and Environmental Engineering, University of California-Santa Barbara, Santa Barbara, CA 93106-5070, and will be accepted until four months after final publication of the paper itself in the ASME JOURNAL OF APPLIED MECHANICS.

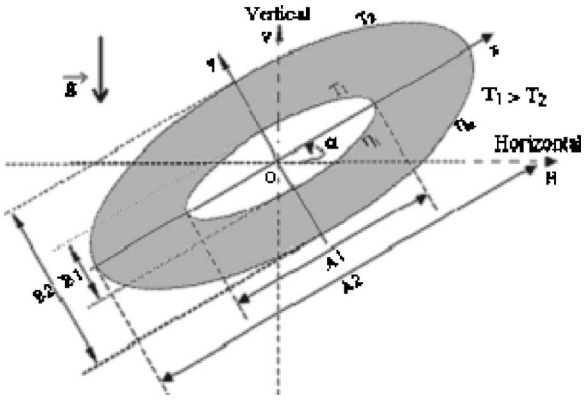

Fig. 1 A cross section of the system

$$(\mathbf{V}\cdot\mathbf{grad})T=\frac{\lambda}{\rho C_p}\nabla^2 T \tag{3}$$

It is convenient to define a reference frame such as the limits of the system result in constant values of the coordinates. The coordinates known as "elliptic" (η,θ) allow in our case to obtain precisely this result. The wall of the external elliptic cylinder is represented by $\eta=\eta_2=$constant, while for the interior elliptic cylinder by $\eta=\eta_1=$constant.

The passage of the Cartesian coordinates to the elliptic coordinates is obtained by the following relations:

$$\left.\begin{aligned} x&=a\,\mathrm{ch}\,\eta\cos\theta\\ y&=a\,\mathrm{sh}\,\eta\sin\theta\end{aligned}\right\} \tag{4}$$

The metric coefficients in elliptic coordinates are given by

$$\left.\begin{aligned} h_1=h_2=h&=a(\mathrm{sh}^2\eta+\sin^2\theta)^{1/2}\\ h_3&=1\end{aligned}\right\} \tag{5}$$

The gravity vector **g** is written in the new system of coordinates as

$$\mathbf{g}=-g\left[\frac{a(\mathrm{sh}\,\eta\cos\theta\sin\alpha+\mathrm{ch}\,\eta\sin\theta\cos\alpha)}{h}\mathbf{e}_\eta+\frac{a(\mathrm{sh}\,\eta\cos\theta\cos\alpha-\mathrm{ch}\,\eta\sin\theta\sin\alpha)}{h}\mathbf{e}_\theta\right] \tag{6}$$

We pass directly to the writing of dimensionless equations, by posing the following dimensionless quantities:

Let us pose

$$h^*=\frac{h}{a}=(\mathrm{sh}^2\eta+\sin^2\theta)^{1/2},\quad V_\eta^*=\frac{V_\eta}{(\nu/a)},\quad V_\theta^*=\frac{V_\theta}{(\nu/a)},\quad P^*=\frac{P-P_0}{\rho_0(\nu^2/a^2)}\ \text{and}\ T^*=\frac{T-T_2}{T_1-T_2}$$

with
characteristic length: a
characteristic velocity: ν/a
so let us introduce the following dimensionless numbers:

– The Prandtl number: $\mathrm{Pr}=\nu\rho c_p/\lambda$
– The Grashof number: $\mathrm{Gr}=g\beta a^3/\nu^2\Delta T$

After some lengthy manipulations, the following set of equations, is obtained:

Equation (1) becomes:

$$\frac{\partial}{\partial\eta}(h^*V_\eta^*)+\frac{\partial}{\partial\theta}(h^*V_\theta^*)=0 \tag{7}$$

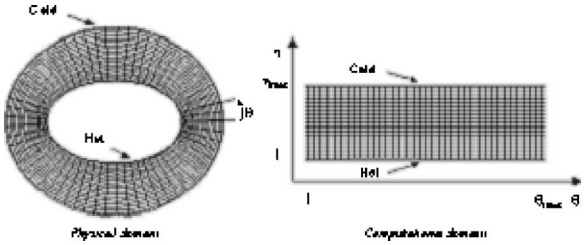

Fig. 2 Physical domain and computational domain

Projection of Eq. (2) following the η axis gives

$$\begin{aligned}&\frac{1}{h^{*2}}\left[\frac{\partial}{\partial\eta}(h^*V_\eta^*V_\eta^*)+\frac{\partial}{\partial\theta}(h^*V_\eta^*V_\theta^*)\right]\\&=-\frac{1}{h^*}\frac{\partial P^*}{\partial\eta}+\mathrm{Gr}T^*\frac{(\mathrm{sh}\,\eta\cos\theta\sin\alpha+\mathrm{ch}\,\eta\sin\theta\cos\alpha)}{h^*}\\&+\frac{2}{h^{*2}}\frac{\partial^2V_\eta^*}{\partial\eta^2}+\frac{1}{h^{*2}}\frac{\partial^2V_\eta^*}{\partial\theta^2}-\frac{1}{h^{*2}}\frac{\partial}{\partial\theta}\left[\frac{V_\eta^*}{h^*}\frac{\partial h^*}{\partial\theta}\right]+\frac{2}{h^{*2}}\frac{\partial}{\partial\eta}\left[\frac{V_\theta^*}{h^*}\frac{\partial h^*}{\partial\theta}\right]\\&+\frac{1}{h^{*2}}\frac{\partial}{\partial\theta}\left[h^*\frac{\partial}{\partial\eta}\left(\frac{V_\theta^*}{h^*}\right)\right]+\frac{1}{h^{*2}}\left[\frac{\partial}{\partial\eta}\left(\frac{V_\theta^*}{h^*}\right)+\frac{\partial}{\partial\theta}\left(\frac{V_\eta^*}{h^*}\right)\right]\frac{\partial h^*}{\partial\theta}\\&-\frac{2}{h^{*2}}\left[\frac{1}{h^*}\frac{\partial V_\theta^*}{\partial\theta}+\frac{V_\eta^*}{h^*}\frac{\partial h^*}{\partial\eta}\right]\frac{\partial h^*}{\partial\eta}+\frac{1}{h^{*2}}V_\theta^{*2}\frac{\partial h^*}{\partial\eta}-\frac{1}{h^{*2}}V_\eta^*V_\theta^*\frac{\partial h^*}{\partial\theta}\end{aligned} \tag{8}$$

And following the θ axis, it gives

$$\begin{aligned}&\frac{1}{h^{*2}}\left[\frac{\partial}{\partial\eta}(h^*V_\eta^*V_\theta^*)+\frac{\partial}{\partial\theta}(h^*V_\theta^*V_\theta^*)\right]\\&=-\frac{1}{h^*}\frac{\partial P^*}{\partial\theta}+GrT^*\frac{(\mathrm{sh}\,\eta\cos\theta\cos\alpha-\mathrm{ch}\,\eta\sin\theta\sin\alpha)}{h^*}\\&+\frac{1}{h^{*2}}\frac{\partial^2V_\theta^*}{\partial\eta^2}+\frac{2}{h^{*2}}\frac{\partial^2V_\theta^*}{\partial\theta^2}-\frac{1}{h^{*2}}\frac{\partial}{\partial\eta}\left[\frac{V_\theta^*}{h^*}\frac{\partial h^*}{\partial\eta}\right]\\&+\frac{2}{h^{*2}}\frac{\partial}{\partial\theta}\left[\frac{V_\eta^*}{h^*}\frac{\partial h^*}{\partial\eta}\right]+\frac{1}{h^{*2}}\left[\frac{\partial}{\partial\eta}\left(\frac{V_\theta^*}{h^*}\right)+\frac{\partial}{\partial\theta}\left(\frac{V_\eta^*}{h^*}\right)\right]\frac{\partial h^*}{\partial\eta}\\&-\frac{2}{h^{*2}}\left[\frac{1}{h^*}\frac{\partial V_\eta^*}{\partial\eta}+\frac{V_\theta^*}{h^*}\frac{\partial h^*}{\partial\theta}\right]\frac{\partial h^*}{\partial\theta}+\frac{1}{h^{*2}}V_\eta^{*2}\frac{\partial h^*}{\partial\theta}\end{aligned}$$

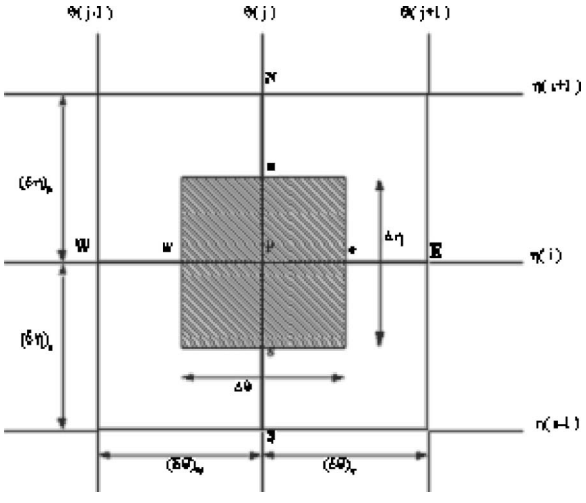

Fig. 3 A typical control volume and its neighbors in a computational

Table 1 Sources and diffusion coefficients

Variable Φ	Source S_Φ	Coefficient Γ_Φ
V_η^*	$-\frac{1}{h^*}\frac{\partial P^*}{\partial \eta}+\mathrm{Gr}T^*\frac{(\mathrm{sh}\eta\cos\theta\sin\alpha+\mathrm{ch}\eta\sin\theta\cos\alpha)}{h^*}-\frac{1}{h^{*2}}\frac{\partial}{\partial\theta}\left[\frac{V_\eta^*}{h^*}\frac{\partial h^*}{\partial\theta}\right]$	$\Gamma_{\Phi\eta}$ 2
	$+\frac{2}{h^{*2}}\frac{\partial}{\partial\eta}\left[\frac{V_\theta^*}{h^*}\frac{\partial h^*}{\partial\theta}\right]+\frac{1}{h^{*2}}\frac{\partial}{\partial\theta}\left[h^*\frac{\partial}{\partial\eta}\left(\frac{V_\theta^*}{h^*}\right)\right]+\frac{1}{h^{*2}}\left[\frac{\partial}{\partial\eta}\left(\frac{V_\theta^*}{h^*}\right)+\frac{\partial}{\partial\theta}\left(\frac{V_\eta^*}{h^*}\right)\right]\frac{\partial h^*}{\partial\theta}$	$\Gamma_{\Phi\theta}$ 1
	$-\frac{2}{h^{*2}}\left[\frac{1}{h^*}\frac{\partial V_\theta^*}{\partial\theta}+\frac{V_\eta^*}{h^{*2}}\frac{\partial h^*}{\partial\eta}\right]\frac{\partial h^*}{\partial\eta}+\frac{1}{h^{*2}}V_\theta^{*2}\frac{\partial h^*}{\partial\eta}-\frac{1}{h^{*2}}V_\eta^*V_\theta^*\frac{\partial h^*}{\partial\theta}$	
V_θ^*	$-\frac{1}{h^*}\frac{\partial P^*}{\partial\theta}+\mathrm{Gr}T^*\frac{(\mathrm{sh}\eta\cos\theta\cos\alpha-\mathrm{ch}\eta\sin\theta\sin\alpha)}{h^*}-\frac{1}{h^{*2}}\frac{\partial}{\partial\eta}\left[\frac{V_\theta^*}{h^*}\frac{\partial h^*}{\partial\eta}\right]$	$\Gamma_{\Phi\eta}$ 1
	$+\frac{2}{h^{*2}}\frac{\partial}{\partial\theta}\left[\frac{V_\eta^*}{h^*}\frac{\partial h^*}{\partial\eta}\right]+\frac{1}{h^{*2}}\frac{\partial}{\partial\eta}\left[h^*\frac{\partial}{\partial\theta}\left(\frac{V_\eta^*}{h^*}\right)\right]\frac{1}{h^{*2}}\left[\frac{\partial}{\partial\eta}\left(\frac{V_\theta^*}{h^*}\right)+\frac{\partial}{\partial\theta}\left(\frac{V_\eta^*}{h^*}\right)\right]\frac{\partial h^*}{\partial\eta}$	$\Gamma_{\Phi\theta}$ 2
	$-\frac{2}{h^{*2}}\left[\frac{1}{h^*}\frac{\partial V_\eta^*}{\partial\eta}+\frac{V_\theta^*}{h^{*2}}\frac{\partial h^*}{\partial\theta}\right]\frac{\partial h^*}{\partial\theta}+\frac{1}{h^{*2}}V_\eta^{*2}\frac{\partial h^*}{\partial\theta}-\frac{1}{h^{*2}}V_\eta^*V_\theta^*\frac{\partial h^*}{\partial\eta}$	
T^*	0	$\frac{1}{P_r}$

$$-\frac{1}{h^{*2}}V_\eta^*V_\theta^*\frac{\partial h^*}{\partial\eta}+\frac{1}{h^{*2}}\frac{\partial}{\partial\eta}\left[h^*\frac{\partial}{\partial\theta}\left(\frac{V_\eta^*}{h^*}\right)\right] \tag{9}$$

And finally Eq. (3) becomes

$$\left[\frac{\partial}{\partial\eta}(h^*V_\eta^*T^*)+\frac{\partial}{\partial\theta}(h^*V_\theta^*T^*)\right]=\frac{1}{\mathrm{Pr}}\left[\frac{\partial^2T^*}{\partial\eta^2}+\frac{\partial^2T^*}{\partial\theta^2}\right] \tag{10}$$

The boundary conditions are the following ones:

– Conditions on the inner surface ($\eta=\eta_i$=constant):

$$\left.\begin{aligned}V_\eta^*=V_\theta^*=0\\T_1^*=1\end{aligned}\right\} \tag{11}$$

– Conditions on the outer surface ($\eta=\eta_e$=constant):

$$\left.\begin{aligned}V_\eta^*=V_\theta^*=0\\T_2^*=0\end{aligned}\right\} \tag{12}$$

To evaluate the stream's function values, we use the following relations:

$$\left\{V_\eta^*=\frac{1}{h^*}\frac{\partial\psi^*}{\partial\theta},\quad V_\theta^*=-\frac{1}{h^*}\frac{\partial\psi^*}{\partial\eta}\right\} \tag{13}$$

3 Numerical Method

To solve Eqs. (8)–(10) with associated boundary conditions (Eqs. (11) and (12)), we consider a numerical solution by the method of finite volumes, presented by Patankar [12] and Nogotov [13].

Figure 2 shows both the physical and the computational domain. Figure 3 shows one typical control volume and its neighbors in a computational domain.

We cut out the annular space according to directions η and θ from the whole of elementary volumes or "control volumes" equal to "$h^{*2}\Delta\eta\Delta\theta$." The problem is bidimensional, the thickness in z direction is assumed to the unity.

The center of a typical control volume is a point P and the center of its side faces "east," "west," "north" and "south," which are the points e, w, n and s, respectively. Four other control volumes surround each interior control volume. The centers of these volumes are points E, W, N and S. While the scalar variables (pressures, temperatures) are stored at the points centered in control volumes, the four velocities components are stored in the centers of the side faces of control volumes [12]. The transfer equations of the scalar variables are integrated in typical control volume; however, those of the velocities components are integrated in staggered control volumes [12]. The control volume of the horizontal component is staggered towards the right and that of the vertical component is staggered upwards. It is well known that this shift is necessary to avoid certain numerical instabilities [12].

3.1 Discretization Equation Transfer of a Variable Φ. The general differential equation is

$$\frac{\partial}{\partial\eta}(h^*V_\eta^*\Phi)+\frac{\partial}{\partial\theta}(h^*V_\theta^*\Phi)=\frac{\partial}{\partial\eta}\left(\Gamma_\Phi\frac{\partial\Phi}{\partial\eta}\right)+\frac{\partial}{\partial\theta}\left(\Gamma_\Phi\frac{\partial\Phi}{\partial\theta}\right)+S_\Phi \tag{14}$$

We illustrate sources and diffusion coefficients in Table 1.

Table 2 Variation of the average Nusselt number according to the number of nodes for e_1=0.86, e_2=0.4, and α=0 deg

		Number of nodes											
		21×15	31×20	41×25	51×31	61×40	71×50	81×56	91×60	101×70	**130×60**	135×65	140×70
Ra	50	0.95	0.97	0.98	0.98	1.02	1.04	1.06	1.09	1.11	**1.12**	1.12	1.12
	500	2.18	2.21	2.24	2.26	2.27	2.27	2.28	2.28	2.29	**2.31**	2.30	2.29
	10^4	2.89	2.91	2.94	3.09	3.17	3.26	3.35	3.37	3.40	**3.41**	3.41	3.41
	5.10^5	6.75	6.81	6.87	6.95	7.01	7.14	7.25	7.29	7.31	**7.30**	7.31	7.31

Table 3 Variation of the average Nusselt number according to the number of nodes for $e_1=0.688$, $e_2=0.4$, and $\alpha=0$ deg

		Number of nodes											
		21×15	31×20	41×25	51×31	61×40	71×50	81×56	91×60	101×70	**130×60**	135×65	140×70
Ra	50	0.82	0.85	0.95	0.99	1.01	1.05	1.07	1.08	1.08	**1.09**	1.10	1.10
	500	1.36	1.40	1.45	1.50	1.56	1.67	1.78	1.82	1.84	**1.85**	1.85	1.86
	10^4	2.54	2.57	2.58	2.60	2.64	2.65	2.70	2.72	2.74	**2.76**	2.76	2.76
	5.10^5	6.07	6.10	6.12	6.16	6.19	6.22	6.21	6.24	6.24	**6.25**	6.25	6.26

The discretization equation is obtained by integrating the conservation equation over the control volume shown in Fig. 3, after some manipulations [12–14]; we have the final discretization equation

$$a_p\Phi_p = a_E\Phi_E + a_W\Phi_W + a_N\Phi_N + a_S\Phi_S + S_\Phi \tag{15}$$

The equation coefficients are well defined in [12], the power law scheme is used to discretize the convective terms in the governing equations.

The discretization equations of the boundary conditions are written in the same form of Eq. (15).

The algorithm of SIMPLER [12] is used for the sequential solution of the system of equations of discretization. The iterative numerical solution of the algebraic system of equations is that of sweeping implying the tridiagonal algorithms of Thomas and cyclic.

Once the temperature distribution is available, the local Nusselt number in the physical domain is defined as

$$\mathrm{Nu} = -\frac{1}{h^*}\frac{\partial T^*}{\partial \eta} \tag{16}$$

The average Nusselt number is obtained by integrating the local Nusselt numbers around the walls

$$\overline{\mathrm{Nu}} = \frac{1}{2\pi}\int_{-\pi}^{+\pi} \mathrm{Nu}\, d\theta \tag{17}$$

4 Results and Discussion

We consider two annular spaces characterized by the eccentricity of the internal elliptic tube ($e_1=0.688, e_2=0.5$) and ($e_1=0.86, e_2=0.6$).

We use four values for the Rayleigh number Ra ($\mathrm{Ra}=10^3$, $\mathrm{Ra}=5.10^4$, $\mathrm{Ra}=10^5$, and $\mathrm{Ra}=5.10^5$). The fluid is assumed as air, so the number of Prandtl is supposed to be constant and equal to 0.7.

4.1 Grid Study. In this study several grids were used arbitrarily, to see their effect on the results. Tables 2 and 3 show us the variation of the average Nusselt number according to the number of nodes for each grid. We choose the grid **130×60** from which we notice that the average Nusselt number does not vary significantly anymore.

4.2 Numerical Code Validation. An annular space ranging between two confocal and horizontal elliptic cylinders [7] has been considered. We present in Fig. 4 the streamlines and the isotherms resulting from our calculation code with the same parameters used by Elshamy et al. [7]. By comparing this figure with Figs. 9 and 10 of Ref. [7], we can notice that the results are similar. Further, we gather in Table 4 the average Nusselt number's values on the two walls resulting from our calculations and those of Ref. [7]. Furthermore, we can notice that these values are in a good agreement.

4.3 Influence of the Rayleigh Number. Figure 5–8 represent the isotherms and the streamlines for different Rayleigh number values.

When the Rayleigh number is weak, as being lower or equal to 10^3, the heat transfer is essentially conductive, so the isotherms in Fig. 5 have the same form as the walls. Nevertheless, there is a movement of the fluid: the particles, which warm up on the wall of the internal elliptic cylinder, tend to rise along this one, then to go down again along the wall of the external elliptic cylinder. Thus the flow is organized in two principal cells which turn very slowly in opposite directions. The laminar convection is weak.

When the Rayleigh number increases to 5.10^4 and 10^5, Figs. 6 and 7 show that the streamline values increase appreciably, which indicates an increase of convection, the flow of the fluid becomes multicellular. Both in the left side and in the right side of the annular space, a secondary flow is done in opposite direction of the principal cell.

It seems to us that the geometry of the two walls is at the origin of the formation of secondary flow, which appears in the case of symmetry, by increasing the number of Rayleigh, the two secondary cells turn between two horizontal planes in the top region of the annular space, and the two principal cells turn between two vertical planes both in the left side and in the right side of this last.

The variation ΔT^* between the isotherms of Figs. 5–8 is equal to 0.1 and the values of the streamlines are given on these figures.

For $\mathrm{Ra}=5.10^5$, the flow which is going up on the side of the hot wall and going down on the side of the cold wall becomes intense and the natural convection is dominant. The streamline values show an appreciable increase in the flow. This means that the convection becomes more important and predominates on the conduction.

The transfer is done primarily by convection. We notice that by increasing the value of the Rayleigh number, the flow of the fluid becomes again bicellular and the isotherms become deformed and inserted at the top where the convection is strong. Figure 8 illustrates it well. An increase in the Rayleigh number, that is to say an intensification of the natural convection, can draw fusion of vortexes, according to the geometry of walls and the viscosity of the fluid. This phenomenon of vortexes destruction is opposite of another, creation of vortexes. This is observed in large values of Rayleigh numbers and is bound to the instability of the flow when it is preturbulent. To study them numerically, it is necessary to arrange calculation codes for an unsteady flow in a tridimensional space. This situation constitutes a priori a limit to the utilization of elaborate calculation codes on a steady flow in a two-dimensional space.

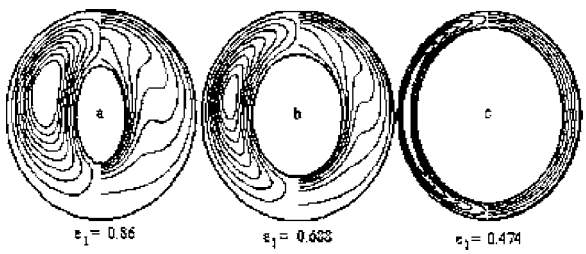

Fig. 4 Streamlines and isotherms for $\mathrm{Ra}=10^4$, $\alpha=0$ deg, and $e_0=0.4$

Table 4 Comparison of average Nusselt number (Ref. [7]) with our results

				Internal wall		External wall	
e_1	e_2	Inclination	Ra	Ref. [7]	Our results	Ref. [7]	Our results
0.688	0.4	$\alpha=90°$	10^4	2.66	2.72	1.38	1.43
0.688	0.4	$\alpha=90°$	10^5	4.94	4.78	2.51	2.52
0.86	0.4	$\alpha=90°$	10^4	3.68	3.46	1.35	1.30
0.86	0.4	$\alpha=90°$	4.10^4	5.34	4.70	1.93	1.77

Figure 9 shows that the average Nusselt number values on the internal and the external walls increase with the increasing of the Rayleigh number.

4.4 Influence of the Inclination Angle. Figures 5–8 and 10 correspond to $\alpha=0$ deg and Fig. 12 corresponds to $\alpha=90$ deg. The vertical fictitious plane passing by system center is a plane of symmetry. The streamlines and the isotherms are symmetrical compared to the vertical plane. On the left side of this plan, the flow turns in the trigonometrical direction. On the right side, the flow is in the opposite direction (the particles of the fluid move upwards, under the action of gravity forces, along the internal hot wall and go down near to the external cold wall).

The variation of the inclination angle α has a considerable effect both on the fields of flow and temperature. We can already notice that for $Ra=10^4$ the flow becomes again bicellular for $\alpha=45$ deg as Fig. 11 shows.

The comparison of Figs. 10 and 12 for $\alpha=0$ deg and $\alpha=90$ deg with Fig. 11 for $\alpha=45$ deg, shows that the angle of inclination α modifies the flow: Initially there is the absence of plans of symmetry of the flows. We also notice that the inclination modifies the flow intensity, (see Fig. 11). The isotherms are also modified by the inclination. The field of temperatures is asymmetrical for α

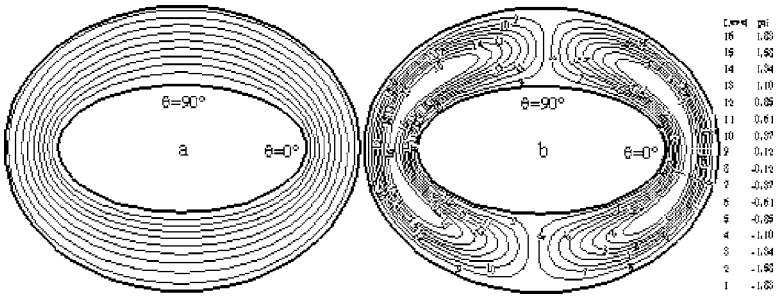

Fig. 5 Isotherms and streamlines for $Ra=10^3$, $\alpha=0°$, $e_1=0.86$, and $e_2=0.6$

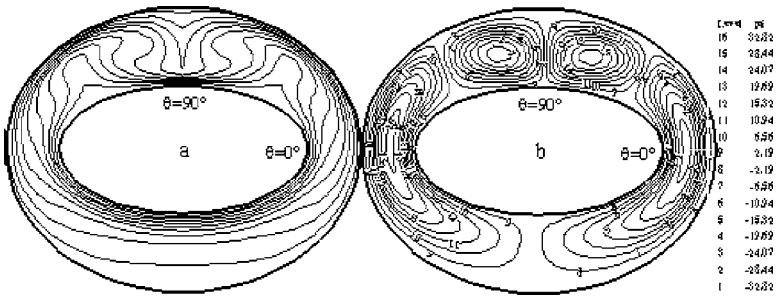

Fig. 6 Isotherms and streamlines for $Ra=5.10^4$, $\alpha=0°$, $e_1=0.86$, and $e_2=0.6$

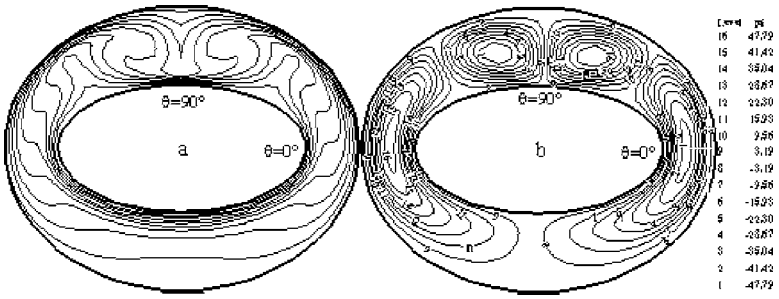

Fig. 7 Isotherms and streamlines for $Ra=10^5$, $\alpha=0$ deg, $e_1=0.86$, and $e_2=0.6$

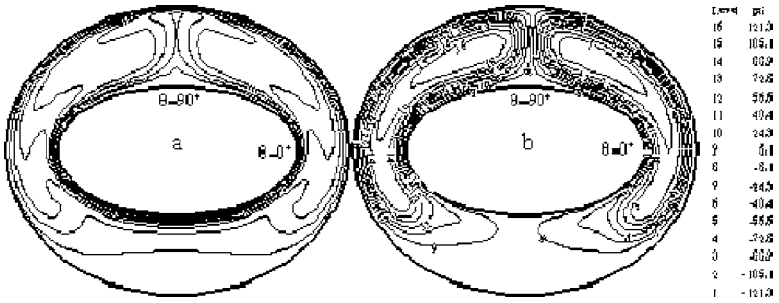

Fig. 8 Isotherms and streamlines for Ra=5.10^5, α=0 deg, e_1=0.86, and e_2=0.6

different from zero as shown through the isotherms of Fig. 11. Thus, the position and the value of the maximum temperature depend on the inclination angle α.

Variation ΔT^* between the isotherms of Figs. 10–12 is also equal to 0.1 and the values of the streamlines are given in these figures.

Figure 13 shows that for α=0 deg the maximum value of the local Nusselt number on the internal wall is located at the angular position θ=90 deg, and the minimal values are located at the angular positions θ=30 deg and θ=150 deg. On the external wall the minimum value of the local Nusselt number is located at the angular position θ=90 deg, and the maximal values are located at the angular positions θ=30 deg and θ=150 deg.

For α=45 deg the minimal value of the local Nusselt number on the internal wall is located at the angular position θ=45 deg, and the maximum value is located at the angular position θ=225 deg (see Fig. 14). On the external wall, the maximal value of the local Nusselt number is located at the angular position θ=45 deg and the minimum value is located at the angular position θ=225 deg.

For α=90 deg the local Nusselt number on the internal wall reaches its maximum at the angular position θ=180 deg, and the minimal value is located at the angular positions θ=45 deg and θ=315 deg (see Fig. 15). On the external wall, the local Nusselt number reaches its maximum in the summit region located at the angular positions θ=45 deg and θ=315 deg; the minimal value is located at the angular position θ=180 deg.

Figure 16 shows that the average Nusselt number values on the internal and the external walls increase with the increasing of inclination angle α.

Table 5 gathers the average Nusselt number values, on the internal and the external walls.

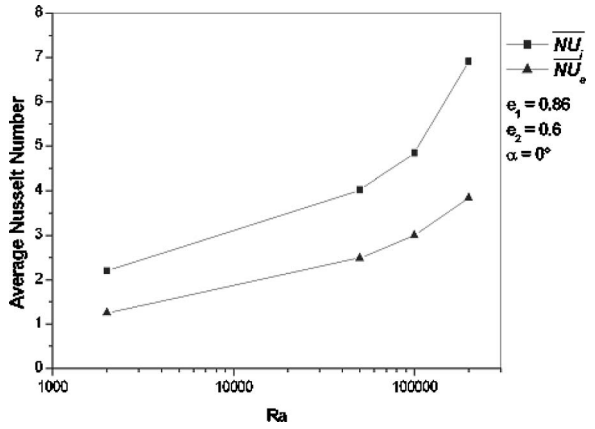

Fig. 9 Average Nusselt number on the internal and external walls

5 Conclusion

The suggested calculation code, which uses the method of finite volumes, with the velocity-pressure formulation, makes it possible to find with a good agreement, the literature results, which solve problems similar to that studied. Thus we theoretically studied the bidimensional thermal natural convection, in laminar flow and permanent, in an annular space located between two confocal elliptic cylinders. We examined, in particular, the influence of the slope's angle α on the convective mode. Three values of α: α=0 deg, α=45 deg, and α=90 deg are considered. Simulations were executed from four values of the Rayleigh number: Ra=10^3, Ra=5.10^4, Ra=10^5, and Ra=5.10^5.

The results underline the influence of the inclination angle on the average Nusselt number ($\overline{Nu_i}$). The maximum value is obtained for α=90 deg when e_1=0.688.

For low Rayleigh number values, the coefficient of heat transfer is dominated by the mechanism of the conduction for the considered values of α.

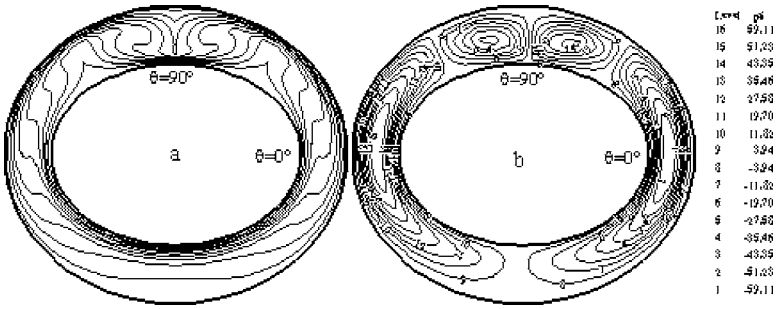

Fig. 10 Isotherms and streamlines for Ra=10^5, α=0 deg, e_1=0.688 and e_2=0.5

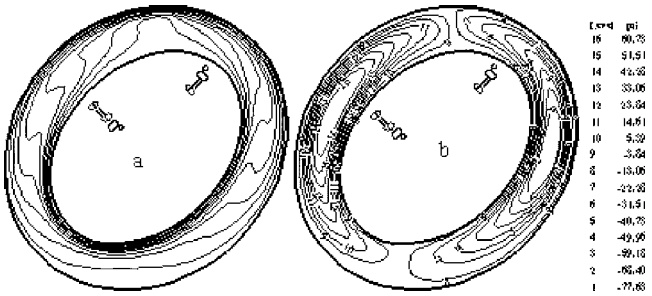

Fig. 11 Isotherms and streamlines for Ra=10^5, α=45 deg, e_1 =0.688, and e_2=0.5

Nomenclature

a = constant defined in the system of elliptic coordinates=characteristic length (m)

a_p, a_E, a_W, a_N, a_s = coefficients of "Eq. (16)," defined in Ref. [12]

$A1$ = length of major axis in internal cylinder (m)

$A2$ = length of major axis in external cylinder (m)

$B1$ = length of minor axis in internal cylinder (m)

$B2$ = length of minor axis in external cylinder (m)

c_p = specific heat at constant pressure (J kg^{-1} K^{-1})

e_1 = eccentricity of internal ellipse, $e_1=\sqrt{A1^2-B1^2}/A1$

e_2 = eccentricity of external ellipse, $e_2=\sqrt{A2^2-B2^2}/A2$

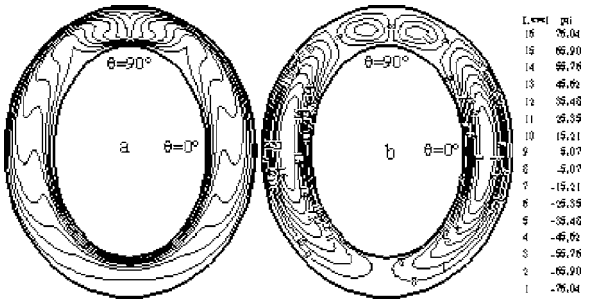

Fig. 12 Isotherms and streamlines for Ra=10^5, α=90 deg, e_1 =0.688, and e_2=0.5

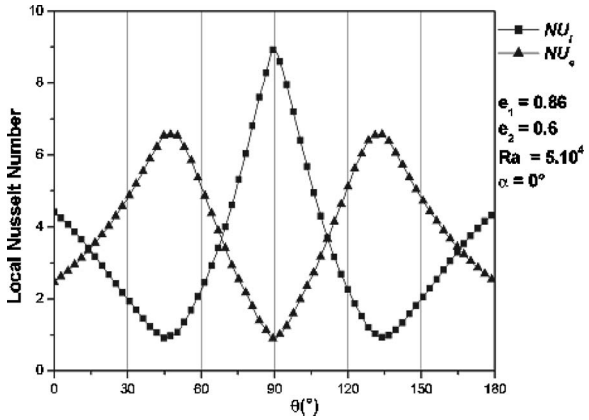

Fig. 13 Local Nusselt number on the internal and external walls

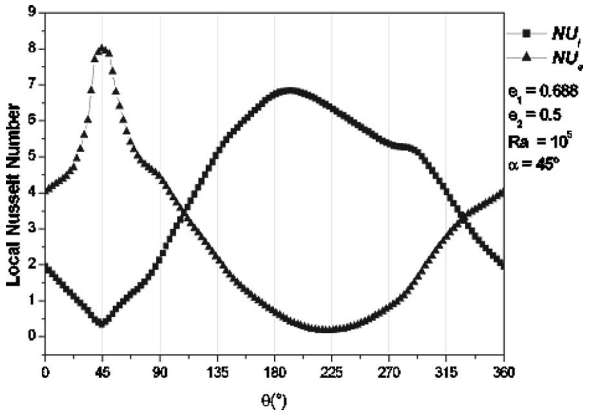

Fig. 14 Local Nusselt number on the internal and external walls

g = gravitational acceleration (m s^{-2})

Gr = Grashof number, $\mathrm{Gr}=g\beta a^3/\nu^2\Delta T$

h = metric coefficient defined in Eq. (5)

$\underline{\mathrm{Nu}}$ = local Nusselt number

$\overline{\mathrm{Nu}}$ = average Nusselt number

P = pressure (Pa)

Pr = Prandtl number, $\mathrm{Pr}=\nu\rho' c_p/\lambda$

Ra = Rayleigh number, Ra=GrPr

S_Φ = Source term in "Eq. (16)"

T = fluid's temperature (K)

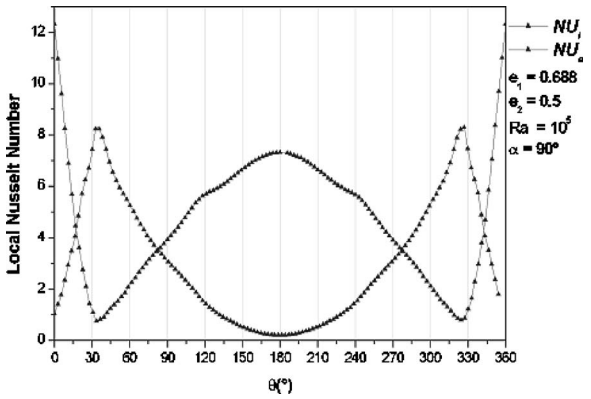

Fig. 15 Local Nusselt number on the internal and external walls

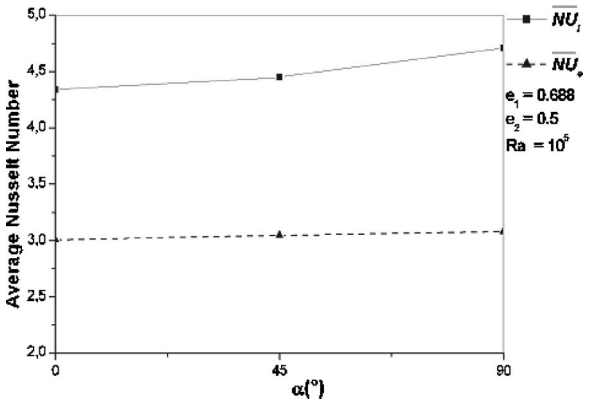

Fig. 16 Average Nusselt number on the internal and external walls

Table 5 The average Nusselt number values, on the internal and external walls

$e_1=0.688$ and $Ra=10^4$	α	$\overline{Nu_i}$	$\overline{Nu_e}$
	0°	**4.34**	**3.01**
	45°	**4.45**	**3.05**
	90°	**4.71**	**3.07**
$e_1=0.86$ and $\alpha=0°$	**Ra**	$\overline{Nu_i}$	$\overline{Nu_e}$
	10^3	**2.20**	**1.25**
	5.10^4	**4.02**	**2.49**
	10^5	**4.85**	**3.00**
	5.10^5	**6.91**	**3.85**

T_1 = temperature of the wall of elliptic internal cylinder (K)
T_2 = temperature of the wall of elliptic external cylinder (K)
T_d = temperature difference, $T_d=T-T_2$ (K)
ΔT = temperature difference between the inner and the outer wall, $\Delta T=T_1-T_2$ (K)
t = time (s)
u = velocity component according to coordinate x (m s^{-1})
v = velocity component according to coordinate y (m s^{-1})
V_η = velocity component according to coordinate η (m s^{-1})
V_θ = velocity component according to coordinate θ (m s^{-1})
$\mathbf{V}$ = velocity vector (m s^{-1})
x,y,z = Cartésien coordinates (m)

Greek letters

α = angle of inclination between OH and OX "Fig. 1" measured positively in the counterclockwise direction (deg)
β = thermal expansion coefficient (K^{-1})
λ = thermal conductivity (W m^{-1} K^{-1})
υ = kinematic viscosity (m^2 s^{-1})
ρ = density (kg m^{-3})
π = stress tensor
η,θ,z = elliptic coordinates
Ψ = stream function (m^2 s^{-1})
ϕ = general function
Γ_Φ = Diffusion coefficient

Exponents

* = dimensionless parameters

Indices

i and 1 = interior
e and 2 = exterior

References

[1] Mack, L. R., and Bishop, E. H., 1968, "Natural Convection Between Horizontal Concentric Cylinders for Low Rayleigh Numbers," Q. J. Mech. Appl. Math., **XXI**, pp. 223–241.
[2] Kuehn, T. H., and Goldstein, R. J., 1976, "An Experimental and Theoretical Study of Natural Convection in the Annulus Between Horizontal Concentric Cylinders," J. Fluid Mech., **74**, pp. 695–719.
[3] Kuehn, T. H., and Goldstein, R. J., 1978, "An Experimental Study of Natural Convection Heat Transfer in Concentric and Eccentric Horizontal Cylindrical Annuli," J. Heat Transfer, **100**, pp. 635–640.
[4] Guj, G., and Stella, F., 1995, "Natural Convection in Horizontal Eccentric Annuli: Numerical Study," Numer. Heat Transfer, Part A, **27**, pp. 89–105.
[5] Lee, J. H., and Lee, T. S., 1981, "Natural Convection in the Annuli Between Horizontal Confocal Elliptical Cylinders," Int. J. Heat Mass Transfer, **24**, pp. 1739–1742.
[6] Schreiber, W. C., and Singh, S. N., 1985, "Natural Convection Between Confocal Horizontal Elliptical Cylinders," Int. J. Heat Mass Transfer, **28**, pp. 807–822.
[7] Elshamy, M. M., Ozisik, M. N., and Coulter, J. P., 1990, "Correlation for Laminar Natural Convection Between Confocal Horizontal Elliptical Cylinders," Numer. Heat Transfer, Part A, **18**, pp. 95–112.
[8] Chmaissem, W., Suh, S. J., and Daguenet, M., 2002, "Numerical Study of the Boussinesq Model of Natural Convection in an Annular Space: Having a Horizontal Axis Bounded by Circular and Elliptical Isothermal Cylinders," Appl. Therm. Eng., **22**, pp. 1013–1025.
[9] Cheng, C. H., and Chao, C. C., 1996, "Numerical Prediction of the Buoyancy-Driven Flow in the Annulus Between Horizontal Eccentric Elliptical Cylinders," Numer. Heat Transfer, Part A, **30**, pp. 283–303.
[10] Guj, G., and Stella, F., 1989, "Vorticity-Velocity Formulation in the Computation of Flows in Multiconnected Domains," Int. J. Opt. Comput., **9**, pp. 1285–1298.
[11] Zhu, Y. D., Shu, C., Qiu, J., and Tani, J., 2004, "Numerical Simulation of Natural Convection Between Two Elliptical Cylinders using DQ Method," Int. J. Heat Mass Transfer, **47**, pp. 797–808.
[12] Patankar, S. V., 1980, *Numerical Heat Transfer and Fluid Flow*, McGraw–Hill, New York.
[13] Nogotov, E. F., 1978, *Applications of Numerical Heat Transfer*, McGraw–Hill, New York.
[14] Saatdjian, E., 1998, *Phénomènes de Transport et Leurs Résolutions Numériques*, Polytechnica, Paris.

Antonio Campo
Professor
Department of Mechanical Engineering,
The University of Vermont,
Burlington, VT 05405
e-mail: acampo@emba.uvm.edu

Oronzio Manca
Professor
e-mail: oronzio.manca@unina2.it

Biagio Morrone
Professor
e-mail: biagio.morrone@unina2.it

Dipartimento di Ingegneria Aerospaziale e Meccanica,
Seconda Università degli Studi di Napoli Real Casa dell'Annunziata,
Via Roma 29,
81301 Aversa (CE), Italy

Numerical Investigation of the Natural Convection Flows for Low-Prandtl Fluids in Vertical Parallel-Plates Channels

Laminar natural convection of metallic fluids ($\mathrm{Pr} \ll 1$) *between vertical parallel plate channels with isoflux heating is investigated numerically in this work. The full elliptic Navier-Stokes and energy equations have been solved with the combination of the stream function and vorticity method and the finite-volume technique. An enlarged computational domain is employed to take into account the flow and thermal diffusion effects. Results are presented in terms of velocity and temperature profiles. The investigation also focuses on the flow and thermal development inside the channel; the outcomes show that fully developed flow is attained up to* $\mathrm{Ra}=10^3$*, whereas the thermal fully developed condition is attained up to* $\mathrm{Ra}=10^4$*. Further, correlation equations for the dimensionless induced flow rate, maximum dimensionless wall temperatures, and average Nusselt numbers as functions of the descriptive geometrical and thermal parameters covering the collection of channel Grashof numbers* $1.32\times10^3 \leqslant \mathrm{Gr}/A \leqslant 5.0\times10^6$ *and aspect ratios* $5 \leqslant A \leqslant 15$*. Comparison with experimental measurements has been presented to assess the validity of the numerical computational procedure.* [DOI: 10.1115/1.1991867]

Introduction

Laminar natural convection between parallel plates has been extensively investigated throughout the years, due to its relevance in a multitude of technological processes [1–4]. In fact, many cooling/heating devices used in engineering applications can be modeled as vertical parallel-plate channels; for example, solar collectors, electronic equipment, channel nuclear reactors, and electric transformers. The investigation of natural convection for such configurations has been mainly focused on two working fluids: air and water [1–6]. The thermal and flow design procedures for simple channel systems are well known, as reported in [7–12].

Due to the renewed interest in nuclear reactor systems this configuration can be of main importance in the design of nuclear reactors safety; in addition, the low Prandtl fluids employed in the thermal design of the core reactors show different behavior than that of air and water.

The numerical studies on natural convection in vertical parallel-plate channels were initiated by Bodoia and Osterle [13] who invoked the boundary layer approach. The investigation was focused only on the channel domain. From a broad framework, it is more suitable to take into account an upstream and downstream regions to obtain more accurate results in terms of local quantities, temperature and velocity, and global quantities, such as Nusselt number and induced mass flow rate, in a large range of Rayleigh numbers, as indicated in detail in [12,14].

The category of liquid metals is of great engineering interest due to their unique heat transfer capabilities. In nuclear power plants in case of failure of the pump cooling system, the heat transfer from the reactor core would be one of the natural convection with the liquid metal being the heat transfer medium. These fluids possess low or very low Prandtl numbers, with an order of magnitude 10^{-2}, and their thermal characteristics are more superior than air and water. These unique fluids present very strong diffusive thermal effects which should be taken into account when the numerical modeling is set up. For this reason, as remarked in [12,14], the boundary layer approach is not suitable and extended computational domains need to be employed to generate accurate numerical solutions.

A short review of publications dealing with the numerical investigation of vertical channels by employing the full elliptic conservation equations articulated with an extended computational domain with both upstream and downstream reservoirs is presented in the forthcoming paragraphs.

Chang and Lin [15,16] solved numerically the elliptic-type governing equations with the primitive variable approach. They employed the SIMPLER method with the finite-difference technique for solving the unsteady two-dimensional flow between symmetrically [15] and asymmetrically [16] isothermally heated parallel plates for air. The main interest of the authors was in the time development of the flow and thermal structures inside the computational domain. For the symmetrically heated channel [15], it was found that the greater the Ra value the shorter the time necessary to attain the steady-state condition. In addition, the authors reported the flow and thermal structures of the whole computational domain. In the paper on the asymmetric heating [16], the authors showed that an inflow from the upper side of the channel exists and, moreover, that at $\mathrm{Ra}=10^6$ the velocity and temperatures showed oscillatory patterns above the heated plates. This investigation elucidated the visualization of the thermal and the flow fields above the heated channel. Ramanahtan and Kumar [17] carried out an extensive parametric study for isoflux vertical parallel plates that included the effects of the Prandtl number and the channel aspect ratio. Also, correlation equations for the maximum wall temperature and the average heat transfer rate were obtained. The main parameters used in the investigation were the Prandtl number, the Grashof number, and the channel Rayleigh number. An adaptive grid solution was performed in [18]. The inflow boundary conditions were imposed as an inviscid flow field generated by an assumed infinite line mass sink located at the center-

Contributed by the Applied Mechanics Division of ASME for publication in the JOURNAL OF APPLIED MECHANICS. Manuscript received July 13, 2004; final manuscript received April 20, 2005. Assoc. Editor: D. Siginer. Discussion on the paper should be addressed to the Editor, Prof. Robert M. McMeeking, Journal of Applied Mechanics, Department of Mechanical and Environmental Engineering, University of California - Santa Barbara, Santa Barbara, CA 93106-5070, and will be accepted until four months after final publication in the paper itself in the ASME JOURNAL OF APPLIED MECHANICS.

line of the inlet plane, coupled with free entrainment boundaries along the side. The downstream region outflow boundary corresponded to an infinite line source plume solution in conjunction with free entrainment boundaries along the sides. The results were obtained with a fixed Prandtl number equal to 0.7, Grashof numbers ranging between 10^3 and 10^5, and a channel aspect ratio equal to 1 or 2. An I-type shaped computational domain was employed, similar to that used in [15]. The vehicle for the numerical computation was the finite volume method in terms of stream function and vorticity approach for air. The relevant problem of optimizing the plate distance was investigated in [19]. The main findings were the dimensionless flow rate as a function of the channel aspect ratio, in terms of the Grashof number based on the channel height and the optimal aspect ratio that maximized the heat transfer coefficient. A numerical investigation for a vertical channel with uniform wall heat flux was reported in [20], where the effect of wall conduction on laminar natural convection between symmetrically heated vertical plates was studied. It was found that the lower the thickness and/or the thermal conductivity of the walls the more uniform the heat flux distribution on the wall. The heat flux and temperature profiles along solid-fluid interfaces for low Rayleigh numbers were significantly influenced by the solid-fluid conductivity and the thickness wall-channel gap ratios. A transient numerical analysis of natural convection in air between two vertical parallel plates with the plates heated at uniform heat flux was addressed in [21]. The computational domain was made up of the channel and two reservoirs, one placed downstream and the other upstream of the channel. The results were presented in terms of wall temperature profiles, air velocity and temperature profiles, and average Nusselt number changing with time for different aspect ratio values and Rayleigh number values. The simulation allowed the authors to detect the complex structures of the flow inside and outside the channel.

A numerical paper dealing with the effect of the Prandtl number on natural convection channel flows was proposed in [22]. The study centered on the elliptic governing equations in a single channel with asymmetric heating conditions, for a wide range of the modified Rayleigh numbers $Ra^*=Ra/A$ and channel aspect ratios. A large spectrum of Prandtl numbers was investigated together with the role of the dimensions of the upstream reservoir on the main thermal parameters. The main results were that for low values of the modified Rayleigh number, the average Nusselt number, due to the upstream conduction outside the channel, does not follow the asymptotic trend corresponding to the fully developed regime unless the channel aspect ratio is small enough. A numerical investigation on the effect of the Prandtl number on natural convection in symmetrically heated isoflux vertical channels with or without coplanar adiabatic extensions downstream was carried out in [23]. Results were obtained for three $Pr=1.0\times10^{-2}$, 0.71, and 10, with $A=10$. The maximum wall temperature attains an asymptotic value with respect to the adiabatic extension length, which decreases for lower values of the Prandtl number. It was also discovered that the increment of the chimney effect is more pronounced for lower Pr.

A detailed experimental program was conducted to study the heat transfer characteristics of mercury in natural convection in a vertical channel in [24,25]. There seems to be a lack of numerical studies on natural convection in isoflux heated vertical channels with low Prandtl number fluids. This study has as practical application the thermal control of nuclear reactors.

The aim of the present paper is to solve the full elliptic Navier-Stokes and energy equations with the stream function and vorticity method and the finite-volume technique. This paper deals with the laminar, steady, two-dimensional (2D) regime natural convection between isoflux vertical parallel plates. An enlarged computational domain has been employed to take into account the flow and thermal diffusion effects. Comparison with the experimental results disclosed in [24,25] is presented to assess the validity of the numerical procedure.

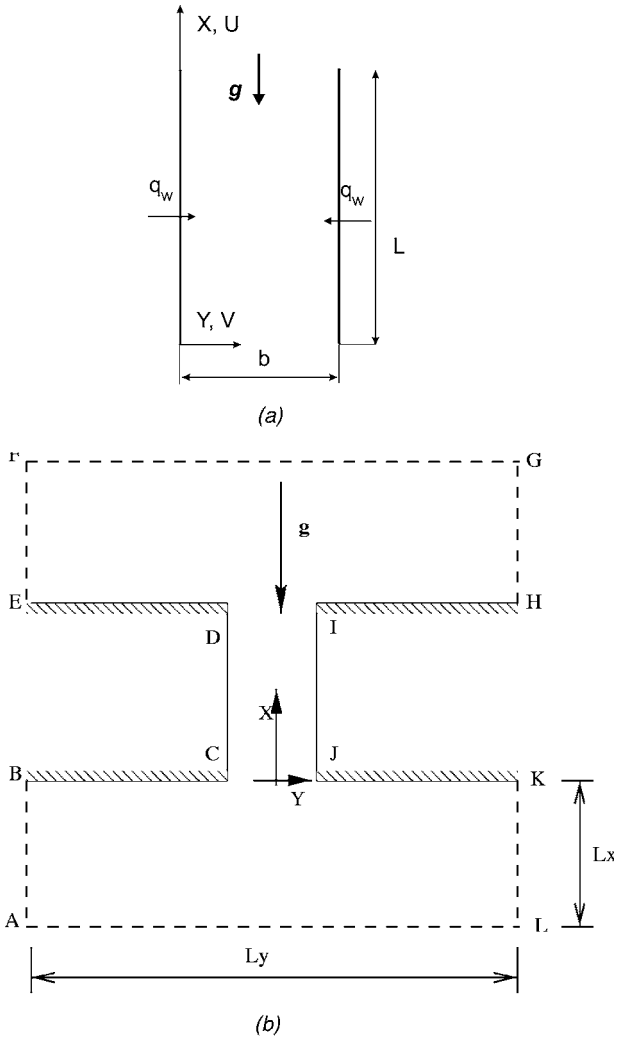

Fig. 1 (*a*) Sketch of the channel, (*b*) computational domain

Results are presented in terms of temperature and velocity profiles since it seems that very low attention was paid to the thermal and flow fields of these fluids in natural convection. In addition, global quantities such as the induced mass flow rate, the maximum wall temperatures, and the average Nusselt numbers as functions of the intervening thermal and geometrical parameters are presented to supply useful data to thermal designers.

Analysis and Numerical Solution Method

The physical system made of a vertical, parallel-plate channel as depicted in Fig. 1(*a*), is characterized by the height of the heated plates L and the channel gap b. The channel aspect ratio $A=L/b$ is the only geometrical parameter arising in the present analysis. The two plates are symmetrically heated with uniform heat flux q_w. As a result, buoyant fluid moves up through the channel gap cooling the heated plates.

Under steady-state and laminar conditions and upon neglecting the variability of thermophysical properties and adopting the Boussinesq approximation, the two-dimensional conservation equations, in terms of stream function ψ and vorticity ω are

$$\frac{\partial(u\omega)}{\partial x}+\frac{\partial(v\omega)}{\partial y}=\nu\nabla^2\omega-g\beta\frac{\partial T}{\partial y} \tag{1}$$

$$\frac{\partial^2\psi}{\partial x^2}+\frac{\partial^2\psi}{\partial y^2}=-\omega \tag{2}$$

Table 1 Comparison for the average Nusselt number for different grid spacing with Ra=10^4 and A=10

Node numbers	11×31	21×61	41×121	Asympt
Nu	2.156	2.180	2.182	2.191
Δ%	−1.60%	−0.50%	−0.40%	0.0

$$\frac{\partial(uT)}{\partial x}+\frac{\partial(vT)}{\partial y}=a\nabla^2 T \tag{3}$$

In the preceding equations, the stream function is obtained by

$$\frac{\partial\psi}{\partial y}=u;\quad \frac{\partial\psi}{\partial x}=-v$$

and the vorticity is

$$\omega=\frac{\partial v}{\partial x}-\frac{\partial u}{\partial y}$$

respectively.

Following arguments raised in [19,26], an enlarged computational domain of finite extension, as illustrated in Fig. 1(*b*), has been employed in this investigation to mimic the free-stream conditions of the fluid flow far away from the region of thermal disturbance induced by the heated plates and to capture the diffusive effects of the low-Prandtl fluids.

The set of imposed boundary conditions is the same as those in [19,26], and is excluded here for sake of brevity.

The choice of the following dimensionless variables:

$$X=\frac{x}{b},\quad Y=\frac{y}{b},\quad U=\frac{ub}{\nu},\quad V=\frac{vb}{\nu},\quad P=\frac{(p-p_\infty)b^2}{\rho\nu^2},$$
$$\Psi=\frac{\psi}{\nu},\quad \Omega=\frac{\omega b^2}{\nu},\quad \theta=\frac{k(T-T_\infty)}{q_w b} \tag{4}$$

gives way to the dimensionless groups

$$\mathrm{Gr}=\frac{g\beta q_w b^4}{k\nu^2},\quad \mathrm{Pr}=\frac{\nu}{a},\quad \mathrm{Ra}=\mathrm{Gr}\,\mathrm{Pr} \tag{5}$$

Further, the channel aspect ratio *A* and the Rayleigh number Ra are embedded into a dimensionless group $\mathrm{Ra}^*=\mathrm{Ra}/A$, called the channel Rayleigh number.

An essential quantity to be evaluated is the induced flow rate between the parallel plates whose dimensionless form is

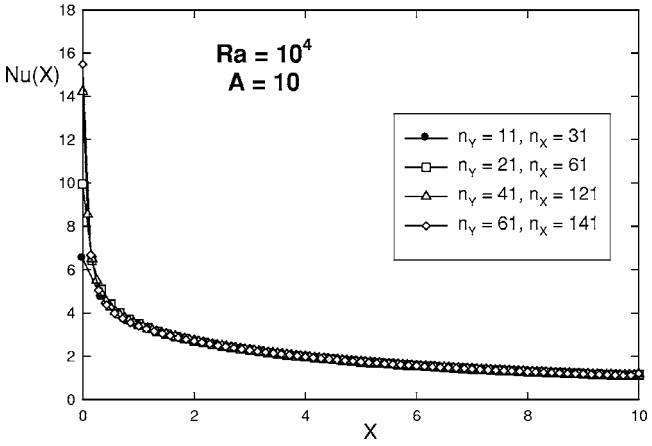

Fig. 2 Local Nusselt number as function of the *X* coordinate at Ra=10^4 and *A*=10 for several meshes

$$\Psi_{w2}-\Psi_{w1}=\Delta\Psi=\int_0^1 U\,dY \tag{6}$$

The key dimensional heat transfer quantity is the local convective coefficient $h(x)$. The wall heat flux has been imposed in this investigation (boundary condition of second kind), so the convective coefficient is related to the wall temperature through the relation

$$h(x)=\frac{q_w}{T_w(x)-T_\infty}$$

Since the local Nusselt number is

$$\mathrm{Nu}(x)=\frac{h(x)b}{k} \tag{7}$$

it can be written in terms of dimensionless wall temperature, by means of Eq. (4), as

$$\mathrm{Nu}(X)=\frac{1}{\theta_w(X)} \tag{8}$$

Thereafter, the average Nusselt number along a single channel wall Nu is defined by

$$\mathrm{Nu}=\frac{1}{A}\int_0^A\frac{dX}{\theta_w(X)} \tag{9}$$

In addition, some other quantities will be employed in the presentation of the results, such as the normalized velocity

$$U^*(X,Y)=\frac{U(X,Y)}{U_{\max}(X)} \tag{10}$$

where $U_{\max}(X)$ is the maximum velocity value at each *X* section and the modified Nusselt number, which employs the bulk temperature

$$\mathrm{Nu}^*(X)=\frac{1}{\theta_w(X)-\theta_b(X)} \tag{11}$$

with $\theta_b(X)$ being the bulk temperature. With reference to [27] the bulk (or mean) temperature in a channel is defined as

$$T_b=\frac{1}{\rho c_p U_m S}\int\int_S \rho c_p u T dS \tag{12}$$

U_m being the average velocity inside the channel and considering a fluid with constant thermophysical properties after rearranging this equation it reads in dimensionless form

$$\theta_b(X)=\frac{\int_0^1 U(X,Y)\theta(X,Y)dY}{\int_0^1 U(X,Y)dY} \tag{13}$$

The numerical computations have been carried out by means of the control volume method. The vorticity and energy equations Eqs. (1) and (3) have been solved by implementing the alternating direction implicit (ADI) method with the false transient procedure, as explained in [28]. The second-order upwind scheme, recommended by [29,30] has been employed to discretize the convective derivatives, while a classical three-point central scheme has been adopted for the diffusive derivatives. The convective terms have been linearized following the iterative procedure suggested by [28]. The second-order upwind used for the convection

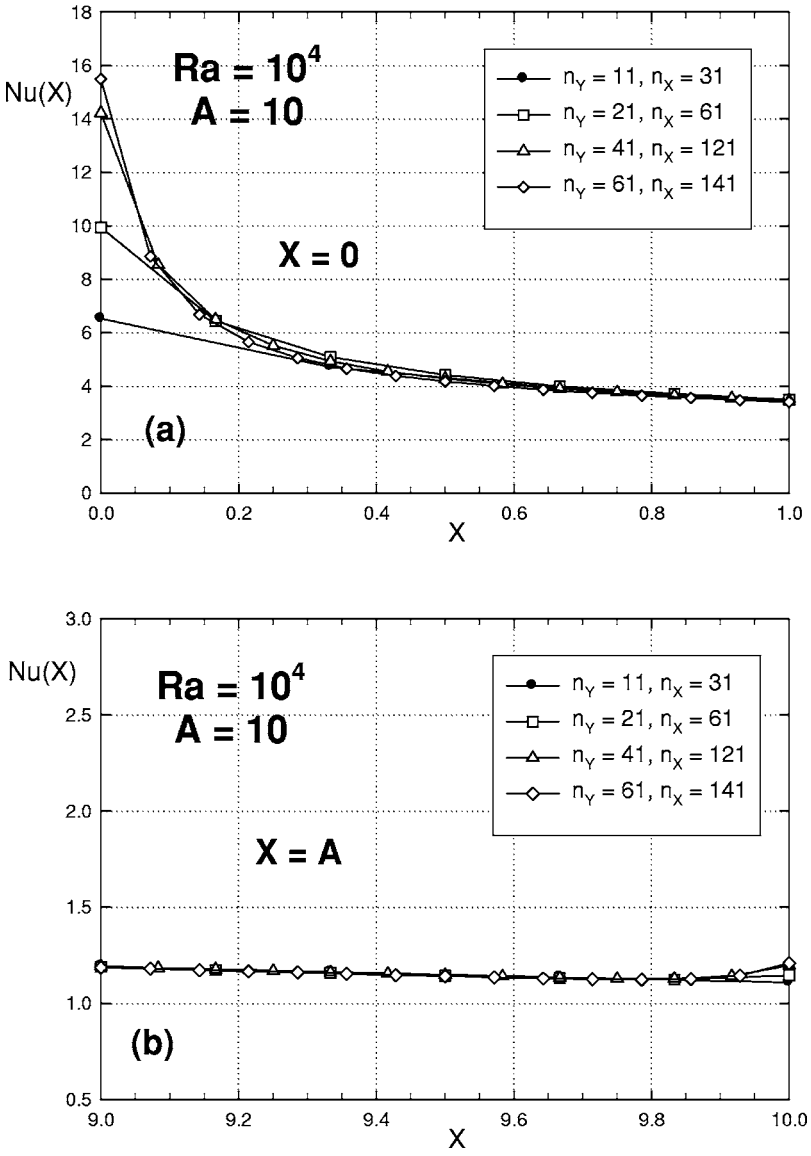

Fig. 3 Local Nusselt number distribution as function of the *X* coordinate for several grids: (*a*) zoom of the inlet section of the channel *X*=0; (*b*) zoom of the exit section of the channel *X*=*A*

terms, both in the vorticity and energy equations, has been demonstrated by [30] that dramatically reduces the numerical diffusion typical of the first-order upwind schemes.

As vividly described by Patankar [31], the problem of numerical diffusion, also called false diffusion, caused by the first-order upwind scheme is never so serious at low Peclet numbers, whereas it can be of importance when the Peclet number increases.

The successive line overrelaxation method (SLOR), with an optimum relaxation factor of about 1.75, has been used to solve the stream function equation. Once the equations of vorticity, stream function, and energy have been solved, then the convergence criteria for the timelike step have to be checked. The steady-statelike condition was considered attained when the percent variation of Ψ, Ω, and θ was less than 10^{-5}.

The computational procedure was implemented by guessing an initial value for the stream functions ψ_{w2} at the right wall 2, and $\psi_{w1}=0$, at the left wall 1. The selected value of the mass flow rate is next verified on a global basis by integrating the momentum equation along the centerline of the vertical, parallel-plate channel in the enlarged computational domain, as recommended by [19].

Validation of the Code. The analysis of validation of the code has been carried out by employing the Richardson extrapolation [32]. The verification of the numerical solutions is obtained by considering several different meshes, successively halving the coarser mesh size.

Indicating the coarse mesh solution at one location of the domain by f_1 and the fine mesh solution at the same location by f_2, the asymptotic value of the function f_{asympt} is given by the Richardson extrapolation relation

$$f_{\text{asympt}} \cong \frac{4}{3}f_2 - \frac{1}{3}f_1$$

as the grid spacing tends to zero, ΔX, $\Delta Y \to 0$, and by halving the grid size.

All the results presented herein refer to fluids with a Prandtl number equal to 0.02. The average Nusselt number is reported in Table 1 as a function of the grid size at $\text{Ra}=10^4$ and an aspect ratio $A=10$; the percent deviations between the grid values and the asymptotic one are displayed in the same table. As it can be observed, the main average heat transfer quantity of interest is very

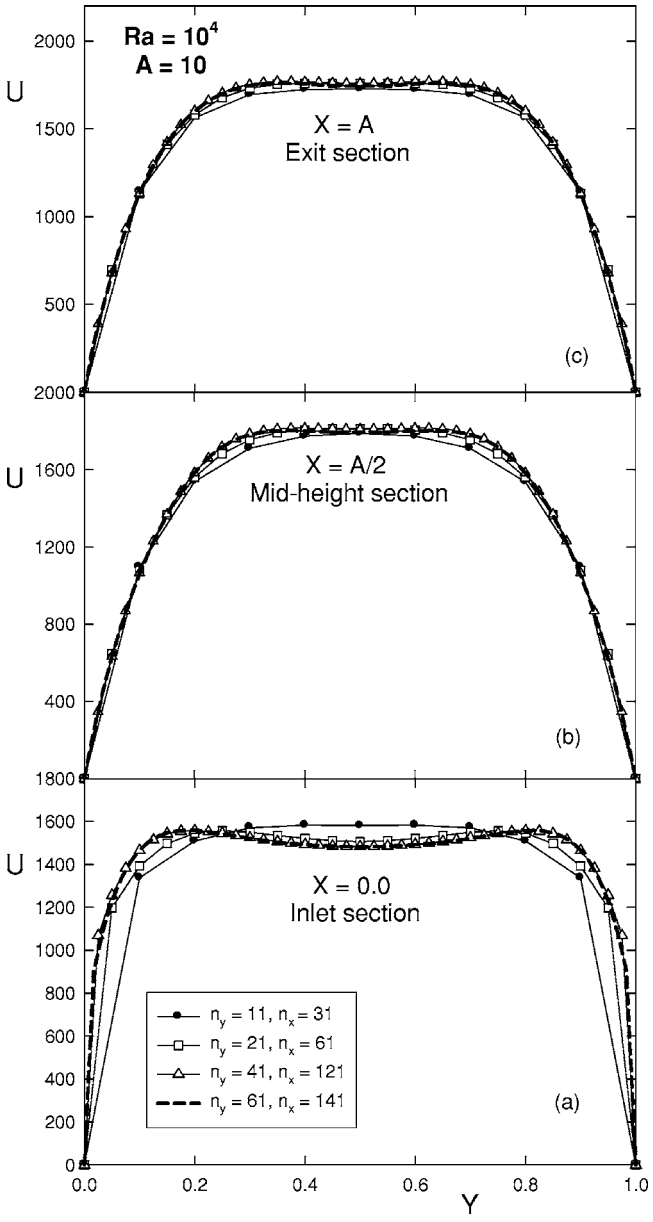

Fig. 4 Velocity profiles as a function of *Y* for different node numbers at three *X* stations: (*a*) *X*=0.0; (*b*) *X*=*A*/2; (*c*) *X*=*A*

weakly affected by the grid nodes. In fact, even with the coarsest mesh, $n_Y \times n_X = 11 \times 31$, the difference with the asymptotic value is lower than 2%.

To investigate the effects of the grid distribution on the the local Nusselt number, Fig. 2 displays this quantity as a function of the X coordinate along the channel walls for different number of grid nodes and the same previous configuration. It can be observed minor differences attained at the channel inlet. In order to visualize the discrepancies at the channel inlet $X=0$ and channel exit $X=A$ for different grid results, Fig. 3 displays the zoomed local Nusselt number at the two aforementioned sections. It can be observed at the channel inlet $X=0.0$ in Fig. 3(a) a strong discrepancy of the local Nusselt number between the coarsest and the finest mesh grids. The difference is about 58% when the 11×31 mesh solution is compared to the 61×141 solution. This difference reduces to about 35% by comparing the 21×61 grid with the 61×141 grid. Anyway, in any case it can be observed that from $X=0.2$ downstream the four profiles show negligible differences. In addition, the 21×61 grid results perfectly overlap to the finer mesh ones from X about 0.05. This is even more true at the channel exit, as observed in Fig. 3(b) where the same profiles are displayed. No discrepancies can be observed, except at the channel exit where the maximum discrepancy between the value of the coarsest and the finest grids is about 6%.

The accuracy of the code has been evaluated also by comparing the velocity and temperature profiles inside the channel, which are displayed in Figs 4 and 5 for different node numbers at $\mathrm{Ra}=10^4$ and the same aspect ratio of $A=10$. The profiles are presented as a function of the transversal coordinate Y at three different stations, $X=0$, $X=A/2$, and $X=A$. The four grid sizes that have been employed for the comparison are $n_Y \times n_X = 11 \times 31$, 21×61, 41×121, and 61×141. Velocity profiles are displayed in Fig. 4 and it can be observed that at the channel inlet $X=0$ in Fig. 4(a) the greatest discrepancies take place. In detail, large deviations can be seen by comparing the grids 11×31 and 21×61. In fact, the percent differences at the centerline between the two velocity profiles are about 5%, whereas the two finer meshes show a discrepancy less than 2%. This behavior is due to the momentum diffusion downward which is not correctly described with the coarsest mesh 11×31. At the channel exit $X=A$ in Fig. 4(b) the velocity profiles show very small changes, not greater than 1% between the coarsest and finest meshes employed.

As far as the temperature profiles are concerned, Fig. 5, the largest deviations are observed at the channel inlet, in Fig. 5(a), with percent variations of about 120% between the coarsest and finest meshes employed, which turns into a smaller difference in terms of the local Nusselt number, about 50% as already seen. In contrast, Fig. 5(b), inside the channel at $X=A/2$, reveals that the discrepancies are quite negligible. Finally, at the channel exit, $X=A$ it is seen in Fig. 5(c) that the differences are slightly larger than 10%.

The numerical diffusion is more relevant at the channel inlet, which implies discrepancies between the profiles for different grid meshes, because the incoming fluid has a velocity vector not parallel to the channel walls, and then to the grid coordinates. This fact is enhanced at the channel inlet with a very coarse mesh, such as the grid with 11×31, but minor effects are present with finer meshes. At the channel exit the effect is dumped because the velocity vector is nearly parallel to the grid coordinate X.

Then, the numerical experiments indicated that a grid consisting of $n_X=71$ and $n_Y=21$ nodes inside the channel furnished satisfactory results as a compromise between the computational time and the accuracy of the code, especially in terms of average quantities for the thermal design, for an aspect ratio ranging between 5 and 15. These grid distributions guaranteed a global energy balance inside the channel with an accuracy of about 0.5%. Both the local and global mass conservation have also been checked and differences of order 10^{-4} between the inflow and outflow mass flow rates were found.

Results and Discussion

All the results presented in the next are for fluids with Prandtl numbers equal to 0.02. The wall temperatures as a function of the X coordinate are plotted in Fig. 6 for two different channel aspect ratios $A=10$ and 15 and several Rayleigh numbers. Both families of curves show increasing values with X and when $A=10$, Fig. 6(a), the increment is linear starting from about $X=0.5$. A similar trend is observed for $A=15$, Fig. 6(b), with the beginning of the linear increment at about $X=1.4$, and the sections close to the channel exit, about $X=14.7$, which show a decrease of the wall temperatures because of the diffusive effects. The percent discrepancy ratio between the maximum temperature values for the $A=10$ case is about 70% by comparing the case with $\mathrm{Ra}=10^4$ and 10^6. A similar discrepancy is obtained for the $A=15$ case.

For an intermediate value of $\mathrm{Ra}=10^4$, Fig. 7 depicts the wall temperatures along the normalized abscissa X/A for the three investigated channel aspect ratios, 5, 10, and 15. It is confirmed that

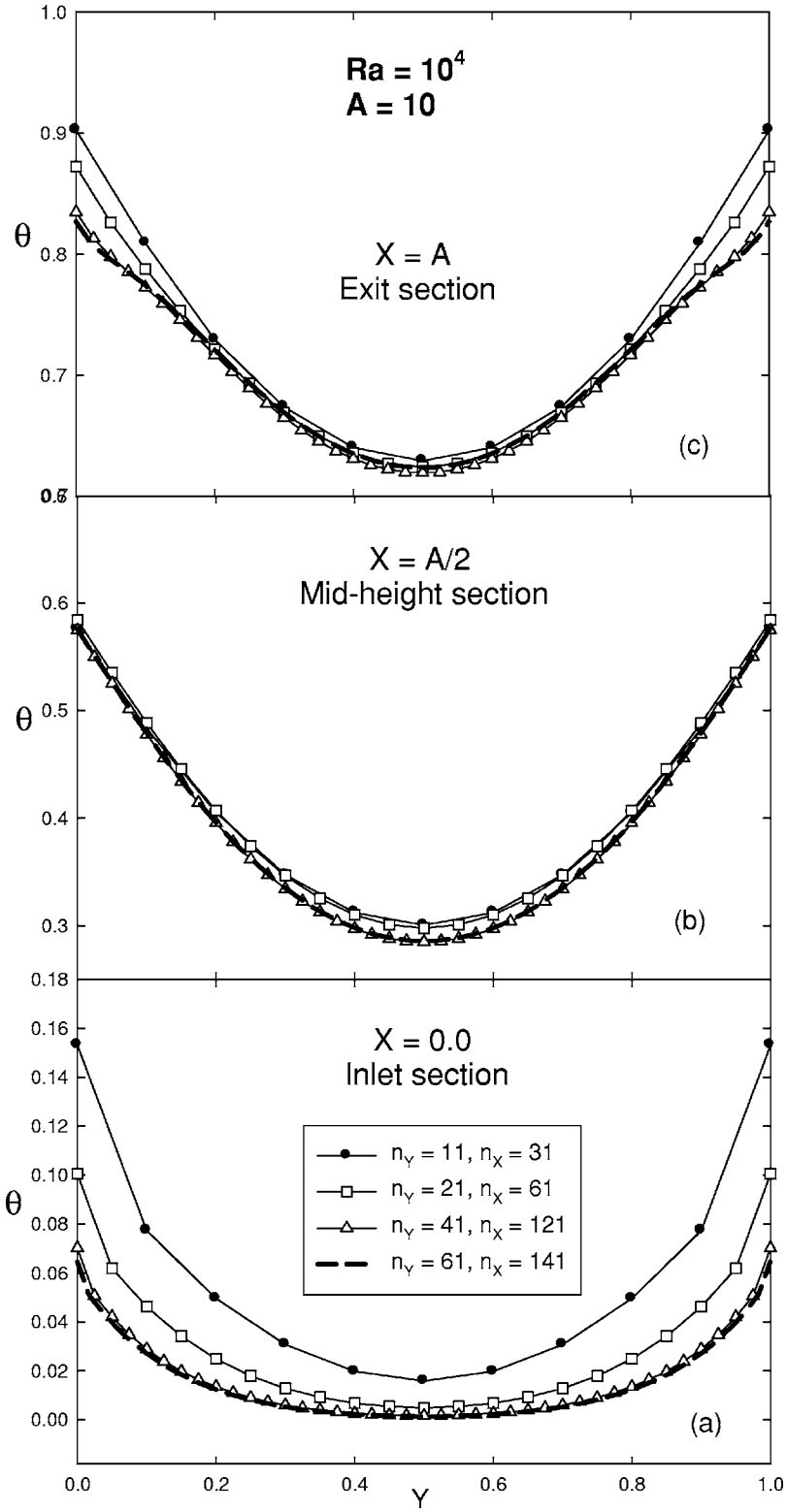

Fig. 5 Temperature profiles as a function of *Y* for different node numbers at three *X* stations: (*a*) *X*=0.0; (*b*) *X*=*A*/2; (*c*) *X*=*A*

the wall temperature values increase with A, whereas the increment of the maximum wall temperature decreases with increasing A value. It can be observed that the channel aspect ratio A can be changed, for example, by fixing b and changing L. In this case the dimensionless temperatures increase with A less than linearly. By doubling L, for the same b and Gr values, the heat rate released to the fluid is doubled. But this does not indicate a subsequent doubling of the dimensionless wall temperatures $\theta_{w,\max}$, in fact the increment is only of order 24%. When the height of the channel is three times, i.e., $A=15$, the percent increment is about 43%. This behavior is motivated by the fact that the increase of the channel height L changes the flow from developing one to a fully developed one.

Figure 8 displays the normalized velocity profiles for a channel

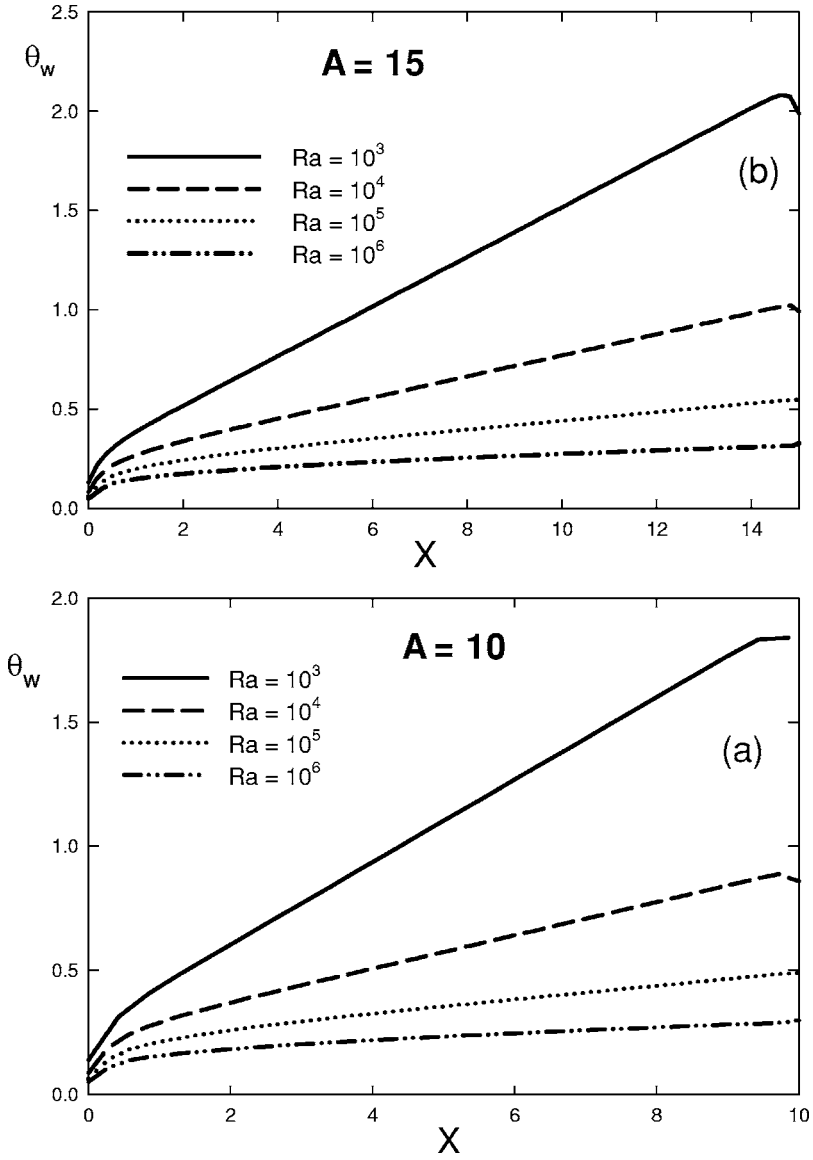

Fig. 6 Wall temperature profiles as a function of *X* for several Ra numbers: (*a*) aspect ratio *A*=10; (*b*) aspect ratio *A*=15

aspect ratio equal to 10 influenced by different Ra numbers as function of the Y coordinate at the channel inlet $X=0$ in Fig. 8(a) and at the exit $X=A$ Fig. 8(b). At the channel inlet, Fig.8(a), the velocity profiles retain the same shape, wherein the maximum values are as follows: 650 at $Ra=10^3$, 1578 at $Ra=10^4$, 3562 at $Ra=10^5$, and 7550 at $Ra=10^6$. The similar patterns are due to the low momentum diffusion downward which do not alter significantly the incoming velocity profile before entering the channel. Conversely, at the channel exit in Fig. 8(b), the velocity patterns are totally dissimilar, because the Ra number plays an important role in the development of the flow and the growth of the boundary layer. In fact, the higher the Ra number the thinner the boundary layer thickness is close to the heated walls. This pattern can be seen in terms of velocity profiles which show a parabolic profile for the case at $Ra=10^3$ and two symmetrical peaks close to the wall at $Ra=10^6$. In terms of ratio between the minimum and maximum velocity values the outcome is 0.55 at $Ra=10^6$, 0.88 at $Ra=10^5$, and 0.99 at $Ra=10^4$.

The normalized temperatures as a function of Y are reported in Fig. 9 at the channel inlet and exit for the same configurations as before in Fig. 8. The higher the Ra value the less developed the temperature profile is at the channel inlet, $X=0$ in Fig. 9(a). In

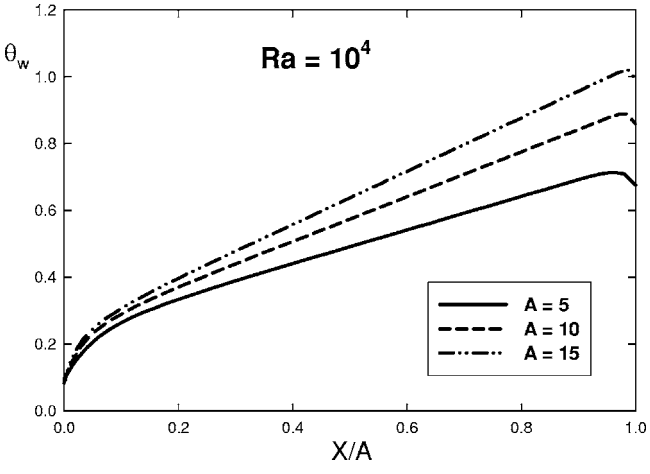

Fig. 7 Wall temperature profiles as a function of the normalized abscissa *X*/*A* for $Ra=10^4$ and several channel aspect ratios *A*

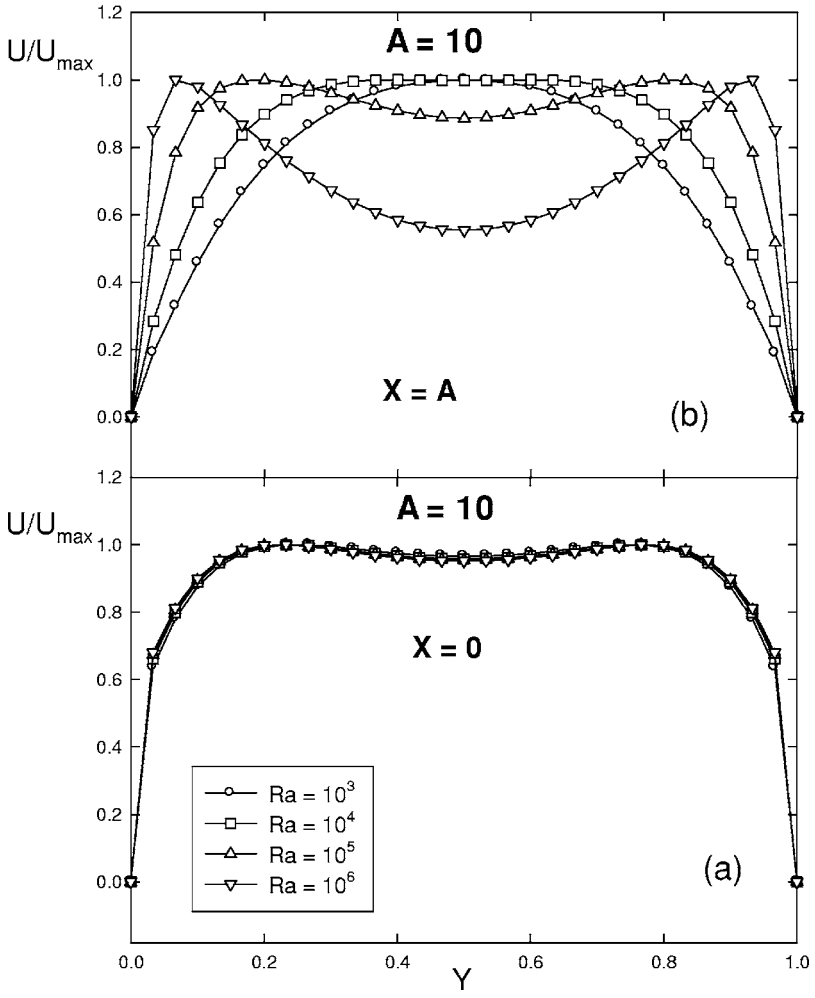

Fig. 8 Normalized velocity profiles as a function of *Y* for *A*=10 and several Ra numbers: (*a*) channel inlet; (*b*) channel exit

fact, at $Ra=10^3$ the thermal disturbance reached the centerline of the channel $Y=0.5$ and the temperature turns out to be about 18% of the wall value. This value descends to 5% when $Ra=10^4$. At $Ra=10^6$ the fluid temperature of the core zone is the same as the ambient temperature when $0.4 \leqslant Y \leqslant 0.6$. At the channel exit, $X=A$ in Fig. 9(*b*), the fluid temperature on the centerline is as low, with respect to the wall value, as the Ra value is higher. In fact, at $Ra=10^3$ the ratio is about 0.92 and at $Ra=10^6$ about 0.23.

The velocity profiles, normalized to the maximum velocity, at $Ra=10^4$ and different channel aspect ratio, $A=5$, 10, 15 are displayed in Fig. 10. It can be seen that the dependence of the shape of the profile both at the channel inlet $X=0$ and exit $X=A$ on the channel aspect ratio is very weak and the velocity profiles are pluglike shaped. The maximum values both at the channel inlet and exit are not located on the centerline. The Y location at which the maxima are attained occur at about $Y=0.2$ and 0.8 at the channel inlet, and tend to the centerline at the channel exit.

The temperature profiles, normalized to the maximum wall value, reported in Fig. 11, are for the same configuration as before. At the channel inlet the temperature profiles are very alike and they present a very small discrepancy on the centerline $Y=0.5$. At the channel exit $X=A$ the greater the A value the higher the normalized temperatures. Anyway, the values are in the 0.66-0.75 range for the investigated A.

In order to investigate the flow and thermal development inside the channel, the axial derivative of the dimensionless normalized velocity and the modified local Nusselt number, Eqs. (10) and (11) are reported. The axial derivatives of the normalized velocity U^* at the symmetry line of the channel $Y=0.5$ for an aspect ratio $A=10$ as a function of the axial coordinate X are displayed in Fig. 12. By neglecting the sections close to the inlet and exit, the fully developed flow is attained for $Ra=10^3$; in fact, when $X \geqslant 3.0$ the derivative is equal to 0.0. For $Ra=10^4$ the derivative attains values close but not equal to zero. On the contrary, higher Ra values display values of the axial derivative different from zero, indicating a still developing flow, since the length of the channel does not permit the flow to fully develop. The modified local Nusselt numbers $Nu^*(X)$ shows that when $Ra=10^3$ the fully thermally developed flow is attained for X coordinate values similiar to those of the flow development. This behavior is not observed for $Ra=10^4$ and 10^5, since the flow attains the thermal developed condition farther downstream than $Ra=10^3$. When the value of Ra is equal to 10^6 this condition is never attained inside the channel.

The temperature fields at $Ra=10^3$ and $Ra=10^6$ are displayed in Fig. 14. When $Ra=10^3$, Fig. 14(*a*), the isolines show a parabolicwise shape inside the channel displaying a behavior typical of thermally fully developed flows. The thermal field at the channel exit shows that the maximum wall temperature is located inside the channel. In addition, the fluid exiting the channel makes a single thermal plume. When $Ra=10^6$, Fig. 14(*b*), the isolines of the temperature display a different behavior. In fact, the isolines are packed to the walls, indicating a stronger temperature gradients in the transversal direction and the flow develops farther downstream than the previous configuration. Also, the boundary

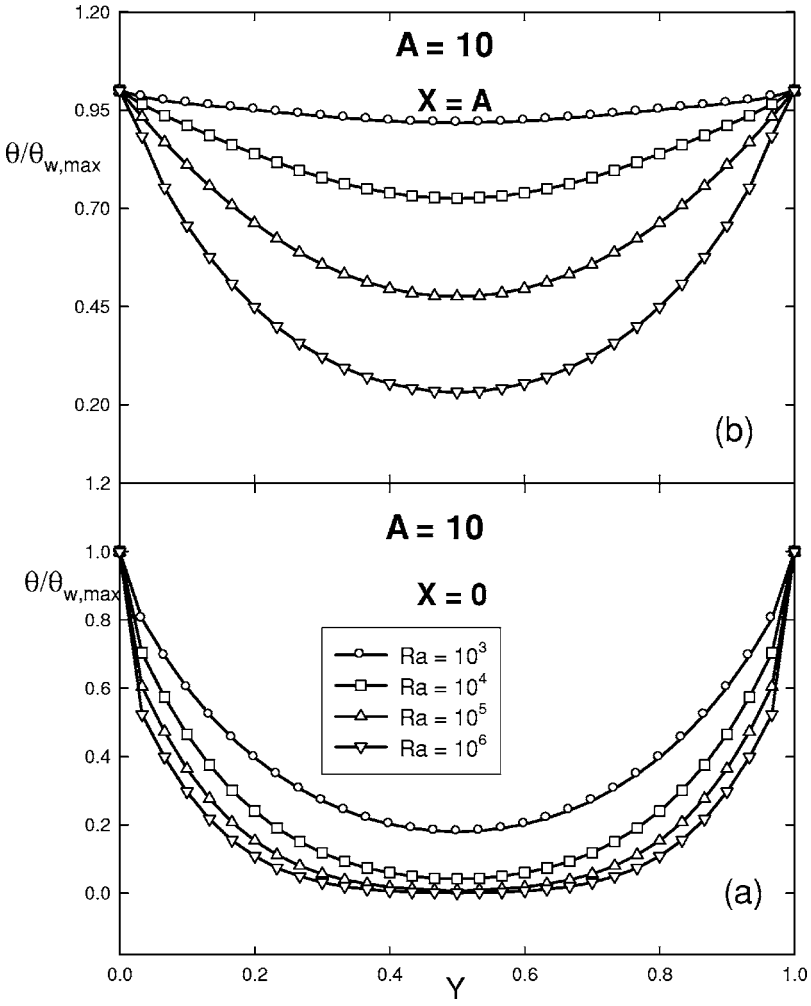

Fig. 9 Normalized temperature profiles as a function of *Y* for *A*=10 and several Ra numbers: (*a*) channel inlet; (*b*) channel exit

layer thickness is thinner than the previous configuration. In addition, the thermal plumes created by the fluid exiting the channel are two distinct.

The $\Delta\Psi$ values, which corresponds to the dimensionless flow rate, has been correlated to the Grashof number and the channel aspect ratio A by the least-squares method. The correlation equation obtained is

$$\Delta\Psi = 3.78(\mathrm{Gr})^{0.352}(A)^{0.585} \tag{14}$$

with a regression coefficient $r^2=0.998$ in the $1.98\times10^3 \leqslant \mathrm{Gr} \leqslant 5.0\times10^7$ and $5 \leqslant A \leqslant 15$ ranges.

Monomial correlation equations for the maximum wall temperature and average Nusselt number in terms of the channel Grashof Grb/L are proposed. The first equation is for the maximum wall temperature

$$\theta_{w,\max} = 19.95\left(\frac{\mathrm{Gr}}{A}\right)^{-0.280} \tag{15}$$

with an $r^2=0.987$ in the $1.32\times10^3 \leqslant \mathrm{Gr}/A \leqslant 5.0\times10^6$ range.

In Fig. 15 the maximum wall temperatures $\theta_{w,\max}$ are displayed in terms of the Gr/A together with the correlation Eq. (15) and a very good agreement is observed. The largest deviations are attained at small and large Gr/A values.

The monomial correlation equation for the average Nusselt number is

$$\mathrm{Nu} = 0.197\left(\frac{\mathrm{Gr}}{A}\right)^{0.215} \tag{16}$$

with $r^2=0.983$ in the same Gr/A range as before.

The comparison between the correlation equation Eq. (16) and the data obtained by the numerical simulation is reported in Fig. 16. To assess the validity of the numerical computations, the experimental measurements by [25] are also included for comparison. The agreement between the numerical and experimental results is excellent. Subtle mismatch occur at the lowest and highest Gr/A values utilized.

Conclusions

A numerical investigation of natural convection between isoflux heated plates for a fluid with the Prandtl number equal to 0.02 has been carried out in the present paper. After having checked the convergence of the numerical procedure, results have been presented as functions of the Rayleigh number in the range 10^3-10^6 and the channel aspect ratio $A=5$, 10, and 15. Results in terms of velocity and temperature distribution as a function of the channel spacing and of wall temperatures show that the higher the Ra number the lower the flow development, with velocity distributions which display large peaks ($\mathrm{Ra}=10^6$) close to the heated plates. The results showed that the thermal diffusion plays an important role up to $\mathrm{Ra}=10^3$ where the temperatures at the channel exit along the channel gap present a nearly uniform distribu-

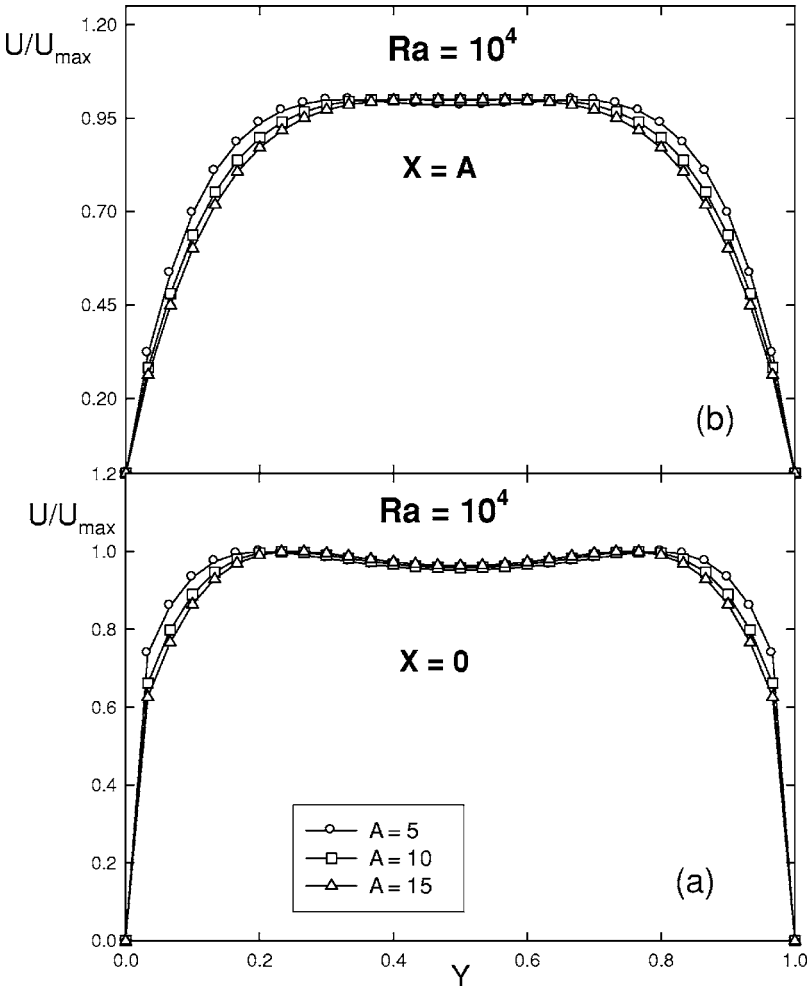

Fig. 10 Normalized velocity profiles as a function of *Y* at Ra=10^4 and several channel aspect ratio *A*: (*a*) channel inlet; (*b*) channel exit

tion with a difference between the minimum and maximum values smaller than 5%, whereas at Ra=10^6 the difference is about 80%.

The results also displayed that the flow is fully developed up to Ra=10^3 for the investigated channel aspect ratio $A=10$, whereas the thermal fully developed condition is attained inside the channel up to Ra=10^4 since the fluid presents a very high thermal diffusion compared to the momentum diffusion.

The temperature fields confirmed the findings of the temperature and velocity profiles. In addition, correlation equations for the induced flow rate, maximum wall temperatures, and average Nusselt numbers are presented as functions of the main thermal Gr or Ra numbers and geometrical A parameters. The present numerical data have been compared to experimental one [25] in terms of the average Nusselt number and the agreement has been excellent. The proposed correlation equations for the average Nusselt number, the dimensionless flow rate, and the maximum wall temperatures are monomial and valid in the whole range of the thermal and geometrical parameters, i.e., modified or channel Grashof numbers $1.32\times10^3\leqslant \mathrm{Gr}/A\leqslant 5.0\times10^6$ and aspect ratios $5\leqslant A\leqslant 15$.

Acknowledgment

This research was supported by MIUR with a PRIN 2003 grant and Seconda Università degli Studi di Napoli with a 2002 and 2003 grants.

Nomenclature

a = thermal diffusivity, m^2/s
A = channel aspect ratio, L/b
b = plate spacing, m
f = dummy function value
g = gravitational acceleration, m/s^2
Gr = Grashof number, Eq. (5)
$h(x)$ = local convective coefficient, W/m^2K
k = thermal conductivity, W/mK
L = plate height, m
Nu(x), Nu(X) = local Nusselt number, Eqs. (7) and (8)
Nu = average Nusselt number, Eq. (9)
Nu^* = modified Nusselt number, Eq. (11)
p = pressure, Pa
P = dimensionless pressure, Eq. (4)
Pr = Prandtl number, Eq. (5)
q_w = wall heat flux, W/m^2
r^2 = correlation coefficient
Ra = Rayleigh number, Eq. (5)
Ra^* = channel Rayleigh number, Ra/A
S = surface area, m^2
T = temperature, K
u, v = velocity components along x,y, m/s
U, V = dimensionless velocities, Eq. (4)
U^* = modified dimensionless velocity, Eq. (10)
x, y = Cartesian coordinates, m

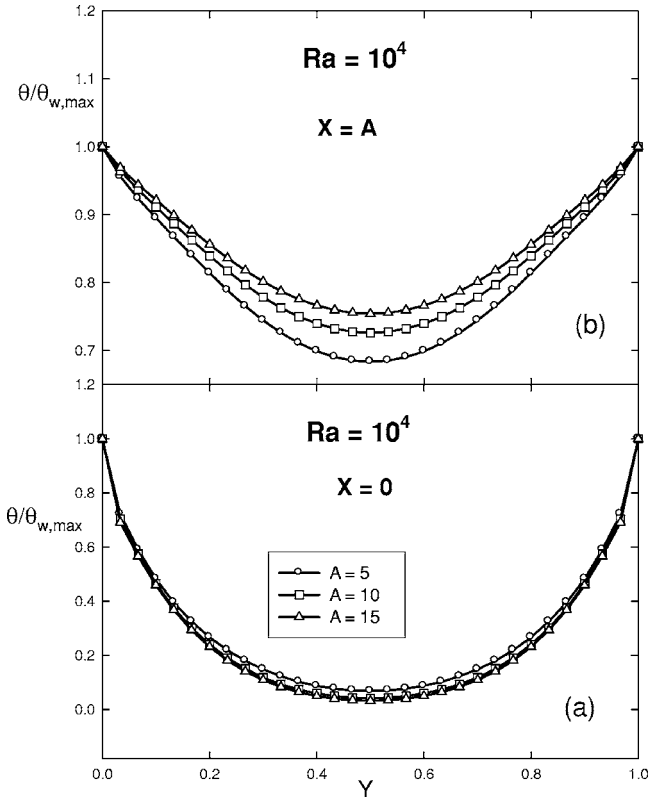

Fig. 11 Normalized temperature profiles as a function of *Y* at Ra=10^4 and several channel aspect ratio *A*: (*a*) channel inlet, (*b*) channel exit

X, Y = dimensionless coordinates, Eq. (4)

Greek Symbols

β = volumetric coefficient of expansion, 1/K
θ = dimensionless temperature, Eq. (4)
ν = kinematic viscosity, m^2/s
ψ = stream function, m^2/s
Ψ = dimensionless stream function, Eq. (4)
ω = vorticity, 1/s
Ω = dimensionless vorticity, Eq. (4)

Subscripts

1 = coarse mesh solution
2 = fine mesh solution

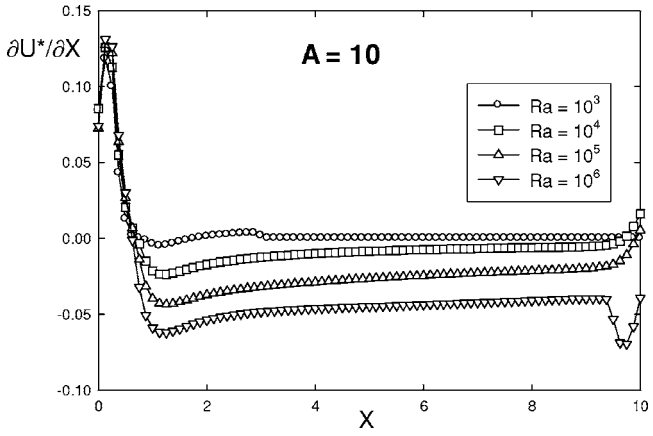

Fig. 12 Axial derivative of the normalized velocity U^* at the centerline, *Y*=0.5, as a function of *X*

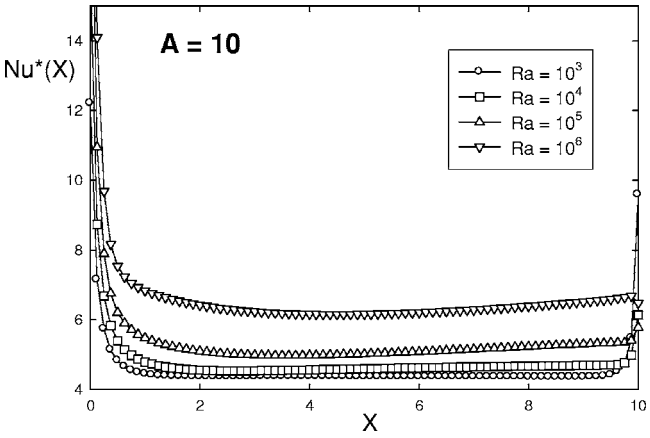

Fig. 13 Local modified Nusselt numbers as a function of the axial coordinate *X* for different Ra values

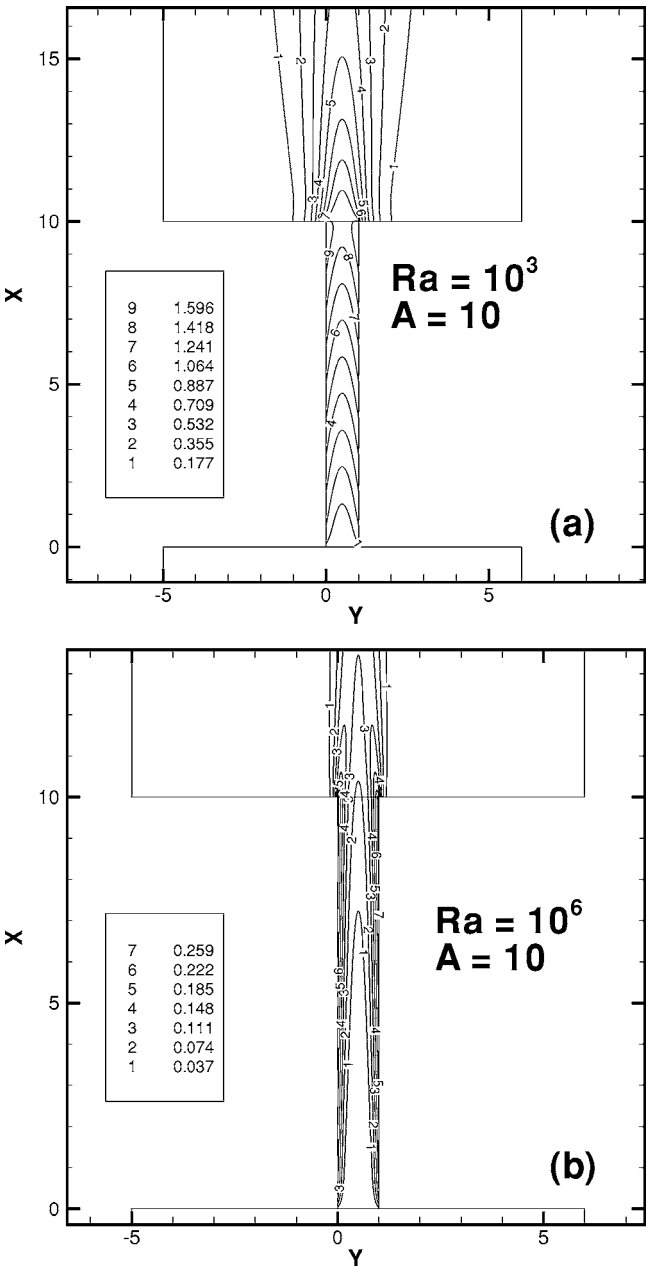

Fig. 14 Temperature isolines with *A*=10: (a) Ra=10^3, (b) Ra =10^6

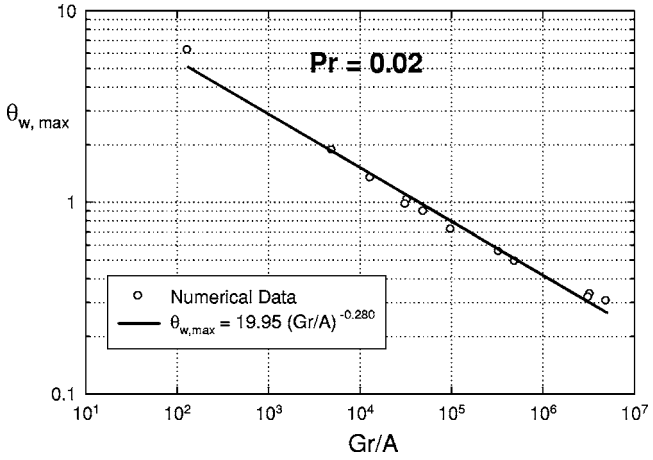

Fig. 15 Maximum wall temperatures as a function of Gr/*A* and the corresponding correlation equation

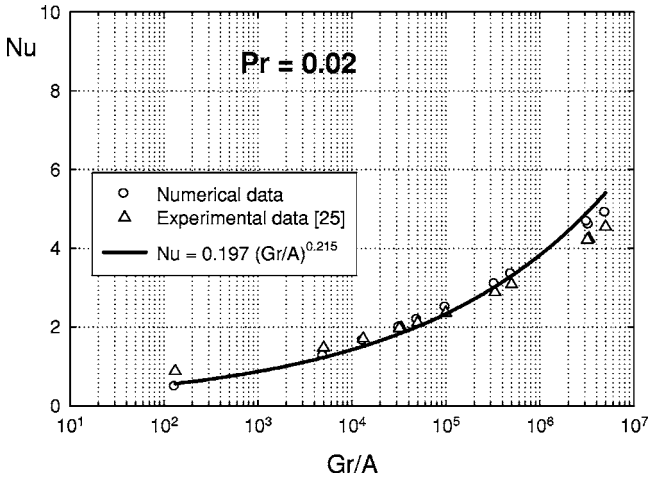

Fig. 16 Average Nusselt number as a function of Gr/*A* and the correlation equation compared with the experimental data [25]

asympt = asymptotic value
b = bulk
max = maximum value
w = wall
∞ = free stream condition

References

[1] Manca, O., Morrone, B., Nardini, S., and Naso, V., 2000, *Computational Analysis of Convection Heat Transfer*, WIT Press, Southampton, GB, Chap. 7.

[2] Kim, S. J., and Lee, S. W., 1996, *Air Cooling Technology for Electronic Equipment*. CRC Press, Boca Raton, FL.

[3] Bar-Cohen, A., and Kraus, A. D., 1998, *Advances in Thermal Modeling of Electronic Componentes and Systems*, Vol. **4**, Hemisphere, New York.

[4] Incropera, F., 1999, *Liquid Cooling of Electronic Devices by Single-Phase Convection*, Wiley, New York.

[5] Gebhart, B., Jaluria, Y., Mahajan, R., and Sammakia, B., 1988, *Buoyancy-Induced Flows and Transport*, Hemisphere, New York.

[6] Kheiriddine, A., Houla Sanda, M., Chaturvedi, S. K., and Mohieldin, T., 1997, "Numerical Prediction of Pressure Loss Coefficient and Induced Mass Flux for Laminar Natural Convective Flow in a Vertical Channel," Energy, **22**, pp. 413–423.

[7] Bar-Cohen, A., and Rohsenow, W. M., 1984, "Thermally Optimum Spacing of Vertical Natural Convection Cooled, Parallel Plates," ASME J. Heat Transfer, **106**, pp. 116–123.

[8] Leigth, J. R., 1987, "Thermal Design Considerations in Vertical-Channel Natural Convection," ASME J. Heat Transfer, **109**, pp. 249–251.

[9] Tsatsaronis, G., Moran, M., and Bejan, A., 1996, *Thermal Design and Optimization*, Wiley Interscience, New York.

[10] Bejan, A., 2000, *Shape and Structure from Engineering to Nature*, Cambridge University, Press, Cambridge, UK.

[11] Manca, O., and Nardini, S., 2001, "Thermal Design of Uniformly Heated Inclined Channels in Natural Convection With and Without Radiative Effects," Heat Transfer Eng. **22**, pp. 1–16.

[12] Carl-Olof, O., 2004, "Prediction of Nusselt Number and Flow Rate of Buoyancy Driven Flow between Vertical Parallel Plates," ASME J. Heat Transfer, **126**, pp. 97–104.

[13] Bodoia, J. R., and Osterle, J. F., 1962, "The Development of Free Convection between Heated Vertical Plates," ASME J. Heat Transfer, **84**, pp. 40–44.

[14] Campo, A., Manca, O., and Morrone, B., 2003, "Comparison of Results Between Different Computational Domains for Natural Convection between Vertical Parallel Plates," *Atti del XXI Congresso Nazionale sulla Transmissione del Calore*, Unione Italiana Termofluidodinamica, Udine, June, pp. 333–338.

[15] Chang, B., and Lin, K., 1989, "Transient Buoyancy-Induced Flow through a Heated, Vertical Channel of Finite Height," Numer. Heat Transfer, Part A, **16**, pp. 15–35.

[16] Chang, B., and Lin, K., 1990. "On the Reversed Flow and Oscillating Wake in an Asymmetrically Heated Channel," Int. J. Numer. Methods Fluids, **10**, pp. 443–459.

[17] Ramanahtan, S., and Kumar, R., 1991, "Correlations for Natural Convection between Heated Vertical Plates," ASME J. Heat Transfer, **113**, pp. 97–107.

[18] Shyy, W., Gingrich, W. K., and Gebhart, B., 1992, "Adaptive Grid Solution for Buoyancy-Induced Flow in Vertical Slots," Numer. Heat Transfer, Part A, **22**, pp. 51–70.

[19] Morrone, B., Campo, A., and Manca, O., 1997, "Optimum Plate Separation in a Vertical Parallel-Plate Channel for Natural Convection Flows: incorporation of Large Spaces at the Channel Extremes," Int. J. Heat Mass Transfer, **40**, pp. 993–1000.

[20] Morrone, B., 2001, "Natural Convection between Parallel Plates with Conjugate Conductive Effects," Numer. Heat Transfer, Part A, **40**, pp. 873–886.

[21] Andreozzi, A., Buonomo, B., and Manca, O., 2003, "Numerical Analysis of Transient Natural Convection in a Vertical Channel," *Atti del 58 Congresso Nazionale*, ATI, pp. 2315–2326.

[22] Hernandez, J., Zamora, B., and Campo, A., 1994, "On the Effect of Prandtl Number and Aspect Ratio upon Laminar Natural Convection Flows in Vertical Channels," *Heat Transfer Conference*, Int. Heat Transfer Conf., Brighton, Aug., pp. 765–770.

[23] Manca, O., and Morrone, B., 1998, "Numerical Analysis of Natural Convection in Partially Heated Vertical Channels for Different Prandtl Numbers," *Atti del XVI Congresso Nazionale sulla Trasmissione del Calore*, Unione Italiana Termfluidodinamica, Siena, June, pp. 501–512.

[24] Humphrey, W. W., and Welty, J. R., 1975, "Natural Convection with Mercury in a Uniformly Heated Vertical Channel During Unstable Laminar and Tansitional Flow," Trans. Am. Inst. Chem. Eng., **21**, pp. 268–274.

[25] Colwell, R., and Welty, J. R., 1974, "An Experimental Investigation of Natural Convection with a Low Prandtl Number Fluid in a Vertical Channel with Uniform Wall Heat Flux," ASME J. Heat Transfer, **96**, pp. 448–454.

[26] Campo, A., Manca, O., and Morrone, B., 1999, "Analysis of Partially Heated Vertical Parallel Plates in Natural Convective Cooling," Numer. Heat Transfer, Part A, **36**, pp. 129–151.

[27] Bejan, A., 2004, *Convection Heat Transfer*, 3rd ed., Wiley, New York.

[28] Roache, J. P., 1972, *Computational Fluid Dynamics*, Hermosa, Albuquerque, NM.

[29] W., S., 1994, *Computational Modeling for Fluid Flow and Interfacial Transport*, Elsevier, NY.

[30] Papadakis, G., and Bergeles, G., 1995, "A Locally Modified Second Order Upwind Scheme for Convection Terms Discretization," Int. J. Numer. Methods Heat Fluid Flow **5**, pp. 49–62.

[31] Patankar, S., 1980, *Numerical Heat Transfer and Fluid Flow*, Hemisphere, Washington, D.C.

[32] Roache, J. P., 1998, *Verification and Validation in Computational Science and Engineering*, Hermosa, Albuquerque, NM.

A. A. Rashaida
e-mail: ali_rashaida@hotmail.com

D. J. Bergstrom

Department of Mechanical Engineering,
University of Saskatchewan,
57 Campus Drive,
Saskatoon, SK S7N 5A9, Canada

R. J. Sumner
Department of Chemical Engineering,
University of Saskatchewan,
Research Annex,
57 Campus Drive,
Saskatoon, SK S7N 5A9, Canada

Mass Transfer From a Rotating Disk to a Bingham Fluid

In the present investigation, an analytical numerical solution is presented for the mass transfer from a rotating disk to a Bingham fluid for the case of laminar boundary layer flow. The analytical approach includes the coupled effects of steady disk rotation and non-Newtonian fluid properties on the mass transfer rate. A dimensionless expression for the wall mass transfer rate based on the Sherwood number, Sh, is obtained in terms of the system parameters (Reynolds number, Re_p*, and Schmidt number,* Sc_p*) which depend on the dimensionless yield stress or Bingham number,* B_y*. The analytical relation indicates that an increase in* B_y *(up to the limit* $B_y \leqslant 1$*) leads to a slight increase in the wall mass transfer rate, and thereafter, for* $B_y > 1$*, the mass transfer rate is reduced.*
[DOI: 10.1115/1.2065607]

1 Introduction

The rotating disk is a popular geometry for studying different fluids, both because of its simplicity and the fact that it represents a classical fluid dynamics problem. A review of mass transfer from rotating disks to Newtonian fluids can be found in Levich [1]. This flow paradigm has also been used to investigate the momentum [2,3] and heat transfer [4] characteristics of non-Newtonian fluids, while relatively less work has been done in relation to mass transfer. Hansford and Litt [5] reported theoretical and experimental studies of mass transfer from a rotating disk for a solute diffusing through power-law fluids. Mishra and Singh [6] extended the work of Hansford and Litt [5] and also compared their results to mass transfer from a flat plate with a non-Newtonian fluid. Greif and Paterson [7] obtained a more accurate prediction for mass transfer from a rotating disk in a power-law fluid by including convective transport in the radial direction. Kawase and Ulbrecht [4] have used power-law velocity profiles in heat and mass transfer analysis for non-Newtonian fluids surrounding rotating bodies and within tubes.

In the previous investigations noted above, the fluid of interest was restricted to either shear thinning or shear thickening fluids (power-law fluids). To the authors' knowledge, no study has yet considered mass transfer for a disk rotating in a Bingham fluid, even though many industrial applications involve slurries or suspensions which exhibit yield stresses. Bingham fluids, unlike Newtonian fluids, can transmit a shear stress in the absence of a velocity gradient. The special flow behavior of a Bingham fluid will also influence the overall mass transfer rates.

The purpose of this study is to present an analytical solution for mass transfer in steady laminar flow of a Bingham fluid over a rotating disk. In this work we extend our previous numerical study [2] of the velocity field to examine the coupled effects of steady disk rotation and a Bingham fluid rheology on the mass transfer rates. Application of the present analysis is limited to flows where the shear stress exceeds the yield stress in the region adjacent to the disk surface. Typically the shear stresses have appreciable values in this region. We first review the concentration profile for a Newtonian fluid, before proceeding to extend the analysis to the case of a Bingham fluid.

Contributed by the Applied Mechanics Division of ASME for publication in the JOURNAL OF APPLIED MECHANICS. Manuscript received June 11, 2005; final manuscript received June 14, 2005. Review conducted by D. A. Siginer. Discussion on the paper should be addressed to the Editor, Prof. Robert M. McMeeking, Journal of Applied Mechanics, Department of Mechanical and Environmental Engineering, University of California—Santa Barbara, Santa Barbara, CA 93106-5070, and will be accepted until four months after final publication in the paper itself in the ASME JOURNAL OF APPLIED MECHANICS.

2 Theoretical Formulation

2.1 Analysis for Newtonian Fluids. We consider laminar flow of a disk rotating in an infinite Newtonian fluid with mass transfer occurring between the surface of the disk and the fluid. The disk rotates about the z axis at a constant angular velocity Ω, and the origin is located where the axis of rotation intersects the disk. Let v_r, v_ϕ, and v_z represent the physical components of the velocity vector in cylindrical coordinates, and ρ and v be the density and kinematic viscosity, respectively. The relevant flow Reynolds number becomes, $\mathrm{Re}=\Omega r^2/v$. It is also assumed that the flow is steady and rotationally symmetric, so that $\partial(\,)/\partial t = \partial(\,)/\partial\phi = 0$ for all dependent variables. The flow field is fully described by the continuity and Navier–Stokes equations. These are given in many standard fluids texts and will not be repeated here. The transport of a species in a flowing liquid is governed by convective and diffusion. For laminar flow, the steady state convection diffusion equation in cylindrical coordinates takes the following form:

$$v_r\frac{\partial c}{\partial r}+\frac{v_\phi}{r}\frac{\partial c}{\partial \phi}+v_z\frac{\partial c}{\partial z}=D\left[\frac{\partial^2 c}{\partial r^2}+\frac{1}{r}\frac{\partial c}{\partial r}+\frac{1}{r^2}\frac{\partial^2 c}{\partial \phi^2}+\frac{\partial^2 c}{\partial z^2}\right] \quad (1)$$

where D is the diffusivity and c is the concentration field of the diffusing species. The relevant boundary conditions are given by

$$c = c_0 \quad \text{at } z = 0$$

$$c \to c_\infty \quad \text{at } z \to \infty \quad (2)$$

Following von Karman (see Ref. [2]), a similarity variable ζ (dimensionless normal distance from the disk) is introduced, along with the following dimensionless representations for the radial, tangential and axial velocity components:

$$\zeta = z\left(\frac{\Omega}{v}\right)^{1/2} \quad (3a)$$

$$F(\zeta)=\frac{v_r}{\Omega r} \quad (3b)$$

$$G(\zeta)=\frac{v_\phi}{\Omega r} \quad (3c)$$

$$H(\zeta) = \frac{v_z}{(\Omega v)^{1/2}} \tag{3d}$$

In addition, a dimensionless concentration may be defined by

$$\Phi(\zeta) = \frac{(c - c_\infty)}{(c_0 - c_\infty)} \tag{4}$$

The approach above assumes that the functions F, G, and H depend only on z and do not depend on r; in particular the flow towards the disk, v_z, is a function of z only and is independent of r. Throughout the fluid the concentration, c, is equal to the bulk value except for a thin layer (the diffusion layer) near the disk. Within the momentum boundary layer, the radial and tangential velocity components are both nonzero, while outside of this region purely axial motion exists. For boundary layer flow, the rate of change of a scalar in the direction normal to the disk is much greater than its rate of change in the radial direction. Thus, the concentration may be approximated as a function of the normal distance from the disk surface, i.e., $c=c(z)$, and not a function of either r or ϕ [4,5]. Accordingly, Eq. (1) reduces to the following ordinary differential equation:

$$v_z \frac{dc}{dz} = D \frac{d^2 c}{dz^2} \tag{5}$$

Introducing the transformations given by Eqs. (3) and (4) into the diffusion Eq. (5), we obtain

$$\Phi'' = ScH\Phi' \tag{6}$$

where the prime denotes differentiation with respect to ζ and $Sc = v/D$ is the Schmidt number of the fluid. From the definition of Φ as given by Eq. (4), the boundary conditions become

$$\Phi = 1 \quad \text{at } \zeta = 0$$

$$\Phi \to 0 \quad \text{at } \zeta \to \infty \tag{7}$$

Following Hansford and Litt [5] we assume high Schmidt number flow, and take $H=-F'(0)\zeta^2$, where $F'(0)$ is the dimensionless radial velocity gradient at the surface of the disk. The physical implication of this approximation is that the mass transfer occurs in a narrow region next to the surface in which the radial velocity profile can be approximated by a linear relation based on its gradient at the surface. Using this result for H, the diffusion equation becomes

$$\Phi'' = -ScF'(0)\zeta^2\Phi' \tag{8}$$

An exact solution of this mass transfer equation under steady state conditions was given by Hansford and Litt [5] as

$$\Phi = 1 - \frac{\Gamma\left(\frac{1}{3}, \frac{F'(0)Sc\zeta^3}{3}\right)}{\Gamma\left(\frac{1}{3}\right)} \tag{9}$$

where $\Gamma(n)$ is the complete gamma function and $\Gamma(n,a)$ is the incomplete gamma function.

The convective mass transfer rate of species A from a rotating disk to the surrounding fluid is given by

$$J_A = K_c(c_0 - c_\infty) \tag{10}$$

K_c is the convective mass transfer coefficient. Since the mass transfer at the surface is entirely the result of molecular diffusion, it can also be described by

$$J_A = -D\left(\frac{dc}{dz}\right)_{z=0} \tag{11}$$

Using the definition of the similarity variable, Eq. (3a), and the dimensionless concentration, Eq. (4), Eq. (11) becomes

$$J_A = 0.776F'(0)^{1/3}(c_0 - c_\infty)\Omega^{1/2}D^{2/3}v^{-1/6} \tag{12}$$

Finally, the mass transfer coefficient can be determined by equating Eq. (12) and Eq. (10) to obtain

$$K_c = 0.776F'(0)^{1/3}\Omega^{1/2}D^{2/3}v^{-1/6} \tag{13}$$

The corresponding expression for the local Sherwood number $Sh=K_c r/D$ becomes

$$Sh = A\,\mathrm{Re}^{1/2}\,Sc^{1/3} \tag{14}$$

where the coefficient A is given by

$$A = 0.776F'(0)^{1/3} \tag{15}$$

From the Newtonian solution, $F'(0)=0.51$ and Eq. (14) reduces to

$$Sh = 0.62\,\mathrm{Re}^{1/2}\,Sc^{1/3} \tag{16}$$

2.2 Analysis for Non-Newtonian Fluids. Now consider the laminar flow over a disk rotating in a non-Newtonian fluid of infinite extent. The non-Newtonian fluid is assumed to be characterized by the Bingham plastic model given by the following expression:

$$\begin{cases} \tau_{ij} = \left(\dfrac{\tau_y}{|\dot{\gamma}|} + \mu_p\right) e_{ij} = \eta e_{ij} & \text{for } \tau \geqslant \tau_y \\ e_{ij} = 0 & \text{for } \tau < \tau_y \end{cases} \tag{17}$$

where μ_p and τ_y are the plastic viscosity and yield stress, respectively, and e_{ij} is the rate-of-deformation tensor, defined in terms of the velocity field u_i by

$$e_{ij} = \frac{\partial u_i}{\partial x_j} + \frac{\partial u_j}{\partial x_i} \tag{18}$$

The magnitudes of the shear stress and deformation rate are defined, respectively, as

$$|\tau| = \sqrt{\left|\frac{1}{2}\tau_{ij}\tau_{ij}\right|} \tag{19a}$$

$$|\dot{\gamma}| = \sqrt{\left|\frac{1}{2}e_{ij}e_{ij}\right|} \tag{19b}$$

using the summation convention for repeated indices. Equation (17) implies that the rheological behavior of a Bingham fluid is characterized by two different flow regimes: if $\tau < \tau_y$ the material behaves as a rigid solid, if $\tau \geqslant \tau_y$, the material flows with an apparent viscosity η.

As shown in Ref. [2], assuming boundary layer flow and rotational symmetry, the apparent viscosity, η, will take the following form:

$$\eta = \left[\mu_p + \frac{\tau_y}{\sqrt{\left(\dfrac{\partial v_r}{\partial z}\right)^2 + \left(\dfrac{\partial v_\phi}{\partial z}\right)^2}}\right] \tag{20}$$

For high Schmidt number convective mass transfer between a Bingham plastic fluid and a rotating disk, the diffusion boundary layer thickness, δ_m, is much smaller than the momentum boundary layer thickness δ. Our mass transfer solution will neglect any unsheared region which might exist outside the boundary layer region, and instead focus on the sheared region which flows with apparent viscosity, η. Calculations based on the numerical solution indicate that for practical rotation rates, the magnitude of the shear stress always exceeds the yield stress in this region.

Rashaida et al. [2] gave the following form for the apparent viscosity at the wall:

$$\eta = \mu_p \left[1 + \frac{2B_y}{[F'(0)^2 + G'(0)^2]^{1/2}} \right] \tag{21}$$

where $F'(0)$ and $G'(0)$ are the gradient of the dimensionless radial and tangential velocity functions at the disk surface, respectively, and B_y is a Bingham number defined as

$$B_y = \frac{\tau_y}{5\rho\Omega r(\upsilon\Omega)^{1/2}} \tag{22}$$

where $\upsilon = \mu_p/\rho$ is the kinematic viscosity of the plastic fluid. The Bingham number is a measure of the ratio of the yield stress to the viscous stress.

Following the approach of Mishra and Singh [6] for the case of a power-law fluid, we can define a shear viscosity at the wall, which is equivalent to the apparent viscosity evaluated at the wall. The apparent viscosity is employed to redefine the Reynolds and Schmidt numbers to take into account the shear dependence of the apparent viscosity, i.e.

$$\mathrm{Re}_p = \frac{\rho\Omega r^2}{\mu_p \left[1 + \dfrac{2B_y}{[F'(0)^2 + G'(0)^2]^{1/2}} \right]} \tag{23}$$

and

$$Sc_p = \frac{\mu_p}{\rho D} \left[1 + \frac{2B_y}{[F'(0)^2 + G'(0)^2]^{1/2}} \right] \tag{24}$$

The mass transfer for a rotating disk in a Bingham plastic fluid will now be discussed based on the appropriate expressions for the apparent viscosity and Reynolds and Schmidt numbers. The mass transfer flux developed for a Newtonian fluid, Eq. (12), can be transformed to represent the mass transfer flux in a Bingham fluid by substituting an appropriate function for the material property υ. Following the approach of Matsumoto et al. [8] for the case of a film on a spinning disk, we substitute $\upsilon = \mu_p/\rho$ to obtain

$$J_A = \frac{0.776F'(0)^{1/3}(c_0 - c_\infty)D^{2/3}\Omega^{1/2}}{(\mu_p/\rho)^{1/6}} \tag{25}$$

The plastic viscosity, μ_p, and the diffusion coefficient, D, can be expressed in terms of the dimensionless parameters Re_p [Eq. (23)] and Sc_p [Eq. (24)], respectively. After substituting Re_p and Sc_p into Eq. (25) and then proceeding with a similar analysis to that adopted for the Newtonian case, we obtain the following expression for the Sherwood number:

$$Sh = \frac{J_A r}{D(c_0 - c_\infty)} = A\,\mathrm{Re}_p^{1/2} Sc_p^{1/3} \tag{26}$$

where

$$A = \frac{0.776F'(0)^{1/3}}{\left[\dfrac{\sqrt{F'(0)^2 + G'(0)^2}}{\sqrt{F'(0)^2 + G'(0)^2 + 2B_y}} \right]^{1/6}} \tag{27}$$

For the Reynolds and Schmidt number expressions adopted, we obtain the same indices as those for a Newtonian fluid. Equation (26) gives the mass transfer rate (in terms of Sherwood number) as a function of Bingham number, including the specific case of $B_y = 0$ for a Newtonian fluid.

3 Results and Discussion

A dimensionless expression for the mass transfer from the surface of a rotating disk has been derived in terms of the system parameters. This expression relates the Sherwood number, Sh, to the Reynolds number Re_p, the Schmidt number Sc_p, and the Bingham number B_y. The present result is expected to be valid as long as the flow in the boundary layer is laminar and the yield stress is exceeded.

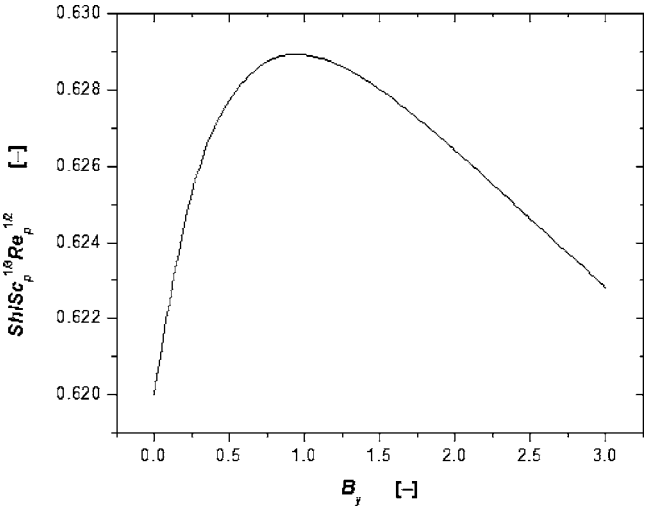

Fig. 1 Effect of Bingham flow behavior on local wall mass transfer rate for a rotating disk

The effect of the dimensionless yield stress or Bingham number on the mass transfer is shown in Fig. 1 in terms of the variation of function A given by Eq. (27) with Bingham number, B_y. The value of A has been calculated for a range of B_y values using the values of $F'(0)$ and $G'(0)$ (the gradient of the two velocity components at the wall) obtained by Rashaida et al. [2]. The Newtonian case corresponds to $B_y = 0$. Figure 1 indicates that increasing the yield stress of the material increases the mass transfer rates for $B_y \leqslant 1$; beyond that, i.e., for $B_y > 1$, the mass transfer begins to decrease. Evidently, the wall mass transfer rate is affected by the complex rheology of the Bingham fluid. However, the overall variation of the coefficient A with B_y is very small: for the range of B_y considered, the variation is less than 2%.

4 Conclusions

An analytical model has been developed to represent the wall mass transfer rate in a non-Newtonian Bingham plastic fluid. The approximate analytical solution is evaluated using the numerical results of Rashaida et al. [2] for the velocity field. It was determined that as the Bingham number increases from 0 to 1, the mass transfer rate increases slightly. Thereafter, when the Bingham number increases beyond 1, the mass transfer rate begins to gradually decrease.

Nomenclature

A = defined by Eqs. (15) and (27)
B_y = Bingham number defined by Eq. (22)
c = concentration at any point in the fluid, kg/m^3
c_0 = concentration at surface, kg/m^3
D = diffusivity coefficient, m^2/s
F, G, H = dimensionless velocities in r, ϕ and z direction
J_A = mass flux of component A, kg/m^2 s
k_c = mass transfer coefficient, m/s
r = radial distance, m
Re_p = Reynolds number based on apparent viscosity defined by Eq. (23)
Sc = general Schmidt number
Sc_p = Schmidt number based on apparent viscosity defined by Eq. (24)
Sh = Sherwood number defined by Eqs. (14) and (26)
$\upsilon_r, \upsilon_\phi, \upsilon_z$ = radial, tangential and axial velocity, m/s
z = axial coordinate, m

Greek symbols

δ = thickness of momentum boundary layer, m
δ_m = thickness of diffusion boundary layer, m
Φ = dimensionless concentration defined by Eq. (4)
ϕ = tangential coordinate
Ω = angular velocity, s^{-1}
$\Gamma(n), \Gamma(n,x)$ = gamma and incomplete gamma function
υ = kinematic viscosity, m^2/s
μ_p = plastic viscosity, Pa s
η = apparent viscosity defined by Eq. (21), Pa s
ρ = density of the fluid, kg/m^3
ζ = dimensionless axial coordinate defined by Eq. (3*a*)

Subscripts

p = plastic
r = radial
z = normal
ϕ = angular
0 = at surface
∞ = in bulk of solution

References

[1] Levich, V. G., 1962, *Physico-Chemical Hydro-dynamics*, Prentice–Hall, Englewood Cliffs, NJ, p. 60.
[2] Rashaida, A., Bergstrom, D., and Sumner, R., "Flow of a Bingham Fluid Over a Rotating Disk," (in preparation).
[3] Andersson, H., De Korte, E., and Meland, R., 2001, "Flow of a Power-Law Fluid Over a Rotating Disk Revisited," Fluid Dyn. Res., **28**, pp. 75–88.
[4] Kawase, Y., and Ulbrecht, J., 1983, "Heat and Mass Transfer in Non-Newtonian Fluid Flow With Power Function Velocity Profiles," Can. J. Chem. Eng., **61**, pp. 791–798.
[5] Hansford, G., and Litt, M., 1968, "Mass Transport From a Rotating Disk Into Power-Law Liquids," Chem. Eng. Sci., **23**, pp. 849–864.
[6] Mishra, P., and Singh, P., 1978, "Mass Transfer From Rotating Disk to Non-Newtonian Fluids," Chem. Eng. Sci. **33**, pp. 1463–1470.
[7] Greif, R., and Paterson, J., 1973, "Mass Transfer to a Rotating Disk in a Non-Newtonian Fluid," Phys. Fluids, **16**, pp. 1816-1817.
[8] Matsumoto, S., and Takashima, Y., 1982, "Film Thickness of a Bingham Liquid on a Rotating Disk," Ind. Eng. Chem. Fundam., **21**, pp. 198–202.

Modeling of Dissolved Gas Effect on Liquid Transients

Mohand Kessal[1]
Département Transport et Equipement Pétrolier,
Faculté des Hydrocarbures et de la Chimie,
Universite de Boumerdès,
Boumerdès 35000, Algeria
e-mail: m.kessal@voilà.fr

Rachid Bennacer
Laboratoire Matériaux et Sciences des Constructions,
Université Cergy-Pontoise,
Paris, France

Transient cavitation of a homogeneous gas-liquid mixture flow is modeled for an elastic pipeline by using the classical conservation equations of each phase, which are, later on, written in dimensionless form. The later is resolved by a second order finite difference scheme for which a flux corrective transport algorithm is added as an additional step, in order to accomplish a suitable treatment of the shock problem. The flow gives rise to a localized vapor+gas cavity for which time and space expansion is calculated from the corresponding compatibility relation, continuity equation and ideal gas law. Also, effect of the degassing phenomenon, on this cavity and on the dynamic parameters, is reproduced from a macroscopic bubble growth model. Obtained results are discussed and compared with ones given by experimental data. [DOI: 10.1115/1.1992513]

Introduction

In order to improve the reliability and the performance of hydraulic systems it is important to be able to predict the onset and the degree of cavitation, during transient flows. Several authors have considered some particular aspects of this phenomenon. Bergant and Simpson [1] have presented a column separation study with a retrospect of different cavity models, followed by a new cavitating region model. Obtained results are in good agreement with experiments. Knowing that a column separation can occur at some points of the system, which leads to cavitiy formation, they have explained in their bibliography three cavity models: the discrete vapor cavity model posed by Streeter [2] and used by Wylie and Streeter [3] and Bergant and Simpson [4]; the interface vapor cavitation model established by Streeter a[5] and used by Bergant and Simpson [6]; the discrete gas cavity model established by Provoost and Wylie [7] and used by Barbero and Coaponi [8] and Bergant and Simpson [4]. In these works, transient cavitation was only considered, i.e., without disolved gas release. In the above models the cavity, induced by the column separation, was calculated by the use of finite difference forms of cavity continuity equation.

In his study on transient pipeline liquids flows, Lee [9] has analyzed effects of air presence and dissolved gas on valves. Basing his investigation on different valve's comportment (i.e., with different characteristics) he has recommended a choice of valve type.

Shu [10] has presented a new two-phase homogeneous equilibrium vaporous cavitation model which was compared with a conventional column separation model. Some serious deficiencies of the later have been avoided by expressing the compatibility equations in terms of pressure (p), ratio between volume flux (Q) and void fraction (α) and mean density time evolution. Good agreement has been found in comparison with experimental data.

Rewriting the classical four equation set of equal velocities homogeneous model, in dimensionless form and all the flow parameters as function of pressure, Kessal and Amaouche [11]) have introduced a new cavity modeling based on continuous medium principle. This technique allows to avoid, in the calculation, the classical procedure of the cavity volume which consumes generally a lot of computational time, especially in the case of transient cavitating flow in pipeline networks.

On the other hand, it is known that, if the pressure drops below its saturated vapor pressure value, a degassing process is observed which leads to gas bubble growth. During the column separation a quantity of gas release will be added to the formed vapor in the cavity. When the pressure increases, these bubbles are not dissolved again as rapidly as the water vapor turns back to liquid. Some authors, among them Kranenburg [12], Wiggert and Sundquist [13] and Kessal and Amaouche [11], have considered this physical phenomenon and approximate models have been obtained. These models, which are almost based on a correlation giving the quantity of gas in a bubble, did not consider the time radius bubble evolution and the parameters affecting the gaseous diffusion. They did the phenomenon depending principally on gas saturated and liquid pressures only. The first author, which has explained and applied this correlation, has performed applications on gaseous and vaporous cavitation with column separation by considering the effect of a supposed number of bubble present in the cavitating flow region. Time cavity volumes are drawn as function of this number. Basing their model on this correlation, Wiggert and Sundquist [13] have introduced, in place of bubble number and others diffusion parameters, a constant with different values depending on initial gas concentration. Considering the gas release phenomena, Kessal and Amaouche [11] have obtained a degassing coefficient which takes into account the fluids properties and the pipe characteristics. However, this model is based on the Wiggert and Sundquist [13] model.

The aim of this paper is to present some applications of a mathematical model, describing a homogeneous transient two-phase flow in a pipeline, taking into account the gas release phenomena and the column separation. The former process, based on the continuity and diffusion equations across the bubble interface, allows calculating the gas rate as function of mixture and bubble interface physical characteristics. The later, which can be conceived as a local phenomenon, is modeled by a new calculation technique based on the corresponding compatibility equation, the continuity equation of the cavity and the gas ideal law. Therefore, the effect of all the flow parameters is considered. Emphasis is also placed on numerical methods adopted and applied to column separation occurring near an instantaneous valve closed.

Theoretical Modeling

Our model considers a homogeneous one-dimensional approach of the liquid-vapor+gas mixture flow, in which the vapor pressure and gas temperature in the cavities can be assumed to be constant. In this model, the two components are treated as a mixture having

[1]Author to whom Correspondence should be addressed.

Contributed by the Applied Mechanics Division of ASME for publication in the JOURNAL OF APPLIED MECHANICS. Manuscript received July 14, 2004; final manuscript received June 4, 2005. Assoc. Editor: D. Siginer. Discussion on the paper should be addressed to the Editor Prof. Robert M. McMeeking, Journal of Applied Mechanics, Department of Mechanical and Environmental Engineering, University of California-Santa Barbara, Santa Barbara, CA 93106-5070, and will be accepted until four months after final publication in the paper itself in the ASME JOURNAL OF APPLIED MECHANICS.

cross sectional duct average flow parameters. So, considering the formulation of Kessal and Amaouche [11], the mass and momentum equations of each component are written in the following conservative form:

$$\frac{\partial \zeta^{\bullet}}{\partial t} + \frac{\partial}{\partial x}(\zeta^{\bullet} V) = 0 \tag{1}$$

$$\frac{\partial}{\partial t}(\zeta^{\bullet} V) + \frac{\partial}{\partial x}(\zeta^{\bullet} V^2 + P') = -\zeta^{\bullet} g \sin\theta - 2C_f \frac{\zeta^{\bullet}}{D_h}|V|V \tag{2}$$

where

$$P' = \frac{p - p_o}{\rho_o}\left(1 - \frac{(p - p_o)D_o}{2eE}\right)^{-1} \tag{3a}$$

or

$$P' = \frac{(P^{\bullet} - 1)Pr\,o}{1 - (P^{\bullet} - 1)Dre} \tag{3b}$$

where

$$\varsigma^{\bullet} = \frac{[1 + Eo^{\bullet}(P^{\bullet} - 1)]P^{\bullet}}{\beta_o + \beta_1 P^{\bullet}} \tag{4}$$

In the previous equations the fluid and pipe physical characteristics are grouped in the following suitable form:

$$\beta_o = \frac{\in_o}{G_r}\left[1 - Eo\ell - \frac{\rho_{vo}}{\rho_{\ell o}}\right]$$

$$\beta_1 = \frac{\in_o}{G_r}\left[Eo\ell - \frac{\rho_{go}}{\rho_{\ell o}}\right] + \frac{\rho_o}{\rho_{\ell o}}$$

$$Eo^{\bullet} = Eo\ell + \frac{D_o}{e}Eos \tag{5}$$

$$Eos = \frac{p_o - p_v}{E}$$

$$Eo\ell = K_{\ell}^{-1}(p - p_v)$$

$$G_r = \exp\left(-\int_0^t \frac{\Gamma_g}{\rho_g \in}\right)$$

G_r is a degassing coefficient and Γ_g the gas release mass rate per unit volume of the mixture (Appendix A).

$P^{\bullet}$ is the equilibrium equation of the bubble in which the dynamics effects are neglected

$$P^{\bullet} = \frac{p - p_v + \dfrac{2\sigma}{R}}{p_o - p_v + \dfrac{2\sigma}{R_o}} \tag{6a}$$

or

$$P^{\bullet} = \frac{p_g}{p_{go}} = \frac{\rho_g}{\rho_{go}} \tag{6b}$$

The void fraction α can be expressed as function of P^* (or pressure p) as

$$\alpha = \frac{\rho_{\ell o}(1 + Eo\ell(P^{\bullet} - 1))}{\rho_{\ell o}(1 + Eo\ell(P^{\bullet} - 1)) - \rho_{vo} - \rho_{go}P^{\bullet} + \dfrac{\rho_o}{\in_o}P^{\bullet}G_r} \tag{7}$$

In order to calculate the pressure p in all points of the pipeline from equation set (1) and (2), where the unknown are $\varsigma^{\bullet}$ and V, $P^{\bullet}$ must be expressed in function of $\varsigma^{\bullet}$. Then from Eq. (4), expression $P^{\bullet} = P^{\bullet}(\varsigma^{\bullet})$ constitutes a second order equation

$$aP^{\bullet 2} + bP^{\bullet} + c = 0$$

Solving for $P^{\bullet}$, yields

$$P^{\bullet} = \frac{\beta_1 \varsigma^{\bullet} - (1 - Eo^{\bullet}) + \sqrt{[(1 - Eo^{\bullet}) - \beta_1 \varsigma^{\bullet}]^2 + 4\beta_o \varsigma^{\bullet} Eo^{\bullet}}}{2Eo^{\bullet}} \tag{8}$$

For a practical application, the resolution of the system (1) and (2) requires the definition of the boundary conditions. In our case, the example considered concerns a flow in a relatively short pipeline with a valve and a tank at upstream and downstream boundary. The calculation of the unknowns, at these points, requires the transformation of the previous system into differential equations corresponding to each boundary. The characteristics method allows to accomplish this transformation (Courant and Hilbert [14]).

Numerical Resolution

Method of Characteristics. The characteristics method, which is based on the propagation celerity of the pressure wave, is applied to obtain ordinary differential equations. In fact, it is not a numerical method but an analytical solution method. However, the necessary integration is generally performed numerically. Following the techniques described by Courant and Hilbert [14] the characteristic roots of (1) and (2) system are:

$$\lambda_{1,2} = V \pm a \tag{9}$$

The parameter **a** is the wave propagation speed in the mixture. It can be expressed in the following form:

$$a = \left(\frac{1}{\dfrac{d\zeta^{\bullet}}{dP'}}\right)^{1/2} \tag{10}$$

where

$$\frac{d\varsigma^{\bullet}}{dP'} = \frac{d\varsigma^{\bullet}}{dP^{\bullet}}\frac{dP^{\bullet}}{dP'}$$

Using Eqs. (3*b*) and (4), the relation (10) becomes

$$a = \frac{A_1}{1 - \dfrac{D_o}{2e}Eos(P^{\bullet} - 1)}\sqrt{\frac{\dfrac{E}{\rho_o}Eos}{(A_2 + P^{\bullet}Eo^{\bullet})A_1 - \beta_1 A_2 P^{\bullet}}} \tag{11}$$

The associated compatibility relations

$$\frac{\delta P'}{\delta t} \pm \zeta^{\bullet} a \frac{\delta V}{\delta t} = \mp\left(\zeta^{\bullet} ag \sin\theta - \frac{2C_f}{D_h}\zeta^{\bullet} a|V|V\right) \tag{12}$$

are valid along the characteristics directions

$$\frac{dx}{dt} = V \pm a \tag{13}$$

The differential operator in Eqs. (12) takes the following form:

$$\frac{\delta}{\delta t} = \frac{\partial}{\partial t} + (V \pm a)\frac{\partial}{\partial x}$$

This equation relates to the propagation of the pressure wave traveling along characteristic lines in the x, t plan defined by Eq. (13) (Fig. 1).

It is assumed that initial and boundary conditions are known and at t time the dependent variables are given at nodes R and S of Fig. 2. The two compatibility relations, given by Eqs. (12), are integrated along the characteristics RP and SP from time **t** to **t** + **Δt** as

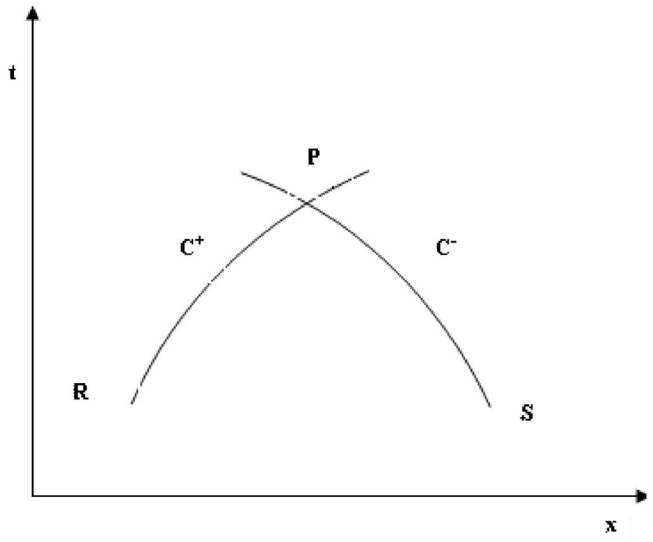

Fig. 1 The characteristic lines in the *x*, *t* plan

$$\int_{R,S}^{P} \delta P' \pm \int_{R,S}^{P} \zeta^{\bullet} a\, \delta V = \mp \int_{R,S}^{P} \left(\zeta^{\bullet} a g \sin\theta - \frac{2C_f}{D_h} \zeta^{\bullet} a |V| V \right) \delta t \tag{14}$$

A specified time grid characteristic is now established in order to accomplish an orderly computer solution. The pipe length L is initially discretized into N equal reaches, $\Delta \mathbf{x} = \mathbf{L}/\mathbf{N}$ (Fig. 2). Flow conditions are known along the pipe at initial time (given by initial steady state conditions). Equations (12) are applied for the downstream and the upstream boundaries, respectively. They are also used in Appendix B for the cavity volume calculation. However, spatially interpolations are necessary at location S and R near the previous boundaries, respectively.

Finite Difference Conservative Method. The set of conservation Eqs. (1) and (2) can be rewritten as

$$\frac{\partial F_1}{\partial t} + \frac{\partial F_2}{\partial x} = 0 \tag{15}$$

$$\frac{\partial F_2}{\partial t} + \frac{\partial F_3}{\partial x} = F_4 \tag{16}$$

This system can be solved by the two-step finite difference S_β^α scheme.

This predictor-corrector scheme corresponds to an explicit form

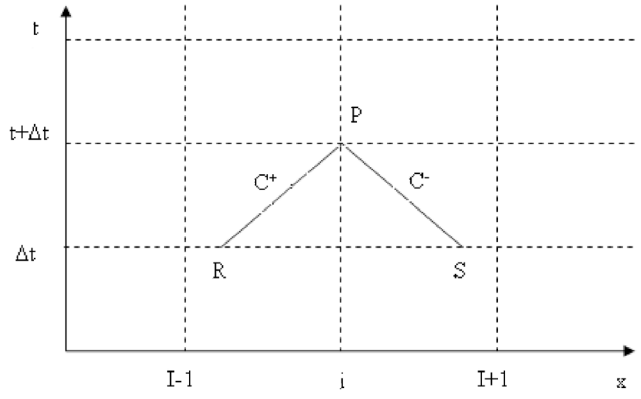

Fig. 2 Linear interpolation on Δ*t* constant grid

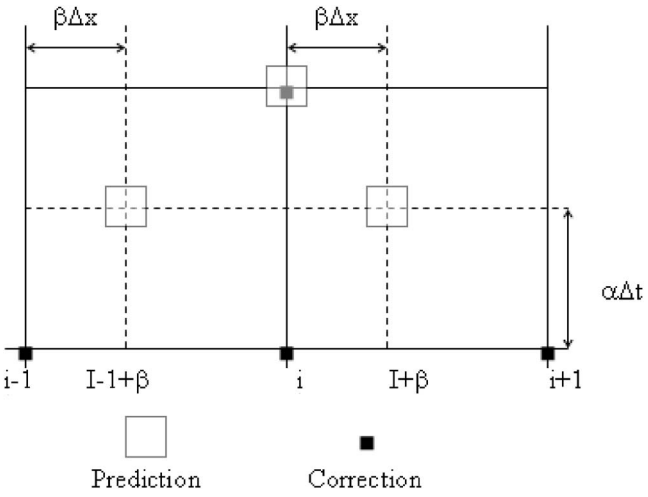

Fig. 3 Finite differences scheme

of the predictor variables in $(i+\beta)$ at time level $(n+\alpha)$. Following the technique described by Lerat and Peret [15]), the two-step finite difference S_β^α scheme, used for any grid point $(i,k+1)$, is as follows, for the predictor:

$$[\bar{F}_1]_i^{n+1} = (1-\beta)[F_1]_i^n + \beta[F_1]_{i+1}^n - \alpha\kappa\{[F_2]_{i+1}^n - [F_2]_i^n\}$$

$$[\bar{F}_2]_i^{n+1} = (1-\beta)[F_2]_i^n + \beta[F_2]_{i+1}^n - \alpha\kappa \begin{Bmatrix} [F_3]_{i+1}^n \\ -[F_3]_i^n \end{Bmatrix} + \alpha\Delta t[F_4]_i^n$$

The corrector step is defined as to obtain overall second order accuracy and can be written as

$$[F_1]_i^{n+1} = [F_1]_i^n - \frac{\kappa}{2\alpha}\{(\alpha-\beta)[F_2]_{i+1}^n + (2\beta-1)[F_2]_i^n + (1-\alpha-\beta)[F_2]_{i-1}^n + [\bar{F}_2]_i^n - [\bar{F}_2]_{i-1}^n\}$$

$$[F_2]_i^{n+1} = [F_2]_i^n - \frac{\kappa}{2\alpha}\{(\alpha-\beta)[F_3]_{i+1}^n + (2\beta-1)[F_3]_i^n + (1-\alpha-\beta)[F_3]_{i-1}^n + [\bar{F}_3]_i^n - [F_3]_{i-1}^n\} + \Delta t[F_4]_i^n$$

in which $\kappa = (\Delta t/\Delta x)$ is calculated in order to satisfy the following stability criteria:

$$\frac{\Delta t}{\Delta x} \leqslant \frac{1}{\mathrm{Max}(|V|+a)} \tag{17}$$

This criteria is also valid for the boundary conditions calculation.

As can be noticed, the S_β^α scheme is a three-point accurate method (Fig. 3). For values of $\alpha=1$ and $\beta=0$ we obtain the predictor-corrector Mac Cormack's scheme (used in this study) which is generally employed in some problems of gas dynamics. The values $\alpha=1/2$ and $\beta=1/2$ correspond to Lax Wendroff scheme.

Considering that the liquid transient flow with gas release phenomenon is not only a hydrodynamic problem but also a phase change problem, the previous scheme, which was generally applied to compressible fluid flow, can be used for our problem. Then in order to accomplish a suitable treatment of the shock problem considered herein (instantaneous valve closure), a flux corrective transport (FCT) algorithm is added to the above scheme as additional steps (Fletcher [16]).

As it was reported by this author, high-order Godunov schemes (for example) produce more accurate solution than FCT algorithms, but more sophistically coding and less economical regarding the computational time. However, FCT algorithm, which is more accurate than artificial viscosity, gives largely acceptable

Table 1 Experimental conditions

Valve localization	Initial velocity	Gas	Gas content[a] (C_o)	Reservoir pressure (KN/M^2)	Fluid temperature (°C)
Upstream	0.77	Air	0.02	172[b]	16
Upstream	0.77	CO_2	0.60	170[b]	16
Upstream	0.77	CO_2	1.15	175[b]	16
Downstream	0.77	Air	0.02	297[c]	18
Downstream	0.77	CO_2	0.60	305[c]	18
Downstream	0.77	CO_2	1.15	308[c]	18

[a]Ratio by volume standard conditions.
[b]Downstream reservoir [Fig. 4(*a*)].
[c]Upstream reservoir [Fig. 4(*b*)].

results for our problem.

During the numerical applications, the above finite difference scheme gives the values of $\zeta^{\bullet}$ and V. Then a direct method is employed to carry out, from Eqs. (6*a*) and (8) (in which $\sigma=0$) and (7) and (6*b*) with (A7), the unknowns p, α and Γ_g. The boundary conditions are calculated from the compatibility relations (12) with spatial interpolations near these boundaries.

Calculation Procedure. In the calculation the unknowns at the boundaries are the pressure p at the valve and the velocity V at the tank. At the valve point, for which $V=Cte$ (or $V=0$ for the upstream valve closure of the duct), the ratio $P^{\bullet}$ can be deduced from Eq. (3*b*) as follows:

$$P^{\bullet} = \frac{P'}{P'Dre + Pro} + 1 \tag{18}$$

Knowing the pressure $p=Cte$ (i.e., $P^{\bullet}=Cte$ and $P'=Cte$) **at** the tank, an integration of the corresponding compatibility relation allows obtaining the velocity V.

For the interior points of the mesh grid used by the numerical procedure, the finite difference scheme gives the parameter $\zeta^{\bullet}$ from which $P^{\bullet}$ can be deduced [Eq. (8)]. The velocity V is obtained directly by ratio F_2/F_1.

Then from the relation (6*a*), in which $\sigma=0$, the pressure p for these cases is

$$p = p_v + P^{\bullet}(p - p_{v_o}) \tag{19}$$

As can be noticed, the parameters $\zeta^{\bullet}$ and $P^{\bullet}$ are dependent on the gas release rate. This phenomenon can be expressed by the degassing coefficient G_r which depends on the pipe and fluids properties. This global formulation allows verifying the impact of these properties on this coefficient.

Besides, a numerical calculation procedure, including these relations, is summarized in Appendix C.

Results

Hypothesis. In addition to habitual assumptions made for single component flow, the following hypothesises should be also stated:

–the steady-state Darcy–Weisbagh formula is used to express the pipe wall shear stress (Wylie and Streeter [2]).

–the initial dissolved gas amount is supposed to be small and uniformly distributed gas bubbles in the liquid.

–the initial void fraction is very small.

–the initial velocity and pressures are calculated from steady-state flow.

–the gas behavior is isothermal.

–the valve closure is instantaneous.

Wiggert and Sundquist [13] have conducted a series of tests, with three initial dissolved gas concentration in water, by considering a pipe loop 295 m in length and 0.0254 m in diameter. Experimental conditions are reported in Table 1. For our model, the

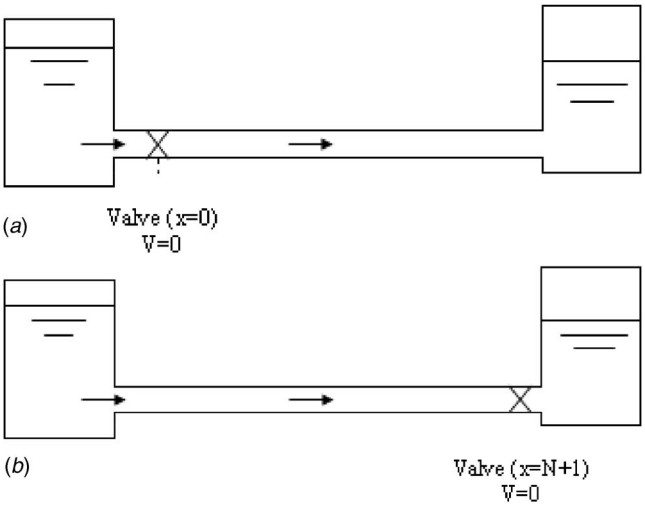

Fig. 4 (*a*) Experimental pipe system with upstream valve closure, (*b*) experimental pipe system with downstream valve closure

numerical calculation is performed by dividing this pipeline into $N=40$ sections. The previous finite difference technique is applied for interior points of the grid (Fig. 3) and the characteristics Eqs. (14) for the boundaries (Fig. 2). For $N>40$ it is noticed to be more time consuming for same results accuracy.

Valve Closure at the Upstream Boundary. Considering experimental and numerical results corresponding to Fig. 4(*a*) (Wiggert and Sundquist [13]), the pressure responses at point $x=0$ are produced in Figs. 5(*a*)–5(*c*), followed by the associated cavity volume near the valve (Fig. 6). This volume is calculated by the method presented in Appendix B. As can be observed, the effect of degassing on cavity closure is noticeable and increases linearly with the time. Pressure peaks are dumped by the subsequent gas release phenomenon. The dumping level depends strongly on initial gas content C_o.

Valve Closure at the Downstream Boundary. Figures 7(*a*)–7(*c*), which correspond to valve closure at $x=L$, show similar results corresponding to Fig. 4(*b*). As can be observed in these figures, the effect of degassing is less pronounced, contrary to the previous case. However, time duration of the cavity (Fig. 8) is shorter and consequently followed by smaller gas release amount.

A comparison between results relative to Figs. 4(*a*) and 4(*b*) shows that upstream valve position has a more pronounced effect on pressure transients than the later. Also, in some plants, the presence of dissolved gas in liquid has some utility, especially in the case of column separation, which is generally followed by a high pressure pulse. In fact, the dissolved gas plays a damping role during this phenomenon. If we consider only a vapor cavity volume (i.e., without gas release) the resulting pressure pulse will be so high that it can be dangerous for the wall pipeline integrity.

The cavity volume calculation for these two practical cases (Figs. 6 and 8) is presented in the Appendix B. It is obtained by combining the corresponding compatibility relation, the cavity continuity equation and the ideal gas law.

Some uncertainties have been noticed in the numerical calculation, especially near the valve closure region where the fluid medium makes the wave speed highly variable. It is also known that the finite difference schema utilizing a fixed grid induce numerical dispersion and attenuation. In the other hand, the characteristics method is less expansive than the Mac Cormack scheme which requires small steps in time because of stability. Nevertheless, the later is more accurate.

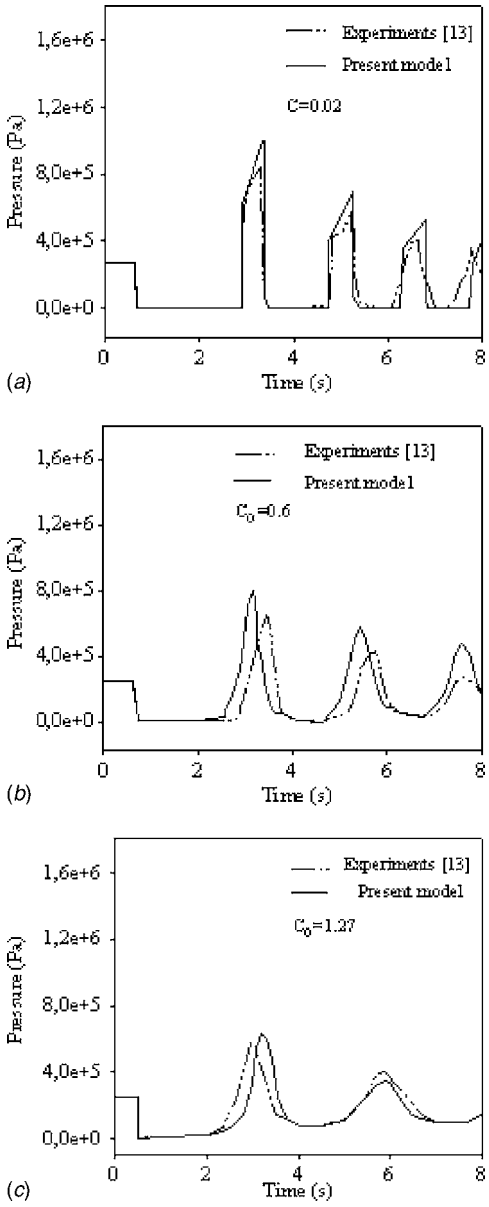

Fig. 5 (*a*) Pressure response at point $x=0$, for $C_o=0.02$, (*b*) pressure response at point $x=0$, for $C_o=0.59$, (*c*) pressure response at point $x=0$, for $C_o=1.15$

Conclusion

A numerical simulation of a gaseous and vaporous cavitation has been performed by introducing a more complete gas release calculation method and a new cavity model for the column separation. The former, which takes into account the physical characteristics of the bubble and the fluid medium, considers the time volume bubble evolution. Cavity volume formation, during transients in a homogeneous gas-liquid mixture flow, is modeled and numerically simulated by taking into account the effect of degassing phenomenon. It has been observed that the gas diffusion into the bubbles and the cavity lead to a depressing of the dynamic parameters and a decrease of time cavity duration. Also, the introduced new model of gas mass rate permits to consider the degassing problem under its physical aspect and its effect on the flow parameters.

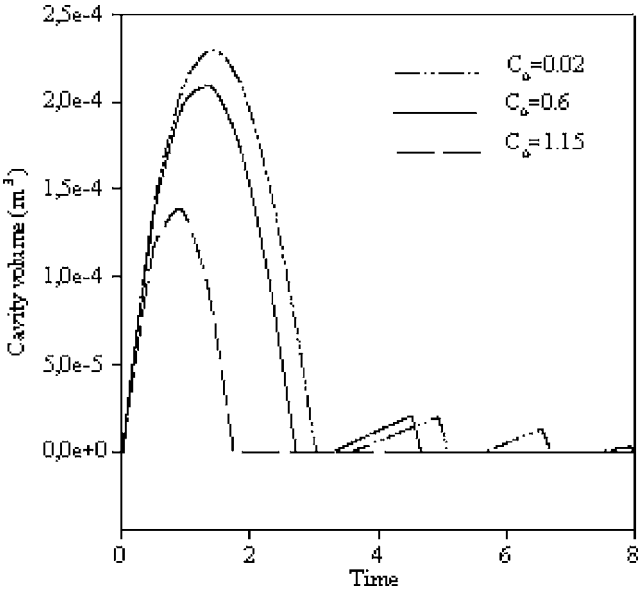

Fig. 6 Time cavity volume expansion at point $x=0$, for $C_o=0.02$, 0.6 and 1.15

Acknowledgment

The authors are grateful to the Associate Editor Dennis Siginer and the reviewers for their constructive comments and suggestions.

Nomenclature

a = wave propagation speed, m/s
C = dissolved gas concentration, moles/moles
C_f = friction coefficient
D_h = hydraulic diameter of the pipe, m
E = Young's modulus of elasticity for pipe material, N/m^2
e = pipe wall thickness, m
G_r = gas release coefficient
g = gravitational acceleration, m/s^2
L = pipe length, m
p = average cross-sectional pressure, N/m^2
p_v = vapor pressure, N/m^2
R = bubble radius, m
S = pipe cross-sectional area, m^2
T = absolute temperature, K
t = time, s
V = average cross-sectional velocity, m/s
W_c = volume of vapor cavity, m^3
x = axial distance along the pipe, m

Greek Symbols

α = average cross-sectional void fraction
β = gas diffusion coefficient, m^2/s^2
Γ_g = rate of gas release per unit volume of the fluid, $Kg/s/m^3$
ρ = mean density of the mixture, kg/m^3
σ = interfacial tension, N/m
τ = boundary shear stress, N/m^2
θ = angle of pipe inclination, deg

Subscripts

c = cavity
f = flux or friction
g = gas
ℓ = liquid
o = reference conditions

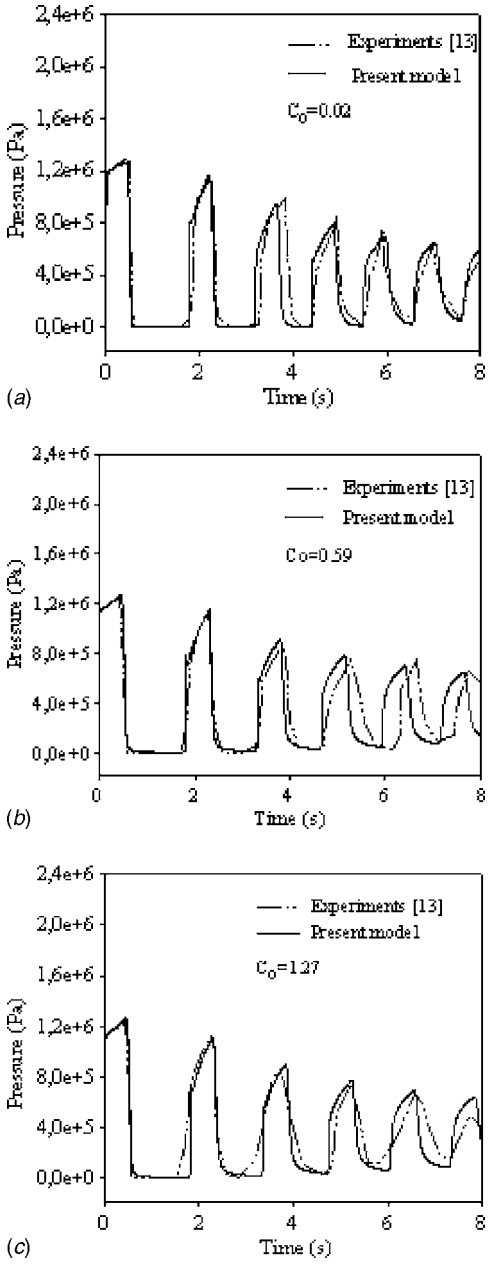

Fig. 7 (*a*) Pressure response at point $x=L$, for $C_o=0.02$, (*b*) pressure response at point $x=L$, for $C_o=0.59$, (*c*) pressure response at point $x=L$, for $C_o=1.27$

s = saturation
v = vapor
w = interface

Appendix A: Gas Mass Rate Calculation (Γ_g)

The mass transfer near the bubble interface can be given by the following form of Fick's law:

$$m_f = \frac{\beta \rho_m}{1 - c_W}\left(\frac{\partial c}{\partial r}\right)_{r=R} \tag{A1}$$

where m_f is the interfacial mass flux across the gas-liquid interface (Fig. 9), β the diffusion coefficient, c the dissolved weight fraction of gas as defined by Henry's law and c_w the solute concentration at the bubble interface.

Also, considering the governing continuity equation for c in the spherical coordinates yields

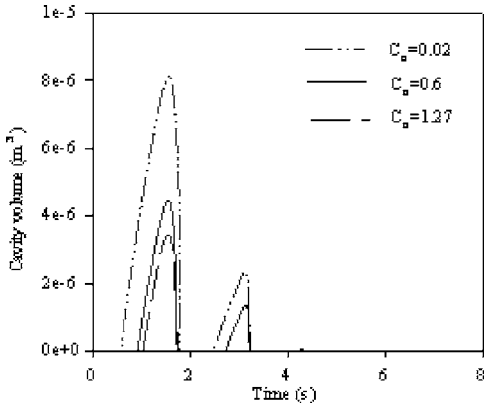

Fig. 8 Time cavity volume expansion at point $x=L$, for C_o =0.02, 0.56 and 1.27

$$\rho\frac{\partial c}{\partial t} + \rho v\frac{\partial c}{\partial r} = \rho\frac{\beta}{r^2}\frac{\partial}{\partial r}\left(r^2\frac{\partial c}{\partial r}\right) \quad \text{for } r \geqslant R(t) \tag{A2}$$

where ρ is the mixture density.

Resolving this equation by an integral method, Kwak and Kim [16] have given a solution for bubble radius R and bubble interface thickness δ. For a constant value of interface tension, the form of this solution is

$$\frac{1}{10}\left(\frac{\delta}{R}\right)^3 + \frac{1}{2}\left(\frac{\delta}{R}\right)^2 + \left(\frac{\delta}{R}\right) = \frac{1 - c_\infty}{c_\infty - c_w}A \tag{A3}$$

where

$$A = \frac{1}{\rho R^3}\left[\left(\rho_\infty + \frac{2\sigma}{R_g T R}\right)R^3 - \left(\rho_\infty + \frac{2\sigma}{R_g T R_o}\right)R_o^3\right]$$

ρ_∞ is the fluid density far from the gas-liquid interface.

Reformulating equation (A1), by replacing the radial gradient of c as function of a concentration profile, the previous authors have obtained

$$m_f = \frac{2\beta\rho}{\delta}\left(\frac{c_\infty - c_w}{1 - c_w}\right) \tag{A4}$$

C_∞ and C_w are the gas concentrations in the liquid (far from the bubble) and near the bubble interface, respectively.

Considering $\delta \ll R$ and replacing δ from equation (A3), yields

$$\delta = AR\frac{1 - c_\infty}{c_\infty - c_w} \tag{A5}$$

Therefore Eq. (A1) becomes

$$m_f = \frac{2\beta\rho^2 R^2}{\left[\left(\rho_\infty + \frac{2\sigma}{R_g T R}\right)R^3 - \left(\rho_\infty + \frac{2\sigma}{R_g T R_o}\right)R_o^3\right]}\frac{(c_\infty - c_w)^2}{(1 - c_w)(1 - c_\infty)} \tag{A6}$$

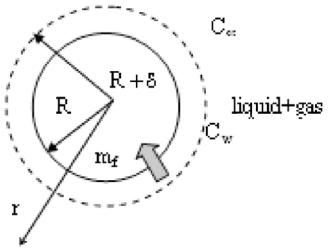

Fig. 9 Bubble growth in gas saturated fluid

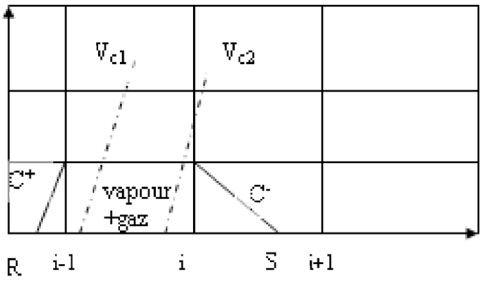

Fig. 10 Cavity position in mesh grid x,t

It must be noticed that gas diffusion calculation requires $c_w < c_\infty$ These concentrations are obtained from experiments (Kwak and Kim [16]).

Writing the mass balance across the bubble interface (Fig. 1 as $m_f 4\pi R^2$, the gas release rate Γ_g becomes

$$\Gamma_g = \frac{8\pi\beta\rho^2 R^4}{\left[\left(\rho_\infty + \frac{2\sigma}{R_g T R}\right)R^3 - \left(\rho_\infty + \frac{2\sigma}{R_g T R_o}\right)R_o^3\right]} \frac{1}{Sdx} \frac{(c_\infty - c_w)^2}{(1-c_w)(1-c_\infty)} \tag{A7}$$

The density ρ depends on the pressure p, as expressed in Equation (4) from which

$$\rho = \varsigma^\bullet \rho_o \frac{S_o}{S} \tag{A8}$$

where: $S_o/S = (1-(D_o/2e)Eos(P^*-1))^2$ (Kessal [17])

The bubble radius R is deduced from the relation (6*a*).

Appendix B: Cavity Volume Modeling

Numerical vapor+gas cavity modeling can be illustrated in a simple manner as shown by Fig. 10, where V_{c1} and V_{c2} are the velocities of cavity boundaries.

Our case corresponds to an upstream pipeline valve closing, as shown in Fig. 4(*a*).

Then integration of one of Eqs. (12), which corresponds to the negative characteristics direction (13), yields

$$P'_{C2} - P'_m = (\zeta^\bullet a)_m (V_{C2} - V_m) + (\zeta^\bullet a)_m \left(g\sin\alpha + \frac{C_f}{D_h} V|V|\right)dt \tag{B1}$$

Also neglecting wall expansion, the relation (3*a*) becomes

$$P'_{C2} \cong \frac{p - p_o}{\rho_o} \tag{B2}$$

which leads to

$$p_{c2} = \rho_o P'_{c2} + p_o \tag{B3}$$

On the other hand, considering the equilibrium equation of a bubble (6*a*) where the surface tension is neglected, equation of state in the cavity takes the following form:

$$p_g Vol = (P_{C2} - P_V)Vol = mRT = RT\int_0^t \Gamma_g dt \tag{B4}$$

Then from (B3) and (B4):

$$P'_{C2} = \frac{RT}{\rho_o Vol}\int_0^t \Gamma_g dt - \frac{p - p_o}{\rho_o} \tag{B5}$$

Considering time cavity expansion, with a volume Vol, Kranenburg [12] has introduced the simple following relation:

$$\frac{dVol}{dt} = S(V_{C2} - V_{C1}) \tag{B6}$$

Replacing V_{C2} and P'_{C2} in (B1) by (B5) and (B6) yields, after simplifications

$$\frac{RT}{\rho_o Vol}\int_t^{t+dt} \Gamma_g dt - \frac{p_o - p_v}{\rho_o} - P_m = \zeta^\bullet a\left(\frac{1}{S}\frac{dV}{dt} + V_{c1} - V_{cm} + \left(g\sin\theta + \frac{C_f}{D_h}V|V|\right)dt\right) \tag{B7}$$

Rearranging in order to calculate time cavity volume expansion yields

$$\frac{dVol}{dt} = \frac{A_1}{Vol} - A_2 \tag{B8}$$

where

$$A_1 = \frac{SRT}{\zeta^\bullet a \rho_o}\int_t^{t+dt} \Gamma_g dt$$

$$A_2 = \frac{S}{\zeta^\bullet a}\left(\frac{p_o - p_V}{\rho_o} + P'_m\right) - S(V_{C1} - V_{cm} + C_1 dt)$$

After some combinations and rearranging for suitable calculations, the time cavity expansion becomes

$$Vol(t+\Delta t) = Vol(t) + (B_1\bar{\Gamma}_g - A_2)dt \tag{B9}$$

where

$$B_1 = \frac{SRT}{\zeta^\bullet a \rho_o}$$

$$C_1 = g\sin\alpha + \frac{C_f}{D_h}V|V|$$

and

$$\bar{\Gamma}_g = \frac{1}{Vol(t)}\int_t^{t+dt} \Gamma_g dt$$

is the relative mass rate of released gas.

It can be noticed that Vol$(t+\Delta t)$ depends on the phases' physical parameters, pipe wall deformation and Γ_g.

Appendix C: Computer Program Chart for the Case of a Valve Closure at Upstream Boundary (Figs. 5(*a*)–5(*c*))

Step 1: Calculate initial steady-state conditions for the parameters p, V and ς^*.

Step 2: Increment the time $\Delta t = \Delta x/V_o + a$

Step 3: Upstream boundary condition corresponding to the negative characteristics direction (Fig. 2).

3.1: Calculate the parameters a_m, V_S, P'_S and ς^*_S, at point S of Fig. 2, by linear interpolation (Hartree method) by using the negative characteristics direction for Eq. (14).

3.2: Calculate $P'(1)$ (for $V(1)=0$) from the one of the compatibility relation (14) corresponding to the negative direction.

3.3: Calculate $P^*(1)$ from the relation (3*b*).

3.4: Calculate $\varsigma^*(1)$ from the relation (4).

3.5: Calculate $p(1)$ from the relation (19).

3.6: Calculate $\alpha(1)$ from the relation (7).

3.7: Calculate the cavity volume Vol$(t+\Delta t)$ from the relation (B9) (Appendix B) by the use the compatibility relation (B1). In our case the velocities V_{C1} and V_{C2} (Fig. 10) are determined from the velocities $V(1)$ and $V(2)$ by linear interpolation. This procedure is repeated for the case a column separation at an interior point position.

Step 4: Downstream boundary condition corresponding to the mesh grid $(n+1)$.

4.1: Calculate $P'(1)$ from the relation (8).

4.2: Calculate the parameters V_R, P'_R and ς^*_R, at point **R** of Fig. 2, by linear interpolation (Hartree method) by using the positive characteristics direction.

4.3: Calculate $V(n+1)$ (for $p(n+1)=\text{const}$) from the one of the compatibility relation (12) corresponding to the positive direction.

Step 5: Calculate, by the use of the previous predictor-corrector scheme, the parameters $\varsigma^*(i)$ and $V(i)$ at the interior points of the mesh grid (Fig. 3).

Step 6: Application of the FCT procedure, as performed by Fletcher [16].

References

[1] Bergant, A., and Simpson, A. R., 1999, "Pipeline Column Separation Flow Regimes," J. Hydraul. Eng. ASCE, pp. 835–848.

[2] Streeter, V. L., 1972, "Water Hammer Analysis," J. Hydraul. Div., Am. Soc. Civ. Eng., **95**(6), pp. 1959–1972.

[3] Wylie, E. B., and Streeter, V. L., 1993, *Fluid Transients in Systems*, Prentice-Hall, Englewood Cliffs, NJ.

[4] Bergant, A., and Simpson, A. R., 1994, "Estimated Unsteady Friction in Transient Cavitating Pipe Flow," *Water Pipeline Systems*, D. S. Miller, ed., Mechanical Engineering, London, pp. 3–16.

[5] Streeter, V. L., 1983, "Transient Cavitating Pipe Flow," J. Hydraul. Eng. ASCE, **109**(11), pp. 1408–1423.

[6] Bergant, A., and Simpson, A. R., 1993, "Interfacial Model for Transient Cavitating Flow in Pipeline," in *Unsteady Flow and Fluid Transient*, R. Bettess and J. Watts, eds., Balkema, Rotterdam, pp. 333–342.

[7] Provoost, G. A., and Wylie, E. B., 1981, "Discrete Gas Model to Represent Distributed Free Gas in Liquids," *Proc. Fifth Int. Symp. on Column Separation, International Association of Hydraulic Research*, Delft, The Netherlands, pp. 249–258.

[8] Barbero, G., and Caponi, C., 1992, "Experimental Validation of a Discrete Free Gas Model for Numerical Simulation of Hydraulic Transients With Cavitation," in *Hydraulic Transients with Water Column Separation*, Fluid Mechanics Group, pp. 51–67.

[9] Lee, T. S., 1999, "Air Influence on Hydraulic Transients on Fluid System With Air Valves," ASME J. Fluids Eng., **121**, pp. 646–650.

[10] Shu, J. J., 2003, "Modeling Vaporous Cavitation on Fluid Transients," Int. J. Pressure Vessels Piping, pp. 1–9.

[11] Kessal, M., and Amaouche, M., 2001, "Numerical Simulation of Vaporous and Gaseous Cavitation in Pipelines," Int. J. Numer. Methods Heat Fluid Flow, **34**, pp. 121–137.

[12] Kranenburg, C., 1974, "Gas Release During Transient Cavitation in Pipes," J. Hydraul. Div., Am. Soc. Civ. Eng., **100**(10), pp. 1383–1398.

[13] Wiggert, D. C., and Sundquist, M. J., 1979, "The Effects of Gaseous Cavitation on Fluid Transients," ASME J. Fluids Eng., **101**, pp. 79–86.

[14] Courant, R., and Hilbert, D., 1962, *Methods of Mathematical Physics*, Interscience, New York, Vol. 2.

[15] Lerat, A., and Peret, R., 1973, "Sur le Choix des Schémas aux Différences du Second Ordre Fournissant des Profils de Choc sans Oscillations," C. R. Acad. de Sci. Paris, **277**.

[16] Kwak, O. Y., and Kim, Y. W., 1998, "Homogeneous Nucleation and Macroscopic Growth of Gas Bubble in Organic Solutions," Int. J. Heat Mass Transfer, **41**(4,5), pp. 757–767.

[17] Kessal, M., 1987, "Modèlisation, en Écoulement Homogène, des Phénomènes de Cavitation lors des Régimes Transitoires en Conduite," thèse de Doctorat d'Ingénieur, INSA de Lyon, France.

[18] Fletcher, C. A. J., 1997, *Computational Techniques for Fluid Dynamics*, 3rd ed., Springer, Berlin.

Numerical Determination of Moment Lyapunov Exponents of Two-Dimensional Systems

Wei-Chau Xie
Professor
Mem. ASME
Solid Mechanics Division, Faculty of Engineering,
University of Waterloo,
Waterloo, ON N2L 3G1, Canada

Ronald M. C. So
Chair Professor and Head
Fellow ASME
Department of Mechanical Engineering,
The Hong Kong Polytechnic University,
Hung Hom, Kowloon, Hong Kong

The pth moment Lyapunov exponent of an n-dimensional linear stochastic system is the principal eigenvalue of a second-order partial differential eigenvalue problem, which can be established using the theory of stochastic dynamical system. An analytical-numerical approach for the determination of the pth moment Lyapunov exponents, for all values of p, is presented. The approach is illustrated through a two-dimensional system under bounded noise or real noise parametric excitation. Series expansions of the eigenfunctions using orthogonal functions are employed to transform the partial differential eigenvalue problems to linear algebraic eigenvalue problems, which are then solved numerically. The numerical values obtained are compared with approximate analytical results with weak noise amplitudes. [DOI: 10.1115/1.2041663]

1 Introduction

In general, the study of the dynamic stability of many engineering structures under random loadings leads to a linear stochastic dynamic system of the form

$$\dot{\mathbf{x}}(t) = \mathbf{A}(\boldsymbol{\xi}(t))\mathbf{x}(t), \quad \mathbf{x}(0) = \mathbf{x}_0, \tag{1}$$

where $\boldsymbol{\xi}(t) = \{\xi_1(t), \xi_2(t), \ldots, \xi_d(t)\}^T$ is a vector of stochastic processes of dimension d characterizing the randomness of the loadings. The sample or almost-sure stability of the trivial solution of system (1) is determined by the Lyapunov exponent, which characterizes the average exponential rate of growth of the solutions of system (1) for t large, defined as

$$\lambda_{\mathbf{x}(t)} = \lim_{t\to\infty} \frac{1}{t} \log\|\mathbf{x}(t)\|, \tag{2}$$

where $\|\mathbf{x}(t)\|$ denotes the Euclidean vector norm. The trivial solution of system (1) is stable with probability one (w.p.1) if the largest Lyapunov exponent is negative, whereas it is unstable w.p.1 if the largest Lyapunov exponent is positive. The theory of Lyapunov exponents was placed on a rigorous mathematical foundation in the Multiplicative Ergodic Theorem [1]. The Lyapunov exponent has been recognized as an ideal avenue for studying the behavior of a dynamical system, because it provides not only the information about stability or instability, but also how rapidly the response grows or diminishes with time. There are many publications on the analytical and numerical determination of the Lyapunov exponents of stochastic dynamical systems.

On the other hand, the stability of the pth moment of the trivial solution of system (1) is determined by the moment Lyapunov exponent

$$\Lambda_{\mathbf{x}(t)}(p) = \lim_{x\to\infty} \frac{1}{t} \log E[\|\mathbf{x}(t)\|^p], \tag{3}$$

where $E[\|\mathbf{x}(t)\|^p]$ denotes expected value. If the moment Lyapunov exponent is negative, then the pth moment approaches 0 as time $t\to\infty$. The pth moment Lyapunov exponent is a convex analytic function in p, which passes through the origin and its slope at the origin is equal to the largest Lyapunov exponent. The non-trivial zero of the moment Lyapunov exponent is called the stability index.

In order to have a complete picture of the dynamic stability of system (1), it is important to study both the sample and moment stability and to determine both the largest Lyapunov exponent and the pth moment Lyapunov exponent.

Although the moment Lyapunov exponents are important in the study of dynamic stability of stochastic systems, the actual evaluations of the moment Lyapunov exponents are very difficult. Various approximate analytical methods have been devised to actually carry out the computation for a number of engineering structural systems with noise excitations of small amplitudes.

Arnold et al. [2] obtained weak noise expansions of the moment Lyapunov exponents of a two-dimensional system in terms of εp, where ε is a small parameter, under both white noise and real noise excitations. Khasminskii and Moshchuk [3] obtained an asymptotic expansion of the moment Lyapunov exponent of a two-dimensional system under white noise parametric excitation in terms of the small fluctuation parameter. Sri Namachchivaya and Vedula [4] obtained a general asymptotic approximation for the moment Lyapunov exponent and the Lyapunov exponent for a four-dimensional system with one critical mode and another asymptotically stable mode driven by a small intensity stochastic process. Sri Namachchivaya and Van Roessel [5] studied the moment Lyapunov exponents of two coupled oscillators driven by real noise. Xie obtained weak noise expansions of the moment Lyapunov exponent, the Lyapunov exponent, and the stability index, in terms of the small fluctuation parameter, of a two-dimensional system under real noise excitation [6] and under bounded noise excitation [7]. Milstein [8] studied the Taylor series expansion of the moment Lyapunov exponent $\Lambda(p)$ in p using the asymptotic behavior of semi-invariants for linear stochastic systems.

The Lyapunov exponents of a general n-dimensional stochastic system can be determined numerically using the algorithm developed in Ref. [9]. However, there are no numerical algorithms for evaluating the moment Lyapunov exponents. Because of this reason, almost all published work has been on the analytical determination of the moment Lyapunov exponents under weak noise excitations. Xie [10] evaluated numerically the moment Lyapunov exponents of a near-nilpotent system under stochastic parametric excitation. The second-order ordinary differential eigenvalue

Contributed by the Applied Mechanics Division of ASME for publication in the JOURNAL OF APPLIED MECHANICS. Manuscript received December 4, 2002; final manuscript received June 1, 2005. Review conducted by I. Mezic. Discussion on the paper should be addressed to the Editor, Prof. Robert M. McMeeking, Journal of Applied Mechanics, Department of Mechanical and Environmental Engineering, University of California—Santa Barbara, Santa Barbara, CA 93106-5070, and will be accepted until four months after final publication in the paper itself in the ASME JOURNAL OF APPLIED MECHANICS.

problem governing the moment Lyapunov exponent is converted to a two-point boundary-value problem, which is solved numerically by the method of relaxation.

Numerical determination of the moment Lyapunov exponents is important for three reasons. Numerically accurate results of the moment Lyapunov exponents are essential in assessing the validity and the ranges of applicability of the approximate analytical results. In many engineering applications, the amplitudes of noise excitations are not small and the approximate analytical methods, such as the method of perturbation and stochastic averaging, cannot be applied. Numerical approaches have to be employed to evaluate the moment Lyapunov exponents. Furthermore, for systems under noise excitations that cannot be described in analytical forms, such as filtered white noise or bounded noise, or if only the time series of the response of the system is known, Monte Carlo simulation approaches have to be resorted to.

This paper presents the first study of numerical determination of the pth moment Lyapunov exponents for all values of p. The formulation of the second-order partial differential eigenvalue problem for the pth moment Lyapunov exponent of a general n-dimensional linear stochastic system is presented in Sec. 2. Analytical-numerical approach for determining the pth moment Lyapunov exponent is illustrated for two-dimensional systems under the parametric excitations of nonwhite noise processes, i.e., the bounded noise and the real noise processes. The second-order partial differential eigenvalue problems are established in Sec. 3. Double series expansions of the eigenfunctions, in terms of orthogonal functions, are used to convert the partial differential eigenvalue problems to linear algebraic eigenvalue problems in Sec. 4. Numerical results of the moment Lyapunov exponents are presented in Sec. 5.

2 Eigenvalue Problems for the Moment Lyapunov Exponents

Suppose Eq. (1) can be rewritten as an n-dimensional system of linear Stratonovich stochastic differential equations

$$d^*\mathbf{x} = \mathbf{a} * \mathbf{x}dt + \sum_{\ell=1}^{d} \sigma^\ell \mathbf{x} dW_\ell, \tag{4a}$$

where $\mathbf{x}=\{x_1,x_2,\ldots,x_n\}^T$ and the superscript $*$ indicates that the stochastic system is understood in the sense of Stratonovich, or the equivalent Itô equations

$$d\mathbf{x} = \mathbf{a}\mathbf{x}dt + \sum_{\ell=1}^{d} \boldsymbol{\sigma}^\ell \mathbf{x} dW_\ell, \quad \mathbf{a} = \mathbf{a}^* + \frac{1}{2}\sum_{\ell=1}^{d} (\boldsymbol{\sigma}^\ell)^2, \tag{4b}$$

in which $W_1(t), W_2(t), \ldots, W_d(t)$ are d mutually independent standard Wiener processes.

Applying the Khasminskii transformation [11]

$$\mathbf{s} = \frac{\mathbf{x}}{\|\mathbf{x}\|}, \quad \|\mathbf{x}\| = \sqrt{\mathbf{x}^T\mathbf{x}}, \quad \|\mathbf{s}\| = 1, \tag{5}$$

which generates a Markov diffusion process on the unit hypersphere S^n in the n-dimensional vector space. The Stratonovich differential equations governing $\mathbf{s}(t)$ are given by

$$d^*\mathbf{s} = \mathbf{h}_0^*(\mathbf{s})dt + \sum_{\ell=1}^{d} \mathbf{h}_\ell(\mathbf{s}) dW_\ell, \tag{6a}$$

or the equivalent Itô differential equations

$$d\mathbf{s} = \mathbf{h}_0(\mathbf{s})dt + \sum_{\ell=1}^{d} \mathbf{h}_\ell(\mathbf{s}) dW_\ell, \tag{6b}$$

where

$$h_{0j}(\mathbf{s}) = h_{0j}^*(\mathbf{s}) + \frac{1}{2}\sum_{k=1}^{n}\sum_{\ell=1}^{d} \frac{\partial h_{j\ell}}{\partial s_k} h_{k\ell},$$

and

$$\mathbf{h}_0(\mathbf{s}) = \mathbf{a}^*\mathbf{s} - q_0\mathbf{s}, \quad q_0 = \mathbf{s}^T\mathbf{a}^*\mathbf{s},$$
$$\mathbf{h}_\ell(\mathbf{s}) = \boldsymbol{\sigma}^\ell\mathbf{s} - q_\ell\mathbf{s}, \quad q_\ell = \mathbf{s}^T\boldsymbol{\sigma}^\ell\mathbf{s}, \quad \text{for } \ell = 1,2,\ldots,d. \tag{7}$$

The infinitesimal generator of the Markov diffusion process $\mathbf{s}(t)$ on the projected space P^n, which is obtained by identifying $\mathbf{s}$ and $-\mathbf{s}$, is ([12,13])

$$\mathcal{A} = \mathbf{h}_0^T\frac{\partial}{\partial\mathbf{s}} + \frac{1}{2}\sum_{\ell=1}^{d}\left(\mathbf{h}_\ell^T\frac{\partial}{\partial\mathbf{s}}\right)^2 = \sum_{j=1}^{n} h_{0j}\frac{\partial}{\partial s_j} + \frac{1}{2}\sum_{j=1}^{n}\sum_{\ell=1}^{d}\left(h_{\ell j}\frac{\partial}{\partial s_j}\right)^2$$
$$= \sum_{j=1}^{n} h_{0j}\frac{\partial}{\partial s_j} + \frac{1}{2}\sum_{j=1}^{n}\sum_{\ell=1}^{d}\left(h_{\ell j}\frac{\partial h_{\ell j}}{\partial s_j}\frac{\partial}{\partial s_j} + h_{\ell j}^2\frac{\partial^2}{\partial s_j^2}\right). \tag{8}$$

To avoid degeneracy, the following ellipticity condition is imposed:

$$\dim \mathrm{LA}(\mathbf{h}_j, j=0,1,\ldots,d)(\mathbf{s}) = n-1, \quad \text{for all } \mathbf{s} \text{ in } P^n,$$

where $\mathrm{LA}(\mathbf{z})$ denotes the Lie algebra generated by the vector fields $\mathbf{z}$. Adopting the following notations

$$\mathcal{B} = \sum_{\ell=1}^{d} q_\ell\left(\mathbf{h}_\ell^T\frac{\partial}{\partial\mathbf{s}}\right) = \sum_{\ell=1}^{d} q_\ell\left(\sum_{j=1}^{n} h_{\ell j}\frac{\partial}{\partial s_j}\right),$$

$$\mathcal{D} = q_0 + \sum_{\ell=1}^{d} r_\ell, \quad r_\ell = \tfrac{1}{2}\mathbf{s}^T[\boldsymbol{\sigma}^\ell + (\boldsymbol{\sigma}^\ell)^T]\boldsymbol{\sigma}^\ell\mathbf{s} - q_\ell^2, \tag{9}$$

$$\mathcal{R} = \sum_{\ell=1}^{d} q_\ell^2,$$

then the pth moment Lyapunov exponent $\Lambda(p)$ is the principal eigenvalue of the differential eigenvalue problem

$$\mathcal{L}(p)T(p) = \Lambda(p)T(p), \tag{10}$$

in which the operator $\mathcal{L}(p)$ is given by

$$\mathcal{L}(p) = \mathcal{A} + p(\mathcal{B}+\mathcal{D}) + \tfrac{1}{2}p^2\mathcal{R}. \tag{11}$$

As an alternative approach, suppose that in system (1) the stochastic process $\xi(t)$ is strongly elliptic, which ensures that the transition probability densities of $(\xi(t),\mathbf{s}(t))$ are smooth in all variables, and the Khasminskii transformation (5) is applied, then the operator $\mathcal{L}(p)$ in Eq. (10) is given by

$$\mathcal{L}(p) = \mathcal{G} + \mathbf{h}^T\frac{\partial}{\partial\mathbf{s}} + pq(\xi,\mathbf{s}) = \mathcal{G} + \sum_{j=1}^{n} h_j\frac{\partial}{\partial s_j} + pq(\xi,\mathbf{s}), \tag{12}$$

where $\mathcal{G}$ is the generator of process $\xi(t)$ and

$$\mathbf{h}(\xi,\mathbf{s}) = [\mathbf{A}(\xi) - q(\xi,\mathbf{s})\mathbf{I}]\mathbf{s}, \quad q(\xi,\mathbf{s}) = \mathbf{s}^T\mathbf{A}(\xi)\mathbf{s}. \tag{13}$$

For the special case when $\xi(t)$ is a stationary ergodic diffusion process described by the Stratonovich stochastic differential equation

$$d^*\xi(t) = X_0(\xi(t))dt + \sum_{\ell=1}^{d} X_\ell(\xi(t))dW_\ell(t), \tag{14}$$

the generator $\mathcal{G}$ of $\xi(t)$ is given by

$$\mathcal{G} = X_0\frac{\partial}{\partial\xi} + \frac{1}{2}\sum_{\ell=1}^{d}\left(X_\ell\frac{\partial}{\partial\xi}\right)^2 = X_0\frac{\partial}{\partial\xi} + \frac{1}{2}\sum_{\ell=1}^{d}\left(X_\ell\frac{\partial X_\ell}{\partial\xi}\frac{\partial}{\partial\xi} + X_\ell^2\frac{\partial^2}{\partial\xi^2}\right). \tag{15}$$

Hence, the pth moment Lyapunov exponent $\Lambda(p)$, for all real values of p, of a general n-dimensional linear stochastic system is the principal eigenvalue of a second-order partial differential eigenvalue problem (10) with $\mathcal{L}(p)$ given by Eqs. (11) and (12).

In the remainder of this paper, two-dimensional systems under parametric excitation of non-white noises are considered to illustrate the analytical-numerical approach for the determination of the pth moment Lyapunov exponent.

3 Eigenvalue Problems for $\Lambda(p)$ of Two-Dimensional Systems

Consider a single degree-of-freedom system under random noise parametric excitation

$$\frac{d^2q(\tau)}{d\tau^2} + 2\beta\frac{dq(\tau)}{d\tau} + [\omega_0^2 - \varepsilon_0\eta(\tau)]q(\tau) = 0, \tag{16}$$

where τ is the time variable, $q(\tau)$ the generalized coordinate, β the damping constant, ω_0 the circular natural frequency of the system, and ε_0 the amplitude of the random fluctuation. An example of system (16) is the transverse vibration of a column under dynamic axial load. In this paper, the random noise $\eta(\tau)$ is considered as a bounded noise or a real noise process.

3.1 Bounded Noise and Real Noise. A bounded noise process is given by

$$\eta(\tau) = \cos[\nu_0\tau + \sigma_0 W(\tau) + \theta], \tag{17}$$

in which θ is a uniformly distributed random number in $(0, 2\pi)$, and $W(\tau)$ is the standard Wiener process in time τ. The inclusion of the phase angle θ in Eq. (17) makes the bounded noise $\eta(\tau)$ a stationary process. The correlation function of $\eta(\tau)$ is given by

$$E[\eta(\tau_1)\eta(\tau_2)] = R(\tau_1 - \tau_2) = \frac{1}{2}\cos\nu_0(\tau_1 - \tau_2)\exp\left(-\frac{\sigma_0^2}{2}|\tau_1 - \tau_2|\right)$$

and the spectral density function of $\eta(\tau)$ is

$$S(\omega) = \int_{-\infty}^{+\infty} R(\tau)e^{i\omega\tau}d\tau = \frac{\sigma_0^2\left(\omega^2 + \nu_0^2 + \frac{1}{4}\sigma_0^4\right)}{2\left[(\omega-\nu_0)^2 + \frac{1}{4}\sigma_0^4\right]\left[(\omega+\nu_0)^2 + \frac{1}{4}\sigma_0^4\right]}.$$

It may be noted that the mean-square value of the bounded noise process $\eta(\tau)$ is fixed at $E[\eta^2(\tau)] = \frac{1}{2}$. The spectral density function can be made to approximate the well-known Dryden and von Karman spectra of wind turbulence by suitable choice of the parameters ν_0, σ_0, and ε_0. In the limit as σ_0 approaches infinite, the bounded noise becomes a white noise of constant spectral density. However, since the mean-square value is fixed at $\frac{1}{2}$, this constant spectral density level reduces to zero in the limit. On the other hand, in the limit as σ_0 approaches zero, the bounded noise becomes a deterministic sinusoidal function.

The bounded noise process (17) was first employed by Stratonovich [14] and has since been applied in many engineering applications, see, e.g., Refs. [15,16].

A real noise process modeled by an Ornstein–Uhlenbeck process is given by

$$d\eta(\tau) = -\alpha_0\eta(\tau)d\tau + \sigma_0 dW(\tau). \tag{18}$$

The Ornstein–Uhlenbeck process is a simple, Gaussian, explicitly representable stationary process that is often used to model a realizable noise process. The correlation function and the spectral density function of the Ornstein–Uhlenbeck process (18) are

$$E[\eta(\tau_1)\eta(\tau_2)] = R(\tau_1 - \tau_2) = \frac{\sigma_0^2}{2\alpha_0}\exp\{-\alpha_0|\tau_1 - \tau_2|\},$$

$$S(\omega) = \int_{-\infty}^{+\infty} R(\tau)e^{i\omega\tau}d\tau = \frac{\sigma_0^2}{2(\alpha_0^2 + \omega^2)},$$

in which α_0 characterizes the bandwidth of the noise and $\sigma_0/(2\alpha_0^2)$ is related to the spectral density of the noise. For the special case $\sigma_0 = \alpha_0 \to \infty$, the Ornstein–Uhlenbeck process $\eta(\tau)$ approaches the unit Gaussian white noise process $\dot{W}(\tau)$.

Equation (16) can be simplified by removing the damping term using the transformation $q(\tau) = x(\tau)e^{-\beta\tau}$ and time scaling $t = \omega\tau$, where $\omega^2 = \omega_0^2 - \beta^2$, to yield

$$\frac{d^2x(t)}{dt^2} + [1 - \varepsilon\xi(t)]x(t) = 0, \tag{19}$$

where $\varepsilon = \varepsilon_0/\omega^2$.

For the bounded noise excitation (17),

$$\xi(t) = \cos\zeta(t), \quad d\zeta(t) = \nu dt + \sigma dW(t), \tag{20}$$

where $\nu = \nu_0/\omega$, $\sigma = \sigma_0/\sqrt{\omega}$, and $W(t)$ is a standard Wiener process in time t.

For the real noise modeled by an Ornstein–Uhlenbeck process (18)

$$\xi(t) = \zeta(t), \quad d\zeta(t) = -\alpha\zeta(t)dt + \sigma dW(t), \tag{21}$$

where $\alpha = \alpha_0/\omega$, $\sigma = \sigma_0/\sqrt{\omega}$.

The moment Lyapunov exponent of systems (16) and (19) are related by

$$\Lambda_{q(\tau)}(p) = -p\beta + \omega\Lambda_{x(t)}(p). \tag{22}$$

3.2 Two-Dimensional System Under Bounded Noise Excitation. The eigenvalue problem governing the pth moment Lyapunov exponent of system (19) can be derived using the formulation for a general n-dimensional linear stochastic system presented in Sec. 2.

For the bounded noise excitation (20), the generator of process $\zeta(t)$ is

$$\mathcal{G} = \frac{\sigma^2}{2}\frac{\partial^2}{\partial\zeta^2} + \nu\frac{\partial}{\partial\zeta}. \tag{23}$$

The generator $\mathcal{G}$ of the bounded noise $\zeta(t)$ is strongly elliptic, which is a required condition for the validity of Eq. (10) and the uniqueness of its solution. Letting $x_1 = x$, $x_2 = \dot{x}$, the single degree-of-freedom system (19) may be written in the form of state equation

$$\begin{Bmatrix}\dot{x}_1\\ \dot{x}_2\end{Bmatrix} = \mathbf{A}(\zeta)\begin{Bmatrix}x_1\\ x_2\end{Bmatrix}, \quad \mathbf{A}(\zeta) = \begin{bmatrix}0 & 1\\ -1 + \varepsilon\cos\zeta & 0\end{bmatrix}. \tag{24}$$

Apply the Khasminskii transformation [11]

$$s_1 = \frac{x_1}{a} = \cos\varphi, \quad s_2 = \frac{x_2}{a} = \sin\varphi, \quad a = \|\mathbf{x}\| = (x_1^2 + x_2^2)^{1/2} \tag{25}$$

and denote $\mathbf{s} = \{s_1, s_2\}^T = \{\cos\varphi, \sin\varphi\}^T$. From Sec. 2, the operator $\mathcal{L}(p)$ is given by Eq. (12), where

$$q(\zeta, \mathbf{s}) = \mathbf{s}^T\mathbf{A}(\zeta)\mathbf{s} = \varepsilon\cos\zeta\cos\varphi\sin\varphi,$$

$$\mathbf{h}(\zeta, \mathbf{s}) = [\mathbf{A}(\zeta) - q(\zeta, \mathbf{s})\mathbf{I}]\mathbf{s} = \begin{Bmatrix}-\varepsilon\cos\zeta\cos^2\varphi\sin\varphi + \sin\varphi\\ (-1 + \varepsilon\cos\zeta)\cos\varphi - \varepsilon\cos\zeta\cos\varphi\sin^2\varphi\end{Bmatrix}. \tag{26a}$$

Hence

$$\mathbf{h}^T\frac{\partial}{\partial \mathbf{s}}=h_1\frac{\partial}{\partial s_1}+h_2\frac{\partial}{\partial s_2}=h_1\left(-\sin\varphi\frac{\partial}{\partial\varphi}\right)+h_2\left(\cos\varphi\frac{\partial}{\partial\varphi}\right)$$

$$=(-1+\varepsilon\cos\zeta\cos^2\varphi)\frac{\partial}{\partial\varphi} \tag{26b}$$

and

$$\mathcal{L}(p)=\frac{\sigma^2}{2}\frac{\partial^2}{\partial\zeta^2}+\nu\frac{\partial}{\partial\zeta^2}+(-1+\varepsilon\cos\zeta\cos^2\varphi)\frac{\partial}{\partial\varphi}$$
$$+\varepsilon p\cos\zeta\cos\varphi\sin\varphi. \tag{27}$$

3.3 Two-Dimensional System Under Real Noise Excitation. For the Ornstein–Uhlenbeck process $\zeta(t)$ given by Eq. (21), the Stratonovich equation is the same as the Itô equation. The generator of process $\zeta(t)$ is

$$\mathcal{G}=-\alpha\zeta\frac{\partial}{\partial\zeta}+\frac{\sigma^2}{2}\frac{\partial^2}{\partial\zeta^2}. \tag{28}$$

Letting $x_1=x$, $x_2=\dot{x}$, the single degree-of-freedom system can be written in the form of state equations

$$\begin{Bmatrix}\dot{x}_1\\ \dot{x}_2\end{Bmatrix}=\mathbf{A}(\zeta)\begin{Bmatrix}x_1\\ x_2\end{Bmatrix},\quad \mathbf{A}(\zeta)=\begin{bmatrix}0 & 1\\ -1+\varepsilon^{1/2}\zeta & 0\end{bmatrix}. \tag{29}$$

Applying the Khasminskii transformation (25), Eqs. (26) become

$$q(\zeta,\varphi)=\mathbf{s}^T\mathbf{A}(\zeta)\mathbf{s}=\varepsilon^{1/2}\zeta\cos\varphi\sin\varphi,$$

$$\mathbf{h}(\zeta,\varphi)=[\mathbf{A}(\zeta)-q(\zeta,\varphi)\mathbf{I}]\mathbf{s}$$
$$=\begin{Bmatrix}-\varepsilon^{1/2}\zeta\cos^2\varphi\sin\varphi+\sin\varphi\\ (-1+\varepsilon^{1/2}\zeta)\cos\varphi-\varepsilon^{1/2}\zeta\cos\varphi\sin^2\varphi\end{Bmatrix}, \tag{30}$$

$$\mathbf{h}^T\frac{\partial}{\partial \mathbf{s}}=h_1\frac{\partial}{\partial s_1}+h_2\frac{\partial}{\partial s_2}=h_1\left(-\sin\varphi\frac{\partial}{\partial\varphi}\right)+h_2\left(\cos\varphi\frac{\partial}{\partial\varphi}\right)$$

$$=(-1+\varepsilon^{1/2}\zeta\cos^2\varphi)\frac{\partial}{\partial\varphi}.$$

Hence, the eigenvalue problem governing the pth moment Lyapunov exponent $\Lambda(p)$ is given by Eq. (10) with the operator $\mathcal{L}(p)$ given by Eq. (12), i.e.,

$$\mathcal{L}(p)=\frac{\sigma^2}{2}\frac{\partial^2}{\partial\zeta^2}-\alpha\zeta\frac{\partial}{\partial\zeta}+(-1+\varepsilon^{1/2}\zeta\cos^2\varphi)\frac{\partial}{\partial\varphi}$$
$$+\varepsilon^{1/2}p\zeta\cos\varphi\sin\varphi. \tag{31}$$

The eigenvalue problems (27) and (31) can also be derived using a more straightforward approach originally applied by Wedig [17] for a two-dimensional linear Itô stochastic system.

4 Transformation of the Eigenvalue Problems for the Moment Lyapunov Exponents

In this section, series expansions of the eigenfunctions are employed to convert the second-order partial differential eigenvalue problems (27) and (31), governing the pth moment Lyapunov exponents, to linear algebraic eigenvalue problems, which can then be easily solved numerically.

4.1 Two-Dimensional System Under Bounded Noise Excitation. For the two-dimensional system (19) under bounded noise excitation (20), the pth moment Lyapunov exponent satisfies the eigenvalue problem (10) with Eq. (27). Since the coefficients of the eigenvalue problem are periodic functions in ζ of period 2π and in φ of period π, the eigenfunction $T(\zeta,\varphi)$ can be expanded in double Fourier series in the complex form, which is much more compact than the real form, as follows [18]:

$$T(\zeta,\varphi)=\sum_{\ell=-\infty}^{\infty}\sum_{k=-\infty}^{\infty}C_{\ell,k}\mathrm{e}^{\mathrm{i}(\ell\zeta+2k\varphi)}, \tag{32}$$

where the coefficients $C_{\ell,k}$ are complex numbers. It can be easily shown that the functions in Eq. (32) possess the orthogonality conditions

$$\int_{\zeta=0}^{2\pi}\mathrm{e}^{\mathrm{i}\ell\zeta}\cdot\mathrm{e}^{-\mathrm{i}m\zeta}d\zeta=2\pi\delta_{\ell,m},\quad \int_{\varphi=0}^{\pi}\mathrm{e}^{\mathrm{i}2k\phi}\cdot\mathrm{e}^{-\mathrm{i}2n\varphi}d\varphi=\pi\delta_{k,n}, \tag{33}$$

where $\delta_{\ell,k}$ denotes the Kronecker delta symbol.

Substituting Eq. (32) into Eq. (10) with $\mathcal{L}(p)$ given by Eq. (27), multiplying the resulting equation by $\mathrm{e}^{-i(m\zeta+2n\varphi)}$, integrating with respect to ζ from 0 to 2π and with respect to φ from 0 to π, and employing the orthogonality conditions (33) yields, for $m,n=0,\pm1,\pm2,\ldots$,

$$\mathrm{i}\tfrac{1}{8}\varepsilon\{[2(n-1)-p](C_{m-1,n-1}+C_{m+1,n-1})$$
$$+[2(n+1)+p](C_{m-1,n+1}+C_{m+1,n+1})\}$$
$$+\mathrm{i}\tfrac{1}{2}\varepsilon n(C_{m-1,n}+C_{m+1,n})+\left(-\tfrac{1}{2}\sigma^2m^2+\mathrm{i}m\upsilon-\mathrm{i}2n\right)C_{m,n}$$
$$=\Lambda C_{m,n}. \tag{34}$$

Equations (34) represent a linear algebraic eigenvalue problem of infinite dimension. In numerical analysis, only a finite number of terms can be taken in the double Fourier series (32). Hence, let m take the values $-M,-M+1,\ldots,M-1,M$, and n take the values $-N,-N+1,\ldots,N-1,N$; that is, there are $2M+1$ terms in ζ and $2N+1$ terms in φ in the double Fourier series (32).

For the ease of formulation, the two-dimensional array of the coefficients $C_{m,n}$ is transformed to the one-dimensional array $y_j=C_{m,n}$, where $j=(2N+1)(M+m)+N+n+1$, for $m=-M:M$, $n=-N:N$. Hence Eqs. (34) result in a linear algebraic eigenvalue problem

$$\mathbf{A}\mathbf{y}=\Lambda\mathbf{y}, \tag{35}$$

in which the dimension of matrix $\mathbf{A}$ is $(2M+1)(2N+1)\times(2M+1)(2N+1)$. For the jth row, $j=(2N+1)(M+m)+N+n+1$, $m=-M:M$, $n=-N:N$, the non-zero elements of $\mathbf{A}$ are

$$A_{j,j}=-\tfrac{1}{2}\sigma^2m^2+\mathrm{i}m\upsilon-\mathrm{i}2n,\quad A_{j,J^-}=A_{j,J^+}=\mathrm{i}\tfrac{1}{2}\varepsilon n,$$

$$A_{j,J^--1}=A_{j,J^+-1}=\mathrm{i}\tfrac{1}{8}\varepsilon[2(n-1)-p],$$

$$A_{j,J^-+1}=A_{j,J^++1}=\mathrm{i}\tfrac{1}{8}\varepsilon[2(n+1)+p],$$

where $J^{\pm}=(2N+1)(M+m\pm1)+N+n+1$.

4.2 Two-Dimensional System Under Real Noise Excitation. The moment Lyapunov exponent of the two-dimensional system (19) under real noise excitation (21) is governed by the eigenvalue problem (31). The coefficients of Eq. (31) are periodic functions in φ of period π. The eigenfunction $T(\zeta,\varphi)$ is expanded in terms of sinusoidal functions and Hermite polynomials as

$$T(\zeta,\varphi)=\sum_{\ell=0}^{\infty}\sum_{k=-\infty}^{\infty}C_{\ell,k}h_\ell(\zeta)\mathrm{e}^{\mathrm{i}2k\varphi}, \tag{36}$$

where $h_\ell(\zeta)$ is the normalized Hermite polynomial

$$h_\ell(\zeta)=\frac{1}{(2^\ell\ell!\sqrt{\pi})^{1/2}}\exp\left(-\frac{\zeta^2}{2}\right)H_\ell(\zeta),\quad \ell=0,1,\ldots, \tag{37}$$

in which $H_\ell(\zeta)$ is the Hermite polynomial [19]. The normalized Hermite polynomials $h_\ell(\zeta),\ell=0,1,\ldots$, form an orthonormal system on the interval $(-\infty,+\infty)$, i.e.,

$$\int_{-\infty}^{+\infty} h_\ell(\zeta)h_m(\zeta)\mathrm{d}\zeta = \delta_{\ell,m}. \tag{38}$$

Some relevant properties of the normalized Hermite polynomials are derived in Appendix A. Double series expansions involving Fourier series and Hermite polynomials have been applied by Wedig [20] in obtaining solutions of two-dimensional Fokker–Planck equations.

Substituting Eq. (36) into Eq. (31), multiplying the resulting equation by $h_m(\zeta)e^{-i2n\varphi}$, for $m=0:+\infty$ and $n=-\infty:+\infty$, integrating with respect to ζ from $-\infty$ to $+\infty$ and with respect to φ from 0 to π, and utilizing the orthogonality condition (38) and identities (43) leads to the equations

$$\begin{aligned}
&\left[-\frac{\sigma^2}{2}\left(m+\frac{1}{2}\right)+\frac{\alpha}{2}-\mathrm{i}2n\right]C_{m,n}\\
&\quad+\mathrm{i}\varepsilon\left[\frac{2(n-1)-p}{4}\left(\sqrt{\frac{m}{2}}C_{m-1,n-1}+\sqrt{\frac{m+1}{2}}C_{m+1,n-1}\right)\right.\\
&\quad+\frac{2(n+1)+p}{4}\left(\sqrt{\frac{m}{2}}C_{m-1,n+1}+\sqrt{\frac{m+1}{2}}C_{m+1,n+1}\right)\\
&\quad\left.+n\left(\sqrt{\frac{m}{2}}C_{m-1,n}+\sqrt{\frac{m+1}{2}}C_{m+1,n}\right)\right]+\\
&\quad\left(\frac{\sigma^2}{2}+\alpha\right)\frac{\sqrt{m(m-1)}}{2}C_{m-2,n}\\
&\quad+\left(\frac{\sigma^2}{2}-\alpha\right)\frac{\sqrt{(m+2)(m+1)}}{2}C_{m+2,n}=\Lambda C_{m,n}.
\end{aligned}\tag{39}$$

Equations (39) are a system of infinity homogeneous linear algebraic equations for the unknown coefficients $C_{m,n}$, $m=0:+\infty$, $n=-\infty:+\infty$. For numerical analysis, the series expansion (36) must be truncated, i.e., m takes the values $0,1,\ldots,M$, and n takes the values $-N,-N+1,\ldots,N-1,N$. Map the two-dimensional array of coefficients $C_{m,n}$ to the one-dimensional array $y_j=C_{m,n}$, $j=(2N+1)m+N+n+1$. Equations (39) can then be written in the form of a linear algebraic eigenvalue problem (35), in which the dimension of matrix $\mathbf{A}$ is $(M+1)(2N+1)\times(M+1)(2N+1)$. For row $j=(2N+1)m+N+n+1$, the non-zero elements of matrix $\mathbf{A}$ are

$$A_{j,j}=-\frac{\sigma^2}{2}\left(m+\frac{1}{2}\right)+\frac{\alpha}{2}+\mathrm{i}2n,$$

$$A_{j,J^--1}=\mathrm{i}\varepsilon\frac{2(n-1)-p}{4}\sqrt{\frac{m}{2}},\quad A_{j,J^-}=\mathrm{i}\varepsilon n\sqrt{\frac{m}{2}},$$

$$A_{j,J^-+1}=\mathrm{i}\varepsilon\frac{2(n+1)+p}{4}\sqrt{\frac{m}{2}},$$

$$A_{j,J^+-1}=\mathrm{i}\varepsilon\frac{2(n-1)-p}{4}\sqrt{\frac{m+1}{2}},\quad A_{j,J^+}=\mathrm{i}\varepsilon n\sqrt{\frac{m+1}{2}},$$

$$A_{j,J^++1}=\mathrm{i}\varepsilon\frac{2(n+1)+p}{4}\sqrt{\frac{m+1}{2}},$$

$$A_{j,J_2^-}=\left(\frac{\sigma^2}{2}+\alpha\right)\frac{\sqrt{m(m-1)}}{2},\quad A_{j,J_2^+}=\left(\frac{\sigma^2}{2}-\alpha\right)\frac{\sqrt{(m+2)(m+1)}}{2},$$

where $J^\pm=(2N+1)(m\pm1)+N+n+1$ and $J_2^\pm=(2N+1)(m\pm2)+N+n+1$.

5 Numerical Results and Discussions

In Sec. 4, double series expansions of the eigenfunctions using orthogonal functions are applied to transform the partial differential eigenvalue problem (10) with $\mathcal{L}(p)$ given by Eqs. (27) and (31), respectively, into linear algebraic eigenvalue problems of the form (35). The resulting large square matrix $\mathbf{A}$ is sparse. To solve system (35) numerically, one must take full advantage of the sparsity of matrix $\mathbf{A}$ in developing or selecting numerical algorithms. *Matlab 6* has an excellent sparse matrix handling facility and functions for determining the eigenvalues of a large sparse matrix. In this paper, the function eigs in *Matlab 6* is used to evaluate a few eigenvalues of system (35). Numerical results are presented in the following.

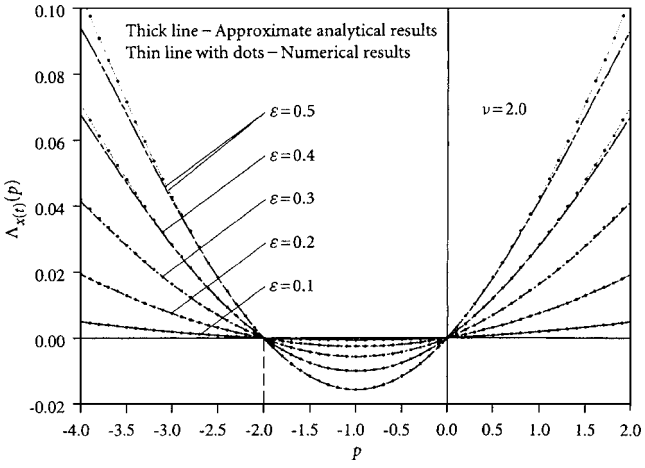

Fig. 1 $\Lambda_{x(t)}(p)$ of system under bounded noise excitation, $\sigma=1.0$, $\nu=2.0$, primary resonance

5.1 Two-Dimensional System Under Bounded Noise Excitation. The bounded noise excitation (20) reduces to harmonic excitation, i.e., $\xi(t)=\cos\nu t$, when $\sigma=0$. It is well known that the resulting Mathieu's Eq. (19) under harmonic excitation is in parametric resonance when $\nu=2,1,\frac{1}{2},\frac{1}{3},\frac{1}{4},\ldots$. The effect of the noise on the parametric resonance or the stability of system (19) is of particular interest.

Using a method of regular perturbation, Xie [7] obtained a fourth-order weak noise expansion of the moment Lyapunov exponent of system (19) under bounded noise excitation (20).

In the numerical solution of the linear algebraic eigenvalue problem (35), the numbers of terms of the series expansion are taken as $N=M=50$, resulting in the dimension of matrix $\mathbf{A}$ being $10\,201\times10\,201$. The number of non-zero elements is 69 800 and the density is

$$\text{density}=\frac{\text{Number of non-zero elements}}{\text{Total number of elements}}=\frac{69\,800}{10\,201^2}=6.708\times10^{-4},$$

which indicates that matrix $\mathbf{A}$ is sparse. The approximate analytical result in Ref. [7] can be used as a seed in the *Matlab* function eigs to determine the largest real eigenvalue of system (35).

Numerical results of the moment Lyapunov exponents are shown in Figs. 1–3 for $\nu=2.0$, 1.0, and 3.0, respectively, $\sigma=1.0$, and various values of ε. When $\nu=2.0$, i.e., system (19) is in primary resonance when $\sigma=0$, the approximate analytical result agrees very well with the numerical results for ε up to 0.5 as shown in Fig. 1. For $\nu=1.0$, i.e., system (19) is in secondary resonance, very good agreement between the two results is observed for ε as large as 0.8 (Fig. 2). Discrepancy between the two results increases rapidly when the value of ε is increased as shown in Figs. 1 and 2. When $\nu=3.0$, as shown in Fig. 3, system (19) is not in parametric resonance and the two results agree extremely well for ε as large as 1.0.

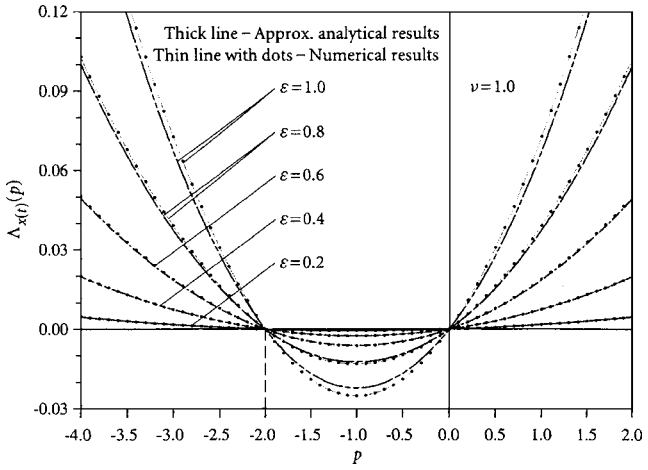

Fig. 2 $\Lambda_{x(t)}(p)$ of system under bounded noise excitation, σ =1.0, ν=1.0, secondary resonance

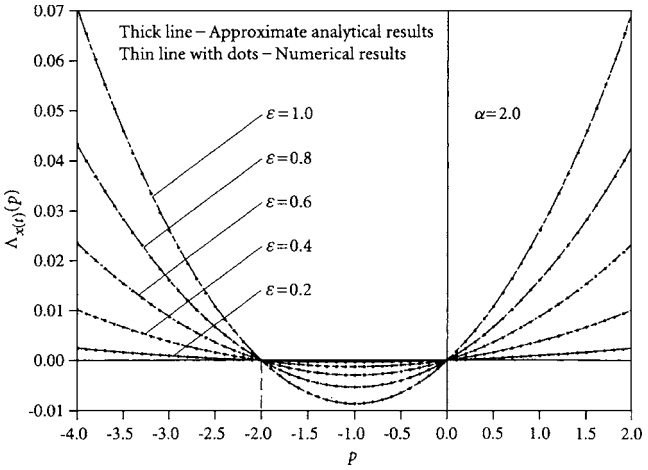

Fig. 4 $\Lambda_{x(t)}(p)$ of system under real noise excitation, α=2.0, σ=1.0

5.2 Two-Dimensional System Under Real Noise Excitation. When the noise amplitude parameter ε is small, a sixth-order perturbation of the moment Lyapunov exponent of system (19) under the real noise excitation (21) is given in Ref. [6]. One extra parameter can be eliminated in Eqs. (19) and (21) as

$$\ddot{x}(t) + [1 - \hat{\varepsilon}\hat{\xi}(t)]x(t) = 0,$$

$$d\hat{\xi}(t) = -\alpha\hat{\xi}(t)dt + dW,$$

where $\hat{\xi}(t)=\xi(t)/\sigma$, $\hat{\varepsilon}=\varepsilon\sigma$. Hence, without loss of generality, the parameter σ can be taken as 1.

In the numerical analysis, the numbers of the double series expansions are taken as $M=N=50$. The dimension of matrix **A** in the linear algebraic eigenvalue problem (35) is 5151×5151 and the number of non-zero elements is 44 849. The density of non-zero elements is $44\,849/5151^2=1.690\times10^{-3}$. Hence, matrix **A** is also sparse and, as in Sec. 5.1, the eigs function in *Matlab* is used to determine the largest real eigenvalue as the moment Lyapunov exponent, with the approximate analytical result in Ref. [6] used as the seed.

Typical results of the moment Lyapunov exponents obtained are shown in Figs. 4–6 for α=2.0, 1.0, and 0.5, respectively, and various values of the noise amplitude parameter ε. The approximate analytical results given in Ref. [6] are also plotted in Figs. 4–6 for comparison.

For α=2.0, the approximate analytical result and the numerical result agree extremely well even for ε as large as 1.0. For α =1.0, some discrepancies are observed between these two results

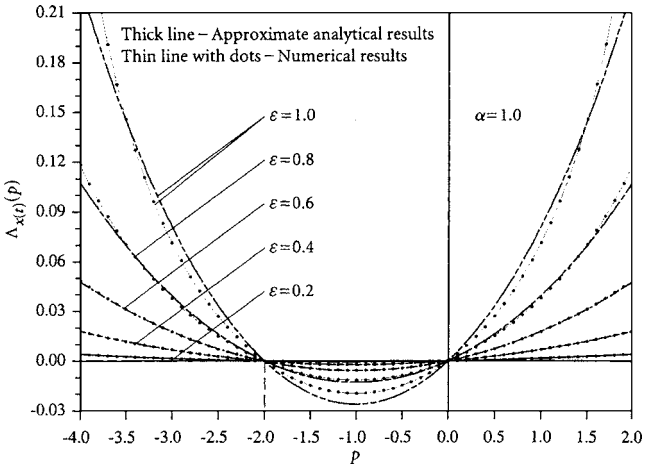

Fig. 5 $\Lambda_{x(t)}(p)$ of system under real noise excitation, α=1.0, σ=1.0

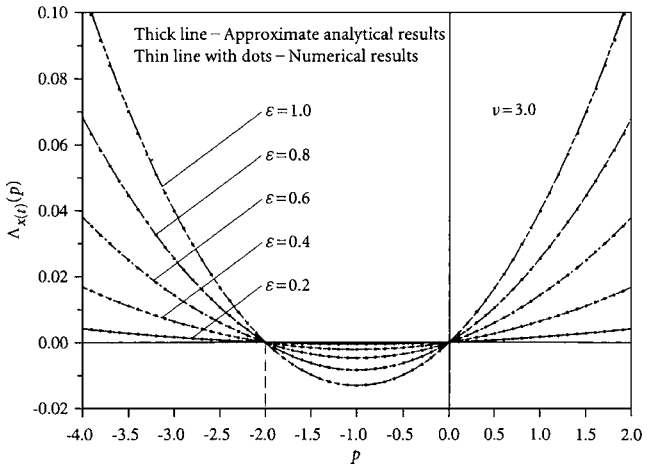

Fig. 3 $\Lambda_{x(t)}(p)$ of system under bounded noise excitation, σ =1.0, ν=3.0, no resonance

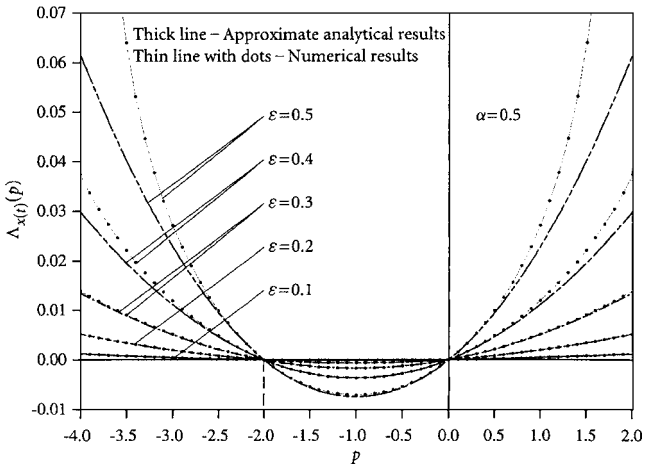

Fig. 6 $\Lambda_{x(t)}(p)$ of system under real noise excitation, α=0.5, σ=1.0

for $\varepsilon=0.8$ and 1.0; as expected, the larger the value of ε, the larger the discrepancy. For $\alpha=0.5$, differences between the analytical and numerical results can be seen for smaller values of $\varepsilon^{1/2}$, such as 0.4 and 0.5.

6 Conclusions

From the theory of stochastic dynamic systems, it is known that the pth moment Lyapunov exponent of a general n-dimensional linear stochastic system is the principal eigenvalue of a second-order partial differential eigenvalue problem, as presented in Sec. 2. An analytical-numerical approach is proposed to obtain numerical values of the pth moment Lyapunov exponents and the method is illustrated using a two-dimensional system under either a bounded noise or a real noise parametric excitation. Double series expansions of the eigenfunctions in terms of orthogonal functions are taken to transform the partial differential eigenvalue problems to linear algebraic eigenvalue problems. The eigs function in *Matlab* for determining a few eigenvalues of a large sparse matrix is then used to solve the linear eigenvalue problem to obtain the pth moment Lyapunov exponents. The numerical results are compared with the approximate analytical results with weak noise obtained earlier (Refs. [6,7]). It is found that for small amplitude of the exciting noise ε, the approximate analytical results agree with the numerical results extremely well. Discrepancies increase for large values of ε. The focus of this study is to present a numerical approach for the determination of the pth moment Lyapunov exponents of linear stochastic systems for all values of p. Detailed discussions on the effect of noise on the parametric resonance and the stability of the dynamical systems can be found in Refs. [6,7].

The analytical-numerical approach presented in this paper is very efficient for lower-dimensional systems, for which the partial differential eigenvalue problems can be easily transformed to linear algebraic eigenvalue problems. For systems of larger dimensions, the conversion from partial differential eigenvalue problems to linear algebraic eigenvalue problems using series expansions of the eigenfunctions could be very involved and the dimensions of the resulting linear algebraic eigenvalue problems could be very large, which may not be handled efficiently even by using a capable algorithm for sparse matrices.

This is the first paper that presents a method for numerically determining the pth moment Lyapunov exponents for all real values of p of two-dimensional systems under non-white noise excitations. Its usefulness and importance is twofold. First, it verifies the validity of the approximate analytical results and determines the range of applicability of the parameter ε. Second, for many engineering applications, the amplitude of the noise ε is not small and numerical approaches must be employed to determine the pth moment Lyapunov exponents.

The analytical-numerical method presented can be applied to systems under noise excitations with explicit analytical descriptions, such as bounded noise or filtered white noise. However, it is not applicable to systems under arbitrary noise excitations with a knowledge of time series only, because it is not possible to set up the partial differential eigenvalue problems. In this case, a Monte Carlo simulation approach may have to be applied. Unfortunately, currently there is no numerical algorithm available. The development of a Monte Carlo simulation algorithm for the determination of the pth moment Lyapunov exponent of a general n-dimensional system will be the focus of future study.

Acknowledgment

The research for this paper was supported, in part, by the Natural Sciences and Engineering Research Council of Canada. W.C.X. is grateful to the Department of Mechanical Engineering, the Hong Kong Polytechnic University, for the financial support provided during his sabbatical leave. R.M.C.S. is grateful for the support given him by the Research Grants Council of the Government of the HKSAR under Grant No. PolyU5174/02E. The authors are grateful to the referee for the constructive comments which helped to improve the paper.

Appendix A. Formulas of the Normalized Hermite Polynomials

It is well known that the Hermite polynomials satisfy the identities

$$H_{m+1}(\zeta)=2\zeta H_m(\zeta)-2mH_{m-1}(\zeta),\qquad H'_m(\zeta)=2mH_{m-1}(\zeta), \tag{40}$$

from which it can be shown that

$$\zeta H_m(\zeta)=\tfrac{1}{2}H_{m+1}(\zeta)+mH_{m-1}(\zeta),$$

$$\zeta^2 H_m(\zeta)=\tfrac{1}{4}H_{m+2}(\zeta)+\left(m+\tfrac{1}{2}\right)H_m(\zeta)+m(m-1)H_{m-2}(\zeta),$$

$$\zeta^2 H'_m(\zeta)=mH_m(\zeta)+2m(m-1)H_{m-2}(\zeta),\qquad H''_m(\zeta)=4m(m-1)H_{m-2}(\zeta). \tag{41}$$

Using Eqs. (40) and (41) and the definition of the generalized Hermite polynomials, one obtains

$$\zeta h_m(\zeta)=\sqrt{\frac{m+1}{2}}h_{m+1}(\zeta)+\sqrt{\frac{m}{2}}h_{m-1}(\zeta),$$

$$\zeta h'_m(\zeta)=-\frac{\sqrt{(m+2)(m+1)}}{2}h_{m+2}(\zeta)-\tfrac{1}{2}h_m(\zeta)+\frac{\sqrt{m(m-1)}}{2}h_{m-2}(\zeta), \tag{42}$$

$$h''_m(\zeta)=\frac{\sqrt{(m+2)(m+1)}}{2}h_{m+2}(\zeta)-\left(n+\tfrac{1}{2}\right)h_m(\zeta)+\frac{\sqrt{m(m-1)}}{2}h_{m-2}(\zeta).$$

Employing the orthogonality condition (38), the following results can be derived:

$$\int_{-\infty}^{+\infty}\zeta h_\ell(\zeta)h_m(\zeta)d\zeta=\sqrt{\frac{m+1}{2}}\delta_{\ell,m+1}+\sqrt{\frac{m}{2}}\delta_{\ell,m-1},$$

$$\int_{-\infty}^{+\infty}\zeta h'_\ell(\zeta)h_m(\zeta)d\zeta=-\frac{\sqrt{(m+2)(m+1)}}{2}\delta_{\ell,m+2}-\tfrac{1}{2}\delta_{\ell,m}+\frac{\sqrt{m(m-1)}}{2}\delta_{\ell,m-2}, \tag{43}$$

$$\int_{-\infty}^{+\infty}h''_\ell(\zeta)h_m(\zeta)d\zeta=\frac{\sqrt{(m+2)(m+1)}}{2}\delta_{\ell,m+2}-\left(n+\tfrac{1}{2}\right)\delta_{\ell,m}+\frac{\sqrt{m(m-1)}}{2}\delta_{\ell,m-2}.$$

References

[1] Oseledec, Y. I., 1968, "A Multiplicative Ergodic Theorem. Lyapunov Characteristic Number for Dynamical Systems," Trans. Mosc. Math. Soc., **19**, pp. 197–231.

[2] Arnold, L., Doyle, M. M., and Sri Namachchivaya, N., 1997, "Small Noise Expansion of Moment Lyapunov Exponents for Two-Dimensional Systems," Dyn. Stab. Syst., **12**(3), pp. 187–211.

[3] Khasminskii, R. Z., and Moshchuk, N., 1998, "Moment Lyapunov Exponent and Stability Index for Linear Conservative System With Small Random Perturbation," SIAM J. Appl. Math., **58**(1), pp. 245–256.

[4] Sri Namachchivaya, N., and Vedula, L., 2000, "Stabilization of Linear Systems by Noise: Application to Flow Induced Oscillations," Dyn. Stab. Syst., **15**(2),

pp. 185–208.
[5] Sri Namachchivaya, N., and Van Roessel, H. J., 2001, "Moment Lyapunov Exponent and Stochastic Stability of Two Coupled Oscillators Driven by Real Noise," Trans. ASME, J. Appl. Mech., **68**(6), pp. 903–914.
[6] Xie, W.-C., 2001, "Moment Lyapunov Exponents of a Two-Dimensional System Under Real Noise Excitation," J. Sound Vib., **239**(1), pp. 139–155.
[7] Xie, W.-C., 2003, "Moment Lyapunov Exponents of a Two-Dimensional System Under Bounded Noise Parametric Excitation," J. Sound Vib., **263**(3), pp. 593–616.
[8] Milstein, G. N., 2002, "The Asymptotic Behavior of Semi-Invariants for Linear Stochastic Systems," Stochastics Dyn., **2**(2), pp. 281–294.
[9] Wolf, A., Swift, J., Swinney, H., and Vastano, A., 1985, "Determining Lyapunov Exponents From a Time Series," Physica D, **16**, pp. 285–317.
[10] Xie, W.-C., 2001, "Lyapunov Exponents and Moment Lyapunov Exponents of a Two-Dimensional Near-Nilpotent System," ASME J. Appl. Mech., **68**(3), pp. 453–461.
[11] Khasminskii, R. Z., 1967, "Necessary and Sufficient Conditions for the Asymptotic Stability of Linear Stochastic Systems," Theor. Probab. Appl., **12**, pp. 144–147 (English translation).
[12] Arnold, L., Oeljeklaus, E., and Pardoux, E., 1986, "Almost Sure and Moment Stability for Linear Itô Equations," *Lyapunov Exponents, Proceedings of a Workshop, Bremen, Germany, 1984, Lecture Notes in Mathematics*, **1186**, Springer Verlag, Berlinpp, 85–125.
[13] Arnold, L., Kliemann, W., and Oeljeklaus, E., 1986, "Lyapunov Exponents of Linear Stochastic Systems," *Lyapunov Exponents, Proceedings of a Workshop, Bremen, Germany, 1984, Lecture Notes in Mathematics*, **1186**, Springer, Verlag Berlin, pp. 129–159.
[14] Stratonovich, R. L., 1967, *Topics in the Theory of Random Noise*, Vol. II. Gordon and Breach, New York.
[15] Lin, Y. K., and Cai, G. Q., 1995, *Probabilistic Structural Dynamics: Advanced Theory and Applications*, McGraw–Hill, New York.
[16] Ariaratnam, S. T., 1996, "Stochastic Stability of Viscoelastic Systems Under Bounded Noise Excitation," *IUTAM Symposium on Advances in Nonlinear Stochastic Mechanics*, Kluwer, Dordrecht, pp. 11–18.
[17] Wedig, W., 1988, "Lyapunov Exponent of Stochastic Systems and Related Bifurcation Problems," *Stochastic Structural Dynamics—Progress in Theory and Applications*, Elsevier, London, pp. 315–327.
[18] Tolstov, G. P., 1962, *Fourier Series* (English translation), Prentice–Hall, Englewood Cliffs, NJ.
[19] Lebedev, N. N., 1972, *Special Functions and Their Applications* (English translation), Dover, New York.
[20] Wedig, W., 1995, *Probabilistic Methods in Applied Physics*, Springer, Berlin, pp. 120–148.

The Load Capacity of a Kagome Based High Authority Shape Morphing Structure

S. L. dos Santos e Lucato

A. G. Evans

Materials Department,
University of California,
Santa Barbara, CA 93106-5050

A protocol for optimizing a high authority shape morphing plate is described. The design incorporates an active Kagome back-plane capable of changing the shape of a solid face by transmitting loads through a tetrahedral truss core. The optimization assesses the required geometric dimensions and actuator specifications in order to maximize the permissible shape changes and load capacity. The critical external loads for all failure mechanisms of the individual components are calculated and used as constraints in the optimization. Resistance of the structure to actuation is presented as an additional constraint. The ensuing relations are subsequently used to choose the best material for a given application. Numerical examples of the procedure are given for a defined structure. [DOI: 10.1115/1.2042482]

1 Introduction

Shape morphing structures are designed to displace surfaces while resisted by large pressure loads (or heavy weights). An approach for addressing this challenge is to seek structures that are simultaneously statically determinate yet stiff [1–6]. One manifestation is the Kagome structure (Fig. 1) [2,3,6] which can be actuated into relatively intricate surface shapes. The structure consists of a solid face sheet with a Kagome, active back-plane and a tetrahedral core. Replacing various truss elements in the back-plane with linear actuators enables the shape of the solid face to be changed. A preliminary demonstration structure has been constructed and used to reveal the practical potential (Fig. 2) [6]. To facilitate fabrication, this structure was made using 304 stainless steel. The length of the panel was chosen to include six hexagonal units of the Kagome plate, while the width incorporated four. Hinging and twisting have been demonstrated and shown to be consistent with linear models [6]. To achieve smooth contour changes at low structural weight, the solid face and the back-plane were stiffness matched. Multiple virtual control points define the shape change [4–6]. The demonstration structure was found to be actuator limited, because the actuators ceased to function at loads much lower than the passive load capacity of the structure.

The intent of the present article is to provide a wider exploration of the authority space for this structure. It will embrace a broad range of material properties and assume actuators having load capacity substantially superior to those used in the preliminary demonstration. A corollary will be an optimization protocol. For tractability and clarity of presentation, the present assessment is limited to simple hinging of the demonstration structure (Fig. 2). Yet, the approach has much wider applicability and its implementation for the attainment of more complex shape changes will be presented in a forthcoming article. The procedure ascertains the stresses, relative to the failure envelope, and determines the actuator authority needed to maximize the load capacity as a function of designated displacements.

Contributed by the Applied Mechanics Division of ASME for publication in the JOURNAL OF APPLIED MECHANICS. Manuscript received July 23, 2004; final manuscript received February 14, 2004. Review conducted by Z. Suo. Discussion on the paper should be addressed to the Editor, Prof. Robert M. McMeeking, Journal of Applied Mechanics, Department of Mechanical and Environmental Engineering, University of California—Santa Barbara, Santa Barbara, CA 93105-5070, and will be accepted until four months after final publication in the paper itself in the ASME JOURNAL OF APPLIED MECHANICS.

2 Passive Load Capability

The passive loads that can be supported without failure have been derived for a cantilever plate subject to a line load, P, imposed at the free end (Fig. 1) [7]. When optimized for loadings that cause the solid face to experience compression, its structural efficiency is competitive with truss and honeycomb core panels [5]. The basic results needed for optimization will be presented with the assumption that the Kagome members are connected by pin joints. Relative to bonded joints this choice allows a fully analytical investigation. It does so without affecting the yield loads, while providing a conservative assessment of the buckling loads.

In the ensuing analysis, the subscripts k, c, and f refer to the Kagome back-plane, core, and solid face, respectively. All truss members have a square cross section, thickness d_x, and a length L_x (Fig. 1). The solid face has thickness d_f. The width and span of the structure are denoted w and s, respectively. The lengths of the Kagome and core members are equal ($L=L_k=L_c$), ensuring maximum resistance to core shear [5]. The Young's modulus is designated E, and yield strength σ_Y. Failure loads are denoted P_{XZ}, with subscript X referring to the component and Z to the failure mode: Y for yielding and B for buckling/wrinkling. The actuator is considered to cease functioning at axial load P_{ACT}.

Kagome back-plane. Initially, the stiffness of the solid face is chosen to match that for the back-plane (by adjusting its thickness). Under this assumption, the nominal stress induced in the back-plane is related to the bending moment, $M=Ps$, and the core height, $H_c=\sqrt{3/2}L$, by [8]

$$\sigma_{11}=\sqrt{\frac{3}{2}}\frac{Ps}{d_f w L}. \tag{1a}$$

Modifications that arise when the system is not stiffness matched are presented in the Appendix. There are three Kagome truss orientations (Fig. 1): one parallel to the width (truss A) and the others at ±30 deg to the span (truss B). For the present loading state, the latter two are equivalent. The nominal stress σ_{11} is related to that on a truss member σ_{truss} by [2]

$$\sigma_{11}=-\sqrt{3}\frac{d_f}{L}\sigma_{\mathrm{truss}}\ \text{(truss A)}\quad\text{and}\quad\sigma_{11}=\frac{\sqrt{3}}{2}\frac{d_f}{L}\sigma_{\mathrm{truss}}\ \text{(truss B)} \tag{1b}$$

If the back-plane is loaded in compression, trusses in orientation A are in tension and those in orientation B are in compression and

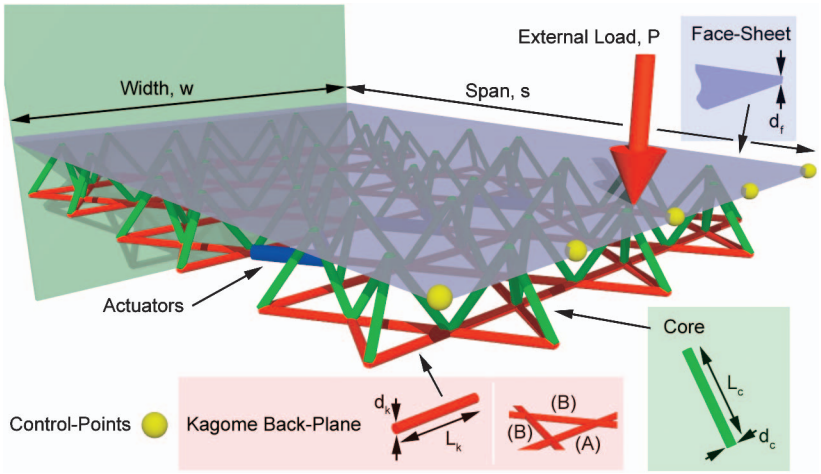

Fig. 1 (Color) Schematic representation of the Kagome-structure. The face sheet is shown in blue, the core in green, and the Kagome back-plane is red. Actuators are placed in lieu of the Kagome members. The control points are used to define the target deformation.

vice versa. Equating $|\sigma_{\text{truss}}|$ to the yield strength, σ_Y, gives the end load that can be supported without failure by yielding as

$$P_{KY} \leqslant \sqrt{2}\frac{wd_k^2}{s}\sigma_{Yk} \text{ (truss A)} \quad \text{and} \quad P_{KY} \leqslant \frac{1}{\sqrt{2}}\frac{wd_k^2}{s}\sigma_{Yk} \text{ (truss B)}. \tag{2}$$

The permissible load is always smaller for trusses in orientation B.

The treatment of buckling is slightly more complex, since the direction of the external load has to be considered. The load that can be supported without buckling if the solid face is in tension (Kagome in compression, i.e., only trusses in B orientation can buckle) is

$$P_{KB} \leqslant \frac{\pi^2}{12\sqrt{2}}\frac{wd_k^4}{L^2 s}E_k \tag{3}$$

Core. The tetrahedral core must sustain the shear force. The end load supported before yielding is [7]

$$P_{CY} \leqslant \frac{1}{\sqrt{6}}\frac{wd_c^2}{L}\sigma_{Yc}. \tag{4}$$

(Note that this core has half the number of tetrahedral element as a truss core sandwich panel [2].) The equivalent result for elastic buckling is

$$P_{CB} \leqslant \frac{\pi}{4\sqrt{6}}\frac{wd_c^4}{L^3}E_c. \tag{5}$$

Solid Face. The solid face has thickness

$$d_f = \lambda_{sm}\frac{E_k}{E_f}\frac{d_k^2}{\sqrt{3}L_k} \tag{6}$$

The scaling factor λ_{sm} is unity when the face is stiffness matched (solid face sheet has the same linear elastic load-deflection behavior as the Kagome back-plane when loaded in tension): $\lambda_{sm} > 1$ signifies a solid face stiffer than the back-plane and vice versa. In this analysis the face sheet stiffness for a given material combi-

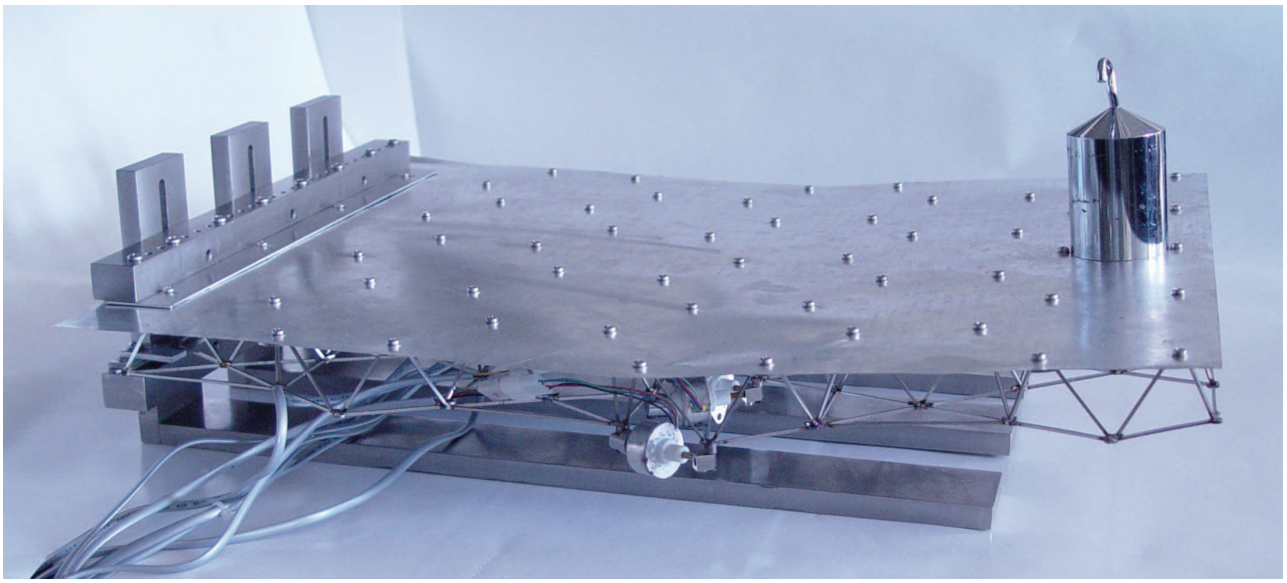

Fig. 2 (Color) Photo of the actual demo structure. The aluminum solid face sheet is used. Actuators are placed along the middle section and extended by 10%.

nation is varied by changing the thickness of the solid face sheet. For example, $\lambda_{sm}=1$ for a stainless steel back-plane ($E_k=200$ GPa) and a polycarbonate ($E_f=4$ GPa) solid face requires both faces to have the same thickness $d_f \approx d_k$. For designs with $d_f \ll H_c$, the load that can be supported is obtained from 1(a) by equating σ_{11} to σ_{Yf}:

$$P_{FY} \leqslant \sqrt{\frac{2}{3}} \frac{w d_f L}{s} \sigma_{Yf} \tag{7}$$

3 Actuation Resistance

When an actuation strain is imposed, the structure induces forces on the actuator, F_{ACT} [6,9]. These forces must be evaluated and compared with the operating characteristics of the actuator. To illustrate the procedure, results are presented for actuators placed along the mid-section, half way between the support and the free end of the cantilever (Fig. 2). For hinging, all actuators experience the same extension and the resistance of the structure scales as [6]

$$\Sigma = \frac{1 + A(E_f/E_c)\alpha + B(E_f/E_c)^2\alpha^2}{C + D(E_f/E_c)\alpha} \tag{8}$$

where Σ is the nondimensional resistance,

$$\Sigma = \frac{F_{ACT} L^3}{E_c \Delta d_c^4} \tag{9}$$

and α is a stubbiness index,

$$\alpha = \left(\frac{d_f}{d_c}\right)^3 \frac{w}{d_c} \tag{10}$$

Here Δ is the actuator displacement and A, B, C, D are nondimensional coefficients. When $E_f=E_c$, Eq. (8) reduces to

$$\frac{F_{ACT} L^3}{E_c \Delta d_c^4} = 0.2 - 0.8\alpha + 13\alpha^2 \tag{11}$$

The passive load induces another force F_{EXT} on the actuators, obtained from (1b) as

$$F_{\mathrm{EXT}} = \frac{0.58\sqrt{3}s}{\sqrt{2}} P_{\mathrm{ACT}} \tag{12}$$

Since the two forces are additive, the total force on the actuators is

$$F_{\mathrm{TOT}} = F_{\mathrm{EXT}} + F_{\mathrm{ACT}}$$

Equating to the load capacity of the actuator, $F_{\mathrm{ACT}}^{\max}$, the maximum permissible external load becomes

$$P_{\mathrm{ACT}} = (F_{\mathrm{ACT}}^{\max} - F_{\mathrm{ACT}}) \frac{\sqrt{2}}{0.58s\sqrt{3}} \tag{13}$$

4 Geometric Optimization

The objectives are to ascertain geometries that satisfy various design criteria, subject to the avoidance of all failure mechanisms. Throughout, the solid face sheet is assumed to be stiffness matched to the back-plane ($\lambda_{sm}=1$). The three criteria are as follows:

(i) Maximize the externally applied load by identifying the first subsystem to fail:

$$P_{\mathrm{ext}}^{\max} = \min(P_{KY}, P_{KB}, P_{CY}, P_{CB}, P_{FY}, P_{FB}, P_{\mathrm{ACT}}) \tag{14}$$

(ii) Maximize the displacement exerted by the actuators without causing failure of any other subsystem:

$$P_{\mathrm{ext}}^{\mathrm{passive}} = \min(P_{KY}, P_{KB}, P_{CY}, P_{CB}, P_{FY}, P_{FB}) \tag{15a}$$

$$\Delta^{\max} = \left(F_{\mathrm{ACT}}^{\max} - P_{\mathrm{ext}}^{\mathrm{passive}} \frac{0.58s\sqrt{3}}{\sqrt{2}}\right) \frac{L^3}{\Sigma E_c d_c^4} \tag{15b}$$

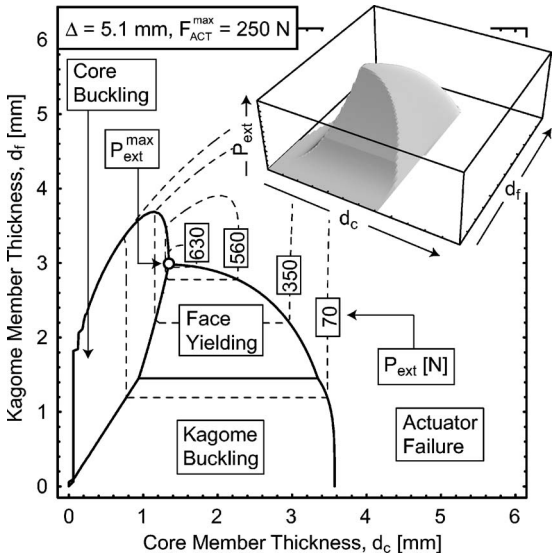

Fig. 3 Maximum load capability for a given actuator capacity and extension. All structure failure mechanisms except face wrinkling are included.

(iii) Determine the actuator load capacity needed to lift a specified passive load:

$$F_{\mathrm{ACT}}^{\mathrm{required}} = P_{\mathrm{ext}}^{\mathrm{passive}} \frac{0.58s\sqrt{3}}{\sqrt{2}} + F_{\mathrm{ACT}} \tag{16}$$

The variables are the thicknesses of the back-plane d_k and the core members d_c. In an application environment the truss length must coincide with the size of the actuators and is not a variable. For simplicity of presentation (as already noted), the other parameters are those applicable to the demonstration structure [6] [$L=L_k=L_c=5.1$ cm, $s=0.53$ m, $w=0.41$ m, $E_c=E_k=E_f=200$ GPa, $\sigma_{Yc}=\sigma_{Yk}=\sigma_{Yf}=200$ MPa (304 stainless steel)].

The load capacity at specified mass is typically the important engineering metric. To ascertain this quantity, note that the mass of the structure is

$$m = 24\left[6\left(L_k - \frac{1}{\sqrt{3}}d_k\right)d_k^2\rho_k + \left(\frac{\sqrt{3}}{2} + 6L_c\right)d_c^2\rho_c + 2\sqrt{3}L_k^2 d_f \rho_f\right] \tag{17}$$

with ρ_k, ρ_c, ρ_f being the densities of the Kagome, core, and solid face sheet materials, respectively. Invoking (14), the specific load capacity becomes

$$\bar{P} = \frac{P_{\mathrm{ext}}^{\max}}{m}. \tag{18}$$

5 Load Capability

The maximum load capability is limited either by structural failure (Eqs. (2)–(5) and (7)) or by the actuator capacity (Eq. (13)). A failure map calculated using (14) is presented as a surface in three-dimensional space comprising the coordinates, $P_{\mathrm{ext}}, d_c, d_k$ (Fig. 3, inset), with the truss thickness, d_c and d_k, as variables. Four failure domains are apparent. For very thin members, failure is dominated by buckling of either the core or the Kagome members. As the members become stubbier the failure mode transitions to face yielding. Eventually (for even greater stubbiness), the load becomes actuator limited. The maximal passive load capability is always at the confluence of the actuator limit and one (or more) of the structural limits. Note that, for a system with a 250 N actuator

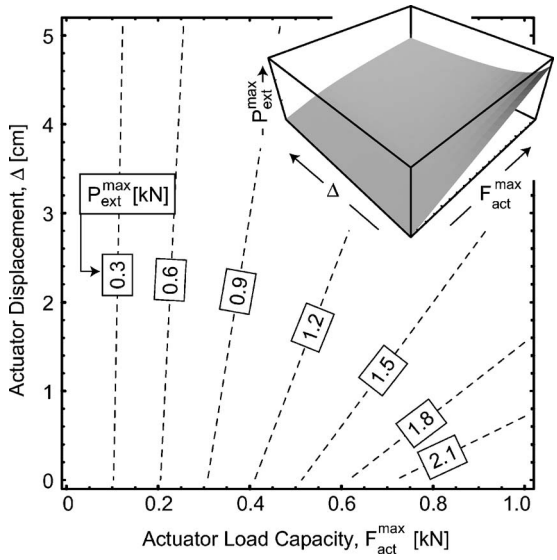

Fig. 4 Maximum load capability as a function of actuator capacity and actuator

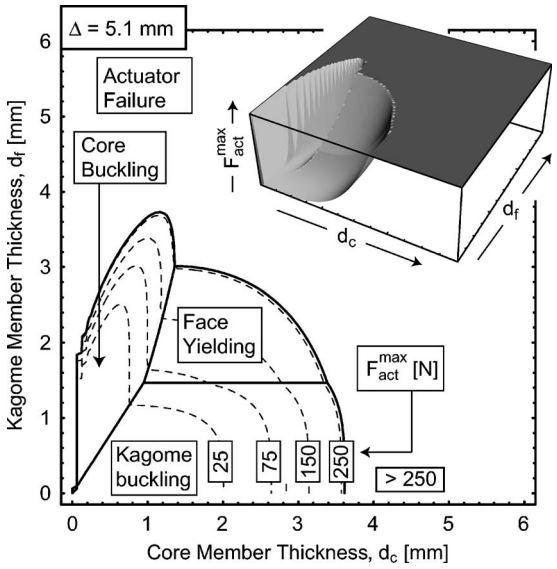

Fig. 6 Required actuator capacity for a given actuator extension of 10%. The plot has been truncated at F_{ACT}^{max}=250 N.

subject to 10% extension, the maximum load capability is 640 N, achieved with core and Kagome cross sections d_c=1.4 mm and d_k=3.0 mm, respectively.

This geometry is only optimal for one material and one actuator. Every other combination will exhibit another point. The *maximum permissible load capability for all possible actuators* is computed using a nonlinear optimization with Mathematica [10]. A typical result (Fig. 4) reveals that the load capability increases monotonically with increasing actuator capacity but decreases with increasing deformation. Since the latter is the limiting feature, Fig. 4 can be used to determine the actuator load capacity required to realize a specified load capability.

The maximum displacement that can be achieved (16) for an actuator capacity of 250 N is plotted in Fig. 5. To avoid the abrupt load drops when failure occurs by buckling, the dimensions of the members have been chosen to reside in the face yield regime. The requirements on the actuator capacity (for 10% extension) are shown on Fig. 6. To assure failure by face yielding, the capacity must be $F_{act}^{max} > 75$ N. Corresponding plots for other values of actuator capacity and displacement can be readily generated.

6 Influence of Material Properties

The previous assessments have been performed for fixed values of the material properties, E and σ_Y. The role of these properties is now explored by optimizing for ranges of Young's modulus (1–300 GPa) and yield strength (50–900 MPa). Many different failure maps have been generated (not shown for conciseness). The results are summarized in Fig. 7, which plots trends with face thickness for five cases. It is apparent that when the face is in tension (no wrinkling) materials with high yield strength ($\sigma_Y > 200$ MPa) provide the greatest load capacity. This maximum occurs for small relative face thickness, $1 < \lambda_{sm} < 3$. The modulus is relatively unimportant in this range. Low modulus only exerts an adverse influence at larger λ_{sm} where the load capacity is suboptimal. Materials with lower yield strength ($\sigma_Y \leqslant 50$ MPa) are clearly inferior (they permit appreciably lower load capability for all λ_{sm}).

The effect of varying the actuator capacity on the *load capability per unit mass* (Eq. (18)) is plotted in Fig. 8 for various engi-

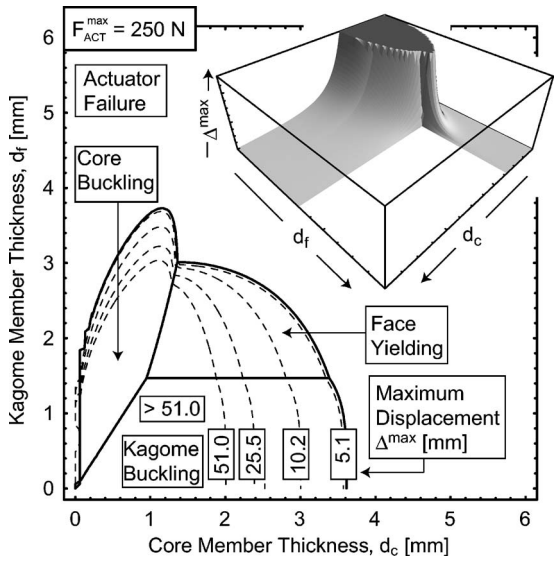

Fig. 5 Contour of actuator extension for a given actuator capacity of 250 N. The plot has been truncated at Δ^{max}=51 mm.

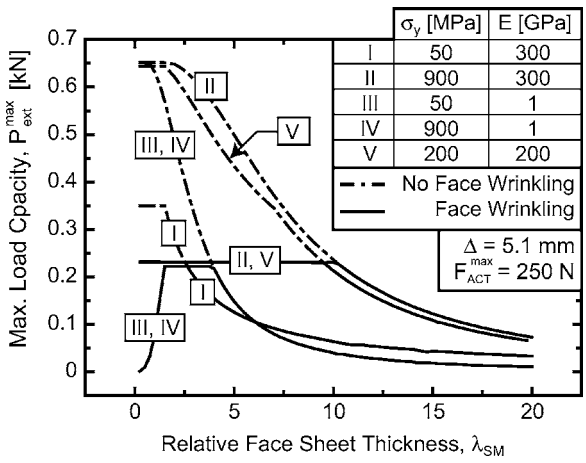

Fig. 7 Effect of variation of face thickness on load capacity for various materials

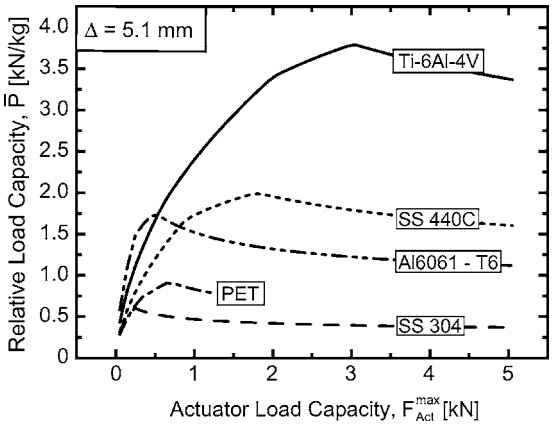

Fig. 8 Specific external load capacity as a function of the actuator load capacity for various engineering materials

neering materials. These materials include a titanium alloy (Ti-6Al-4V), an aluminum alloy (Al 6061-T6), two stainless steels (304 and 440C), and a polymer (PET). Every location on this figure represents a nonlinear optimization with the specified material parameters and actuator capacity. The calculations are based on a 10% actuator extension. For each material, there is a peak specific load capability and associated actuator capacity. The decrease at large actuator capacity arises because stubbier trusses and a thicker face are needed to support the larger loads, causing the weight to increase more rapidly than the rise in load capability. Note that, when only low capacity actuators are available, Al alloys are preferred. Conversely, when actuator capacity is unlimited, Ti alloys provide a much greater load capability per unit mass than all other materials.

7 Concluding Remarks

An assessment of the requirements and properties of a Kagome based shape morphing structure has been conducted. The fully optimized structure always resides at the confluence of the actuator limit and one (or more) structural failure mechanism. The most robust design is located just within the actuator-limited domain. Designs within the buckling domain should be avoided, because of the drop in load capacity. Those located in yield domains might be acceptable, since strain hardening provides some safety margin.

The load capability scales almost linearly with the actuator capacity but decreases at large deformations. When the passive face is loaded in tension, materials with high yield strength provide the greatest load capacity. The modulus is relatively unimportant. The load capability per unit mass exhibits a maximum. When the actuator capacity is unlimited, Ti alloys provide the greatest load capability per unit mass. Also the greatest load capacity is obtained with solid face sheet thickness of one to three times that of the stiffness matched thickness. Thicker faces increase the resistance against actuation without increasing the overall load capacity of the passive structure.

Since the constraint equations are quite general (except that the length of the Kagome and core members must be equal) other actuator locations and shape changes can be readily introduced by changing Eqs. (11) and (12).

Nomenclature

d_k, d_c, d_f = thickness of Kagome members, core members, solid face sheet
L_k, L_c = length of Kagome members, core members
L = length of Kagome and core members (L_k=L_c required)

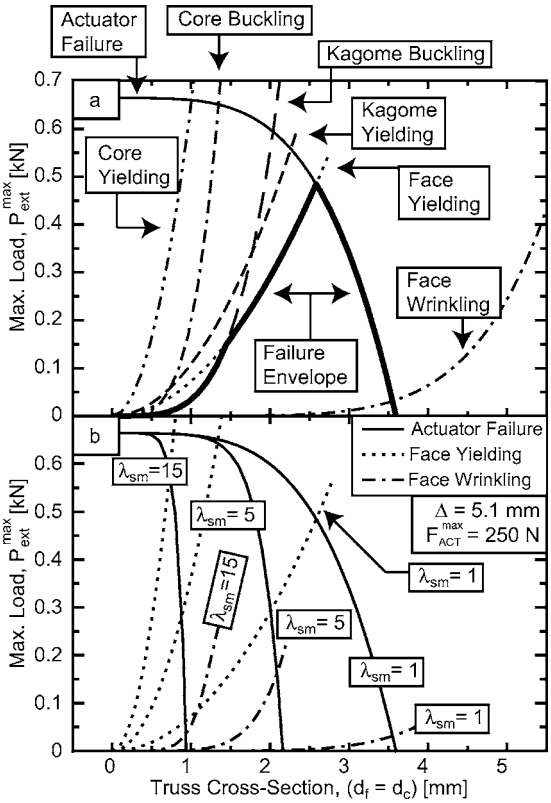

Fig. 9 Variation of the face thickness and comparison of face wrinkling to face yielding. (*a*) Face thickness fixed at λ_{sm}=1. (*b*) Face thickness fixed varied λ_{sm}=1, 5 and 15.

w, s, H_c = width and span of the structure, height of the core
λ_{sm} = solid face thickness scaling factor
E_k, E_c, E_f = Young's modulus of Kagome, core, and solid face
$\sigma_{Yk}, \sigma_{Yc}, \sigma_{Yf}$ = yield strength of Kagome, core, and solid face
ρ_k, ρ_c, ρ_f = Density of the Kagome, core, and solid face sheet
P_{KY}, P_{CY}, P_{FY} = external load to yield Kagome, core, and solid face
P_{KB}, P_{CB}, P_{FB} = external load to buckle Kagome, core, and solid face
P_{ACT} = external load to cease actuator function
$F_{\mathrm{ACT}}, F_{\mathrm{EXT}}$ = force on actuators due to structural resistance and external load
$F^{\max}_{\mathrm{ACT}}$ = load limit of actuator
P_{ext}, Δ = permissible external load, displacement of actuator
$P^{\max}_{\mathrm{ext}}, \Delta^{\max}$ = maximum permissible external load and actuator displacement

Appendix: Solid Face in Compression

In normal operation, the passive loads place the solid face in tension. Should the design require the face to experience compression, it would be susceptible to wrinkling at the load:

$$P_{FB} \leq \frac{2.24\sqrt{3}}{\sqrt{2}} \frac{d_f^3}{L} E_f \tag{A1}$$

The ratio of the loads that cause failure by yielding and wrinkling is given by combining Eqs. (7) and (A1):

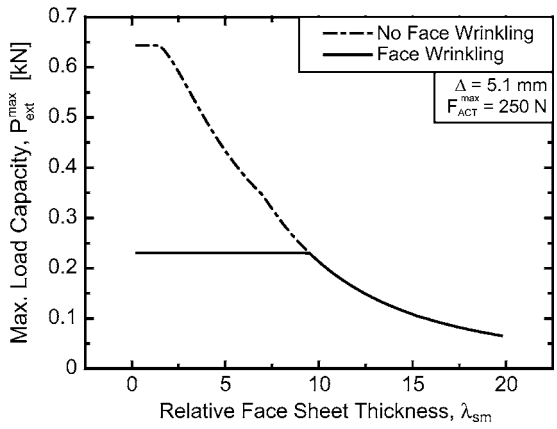

Fig. 10 Maximum load capability as a function of the solid face sheet thickness with and without face wrinkling

$$\frac{P_{FY}}{P_{FB}} = \frac{1}{3.36}\frac{wL^2}{sd_f^2}\varepsilon_{Yf} \tag{A2}$$

where $\varepsilon_{Yf}=\sigma_{Yf}/E_f$ is the yield strain of the solid face. The trends for a stiffness-matched system ($\lambda_{sm}=1$) are shown in Fig. 9(*a*); while those for systems with different λ_{sm} are shown on Fig. 9(*b*). For clearance of visualization only a cut along the $d_k=d_c$ plane is shown. When stiffness matched and loaded in tension, the maximum load capacity (Fig. 9(*a*)) occurs at the confluence of face yielding and actuator failure: with load capability, $P_{\text{ext}}^{\max}\approx 0.5$ kN. However, when loaded in compression, failure is limited by wrinkling and occurs at a much lower load, $P_{\text{ext}}^{\max}\approx 30$ N. Increasing the face thickness ($\lambda_{sm}>1$) dramatically increases the wrinkling resistance (Fig. 9(*b*)): but the benefits are offset by a corresponding increase in actuation resistance. The highest load capability in compression is $P_{\text{ext}}^{\max}\approx 150$ N when $\lambda_{sm}\approx 5$. Note that the load capability can be increased by lifting the restriction $d_k=d_c$.

The trends in maximum load capability with relative face thickness obtained using Mathematica are plotted in Fig. 10. Thicker faces have no benefit when in tension: they only serve to increase the actuation resistance. When in compression, while thicker faces resist wrinkling, they also increase the actuation resistance. Upon optimizing, these effects compensate at thickness $\lambda_{sm}\sim 9$. For even thicker faces, wrinkling is no longer an active constraint and the structure always fails by Kagome buckling.

References

[1] Lu, T. J., Hutchinson, J. W., and Evans, A. G., 2001, "Optimal Design of a Flexural Actuator," J. Mech. Phys. Solids, **49**, pp. 2071–2093.

[2] Hutchinson, R. G., Wicks, N., Evans, A. G., Fleck, N. A., and Hutchinson, J. W., 2003, "Kagome Plate Structures for Actuation," Int. J. Solids Struct., **40**, pp. 6969–6980.

[3] Hyun, S., and Torquato, S., 2002, "Optimal and Manufacturable Two-Dimensional, Kagomé-Like Cellular Solids," J. Mater. Res., **17**, pp. 137–144.

[4] Christensen, R. M., 2000, "Mechanics of Cellular and Other Low-Density Materials," Int. J. Solids Struct., **37**, pp. 93–104.

[5] Wicks, N., 2003, "Optimization and Actuation of Truss Structures," Ph.D. thesis, Engineering Sciences, Harvard University, Cambridge, MA.

[6] Dos Santos e Lucato, S. L., Wang, J., McMeeking, R. M., and Evans, A. G., 2004, "Design and Demonstration of a High Authority Shape Morphing Structure," Int. J. Solids Struct., **41**, pp. 3521–3543.

[7] Wicks, N., and Hutchinson, J. W., 2001, "Optimal Truss Plates," Int. J. Solids Struct., **38**, pp. 5165–5183.

[8] Ashby M. F., Evans, A. G., Fleck, N. A., Gibson, L. J., Hutchinson, J. W., and Wadley, H. N. G., 2000, *Metal Foams: A Design Guide*, Butterworth-Heinemann, Boston.

[9] Symons, D. D., Hutchinson, R. G., and Fleck, N. A., 2004, "Actuation Performance of the Kagome Double Layer Grid," J. Mech. Phys. Solids, **53**, pp. 1855–1874.

[10] Mathematica 5.0, 2003, www.wolfram.com, Wolfram Research, Champaign, IL, USA.

Periodic Antiplane Cracks in Graded Coatings Under Static or Transient Loading

B. L. Wang

Y.-W. Mai
Fellow ASME

Centre for Advanced Materials Technology (CAMT),
School of Aerospace, Mechanical and Mechatronic Engineering J07,
The University of Sydney,
Sydney NSW 2006, Australia

A periodic array of cracks in a functionally graded coating bonded to a homogeneous substrate is considered. The medium is subjected to transient or static mechanical loads. The problem is formulated in terms of a singular integral equation with the crack face displacement as the unknown variable. In addition to the time-varied stresses and stress intensity factors for various parameters of the problem, the effect of periodic cracking on the relaxation of the transient stress on the coating surface is discussed. Also included is the influence of the material gradient (material nonhomogeneity) on the crack tip intensity factors and stresses. Solutions for a single graded layer and a graded coating bonded to an infinite substrate are given. [DOI: 10.1115/1.2043190]

1 Introduction

In functionally graded materials (FGMs), the spatial variation of thermal and mechanical properties strongly influences the response to loading [1]. The presence of a functionally graded interface between two dissimilar materials, for example, can lead to a relaxation in stresses associated with discontinuities at bimaterial interfaces [2–6]. In fracture mechanics applications in nonhomogeneous materials, assuming an exponential spatial variation of the elastic modulus, Erdogan and his coworkers (see, for example, [7–10]) have provided a series of analytical solutions for cracks in nonhomogeneous elastic solids under mechanical loading. A number of other similar studies include [11–17].

Because fracture remains a key failure mode of FGMs, successful application of these materials depends on an understanding of their fracture mechanics. Jin and Noda [18] demonstrated the correspondence between near-tip field in homogeneous and nonhomogeneous bodies, which permits the application of standard analysis techniques to cracks in FGMs. Delamination and cracking of FGMs at coating-substrate interfaces due to thermal loads are the focus of investigations [3,19–21]. Kim and Paulino [22] developed a finite element methodology for the fracture analysis of orthotropic functionally graded materials where cracks are arbitrarily oriented with respect to the principal axes of material orthotropy. Wang et al. [23] proposed a multilayered model for a functionally graded interfacial zone between two dissimilar elastic solids. Recently, some authors have addressed several dynamic fracture problems in functionally graded materials. Li et al. [24] investigated the dynamic behavior of a cylindrical crack in a functionally graded interlayer under torsional loading. Zhang et al. [25] investigated a transient dynamic crack in a FGM by using a hypersingular time-domain boundary integral equation method. Investigated in [26,27] are the plane dynamic fracture problems of functionally graded materials. Developed in [28] are stress and displacement fields for a crack propagating along the gradient in a functionally gradient material, which has (i) a linear variation of shear modulus with a constant density and Poisson's ratio, and (ii) an exponential variation of shear modulus and density under a constant Poisson's ratio. In [29], a generalized elastic solution for an arbitrarily propagating crack in FGMs was obtained through an asymptotic analysis. Experimental research was conducted for a functionally graded material under low-velocity impact loading in [30]. A theoretical investigation of the singular behavior of a propagating crack in a FGM with spatially varying elastic properties under plane elastic deformation is investigated in [31]. Experimentally, the behavior of a propagating crack in functionally graded materials was characterized using dynamic photoelasticity in conjunction with high-speed photography [32], and the crack tip deformations and fracture parameters in a functionally graded beam are evaluated under static and dynamic loading conditions [33].

Despite a variety of challenging issues related to certain crack problems in the functionally graded nonhomogeneous media have been addressed, one remaining problem that needs to be fully understood is that of a periodic array of parallel cracks in such media. Past experience suggests that cracks in nonhomogeneous materials may be either a single dominant crack or a roughly regular array of periodic cracks [34–38]. To date, such periodic array of cracks in functionally graded materials has been solved for the antiplane shear deformation [39], in-plane mechanical deformation [40], and thermal load [41]. To our best understanding, no paper has been published for the transient fracture of functionally graded materials with periodic surface cracks.

This paper focuses on the static and transient solutions for a periodic array of cracks in a functionally graded coating bonded to a homogeneous half-plane. For simplicity, the antiplane problem is considered. Such a problem is important not only because a practical FGM may subject to an antiplane mechanical deformation, but also because it can provide a useful analogy to the most important in-plane crack problem. It is assumed that the thickness variation of the shear modulus of the coating is exponential. By defining the crack surface displacement as the unknown function, a singular integral equation is derived and is solved numerically. The objective of the study is to obtain a series of solutions for examining the influence of such factors as material nonhomogeneity constants, crack spacing on the stress and stress intensity factors, both at transient state and steady state.

Contributed by the Applied Mechanics Division of ASME for publication in the JOURNAL OF APPLIED MECHANICS. Manuscript received September 17, 2004; final manuscript received March 8, 2005. Review conducted by Z. Suo. Discussion on the paper should be addressed to the Editor, Prof. Robert M. McMeeking, Journal of Applied Mechanics, Department of Mechanical and Environmental Engineering, University of California-Santa Barbara, Santa Barbara, CA 93106-5070, and will be accepted until four months after final publication in the paper itself in the ASME JOURNAL OF APPLIED MECHANICS.

2 Description of the Problem

Consider a graded coating bonded to a homogeneous substrate. There is a row of periodic cracks vertical to the surface of the medium, as shown in Fig. 1. The upper and lower tips of the cracks terminate at $y=b$ and $y=d$, respectively. The length of the cracks is $2a$. The principal axes of the medium are along the x-

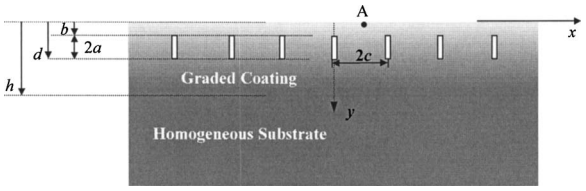

Fig. 1 Periodic array of cracks in a graded coating bonded to a semi-infinite homogeneous substrate; *h* is the coating thickness; crack tips are located at *y=b* and *y=d*. 2*c* is the crack spacing. If *b* is larger than zero the cracks are embedded in the strip. For edge cracks, *b* equals zero.

and y-axes. The thickness of the coating layer is as h, which is considerably smaller than the thickness of the substrate.

In this paper we assume that the medium has orthotropic properties. To make the analysis tractable, it is further assumed that the shear moduli and the mass density of the graded region are given by the following two-parameter expression:

$$\mu_x(y) = c_{x0}e^{\beta y}, \quad \mu_y(y) = c_{y0}e^{\beta y}, \quad \rho(y) = \rho_0 e^{\beta y} \tag{1}$$

where ρ_0 is the mass density, and c_{x0} and c_{y0} are elastic constants on the surface $y=0$. Many authors have used the assumptions shown in Eq. (1) for FGM applications (e.g., [7–17,26,27,42–44]). Wang et al. have demonstrated that the assumption of an exponentially varied gradient is reasonable for FGMs subjected to mechanical loading [45], provided that the crack is not too long compared to the medium size.

Under out-of-plane displacement $w(x,y)$, the constitutive equations have the following forms:

$$\sigma_{xz} = c_{x0}e^{\beta y}\frac{\partial w}{\partial x}, \quad \sigma_{yz} = c_{y0}e^{\beta y}\frac{\partial w}{\partial y}, \quad \text{for the graded layer} \tag{2a}$$

and

$$\sigma_{xz} = c_{xh}\frac{\partial w}{\partial x}, \quad \sigma_{yz} = c_{yh}\frac{\partial w}{\partial y}, \quad \text{for the substrate} \tag{2b}$$

in which c_{xh} and c_{yh} are elastic constants in the substrate (i.e., $y \geqslant h$).

The equilibrium equation, $\sigma_{zx,x}+\sigma_{zy,y}=\rho w_{,tt}$, with the substitution of Eqs. (2), becomes

$$c_{x0}\frac{\partial^2 w}{\partial x^2} + c_{y0}\frac{\partial^2 w}{\partial y^2} + c_{y0}\beta\frac{\partial w}{\partial y} = \rho_0\frac{\partial^2 w}{\partial t^2}, \quad \text{for the graded layer} \tag{3a}$$

and

$$c_{xh}\frac{\partial^2 w}{\partial x^2} + c_{yh}\frac{\partial^2 w}{\partial y^2} = \rho_h\frac{\partial^2 w}{\partial t^2}, \quad \text{for the substrate} \tag{3b}$$

in which $\rho_h=\rho_0 e^{\beta h}$ is the density of the substrate.

Since we are interested in the crack tip behaviors, the problem can be reduced to a perturbation problem in which the crack surface tractions are the only nonzero external loads. Therefore, all the field quantities are zero at infinity. The stress also vanishes on the top surface of the medium such that

$$\sigma_{yz}(x, y=0) = 0 \tag{4}$$

At the interface $y=h$ the displacement w and the stress component σ_{yz} must be continuous. Therefore, we have

$$\sigma_{yz}(x, h-0) = \sigma_{yz}(x, h+0) \tag{5a}$$

$$w(x, h-0) = w(x, h+0) \tag{5b}$$

In the problem under consideration, the loading condition is antisymmetric with respect to the $x=0$ plane. Therefore, it is sufficient to consider the right half of the medium (i.e., the $x>0$ part). Because of periodicity, the problem can be considered for the strip $0<x<c$, subjected to an additional homogeneous boundary condition:

$$w(c, y) = 0 \tag{6}$$

Generally, the crack surfaces are traction free. By considering field quantities near the crack front, the crack problem can be treated by the superposition technique. That is, one first solves the problem without any cracks and then adds equal and opposite values of the stresses to the crack faces to form the applied loads. Then, the mixed boundary conditions on the cracked planes can be stated as follows:

$$\sigma_{xz}(0, y) = -\tau_0(y)H(t), \quad y \in [b, d] \tag{7a}$$

$$w(0, y) = 0, \quad y \notin [b, d] \tag{7b}$$

in which $H(t)$ denotes the Heaviside function, the quantity τ_0 is the stress in the absence of any cracks.

The solution of the strip is obtained in terms of some unknown coefficients. These unknown coefficients are then determined by applying the surface condition (4), interface conditions (5), periodic condition (6), and by introducing an auxiliary function along the cracked plane (i.e., the $x=0$ plane). The auxiliary function would then be determined from the crack face boundary conditions (7).

3 Solution for the Graded Layer and the Substrate

In the following analysis, the Laplace transform will be adopted. The Laplace transform of a function $f(t)$ is defined as

$$f^*(p) = \int_0^\infty f(t)\exp(-pt)dt \tag{8a}$$

whose Laplace inversion is

$$f(t) = \frac{1}{2\pi i}\int_{\mathrm{Br}} f^*(p)\exp(pt)dp \tag{8b}$$

in which Br stands for the Bromwich path of integration. The time-dependence in Eqs. (3) can be eliminated by the application of Eqs. (8).

3.1 Solution for the Graded Layer. As pointed out above, the problem can be considered for the strip $0<x<c$. Employing the Fourier transform, the displacement can be expressed in terms of unknowns F_{mn} and $G_m(\xi)$ in the following form:

$$w^*(x, y, p) = \sum_{n=1}^{\infty}\sum_{m=1}^{2} F_{mn}\exp(s_n\lambda_m y)\sin(s_n x) + \frac{1}{2\pi}\int_{-\infty}^{\infty}[G_1\exp(|\xi|\gamma x) + G_2\exp(-|\xi|\gamma x)] \times \exp(-i\xi y)d\xi \tag{9}$$

where $s_n=n\pi x/c$ and

$$\lambda_1(s_n) = \sqrt{\frac{c_{x0}}{c_{y0}} + \frac{\rho_0 p^2}{c_{y0}s_n^2} + \left(\frac{\beta}{2s_n}\right)^2} - \frac{\beta}{2s_n} \tag{10a}$$

$$\lambda_2(s_n) = -\sqrt{\frac{c_{x0}}{c_{y0}} + \frac{\rho_0 p^2}{c_{y0}s_n^2} + \left(\frac{\beta}{2s_n}\right)^2} - \frac{\beta}{2s_n} \tag{10b}$$

$$\gamma(\xi) = \sqrt{\frac{c_{y0}}{c_{x0}} + \frac{i\xi c_{y0}\beta + \rho_0 p^2}{c_{x0}\xi^2}} \tag{10c}$$

Substituting Eq. (9) into the constitutive equations (2), the stresses can be obtained

$$\sigma_{xz}^{*}(x,y,p) = c_{x0}e^{\beta y}\sum_{n=1}^{\infty} s_n \sum_{m=1}^{2} F_{mn}\exp(s_n\lambda_m y)\cos(s_n x) + \frac{1}{2\pi}c_{x0}e^{\beta y}\int_{-\infty}^{\infty} |\xi|\gamma[G_1 \times \exp(|\xi|\gamma x) - G_2\exp(-|\xi|\gamma x)]\exp(-i\xi y)d\xi \tag{11a}$$

$$\sigma_{yz}^{*}(x,y,p) = c_{y0}e^{\beta y}\sum_{n=1}^{\infty} s_n \sum_{m=1}^{2} \lambda_m F_{mn}\exp(s_n\lambda_m y)\sin(s_n x) - \frac{i}{2\pi}c_{y0}e^{\beta y}\int_{-\infty}^{\infty} \xi[G_1\exp(|\xi|\gamma x) + G_2 \times \exp(-|\xi|\gamma x)]\exp(-i\xi y)d\xi \tag{11b}$$

3.2 Solution for the Substrate. Considering regularity conditions at infinity ($y\to\infty$), the displacement for the strip $0<x<c$ in the homogeneous substrate can be expressed in terms of unknowns F_n as

$$w^{*}(x,y,p) = \sum_{n=1}^{\infty} F_n \exp(s_n\lambda y)\sin(s_n x) \tag{12}$$

in which

$$\lambda(s_n) = -\sqrt{\frac{c_{xh}}{c_{yh}} + \frac{\rho_h p^2}{c_{yh}s_n^2}} \tag{13}$$

The stresses in the substrate associated with Eq. (12) are

$$\sigma_{xz}^{*}(x,y,p) = c_{xh}\sum_{n=1}^{\infty} s_n F_n \exp(s_n\lambda y)\cos(s_n x) \tag{14a}$$

$$\sigma_{yz}^{*}(x,y,p) = c_{yh}\sum_{n=1}^{\infty} \lambda F_n \exp(s_n\lambda y)\sin(s_n x) \tag{14b}$$

The problem under consideration has been reduced to the determination of the coefficients F_{mn}, G_1, G_2, and F_n. To this end, the surface and periodicity conditions must be satisfied.

4 Satisfying the Periodicity, Surface, and Interface Conditions

Introduce an auxiliary function g in the following manner [35,39]:

$$g(y) = w^{*}(+0,y,p), \quad y\in[b,d] \tag{15a}$$

$$g(y) = 0, \quad y\in[0,b]+[d,h] \tag{15b}$$

In what follows, the unknown coefficients F_{mn}, G_m, and F_n will be expressed in terms of the auxiliary function $g(y)$ from the surface, interface, and periodicity conditions.

4.1 Satisfying the Periodicity Conditions. From the periodicity condition (6) and with the substitution of Eq. (9) into Eqs. (15), G_m can be expressed in terms of the auxiliary function g as

$$G_m(\xi) = b_m\int_b^d g(r)\exp(i\xi r)dr \tag{16}$$

where $(m=1,2)$, b_m are known coefficients

$$b_1(\xi) = \frac{1}{1-\exp(2|\xi|\gamma c)}, \quad b_2(\xi) = -\frac{\exp(2|\xi|\gamma c)}{1-\exp(2|\xi|\gamma c)} \tag{17}$$

Equation (16) relates the functions $G_m(m=1,2)$ to the auxiliary function g. To relate the coefficients F_{mn} and F_n to $g(y)$, the surface and interface conditions (4) and (5) must be considered.

4.2 Satisfying the Surface and Interface Conditions. On the top surface $y=0$, the stress free boundary condition (4) gives

$$\sum_{m=1}^{2}\lambda_m F_{mn} = \frac{1}{\pi c}\int_b^d \delta_1(n,r)g(r)dr \tag{18}$$

in which the coefficient δ_1 is obtained from the theory of residues as

$$\delta_1(n,r) = -\pi\lambda_1^2\exp(-s_n\lambda_1 r) \tag{19}$$

At the interface $y=h$, the stress continuity condition (5a) gives

$$\sum_{m=1}^{2}\lambda_m F_{mn}\exp(s_n\lambda_m h) - \lambda F_n\exp(s_n\lambda h) = \frac{1}{\pi c}\int_b^d \delta_2(n,r)g(r)dr \tag{20}$$

in which the coefficient δ_2 is also evaluated from the theory of residues as

$$\delta_2(n,r) = \pi\lambda_2^2\exp[s_n\lambda_2(h-r)] \tag{21}$$

Furthermore, from the displacement continuity condition (5b), we obtain

$$\sum_{m=1}^{2} F_{mn}\exp(s_n\lambda_m h) - F_n\exp(s_n\lambda h) = -\frac{1}{\pi c}\int_b^d \delta_2(n,r)g(r)dr \tag{22}$$

The linear algebraic equations (18), (20), and (22) can be used to determine the remaining coefficients F_{mn} and F_n, in terms of the auxiliary function g. The coefficients F_{mn}, which will be used later, can be expressed as

$$F_{mn} = \frac{1}{\pi c}\int_b^d f_{mn}(r)g(r)dr \tag{23}$$

where f_{mn} are known functions of r.

Equation (23) gives the coefficient F_{mn} in terms of the auxiliary function $g(y)$. In the case of a single coating, F_n are zero and the remaining coefficients F_{mn} can be determined from Eqs. (18) and (20) (if the surface $y=h$ is stress free) or from Eqs. (18) and (22) (if the surface $y=h$ is mechanically constrained).

Subsequently, the auxiliary function $g(y)$ will be determined from the mixed-mode boundary condition on the cracked plane through an integral equation.

5 Crack Problem

From Eq. (11a), and with the substitution of Eqs. (16) and (23), the stress σ_{xz} on the $x=0$ plane in the Laplace transform domain can be expressed as

$$\sigma_{xz}^{*}(0,y,p) = c_{x0}e^{\beta y}\left[\int_b^d \Omega(y,r)g(r)dr + \int_b^d \Psi(y,r)g(r)dr\right] \tag{24}$$

with

$$\Omega(y,r) = \frac{1}{\pi c}\sum_{n=1}^{\infty} s_n\sum_{m=1}^{2}\exp(s_n\lambda_m y)f_{mn}(r) \tag{25}$$

$$\Psi(y,r)=\frac{1}{2\pi}\lim_{x\to+0}\int_{-\infty}^{\infty}|\xi|\gamma[b_1\exp(|\xi|\gamma x)-b_2 \times\exp(-|\xi|\gamma x)]\exp[i\xi(r-y)]d\xi \tag{26}$$

In order to determine the possible singular behavior of Eq. (24), the behavior of the kernel $\psi(y,r)$ at $y=r$ needs to be examined. It can be seen from Eqs. (17) and (26) that as ξ approaches infinity, the quantity $I(\xi)=\lim_{x\to+0}\gamma[b_1\exp(|\xi|\gamma x)-b_2\exp(-|\xi|\gamma x)]$ becomes $I(\infty)=-\sqrt{c_{y0}/c_{x0}}$. By adding and subtracting the asymptotic value $I(\infty)$ to and from $I(\xi)$ in Eq. (26) and using the known result

$$\lim_{x\to+0}\int_0^{\infty}\xi\exp(-\xi\gamma x)\cos[\xi(r-y)]d\xi=-\frac{1}{(r-y)^2} \tag{27}$$

it can be shown that

$$\Psi(y,r)=\Theta(y,r)+\frac{1}{\pi}\sqrt{\frac{c_{y0}}{c_{x0}}}\frac{1}{(r-y)^2} \tag{28}$$

where

$$\Theta(y,r)=\frac{1}{2\pi}\int_{-\infty}^{\infty}|\xi|\left[\sqrt{\frac{c_{y0}}{c_{x0}}}-\gamma(\xi)\coth(|\xi|\gamma(\xi)c)\right]\exp[i\xi(r-y)]d\xi \tag{29}$$

For $r\to y$, Eq. (29) gives $\Theta(y,r)=0$.

To improve the convergence of the series sum in Eq. (25), the behavior of the kernel Ω as $s_n\to\infty$ can be examined. It can be shown from Sec. 4.2 that as s_n becomes sufficiently large, the coefficients f_{1n} are zero and the remaining coefficients f_{2n} behave like

$$f_{2n\infty}(r)=\frac{\pi}{\lambda_0}\exp(-s_n\lambda_0 r),\quad \lambda_0=\sqrt{\frac{c_{x0}}{c_{y0}}} \tag{30}$$

in which the subscript ∞ denotes the corresponding value as s_n becomes infinity. It can also be shown that as $s_n\to\infty$, λ_1 becomes λ_0 and λ_2 becomes $-\lambda_0$. By adding and subtracting $f_{2n\infty}$ to and from f_{2n} in Eq. (25), and evaluating the series sum, we obtain

$$\Omega(y,r)=\frac{1}{\pi c}\sum_{n=1}^{\infty}s_n\left[\sum_{m=1}^{2}\exp(s_n\lambda_m y)f_{mn}(r)-\exp(-s_n\lambda_0 y)f_{2n\infty}(r)\right] +\frac{\pi}{\lambda_0 c^2}\frac{\exp\left[-\frac{\pi}{c}\lambda_0(y+r)\right]}{\left\{1-\exp\left[-\frac{\pi}{c}\lambda_0(y+r)\right]\right\}^2} \tag{31}$$

The convergence of Eq. (31) is considerably better than Eq. (25), especially for edge cracks with large values of the crack spacing c or small values of the strip thickness h.

6 Singular Integral Equation

Combining Eq. (28) with Eq. (24), the crack face boundary conditions (7) give the following integral equations for the auxiliary function $g(r)$:

$$\left[\frac{1}{\pi}\sqrt{\frac{c_{y0}}{c_{x0}}}\int_b^d\frac{1}{(r-y)^2}g(r)dr+\int_b^d H(y,r)g(r)dr\right] =-c_{x0}^{-1}e^{-\beta y}\tau_0^*(y,p) \tag{32}$$

where $\tau_0^*(y,p)$ is the Laplace transform of $\tau_0(y)\mathrm{H}(t)$ in Eq. (7*a*), and

$$H(y,r)=\Theta(y,r)+\Omega(y,r) \tag{33}$$

is a bonded integral kernel in interval $[b,d]$.

Equation (32) is the desired singular integral equation for a row of cracks in a FGM layer bonded to an elastic substrate. This equation can be solved by expanding $g(y)$ in terms of a Chebyshev polynomial series of the second kind [35].

6.1 Internal Crack Solution. For the case of internal (embedded) cracks, the integral equation (32) can be normalized between −1 and 1 with the substitutions

$$y=\bar{y}a+(d+b)/2,\quad r=\bar{r}a+(d+b)/2 \tag{34}$$

$$g(y)=a\bar{g}(\bar{y}) \tag{35}$$

where $a=(d-b)/2$ is the half crack length. The normalized integral equations in this case are

$$\frac{1}{\pi}\sqrt{\frac{c_{y0}}{c_{x0}}}\int_{-1}^{1}\frac{1}{(\bar{r}-\bar{y})^2}\bar{g}(\bar{r})d\bar{r}+a^2\int_{-1}^{1}H(y,r)\bar{g}(\bar{r})d\bar{r} =-c_{x0}^{-1}e^{-\beta y}\tau_0^*(y,p) \tag{36}$$

The solution of Eq. (36) can be expressed as [35]

$$\bar{g}(\bar{r})=\left[\sum_{j=0}^{\infty}m_j U_j(\bar{r})\right]\sqrt{1-\bar{r}^2} \tag{37}$$

where $U_j(\bar{r})=\sin[(j+1)\arccos(\bar{r})]/\sqrt{1-\bar{r}^2}$ is the Chebyshev polynomial of the second kind and m_j are unknown coefficients. Direct substitution of Eq. (37) into Eq. (36) and evaluation of the finite-part integral given by

$$\frac{1}{\pi}\int_{-1}^{1}\frac{\sqrt{1-\bar{r}^2}U_i(\bar{r})}{(\bar{r}-\bar{y})^2}d\bar{r}=-(i+1)U_i(\bar{y}) \tag{38}$$

result in

$$\sum_{j=0}^{\infty}m_j\left[-\sqrt{\frac{c_{y0}}{c_{x0}}}(j+1)U_i(\bar{y})+a^2\int_{-1}^{1}H(y,r)U_j(\bar{r})\sqrt{1-\bar{r}^2}d\bar{r}\right] =-c_{x0}^{-1}e^{-\beta y}\tau_0^*(y,p) \tag{39}$$

Equation (39) can be solved by simple collocation [35], where the roots of the Chebyshev polynomial are used as collocation points for $\bar{y}$. Once m_j are known, the full field solution is obtained. Because of the antisymmetry of the problem, only mode III stress intensity factor k_3 exists at the crack tips. The values of k_3 at the crack tips are defined and obtained as

$$k_3(b)=[\sqrt{2\pi(b-y)}]_{y\to b-0}\sigma_{xz}(0,y) =-\sqrt{\pi a}\sqrt{c_{x0}c_{y0}}e^{\beta b}\sum_{j=0}^{\infty}m_j U_j(-1) \tag{40a}$$

$$k_3(d)=[\sqrt{2\pi(y-d)}]_{y\to d+0}\sigma_{xz}(0,y)=-\sqrt{\pi a}\sqrt{c_{x0}c_{y0}}e^{\beta d}\sum_{j=0}^{\infty}m_j U_j(1) \tag{40b}$$

where the values of U_j at either end-point is

$$U_i(-1)=(i+1)(-1)^i,\quad U_i(1)=(i+1) \tag{41}$$

After determining the coefficients m_j, the crack surface sliding displacement $g(y)$ on the upper surface of the cracks can be obtained from Eqs. (37) and (35) as

$$g(y)=a\left[\sum_{j=0}^{\infty}m_j U_j(\bar{y})\right]\sqrt{1-\bar{y}^2} \tag{42}$$

in which $\bar{y}$ is related to y through Eq. (34).

6.2 Edge Crack Solution. For the case of edge cracks, i.e., when $b=0$, the normalized integral equation has the form

$$\frac{1}{\pi}\sqrt{\frac{c_{y0}}{c_{x0}}}\int_0^1 \frac{1}{(\bar{r}-\bar{y})^2}\bar{g}(\bar{r})d\bar{r} + d^2\int_0^1 H(y,r)\bar{g}(\bar{r})d\bar{r} = -c_{x0}^{-1}e^{-\beta y}\tau_0^*(y,p) \tag{43}$$

with:

$$y=\bar{y}d, \quad r=\bar{r}d, \quad g(y)=d\bar{g}(\bar{y}) \tag{44}$$

As in the case of internal cracks, the functions $\bar{g}_k(\bar{r})$ can be expressed as Eq. (37). The integral equation (43), after being substituted with Eq. (37), leads to the following equations for the evaluation of the unknown coefficients m_j:

$$\sum_{j=0}^{\infty} m_j\left[-\frac{1}{\pi}\sqrt{\frac{c_{y0}}{c_{x0}}}\int_0^1 \frac{\sqrt{1-\bar{r}^2}}{(\bar{r}-\bar{y})^2}U_j(\bar{r})d\bar{r} + d^2\int_0^1 H(y,r)U_j(\bar{r})\sqrt{1-\bar{r}^2}d\bar{r}\right] = -c_{x0}^{-1}e^{-\beta y}\tau_0^*(y,p) \tag{45}$$

The difference between the edge crack case and internal crack case is that a closed-form expression for the finite-part integral in Eq. (45) is not known. We can take advantage of the identity (38) by rewriting Eq. (45) as

$$\sum_{j=0}^{\infty} m_j\left[-\frac{1}{\pi}\sqrt{\frac{c_{y0}}{c_{x0}}}\int_{-1}^1 \frac{\sqrt{1-\bar{r}^2}}{(\bar{r}-\bar{y})^2}U_j(\bar{r})d\bar{r} + Q_j(y)\right] = -c_{x0}^{-1}e^{-\beta y}\tau_0^*(y,p) \tag{46}$$

where

$$Q_j(y) = \frac{1}{\pi}\sqrt{\frac{c_{y0}}{c_{x0}}}\int_{-1}^1 \frac{\sqrt{1-\bar{r}^2}}{(\bar{r}+\bar{y})^2}U_j(-\bar{r})d\bar{r} + d^2\int_0^1 H(y,r)U_j(\bar{r})\sqrt{1-\bar{r}^2}d\bar{r} \tag{47}$$

and thus the algebraic system of equations for solution of the unknown coefficients m_j, if collocation is used, becomes

$$\sum_{j=0}^{\infty} m_j\left(-\sqrt{\frac{c_{y0}}{c_{x0}}}(j+1)U_i(\bar{y}) + Q_j(y)\right) = -c_{x0}^{-1}e^{-\beta y}\tau_0^*(y,p) \tag{48}$$

Once the coefficients m_j are known for the edge crack problem, the stress intensity factor can be determined from Eq. (40*b*), and the displacement on the crack faces can be calculated from Eq. (42) (replace a in Eqs. (40*b*) and (42) with d).

After the solution in the Laplace transform domain is obtained, the solution in time domain is obtained by the Laplace inversion from the method of Miller and Guy [46]. To obtain the dynamic solution more efficiently, an additional constraint is adopted here. This additional constraint is that as t approaches infinity, the dynamic solution equals the corresponding static solution, which is obtained from the model outlined above by setting the Laplace transform parameter p to zero.

After obtaining the stress intensity factors in time domain, the energy release rate at the crack tips $y=b$ and $y=d$ can be evaluated from

$$G(b) = \frac{1}{2}\frac{1}{c_{x0}\exp(\beta b)}k_3^2(b) \quad \text{and} \quad G(d) = \frac{1}{2}\frac{1}{c_{x0}\exp(\beta d)}k_3^2(d) \tag{49}$$

respectively.

This section competes the crack tip field intensity factor solution. The stress in the cracked medium will be discussed subsequently.

7 Stress in the Cracked Medium

A quantity of practical interest is the stress $\sigma_{xz}(x,y)$, as it may have an effect on further cracking. For simplicity, only the stress at the plane $x=c$ in the graded layer is given (we expect that the overall stress is maximized there since it is furthest away from the crack, which is a stress-free zone). Substituting Eqs. (16) and (23) into Eq. (11*a*), the stress can be obtained as follows:

$$\sigma_{xz}^*(c,y,p) = c_{x0}e^{\beta y}\int_b^d \Pi(y,r)g(r)dr \tag{50}$$

where

$$\Pi(y,r) = \Pi_a(y,r) + \Pi_b(y,r) \tag{51}$$

with

$$\Pi_a(y,r) = \frac{1}{c^2}\sum_{n=1}^{\infty} n(-1)^n\sum_{m=1}^{2}\exp(s_n\lambda_m y)f_{mn}(r) \tag{52a}$$

$$\Pi_b(y,r) = \frac{1}{\pi}\int_{-\infty}^{\infty}|\xi|\gamma\frac{\exp(|\xi|\gamma c)}{1-\exp(2|\xi|\gamma c)}\exp[i\xi(r-y)]d\xi \tag{52b}$$

On the right-hand side of Eq. (51), the first term is the contribution due to the finite size of the medium, and the second term is the contribution due to the finite spacing of the cracks. If the medium is infinite (e.g., $h \gg d$ and $b \gg a$) then $\Pi_a=0$.

The convergence of Eq. (52*a*) can be improved considerably by adding and subtracting $f_{2n\infty}$ in Eq. (30) to and from f_{2n}, and evaluating the infinite sum. As a result, we have

$$\Pi_a(y,r) = \frac{1}{c^2}\sum_{n=1}^{\infty} n(-1)^n \times\left[\sum_{m=1}^{2}\exp(s_n\lambda_m y)f_{mn}(r) - \exp(-s_n\lambda_0 y)f_{2n\infty}(r)\right] + \frac{\pi}{\lambda_0 c^2}\frac{\exp\left[-\frac{\pi}{c}\lambda_0(y+r)\right]}{\left[1+\exp\left[-\frac{\pi}{c}\lambda_0(y+r)\right]\right]^2}. \tag{53}$$

As n increase, Eq. (53) converges faster than Eq. (52*a*), especially for edge cracks with large values of crack spacing c or small values of layer thickness h.

It should be note that Eq. (50) would give the stress for the perturbation problem solved under the conditions (4)–(7). To obtain the correct stress in the cracked medium, the solution of the uncracked medium under prescribed external loads must be added to that given by Eq. (50).

8 Numerical Results

Since the surface crack problem is the only practical case,[39] all results presented in this section are obtained for $b=0$ (see Fig. 1). Since the main purpose of this paper is to explore the effect of the crack spacing on the dynamic stress intensity factors (DSIFs) and the static stress intensity factors (SSIFs), the material system considered here is an isotropic coating/substrate system. Denote the shear moduli on the coating surface ($y=0$) and the coating/substrate interface ($y=h$) as $\mu(0)$ and $\mu(h)$, respectively. Because the material property is a continuous function of y, the shear modulus of the substrate would also be $\mu(h)$. For the graded coating the parameter β can be determined from

$$\beta = \frac{1}{h}\log\left(\frac{\mu(h)}{\mu(0)}\right) \tag{54}$$

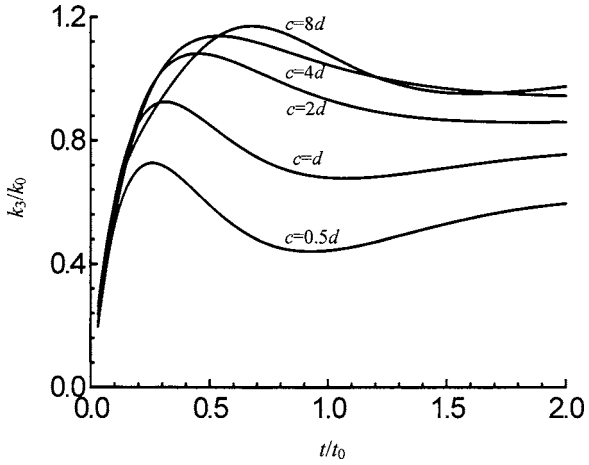

Fig. 2 Normalized transient stress intensity factor for surface cracks in a graded layer; $k_0=\tau_0\sqrt{\pi d}$, $t_0=h\sqrt{\rho_0/\mu_0}$, $\mu(h)/\mu(0)=1/3$, $b=0$, $d=0.25h$

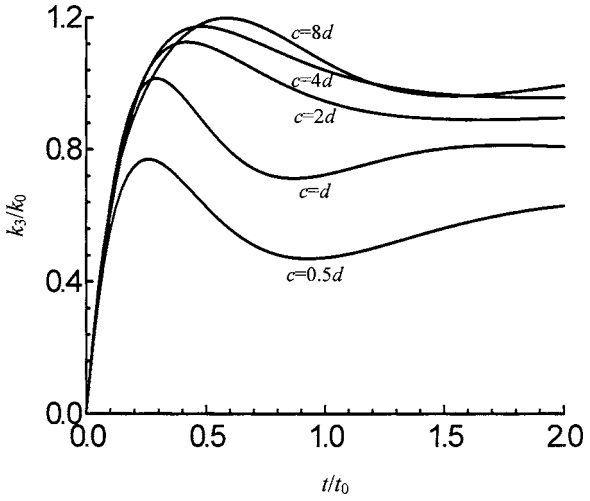

Fig. 4 Same as Fig. 2; $\mu(h)/\mu(0)=3$

8.1 A Single Graded Layer. We first consider a single graded layer (which means there is no substrate attached to the graded layer) subjected to a sudden antiplane shearing force τ_0 applied on the crack faces. The crack length for this problem is fixed as $d=0.25h$, where h is the thickness of the graded layer.

In Figs. 2–4 the normalized DSIFs are plotted against time for selected values of crack spacing c. All the curves reach a peak and then decrease in magnitude. The peaks are more pronounced if the crack spacing is increased. Note that the curves for small crack spacing reach the peaks those for larger crack spacing. This represents the disturbance of the waves reflected from the adjacent crack faces. At sufficiently large time, the dynamic stress intensity factor solutions are reduced to the corresponding static solutions.

In Fig. 5, the normalized peak and steady values of k_3 are plotted for different values of crack spacing and material nonhomogeneity. Obviously, the stress intensity factors are enhanced if the graded layer has an increasing stiffness from its surface $y=0$ to surface $y=h$. Vice verse, this is if the stiffness of the graded layer is a decreasing function of y then the stress intensity factor is released. Most functionally graded materials are ceramic and metal composites. The stiffness of the ceramic phase is usually higher than that of the metal phase. Therefore, the metal and ceramic FGMs have a potential to reduce both transient and static stress intensity factors.

Further consideration of Fig. 5 shows that multiple cracking has a great tendency to reduce the stress intensity factor. As crack spacing becomes infinity, the present solution for a homogeneous layer tends to the existing result $k_3=\tau_0\sqrt{2h\tan[\pi a/(2h)]}=1.027\tau_0\sqrt{\pi a}$, which can be found from the handbook (e.g., [47]). It is interesting to note that for $c=0.5d$ ($c=0.125h$) the static stress intensity factor for a homogeneous layer $k_3=0.5632\tau_0\sqrt{\pi a}$; a value that is only 55% of the stress intensity factor for infinity crack spacing, which is $k_3=\tau_0\sqrt{2h\tan[\pi a/(2h)]}=1.027\tau_0\sqrt{\pi a}$. Similar to the static solution, the peak values of the stress intensity factors are also reduced considerably by multiple cracking.

Some examples for the stress $\sigma_{xz}(c,0)$ on the surface of the graded layer calculated from Eq. (50) are shown in Figs. 6–8. The corresponding peak values and steady values are displayed in Figs. 9 and 10, respectively. Note that the stress is negative since are applied crack face pressure loads are applied. Similar to the DSIFs, the stresses show significant oscillation with time. In all cases the peak and steady values of $\sigma_{xz}(c,0)$ are monotonously decreasing functions of the crack spacing c/h and have the limiting values of zero for $c\to\infty$. Since the solutions are obtained for the perturbation problem, results in Figs. 6–10 represent the

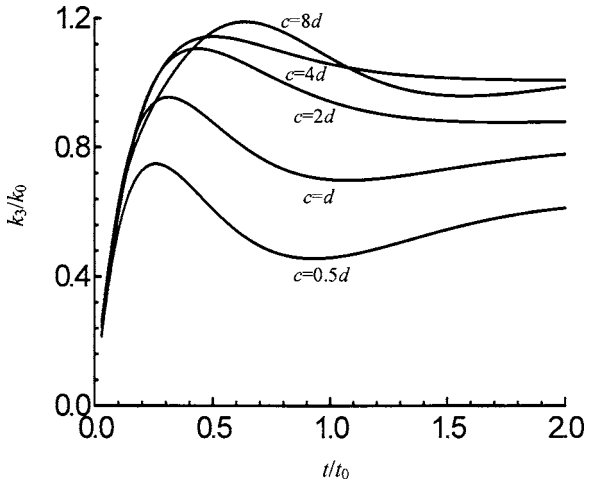

Fig. 3 Same as Fig. 2; $\mu(h)/\mu(0)=1$

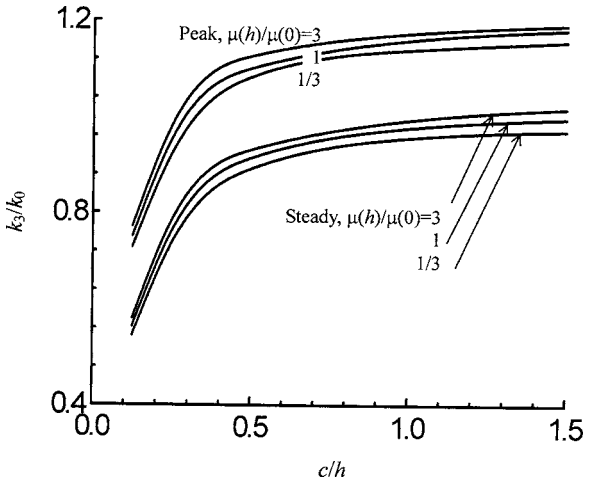

Fig. 5 Normalized peak and steady values of the stress intensity factor for surface cracks in a graded layer; $k_0=\tau_0\sqrt{\pi d}$, $b=0$, $d=0.25h$

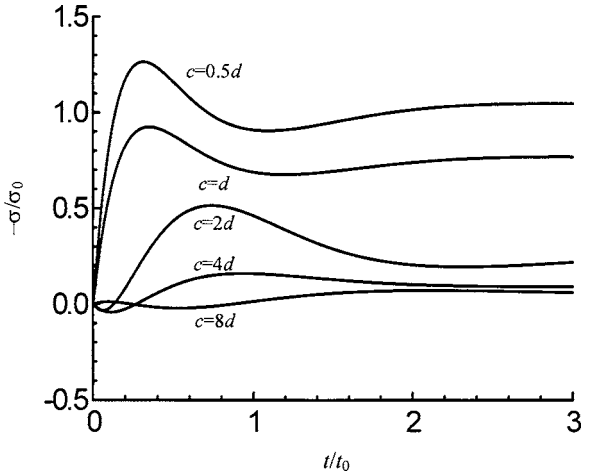

Fig. 6 Normalized transient stress σ at the point A: $(x,y)=(c,0)$ in a periodically cracked graded layer; $t_0=h\sqrt{\rho_0/\mu_0}$, $\mu(h)/\mu(0)=1/3$, $b=0$, $d=0.25h$

stresses that the cracked medium can release. The corrected stresses in the cracked medium should be obtained by adding those in Figs. 6–10 to the corresponding solutions of the uncracked medium under prescribed external loads. Considering such a fact, it is understood that the increasing crack density (or

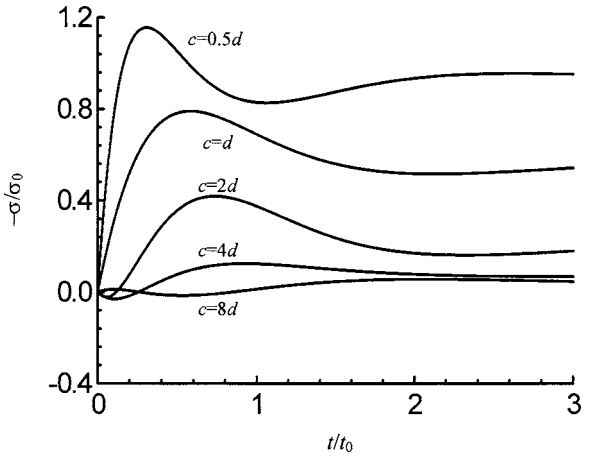

Fig. 7 Same as Fig. 6; $\mu(h)/\mu(0)=1$

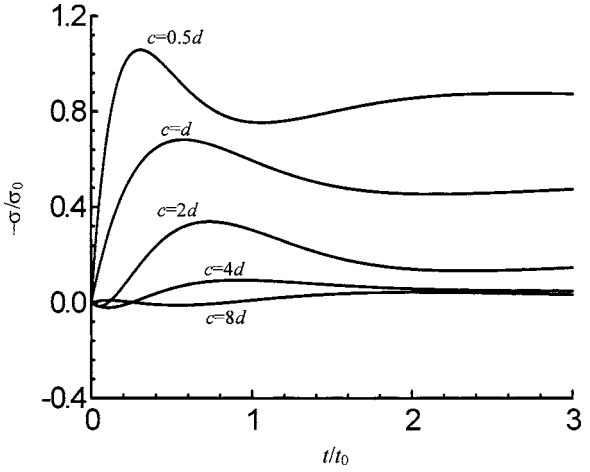

Fig. 8 Same as Fig. 6; $\mu(h)/\mu(0)=3$

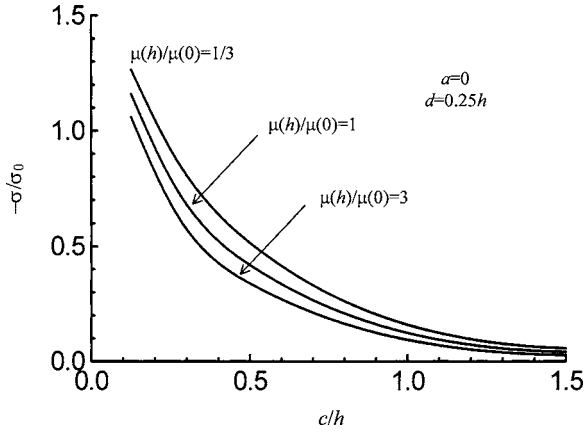

Fig. 9 Normalized peak values of the stress σ_{xz} at the point A: $(x,y)=(c,0)$ in a periodically cracked graded layer

decreasing crack spacing) has a significant effect to release the overall stress in the cracked medium. An explanation for this can be that a single crack would most seriously disturb the local stress state, and the stress distribution in a system with more cracks is smoother than a system with fewer cracks. As a result, both the stress and the stress intensity factor are minimized by multiple cracking.

8.2 A Coating/Substrate System. In this section a graded coating/substrate system are investigated. The results for some simplified cases are compared to the solutions available from the literature. Since the crack is usually arrested at the interface, the stress intensity factors and stresses are computed for $d=h$.

Graphically depicted in Figs. 11 and 12 are the values of $k_3(t)$ and $\sigma(c,0)$ with time for selected values of crack spacing. The graded index is zero so that the entire medium is homogeneous. The interpretation for the effects of time and crack spacing on k_3 and $\sigma(c,0)$ is similar to the case of the single graded layer. Since the cracks considered here are longer than those in the single graded layer, in each curve k_3 and $\sigma(c,0)$ take a longer time to attain their peak and steady values. From our results, we find that results for $c=4d$ are almost identical to curves for $c>4d$. Hence, the results for $c=4d$ can be qualitatively considered as the single crack solution. The curve for $c=4d$ in Fig. 11 is in good agreement with that by Sih for a single crack in a semi-infinite medium [48].

We have also obtained the solutions for various values of the

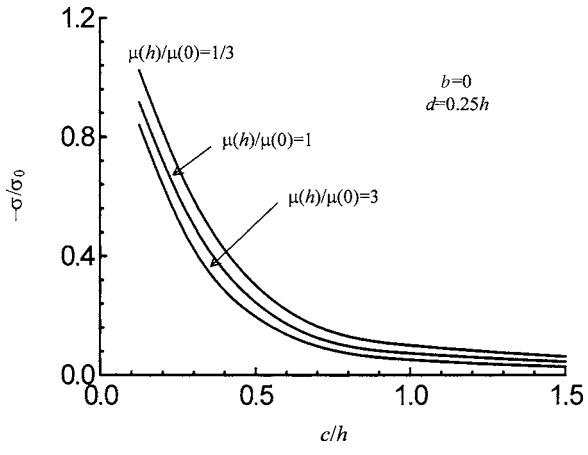

Fig. 10 Normalized steady values of the stress σ_{xz} at the point A: $(x,y)=(c,0)$ in a periodically cracked graded layer

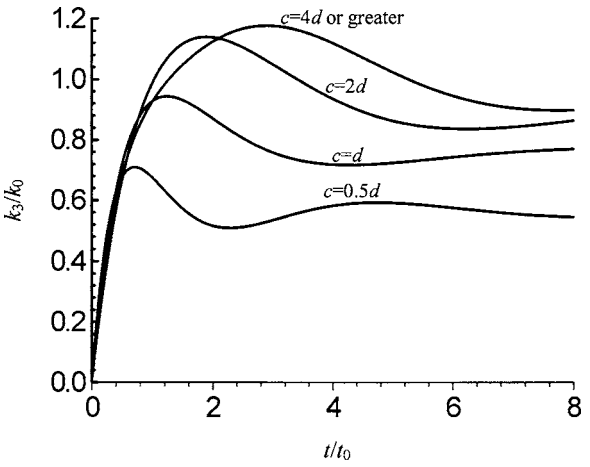

Fig. 11 Normalized transient stress intensity factor for periodic cracks in a coating/substrate system; $k_0=\tau_0\sqrt{\pi h}$, $t_0=h\sqrt{\rho_0/\mu_0}$, $\mu(h)/\mu(0)=1$, $b=0$, $d=h$

material nonhomogeneity parameter β (or $\mu(h)$ to $\mu(0)$ ratio). The results are not given here since the effect of β on k_3 and $\sigma(c,0)$ in the graded coating/substrate system is similar to that in the single graded layer. A main conclusion from the results is that k_3 decreases with decreasing β, and conversely, the magnitude of $\sigma(c,0)$ decreases with increasing β. This suggests that in graded coating applications, it is better that the coating has a higher stiffness than the substrate (i.e., $\mu(y)$ is a decreasing function of y).

As mentioned above, the model developed in this paper is applicable to transient as well as steady problems. Table 1 gives the stress intensity factors for a row of edge cracks in homogeneous semi-infinite medium. The exact solution for this crack configuration can be found from the handbook (e.g., [47]) and the results are also listed in Table 1. It can be seen that the present solution and the exact solution are completely identical.

9 Conclusion

A theoretical model is developed for the interactions of a row of cracks periodically located in a functionally graded coating bonded to a homogeneous substrate. To simplify the analysis, we considered the antiplane mechanical loading. Such a problem is important not only because a practical material may be subjected to an antiplane mechanical deformation, but also because it can provide a useful analogy to the most important in-plane crack-dislocation problem.

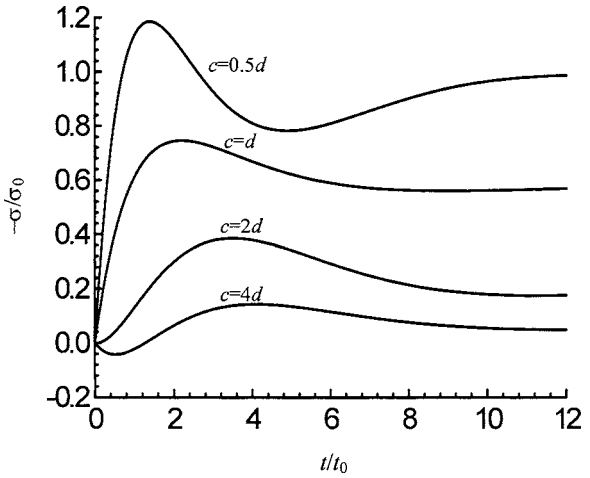

Fig. 12 Normalized transient stress at the point A: $(x,y)=(c,0)$ in a coating/substrate system; $t_0=h\sqrt{\rho_0/\mu_0}$, $\mu(h)/\mu(0)=1$, $b=0$, $d=h$

Table 1 Stress intensity factors for a row of edge cracks in a semi-infinite homogeneous medium (d is the crack length; numbers in parentheses denote exact solutions obtained from $k_3=\tau_0\sqrt{2c\tanh[\pi d/(2c)]}$)

c/d	Stress intensity factor $k_3/\tau_0\sqrt{\pi d}$ (present solution)	Stress intensity factor $k_3/\tau_0\sqrt{\pi d}$ (exact solutions)
∞	1.0000	(1.0000)
5	0.9840	(0.9840)
2.5	0.9414	(0.9414)
1.5	0.8634	(0.8634)
1	0.7641	(0.7641)
0.5	0.5631	(0.5631)

Both transient solution and static solution are obtained. The numerical Laplace inversion we used here ensures the transient solution reduces to the corresponding static solution, when time becomes infinity. The stresses and the stress intensity factors are illustrated for different values of the nonhomogeneity parameter as well as the crack spacing. The results show that both the stress and stress intensity factor can be reduced significantly by increasing crack density (decreasing crack spacing).

Acknowledgment

The authors wish to thank the Australian Research Council (ARC) (Grant No. #DP0346037) for their support of the work reported in this paper. They also acknowledge the ARC for the awards of an Australian Research Fellowship and an Australian Federation Fellowship, respectively.

References

[1] Miyamoto, Y., Kaysser, W. A., Rabin, B. H., Kawasaki, A., and Ford, A. G., 1999, *Functionally Graded Materials: Design, Processing and Applications*, Kluwer, Boston.
[2] Hasselman, D. P. H., and Youngblood, G. E., 1978, "Enhanced Thermal Resistance of Structural Ceramics With Thermal Conductivity Gradients," J. Am. Ceram. Soc., **61**, pp. 49–52.
[3] Lee, Y.-D., and Erdogan, F., 1995, "Residual/Thermal Stresses in FGM and Laminated Thermal Barrier Coatings," Int. J. Fract., **69**, pp. 145–165.
[4] Ravichandran, K. S., 1995, "Thermal Residual Stresses in a Functionally Graded Material System," Mater. Sci. Eng., A, **201**, pp. 269–276.
[5] Noda, N., 1999, "Thermal Stresses in Functionally Graded Materials," J. Therm. Stresses, **22**(1), pp. 477–512.
[6] Nomura, N., Gasik, M., Kawasaki, A., and Watanabe, R., 2001, "Thermomechanical Modelling of Functionally Graded Thermal Barrier Coatings," Ceram. Trans., **114**, pp. 223–229.
[7] Delale, F., and Erdogan, F., 1988, "Interface Crack in a Nonhomogeneous Elastic Medium," Int. J. Eng. Sci., **26**, pp. 559–568.
[8] Ozturk, M., and Erdogan, F., 1993, "The Axisymmetric Crack Problem in a Nonhomogeneous Medium," ASME J. Appl. Mech., **60**, pp. 406–413.
[9] Konda, N., and Erdogan, F., 1994, "The Mixed Mode Crack Problem in a Nonhomogeneous Elastic Medium," Eng. Fract. Mech., **47**, pp. 533–545.
[10] Erdogan, F., and Wu, B. H., 1997, "The Surface Crack Problem for a Plate With Functionally Graded Properties," ASME J. Appl. Mech., **64**, pp. 449–456.
[11] Dhaliwal, R. S., and Singh, B. M., 1978, "On the Theory of Elasticity of a Nonhomogeneous Medium," J. Elast., **8**, pp. 211–219.
[12] Gerasoulis, A., and Srivastav, R. P., 1980, "A Griffith Crack Problem for a Nonhomogeneous Medium," Int. J. Eng. Sci., **18**, pp. 239–247.
[13] Schovanec, L., and Walton, J. R., 1988, "On the Order of the Stress Singularity for an Antiplane Shear Crack at the Interface of Two Bonded Inhomogeneous Elastic Materials," ASME J. Appl. Mech., **55**, pp. 234–236.
[14] Ang, W. T., and Clements, D. L., 1987, "On Some Crack Problems for Inhomogeneous Elastic Materials," Int. J. Solids Struct., **23**, pp. 1089–1104.
[15] Eischen, J. W., 1987, "Fracture of Nonhomogeneous Materials," Int. J. Fract., **34**, pp. 3–22.
[16] Craster, R. V., and Atkinson, C., 1994, "Mixed Boundary-Value Problems in Nonhomogeneous Elastic Materials," Q. J. Mech. Appl. Math., **47**, pp. 183–206.
[17] Vrbik, J., Singh, B. M., Rokne, J., and Dhaliwal, R. S., 2002, "The Problem of a Penny-Shaped Crack in a Non-Homogeneous Medium Under Shear," Eur. J. Mech. A/Solids, **21**, pp. 773–777.

[18] Jin, Z. H., and Noda, N., 1994, "Crack Tip Singular Fields in Nonhomogeneous Materials," ASME J. Appl. Mech., **61**(3), pp. 738–740.
[19] Bao, G., and Cai, H., 1997, "Delamination Cracking in Functionally Graded Coating/Metal Substrate Systems," Acta Mater., **45**(3), pp. 1055–1066.
[20] Quian, G., Nakamura, T., and Berndt, C. C., 1998, "Effects of Thermal Gradient and Residual Stresses on Thermal Barrier Coating Fracture," Mech. Mater., **27**, pp. 91–110.
[21] Gaudette, F. G., Giannakopoulos, A. E., and Suresh, S., 2001, "Interface Cracks in Layered Materials Subjected to a Uniform Temperature Change," Int. J. Fract., **110**(4), pp. 325–349.
[22] Kim, J. H., and Paulino, G. H., 2002, "Mixed-Mode Fracture of Orthotropic Functionally Graded Materials Using Finite Elements and the Modified Crack Closure Method," Eng. Fract. Mech., **69**, pp. 1557–1586.
[23] Wang, Y. S., Huang, G. Y., and Gross, D., 2004, "On the Mechanical Modeling of Functionally Graded Interfacial Zone With a Griffith Crack: Plane Deformation," Int. J. Fract., **125**, pp. 189–205.
[24] Li, C. Y., Weng, G. J., and Duan, Z. P., 2001, "Dynamic Behavior of a Cylindrical Crack in a Functionally Graded Interlayer Under Torsional Loading," Int. J. Solids Struct., **38**, pp. 7473–7485.
[25] Zhang, C., Sladek, J., and Sladek, V., 2003, "Effects of Material Gradients on Transient Dynamic Mode-III Stress Intensity Factors in a FGM," Int. J. Solids Struct., **40**, pp. 5251–5270.
[26] Guo, L. C., Wu, L. Z., Zeng, T., and Ma, L., 2004, "Fracture Analysis of a Functionally Graded Coating-Substrate Structure With a Crack Perpendicular to the Interface, Part II: Transient Problem," Int. J. Fract., **127**, pp. 39–59.
[27] Ma, L., Wu, L. Z., Zhou, Z. G., and Zeng, T., 2004, "Crack Propagating in a Functionally Graded Strip Under the Plane Loading," Int. J. Solids Struct., **126**(1), pp. 39–55.
[28] Lee, K. H., 2004, "Characteristics of a Crack Propagating Along the Gradient in Functionally Gradient Materials," Int. J. Solids Struct., **41**(11–12), pp. 2879–2898.
[29] Chalivendra, V. B., Shukla, A., and Parameswaran, V., 2002, "Dynamic Out of Plane Displacement Fields for an Inclined Crack in Graded Materials," J. Elast., **69**(1–3), pp. 99–119.
[30] El-Hadek, M. A., and Tippur, H. V., 2003, "Dynamic Fracture Parameters and Constraint Effects in Functionally Graded Syntactic Epoxy Foams," Int. J. Solids Struct., **40**(8), pp. 1885–1906.
[31] Meguid, S. A., Wang, X. D., and Jiang, L. Y., 2002, "On the Dynamic Propagation of a Finite Crack in Functionally Graded Materials," Eng. Fract. Mech., **69**(14–16), pp. 1753–1768.
[32] Shukla, A., and Jain, N., 2004, "Dynamic Damage Growth in Particle Reinforced Graded Materials," Int. J. Impact Eng., **30**(7), pp. 777–803.
[33] Rousseau, C. E., and Tippur, H. V., 2002, "Influence of Elastic Variations on Crack Initiation in Functionally Graded Glass-Filled Epoxy," Eng. Fract. Mech., **69**(14–16), pp. 1679–1693.
[34] Grot, A. S., and Martyn, J. K., 1981, "Behavior Plasma-Sprayed Ceramic Thermal Barrier Coating for Gas Turbine Engines," Bull. Am. Ceram. Soc., **60**(8), pp. 807–811.
[35] Nied, H. F., 1987, "Periodic Array of Cracks in a Half Plane Subjected to Arbitrary Loading," ASME J. Appl. Mech., **54**, pp. 642–648.
[36] Rizk, Abd El-Fattah, 2004, "Periodic Array of Cracks in a Strip Subjected to Surface Heating," Int. J. Solids Struct., **41**(16–17), pp. 4685–4696.
[37] Schulze, G. W., and Erdogan, F., 1998, "Periodic Cracking of Elastic Coatings," Int. J. Solids Struct., **35**, pp. 3615–3634.
[38] Timm, D. H., Guzina, B. B., and Voller, V. R., 2003, "Prediction of Thermal Crack Spacing," Int. J. Solids Struct., **40**, pp. 125–142.
[39] Erdogan, F., and Ozturk, M., 1995, "Periodic Cracking of Functionally Graded Coatings," Int. J. Eng. Sci., **33**(15), pp. 2179–2195.
[40] Choi, H. J., 1997, "A Periodic Array of Cracks in a Functionally Graded Nonhomogeneous Medium Loaded Under In-Plane Normal and Shear," Int. J. Fract., **88**, pp. 107–128.
[41] Bao, G., and Wang, L., 1995, "Multiple Cracking in Functionally Graded Ceramic-Metal Coatings," Int. J. Solids Struct., **32**, pp. 2853–2871.
[42] Guler, M. A., and Erdogan, F., 2004, "Contact Mechanics of Graded Coatings," Int. J. Solids Struct., **41**, pp. 3865–3889.
[43] Giannakopoulos, A., and Suresh, S., 1997, "Indentation of Solids With Gradients in Elastic Properties: Part I. Point Force Solution," Int. J. Solids Struct., **34**(19), pp. 2357–2392.
[44] Giannakopoulos, A., and Suresh, S., 1997, "Indentation of Solids With Gradients in Elastic Properties: Part II. Axisymetric Indenters," Int. J. Solids Struct., **34**(19), pp. 2393–2428.
[45] Wang, B. L., Mai, Y.-W., and Noda, N., 2002, "Fracture Mechanics Analysis Model for Functionally Graded Materials With Arbitrarily Distributed Properties," Int. J. Fract., **116**, pp. 161–177.
[46] Miller, M. K., and Guy, W. T., 1966, "Numerical Inversion of the Laplace Transform by Use of Jacobi Polynomials," SIAM (Soc. Ind. Appl. Math.) J. Numer. Anal., **3**, pp. 624–635.
[47] Murakami, Y., 1987, *Stress Intensity Factors Handbook*, Pergamon, New York.
[48] Sih, G. C., 1977, "Elastodynamics Crack Problems," *Mechanics of Fracture Mechanics*, Noordhoff, Leyden, Vol. 4.

Variation in Fractal Properties and Non-Gaussian Distributions of Microcontact Between Elastic-Plastic Rough Surfaces With Mean Surface Separation

Jung Ching Chung

Jen Fin Lin
Professor
e-mail: jflin@mail.ncku.edu.tw

Department of Mechanical Engineering,
National Cheng Kung University,
Tainan City, 70101, Taiwan

The fractal parameters (fractal dimension and topothesy), describing the contact behavior of rough surface, were considered as constant in the earlier models. However, their results are often significantly different from the experimental results. In the present study, these two roughness parameters have been derived analytically as a function of the mean separation first, then they are found with the aid of the experimental results. By equating the structure functions developed in two different ways, the relationship among the scaling coefficient in the power spectrum function, the fractal dimension, and topothesy of asperity heights can be established. The variation of topothesy can be determined when the fractal dimension and the scaling coefficient have been obtained from the experimental results of the number of contact spots and the power spectrum function at different mean separations. The probability density function of asperity heights, achieved at a different mean separation, was obtained from experimental results as a non-Gaussian distribution; it is expressed as a function of the skewness and the kurtosis. The relationship between skewness and mean separation can be established through the fitting of experimental results by this non-Gaussian distribution. For a sufficiently small mean separation, either the total load or the real contact area predicted by variable fractal parameters, as well as non-Gaussian distribution, is greater than that predicted by constant fractal parameters, as well as Gaussian distribution. The difference between these two models is significantly enhanced as the mean separation becomes small.
[DOI: 10.1115/1.2061967]

1 Introduction

The contact between two rough surfaces has a strong influence on the phenomena of friction, wear, and lubrication, as well as on the conduction of heat and electricity. In general, the structure of most surfaces appears to be random on a small scale. Statistical parameters such as the root-mean-square (rms) of surface height σ, slope σ', and curvature σ'' are conventionally used to characterize surface roughness [1,2]. Several theories based on these parameters have been developed to model rough surfaces in contact. The most popular of these is the Greenwood and Williamson (GW) model [1], which is based on the assumption that the surface is composed of hemispherical asperities having equal radii given by $1/\sigma''$.

Nayak [3] considered rigid-plastic contact of two Gaussian rough surfaces and noticed that the GW model is not applicable for all microcontact sizes. McCool [4] took account of the interaction between two neighboring asperities and modeled the elastic-plastic contact of isotropic and anisotropic solid bodies. Chang et al. (the CEB model) [5] modified the original GW model [1] to incorporate the effect of volume conservation when an asperity deforms plastically. Numerical results obtained from their model are compared with existing models [1,6]. Kogut and Etsion [7] presented an elastic-plastic finite element solution for the contact of a deformable sphere pressed by a rigid flat. Their solution provides dimensionless expressions for contact load and contact area covering a large range, from yielding inception to fully plastic contact of the sphere. The finite element solution of Kogut and Etsion [8] enabled a revision of the CEB model developed for rough surface contacts and showed substantial differences in contrast with solutions of the CEB model. The microcontact model which was developed by Kogut and Etsion [7] is adopted in the present study to obtain the contact area, contact load, and contact pressure of an asperity.

The power spectra of engineering surfaces produced by random processes have been observed to follow inverse power laws over a wide range of the length scale [9–11]. Microscopic observations have shown that engineering surfaces can be characterized by fractals, from the nanometer to the millimeter scale [10–12]. The assumption of a surface being composed of hemispherical asperities belonging to a single length scale is an oversimplification of the real surface, which contains several roughness scales. Majumdar and Bhushan [13] and Bhushan and Majumdar [14] imposed scale-independent parameters (fractal dimension D), instead of employing conventional statistical parameters, to describe the load contact of rough surfaces.

A power law size distribution of contact spots, resulting from a geomorphology fractal model, calculated the real contact area. Zhou et al. [15] developed a fractal geometry model, which predicts the wear rate in terms of the fractal dimension and topothesy. It should be mentioned that they had found the fractal dimension changing with the wear process. A new fractal-based functional model for anisotropic rough surface, developed by Blackmore and

Contributed by the Applied Mechanics Division of ASME for publication in the JOURNAL OF APPLIED MECHANICS. Manuscript received June 16, 2004; final manuscript received May 12, 2005. Review conducted by K. Ravi-Chandar. Discussion on the paper should be addressed to the Editor, Prof. Robert M. McMeeking, Journal of Applied Mechanics, Department of Mechanical and Environmental Engineering, University of California - Santa Barbara, Santa Barbara, CA 93106-5070, and will be accepted until four months after final publication in the paper itself in the ASME JOURNAL OF APPLIED MECHANICS.

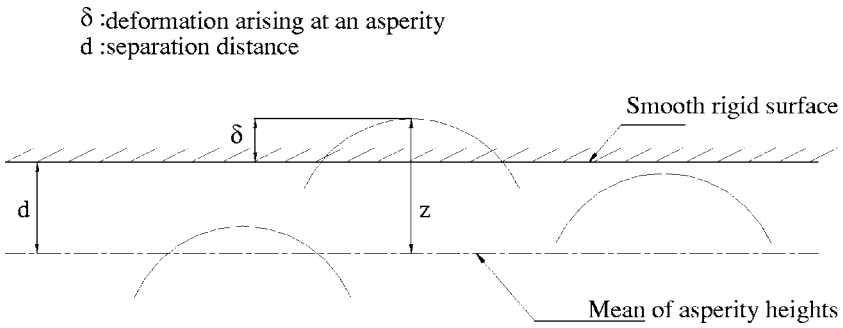

Fig. 1 The schematic diagram of two contact surface with deformation

Zhou [16], was devised to test two methods for the approximate computation of the fractal dimension (D) of surfaces ($2<D<3$). A general distribution function for the heights of an anisotropic engineering surface has been derived by Blackmore and Zhou [17]. The two-dimensional method for determining G and D was extended by Zahouani et al. [18] to three-dimensional measurements of rough surfaces. A two variable fractal surface description was also incorporated in a three-dimensional elastic-plastic contact mechanics analysis by Yan and Komvopoulos [19]. The fractal surface descriptions developed by Yan and Komvopoulos [19] are helpful to describe the interference and the radius of curvature of a spherical asperity in the present study.

The power law model was developed for the number N by Mandelbrot [20] to deal with the cumulative distribution of islands on the earth's relief, where D is the fractal dimension of its coastline. The study of Chung and Lin [21] considers developments of the size distribution functions, $n(a')$, for elastic, elastoplastic, and fully plastic deformation. They are used to evaluate the number N of contact spots with an area larger than an area of a' in per unit apparent area, rather than using the power law model commonly adopted in several other studies [13,14,19,22]. Nevertheless, all of these studies related to the fractal theory assumed that fractal dimension and the topothesy are invariant with mean separation, and the probability density function is assumed to be the Gaussian distribution except in the studies of Blackmore and Zhou [16,17]. These two studies have obtained a non-Gaussian distribution for anisotropic rough surfaces; the results show good agreement between theory and experiment.

The fractal parameters (fractal dimension and topothesy), describing the contact of rough surface, were always considered as constant in the earlier models [13,14,19,22]. The behavior predicted by the assumption of constant fractal parameters is significantly different from the experimental results. Instead of considering the fractal dimension D and topothesy G as two invariants in the fractal analysis of asperity heights, these two roughness parameters are varied by differing the mean separation in the present study. The probability density function of asperity heights, achieved at different mean separations, was identified by the experimental results to be a non-Gaussian distribution [23]; it is expressed as a function of the skewness and the kurtosis of surface asperities. The objective of this study is to establish the relationships among these fractal parameters and investigate the effect of these variable fractal parameters on the contact behavior. The solutions are obtained by the following assumptions: (a) the geometry of an asperity tip is assumed to be spherical; (b) the material of all asperities is assumed to have the elastic-perfectly plastic behavior in either tension or compression. The von Mises yielding criterion was used to detect the local transition from elastic to plastic deformation.

The results shown in the experimental study of Othmani and Kaminsky [23], which provide the fractal dimension data varying with the mean separation, are exhibited in this study as the example to illustrate the variable behavior of the fractal dimension D, the topothesy G, and the scaling coefficient C_p. By equating the structure functions developed in two different ways, the relationship among C_p, D, and G is thus established. However, the variations of either C_p or G with the mean separation are still not available in the experimental study [23]. A relationship between C_p and G has to be found from the G-D-C_p diagram by connecting the intersection points of constant-G curves and constant-C_p curves. The topographies of a surface obtained from the experimental results at different separations [23] show the probability density function g to be no longer a Gaussian distribution. This non-Gaussian probability density function has been expressed as a function of the skewness Sk and the kurtosis Kt. The relationship between the skewness and the mean separation is thus established if the experimental results [23] can be fitted by the probability density function g. The relationship between fractal dimension and skewness is thus obtained by means of the relationship developed between the fractal dimension and the mean separation. The results obtained by assuming constant D and G as well as the Gaussian distribution are compared with those obtained by variable D and G as well as the non-Gaussin distribution.

2 Theoretical Analysis for Contact Surfaces

The contact of two rough surfaces (see Fig. 1) can be modeled by a flat and smooth surface in contact with a rough surface. If the mean radii of curvature of the asperities on surface 1 and surface 2 are R_1 and R_2, respectively, the equivalent rough surface can be expressed as having the radius of curvature, R, satisfying $1/R=1/R_1+1/R_2$. If σ_1 and σ_2 denote the standard deviations of the surface roughness of surface 1 and surface 2, respectively. The standard deviation, σ, for this equivalent rough surface satisfies $\sigma=\sqrt{\sigma_1^2+\sigma_2^2}$.

2.1 Contact of Elastic and Fully Plastic Deformations. According to Hertz theory, the elastic contact area, a_e, the elastic contact load, F_e, and the average contact pressure, P_e, produced by a sphere with a radius of R in contact with a flat, smooth plate with an elastic interference, δ, are given as [24]

$$a_e=\pi R\delta \tag{1}$$

$$F_e=\tfrac{4}{3}ER^{1/2}\delta^{3/2} \tag{2}$$

$$P_e=\frac{4}{3}\frac{E}{\pi}\left(\frac{\delta}{R}\right)^{1/2} \tag{3}$$

where E denotes the effective Young's modulus of two solid contact surfaces (surface 1 and surface 2) with the Young's modului, E_1 and E_2, and the Poisson ratios, ν_1 and ν_2, respectively. It is stated as

$$\frac{1}{E}=\frac{1-\nu_1^2}{E_1}+\frac{1-\nu_2^2}{E_2}$$

In the fully plastic deformation regime, the asperity's contact area, a_p, the contact load, F_p, and the average contact pressure, P_p, can be expressed as [24]

$$a_p = 2\pi R\delta \tag{4}$$

$$F_p = H \cdot a_p \tag{5}$$

$$P_p = H \tag{6}$$

2.2 The Critical Interference and Contact of Elastoplastic Deformation. The critical interference, δ_c, that marks the transition from the elastic deformation to the elastoplastic deformation (i.e., the yielding inception) is given as [5,7,8,12,19]

$$\delta_c = \left(\frac{\pi KH}{2E}\right)^2 R \tag{7}$$

where H denotes the hardness of the softer material and its relationship with the yield strength (Y) is generally expressed by $H = CY$. $C = 2.8$ [25] is valid only for a small region of indentations; this C value is brought down by large indentations due to the softening effect formed at large deformations, and the hardness coefficient K is related to the Poisson ratio of the softer material [5,7,8]

$$K = 0.454 + 0.41\nu \tag{8}$$

From the results provided by Mesarovic and Fleck [26] for a half-space indention, the depth generated by a rigid sphere is deep into the fully plastic deformation regime. The plastic deformation in response to this depth is characterized by two parameters: a yielding strength and a non-dimensional strain-hardening exponent. The results reveal that the normalized contact radius and the average contact pressure of an asperity can be obtained as functions of the normalized indentation depth and the strain-hardening exponent. The elastic-plastic finite element model developed by Kogut and Etsion [7] for the frictionless contact of a deformable sphere pressed by a rigid flat plate is adopted in the present work. In their study, the sphere is assumed to be an elastic-perfectly plastic material with an identical behavior in tension and compression. The validity of the dimensionless contact pressure, P/Y (P: contact pressure), was tested by solving the problem for several different material properties ($100 < E/Y < 1000$, $\nu = 0.3$) and sphere radii ($0.1\ \text{mm} < R < 10\ \text{mm}$). The dimensionless results of contact load, contact area, and P/Y versus the dimensionless interference, δ/δ_c, are always the same regardless of the selection of material properties and sphere radius. From the results provided by Kogut and Etsion [7], they showed that the normalized contact area and the average contact pressure can be expressed by curve-fitting as a function of the dimensionless interference only. This model can be easily modified to accommodate the strain hardening effect, it is, however, applied in the present study simply for the purpose of comparing the results with that of the earlier studies.

Kogut and Etsion [7] used the finite element method to solve the microcontact problem of a single asperity, and found that the elastoplastic regime extends over the dimensionless interference values in a range of $1 \leqslant \delta/\delta_c \leqslant 110$, with a distinct transition in the contact behavior at $\delta/\delta_c = 6$. In a range that $1 \leqslant \delta/\delta_c < 6$, a plastic region develops beneath the contact surface, while the entire contact area is in the elastic deformation. In a range that $\delta/\delta_c \geqslant 6$, the contact area contains an inner elastic circular core surrounded by an external plastic annulus. This elastic core shrinks with increasing interference and finally disappears completely at $\delta/\delta_c = 68$. Thereafter, the entire contact area is in the plastic deformation, but the average contact pressure continues to rise until it becomes a constant value equal to the material hardness as $\delta/\delta_c = 110$, which marks the beginning of the fully plastic deformation.

The dependence of the asperity's contact area, a_{ep}, the contact load, F_{ep}, and the average contact pressure, P_{ep}, in the elastoplastic deformation regime were presented by Kogut and Etsion [7] in a dimensionless form as

$$\frac{a_{ep}}{\pi R\delta_c} = a_1\left(\frac{\delta}{\delta_c}\right)^{b_1} \tag{9}$$

$$\frac{F_{ep}}{2/3KH\pi R\delta_c} = a_2\left(\frac{\delta}{\delta_c}\right)^{b_2} \tag{10}$$

$$\frac{P_{ep}}{H/2.8} = a_3\left(\frac{\delta}{\delta_c}\right)^{b_3} \tag{11}$$

where the coefficients, a_1–a_3, and the exponents, b_1–b_3, for the first and second elastoplastic regimes were given in this study [7].

2.3 Contact Loads of Elastic, Elastoplastic, and Fully Plastic Deformations in the Fractal Model. Yan and Komvopoulos [19] used a modified two-variable Weierstrass-Mandelbrot function, $z(x,y)$, to characterize the rough surface geometry. To obtain the deformation force at a microcontact of given size, its interference with the opposing rigid smooth flat must be determined first. They assumed spherical asperity microcontacts to be the isotropic distribution and derived a single-variable equivalent relationship for the surface represented by

$$z(x) = L(G/L)^{(D-2)}(\ln\alpha)^{1/2}\sum_{n=0}^{n_{\max}} \alpha^{(D-3)n}\cos\phi - \cos(2\pi\alpha^n x/L - \phi),$$

where $D(2 < D < 3)$ denotes the fractal dimension of the surface [19]; G denotes the topothesy which is a height scaling parameter independent of the frequency of the wave form shown in asperity heights; L is the sample length; α represents a parameter that determines the density of frequency shown in the surface asperities, it was chosen to be 1.5; and ϕ is a random phase which is used to prevent the coincidence of different frequencies at any point of the surface profile. Since the expression of $z(x)$ is still a series of cosine functions, a profile consisting of smaller asperities residing on the top of larger asperities is produced. For an asperity with its truncated microcontact radius r', the longest wavelength in the asperity wave form is $2r'$. It is reasonable to assume that the microcontact force is principally due to the deformation of an asperity with the base wavelength, and the corresponding frequency index n, where $n = \ln(L/2r')/\ln\alpha$ [19]. Therefore, $\alpha^n = L/2r'$, The substitution of α^n into this $z(x)$ expression allows the $z(x)$ function to be reduced to $z_0(x)$ which can be expressed as [19]: $z_0(x) = G^{(D-2)}(\ln\alpha)^{1/2}(2r')^{(3-D)}[\cos\phi - \cos(\pi x/r' - \phi)]$. The interference of a spherical asperity, δ, is determined by the $z_0(x)$ function and it is equal to the peak-to-valley amplitude of the $z_0(x)$ function. For a given contact spot with an area ($a' = \pi r'^2$), δ is given as [19]

$$\delta = 2^{(4-D)}G^{(D-2)}(\ln\alpha)^{1/2}\pi^{(D-3)/2}a'^{(3-D)/2} \tag{12a}$$

The radius of curvature, R, for the circular contact spot is thus obtained by $R = -[1 + (dz_0/dx)^2]^{1/2}(d^2z_0/dx^2)^{-1}$ [27]. The r' value in the $z_0(x)$ expression can be determined by the expression that $r' = [\delta(R-\delta)]^{1/2}$ [27]. By the relationship that $a' = \pi r'^2$; the effective radius of curvature of an asperity, R, is thus obtained as

$$R = \frac{2^{(D-4)}G^{(2-D)}a'^{(D-1)/2}}{\pi^{(D-1)/2}(\ln\alpha)^{1/2}} \tag{12b}$$

The dimensionless topothesy, $\bar{G}$, and the dimensionless contact area, $\overline{a'}$, through normalizing of the relevant parameter by the standard deviation of surface height, σ, can be expressed as

$$\bar{G} \equiv G/\sigma$$

$$\overline{a'} \equiv a'/\sigma^2$$

then, the dimensionless interference, $\bar{\delta}(\bar{\delta} \equiv \delta/\sigma)$, and the dimensionless effective radius of curvature, $\bar{R}(\bar{R} \equiv R/\sigma)$, can be expressed as

$$\bar{\delta} = 2^{(4-D)}\bar{G}^{(D-2)}(\ln \alpha)^{1/2}\pi^{(D-3)/2}\overline{a'}^{(3-D)/2} \tag{13a}$$

$$\bar{R} = \frac{2^{(D-4)}\bar{G}^{(2-D)}\overline{a'}^{(D-1)/2}}{\pi^{(D-1)/2}(\ln \alpha)^{1/2}} \tag{13b}$$

Substitutions of Eqs. (13*a*) and (13*b*) into two sides of Eq. (7), and subsequent simplification, give

$$\bar{a}_c = \left[2^{(10-2D)}\pi^{(D-4)}\bar{G}^{(2D-4)}(\ln \alpha)\left(\frac{E}{KH}\right)^2\right]^{1/(D-2)} \tag{14}$$

here, $\bar{a}_c$ is the dimensionless critical contact area corresponding to the inception of the elastoplastic deformation. Asperities are elastically deformed as $\delta < \delta_c$. The substitutions of Eq. (13*a*) and Eq. (7) into the above mentioned inequality yields $a' > a_c$. When asperities are deformed, such as $\delta \geq \delta_c$, they are in the elastoplastic deformation; even in the fully plastic deformation, the result of $a' \leq a_c$ is obtained. The same conclusion has also been drawn in several other studies [13,19,22].

By substituting Eqs. (13*a*) and (13*b*) into Eqs. (2), (5), and (10), respectively, the dimensionless contact load of an asperity for elastic, elastoplastic, and fully plastic deformations in fractal form can be obtained as follows.

(a) For the elastic deformation $(\delta/\delta_c \leq 1)$

$$\bar{F}_e \equiv F_e/(E \cdot \sigma^2) = \tfrac{1}{3} \cdot 2^{(6-D)}\pi^{(D-4)/2}(\ln \alpha)^{1/2}\bar{G}^{(D-2)}\overline{a'}^{(4-D)/2} \tag{15}$$

(b) For the first elastoplastic deformation $(1 \leq \delta/\delta_c \leq 6)$

$$\bar{F}_{ep1} \equiv F_{ep1}/(E \cdot \sigma^2) = 1.2377 \cdot \left(\frac{KH}{E}\right)^{0.144} 2^{-0.85D+3.4}\bar{G}^{0.85D-1.7} \times (\ln \alpha)^{0.425}\pi^{0.425D-1.7}\overline{a'}^{(-0.425D+1.85)} \tag{16a}$$

For the second elastoplastic deformation $(6 \leq \delta/\delta_c \leq 110)$

$$\bar{F}_{ep2} \equiv F_{ep2}/(E \cdot \sigma^2) = 1.3439 \cdot \left(\frac{KH}{E}\right)^{0.474} 2^{-0.526D+2.104}\bar{G}^{0.526D-1.052} \times (\ln \alpha)^{0.263}\pi^{0.263D-1.052}\overline{a'}^{(-0.263D+1.526)} \tag{16b}$$

(c) For the fully plastic deformation $(110 \leq \delta/\delta_c)$

$$\bar{F}_p = (H \cdot a')/(E \cdot \sigma^2) = (H/E) \cdot \overline{a'} \tag{17}$$

2.4 Relationship between Fractal Dimension and Mean Separation. In the present study, the variations of G and D with mean separation, $\bar{d}$, of two contact surfaces can be obtained. For a fractal surface, the number $(N(a'))$ of contact spots with area larger than a' follows the power law relation in the form [21]

$$N(a') \approx B \cdot a'^{(1-D)/2} \tag{18}$$

If the $N(a')-a'$ plot in the log-log form can be obtained from the experimental results of $N(a')$ and a', the slope of an $N(a')-a'$ curve is equal to $(1-D)/2$. Then, the fractal dimension D can be determined if the slope is available. As Fig. 2 shows, all $N(a')/Aa-a'$ curves involved experimental data obtained at different separations [23]. The fractal dimension for each $\bar{d}$ can then be determined. Define $\bar{d}$ as the dimensionless mean separation. The empirical expression obtained from the curve fitting of the D data is expressed as

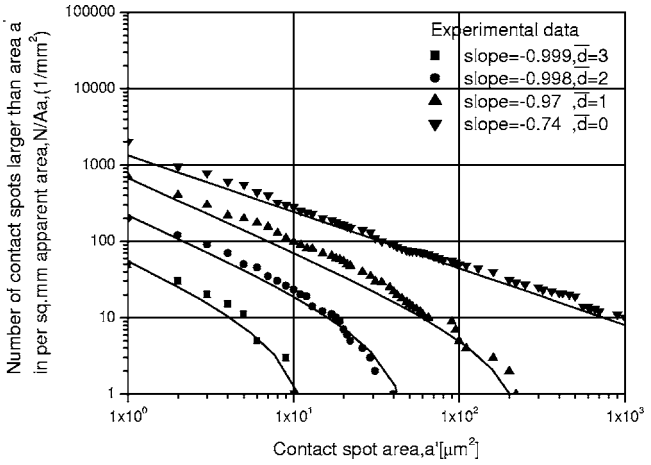

Fig. 2 The experimental results of $N(a')/Aa$ shown in the study of Othmani and Kaminsky [23] as a function of the contact spot area a'. The solid curves are applied to fit the experimental data by adjusting the slope value.

$$D = y_1 + A_1 e^{(-\bar{d}/t_1)} \tag{19}$$

where $y_1 = 3.0$, $A_1 = -0.52395$, and $t_1 = 0.47258$. The curve is shown in Fig. 3.

2.5 Relationship among Topothesy, Fractal Dimension, and Scaling Constant. The relationship among topothesy, G, fractal dimension, D, and scaling constant, C_p, needs to be derived. In the study of Yan and Komvopoulos [19], the structure function, S, of a surface with surface asperities is expressed as

$$S(\tau) = 2^{2(4-D)}G^{2(D-2)}(\ln \alpha)(\tau)^{2(3-D)} \tag{20}$$

where τ denotes the resolution of an instrument applied to measure the surface heights of points separated by a distance, τ. The structure function can also be obtained from the power spectrum function, $P(\omega)$, of surface asperities. This function is written as [28]

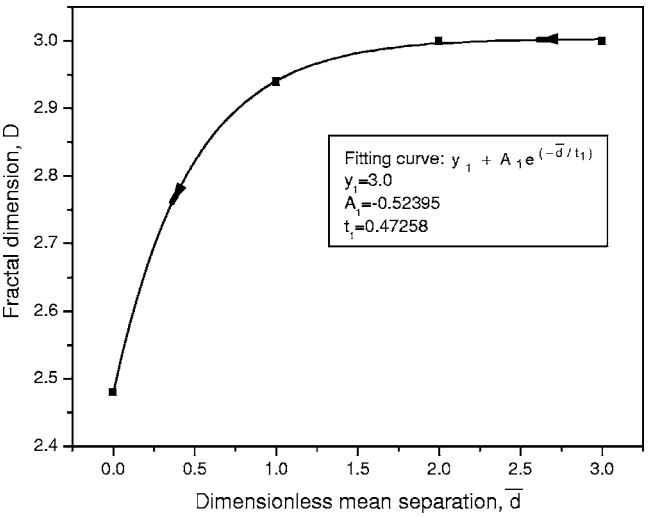

Fig. 3 The fractal dimensions varying with the dimensionless mean separation. These data of D are obtained from the slope values of the four curves shown in Fig. 2.

$$P(\omega) = \frac{C_p}{\omega^{\eta}} \tag{21}$$

where $\omega = 1/\tau$ and η denotes the exponent value of ω. C_p is a scaling constant which depends on the amplitude of surface roughness. The structure function corresponding to this power spectrum is given as [28]

$$S(\tau) = \int_{-\infty}^{\infty} P(\omega)[\exp(i\omega\tau) - 1]d\omega = \frac{2C_p}{\eta - 1}\sin\left(\frac{\pi}{2}(2-\eta)\right)\Gamma(2-\eta) \times |\tau|^{\eta-1} \tag{22}$$

Equating Eqs. (20) and (22) gives the exponent value of τ, satisfying $\eta - 1 = 6 - 2D$; therefore, $\eta = 7 - 2D$. Substituting $\eta = 7 - 2D$ into Eq. (22) produces the structure function as

$$S(\tau) = \frac{C_p}{3-D}\sin\left(\frac{\pi}{2}(2D-5)\right)\Gamma(2D-5)\tau^{2(3-D)} \tag{23}$$

Here, Γ denotes the gamma function. Equating the coefficients of τ, shown in Eqs. (20) and (23), yields the C_p parameter as

$$C_p = \frac{(3-D)2^{2(4-D)}G^{2(D-2)}\ln\alpha}{\sin\left(\frac{\pi(2D-5)}{2}\right)\Gamma(2D-5)} \tag{24}$$

Equation (24) can also be rewritten as

$$G = \left\{\frac{Cp \cdot \sin\left(\frac{\pi(2D-5)}{2}\right)\Gamma(2D-5)}{(3-D)2^{2(4-D)}\ln\alpha}\right\}^{1/(2D-4)} \tag{25}$$

In either Eq. (24) or Eq. (25), three parameters, D, G, and C_p, can be uniquely determined, but only when any two of these parameters are available. As Eq. (21) shows, the power spectrum $P(\omega)$, as a function of frequency ω, can be determined by measuring surface topographies achieved at different mean separations of two contact surfaces. The logarithmic form of Eq. (21) gives $\log P(\omega) = \log C_p + \eta \cdot \log \omega$. C_p is thus the intersection of this straight line with the $\log P(\omega)$ coordinate, when the experimental data are revealed in the $\log P(\omega) - \log \omega$ plot. As to the fractal dimension, D, a three-dimensional surface profile yields its value, varying in the range of 2 to 3. In the present study, the variations of G with D in this range can therefore be determined in Eq. (25), if the C_p parameter is obtained directly from surface roughness measurements.

In order to satisfy Eq. (25), there exists a manipulating region suitable for parameters, G and C_p, when the fractal dimension D is varied from 2 to 3. As Fig. 4 shows, the upper boundary of this region is denoted by line 1 having a constant G value. This constant value is the original topothesy of the profile before incurring any contact deformation. The lower boundary of this region is denoted by curve 3. This curve is determined as follows: substituting the initial values of D and G for a surface before surface contacts into Eq. (24) obtains the C_p value. This C_p value is denoted by $(C_p)_{\text{initial}}$, as shown in Fig. 4. Then, curve 3 is obtained by fixing the $(C_p)_{\text{initial}}$ value, but changing the fractal dimension. The real contact behavior arising at different mean separation must be within the region laying between line 1 and curve 3. However, this activity does not suggest that contact behavior can follow any arbitrary relationship within this region. The choice of the G-C_p relationship must satisfy the necessary condition that the G parameter is lowered by decreasing the fractal dimension (D) in order to conform to the reality of contact behavior.

Due to the lack of C_p data in the experimental study of Othmani and Kaminsky [23], curve 2(a)-curve 2(c) in Fig. 4, are shown as three examples. The prerequisite validity of these three curves will be illustrated in the "Results and Discussion" section. The evaluation about the effect of variable G, D, and C_p on the tribological behavior is now on the base of curves 2(a)–2(c). Theoretically, a genuine curve 2 should be determined by the measurements of surface topography.

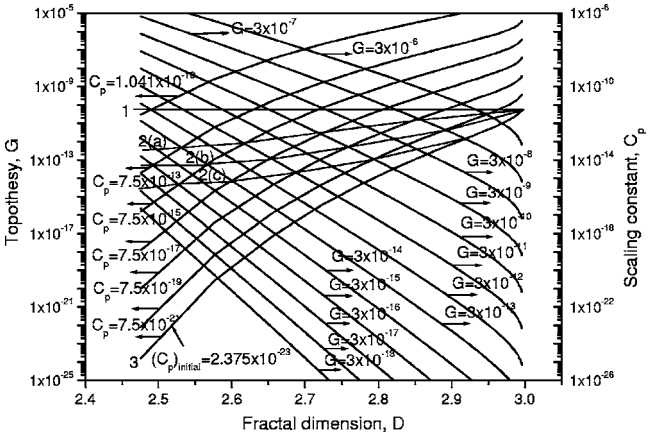

Fig. 4 Determination of the region satisfying Eq. (25). The tribological behavior in the present study is analyzed according to curve 2(a)-curve 2(c).

2.6 Size Distributions at Elastic, Elastoplastic, and Fully Plastic Deformations. In the present study, all parameters with a bar above them are now defined to be dimensionless. Define $\bar{a}_1 \equiv \left[\left(\frac{1}{110}\right)^{1/(D-2)}\right] \cdot \bar{a}_c$ and $\bar{a}_2 \equiv \left[\left(\frac{1}{6}\right)^{1/(D-2)}\right] \cdot \bar{a}_c$. If the size distribution parameter, $n(\bar{a}')$, of asperities at each of the elastic, elastoplastic, and fully plastic deformation regimes is available, the real contact area of a surface in the dimensionless form ($\bar{A}r = Ar/\sigma^2$) can be expressed as

$$\begin{aligned}\bar{A}r &= \bar{A}_e + \bar{A}_{\text{ep}_1} + \bar{A}_{\text{ep}_2} + \bar{A}_p \\ &= \int_{\bar{a}_c}^{\bar{a}_L} n_e(\bar{a}')\bar{a}'d\bar{a}' + \int_{\bar{a}_2}^{\bar{a}_c} n_{\text{ep1}}(\bar{a}')\bar{a}'d\bar{a}' \\ &\quad + \int_{\bar{a}_1}^{\bar{a}_2} n_{\text{ep2}}(\bar{a}')\bar{a}'d\bar{a}' + \int_{o}^{\bar{a}_1} n_p(\bar{a}')\bar{a}'d\bar{a}'\end{aligned} \tag{26}$$

where n_{ep1} and n_{ep2} represent the size distribution function in the first and second elastoplastic regimes, respectively. The size distribution functions in the three deformation regimes, $n_e(\bar{a}')$, $n_{\text{ep1}}(\bar{a}')$, $n_{\text{ep2}}(\bar{a}')$, and $n_p(\bar{a}')$ can be determined if the real contact area, $\bar{A}r$ in Eq. (26), can be obtained in another way. If the probability density function of asperity heights, $g(\bar{z})$, is known, the asymptotic expression of the real contact area, developed by Bush et al. [29], can be expressed as

$$\begin{aligned}\bar{A}r &= \frac{\lambda \cdot \kappa}{\lambda^2 + \kappa^2}\bar{A}a\left\{\int_{\bar{d}}^{(\bar{d}+\bar{\delta}_c)} g(\bar{z})d\bar{z} + \int_{(\bar{d}+\bar{\delta}_c)}^{(\bar{d}+6\bar{\delta}_c)} g(\bar{z})d\bar{z}\right. \\ &\quad \left. + \int_{(\bar{d}+6\bar{\delta}_c)}^{(\bar{d}+110\bar{\delta}_c)} g(\bar{z})d\bar{z} + \int_{(\bar{d}+110\bar{\delta}_c)}^{\infty} g(\bar{z})d\bar{z}\right\}\end{aligned} \tag{27}$$

where

$$\bar{\delta}_c = \delta_c/\sigma$$

$$\bar{z} = z/\sigma$$

$$\lambda = \left\{\frac{(m_2)_{\min}}{(m_2)_{\max}}\right\}^{1/2}$$

$$\kappa = \frac{0.4777\lambda}{1 - 1.3211\lambda}$$

and where the m_2 parameter is known as the second spectral moment of a profile. It gives

$$m_2 = E\{(dz/dx)^2\}$$

where $z(x)$ is a surface profile varying in an arbitrary direction, x, and $E\{\}$ denotes a statistical expectation. The direction in which m_2 has a maximum value is known as the principal direction. Then, $m_2(0) = (m_2)_{\max} = m_{20}$ and $m_2(\pi/2) = (m_2)_{\min} = m_{02}$. The λ parameter in the present analysis is assumed to be a fixed value.

In Eq. (26), a dummy variable should be used to express the first integral as

$$\bar{A}_e(\overline{a'}) = \int_{\overline{a'}}^{\bar{a}_L} n_e(\bar{\alpha})\bar{\alpha} d\bar{\alpha},$$

where $\overline{a'}$ is treated as the variable lower limit of integration. Then the fundamental theorem of calculus yields

$$\frac{d\bar{A}_e}{d\overline{a'}} = -n_e(\overline{a'})\overline{a'}$$

therefore,

$$n_e(\overline{a'}) = -\frac{1}{\overline{a'}}\frac{d\bar{A}_e}{d\overline{a'}}.$$

Appling the chain rule to this, one obtains

$$n_e(\overline{a'}) = -\frac{1}{\overline{a'}}\frac{d\overline{A_e}}{d\overline{a'}} = -\frac{1}{\overline{a'}}\frac{d\overline{A_e}}{d\bar{z}}\frac{d\bar{z}}{d\overline{a'}}$$

From Fig. 1, $\bar{z} = \bar{\delta} + \bar{d}$, whence $d\bar{z}/d\overline{a'} = d\bar{\delta}/d\overline{a'}$, so the above-noted formula yields

$$n_e(\overline{a'}) = -\frac{1}{\overline{a'}}\frac{d\overline{A_e}}{d\bar{z}}\frac{d\bar{\delta}}{d\overline{a'}} \tag{28}$$

In Eq. (27), a dummy variable should also be used to express the first integral as

$$\bar{A}_e(\bar{z}) = \frac{\lambda \cdot \kappa}{\lambda^2 + \kappa^2}\overline{Aa}\int_{\bar{z}}^{\bar{d}+\bar{\delta}_c} g(\varsigma) d\varsigma,$$

with $\bar{z}$ as the lower limit of integration. Applying the fundamental theorem of calculus to the above equation, one obtains

$$\left.\frac{d\bar{A}_e}{d\bar{z}}\right|_{\bar{d}} = -\frac{\lambda \cdot \kappa}{\lambda^2 + \kappa^2}\overline{Aa} \cdot g(\bar{d}) \tag{29}$$

The area derivative of the deformation parameter ($\bar{\delta}$) shown in Eq. (13*a*) with respect to the contact area $\overline{a'}$ is expressed as

$$\frac{d\bar{\delta}}{d\overline{a'}} = \left[\frac{3-D}{2}\right] 2^{4-D}\bar{G}^{(D-2)}(\ln \alpha)^{1/2}\pi^{(D-3)/2}\overline{a'}^{(1-D)/2} \tag{30}$$

where $\bar{G} = G/\sigma$. Substituting Eqs. (29) and (30) into Eq. (28) gives

$$n_e(\overline{a'}) = \frac{\lambda \cdot \kappa}{\lambda^2 + \kappa^2}\overline{Aa} \cdot g(\bar{d})\left[\frac{3-D}{2}\right] 2^{4-D}\bar{G}^{(D-2)} \times (\ln \alpha)^{1/2}\pi^{(D-3)/2}\overline{a'}^{(-1-D)/2} \tag{31}$$

The number of contact spots (N) in the elastic deformation region, whose area is larger than the contact spot area $\overline{a'}$, takes $N(\overline{a'}) = \int_{\overline{a'}}^{\bar{a}_L} n_e(\overline{a'})d\overline{a'}$. The size distribution function, $n_{ep1}(\overline{a'})$, for the first elastoplastic regime, $n_{ep2}(\overline{a'})$ for the second elastoplastic regime, and $n_p(\overline{a'})$ for the fully plastic regime are shown in Appendix.

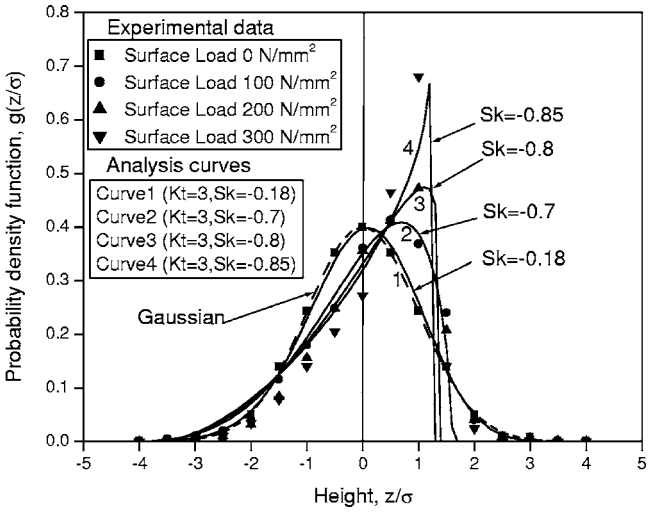

Fig. 5 Probability density functions of asperity heights [23]

2.7 Non-Gaussian Probability Density Function Varying With Mean Separation. The topographies of a surface obtained from surface contacts at different separations are generally no longer the Gaussian distribution, and the probability density function of surface asperities varies with the mean separation of two surfaces. According to the experimental results shown in the study of Othmani and Kaminsky [23], surface asperities, after experiencing contacts of different separations, were found to be satisfied by a non-Gaussian probability density function.

The equation for the non-Gaussian probability density function, $g(\bar{z})$, can be expressed as [30]

$$g(\bar{z}) = y_e(1 + \bar{z}/B_1)^{m_1}(1 - \bar{z}/B_2)^{m_2}, \quad (-B_1 < \bar{z} < B_2) \tag{32}$$

In Eq. (32), m_1, m_2, B_1, B_2 are obtained by solving [30]

$$(m_1 + 1)/B_1 = (m_2 + 1)/B_2 \tag{33}$$

$$B_1 + B_2 = \tfrac{1}{2}\{\mathrm{Sk}^2(r+2)^2 + 16(r+1)\}^{1/2} \tag{34}$$

where Sk in Eq. (34) denotes the skewness, the measure of the asymmetry of the profile about the mean line; and r is written as [30]

$$r = \frac{6(\mathrm{Kt} - \mathrm{Sk}^2 - 1)}{(6 + 3\mathrm{Sk}^2 - 2\mathrm{Kt})} \tag{35}$$

where Kt in Eq. (35) represents a measure of the sharpness of the surface profile. The m_1 and m_2 values are given by [30]

$$m_1 = \frac{1}{2}\left\{r - 2 - r(r+2)\left(\frac{\mathrm{Sk}^2}{\mathrm{Sk}^2(r+2)^2 + 16(r+1)}\right)^{1/2}\right\} \tag{36a}$$

$$m_2 = \frac{1}{2}\left\{r - 2 + r(r+2)\left(\frac{\mathrm{Sk}^2}{\mathrm{Sk}^2(r+2)^2 + 16(r+1)}\right)^{1/2}\right\} \tag{36b}$$

and

$$y_e = \frac{1}{B_1 + B_2}\frac{(m_1+1)^{m_1}(m_2+1)^{m_2}}{(m_1+m_2+2)^{m_1+m_2}}\frac{\Gamma(m_1+m_2+2)}{\Gamma(m_1+1)\Gamma(m_2+1)} \tag{37}$$

where Γ is the gamma function. Once Sk and Kt are obtained, the non-Gaussian probability density function, $g(\bar{z})$, is determined. The kurtosis, Kt, is generally fixed to be 3 [30], and the skewness, Sk, is derived by adjusting its value so that the curve predicted by Eq. (32) shows good agreement with the experimental results. Figure 5 indicates the solid curves predicted by Eq. (32) at differ-

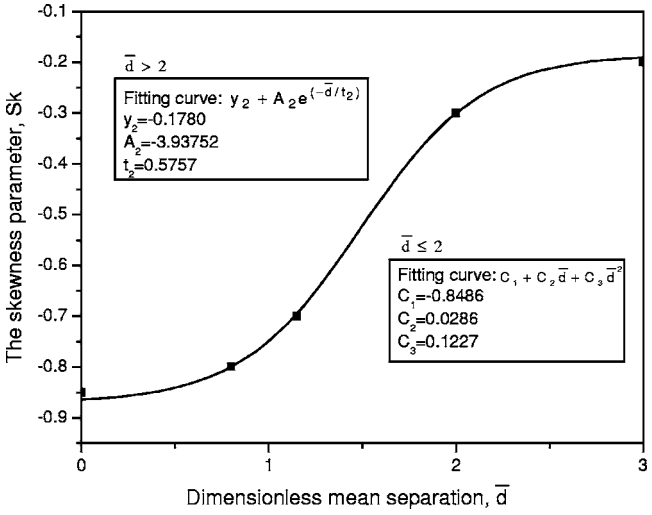

Fig. 6 Variations of the skewness parameter with the dimensionless mean separation. These skewness data are obtained from the fittings shown in Fig. 5.

ent skewness values. The experimental results corresponding to these Sk values are noted by different symbols.

From the preceding experimental results, surface skewness changes are shown to be dependent upon different dimensionless mean separation, $\bar{d}$. The point data in Fig. 6 show the variation of surface skewness with $\bar{d}$ for the experimental results in Fig. 5. No single expression fits all these points accurately. Therefore, in the present study two skewness expressions are needed to describe the behavior exhibited in the two subregions of $\bar{d}$. The empirical expression for $\bar{d} > 2$ is given as

$$\mathrm{Sk} = y_2 + A_2 \cdot e^{(-\bar{d}/t_2)} \tag{38}$$

where $y_2 = -0.1780$, $A_2 = -3.93752$, and $t_2 = 0.5757$. The expression for $\bar{d} \leqslant 2$ is given as

$$\mathrm{Sk} = C_1 + C_2 \cdot \bar{d} + C_3 \cdot \bar{d}^2 \tag{39}$$

where $C_1 = -0.8486$, $C_2 = 0.0286$, and $C_3 = 0.1227$. Then the real contact area, $\overline{Ar}$, shown in Eq. (27), can be rewritten as

$$\overline{Ar} = \frac{\lambda \cdot \kappa}{\lambda^2 + \kappa^2} \overline{Aa} \cdot \int_{\bar{d}}^{\infty} g(\bar{z}) d\bar{z} \tag{40}$$

The equivalence between Eqs. (26) and (40) is established first; then, the substitution of the $g(\bar{d})$ expression, shown in Eq. (32), into the resulting equivalence allows us to obtain the largest contact area $(\overline{a_L})$ of an asperity among all real contact spot areas.

The total load, F_t, acting on an apparent surface, can be evaluated by the size distribution of contact spots. If the largest contact spot area is larger than the critical area, i.e., $\overline{a_L} > a_c$, the dimensionless total load $(\overline{F_t} \equiv F_t/(E \cdot \sigma^2))$ is expressed as

$$\overline{F_t} = \int_{\bar{a}_c}^{\bar{a}_L} \overline{F_e} \cdot n_e(\overline{a'}) \cdot d\overline{a'} + \int_{\bar{a}_2}^{\bar{a}_c} \overline{F}_{\mathrm{ep1}} \cdot n_{\mathrm{ep1}}(\overline{a'}) \cdot d\overline{a'} + \int_{\bar{a}_1}^{\bar{a}_2} \overline{F}_{\mathrm{ep2}} \cdot n_{\mathrm{ep2}}(\overline{a'}) \cdot d\overline{a'} + \int_{0}^{\bar{a}_1} \overline{F_p} \cdot n_p(\overline{a'}) \cdot d\overline{a'} \tag{41}$$

2.8 Relationship Between Fractal Dimension and Skewness. The dimensionless mean separation, $\bar{d}$, shown in Eqs. (19), (38), and (39), reveals that the relationship between the fractal dimension D and the skewness Sk can be established. There exist two cases for the dimensionless mean separation. In the case that $\bar{d} > 2$, Eq. (19) gives

$$D = y_1 + A_1 e^{(-\bar{d}/t_1)} = y_1 + A_1 e^{(-\bar{d}/t_2)(t_2/t_1)} = y_1 + A_1 \cdot [e^{(-\bar{d}/t_2)}]^{(t_2/t_1)} \tag{42}$$

By the use of Eq. (38), Eq. (42) can be rewritten as

$$D = y_1 + A_1 \cdot \left[\frac{\mathrm{Sk} - y_2}{A_2}\right]^{(t_2/t_1)} \tag{43}$$

In the case that $\bar{d} \leqslant 2$, Eq. (39) can be rewritten as

$$C_3 \cdot \bar{d}^2 + C_2 \cdot \bar{d} + (C_1 - \mathrm{Sk}) = 0 \tag{44}$$

Since $\bar{d}$ is a positive value, the $\bar{d}$ solution of Eq. (44) is obtained as

$$\bar{d} = \frac{-C_2 + \sqrt{C_2^2 - 4C_3(C_1 - \mathrm{Sk})}}{2C_3} = \frac{-0.0286 + \sqrt{0.00081796 - 0.4908(-0.8486 - \mathrm{Sk})}}{0.2454} \tag{45}$$

Since $\bar{d}$ is expressed as a function of the skewness, the relationship between fractal dimension, D, and skewness, Sk, can be established by substituting the $\bar{d}$ expression shown in Eq. (45) to the D expression shown in Eq. (19). Final conclusions drawn from the present analysis are that the fractal dimension D can be obtained from Eq. (19) by giving a $\bar{d}$ value; this D value can be used to obtain G from Eq. (25), if C_p is given as a constant value. For the case that $\bar{d} > 2$, Eq. (43) is directly applied to solve Sk, if D is known; whereas, for the case that $\bar{d} \leqslant 2$, Eqs. (19) and (45) are combined to obtain Sk, if D is known.

3 Results and Discussion

In the present study, the fractal theory developed in previous studies [13,19] analyzing the contact of rough surfaces is adopted here to study microcontact behavior exhibited at different mean separations. Instead of considering the fractal dimension D and topothesy G as invariants at various mean separations (d), these two roughness parameters are actually varied with the mean separation. The solid curves shown in Fig. 2 present theoretical results predicted by the different fractal dimensions in Eq. (18); each of these curves shows fairly good fitting with the experimental data [23]. Then, the slope of each curve is determined. Mean separation data have been provided in the experimental study of Othmani and Kaminsky [23]. The slopes of these curves involve negative values; they become steep as the mean separation between two contact surfaces is increased. Figure 3 shows the variation of fractal dimension with the mean separation for experimental results shown in Fig. 2. The fractal dimension for the cases of large separation is 3; it is decreased as the mean separation is reduced. The fractal dimension corresponding to zero separation is lowered to about 2.475.

In Fig. 4, the intersection point (a) of line 1 and curve 3 indicates the surface state, before it experiences any asperity interference. These intersection points of constant-G and constant-C_p curves show the values of G, D, and C_p satisfying Eq. (25). With the aid of Fig. 3, curves 2(a)–2(c) in Fig. 4 are here obtained by connecting part of these intersection points so that the G parameter is always lowered by decreasing the fractal dimension. The topothesies of these three curves satisfy: $(G)_{2(a)} > (G)_{2(b)} > (G)_{2(c)}$. These specific curves may not conform precisely to real G-C_p behavior for the material used in the experimental study of

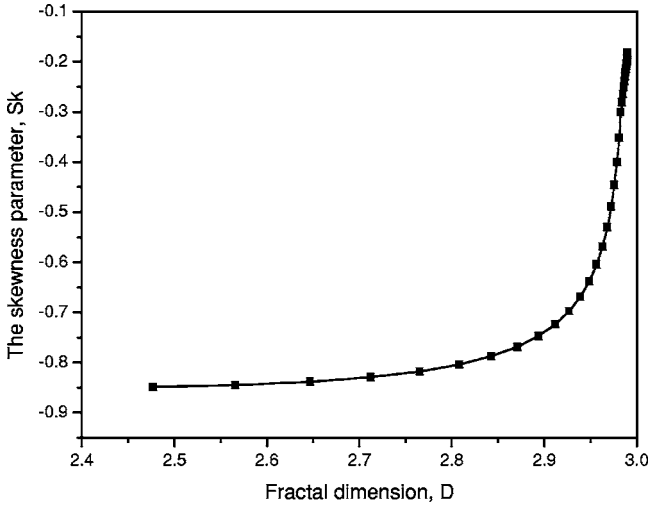

Fig. 7 Variations of the skewness parameter with the fractal dimension. They are established using Figs. 3 and 6.

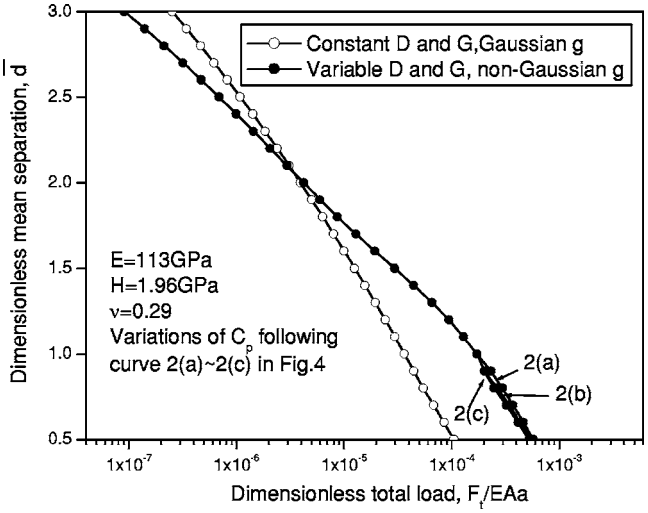

Fig. 8 Variations of the dimensionless mean separation with the dimensionless total load. They are presented to compare the evaluations based on variable *G* and *D* as well as non-Gaussian $g(\bar{z})$, with the evaluations based on constant *G* and *D* as well as Gaussian $g(\bar{z})$.

Othmani and Kaminsky [23]; however, these three curves can provide us with information about the influence of variable G, D, and C_p on tribological behavior.

The topographies of a surface obtained from surface contacts at different separations generally do not follow the Gaussian distribution; the non-Gasussian density function was formulated in the Kotwal and Bhushan study [30] as a function of the skewness (Sk) and the kurtosis (Kt). In this study, a given mean separation (d) is sufficient to determine the fractal dimension, the topothesy, and the skewness. Figure 5 shows the variations of the probability density function $g(\bar{z})$ under four different surface loads (unit: N/mm^2). The skewnesses of these solid curves are all negative values; their absolute values are increased by increasing the surface load. Figure 6 shows the variations of the skewness with the mean separation $\bar{d}$. The skewness parameter becomes more negative as the mean separation is reduced.

The combination of the D-$\bar{d}$ relationship, shown in Fig. 3, and the Sk-$\bar{d}$ relationship, shown in Fig. 6, reveals the Sk-D relationship in Fig. 7. For the fractal dimension in the region smaller than 2.8, the skewness of surface asperities is almost invariant with D. However, a further increase in the fractal dimension causes a significant lowering of skewness in the absolute value, especially for the fractal dimension close to 3.0.

The probability density function $g(\bar{z})$ of surface asperities is usually assumed to be a Gaussian distribution, and D and G remain invariant with changing mean separation. However, experimental results in Othmani and Kaminsky [23] reveal that $g(\bar{z})$ actually varies with mean separation, and D and G are no longer taken to be invariant. Figure 8 shows the dimensionless total loads predicted by these two models from different viewpoints. In the case of variable G and D and non-Gaussian $g(\bar{z})$, the relationship among G, D, and C_p obeys the behavior of curve 2 in Fig. 4; whereas $g(\bar{z})$ obtained from the experimental results, shown in Fig. 5, is applied to obtain theoretical solutions in the present study. In the region of $\bar{d}$ smaller than about 2.0, the total load predicted by a non-Gaussian $g(\bar{z})$ is higher than that predicted by a Gaussian $g(\bar{z})$. The difference in the total load is enhanced by decreasing the mean separation.

Conversely, the total load predicted by a non-Gaussian $g(\bar{z})$ is lower than that predicted by a Gaussian $g(\bar{z})$, if $\bar{d}$ is greater than about 2. The existence of the $F_t/(E\cdot Aa)$ difference between these two models, for a mean separation greater than about 2, is not actually correct. This difference should be narrowed to be negligibly small as the mean separation $\bar{d}$ is increased to larger values. The interpretation of this error can be given by the probability density curves shown in Fig. 5 for Sk=0 (Gaussian) and Sk =−0.18. From an investigation of Fig. 6, the skewness (Sk) varies roughly in the range of −0.3 to −0.18, if the mean separation ($\bar{d}$) is greater than 2.0. Therefore, differences in $F_t/(E\cdot Aa)$, shown in Fig. 8, for $\bar{d}\geqslant 2$ are only pertinent to the probability density profiles with Sk=0 (Gaussian) and Sk=−0.18. As Sk=−0.18, Fig. 6 shows the dimensionless mean separation corresponding to this Sk value is about 3. The g curve corresponding to Sk=−0.18 as well as in the region of $z/\sigma\geqslant 3$ is slightly different from that of Sk =0.0 (Gaussian). The differences between these two curves in this region become the primary factors of those differences shown in Fig. 8. This behavior is theoretically abnormal; however, the differences shown in the region of $\bar{d}\geqslant 2$ are quite small.

As Fig. 8 shows, the three curves marked by 2(a), 2(b), and 2(c) are, respectively, obtained by following curve 2(a)-curve 2(c) as shown in Fig. 4. Small differences are shown among them only when the mean separation is quite small. Nevertheless, the total loads satisfy: $(F_t/E\cdot Aa)_{2(a)}>(F_t/E\cdot Aa)_{2(b)}>(F_t/E\cdot Aa)_{2(c)}$ if they are evaluated at the same mean separation ($\bar{d}$). This ordering is the same as that shown in Fig. 4 for the topothesies (G) of these three curves. Therefore, a higher total load is created by a contact surface with a larger G which varies with the mean separation.

The effect of variable D, G and $g(\bar{z})$ on the dimensionless real contact area is shown in Fig. 9. This figure exhibits the characteristic that a decrease in the mean separation can result in an increase in the total load, thereby increasing the real contact area. However, under a fixed total load, the real contact area predicted by the Gaussian $g(\bar{z})$ (D and G are two invariants) is always larger than that predicted by the variable $g(\bar{z})$; and the difference between them is significantly enlarged by increasing the total load. The conjunction of the results shown in Figs. 8 and 9 implies that the real contact area predicted by variable G and D, as well as non-Gaussian $g(\bar{z})$, is larger than that predicted by constant G and D, as well as Gaussian $g(\bar{z})$, if they are evaluated at a small mean separation. The results of Ar/Aa corresponding to curves 2(a)–2(c) shown in Fig. 4 are so close that the differences among them are negligibly small.

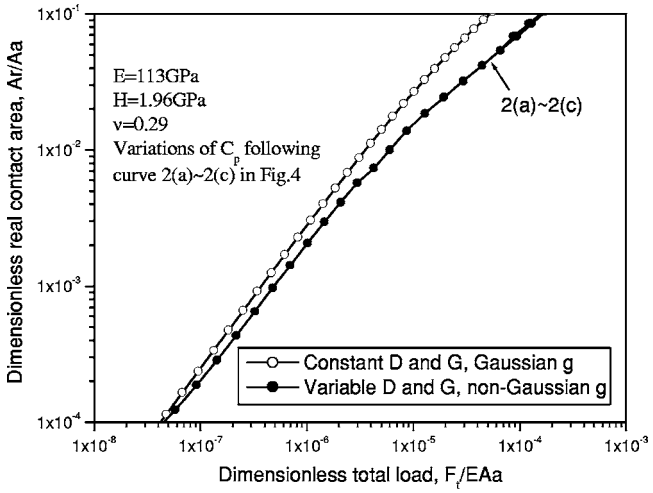

Fig. 9 Variations of the dimensionless real contact area with the dimensionless total load. They are presented to compare the evaluations based on the two different models described in Fig. 8.

Figure 10 shows the variations of $N(a')/Aa$, with the mean separation $\bar{d}$ for these two different evaluation models. The behavior exhibited in the dimensionless mean separations smaller than about 2.0 shows that the $N(a')/Aa$ value predicted by variable D,G, and non-Gaussian $g(\bar{z})$, is higher than that predicted by assuming constant D,G, and Gaussian $g(\bar{z})$. However, the behavior exhibited in mean separations larger than 2.0 is exactly opposite. Theoretically, these two curves should be grouped together when $\bar{d} \geqslant 2$ because the difference in $N(a')/Aa$ between these two models should be very small as the mean separation becomes large. This difference can be accounted for by the conclusion derived in the interpretation of differences shown in Fig. 8 for the region of $\bar{d} \geqslant 2$. The evaluations of N/A_a based on curves 2(a)–2(c) exhibited in Fig. 4 show significant differences among them as the mean separation becomes small. The results satisfy: $(N/Aa)_{2(c)} > (N/Aa)_{2(b)} > (N/Aa)_{2(a)}$.

4 Conclusions

1. The reported experimental results show the characteristic that the fractal dimension varies with the mean separation of two contact surfaces. In the present study, the relationship between the fractal dimension and the topothesy can be established by incorporating the theoretical deductions with the experimental data. The probability density function $g(\bar{z})$ of surface asperities is also changed to be a non-Gaussian distribution according to the experimental results. All these roughness parameters can be expressed as functions of the mean separation.
2. The relationship among D, G, and C_p can be derived from the equivalence of two structure function expressions, which are developed in different ways. The variations of G are thus determined when the fractal dimension D and the scaling coefficient C_p can be obtained from the experimental results of the number of contact spots, $N(a')$, and the power spectrum function $P(\omega)$ shown at different mean separations.
3. The probability density functions shown in the experimental results of different loads can be expressed as a function of the skewness parameter (Sk) of asperity heights. The absolute value of the skewness is increased by reducing the mean separation.
4. The total load predicted by variable D and G, as well as non-Gaussian g, is greater than that predicted by constant D and G, as well as Gaussian g. The differences become significant as the mean separation is reduced to small values. The real contact area and the number of contact spots have shown the same behavior as the total load.

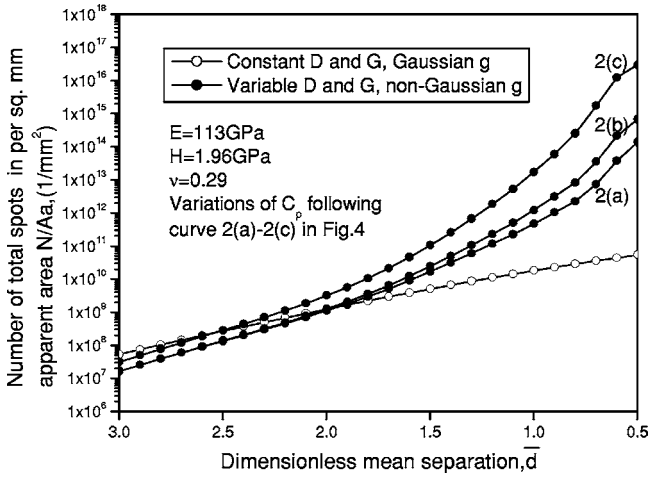

Fig. 10 Variations of $N(a')/Aa$ with the dimensionless mean separation. They are presented to compare the evaluations based on the two different models described in Fig. 8.

Nomenclature

a_c = critical contact spot area
$\bar{a}_c$ = dimensionless critical contact spot area, a_c/σ^2
a_L = largest contact spot area
$\bar{a}_L$ = dimensionless largest contact spot area, a_L/σ^2
$\overline{a'}$ = dimensionless contact area of an asperity
$\bar{a}_1$ = $\left[\left(\frac{1}{110}\right)^{1/(D-2)}\right]\cdot\bar{a}_c$
$\bar{a}_2$ = $\left[\left(\frac{1}{6}\right)^{1/(D-2)}\right]\cdot\bar{a}_c$
$\underline{Ar}$ = real contact area
$\overline{Ar}$ = dimensionless real contact area, Ar/σ^2
$\underline{Aa}$ = apparent area
$\overline{Aa}$ = dimensionless apparent area, Aa/σ^2
$\bar{d}$ = dimensionless mean separation, d/σ
D = 3-D fractal dimension $(2<D<3)$
E = effective Young's modulus
F = contact load of an asperity
$\bar{F}$ = dimensionless contact load
F_t = total contact load
$\overline{F_t}$ = dimensionless total contact load, $F_t/(E\cdot\sigma^2)$
$g(\bar{z})$ = probability density function of asperity heights
G = topothesy
$\bar{G}$ = dimensionless topothesy, G/σ
H = hardness of the softer material in contact
Kt = kurtosis
$n(\overline{a'})$ = size distribution of contact spots of area $\overline{a'}$
N = number of contact spots
P = mean contact pressure
$\bar{P}$ = dimensionless mean contact pressure
R = equivalent radius of curvature of an asperity
$\bar{R}$ = dimensionless equivalent radius, R/σ
Sk = skewness
Y = yield strength of softer material
$z(x,y)$ = modified two-variable Weierstrass-Mandelbrot function

Greek symbols

α = a parameter that determines the density of frequencies in the surface (=1.5)
δ = deformation at an asperity
$\bar{\delta}$ = dimensionless deformation at an asperity, δ/σ
δ_c = critical deformation
σ = standard deviation of surface heights
τ = length scale
ν_1, ν_2 = Poisson ratios of surface 1 and surface 2, respectively

Subscripts

e = elastic deformation
ep = elastoplastic deformation
p = plastic deformation

Appendix

Equations (13*a*) and (13*b*) are now substituted into Eqs. (4) and (9) to obtain the $\overline{a'}$-$\bar{\delta}$ relationships in the fractal form for the elastoplastic and the fully plastic deformation regimes, respectively. By following the same procedures deduced to

$$n_e(\overline{a'})\left(=-\frac{1}{\overline{a'}}\frac{d\bar{A}_e}{d\overline{a'}}\right),$$

the size distribution function, $n_{\mathrm{ep1}}(\overline{a'})$, for the first elastoplastic regime, $n_{\mathrm{ep2}}(\overline{a'})$ for the second elastoplastic regime, and $n_p(\overline{a'})$ for the fully plastic regime, respectively, are obtained as follows:

$$n_{\text{ep1 or ep2 or }p}(\overline{a'}) = -\frac{1}{\overline{a'}}\frac{d\bar{A}_{\text{ep1 or ep2 or }p}}{d\bar{z}}\frac{d\bar{\delta}}{d\overline{a'}} \tag{A1}$$

The value of $d\bar{A}_{\text{ep1 or ep2 or }p}/d\bar{z}$ in Eq. (A1), by the use of Eq. (27), gives

$$\frac{d\bar{A}_{\text{ep1 or ep2 or }p}}{d\bar{z}} = -\frac{\lambda\kappa}{\lambda^2+\kappa^2}[\overline{Aa}\cdot g]_{\text{ep1 or ep2 or }p} \tag{A2}$$

The substitutions of the $\overline{a'}$-$\bar{\delta}$ relationship developed for each of these three regimes and the corresponding $d\bar{A}_{\text{ep1 or ep2 or }p}/d\bar{z}$ expression shown in Eq. (A2) into Eq. (A1) give the size distribution functions for these three regimes as

$$n_{\mathrm{ep1}}(\overline{a'}) = \frac{\lambda\cdot\kappa}{\lambda^2+\kappa^2}\overline{Aa}\cdot g(\bar{d}+\bar{\delta}_c)\cdot\left\{(1.1236-0.3386D)\times\left(\frac{KH}{E}\right)^{0.239}\pi^{(0.38D-1.021)}(\ln\alpha)^{0.38}\times 2^{(3.044-0.76D)}\bar{G}^{(0.76D-1.522)}\cdot\overline{a'}^{(-0.38D-0.739)}\right\} \tag{A3}$$

$$n_{\mathrm{ep2}}(\overline{a'}) = \frac{\lambda\cdot\kappa}{\lambda^2+\kappa^2}\overline{Aa}\cdot g(\bar{d}+6\bar{\delta}_c)\cdot\left\{(1.1-0.33D)\times\left(\frac{KH}{E}\right)^{0.255}\pi^{(0.373D-0.99)}(\ln\alpha)^{0.373}\times 2^{(2.981-0.746D)}\bar{G}^{(0.746D-1.49)}\cdot\overline{a'}^{(-0.373D-0.755)}\right\} \tag{A4}$$

$$n_p(\overline{a'}) = \frac{\lambda\cdot\kappa}{\lambda^2+\kappa^2}\overline{Aa}\cdot g(\bar{d}+110\bar{\delta}_c)\cdot 2^{4-D}\bar{G}^{(D-2)}\times(\ln\alpha)^{1/2}\pi^{(D-3)/2}\overline{a'}^{(-1-D)/2}\left[\frac{3-D}{4}\right] \tag{A5}$$

References

[1] Greenwood, J. A., and Williamson, J. B. P., 1966, "Contact of Nominally Flat Surfaces," Proc. R. Soc. London, Ser. A, **295**, pp. 300–319.
[2] Nayak, P. R., 1971, "Random Process Model of Rough Surfaces," ASME J. Lubr. Technol., **93**, pp. 398–407.
[3] Nayak, P. R., 1973, "Random Process Model of Rough Surfaces in Plastic Contact," Wear, **26**, pp. 305–333.
[4] McCool, J. I., 1986, "Comparison of Model for Contact of Rough Surfaces," Wear, **107**, pp. 37–60.
[5] Chang, W. R., Etsion, I., and. Bogy, D. B, 1987, "An Elastic-Plastic Model for The Contact of Rough Surfaces," ASME J. Tribol., **109**, pp. 257–263.
[6] Pullen, J., and Williamson, J. B. P., 1972, "On The Plastic Contact of Rough Surfaces," Proc. R. Soc. London, Ser. A **327**, pp. 159–173.
[7] Kogut, L., and Etsion, I., 2002, "Elastic-Plastic Contact Analysis of a Sphere and a Rigid Flat," ASME J. Appl. Mech., **69**, pp. 657–662.
[8] Kogut, L., and Etsion, I., 2003, "A Finite Element Based Elastic-Plastic Model for the Contact of Rough Surface," Tribol. Trans., **46**, pp. 383–390.
[9] Gagnepain, J. J., and Roques-Carmes, C., 1986, "Fractal Approach to Two-Dimensional and Three-Dimensional Surface Roughness," Wear, **109**, pp. 119–126.
[10] Majumdar, A., and Tien, C. L., 1990, "Fractal Characterization and Simulation of Rough Surfaces," Wear, **136**, pp. 313–327.
[11] Russ, J. C., 1994, *Fractal Surfaces*, Plenum, New York.
[12] Majumdar, A., and Bhushan, B., 1990, "Role of Fractal Geometry in Roughness Characterization and Contact Mechanics of Surfaces," ASME J. Tribol., **112**, pp. 205–216.
[13] Majumdar, A., and Bhushan, B., 1991, "Fractal Model of Elastic-Plastic Contact between Rough Surfaces," ASME J. Tribol., **113**, pp. 1–11.
[14] Bhushan, B., and Majumdar, A., 1992, "Elastic-Plastic Contact Model for Bifractal Surfaces," Wear, **153**, pp. 53–64.
[15] Zhou, G. Y., Leu, M. C., and Blackmore, D., 1993, "Fractal Geometry Model for Wear Prediction," Wear, **170**, pp. 1–14.
[16] Blackmore, D., and Zhou, G., 1998, "A New Fractal Model for Anisotropic Surfaces," Int. J. Mach. Tools Manuf., **38**, pp. 551–557.
[17] Blackmore, D., and Zhou, J. G., 1998, "Fractal Analysis of Height Distributions of Anisotropic Rough Surfaces," Fractals, **6**, pp. 43–58.
[18] Zahouani, H, Vargiolu, R., and Loubet, J. L, 1998, "Fractal Models of Surface Topography and Contact Mechanics," Math. Comput. Modell., **28**, pp. 517–534.
[19] Yan, W., and Komvopoulos, K., 1998, "Contact Analysis of Elastic-Plastic Fractal Surfaces," J. Appl. Phys., **84**, pp. 3617–3624.
[20] Mandelbort, B. B., 1982, *The Fractal Geometry of Nature*, Freeman, New York.
[21] Chung, J. C., and Lin, J. F., 2004, "Fractal Model Developed for Elliptic Elastic-Plastic Asperity Microcontacts of Rough Surfaces," ASME J. Tribol., **126**, pp.646–654.
[22] Komvopoulos, K., and Ye, N., 2001, "Three-Dimensional Contact Analysis of Elastic-Plastic Layered Media With Fractal Surface Topographies," ASME J. Tribol., **123**, pp. 632–640.
[23] Othmani, A., and Kaminsky, C., 1998, "Three Dimensional Fractal Analysis of Sheet Metal Surfaces," Wear, **214**, pp. 147–150.
[24] Johnson, K. L, 1987, *Contact Mechanics*, Cambridge University Press, Cambridge, UK.
[25] Tabor, D., 1951, *The Hardness of Metals*, Clarendon Press, Oxford, UK.
[26] Mesarovic, S. D., and Fleck, N. A., 1999, "Spherical Indentation of Elastic-Plastic solids," Proc. R. Soc. London, Ser. A, **455**, pp. 2707–2728.
[27] Ogilvy, J. A., 1991, "Numerical Simulation of Friction between Contacting Rough Surfaces," J. Phys. D, **24**, pp. 2098–2109.
[28] Berry, M. V., 1979, "Diffractals," J. Phys. A, **12**, pp. 781–797.
[29] Bush, A. W., Gibson, R. D., and Keogh, G. P., 1979, "Strongly Anisotropic Rough Surface," ASME J. Lubr. Technol., **101**, pp. 15–20.
[30] Kotwal, C. A., and Bhushan, B., 1996, "Contact Analysis of Non-Gaussian Surfaces for Minimum Static and Kinetic Friction and Wear," Tribol. Trans., **39**, pp. 890–898.

Guillermo Franco
Postdoctoral Research Fellow
The Earth Institute,
Columbia University,
634A S. W. Mudd Building,
New York, NY 10027
e-mail: franco@civil.Columbia.edu.

Raimondo Betti
Professor
Department of Civil Engineering and Engineering Mechanics,
Columbia University,
640 S. W. Mudd Building,
New York, NY 10027
e-mail: betti@civil.Columbia.edu

Richard W. Longman
Professor
Department of Mechanical Engineering,
Columbia University,
232 S. W. Mudd Building,
New York, NY 10027
e-mail: RWL14@Columbia.edu

On the Uniqueness of Solutions for the Identification of Linear Structural Systems

This work tackles the problem of global identifiability of an undamped, shear-type, N degrees of freedom linear structural system under forced excitation without any prior knowledge of its mass or stiffness distributions. Three actuator/sensor schemes are presented, which guarantee the existence of only one solution for the mass and stiffness identification problem while requiring a minimum amount of instrumentation (only 1 actuator and 1 or 2 sensors). Through a counterexample for a 3DOF system it is also shown that fewer measurements than those suggested result invariably in non-unique solutions. [DOI: 10.1115/1.2062829]

Introduction

Parametric system identification consists of two basic steps: First, a model for the actual system to be identified is formalized in terms of a set of differential equations, which target to describe with reasonable fidelity the physical response of the system to applied stimuli if the coefficients or parameters involved are chosen appropriately. The second step in the identification procedure consists of optimizing these parameters so that the model behaves as closely to the actual system as possible. Once the mathematical model with its parameters has been determined, it can be used, for instance, to simulate the behavior of the system under different conditions of external forcing. With successive identifications, the variation of the model parameters can be calculated and used to infer the deterioration of the physical system as a damage detection procedure.

The behavior of the system can be understood in a broad sense as a response of the system (output) to a set of stimuli (inputs). In structural engineering, a typical way to describe this behavior is through the dynamic signature of the structure, that is the characteristic motion undergone by the system when a set of dynamic forces are applied. Therefore, to obtain the dynamic signature of a structure it is necessary to record its movements at different locations as well as the forces applied. Ideally, the more measurements obtained, the more complete the dynamic characterization of the structure will be. On the other side, for practical purposes, instrumentation has to be kept at a minimum for economic reasons.

Through the years, the identification algorithms that have been developed have tried to obtain a complete characterization of the system with a minimum amount of input and output measurements in order to lower the economic requirements while still accomplishing the final task of identifying the system accurately. The question that arises naturally then is what is the minimum amount of measurements needed to identify the structure completely and unambiguously?

The problem of determining whether a system can be identified uniquely with a given set of inputs and outputs is known as the problem of global identifiability. A linear model structure characterized by the transfer function $G(s,\theta)$, which depends on the set of parameters θ, is said to be globally identifiable at θ^* if $G(s,\theta)\equiv G(s,\theta^*)$ for all s implies that $\theta=\theta^*$. A comprehensive treatment of the subject and the existent methodologies to tackle this problem can be found in the works of Nguyen and Wood [1] and Walter [2]. It is quite difficult to provide an answer to the question of identifiability for general models, without using the specific equations and properties of the system at hand. These difficulties notwithstanding, Katafygiotis and Beck [3] present a procedure to test global identifiability of structural models applicable in general, and with a similar philosophy, Ljung and Glad [4] develop a methodology based on differential algebra to answer the question of identifiability for general models. However, both approaches require the assistance of computer programs and the manipulation of all the equations of the problem. Therefore, it is difficult to obtain a general answer for general N-dimensional systems. Instead, a tailored approach for the problem of identification of shear-type structures, as presented by Udwadia et al. [5,6], offers a more straightforward test for identifiability using the particular structure of this specific problem. This approach is, nevertheless, applicable to linear structures, whereas the other more general approaches apply to nonlinear models as well. For nonlinear shear-type building structures, it may be possible to adapt these formerly cited general approaches to the model structure at hand to obtain similar conclusions to those presented here but of application to nonlinear problems as well.

In this paper, the problem of identification of a linear shear-type building structure with N degrees of freedom is analyzed using the polynomial regularity of the problem, already pointed out by Udwadia and Sharma [5] in their analysis of uniqueness for the stiffness distribution of a structure excited by a single actuator located at the first floor. Their results are expanded here and are general-

Contributed by the Applied Mechanics Division of THE AMERICAN SOCIETY OF MECHANICAL ENGINEERS for publication in the ASME JOURNAL OF APPLIED MECHANICS. Manuscript received by the Applied Mechanics Division, July 9, 2003; final revision, July 30, 2005. Review conducted by I. Mezic. Discussion on the paper should be addressed to the Editor, Prof. Robert M. McMeeking, Journal of Applied Mechanics, Department of Mechanical and Environmental Engineering, University of California–Santa Barbara, Santa Barbara, CA 93106-5070, and will be accepted until four months after final publication of the paper itself in the ASME JOURNAL OF APPLIED MECHANICS.

ized to the case of a single actuator located at any degree of freedom of the structure. The hypothesis of known mass distribution is removed in this analysis and the structure identification is performed here without any prior knowledge of mass or stiffness. Three sufficient conditions for guaranteeing uniqueness are proposed using just one or two sensors, depending on the location of the actuator.

Note that satisfying global identifiability does not mean that the unique solution is found. Indeed, to find this solution it is usually necessary to solve a nonlinear optimization problem that can be quite complex. In the last section of the paper a simple 3DOF system is studied analytically. It will be shown how the complexity of the problem grows quickly with the degrees of freedom of the system. An algorithm that is not sensitive to entrapment in local minima or to initial estimates could, in theory, tackle the problem appropriately. See for example the works of Koh et al. [7], Chou and Ghaboussi [8], and Franco et al. [9], where the problem of structural system identification is approached with optimization techniques based on evolutionary computation.

The input and output records used in the mathematical proofs are supposed to be noise-free, as is customary in the analysis of global identifiability. The existence of noise may cause the appearance of local minima in the parameter optimization problem and it may cause the global optimum to shift from the location of the actual desired values, but this concerns the optimization process and not the question of identifiability. The conclusions and results presented here are naturally applicable to any dynamic system that can be described by the same mathematical expression, that is a positive definite diagonal mass matrix and a positive definite tridiagonal stiffness matrix as described in the following section.

Problem Statement

Consider the one-dimensional model of an N degree of freedom undamped oscillator represented by the floor masses m_i, $i=1,2,\ldots,N$, and the corresponding stiffnesses k_i, $i=1,2,\ldots,N$ as can be seen in Fig. 1. Both masses and stiffnesses have positive values ($m_i>0$ and $k_i>0$ for $i=1,2,\ldots,N$). The identification problem consists of determining the stiffnesses k_i and masses m_i from a knowledge of the time history of the input force $f(t)$, applied at the jth degree of freedom ($1\leqslant j\leqslant N$), and a set of responses recorded at particular locations. All time functions in this discussion are assumed to be Laplace transformable. Although damping is generally present in real structures, it was shown by Udwadia et al. [6] that damping did not alter their conclusions on uniqueness reached with the analysis of the undamped oscillator. Therefore, for the sake of simplicity, the study presented here focuses on the uniqueness of the solution for the case of undamped structures.

The equations of motion governing this problem can be expressed as:

$$\mathbf{M}\ddot{\mathbf{x}}(t)+\mathbf{K}\mathbf{x}(t)=\mathbf{B}f(t) \tag{1}$$

$$\mathbf{M}=\begin{bmatrix} m_1 & & & & \\ & m_2 & & & \\ & & \ddots & & \\ & & & m_{N-1} & \\ & & & & m_N \end{bmatrix};$$

$$\mathbf{K}=\begin{bmatrix} k_1 & -k_1 & & & \\ -k_1 & k_1+k_2 & -k_2 & & \\ & -k_2 & \ddots & & \\ & & & & -k_{N-1} \\ & & & -k_{N-1} & k_{N-1}+k_N \end{bmatrix} \tag{2}$$

where $\mathbf{M}$ and $\mathbf{K}$ are the mass and stiffness matrices of the structural system, respectively. $\mathbf{B}$ is the input vector, whose components are all zero except for the jth component, where the input force $f(t)$ is applied, which is equal to 1. Vector $\mathbf{x}(t)$ contains the responses of the system for all degrees of freedom, $x_i(t)$ for $i=1,2,\ldots,N$, with $\ddot{}$ indicating double differentiation with respect to time. Since m_i and k_i for all $i=1,2,\ldots,N$ are real and positive, we can reduce the system of equations (1) to

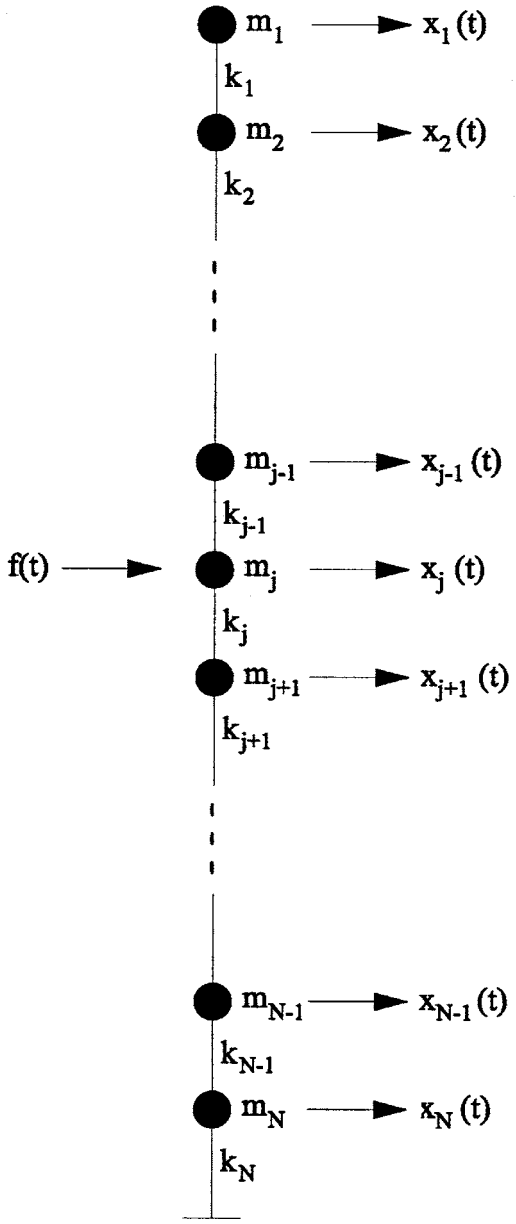

Fig. 1 One-dimensional shear-type building model with *N* degrees of freedom, input located at the *j*th story and output measured at all locations

$$\ddot{\mathbf{y}}(t)+\mathbf{A}\mathbf{y}(t)=\mathbf{\Phi}f(t) \tag{3}$$

$$\mathbf{y}=\mathbf{M}^{1/2}\mathbf{x},\quad \mathbf{\Phi}=\mathbf{M}^{-1/2}\mathbf{B}=\left(0,\ldots,0,\frac{1}{\sqrt{m_j}},0,\ldots,0\right)^T,$$

$$\mathbf{A}=\mathbf{M}^{-1/2}\mathbf{K}\mathbf{M}^{-1/2} \tag{4}$$

where the only nonzero component of vector $\mathbf{\Phi}$ is the jth component, corresponding to the location where the input force is applied. The matrix $\mathbf{A}$ thus obtained is a symmetric tridiagonal matrix and can be expressed as:

$$\mathbf{A}=\begin{bmatrix} b_1 & -a_1 & & & & \\ -a_1 & b_2 & -a_2 & & & \\ & -a_2 & \ddots & & & \\ & & & & -a_{N-1} & \\ & & & -a_{N-1} & b_N \end{bmatrix} \tag{5}$$

where

$$a_i=\frac{k_i}{\sqrt{m_i m_{i+1}}},\quad 1\leq i\leq N-1,\quad b_i=\frac{k_{i-1}+k_i}{m_i},\quad 1\leq i\leq N,\quad k_0=0 \tag{6}$$

with all a_i and b_i coefficients strictly positive.

Taking the Laplace transform of Eq. (3) and replacing the transform variable by $\sqrt{-\lambda}$, the equation of motion yields $(\mathbf{A}-\lambda\mathbf{I})\mathbf{Y}(\lambda)=\mathbf{\Phi}F(\lambda)$. The symbols used for the Laplace transforms are the capitalized symbols of each function and they are functions of the transform variable $\sqrt{-\lambda}$, or simply, functions of λ. The Laplace transform of the ith component of $\mathbf{Y}(\lambda)$, $Y_i(\lambda)$, can be expressed, using Cramer's rule, as $Y_i(\lambda)=(\Delta_i/\Delta)F(\lambda)$, where $\Delta=\det(\mathbf{A}-\lambda\mathbf{I})$, and Δ_i is the determinant of the matrix obtained from $(\mathbf{A}-\lambda\mathbf{I})$ by replacing its ith column with $\mathbf{\Phi}$.

For notational convenience, let us denote by $P_i(\lambda)$ the determinant of the upper left $i\times i$ submatrix of $(\mathbf{A}-\lambda\mathbf{I})$ and by $Q_i(\lambda)$, the determinant of the lower right $(N-i+1)\times(N-i+1)$ submatrix of $(\mathbf{A}-\lambda\mathbf{I})$. In this way, note that $P_N(\lambda)=Q_1(\lambda)=\det(\mathbf{A}-\lambda\mathbf{I})$. It is possible to express then the Laplace transforms of the outputs $X_{j-n}(\lambda)$ (at location above the one where the input excitation is applied), $X_j(\lambda)$ (at the same location where the excitation is applied), and $X_{j+l}(\lambda)$ (for locations below the one of the input excitation), for $1\leq j\leq N$, $1\leq n\leq j-1$, and $1\leq l\leq N-j$, as

$$X_{j-n}(\lambda)=\frac{1}{\sqrt{m_{j-n}}}a_{j-n}\cdots a_{j-1}\frac{P_{j-n-1}(\lambda)Q_{j+1}(\lambda)}{\Delta(\lambda)}\frac{F(\lambda)}{\sqrt{m_j}} \tag{7}$$

$$X_j(\lambda)=\frac{1}{\sqrt{m_j}}\frac{P_{j-1}(\lambda)Q_{j+1}(\lambda)}{\Delta(\lambda)}\frac{F(\lambda)}{\sqrt{m_j}} \tag{8}$$

$$X_{j+l}(\lambda)=\frac{1}{\sqrt{m_{j+l}}}a_{j+l-1}\cdots a_j\frac{P_{j-1}(\lambda)Q_{j+l+1}(\lambda)}{\Delta(\lambda)}\frac{F(\lambda)}{\sqrt{m_j}} \tag{9}$$

where, by definition, $P_0(\lambda)=Q_{N+1}(\lambda)=1$ and $X_j(\lambda)$ is the transform of $x_j(t)$, the response of the structure at the jth degree of freedom. Using the definitions introduced in Eq. (6), the previous relationships can be rewritten as

$$X_{j-n}(\lambda)=\frac{k_{j-n}}{m_{j-n}}\cdots\frac{k_{j-1}}{m_{j-1}}\frac{1}{m_j}\frac{P_{j-n-1}(\lambda)Q_{j+1}(\lambda)}{\Delta(\lambda)}F(\lambda) \tag{10}$$

$$X_j(\lambda)=\frac{1}{m_j}\frac{P_{j-1}(\lambda)Q_{j+1}(\lambda)}{\Delta(\lambda)}F(\lambda) \tag{11}$$

$$X_{j+l}(\lambda)=\frac{1}{m_{j+l}}\frac{k_{j+l-1}}{m_{j+l-1}}\cdots\frac{k_j}{m_j}\frac{P_{j-1}(\lambda)Q_{j+l+1}(\lambda)}{\Delta(\lambda)}F(\lambda) \tag{12}$$

Some Useful Properties

In this section, some useful lemmas are developed that will make it easier to draw conclusions regarding the uniqueness of solution of the identification problem for different input-output schemes presented in the following sections. Lemmas 1 and 4, whose proofs have been omitted here, are obtained directly from the structure of matrix **A** and are well described in the literature [10,5].

LEMMA 1: (a) *The functions $P_i(\lambda)$ defined in the previous section satisfy the recursion relation*

$$P_i(\lambda)=(b_i-\lambda)P_{i-1}(\lambda)-a_{i-1}^2P_{i-2}(\lambda),\quad 2\leq i\leq N,$$
$$P_1(\lambda)=(b_1-\lambda) \tag{13}$$

(b) *Each $P_i(\lambda)$ mentioned above is a polynomial of degree i with $(-1)^i\lambda^i$ as the leading term, that is* $\lim_{\lambda\to\infty}P_i(\lambda)/\lambda^i=(-1)^i$.

Proof: (a) is a known result related to the structure of the matrix **A** [10]. (b) follows through induction as indicated by Udwadia and Sharma [5].

LEMMA 2: (a) *The functions $Q_i(\lambda)$ defined above satisfy the recursion relation*

$$Q_i(\lambda)=(b_i-\lambda)Q_{i+1}(\lambda)-a_i^2Q_{i+2}(\lambda),\quad 1\leq i\leq N-1,\quad Q_N(\lambda)=(b_N-\lambda) \tag{14}$$

(b) *Each $Q_i(\lambda)$ mentioned above is a polynomial of degree $N-i+1$ with $(-1)^{N-i+1}\lambda^{N-i+1}$ as the leading term, that is* $\lim_{\lambda\to\infty}Q_i(\lambda)/\lambda^{N-i+1}=(-1)^{N-i+1}$.

Proof: (a) follows from the structure of the $(N-i+1)\times(N-i+1)$ lower right submatrix of **A**. There are only two nonzero coefficients in the first column of such matrix, namely $(b_i-\lambda)$ at location (1,1), and $-a_i$ at location (2,1). The determinant of this matrix, $Q_i(\lambda)$, can be calculated using Laplace expansion with these coefficients, obtaining

$$Q_i(\lambda)=(b_i-\lambda)\begin{vmatrix} (b_{i+1}-\lambda) & -a_{i+1} & & \\ -a_{i+1} & \ddots & -a_{N-1} & \\ & -a_{N-1} & (b_N-\lambda) & \end{vmatrix}-(-a_i)\times\begin{vmatrix} -a_i & & \\ -a_{i+1} & (b_{i+2}-\lambda) & -a_{i+2} \\ & -a_{i+2} & \ddots \end{vmatrix}. \tag{15}$$

The first determinant is, by definition, $Q_{i+1}(\lambda)$. The second determinant is the determinant of a block lower triangular matrix, which is equal to the determinant of the block matrices on the diagonal [11], namely $-a_iQ_{i+2}(\lambda)$. Substituting these values into expression (15) leads us to Eq. (14). (b) can be easily proved by induction analogously to lemma 1(b).

LEMMA 3: *The determinant $\Delta(\lambda)$ can be expressed as*

$$\Delta(\lambda)=(b_i-\lambda)P_{i-1}(\lambda)Q_{i+1}(\lambda)-a_{i-1}^2P_{i-2}(\lambda)Q_{i+1}(\lambda)-a_i^2P_{i-1}(\lambda)Q_{i+2}(\lambda) \tag{16}$$

for any $i=2,3,\ldots,N-1$.

Proof: The result is obtained by considering the Laplace expansion of the determinant of matrix **A**. Consider the ith column of **A**, which contains only three nonzero elements, namely $-a_{i-1}$ at location $(i-1,i)$, $(b_i-\lambda)$ at location (i,i), and a_i at location $(i+1,i)$. This yields that

$$\Delta(\lambda)=(b_i-\lambda)\begin{vmatrix} \ddots & -a_{i-2} & & & \\ -a_{i-2} & (b_{i-1}-\lambda) & & & \\ & & (b_{i+1}-\lambda) & -a_{i+1} & \\ & & -a_{i+1} & \ddots & \end{vmatrix}-(-a_{i-1})\times\begin{vmatrix} \ddots & -a_{i-3} & & & \\ -a_{i-3} & (b_{i-2}-\lambda) & -a_{i-2} & & \\ & & -a_{i-1} & -a_i & \\ & & & (b_{i+1}-\lambda) & -a_{i+1} \\ & & & -a_{i+1} & \ddots \end{vmatrix}-(-a_i)\times\begin{vmatrix} \ddots & -a_{i-2} & & & \\ -a_{i-2} & (b_{i-1}-\lambda) & & & \\ & -a_{i-1} & -a_i & & \\ & & -a_{i+1} & (b_{i+2}-\lambda) & -a_{i+2} \\ & & & -a_{i+2} & \ddots \end{vmatrix} \tag{17}$$

The first determinant is that of a block diagonal matrix and, therefore, it is equal to the product of their determinants, namely $P_{i-1}(\lambda)Q_{i+1}(\lambda)$. The second determinant is that of an upper triangular block matrix and it is equal to $-a_{i-1}P_{i-2}(\lambda)Q_{i+1}(\lambda)$. Similarly, the third one is equal to $-a_iP_{i-1}(\lambda)Q_{i+2}(\lambda)$. Thus, substitution of these values into Eq. (17) immediately yields the result of lemma 3.

LEMMA 4: *For* $i=1,2,\ldots,N$ *the polynomials* $P_j(\lambda)$ *and* $P_{j-1}(\lambda)$ *do not have any common zeros*.

Proof: This result can be obtained by induction, as indicated by Udwadia and Sharma [5].

LEMMA 5: *For* $i=1,2,\ldots,N$ *the polynomials* $Q_j(\lambda)$ *and* $Q_{j+1}(\lambda)$ *do not have any common zeros*.

Proof: Analogous to the proof of lemma 4, this result follows by induction (reverse induction in this occasion). Consider that the polynomials

$$Q_N(\lambda)=(b_N-\lambda) \text{ and } Q_{N-1}(\lambda)=(b_{N-1}-\lambda)(b_N-\lambda)-a_{N-1}^2 \tag{18}$$

could only have $\lambda=b_N$ as their common zero because it is the only zero of $Q_N(\lambda)$. This, though, would imply that necessarily $a_{N-1}=0$, which is not possible by the definition of all a_i as strictly positive real values. Now suppose that $Q_i(\lambda)$ and $Q_{i+1}(\lambda)$ do not have common zeros for $n\leqslant i\leqslant N$, and let

$$Q_{n-1}(\lambda^*)=Q_n(\lambda^*)=0 \tag{19}$$

Using the recursion relation of lemma 2, $Q_{n-1}(\lambda^*)$ can be written as

$$Q_{n-1}(\lambda^*)=(b_{n-1}-\lambda^*)Q_n(\lambda^*)-a_n^2Q_{n+1}(\lambda^*)=-a_n^2Q_{n+1}(\lambda^*)=0 \tag{20}$$

which implies that $Q_{n+1}(\lambda^*)=0$ since $a_n\neq 0$. This is a contradiction since $Q_n(\lambda)$ and $Q_{n+1}(\lambda)$ do not have common zeros for $n\leqslant i\leqslant N$. Thus the lemma is proved.

Two more lemmas are included in this section which refer explicitly to the problem of identification and uniqueness. It is necessary at this point to introduce some additional notation. Suppose that there exist two distinct systems, one denoted by the already introduced variables $m_1,\ldots,m_N$ and $k_1,\ldots,k_N$ and another by $\hat{m}_1,\ldots,\hat{m}_N$ and $\hat{k}_1,\ldots,\hat{k}_N$. Since both systems have the same structure, for both it is possible to build the matrices $\mathbf{A}$ and $\hat{\mathbf{A}}$ as indicated in Eq. (5) with the coefficients a_i and b_i defined in Eq. (6) for one system, and the respective coefficients $\hat{a}_i$ and $\hat{b}_i$ for the $\hat{\cdot}$-system. Similarly, a set of $\hat{P}(\lambda)$ and $\hat{Q}(\lambda)$ polynomials are defined for the $\hat{\cdot}$-system. The two following lemmas relate the polynomials of one system to the polynomials of the other system given certain conditions.

LEMMA 6: *If*

$$P_j(\lambda)\hat{P}_{j-1}(\lambda)=\hat{P}_j(\lambda)P_{j-1}(\lambda), \tag{21}$$

then

$$P_i(\lambda)=\hat{P}_i(\lambda),\quad b_i=\hat{b}_i,$$

$$\forall\, i=1,2,\ldots,j,\quad \hat{a}_i=a_i\quad \forall\, i=1,2,\ldots,j-1 \tag{22}$$

Proof: Considering Lemma 1(a), substitute $P_j(\lambda)$ and $\hat{P}_j(\lambda)$ in Eq. (22) with the equivalent expression obtained from Eq. (13) so that

$$\hat{P}_{j-1}(\lambda)[(b_j-\lambda)P_{j-1}(\lambda)-a_{j-1}^2P_{j-2}(\lambda)]=P_{j-1}(\lambda)[(\hat{b}_j-\lambda)\hat{P}_{j-1}(\lambda)-\hat{a}_{j-1}^2\hat{P}_{j-2}(\lambda)] \tag{23}$$

$$(b_j-\lambda)\hat{P}_{j-1}(\lambda)P_{j-1}(\lambda)-a_{j-1}^2\hat{P}_{j-1}(\lambda)P_{j-2}(\lambda)=(\hat{b}_j-\lambda)P_{j-1}(\lambda)\hat{P}_{j-1}(\lambda)-\hat{a}_{j-1}^2P_{j-1}(\lambda)\hat{P}_{j-2}(\lambda) \tag{24}$$

$$[b_j-\hat{b}_j]\hat{P}_{j-1}(\lambda)P_{j-1}(\lambda)=a_{j-1}^2\hat{P}_{j-1}(\lambda)P_{j-2}(\lambda)-\hat{a}_{j-1}^2P_{j-1}(\lambda)\hat{P}_{j-2}(\lambda) \tag{25}$$

Dividing by $\hat{P}_{j-1}(\lambda)P_{j-1}(\lambda)$ and letting $\lambda\to\infty$, the equality $b_j=\hat{b}_j$ is obtained with help of lemma 1(b). Thus it follows that

$$0=a_{j-1}^2\hat{P}_{j-1}(\lambda)P_{j-2}(\lambda)-\hat{a}_{j-1}^2P_{j-1}(\lambda)\hat{P}_{j-2}(\lambda) \tag{26}$$

In both polynomial products, the highest power of λ is $\lambda^{j-1}\lambda^{j-2}=\lambda^{2j-3}$. This allows us to divide Eq. (26) by λ^{2j-3} and to let λ approach ∞ again, obtaining the result $\hat{a}_{j-1}^2=a_{a-1}^2$. Given that all a_i's are defined to be positive, this is equivalent to $\hat{a}_{j-1}=a_{j-1}$. Substituting this into Eq. (26) yields also that $\hat{P}_{j-1}(\lambda)P_{j-2}(\lambda)=P_{j-1}(\lambda)\hat{P}_{j-2}(\lambda)$. This equation is analogous in its structure to the original hypothesis of the lemma, thus the process can be repeated, obtaining that $\hat{P}_i(\lambda)P_{i-1}(\lambda)=P_i(\lambda)\hat{P}_{i-1}(\lambda)$ and $b_i=\hat{b}_i$ for all $i=2,3,\ldots,j$, and $a_i=\hat{a}_i$ for all $i=2,3,\ldots,j-1$. This recursion process leads finally to the last product of polynomials, namely $\hat{P}_1(\lambda)P_0(\lambda)=P_1(\lambda)\hat{P}_0(\lambda)$. Since $P_0(\lambda)=\hat{P}_0(\lambda)=1$, substitution yields that $\hat{P}_1(\lambda)=P_1(\lambda)$, which implies that $b_1=\hat{b}_1$ as well. This can be used in turn in the previously obtained product $\hat{P}_2(\lambda)P_1(\lambda)=P_2(\lambda)\hat{P}_1(\lambda)$ to state that also $P_2(\lambda)=\hat{P}_2(\lambda)$. These recursions can be applied for all $P_i(\lambda)$, with $i=1,2,\ldots,j$ thus proving the lemma.

LEMMA 7: *If*

$$Q_{j+1}(\lambda)\hat{Q}_j(\lambda)=\hat{Q}_{j+1}(\lambda)Q_j(\lambda) \tag{27}$$

then

$$Q_i(\lambda)=\hat{Q}_i(\lambda),\quad b_i=\hat{b}_i,$$

$$\forall\, i=j,j+1,\ldots,N,\quad \hat{a}_i=a_i\quad \forall\, i=j,j+1,\ldots,N-1. \tag{28}$$

Proof: The proof follows in the same way as in lemma 6. Substitute the expressions for $Q_j(\lambda)$ and $\hat{Q}_j(\lambda)$, introduced in lemma 2(a), into Eq. (27) and develop it as follows

$$Q_{j+1}(\lambda)[(\hat{b}_j-\lambda)\hat{Q}_{j+1}(\lambda)-\hat{a}_j^2\hat{Q}_{j+2}(\lambda)]=\hat{Q}_{j+1}(\lambda)[(b_j-\lambda)Q_{j+1}(\lambda)-a_j^2Q_{j+2}(\lambda)] \tag{29}$$

$$(\hat{b}_j-\lambda)\hat{Q}_{j+1}(\lambda)Q_{j+1}(\lambda)-\hat{a}_j^2\hat{Q}_{j+2}(\lambda)Q_{j+1}(\lambda)=(b_j-\lambda)Q_{j+1}(\lambda)\hat{Q}_{j+1}(\lambda)-a_j^2Q_{j+2}(\lambda)\hat{Q}_{j+1}(\lambda) \tag{30}$$

$$[\hat{b}_j-b_j]\hat{Q}_{j+1}(\lambda)Q_{j+1}(\lambda)=\hat{a}_j^2\hat{Q}_{j+2}(\lambda)Q_{j+1}(\lambda)-a_j^2Q_{j+2}(\lambda)\hat{Q}_{j+1}(\lambda) \tag{31}$$

Using the same strategy as before, that is dividing by $\hat{Q}_{j+1}(\lambda)Q_{j+1}(\lambda)$ and letting $\lambda\to\infty$, it can be concluded that $b_j=\hat{b}_j$. Substitution of this result into Eq. (31) leads to

$$0=\hat{a}_j^2\hat{Q}_{j+2}(\lambda)Q_{j+1}(\lambda)-a_j^2Q_{j+2}(\lambda)\hat{Q}_{j+1}(\lambda) \tag{32}$$

Dividing Eq. (32) by $\lambda^{2N-2j-1}$ and letting λ approach ∞ again, it follows that $\hat{a}_j^2=a_j^2$, which implies after substitution that $\hat{Q}_{j+2}(\lambda)Q_{j+1}(\lambda)=Q_{j+2}(\lambda)\hat{Q}_{j+1}(\lambda)$. As before, this recursion can be applied up to the last product of polynomials, namely $\hat{Q}_N(\lambda)Q_{N+1}(\lambda)=Q_N(\lambda)\hat{Q}_{N+1}(\lambda)$. Since $Q_{N+1}(\lambda)=\hat{Q}_{N+1}(\lambda)=1$, substitution yields that $\hat{Q}_N(\lambda)=Q_N(\lambda)$, which implies that $b_N=\hat{b}_N$ as

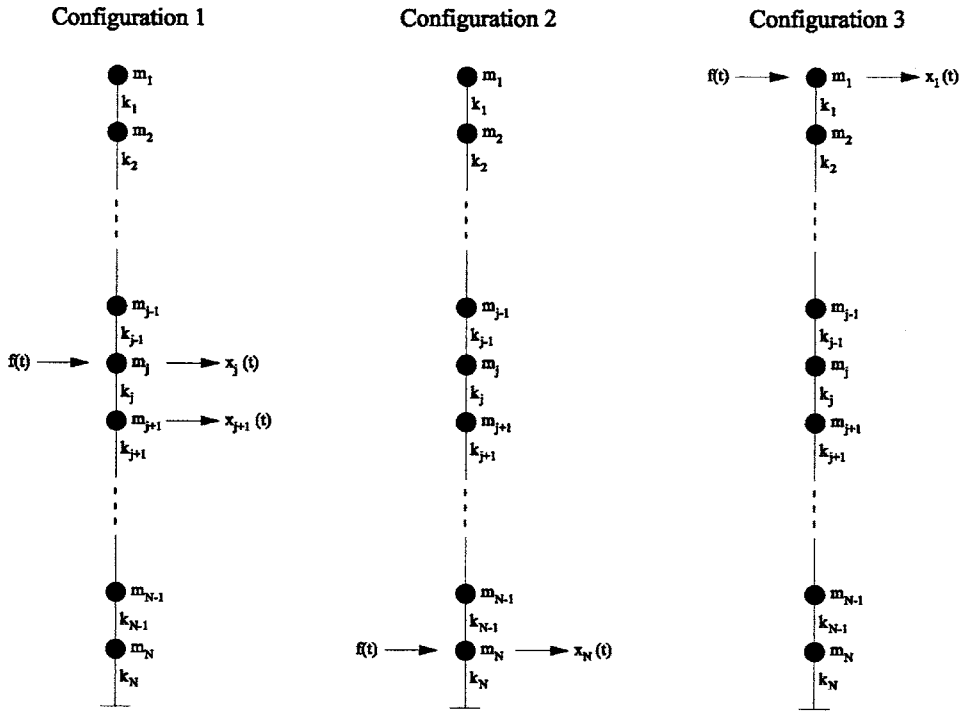

Fig. 2 Possible configurations for unique identification

well. Applying the recursion backwards for all $Q_i(\lambda)$, with $i=j,j+1,\ldots,N-1$ the lemma is proved.

Sufficient Conditions to Guarantee Uniqueness

Now let us focus on the question: What is the minimum amount of information that is required to guarantee the uniqueness of the solution for the identification of a shear-type one-dimensional building model? This question is important because the cost of the identification of an actual structure grows with the number of measurements. Therefore, it is of interest to know whether or not a configuration of measurements that uses very few sensors can provide information that leads to a unique solution.

In this section we will analyze three configurations (see Fig. 2) of input and output measurements that yield a unique identification of mass and stiffness distribution for a one-dimensional *N*DOF shear-type building model.

Configuration 1: 2 Sensors and 1 Actuator at Any Degree of Freedom. Suppose that the known excitation force is applied solely at floor j, with $2\leqslant j\leqslant N-1$, and that two output measurements are available at floors j and $j+1$, as seen in configuration 1 of Fig. 2. The question we are addressing is the following: Can we find two distinct mass and stiffness distributions that yield the same outputs at various degrees of freedom when excited by the same force? To answer this question, let us suppose that the same excitation force $f(t)$ is applied at the jth floor of two distinct systems characterized by $m_1,\ldots,m_N,k_1,\ldots,k_N$ and by $\hat{m}_1,\ldots,\hat{m}_N,\hat{k}_1,\ldots,\hat{k}_N$, respectively. Following Eqs. (10)–(12), we can express the Laplace transforms of the measurements for one system as

$$X_j(\lambda)=\frac{1}{m_j}\frac{P_{j-1}(\lambda)Q_{j+1}(\lambda)}{\Delta(\lambda)}F(\lambda) \tag{33}$$

$$X_{j+1}(\lambda)=\frac{1}{m_{j+1}}\frac{k_j}{m_j}\frac{P_{j-1}(\lambda)Q_{j+2}(\lambda)}{\Delta(\lambda)}F(\lambda) \tag{34}$$

and for the $\hat{\cdot}$-system as

$$\hat{X}_j(\lambda)=\frac{1}{\hat{m}_j}\frac{\hat{P}_{j-1}(\lambda)\hat{Q}_{j+1}(\lambda)}{\hat{\Delta}(\lambda)}F(\lambda) \tag{35}$$

$$\hat{X}_{j+1}(\lambda)=\frac{1}{\hat{m}_{j+1}}\frac{\hat{k}_j}{\hat{m}_j}\frac{\hat{P}_{j-1}(\lambda)\hat{Q}_{j+2}(\lambda)}{\hat{\Delta}(\lambda)}F(\lambda) \tag{36}$$

Since the outputs obtained at the jth and $(j+1)$th degrees of freedom of one system are supposed to be identical to the corresponding ones from the second system, we can equate the Laplace transforms of the outputs of both systems and obtain the following equations, where the transform of the excitation, $F(\lambda)$, has been eliminated because it is the same for both systems

$$\frac{1}{m_j}\frac{P_{j-1}(\lambda)Q_{j+1}(\lambda)}{\Delta(\lambda)}=\frac{1}{\hat{m}_j}\frac{\hat{P}_{j-1}(\lambda)\hat{Q}_{j+1}(\lambda)}{\hat{\Delta}(\lambda)} \tag{37}$$

$$\frac{1}{m_{j+1}}\frac{k_j}{m_j}\frac{P_{j-1}(\lambda)Q_{j+2}(\lambda)}{\Delta(\lambda)}=\frac{1}{\hat{m}_{j+1}}\frac{\hat{k}_j}{m_j}\frac{\hat{P}_{j-1}(\lambda)\hat{Q}_{j+2}(\lambda)}{\hat{\Delta}(\lambda)} \tag{38}$$

Note that in both equations, the numerator of the polynomial fraction is of a lesser order in λ than the denominator. In particular, the numerator of Eq. (37) has a degree of $\lambda^{j-1}\lambda^{N-(j+1)+1}=\lambda^{N-1}$ and the numerator of Eq. (38) has a degree of $\lambda^{j-1}\lambda^{N-(j+2)+1}=\lambda^{N-2}$, while both denominators, $\Delta(\lambda)$ and $\hat{\Delta}(\lambda)$, are polynomials of degree λ^N. Thus, multiplying both sides of Eq. (37) by λ and Eq. (38) by λ^2, and letting $\lambda\to\infty$, it is possible to obtain this new set of equations

$$\frac{1}{m_j}=\frac{1}{\hat{m}_j} \tag{39}$$

$$\frac{1}{m_{j+1}}\frac{k_j}{m_j}=\frac{1}{\hat{m}_{j+1}}\frac{\hat{k}_j}{\hat{m}_j} \tag{40}$$

which implies that

$$m_j=\hat{m}_j \tag{41}$$

$$\frac{k_j}{m_{j+1}} = \frac{\hat{k}_j}{\hat{m}_{j+1}} \tag{42}$$

Substituting Eqs. (39) and (40) into (37) and (38), respectively, provides also the following equalities for the ratios of polynomials

$$\frac{P_{j-1}(\lambda)Q_{j+1}(\lambda)}{\Delta(\lambda)} = \frac{\hat{P}_{j-1}(\lambda)\hat{Q}_{j+1}(\lambda)}{\hat{\Delta}(\lambda)} \tag{43}$$

$$\frac{P_{j-1}(\lambda)Q_{j+2}(\lambda)}{\Delta(\lambda)} = \frac{\hat{P}_{j-1}(\lambda)\hat{Q}_{j+2}(\lambda)}{\hat{\Delta}(\lambda)} \tag{44}$$

Since all polynomials involved are in general different than zero for an arbitrary λ, division of Eq. (44) by Eq. (43) yields

$$\frac{Q_{j+2}(\lambda)}{Q_{j+1}(\lambda)} = \frac{\hat{Q}_{j+2}(\lambda)}{\hat{Q}_{j+1}(\lambda)} \tag{45}$$

which can also be expressed as

$$Q_{j+2}(\lambda)\hat{Q}_{j+1}(\lambda) = \hat{Q}_{j+2}(\lambda)Q_{j+1}(\lambda) \tag{46}$$

By lemma 5, we can conclude that

$$Q_i(\lambda) = \hat{Q}_i(\lambda), \quad b_i = \hat{b}_i, \quad \forall\, i = j+1, j+2, \ldots, N, \quad \hat{a}_i = a_i$$

$$\forall\, i = j+1, j+2, \ldots, N-1 \tag{47}$$

Let us consider now Eq. (43) and clear the denominators to obtain

$$P_{j-1}(\lambda)Q_{j+1}(\lambda)\hat{\Delta}(\lambda) = \hat{P}_{j-1}(\lambda)\hat{Q}_{j+1}(\lambda)\Delta(\lambda) \tag{48}$$

Using lemma 3 to substitute the $\Delta(\lambda)$ and $\hat{\Delta}(\lambda)$ polynomials, it is possible to express the previous equation as

$$P_{j-1}(\lambda)Q_{j+1}(\lambda)[(\hat{b}_j - \lambda)\hat{P}_{j-1}(\lambda)\hat{Q}_{j+1}(\lambda) - \hat{a}_{j-1}^2\hat{P}_{j-2}(\lambda)\hat{Q}_{j+1}(\lambda) - \hat{a}_j^2\hat{P}_{j-1}(\lambda)\hat{Q}_{j+2}(\lambda)] \tag{49}$$

$$= \hat{P}_{j-1}(\lambda)\hat{Q}_{j+1}(\lambda)[(\hat{b}_j - \lambda)\hat{P}_{j-1}(\lambda)\hat{Q}_{j+1}(\lambda) - a_{j-1}^2\hat{P}_{j-2}(\lambda)\hat{Q}_{j+1}(\lambda) - a_j^2 P_{j-1}(\lambda)Q_{j+2}(\lambda)] \tag{50}$$

expression that, by grouping the polynomial products, reduces to

$$\begin{aligned}(\hat{b}_j - b_j)\hat{P}_{j-1}(\lambda)\hat{Q}_{j+1}(\lambda)P_{j-1}(\lambda)Q_{j+1}(\lambda) &- \hat{a}_{j-1}^2\hat{P}_{j-2}(\lambda)\hat{Q}_{j+1}(\lambda)P_{j-1}(\lambda)Q_{j+1}(\lambda) - \hat{a}_j^2\hat{P}_{j-1}(\lambda)\hat{Q}_{j+2}(\lambda)P_{j-1}(\lambda)Q_{j+1}(\lambda) \\ &= -a_{j-1}^2 P_{j-2}(\lambda)Q_{j+1}(\lambda)\hat{P}_{j-1}(\lambda)\hat{Q}_{j+1}(\lambda) - a_j^2 P_{j-1}(\lambda)Q_{j+2}(\lambda)\hat{P}_{j-1}(\lambda)\hat{Q}_{j+1}(\lambda)\end{aligned} \tag{51}$$

Since the product $\hat{P}_{j-1}(\lambda)\hat{Q}_{j+1}(\lambda)P_{j-1}(\lambda)Q_{j+1}(\lambda)$ is a polynomial of higher order in λ than the rest of the polynomial products in Eq. (51), it is possible to divide all terms by the highest power, i.e., λ^{2N-2}, and let $\lambda \to \infty$. In this way, we obtain the following equality

$$b_j = \hat{b}_j \tag{52}$$

that allows us to express Eq. (51) as

$$\begin{aligned}-\hat{a}_{j-1}^2\hat{P}_{j-2}(\lambda)\hat{Q}_{j+1}(\lambda)P_{j-1}(\lambda)Q_{j+1}(\lambda) &- \hat{a}_j^2\hat{P}_{j-1}(\lambda)\hat{Q}_{j+2}(\lambda)P_{j-1}(\lambda)Q_{j+1}(\lambda) \\ &= -a_{j-1}^2 P_{j-2}(\lambda)Q_{j+1}(\lambda)\hat{P}_{j-1}(\lambda)\hat{Q}_{j+1}(\lambda) - a_j^2 P_{j-1}(\lambda)Q_{j+2}(\lambda)\hat{P}_{j-1}(\lambda)\hat{Q}_{j+1}(\lambda)\end{aligned} \tag{53}$$

Since all the polynomial products have the same order, dividing by the highest power λ^{2N-3}, and letting $\lambda \to \infty$, leads to the relationship

$$\hat{a}_j^2 - a_j^2 = a_{j-1}^2 - \hat{a}_{j-1}^2 \tag{54}$$

Now consider that from Eq. (42), $k_j/k_j = m_{j+1}/\hat{m}_{j+1} = \alpha$ so that

$$k_j = \alpha\hat{k}_j \text{ and } m_{j+1} = \alpha\hat{m}_{j+1} \tag{55}$$

Recalling that from Eq. (41), $m_j = \hat{m}_j$ and using Eq. (55), it is possible to obtain a similar expression of a_j^2 as

$$a_j^2 = \frac{k_j^2}{m_j m_{j+1}} = \frac{\alpha^2\hat{k}_j^2}{\hat{m}_j\alpha\hat{m}_{j+1}} = \alpha\frac{\hat{k}_j^2}{\hat{m}_j\hat{m}_{j+1}} = \alpha\hat{a}_j^2 \tag{56}$$

so that a_{j-1}^2 can be expressed as

$$a_{j-1}^2 = \hat{a}_{j-1}^2 + \hat{a}_j^2 - a_j^2 = \hat{a}_{j-1}^2 + \hat{a}_j^2 - \alpha\hat{a}_j^2 = \hat{a}_{j-1}^2 + \hat{a}_j^2(1-\alpha) \tag{57}$$

Since it is also known [Eq. (47)] that $Q_{j+1}(\lambda) = \hat{Q}_{j+1}(\lambda)$, it is possible to simplify Eq. (53) so that

$$\begin{aligned}-\hat{a}_{j-1}^2\hat{P}_{j-2}(\lambda)\hat{Q}_{j+1}(\lambda)P_{j-1}(\lambda) - \hat{a}_j^2\hat{P}_{j-1}(\lambda)\hat{Q}_{j+2}(\lambda)P_{j-1}(\lambda) &= -(\hat{a}_{j-1}^2 + \hat{a}_j^2(1-\alpha))P_{j-2}(\lambda)\hat{P}_{j-1}(\lambda)\hat{Q}_{j+1}(\lambda) \\ &\quad - \alpha\hat{a}_j^2 P_{j-1}(\lambda)Q_{j+2}(\lambda)\hat{P}_{j-1}(\lambda)\end{aligned} \tag{58}$$

where a_j^2 and a_{j-1}^2 have been replaced by the relations (56) and (57), respectively. Considering $Q_{j+1}(\lambda) = \hat{Q}_{j+1}(\lambda)$ and $Q_{j+2}(\lambda) = \hat{Q}_{j+2}(\lambda)$ [as shown in Eq. (47)] and rearranging the expression, leads to

$$\begin{aligned}\hat{a}_{j-1}^2\hat{Q}_{j+1}(\lambda)[P_{j-2}(\lambda)\hat{P}_{j-1}(\lambda) - \hat{P}_{j-2}(\lambda)P_{j-1}(\lambda)] &= \hat{a}_j^2(1-\alpha)\hat{P}_{j-1}(\lambda)[\hat{Q}_{j+2}(\lambda)P_{j-1}(\lambda) - \hat{Q}_{j+1}(\lambda)P_{j-2}(\lambda)]\end{aligned} \tag{59}$$

Let us now introduce the scalar parameter $\gamma \in \mathbb{R}$ defined as

$$\gamma = \frac{\hat{a}_j^2(1-\alpha)}{\hat{a}_{j-1}^2}, \tag{60}$$

so that Eq. (59) can be rewritten as

$$\begin{aligned}\hat{Q}_{j+1}(\lambda)[P_{j-2}(\lambda)\hat{P}_{j-1}(\lambda) - \hat{P}_{j-2}(\lambda)P_{j-1}(\lambda)] &= \gamma\hat{P}_{j-1}(\lambda)[\hat{Q}_{j+2}(\lambda)P_{j-1}(\lambda) - \hat{Q}_{j+1}(\lambda)P_{j-2}(\lambda)]\end{aligned} \tag{61}$$

Equation (61) is equivalent to saying that, if γ exists and is different from zero, the two polynomial functions are linearly dependent. To show that this is impossible, let us rearrange the functions so that we can factor out $P_{j-1}(\lambda)$ and $P_{j-2}(\lambda)$ as

$$\begin{aligned}P_{j-2}(\lambda)[\hat{Q}_{j+1}(\lambda)\hat{P}_{j-1}(\lambda) + \gamma\hat{Q}_{j+1}(\lambda)\hat{P}_{j-1}(\lambda)] &= P_{j-1}(\lambda)[\hat{Q}_{j+1}(\lambda)\hat{P}_{j-2}(\lambda) + \gamma\hat{P}_{j-1}(\lambda)\hat{Q}_{j+2}(\lambda)]\end{aligned} \tag{62}$$

This equation must hold for all $\lambda \in \mathbb{R}$. In particular, consider $\lambda = q_1$, where q_1 is a zero of $Q_{j+1}(\lambda)$. Since $Q_{j+1}(\lambda) = \hat{Q}_{j+1}(\lambda)$ [Eq. (47)], it holds that q_1 is also a zero of $\hat{Q}_{j+1}$. Then, evaluating expression (62) for $\lambda = q_1$ we obtain that

$$0 = \gamma P_{j-1}(q_1)\hat{P}_{j-1}(q_1)\hat{Q}_{j+2}(q_1) \tag{63}$$

By lemma 5 we know that $Q_{j+1}(\lambda)$ and $Q_{j+2}(\lambda)$ do not have zeros in common. Therefore, using the equality $Q_{j+2}(\lambda) = \hat{Q}_{j+2}(\lambda)$ from Eq. (47), we can conclude that $\hat{Q}_{j+2}(q_1) \neq 0$. In addition, the type of structure at hand also requires that all eigenvalues of the matrix $\mathbf{A}$ are distinct. Proof of this statement can be found in [5]. Since the eigenvalues of $\mathbf{A}$ are distinct, the rank deficiency of matrix $(\mathbf{A} - \lambda\mathbf{I})$ evaluated at an eigenvalue of $\mathbf{A}$ is exactly one.

If $P_{j-1}(\lambda)$ and $Q_{j+1}(\lambda)$ had a zero $\lambda = \lambda^*$ in common, through

lemma 3 it follows that it would also be a zero of the determinant of $(\mathbf{A}-\lambda\mathbf{I})$ and therefore an eigenvalue of $\mathbf{A}$. Moreover, it can be shown that this zero would be of multiplicity higher than one. In fact, this eigenvalue problem can be considered as a linear system of equations involving three subsystems, one characterized by the upper left $(j-1)\times(j-1)$ submatrix of $(\mathbf{A}-\lambda\mathbf{I})$, one characterized by the lower right $(N-j)\times(N-j)$ submatrix, and one characterized by the jth row of $(\mathbf{A}-\lambda\mathbf{I})$. If λ^* is a common zero of $P_{j-1}(\lambda)$ and $Q_{j+1}(\lambda)$, $P_{j-1}(\lambda^*)=Q_{j+1}(\lambda^*)=0$, then the ranks of these matrices are lower than $j-1$ and $N-j$, respectively. This implies that the rank of the complete system $(\mathbf{A}-\lambda^*\mathbf{I})$ is lower than $N-1$ and that thus the rank deficiency induced by the eigenvalue λ^* is higher than one. This contradicts the initial statement that λ^*, being an eigenvalue of $\mathbf{A}$, cannot have multiplicity higher than one. Thus $P_{j-1}(\lambda)$ and $Q_{j+1}(\lambda)$ cannot have any zeros in common. Hence, in Eq. (63), $P_{j-1}(q_1)\neq 0$. Using the equivalence between $Q_{j+1}(\lambda)$ and $\hat{Q}_{j+1}(\lambda)$ expressed in Eq. (47), it is possible to conclude that also $\hat{P}_{j-1}(q_1)\neq 0$.

With this knowledge, it can be immediately concluded from Eq. (63) that $\gamma=0$. Substitution of this value into Eqs. (60) and (61) yields, respectively,

$$\alpha = 1 \tag{64}$$

$$[P_{j-2}(\lambda)\hat{P}_{j-1}(\lambda) - \hat{P}_{j-2}(\lambda)P_{j-1}(\lambda)] = 0 \tag{65}$$

which allows us to apply lemma 6 obtaining that

$$P_i(\lambda) = \hat{P}_i(\lambda), \quad b_i = \hat{b}_i,$$

$$\forall\, i = 1,2,\ldots,j-1, \quad \hat{a}_i = a_i \quad \forall\, i = 1,2,\ldots,j-2 \tag{66}$$

Substituting $\alpha=1$ in Eqs. (56) and (57) immediately yields that

$$a_j = \hat{a}_j \tag{67}$$

$$a_{j-1} = \hat{a}_{j-1} \tag{68}$$

thus completing the unique determination, together with the results from Eqs. (47) and (52), of all a_i for all $i=1,2,\ldots,N-1$ and all b_i for all $i=1,2,\ldots,N$. It is straightforward to observe that this allows one now to uniquely determine all stiffnesses and masses cascading up and down the structure, starting with the values $m_j=\hat{m}_j$ from Eq. (39) and $k_j=\hat{k}_j$, $m_{j+1}=\hat{m}_{j+1}$ from Eq. (55).

Similarly, following an analogous procedure, it is possible to obtain a unique determination of structural masses and stiffnesses when a sensor is located directly above the actuator.

At this point, we can conclude that two systems, which have equal outputs at two adjacent degrees of freedom when subjected to the same input, are identical independent of the number of DOFs of the system. Conversely, an identification problem that relies on a collocated set of input-output and on an adjacent output, must have a unique solution. This is an important statement to guarantee the existence of a unique solution.

Configuration 2: 1 Sensor and 1 Actuator at the *N*th Degree of Freedom. Let us suppose now that a known input excitation is solely applied on the lower floor (first floor) of the building and that only one output measurement is available at that same floor, as seen in configuration 2 of Fig. 2. Assuming that there might be two structural systems, as before, that yield the same input-output relation, let us equate the Laplace transforms of the outputs at the first floor (index N in our notation). For the first system, the Laplace transform of the output at the lower floor can be expressed as

$$X_N(\lambda) = \frac{1}{m_N}\frac{P_{N-1}(\lambda)Q_{N+1}(\lambda)}{\Delta(\lambda)}F(\lambda) \tag{69}$$

which can be simplified, since $P_N(\lambda)=\Delta(\lambda)$ and $Q_{N+1}(\lambda)=1$ by definition, as

$$X_N(\lambda) = \frac{1}{m_N}\frac{P_{N-1}(\lambda)}{P_N(\lambda)}F(\lambda) \tag{70}$$

Analogously, for the second structural system (the $\hat{\cdot}$-system) we obtain that

$$\hat{X}_N(\lambda) = \frac{1}{\hat{m}_N}\frac{\hat{P}_{N-1}(\lambda)}{\hat{P}_N(\lambda)}F(\lambda) \tag{71}$$

Since the two systems experience the same output at the first floor, it is possible to equate the two output transforms and obtain

$$\frac{1}{m_N}\frac{P_{N-1}(\lambda)}{P_N(\lambda)} = \frac{1}{\hat{m}_N}\frac{\hat{P}_{N-1}(\lambda)}{\hat{P}_N(\lambda)} \tag{72}$$

Multiplying the expression by λ on both sides and letting $\lambda\to\infty$, it follows that

$$\frac{1}{m_N} = \frac{1}{\hat{m}_N} \tag{73}$$

and consequently,

$$m_N = \hat{m}_N \tag{74}$$

$$P_{N-1}(\lambda)\hat{P}_N(\lambda) = \hat{P}_{N-1}(\lambda)P_N(\lambda) \tag{75}$$

Through the use of lemma 6 with $j=N$, this equation implies that

$$P_i(\lambda) = \hat{P}_i(\lambda), \quad b_i = \hat{b}_i,$$

$$\forall\, i = 1,2,\ldots,N, \quad \hat{a}_i = a_i \quad \forall\, i = 1,2,\ldots,N-1 \tag{76}$$

stating then that all b_i and a_i coefficients are uniquely determined. As described in [5], the following identity can be used

$$\frac{P_{i-1}(0)}{P_i(0)} = \frac{m_i}{k_i} \tag{77}$$

which for the case of $i=N$, leads to

$$\frac{P_{N-1}(0)}{P_N(0)} = \frac{m_N}{k_N} \text{ and } \frac{\hat{P}_{N-1}(0)}{\hat{P}_N(0)} = \frac{\hat{m}_N}{\hat{k}_N} \tag{78}$$

Since $P_i(\lambda)=\hat{P}_i(\lambda)$ (Eq. (76)) and $m_N=\hat{m}_N$ (Eq. (74)), we can equate these two expressions and obtain $k_N=\hat{k}_N$. Having determined m_N and k_N and considering the uniqueness of the b_i and a_i coefficients, it is straightforward to show in a cascading fashion, starting at the Nth degree of freedom, the uniqueness of solution for the entire distribution of mass and stiffness of the structure.

Configuration 3: 1 Sensor and 1 Actuator at the First Degree of Freedom. In a similar fashion, the uniqueness of the solution can be proven for the case of a collocated set of input-output measurements applied on the top floor (configuration 3 of Fig. 2). Again, let us assume that there might be two structural systems that yield the same input-output relation on the top floor. Following a procedure analogous to the one presented in the previous section, it is possible to equate the Laplace transforms of the outputs at the roof to obtain

$$\frac{1}{m_1}\frac{Q_2(\lambda)}{Q_1(\lambda)} = \frac{1}{\hat{m}_1}\frac{\hat{Q}_2(\lambda)}{\hat{Q}_1(\lambda)} \tag{79}$$

Multiplying the expression by λ on both sides and letting $\lambda\to\infty$, leads to

$$m_1 = \hat{m}_1 \tag{80}$$

and, consequently,

$$Q_2(\lambda)\hat{Q}_1(\lambda) = \hat{Q}_2(\lambda)Q_1(\lambda) \tag{81}$$

Applying lemma 7 with $j=1$ the following result is obtained

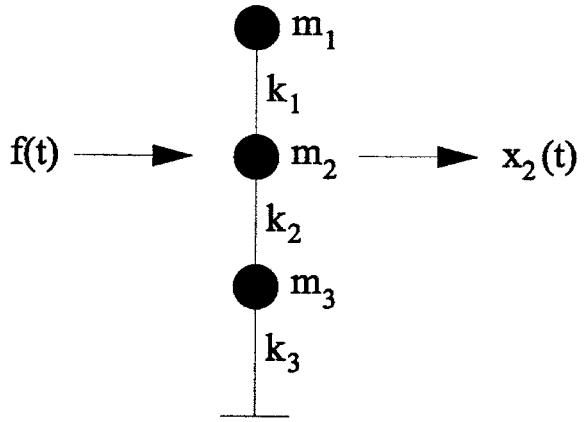

Fig. 3 Collocated configuration for the 3DOF system

$$Q_i(\lambda) = \hat{Q}_i(\lambda), \quad b_i = \hat{b}_i,$$

$$\forall\, i = 1,2,\ldots,N, \quad \hat{a}_i = a_i \quad \forall\, i = 1,2,\ldots,N-1 \tag{82}$$

Again, all b_i and a_i coefficients are then uniquely determined. Using $m_1 = \hat{m}_1$ and $b_1 = \hat{b}_1$ from Eqs. (80) and (82), respectively, it immediately follows that $k_1 = \hat{k}_1$. Plugging these two values into the equality $a_1 = \hat{a}_1$ yields that $m_2 = \hat{m}_2$ and so, in cascade, all masses and stiffnesses can then be determined. Therefore, also in the case of 2 structures having the same input-output relations at the top floor (configuration 3), it is possible to affirm that these 2 structures are identical. This is also an important statement of the uniqueness of solution in the identification of the mass and stiffness distribution.

Collocation is Not a Sufficient Condition to Guarantee Uniqueness

After seeing the results of uniqueness of the solution for configurations 2 and 3, one might ask if the condition of collocation, in general, would be a sufficient condition to ensure uniqueness. Here, an example is presented that shows such a condition is insufficient.

Consider the 3-story system of Fig. 3 with collocated measurements of input and output at the second floor. This case does not fit into configurations 2 and 3 presented in Fig. 2, hence uniqueness of the solution cannot be guaranteed a priori. The equations of motion are analyzed to find out if there are multiple systems that yield the same output at the measured floor given the input excitation at that same floor (collocated). Let us assume that there are two structural systems whose mass matrices ($\mathbf{M}$ and $\hat{\mathbf{M}}$) and stiffness matrices ($\mathbf{K}$ and $\hat{\mathbf{K}}$) can be represented as

$$\mathbf{M} = \begin{bmatrix} m_1 & 0 & 0 \\ 0 & m_2 & 0 \\ 0 & 0 & m_3 \end{bmatrix}, \quad \mathbf{K} = \begin{bmatrix} k_1 & -k_1 & 0 \\ -k_1 & k_1+k_2 & -k_2 \\ 0 & -k_2 & k_2+k_3 \end{bmatrix} \tag{83}$$

$$\hat{\mathbf{M}} = \begin{bmatrix} \hat{m}_1 & 0 & 0 \\ 0 & \hat{m}_2 & 0 \\ 0 & 0 & \hat{m}_3 \end{bmatrix}, \quad \hat{\mathbf{K}} = \begin{bmatrix} \hat{k}_1 & -\hat{k}_1 & 0 \\ -\hat{k}_1 & \hat{k}_1+\hat{k}_2 & -\hat{k}_2 \\ 0 & -\hat{k}_2 & \hat{k}_2+\hat{k}_3 \end{bmatrix} \tag{84}$$

The Laplace transform of the output at the second floor for the two systems can be expressed as

$$X_2(\lambda) = \frac{\Delta_2(\lambda)}{\Delta(\lambda)} F(\lambda); \quad \hat{X}_2(\lambda) = \frac{\hat{\Delta}_2(\lambda)}{\hat{\Delta}(\lambda)} F(\lambda) \tag{85}$$

where

$$\Delta_2(\lambda) = m_1 m_3 \lambda^2 + (k_1 m_3 + m_1 k_2 + m_1 k_3)\lambda + k_1 k_2 + k_1 k_3 \tag{86}$$

$$\begin{aligned}\Delta(\lambda) = {} & \lambda^3 m_1 m_2 m_3 + (m_1 m_2 k_3 + k_1 m_2 m_3 + m_1 m_2 k_2 + m_1 k_2 m_3 \\ & + m_1 k_1 m_3)\lambda^2 + (m_1 k_1 k_3 + k_1 m_2 k_3 + m_1 k_2 k_3 + m_1 k_1 k_2 \\ & + k_1 m_2 k_2 + k_1 k_2 m_3)\lambda + k_1 k_2 k_3,\end{aligned} \tag{87}$$

while $\hat{\Delta}_2$ and $\hat{\Delta}$ have identical expressions but with k_i and $m_i (i = 1,2,3)$ replaced by $\hat{k}_i$ and $\hat{m}_i (i = 1,2,3)$.

Let us assume that the $\hat{\cdot}$-system represents the actual system and that, therefore, the parameters $\hat{m}_1$, $\hat{m}_2$, $\hat{m}_3$, $\hat{k}_1$, $\hat{k}_2$, and $\hat{k}_3$ are fixed. We now suppose that the other m_1, m_2, m_3, k_1, k_2, and k_3, has the same input-output relation at the second degree of freedom as the $\hat{\cdot}$-system. In this way, by equating $X_2(\lambda) = \hat{X}_2(\lambda)$, it is possible to obtain

$$\Delta_2(\lambda)\hat{\Delta}(\lambda) - \hat{\Delta}_2(\lambda)\Delta(\lambda) = 0 \tag{88}$$

which corresponds to a fifth-order polynomial in λ. Since this equation must hold for all $\lambda \in \mathbb{R}$, all coefficients of the polynomial in λ must be identically equal to zero. The 6 coefficients of the polynomial thus result in 6 nonlinear equations that relate the parameters m_1, m_2, m_3, k_1, k_2, and k_3 to their counterparts of the $\hat{\cdot}$-system.

Solving the nonlinear system of equations for the variables m_1, m_2, m_3, k_1, k_2, and k_3 in function of the parameters $\hat{m}_1$, $\hat{m}_2$, $\hat{m}_3$, $\hat{k}_1$, $\hat{k}_2$, and $\hat{k}_3$, will allow us to find all possible solutions.

Let us analyze first the coefficient of the highest order term (λ^5) of Eq. (88)

$$-\hat{m}_1 \hat{m}_3 m_1 m_2 m_3 + m_1 m_3 \hat{m}_1 \hat{m}_2 \hat{m}_3 = 0 \tag{89}$$

from which it can be immediately concluded, since all the masses are strictly positive, that $m_2 = \hat{m}_2$. This important, preliminary result tells us that the two systems must have an identical mass at the second level and thus the identification of the second floor mass is unique. The coefficient equation for λ^4 yields then

$$m_1 m_3 \hat{m}_1 \hat{k}_1 \hat{m}_3 - \hat{m}_1 \hat{m}_3 m_1 k_1 m_3 + m_1 m_3 \hat{m}_1 \hat{k}_2 \hat{m}_3 - \hat{m}_1 \hat{m}_3 m_1 k_2 m_3 = 0 \tag{90}$$

Dividing by $m_1 m_3 \hat{m}_1 \hat{m}_3$, the previous equation can be reduced to a much simpler one as: $k_1 + k_2 = \hat{k}_1 + \hat{k}_2$, from which $k_1 = \hat{k}_1 + \hat{k}_2 - k_2$. By using the results from Eqs. (89) and (90), it is possible to reduce the initial system of equations to a system of 4 nonlinear equations in the unknown parameters m_1, m_3, k_2, and k_3.

Such a system of equations is quite complex but it can be solved analytically through the use of Sylvester's Dyalitic Elimination [12,13]. The first step of this technique consists in selecting one of the unknown variables as a fixed parameter, ρ. Here, the variable k_2 has been chosen equal to ρ since it substantially simplifies the problem. Then, let us select combinations of the rest of the variables as the new unknowns of what will become a linear system of equations. The following initial variables are considered

$$x_1 = m_1; \quad x_2 = m_3; \quad x_3 = m_1 m_3 \tag{91}$$

$$x_4 = k_4; \quad x_5 = m_1 k_3; \quad x_6 = 1 \tag{92}$$

The choice of $x_6 = 1$ as a variable will later allow us to impose that the solution may not be the trivial (zero) one, as indicated in [13]. Considering these newly defined variables, the initial system of 4 equations can now be expressed in terms of a linear combination of the new variables as

$$\mathbf{H}\mathbf{x} = \mathbf{0} \tag{93}$$

where $\mathbf{H}$ is a matrix of dimension 4×6 whose components are zero except the ones listed in Eqs. (94)–(109). Using this new

notation, the first equation, represented by the first row of $\mathbf{H}$, will have the nonzero components of $\mathbf{H}$ as

$$\mathbf{H}_{1,1} = \hat{m}_1\hat{m}_3\rho^2 \tag{94}$$

$$\mathbf{H}_{1,2} = \hat{m}_1\hat{k}_1^2\hat{m}_3 + \hat{m}_1\hat{m}_3\rho^2 + 2\hat{m}_1\hat{k}_2\hat{m}_3\hat{k}_1 - 2\hat{m}_1\hat{m}_3\rho\hat{k}_2 - 2\hat{m}_1\hat{m}_3\rho\hat{k}_1 + \hat{m}_1\hat{k}_2^2\hat{m}_3 \tag{95}$$

$$\mathbf{H}_{1,3} = -\hat{m}_1\hat{k}_2^2 - \hat{k}_1^2\hat{m}_3 \tag{96}$$

The second equation will have the following components

$$\mathbf{H}_{2,1} = \hat{m}_1\hat{k}_3\rho^2 + \rho^2\hat{m}_1\hat{k}_2 - \rho\hat{m}_1\hat{k}_2^2 + \hat{k}_1\hat{m}_3\rho^2 - \hat{k}_1^2\hat{m}_3\rho \tag{97}$$

$$\mathbf{H}_{2,2} = -2\hat{m}_1\hat{k}_1\hat{k}_3\rho + 2\hat{m}_1\hat{k}_2\hat{k}_3\hat{k}_1 - 2\hat{m}_1\hat{k}_2\hat{k}_3\rho - 2\hat{m}_1\hat{k}_2\rho\hat{k}_1 - 2\hat{k}_1\hat{k}_2\hat{m}_3\rho + \hat{k}_1\hat{m}_3\rho^2 + \hat{k}_1\hat{k}_2^2\hat{m}_3 + \hat{k}_1^2\hat{k}_2\hat{m}_3 + \hat{m}_1\hat{k}_1^2\hat{k}_3 + \hat{m}_1\hat{k}_1\hat{k}_2^2 + \hat{m}_1\hat{k}_2^2\hat{k}_3 + \hat{m}_1\hat{k}_1^2\hat{k}_2 + \hat{m}_1\hat{k}_2\rho^2 - \hat{m}_1\hat{k}_2^2\rho + \hat{m}_1\hat{k}_3\rho^2 - \hat{k}_1^2\hat{m}_3\rho \tag{98}$$

$$\mathbf{H}_{2,3} = -\hat{k}_1\hat{k}_2^2 - \hat{k}_1^2\hat{k}_2 - \hat{k}_1^2\hat{k}_3 \tag{99}$$

$$\mathbf{H}_{2,4} = \hat{m}_1\hat{m}_3\rho^2 - 2\hat{m}_1\hat{k}_2\hat{m}_3\rho - 2\hat{m}_1\hat{k}_1\hat{m}_3\rho + 2\hat{m}_1\hat{k}_2\hat{m}_3\hat{k}_1 + \hat{m}_1\hat{k}_1^2\hat{m}_3 + \hat{m}_1\hat{k}_2^2\hat{m}_3 \tag{100}$$

$$\mathbf{H}_{2,5} = -\hat{k}_1^2\hat{m}_3 - \hat{m}_1\hat{k}_2^2 \tag{101}$$

$$\mathbf{H}_{2,6} = \rho\hat{m}_1\hat{k}_2^2\hat{m}_3 + 2\rho\hat{m}_1\hat{k}_2\hat{m}_3\hat{k}_1 - \rho^2\hat{m}_1\hat{k}_1\hat{m}_3 + \rho\hat{m}_1\hat{k}_1^2\hat{m}_3 - \rho^2\hat{m}_1\hat{k}_2\hat{m}_3 \tag{102}$$

while, for the third and fourth equations, the only nonzero components of $\mathbf{H}$ are

$$\mathbf{H}_{3,1} = \rho^2\hat{k}_1\hat{k}_2 - \rho\hat{k}_1^2\hat{k}_2 - \rho\hat{k}_1^2\hat{k}_3\rho + \hat{k}_1\hat{k}_3\rho^2 - \rho\hat{k}_1\hat{k}_2^2 \tag{103}$$

$$\mathbf{H}_{3,2} = \hat{k}_1^2\hat{k}_2\hat{k}_3 + \hat{k}_1\hat{k}_2^2\hat{k}_3 - 2\hat{k}_1\hat{k}_3\rho\hat{k}_2 + \hat{k}_1\hat{k}_3\rho^2 - \hat{k}_1^2\hat{k}_3\rho - \hat{k}_1\hat{k}_2^2\rho - \hat{k}_1^2\hat{k}_2\rho + \hat{k}_1\hat{k}_2\rho^2 \tag{104}$$

$$\mathbf{H}_{3,4} = \hat{m}_1\hat{k}_1^2\hat{k}_2 - \hat{k}_1^2\hat{m}_3\rho + \hat{m}_1\hat{k}_1\hat{k}_2^2 - 2\hat{m}_1\hat{k}_2\rho\hat{k}_1 - 2\hat{k}_1\hat{k}_3\rho\hat{k}_2 - 2\hat{m}_1\hat{k}_3\rho\hat{k}_2 + 2\hat{m}_1\hat{k}_2\hat{k}_3\hat{k}_1 - 2\hat{m}_1\hat{k}_3\rho\hat{k}_1 - \hat{m}_1\hat{k}_2^2\rho + \hat{m}_1\hat{k}_2\rho^2 + \hat{k}_1\hat{m}_3\rho^2 + \hat{k}_1\hat{k}_2^2\hat{m}_3 + \hat{k}_1^2\hat{k}_2\hat{m}_3 + \hat{m}_1\hat{k}_1^2\hat{k}_3 + \hat{m}_1\hat{k}_3\rho^2 + \hat{m}_1\hat{k}_2^2\hat{k}_3 \tag{105}$$

$$\mathbf{H}_{3,5} = -\hat{k}_1^2\hat{k}_3 - \hat{k}_1\hat{k}_2^2 - \hat{k}_1^2\hat{k}_2 \tag{106}$$

$$\mathbf{H}_{3,6} = \rho\hat{m}_1\hat{k}_1^2\hat{k}_3 - \rho^2\hat{m}_1\hat{k}_1\hat{k}_3 + \rho\hat{m}_1\hat{k}_1\hat{k}_2^2 - \rho^2\hat{m}_1\hat{k}_1\hat{k}_2 + 2\rho\hat{m}_1\hat{k}_2\hat{k}_3\hat{k}_1 - \rho^2\hat{m}_1\hat{k}_2\hat{k}_3 + \rho\hat{m}_1\hat{k}_1^2\hat{k}_2 + \rho\hat{m}_1\hat{k}_2^2\hat{k}_3 - \rho^2\hat{k}_1\hat{k}_2\hat{m}_3 + \rho\hat{k}_1\hat{k}_2^2\hat{m}_3 + \rho\hat{k}_1^2\hat{k}_2\hat{m}_3 \tag{107}$$

$$\mathbf{H}_{4,4} = -\hat{k}_1^2\hat{k}_2\rho - \hat{k}_1\hat{k}_2^2\rho + \hat{k}_1\hat{k}_2\rho^2 + \hat{k}_1\hat{k}_3\rho^2 + \hat{k}_1^2\hat{k}_2\hat{k}_3 + \hat{k}_1\hat{k}_2^2\hat{k}_3 - \hat{k}_1^2\hat{k}_3\rho - 2\hat{k}_1\hat{k}_3\rho\hat{k}_2 \tag{108}$$

$$\mathbf{H}_{4,6} = -\rho^2\hat{k}_1\hat{k}_2\hat{k}_3 + \rho\hat{k}_1^2\hat{k}_2\hat{k}_3 + \rho\hat{k}_1\hat{k}_2^2\hat{k}_3 \tag{109}$$

Since the system has only 4 equations, more linearly independent equations are needed in order to complete the system. These additional equations can be obtained by properly multiplying the initial equations by the unknown variables. In this case, 6 additional equations have been obtained by multiplying:

$$\text{Fourth equation} \times m_1 \tag{110}$$

$$\text{Fourth equation} \times m_3 \tag{111}$$

$$\text{First equation} \times k_3 \tag{112}$$

$$\text{Third equation} \times m_3 \tag{113}$$

$$\text{First equation} \times m_3 \tag{114}$$

$$\text{Second equation} \times m_3 \tag{115}$$

It is important to note that the newly introduced equations are not linearly dependent on the original ones since the multiplicative factors are the unknowns of the original system. The addition of these new equations carries the appearance of new variables in the system, namely

$$x_7 = m_3k_3; \quad x_8 = m_1m_3k_3; \quad x_9 = m_3^2; \quad x_{10} = m_1m_3^2 \tag{116}$$

Ultimately, by considering all the equations, a system of 10 equations in 10 variables $x_1, x_2, \ldots, x_{10}$ is obtained. By adding these new equations and variables, the original matrix $\mathbf{H}$, of dimension 4×6, has been expanded to a 10×10 matrix with the following properties

$$\mathbf{H}_{5,1} = \mathbf{H}_{4,6}; \quad \mathbf{H}_{5,5} = \mathbf{H}_{4,4} \tag{117}$$

$$\mathbf{H}_{6,2} = \mathbf{H}_{4,6}; \quad \mathbf{H}_{6,7} = \mathbf{H}_{4,4} \tag{118}$$

$$\mathbf{H}_{7,5} = \mathbf{H}_{1,1}; \quad \mathbf{H}_{7,7} = \mathbf{H}_{1,2}; \quad \mathbf{H}_{7,8} = \mathbf{H}_{1,3} \tag{119}$$

$$\mathbf{H}_{8,3} = \mathbf{H}_{3,1}; \quad \mathbf{H}_{8,9} = \mathbf{H}_{3,2}; \quad \mathbf{H}_{8,7} = \mathbf{H}_{3,4}; \quad \mathbf{H}_{8,8} = \mathbf{H}_{3,5}; \quad \mathbf{H}_{8,2} = \mathbf{H}_{3,6} \tag{120}$$

$$\mathbf{H}_{9,3} = \mathbf{H}_{1,1}; \quad \mathbf{H}_{9,9} = \mathbf{H}_{1,2}; \quad \mathbf{H}_{9,10} = \mathbf{H}_{1,3} \tag{121}$$

$$\mathbf{H}_{10,3} = \mathbf{H}_{2,1}; \quad \mathbf{H}_{10,9} = \mathbf{H}_{2,2}; \quad \mathbf{H}_{10,10} = \mathbf{H}_{2,3} \tag{122}$$

$$\mathbf{H}_{10,7} = \mathbf{H}_{2,4}; \quad \mathbf{H}_{10,8} = \mathbf{H}_{2,5}; \quad \mathbf{H}_{10,2} = \mathbf{H}_{2,6} \tag{123}$$

The matrix thus built represents a linear system of 10 equations in 10 unknowns: $\mathbf{Hx}=\mathbf{0}$. Having set $x_6=1$ will make the trivial solution $\mathbf{x}=\mathbf{0}$ not a possible one. Therefore, the nullspace of matrix $\mathbf{H}$ cannot be empty and thus the determinant of $\mathbf{H}$ must be zero. Matrix $\mathbf{H}$ depends solely on the parameter ρ, therefore, it will be possible to find the values of ρ that make the determinant zero imposing $\det(\mathbf{H})=0$. After lengthy manipulation, the determinant of matrix $\mathbf{H}$ can be expressed as

$$\det(\mathbf{H}) = \rho^6(\rho-\hat{k}_2)(\rho-\hat{k}_1-\hat{k}_2)^6\left(\rho - \frac{\hat{k}_2\hat{k}_1 + \hat{k}_1\hat{k}_3 + \hat{k}_2\hat{k}_3}{\hat{k}_2+\hat{k}_3}\right) \tag{124}$$

where it is clear that there are four distinct solutions for ρ. Recalling that $\rho=k_2$ as defined earlier, the first root, the trivial solution $\rho=k_2=0$, does not yield a physically possible system. The second root, $\rho=k_2=\hat{k}_2$, yields the actual solution for the stiffness k_2. The third root yields $\rho=k_2=\hat{k}_1+\hat{k}_2$. However, from Eq. (90), it was found that $k_1+k_2=\hat{k}_1+\hat{k}_2$, and so this root would imply that $k_1=0$. This solution does not yield a possible physical system either. In absence of any other roots, the analysis would conclude that the only physically possible solution corresponds to the second root $\rho=k_2=\hat{k}_2$. Substitution of this equation in expression (90) yields that $k_1=\hat{k}_1$ and it can be shown that further substitution of these values into the rest of the equations yields that all parameters of both systems are equal. This would imply uniqueness of the solutions, meaning that there is only one 3DOF structure that can be represented by a given set of input-output measurements at the

second floor. Any efficient identification algorithm should converge to this solution. However, the existence of the fourth root complicates the matter significantly since $\rho=k_2=(\hat{k}_2\hat{k}_1+\hat{k}_1\hat{k}_3+\hat{k}_2\hat{k}_3)/(\hat{k}_2+\hat{k}_3)$ does indeed lead to a plausible physical solution different from the actual one. In fact, substituting this value of k_2 into the equations of the system will lead to

$$m_1=\frac{\hat{m}_3\hat{k}_2^2}{\hat{k}_2^2+2\hat{k}_2\hat{k}_3+\hat{k}_3^2} \tag{125}$$

$$m_2=\hat{m}_2 \tag{126}$$

$$m_3=\hat{m}_1\frac{\hat{k}_2^2\hat{k}_2^2+2\hat{k}_1^2\hat{k}_2\hat{k}_3+\hat{k}_1^2\hat{k}_3^2+2\hat{k}_1\hat{k}_2^2\hat{k}_3+2\hat{k}_1\hat{k}_2\hat{k}_3^2+\hat{k}_2^2\hat{k}_3^2}{\hat{k}_1^2(\hat{k}_2^2+2\hat{k}_2\hat{k}_3+\hat{k}_3^2)} \tag{127}$$

$$k_1=\hat{k}_1+\hat{k}_2-\frac{\hat{k}_2\hat{k}_1+\hat{k}_1\hat{k}_3+\hat{k}_2\hat{k}_3}{\hat{k}_2+\hat{k}_3} \tag{128}$$

$$k_2=\frac{\hat{k}_2\hat{k}_1+\hat{k}_1\hat{k}_3+\hat{k}_2\hat{k}_3}{\hat{k}_2+\hat{k}_3} \tag{129}$$

$$k_3=\frac{(\hat{k}_2\hat{k}_1+\hat{k}_1\hat{k}_3+\hat{k}_2\hat{k}_3)\hat{k}_2\hat{k}_3}{\hat{k}_1(\hat{k}_2^2+2\hat{k}_2\hat{k}_3+\hat{k}_3^2)} \tag{130}$$

Such a set of masses and stiffnesses represents a physically plausible structural system with the same input-output relation at the second degree of freedom as the original one. Thus, for a 3DOF system as in Fig. 3, two different solutions might be identified if only the collocated input-output pair at the second floor is known. One is the actual desired solution, the other is a misleading solution, corresponding to a different system which has the same input-output transfer function at the second floor.

To illustrate these findings, let us consider the following numerical example. Suppose that $\hat{m}_1=1.1$, $\hat{m}_2=1.3$, $\hat{m}_3=0.85$, $\hat{k}_1=11.0$, $\hat{k}_2=12.0$, and $\hat{k}_3=9.0$. Equations (125)–(130) yield that $m_1=0.2776$, $m_2=1.3$, $m_3=2.3690$, $k_1=6.8571$, $k_2=16.1429$, and $k_3=7.5473$. The responses of both systems at all floors under a known random force excitation at floor 2 are plotted in Fig. 4. It is clear from the plot that the responses of both systems at floors 1 and 3 are different, while they cannot be distinguished at floor 2. Therefore, if only the measurements at the second floor are known, a unique identification will not be possible since there will be 2 different systems that have the same input-output set at the 2nd degree of freedom but different responses at the other 2 DOFs.

Conclusions

In this paper, the global identifiability problem of a linear shear-type N-degrees of freedom building structure has been tackled. It has been shown that there are certain configurations of input and output measurements that yield a unique solution for the identification of mass and stiffness properties of the structure. These proposed configurations require a minimum amount of sensors (only one or two) and just one actuator. Fewer measurements, like in the case of only the collocated input-output pair at one single degree of freedom, yield multiple solutions of identification as it has been shown for the 3DOF system.

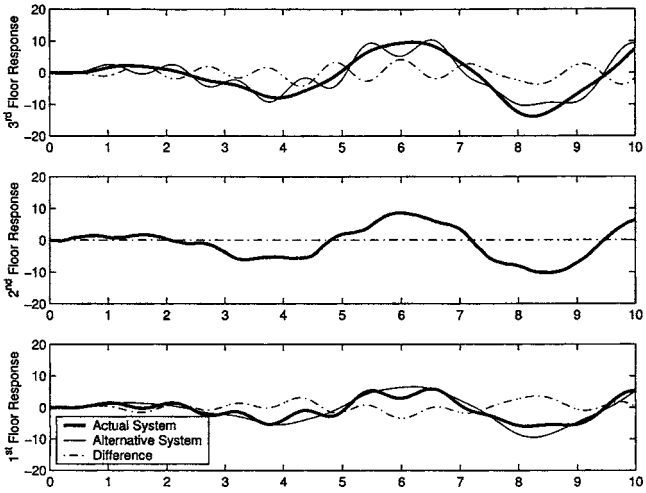

Fig. 4 Comparison of measurements between the two physically possible solutions for the 3DOF system with collocated input-output measurement at the second DOF

These results are especially useful to those identification methods, whose objective is to find a full order model solution with only a reduced set of measurements. If the identification algorithm is able to find the global optimum in a highly nonlinear optimization landscape, the usage of the actuator/sensor configurations proposed herein guarantees that one and only one possible physical solution exists.

References

[1] Nguyen, V. V., and Wood, E. F., 1982, "Review and Unification of Linear Identifiability Concepts," SIAM Rev., **24**, pp. 34–51.

[2] Walter, E., 1987, *Identifiability of Parametric Models*, 1st ed., Pergamon Press, New York.

[3] Katafygiotis, L. S., and Beck, J. L., 1990, "Uniqueness in Structural System Identification," *Proceedings of the U. S. National Workshop on Structural Control Research*, pp. 136–140.

[4] Ljung, L., and Glad, T., 1994, "On Global Identifiability for Arbitrary Model Parametrizations," Automatica, **30**, pp. 265–276.

[5] Udwadia, F. E., and Sharma, D. K., 1978, "Some Uniqueness Results Related to Building Structural Identification," SIAM J. Appl. Math., **34**, pp. 104–118.

[6] Udwadia, F. E., Sharma, D. K., and Shah, P. C., 1978, "Uniqueness of Damping and Stiffness Distributions in the Identification of Soil and Structural Systems," J. Appl. Mech., **45**, pp. 181–187.

[7] Koh, C. G., Hong, B., and Liaw, C.-Y., 2000, "Parameter Identification of Large Structural Systems in Time Domain," J. Struct. Eng., **126**, pp. 957–963.

[8] Chou, J.-H., and Ghaboussi, J., 2001, "Genetic Algorithm in Structural Damage Detection," Comput. Struct., **79**, pp. 1335–1353.

[9] Franco, G., Betti, R., and Lus, H., 2004, "Identification of Structural Systems Using in Evolutionary Strategy," ASCE J. Eng. Mech., **130**(10), pp. 1125–1139.

[10] Wilkinson, J. H., 1965, *The Algebraic Eigenvalue Problem*, 1st ed., Oxford University Press, New York.

[11] Friedberg, S. H., Insel A. J., and Spence, L. E., 1979, *Linear Algebra*, 1st ed., Prentice-Hall Inc., New York.

[12] Salmon, G., 1964, *Lessons Introductory to the Modern Higher Algebra*, 1st ed., Chelsea Publishing Co., New York.

[13] Raghavan, M., and Roth, B., 1995, "Solving Polynomial Systems for the Kinematic Analysis and Synthesis of Mechanism and Robot Manipulators," ASME J. Mech. Des., **117**, pp. 71–79.

Journal of Applied Mechanics

Technical Briefs

Cross Relations Between the Planar Elastic Moduli of Perforated Structures

Shmuel Vigdergauz
R&D Division, The Israel Electric Corporation, Ltd.,
P. O. Box 10, Haifa 31000, Israel
e-mail: smuel@iec.co.il

The effective compliance moduli of a plate with a doubly periodic set of traction-free holes are considered. Attention is drawn to the perturbation form in which they are expressed by applying the complex variable methods in two-dimensional elasticity. This permits one to derive specific dimensionless combinations of the effective moduli, which are independent of the solid Poisson ratio. Using them saves computations of the structure moduli by FEM-like methods and helps one to evaluate their practical accuracy. Thus far, the only result of this kind has been observed numerically by Day, Snyder, Garboczi, and Thorpe (J. Mech. Phys. Solids. ***40****, pp. 1031–1051, 1992) and later proved by Cherkaev, Lurie, and Milton (Proc. R. Soc. London, Ser. A* ***458****, pp. 519–529, 1992).* [DOI: 10.1115/1.1938202]

1 Local Structure Description

Consider a two-dimensional (2D) perforated structure that is formed by replicating a basic polygonal cell over an (x,y) plane in two noncoinciding dimensions with the periods $\omega_1,\omega_2:\mathrm{Im}(\omega_2/\omega_1)>0$. The cell is supposed to contain only one strictly centered interior hole with a smooth traction-free boundary L and the volume fraction $c<1$. Let the cell be a square, $\omega_2/\omega_1=i$, and let the hole also have a square symmetry. This corresponds to the simplest anisotropic model with only three different effective moduli: the bulk modulus K_e and two shear moduli $\mu_e^{(j)}$, $j=1, 2$.

At given cell geometry the effective moduli depend on the solid-phase isotropic moduli K,μ, which are used in parallel with the Young's modulus E and the Poisson ratio ν. This dependence may be explicitly derived through the analytical Kolosov-Muskhelishvili (KM) potentials $\varphi(z),\psi(z)$, $z=x+iy\in S$ [1], which express the hole-distorted stress field in the solid phase S

$$\sigma(x,y)=\{\sigma_{xx},\sigma_{yy},\sigma_{xy}\} \tag{1}$$

by automatically satisfying the equilibrium equations.

Because of the stress field periodicity, $\varphi(z),\psi(z)$ are written [2] through more simple doubly periodic functions $\theta(z),\xi(z)$:

$$\varphi(z)=D_1z+D_2\zeta_0(z)+\theta(z) \tag{2}$$

$$\psi(z)=R_1z+R_2\zeta_0(z)-\zeta_0(z)\varphi'(z)+\xi(z);\quad \zeta_0(z)\equiv\frac{F}{\pi}\zeta(z)\quad z\in S \tag{3}$$

where F is the cell area and $\zeta(z)$ is the quasi-periodic Weierstrassian ζ, function [3].

Physically, the constants D_1,D_2,R_1,R_2 are the quasi periods of the local displacements in S_2. They are linearly related to given stress averages (angular brackets) over the cell

$$\langle\mathrm{Tr}\rangle=\langle\sigma_{xx}+\sigma_{yy}\rangle=2\,\mathrm{Re}(D_1+R_2) \tag{4}$$

$$\langle\mathrm{Dev}\rangle=\langle\sigma_{xx}-\sigma_{yy}\rangle=2\,\mathrm{Re}(D_2+R_1) \tag{5}$$

$$\langle\sigma_{xy}\rangle=\mathrm{Im}(D_2-R_1) \tag{6}$$

Together with the traction-free boundary condition along the hole contour L

$$\overline{\varphi(t)}+\bar{t}\varphi'(t)+\psi(t)=0;\quad t\in L \tag{7}$$

the loading conditions (4)–(6) form a uniquely solvable boundary value problem for the potentials (2) and (3) by which the local stresses and all the related quantities are then found.

An important point here is that the problem's governing equations (4)–(7) involve no phase moduli K,μ and hence depend only on the cell geometry. In particular,

$$D_j=D_j(L,c),\quad R_j=R_j(L,c),\quad j=1,2 \tag{8}$$

Though the KM approach is essentially limited to planar problems, it also works for a cylinder body infinitely elongated in the axial direction. These states are referred to as plane stress and plane strain, respectively. In either state all solid moduli, but μ, specifically differ from their three-dimensional (3D) counterparts [1] and obey the following interrelations:

$$\mu/K=(1-2\nu)\,(\text{plane strain}),\quad \mu/K=(1-\nu)/(1+\nu)\,(\text{plane stress}) \tag{9}$$

$$4E^{-1}=K^{-1}+\mu^{-1}(\text{plain strain, plain stress}) \tag{10}$$

2 Stress-Strain Averages

The energy density W of the field (1) is written (see, for instance, [4]) as a quadratic form

$$4W=\frac{\langle\mathrm{Tr}\rangle^2}{K_e}+\frac{\langle\mathrm{Dev}\rangle^2}{\mu_e^{(1)}}+\frac{\langle\sigma_{xy}\rangle^2}{\mu_e^{(2)}} \tag{11}$$

in the stress averages (4)–(6) The plate effective moduli $K_e,\mu_e^{(1)},\mu_e^{(2)}$ in (11) are obtained as the cell harmonic means under the unit loadings. Using the KM potentials we derive them in a perturbation form [2]

Contributed by the Applied Mechanics Division of ASME for publication in the JOURNAL OF APPLIED MECHANICS. Manuscript received July 8, 2004; final manuscript received November 1, 2004. Assoc. Editor: A. Maniatty.

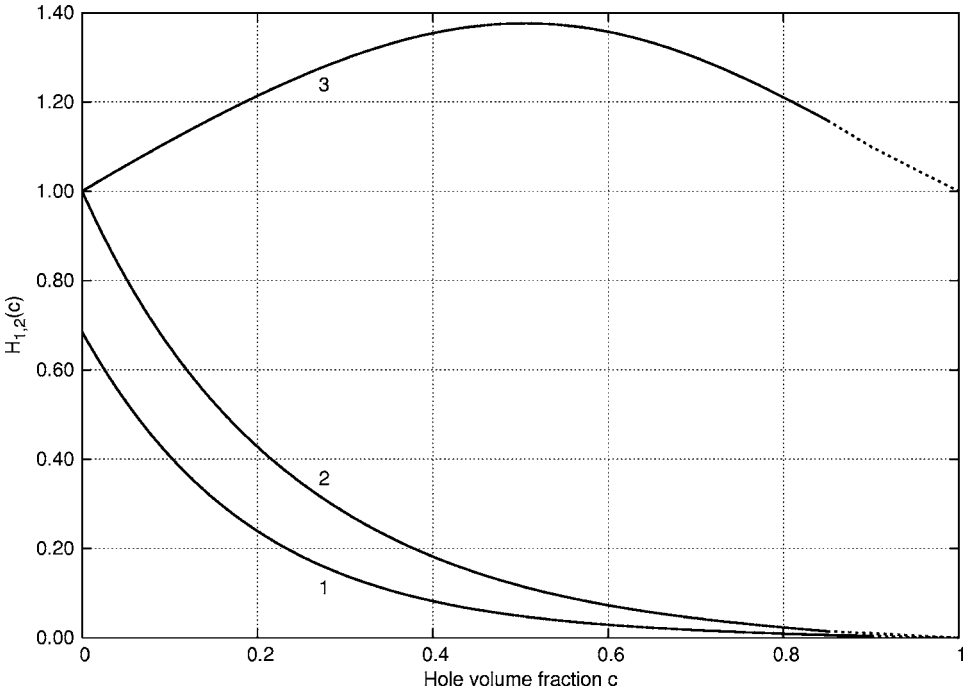

Fig. 1 The combined increment $H_{1,2(c)}$ from (24) in a square lattice: $H_1(c)$ for a square hole (1) and $H_1(c), H_2(c)$ for the equistress hole (2 and 3, respectively). The dotted segments visually extrapolate the computed results up to the cellular limit $c=1$. The required dilute limits $A^0, B^0_{1,2}$ (16) are borrowed from [15].

$$\Delta\left(\frac{1}{K_e}\right) \equiv \frac{1}{K_e} - \frac{1}{K} = \frac{4A}{E}; \quad \mathrm{Tr} = 1, \quad \mathrm{Dev} = \langle \sigma_{xy} \rangle = 0 \tag{12}$$

$$\Delta\left(\frac{1}{\mu_e^{(1)}}\right) \equiv \frac{1}{\mu_e^{(1)}} - \frac{1}{\mu} = \frac{4B_1}{E}; \quad \mathrm{Dev} = 1, \quad \mathrm{Tr} = \langle \sigma_{xy} \rangle = 0 \tag{13}$$

$$\Delta\left(\frac{1}{\mu_e^{(2)}}\right) \equiv \frac{1}{\mu_e^{(2)}} - \frac{1}{\mu} = \frac{4B_2}{E}; \quad \langle \sigma_{xy} \rangle = 1, \quad \mathrm{Tr} = \mathrm{Dev} = 0 \tag{14}$$

The dimensionless coefficients $A, B_{1,2} > 0$ describe the hole-induced increments in the inverses of the local moduli K and μ, respectively. They are related to the quasi-periods in (4)–(6) by [2]

$$4\,\mathrm{Re}\,D_1 - 1 = A, \quad -4\,\mathrm{Re}\,D_2 = B_1, \quad 2\,\mathrm{Im}\,D_2 = B_2 \tag{15}$$

To avoid confusion we note that A, B_1, B_2 have been less aptly introduced in [2] as A_1, A_2, A_3. The different letters should stress the relation to the different moduli.

For a dilute concentration of holes $c \ll 1$, the increments are proportional to the hole area [4]

$$A(c) = A^0 c + o(c), \quad B_{1,2}(c) = B^0_{1,2} c + o(c) \quad c \to 0 \tag{16}$$

In the opposite limiting case of $c \to 1$, perforated structures transform to cellular solids, which are arrays of thin-walled elastic squares with the asymptotics

$$A, B_1 \to c(1-c)^{-1}, \quad B_2 \to 4c(1-c)^{-3}, \quad c \to 1 \tag{17}$$

rigorously obtained by simple beam theory [7].

Though seemingly simple, the increments cannot be found without solving the full-scale elastostatic problem for the local stresses (1). In turn, this problem most likely has no closed-form solution, apart from the equistress hole shapes L_0 [4], which provide the global minimum for the bulk-related increment A at given volume fraction c

$$A(c,L) \underset{\{L\}}{\to} \min = A(c,L_0) = \frac{c}{1-c}, \quad \forall\, c < 1 \tag{18}$$

3 Analytical Conclusions

In the absence of analytical solutions to the stress-strain problem, the closed-form relations, such as (18), are valuable in verifying the numerical results. Three other useful identities of this kind immediately follow from (8) and (15) which show the independence of the increments and the local moduli. With (9) and (10) this equivalently implies an explicit dependence of the relative effective moduli on the solid Poisson ratio

$$\frac{K_e}{K} = \left(1 + 2A\frac{1-\nu}{1-2\nu}\right)^{-1}, \quad \frac{\mu_e^{(j)}}{\mu} = [1 + 2B_j(1-\nu)]^{-1}; \quad \text{(plane stress)} \tag{19}$$

$$\frac{K_e}{K} = \left(1 + \frac{2A}{1-\nu}\right)^{-1}, \quad \frac{\mu_e^{(j)}}{\mu} = \left(1 + \frac{2B_j}{1+\nu}\right)^{-1}; \quad \text{(plane strain)} \tag{20}$$

$$E\left(\frac{1}{\mu_e^{(j)}} - \frac{1}{\mu}\right) = B_j(c,L,); \quad j = 1,2 \text{ (the both)} \tag{21}$$

Combining also (10) with either of the above-obtained relations, we get that the relative Young's moduli of a perforated structure are independent of the solid Poisson ratio

$$\frac{E_e^{(j)}}{E} = 1 + A + B_j, \quad j = 1,2 \tag{22}$$

First found numerically in [5] for $j=1$, this remarkable feature was later derived analytically in [6] from quite different considerations. However, to our best knowledge, the separate relations (19) and (20) have not yet been reported in the literature.

Table 1 The effective bulk modulus and the related quantities for a square honeycomb at $c=0.9$ [12]

ν	K_e/K	A	$me(K_e)$ (%)	$\Delta A(\%)$
−0.95	0.07521498	9.1426024	0.021	0.00145
−0.90	0.07458332	9.1426069	0.021	0.00140
−0.80	0.07321184	9.1426060	0.021	0.00141
−0.70	0.07167391	9.1426435	0.021	0.00100
−0.60	0.06993791	9.1426479	0.021	0.00095
−0.50	0.06796250	9.1426645	0.021	0.00077
−0.40	0.06569467	9.1426725	0.022	0.00068
−0.30	0.06306418	9.1426843	0.022	0.00056
−0.20	0.05907645	9.1426843	0.022	0.00031
−0.10	0.05630105	9.1427226	0.023	0.00014
0.00	0.05185260	9.1427180	0.023	0.00019
0.10	0.04635822	9.1427322	0.024	0.00003
0.20	0.03940013	9.1427351	0.024	0.00000
0.30	0.03030352	9.1427048	0.026	0.00033
0.40	0.01790323	9.1426405	0.027	0.00104
0.45	0.00984560	9.1425648	0.030	0.00186
the maximum A^+		9.1427351		
the cellular approximation (17)		9.0		

Table 2 The effective shear modulus and the related quantities for a square honeycomb at $c=0.9$ [12]

ν	$\mu_e^{(1)}/\mu$	B_1	$me(\mu_e^1)$ (%)	ΔB_1 (%)
−0.95	0.02710925	9.2019944	0.00138	0.00043
−0.90	0.02780280	9.2020001	0.00137	0.00036
−0.80	0.02930220	9.2019807	0.00134	0.00058
−0.70	0.03097230	9.2020337	0.00132	0.00000
−0.60	0.03284460	9.2020016	0.00129	0.00035
−0.50	0.03495770	9.2020003	0.00127	0.00036
−0.40	0.03736140	9.2019972	0.00124	0.00040
−0.30	0.04012001	9.2020070	0.00121	0.00029
−0.20	0.04331856	9.2019972	0.00118	0.00040
−0.10	0.04707117	9.2020119	0.00115	0.00024
0.00	0.05153570	9.2020124	0.00112	0.00023
0.10	0.05693589	9.2020078	0.00108	0.00028
0.20	0.06360024	9.2020069	0.00105	0.00029
0.30	0.07203144	9.2020191	0.00101	0.00016
0.40	0.08303974	9.2020224	0.00098	0.00012
0.45	0.08991015	9.2020134	0.00096	0.00022
the maximum B_1^+		9.2020337		
the cellular approximation (17)		9.0		

Along with (22), the cell energy increment multiplied by the solid Young's modulus is also independent of the phase moduli

$$E\Delta(W) = A\langle \mathrm{Tr}\rangle^2 + B_1\langle \mathrm{Dev}\rangle^2 + B_2\langle \sigma_{xy}\rangle^2 \tag{23}$$

In view of (16) and (17) the ratios (19), (20), and (23) tend to zero with $c\to 0$ and to infinity with $c\to 1$. Contrastingly, the following ν-independent combination

$$H_j(c,L) \equiv \frac{\Delta\left(\frac{1}{K_e}\right) - \Delta\left(\frac{1}{\mu_e^{(j)}}\right)}{c\left(1+\frac{1}{K_e}+\frac{1}{\mu_e^{(j)}}\right)} = \frac{B_j - A}{c(1+A+B_j)}; \quad j=1,2 \tag{24}$$

has a finite cellular limit and a nonzero dilute limit

$$\lim_{c\to 0} H_j(c,L) = B_j^0(L) - A^0(L), \quad \lim_{c\to 1} H_j(c,L) = j-1, \quad j=1,2 \tag{25}$$

All the results obtained equally hold for a macroisotropic ($\mu_e^{(1)} = \mu_e^{(2)}$) hexagon lattice: $\omega_2/\omega_1 = \exp(2i\pi/3)$ when [8]

$$A \to c(1-c)^{-1}, \quad B_1 = B_2 \to 3c(1-c)^{-3}/2, \quad c\to 1 \tag{26}$$

4 Numerical Implications

Potential-related identities (19)–(21) reduce the problem of computing the effective moduli to finding the ν-independent increments (12)–(14) or, equivalently, the quasi-periods from (2) and (3). In parallel with the series expansions of the functions $\theta(z)$ and $\xi(z)$, they may be calculated from the infinite system of linear algebraic equations. For smooth hole shapes the system coefficients are routinely derived using the complex variable technique as exemplified in [9]. Specifically, they take a closed form for a circle of radius r centered at a point a

$$\bar{t} - \bar{a} = r^2(t-a)^{-1}; \quad t\in L \tag{27}$$

(see [10] and more advanced recent results in [11]).

Nonsmooth contours are more amenable to finite element methods (FEM), which find the effective moduli by directly solving the stress-strain relations in a meshed cell with given solid constants under periodic boundary conditions [12]. The explicit ν dependencies (19)–(21) remain outside of this numerical scheme and hence may estimate its computational error through the relative deviations in the increment value, which should be found independently for at least two different Poisson ratios. The deviations are measured from the sample maximum since the FEM calculations yield a conservative result for the moduli inverses [12]

$$\Delta A(\%) = 100\frac{A^- - A(\nu)}{A^-}, \quad A^+ = \max_\nu(A(\nu)) \tag{28}$$

$$\Delta B_j(\%) = 100\frac{B_j^+ - B_j(\nu)}{B_j^+}, \quad B_j^+ = \max_\nu(B_j(\nu)), \quad j=1,2 \tag{29}$$

A good case in point is provided by [13] where the plain-strain ratios K_e/K and $\mu_e^{(1)}/\mu$ from (19) for a square honeycomb are computed by FEM simulation over a wide range of c and ν with the results error $meA(\%), meB_1(\%)$ evaluated through the Zienkiewicz-Zhu error estimator (ZZEE) [14].

At each given c we use these results to obtain a set of the increment values A, B_1 slightly varying with ν as exemplified in Tables 1 and 2 for the case of $c=0.9$ near the cellular limit. It is seen that the increment related error tolerances are much lesser than those obtained by ZZEE. It gives good reason to think that the actual accuracy in [12] is orders better.

In Fig. 1 we finally combine their results with ours [9] to display the curves $H_{1,2}(c)$ for two different hole shapes.

References

[1] Muskhelishvili, N. I., 1975, *Some Basic Problems of the Mathematical Theory of Elasticity*, 2nd ed., Noordhoff, Leiden, The Netherlands.

[2] Vigdergauz, S., 1999, "Complete Elasticity Solution to the Stress Problem in a Planar Grained Structure," Math. Mech. Solids **4**, pp. 407–441.

[3] Abramowtz, M., and Stegun, I., eds., 1965, *Handbook of Mathematical Functions*, Dover, New York.

[4] Milton, G. W., 2002, *The Theory of Composites*, Cambridge University Press, Cambridge, UK.

[5] Day, A. R., Snyder, K. A., Garboczi, E. J., and Thorpe, M. F., 1992, "The Elastic Moduli of Sheets Containing Circular Holes" J. Mech. Phys. Solids **40**, pp. 1031–1051.

[6] Cherkaev, A. V., Lurie, K. A., and Milton, G. W., 1992, "Invariant Properties of the Stress in Plane Elasticity and Equivalent Classes of Comnposites," Proc. R. Soc. London, Ser. A **458**, pp. 519–529.

[7] Gibson, L. J., and Ashby, M. F., 1999, *Cellular Solids: Structure and Properties*, 2nd ed., Cambridge University Press, Cambridge, UK.

[8] Eichen, J. W., and Torquato, S., 1993, "Determining Elastic Behavior of Composites by the Boundary Element Method," J. Appl. Phys. **74**, pp. 159–170.

[9] Vigdergauz, S., 2001, "The Effective Properties of a Perforated Elastic Plate. Numerical Optimization by Genetic Algorithm," Int. J. Solids Struct. **38**, pp. 8593–8616.
[10] Vigdergauz, S., 1974, "On the Plane Problem of the Theory of Elasticity for Multiply-Connected Domains with Cyclic Symmetry," J. Appl. Math. Mech. **38**, pp. 937–941.
[11] Wang, J., Crouch, S. L., and Mogilevskaya, S. G., 2003, "A Complex Boundary Integral Method for Multiple Circular Holes in an Infinite Plane," Eng. Anal. Boundary Elem. **27**, pp. 789–802.
[12] Berggren, S. A., Lukkassen, D., Meidell, A., and Simula, L., 2003, "Some Methods for Calculating Stiffness Properties of Periodic Structures," Appl. Math. **48**, pp. 97–110.
[13] Berggren, S. A., Lukkassen, D., Meidell, A., and Simula, L., 2001, "On Stiffness Properties of Square Honeycombs and Other Unidirectional Properties", Composites, Part B **32**, pp. 503–511.
[14] Zienkiewicz, O. C., and Zhu, J. Z., 1987, "A Simple Error Estimator and Adaptive Procedure for Practical Engineering Analysis," Int. J. Numer. Methods Eng. **24**, pp. 337–357.
[15] Jasiuk, I., 1995, "Cavities vis-a-vis rigid inclusions: elastic moduli with polygonal inclusions," Int. J. Solids Struct. **32**, pp. 407–422.

Quasi-One-Dimensional Periodic Structure with Locally Resonant Band Gap

Gang Wang[1]
e-mail: wang–g@vip.sina.com

Xisen Wen

Jihong Wen

Yaozong Liu

Institute of Mechatronical Engineering, National University of Defense Technology, Changsha 410073, China
and
PBG Research Center, National University of Defense Technology, Changsha 410073, China

The propagation of longitudinal elastic waves in quasi one-dimensional structure consisting of harmonic oscillators periodically jointed on a slender beam is studied. Sub-frequency locally resonant band gap with highly asymmetric attenuation is observed in both theoretical and experimental results, and both results match well. The stiffness and mass ratios are found analytically as two factors that influence the actual attenuation in the band gap of the locally resonant phononic crystals. The study on the weights of the two factors shows that the stiffness ratio is the key one. Thus, the reason for the mismatch between the regions of the sharp attenuation and the theoretical band gap in the locally resonant phononic crystals is discovered. [DOI: 10.1115/1.2061947]

1 Introduction

The theory of wave propagation in periodic structures was developed by solid state physicists and electrical engineers several decades ago [1,2]. Periodic structures act as a filter for traveling waves of any kind whether they are electromagnetic, acoustic, bending among others [3]. This principle can be used to reduce the vibration level in one part of a structure when it is excited at another. Numerous works have been devoted to the study of the continuous periodic engineering structures [3–6].

These works have enlightened the study of the elastic/acoustic wave propagation in phononic crystals (PCs) composed of artificial periodic elastic structures, which has received a great deal of attention [7–18] in recent years. The emphasis was laid on the existence of complete elastic/acoustic band gaps within which sound and vibrations are all forbidden. This is of interest for applications such as elastic/acoustic filters, improvements in the design of transducers, noise control and vibration shield; as well as for pure physics concerned with the Anderson localization of sound and vibration [12].

The low frequency band gap of PCs with small dimension is crucial to applications in low frequency sound or vibration shelters. Conventional PCs controlled by the Bragg reflection mechanism can hardly reach the requirement because the wavelength of low frequency elastic wave in common solids is long [13]. This would bring on structures with the size of outdoor sculptures in order to prevent environmental noises [8], or with bigger size for the vibration shielding in common machines.

Liu et al. advanced in their pioneering work [7] the locally resonant (LR) mechanism of band gap in researching the three-dimensional (3D) PCs consisting of cubic arrays of coated spheres immersed in an epoxy matrix. They also constructed simple cubic 3D PCs with lattice constant of 1.55 cm and sharp attenuation at the frequency around 400 Hz. Similar work by Goffaux et al. [9] shows that narrow attenuation with low frequency also exists in its two-dimensional (2D) counterpart, the array of coated cylinders in epoxy. The actual attenuation in these locally resonant band gaps is too narrow to be used as low frequency sound or vibration shelters.

The mechanical analog composed of lumped masses jointed by massless springs in the works [9,10] of Goffaux is introduced in order to get a physical insight into the LR mechanism. A similar model has also been proposed recently by us in the study of the 2D binary LR PCs [14]. The study has motivated the work in this paper. As the LR PCs can be simulated with simple analog models such as Kelvin's in textbooks [1], such models can also be used to study the attenuation property in it. Therefore, the quasi-one-dimensional LR PCs composed of a continuous slender beam with periodically jointed harmonic oscillators is studied in order to find the key factor that influences the attenuation property in the band gap of the LR PCs, which is necessary in the improvements of the original sharp attenuation spectra as well as the design of the LR PCs.

2 Theory

Figure 1(*a*) illustrates a continuous elastic beam with periodically attached oscillators, i.e., the quasi-1D LR PC. The Young's module, density and cross-section area of the slender beam is E, ρ, and A, respectively. The stiffness and mass of each oscillator are k and m. The regular interval of the oscillators is L_x, i.e., the lattice constant.

Using the well-known transfer matrix method [13] and the Bloch theorem [16,19], the solution for the longitudinal elastic wave in the infinite periodic structure is clearly

$$\cos(\pm\varepsilon) = \cosh(\pm\mu) = \cos(\beta L_x) - \frac{km\omega^2}{2\beta c^2 \rho A(k - m\omega^2)}\sin(\beta L_x) \tag{1}$$

where ω is the angular frequency of the wave, $\beta=\omega/c$ is the longitudinal wave number of the uninterrupted uniform beam at frequency ω, and $c=(E/\rho)^{1/2}$ is the velocity of longitudinal elastic wave in the beam, μ and ε are the attenuation and phase constants [6], respectively.

For a finite sample consisting of N periods, the transmission factor is also needed, besides the attenuation and phase curves of infinite system. It can also be calculated with the transfer matrix method [13].

3 Theoretical and Experimental Results

Figure 2(*a*) illustrates the calculated attenuation and phase constants μ,ε of a quasi-1D LR PC illustrated in Fig. 1(*b*) with lattice constants $L_x=0.05$ m, which is composed of a slender organic glass beam (with parameters of $A=50\times10^{-6}$ m^2, $E=1.5\times10^{10}$ Pa, and $\rho=1200$ kg m^{-3}) and the same harmonic oscillators periodically jointed on it. Each oscillator is composed of a pair of steel slices (act as a spring) and masses. They are set symmetrically on the beam in order to counteract the torsions. The stiffness and mass of the oscillators are $k=5.12\times10^6$ N·m^{-1} and $m=47.6$ g. The accessional mass of the joints connecting the steel slices with the beam per period $m_{\text{joint}}=16$ g. The frequency is given in the normalized unit $\beta L_x/2\pi$ on the upper abscissa compared with that in Hz on the lower abscissa. The transmission frequency response function (FRF) of a finite sample with eight

[1]Corresponding author.

Contributed by the Applied Mechanics Division of ASME for publication in the JOURNAL OF APPLIED MECHANICS. Manuscript received July 14, 2004; final manuscript received May 12, 2005. Review conducted by O. M. O'Reilly.

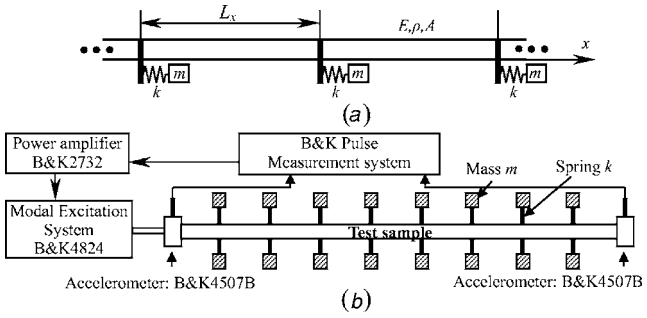

Fig. 1 (*a*) Quasi-one-dimensional phononic crystal composed of infinitely extended continuous slender beam with periodically jointed harmonic oscillators. We consider the longitudinal waves propagating along *x* direction. (*b*) The actual sample of the quasi-one-dimensional phononic crystal with eight periods and the experimental instruments.

periods is also calculated and illustrated as dashed lines in Fig. 2(*b*). The attenuation region (also called the band gap) settles between 1584 and 3047 Hz (from 0.0564 to 0.1084 in the normalized unit). They are about 1/10 and 1/5 of that controlled by the Bragg reflection mechanism, which ordinarily locate near 0.5 in the normalized frequency.

In order to validate the theoretical model, vibration experiments on the laboratory model shown in Fig. 1(*b*) are performed. In the experiment, the white noise signal is generated and fed to the vibration shaker through the power amplifier, which transmits vibrations to the test sample across an accelerometer. The elastic waves propagate through the sample, and the acceleration on the right of the beam is measured with another accelerometer. Two samples of different period number $N=6$ and 8 are measured. The measured results are illustrated in Fig. 2(*b*) compared with the calculated ones, where good agreement can be found and highly asymmetric attenuation in the band gap is observed. As to the measured transmission spectra, the peaks corresponding to the natural frequencies in the calculated results are erased by the damping in the beam and submerged in the measurement noise. The random noise in the measured curves below −50 dB originates in the limit of the signal noise ratio of the experimental setup. The viscoelastic of the organic glass beam results in additional attenuations at higher frequencies.

4 Discussion

For the attenuation constant and transmittance spectra illustrated in Fig. 2, we can observe highly asymmetric attenuation in the band gap. The maximal attenuation, which corresponds to the resonant eigenfrequency (1651 Hz) of the oscillators, locates near the lower edge (1584 Hz) of the band gap. When the frequency rises from it, the transmittance factor rises sharply at first (also observed in the 2D/3D LR PCs [7,10,11]) and slowly whereafter. This is obviously different with that of a band gap controlling by the Bragg scattering mechanism, where the maximal attenuations always locate near the mid-gap frequency. As the attenuation constant in the band gap represents the attenuation per period, it is an impersonal description of the band gap attenuations of the LR

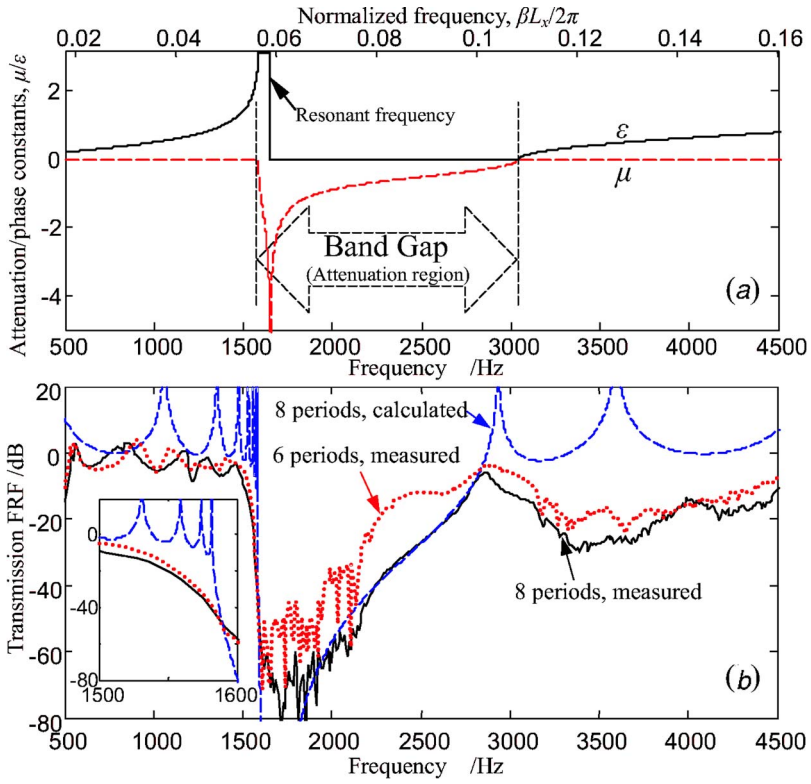

Fig. 2 (*a*) Calculated attenuation and phase constants μ, ε of the quasi-1D LR PCs illustrated in Fig. 1(*b*) for several frequencies that are given in the normalized units $\beta L_x/2\pi$ and Hz on the upper and lower abscissas, respectively. (*b*) Measured (solid line for the sample with eight periods, and dots for that with six periods) and calculated (dashed line for the sample with eight periods) transmission frequency response function for this quasi-1D LR PC. The subfigure illustrates a zoom from 1500 to 1600 Hz in order to give a clear description the eight peaks corresponding to the natural frequencies.

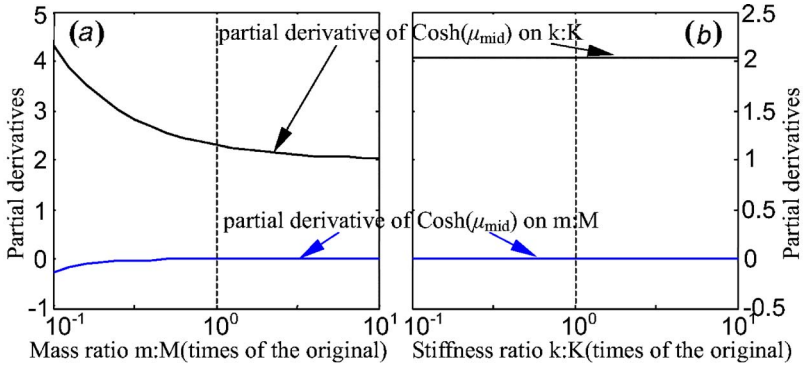

Fig. 3 The partial derivative of cosh(μ_{mid}) on the stiffness ratio $k:K$ (upper line) and the mass ratio $m:M$ (lower line) for several (*a*) mass and (*b*) stiffness ratios

PCs. When it is too small at the mid-gap, the transmission FRF in the band gap of a finite LR PC will become only a sharp attenuation near the resonant eigenfrequency.

For simplicity, the resonant eigenfrequency of the oscillator is considered as the frequency on the lower edge of the band gap. Given M as the mass of the beam per period, the band gap frequency range is [14]

$$\sqrt{\frac{k}{m}} < \omega < \sqrt{\frac{k}{m}\left(1+\frac{m}{M}\right)} \tag{2}$$

Thus

$$\omega = \sqrt{\frac{k}{m}}[1+(p-1)\alpha], \quad (p>1, 0<\alpha<1) \tag{3}$$

where $p=\sqrt{1+m/M}$, and α is a linear factor stands for the normalized position in the band gap.

As the normalized frequency βL_x in the LR band gap is very small, the following approximations can be taken for simplicity:

$$\cos(\beta L_x) \cong 1, \quad \sin(\beta L_x) \cong \beta L_x \tag{4}$$

Inserting Eqs. (3) and (4) into Eq. (1), we have the analytical description of the attenuation constants in the LR band gap as

$$\cosh(\mu) \cong 1 + 2\frac{k}{K}\left\{1 - \frac{1}{[1+(p-1)\alpha]^2}\right\}^{-1} \tag{5}$$

where $K=\mathrm{ES}/L_x$ is the equivalent stiffness of the beam in a period.

When $\alpha=0.5$, the mid-gap attenuation constants μ_{mid} can be described with

$$\cosh(\mu_{\mathrm{mid}}) \cong 1 + 2\frac{k}{K}\left[1 - \frac{4}{(1+p)^2}\right]^{-1} \tag{6}$$

From Eqs. (5) and (6), it is obvious that for a specific normalized position α in the band gap, the attenuation is in the direct ratio with the stiffness ratio $k:K$ and in the inverse ratio with the mass ratio $m:M$. In order to find the weights of the two factors corresponding to the LR PCs, we studied the partial derivative of $\cosh(\mu_{\mathrm{mid}})$ on the stiffness ratio $k:K$ and the mass ratio $m:M$ for several mass and stiffness ratios in Fig. 3. The stiffness ratio has much greater weight than the mass ratio in affecting the mid-gap attenuation of the LR PCs. Therefore, except for some occasions with very low mass ratio, the influence of the mass ratio on the mid-gap attenuation can be ignored. As the attenuation constant is analytically described with Eq. (5), there exists no direct relation between the attenuation in the band gap and other parameters, such as the mid-gap frequency or width of the band gap.

When the stiffness of the beam (corresponding to elastic constants of the hosting) is much bigger than that of the spring (corresponding to elastic constants of the coating), the mid-gap attenuation in the band gap will be too small to be observed. In other words, as the stiffness ratio decreases the band gap attenuation tends to vanish because the system tends to be no longer periodic. This is the reason why there exists only a sharp attenuation near the eigenfrequency of the oscillators in the 2D or 3D LR PCs, while their corresponding theoretical band gaps are much wider.

5 Conclusion

In conclusion, we have studied the propagation of longitudinal elastic waves in quasi-one-dimensional locally resonant phononic crystals consisting of harmonic oscillators periodically jointed on a slender beam. Sub-frequency band gap with highly asymmetric attenuation is observed in theoretical and experimental results, and both results matches well. The two factors that influence the actual attenuation in the band gap of the locally resonant phononic crystals are found analytically, and the weights of them is studied. Thus, the reason for the mismatch between the regions of the sharp attenuation and the theoretical band gap in the locally resonant phononic crystals is discovered. These results will facilitate the design of the low frequency sound/vibration shelter with the idea of the phononic crystals.

Acknowledgment

This work was supported by the State Key Development Program for Basic Research of China (Grant No. 51307). The authors would like to thank the anonymous referees for valuable recommendations and criticisms.

References

[1] Brillouin, L., 1953, *Wave Propagation in Periodic Structures*, Dover Publications, New York, Chap. 1.
[2] Elachi, C., 1976, "Waves in Active and Passive Periodic Structure: A Review," Proc. IEEE, **64**, pp. 1666–1698.
[3] Roy, A. K., and Plunkett, R., 1986, "Wave Attenuation in Periodic Structures," J. Sound Vib., **104**, pp. 395–410.
[4] Romeo, F., and Luongo, A., 2003, "Vibration Reduction in Piecewise Bi-coupled Periodic Structures," J. Sound Vib., **268**, pp. 601–615.
[5] Yong, Y., and Lin, Y. K., 1989, "Propagation of Decaying Waves in Periodic and Piecewise Periodic Structures of Finite Length," J. Sound Vib., **129**, pp. 99–118.
[6] Mead, D. J., 1996, "Wave Propagation in Continuous Periodic Structures: Research Contributions From Southampton, 1964-1995," J. Sound Vib., **190**, pp. 495–524.
[7] Liu, Z., Zhang, X., Mao, Y. et al., 2000, "Locally Resonant Sonic Materials," Science, **289**, pp. 1734–1736.
[8] Martínez-Sala, R., Sancho, J., Sánchez, J. V. et al., 1995, "Sound Attenuation by Sculpture," Nature (London), **378**, p. 241.
[9] Goffaux, C., and Sánchez-Dehesa, J., 2003, "Two-Dimensional Phononic Crystals Studied using a Variational Method: Application to Lattices of Locally Resonant Materials," Phys. Rev. B, **67**, p. 144301.
[10] Goffaux, C., Sánchez-Dehesa, J., Yeyati, A. L. et al., 2002, "Evidence of Fano-like Interference Phenomena in Locally Resonant Materials," Phys. Rev.

Lett., **88**, p. 225502.
[11] Hirsekorn, M., 2004, "Small-Size Sonic Crystals with Strong Attenuation Bands in the Audible Frequency Range," Appl. Phys. Lett., **84**, pp. 3364–3366.
[12] Klironomos, A. D., and Economou, E. N., 1998, "Elastic Wave Band Gaps and Single Scattering," Solid State Commun., **105**, pp. 327–332.
[13] Wang, G., Yu, D., Wen, J. et al., 2004, "One-Dimensional Phononic Crystals with Locally Resonant Structures," Phys. Lett. A, **327**, pp. 512–521.
[14] Wang, G., Wen, X., Wen, J. et al., 2004, "Two-Dimensional Locally Resonant Phononic Crystals with Binary Structures," Phys. Rev. Lett., **93**, p. 154302.
[15] Wang, G., Wen, J., Liu, Y. et al., 2004, "Lumped-Mass Method for the Study of Band Structure in Two-Dimensional Phononic Crystals," Phys. Rev. B, **69**, p. 184302.
[16] Djafari-Rouhani, B., Dobrzynski, L., and Duparc, O. H., 1983, "Sagittal Elastic Waves in Infinite and Semi-infinite Superlattices," Phys. Rev. B, **28**, pp. 1711–1720.
[17] Platts, S. B., Movchan, N. V., McPhedran, R. C. et al., 2003, "Transmission and Polarization of Elastic Waves in Irregular Structures," ASME J. Eng. Mater. Technol., **125**, pp. 2–6.
[18] Jensen, J. S., 2003, "Phononic Band Gaps and Vibrations in One- and Two-Dimensional Mass-Spring Structures," J. Sound Vib., **266**, pp. 1053–1078.
[19] Madelung, O., 1978, *Introduction to Solid-State Theory*, Springer-Verlag, Berlin, Chap. 2.

Modeling Flow of a Biviscous Fluid From Borehole Into Rock Fracture

A. Lavrov
SINTEF Petroleum Research, Formation Physics Department, 7465 Trondheim, Norway
e-mail: alexandre.lavrov@iku.sintef.no

Flow of bi-viscous fluid, i.e., non-Newtonian fluid with the shear stress versus shear rate function composed of two straight segments, from a borehole into a nonpropagating deformable horizontal fracture of circular shape was modeled within the lubrication approximation. The volume of the fluid lost into the fracture was found to be an almost-linearly decreasing function of the fluid yield stress and a linearly increasing function of the borehole pressure, under assumption of linear fracture deformation law. The model developed serves as a first approximation of mud loss during drilling of low-permeability naturally fractured rocks. [DOI: 10.1115/1.2061927]

Introduction

Drilling naturally fractured rocks in overbalance, i.e., with borehole pressure exceeding the reservoir fluid pressure, is accompanied with losses of drilling fluid. The main reason for this drilling problem in low-permeability formations is the presence of natural fractures that can extend sometimes over hundreds and thousands of meters. A solid understanding of fluid loss mechanics is necessary for an appropriate drilling fluid design. Such understanding is also required when fluid loss measurements are used for reservoir characterization purposes [1,2].

Bingham fluid flow from borehole into a single nondeformable fracture (constant aperture case) was modeled in Ref. [3]. Fluid flow of Newtonian fluid into a deformable fracture was investigated in Ref. [4]. Non-Newtonian power-law fluid flow into a deformable fracture was studied in Ref. [5]. Non-Newtonian Bingham rheology is typical for most types of drilling fluids currently in use.

Here, flow of a bi-viscous fluid into a deformable fracture is investigated theoretically. Under bi-viscous fluid, we mean a non-Newtonian fluid having the shear stress versus shear rate function composed of two straight segments. As discussed in Refs. [6,7], a bi-viscous model with a large viscosity ratio can serve as a realistic approximation for the Bingham rheology. Using bi-viscous instead of Bingham model allows the shear stress versus shear rate dependency to be continuous, which facilitates numerical solution. Besides, and perhaps most important, the flow of bi-viscous fluid in a narrow channel is much better understood, i.e., the question about hard core formation in such flow is unambiguously answered negatively in this case. Other, more complicated fluid rheologies, e.g., Herschel-Bulkley fluid, were not considered in the present work since many real drilling fluids are well described by Bingham or bi-viscous model.

Governing Equations; Boundary and Initial Conditions

A horizontal disk-shaped fracture of radius r_{ext} located in an impermeable rock mass is considered. Initially, the fracture is fully saturated with a liquid under the static reservoir pressure, p_0. A simplified fracture deformation law is adopted, namely: Fracture aperture w in each point is assumed to be a linear function of fluid pressure, p, inside the fracture: $w=w_0+p/K_n$, where w_0 is the fracture aperture when the fluid pressure is zero; K_n is the normal fracture deformation modulus. The initial fracture aperture is thus equal to w_0+p_0/K_n. The assumed local linear relation between fluid pressure and fracture aperture is a large simplification. During further development of the model, more realistic nonlinear and nonlocal deformation laws [8] should be allowed. However, as a first approximation, linear fracture deformation seems an acceptable assumption.

At time $t=0$, a vertical borehole of radius r_w intersects the fracture in its center. The borehole axis coincides with the z axis of the cylindrical coordinate system. Cylindrical coordinate r denotes the distance in the fracture plane from the borehole axis. All properties of the fluid coming from the borehole are assumed to be identical to those of the reservoir fluid being originally in the fracture, thus neglecting fluid displacement effects. Based on Ref. [7], bi-viscous fluid rheology can be described in one-dimensional form as follows:

$$\tau=\mu_0\dot{\gamma} \quad \text{for } |\dot{\gamma}|<|\dot{\gamma}_c|$$
$$\tau=\tau_y+\mu_1\dot{\gamma} \quad \text{for } |\dot{\gamma}|>|\dot{\gamma}_c| \tag{1}$$

where τ and $\dot{\gamma}$ are shear stress and shear rate, respectively; μ_0, μ_1 are dynamic fluid viscosities at low and high shear rates, respectively; τ_y is a constant, further termed "yield stress;" $\dot{\gamma}_c=\tau_y/(\mu_0-\mu_1)$.

After being penetrated by the borehole, fluid pressure at $r=r_w$ linearly increases from $p=p_0$ to $p=p_w$ during 1 s, and then stays constant and equal to p_w. At $r=r_{\text{ext}}$, no flow in r direction is assumed, i.e., $\partial p/\partial r=0$. The latter type of boundary condition is a standard one in hydraulic fracture modeling, e.g., Ref. [8]. The problem of fluid loss during drilling is characterized by a much lesser pressure difference between the fracture and the formation than is the case in hydraulic fracturing problems. The assumption of zero fluid flow through the fracture tip is thus realistic. Stress conditions at infinity are assumed such that the fracture does not propagate.

Assume the fracture surfaces are smooth enough for the lubrication approximation to be valid. Applying momentum conservation and no-slip conditions on the surfaces, the fluid average velocity, $\langle v\rangle$, at a distance r from the borehole axis is obtained as follows

$$\langle v\rangle=-\frac{w^2}{12\mu_0}\frac{\partial p}{\partial r} \quad \text{for } z_0>w/2 \tag{2a}$$

$$\langle v\rangle=-\frac{w^2}{12\mu_1}\frac{\partial p}{\partial r}+\left(\frac{wz_0}{4}-\frac{z_0^3}{3w}\right)\frac{\mu_0-\mu_1}{\mu_0\mu_1}\frac{\partial p}{\partial r} \quad \text{for } z_0<w/2 \tag{2b}$$

where

$$z_0=\left|\frac{\mu_0}{\mu_0-\mu_1}\frac{\tau_y}{\partial p/\partial r}\right|.$$

Mass conservation equation is given by

$$\frac{\partial}{\partial r}(w\langle v\rangle)+\frac{1}{r}w\langle v\rangle+\frac{\partial w}{\partial t}=0 \tag{3}$$

Although the rheological drilling fluid model and the fracture deformation law employed are quite simple, the strong nonlinearity of the resulting governing equation motivates the use of numerical solution. Equation (3) was solved using an explicit second-order finite-difference scheme with a time step of 0.00001 s to obtain the fluid loss rate from borehole into the fracture given by the value of $(2\pi rw\langle v\rangle)$ at $r=r_w$, as a function of time. The so calculated flow rate corresponds to the difference between flow-in and flow-out measured by flowmeters during drilling.

Contributed by the Applied Mechanics Division of ASME for publication in the JOURNAL OF APPLIED MECHANICS. Manuscript received July 22, 2004; final manuscript received March 9, 2005. Review conducted by B. A. Younis.

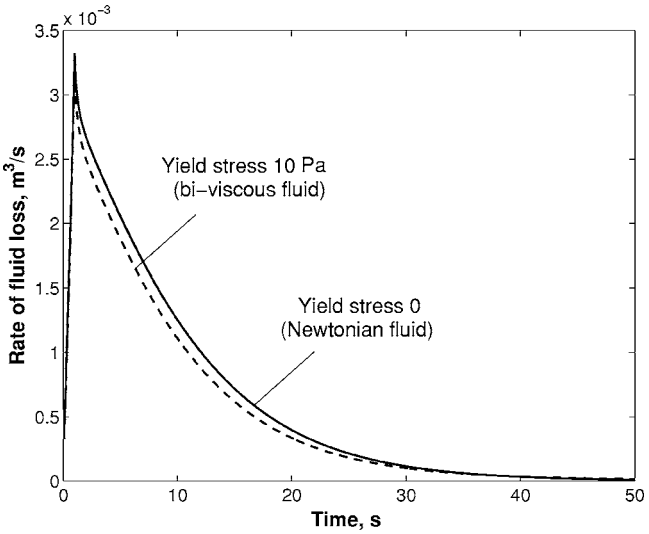

Fig. 1 Fluid loss dynamics for two fluids: Newtonian (yield stress 0) and non-Newtonian bi-viscous (yield stress 10 Pa). Values of other parameters are the same for both curves and are given in the text.

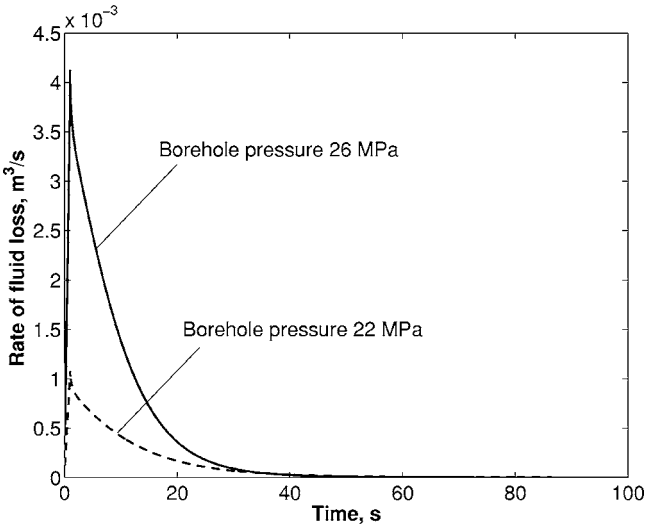

Fig. 3 Fluid loss dynamics for two borehole pressure values, 22 and 26 MPa. Values of other parameters are the same for both curves and are given in the text.

Modeling Results

Simulation results are presented in Fig. 1 for the following set of parameters: r_w=0.1 m; r_{ext}=10 m; p_0=20 MPa; p_w=25 MPa; w_0=0.1 mm; K_n=5·10^4 MPa/m; μ_0=40 Pa·s; μ_1=0.04 Pa·s, the ratio μ_0/μ_1 being 1000 as suggested in Ref. [7] for an approximation of a Bingham fluid. Target time of 2000 s was used in both simulations shown in Fig. 1, although only the first 50 s are shown in order to highlight the fluid loss dynamics at this early stage. As Fig. 1 demonstrates, fluid loss dynamics is affected by the yield stress value at the very beginning ($t \leqslant 40$ s). This effect also becomes clear from the dependency of the total volume of fluid lost during the time interval from t=0 to t=2000 s on the yield stress (Fig. 2). As Fig. 2 indicates, the total volume of the lost fluid decreases virtually linearly with yield stress, in the range of yield stresses examined. It should be noted that this range of yield stress values is typical of drilling fluids.

The shape of the flow rate versus time curve obtained from the simulations (rapid increase in the beginning and a subsequent gradual decrease, Fig. 1) is qualitatively the same as the shape of corresponding curves obtained during field measurements while drilling in naturally fractured formations [1]. Varying parameters of the model might allow us to fit the observed data exactly. However, such validation would be appropriate only if geological conditions and mechanical properties of the rock in the reported field studies were documented in detail, to impose constraints on the possible values of the model's input parameters. Also, independent measurements of fracture parameters are required to verify the performance of the model against real-world data.

The model allows an estimation of the effect different formation properties and operational parameters have on fluid loss dynamics in fractured reservoirs. Of utmost interest from practical viewpoint is the effect of borehole pressure, determined by drilling fluid composition (mud weight). Four simulations, for borehole pressure values of 22 MPa, 24 MPa, 26 MPa, and 28 MPa, were conducted. A comparison between two of them (22 MPa and 26 MPa) is presented in Fig. 3. The rheological parameters of the fluid are the same for both curves in Fig. 3, i.e., μ_0=40 Pa·s;

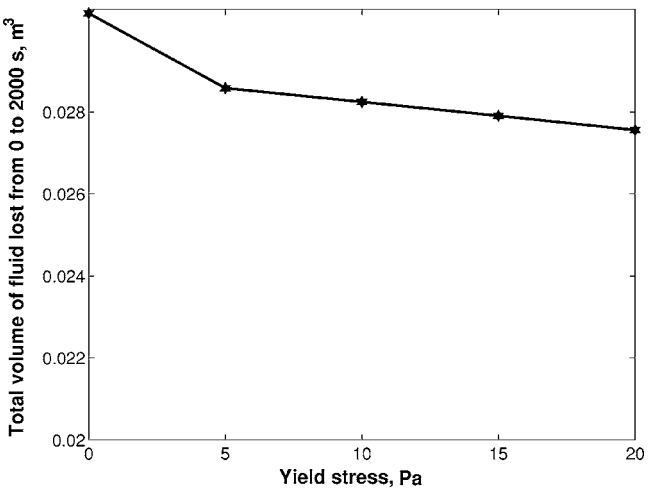

Fig. 2 Total volume of fluid lost within the first 2000 s as a function of the fluid yield stress. Values of parameters are given in the text.

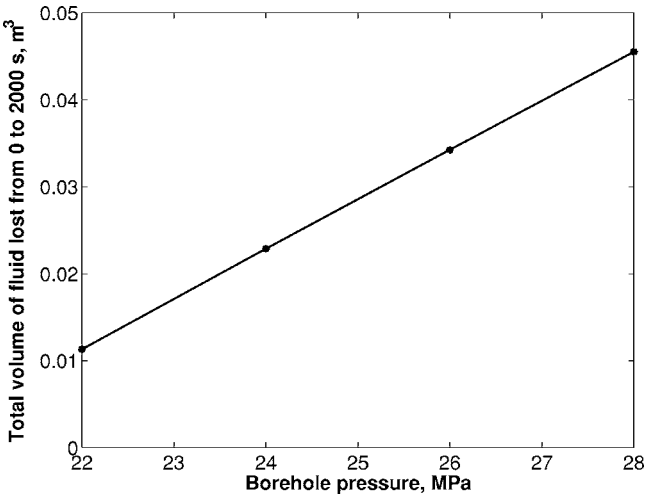

Fig. 4 Total volume of fluid lost within the first 2000 s as a function of borehole pressure. Values of other parameters are given in the text.

$\mu_1 = 0.04$ Pa·s; $\tau_y = 5$ Pa. Other parameters have the same values as in Fig. 1. As Fig. 3 indicates, the borehole pressure strongly affects the initial peak of the fluid loss curve and virtually does not affect the duration of the "tail." The total volume of fluid lost into the fracture within the time interval from $t = 0$ to $t = 2000$ s increases linearly with the borehole pressure (Fig. 4), which has to be attributed to the assumed linear fracture deformation law.

Conclusions

Flow of a non-Newtonian drilling fluid from a borehole into a nonpropagating fracture was modeled under the assumptions of linear fracture deformation (opening) and bi-viscous fluid rheology. The volume of the fluid lost into the fracture was shown to be an almost-linearly decreasing function of the fluid yield stress and a linearly increasing function of the borehole pressure. The model can be used in order to optimize drilling regime in naturally fractured reservoirs. It can also provide an aid when using mud loss data for formation characterization purposes.

Acknowledgment

The author is grateful to anonymous reviewers for helpful comments. Financial support of the Norwegian Research Council for this work is gratefully appreciated.

References

[1] Beda, G., and Carugo, C., 2001, "Use of Mud Microloss Analysis While Drilling to Improve the Formation Evaluation in Fractured Reservoirs," Paper SPE 71737 presented at the 2001 SPE Annual Technical Conference and Exhibition, New Orleans, LA, 30 September–3 October, 2001.

[2] Sanfillippo, F., Brignoli, M., Santarelli, F. J., and Bezzola, C., 1997, "Characterization of Conductive Fractures While Drilling," Paper SPE 38177 presented at the 1997 SPE European Formation Damage Conference, The Hague, The Netherlands, 2–3 June, 1997.

[3] Liétard, O., Unwin, T., Guillot, D. J., and Hodder, M. H., 1999, "Fracture Width Logging While Drilling and Drilling Mud/Loss-Circulation-Material Selection Guidelines in Naturally Fractured Reservoirs," SPE Drill. Completion, **14**, pp.168–177.

[4] Lavrov, A., and Tronvoll, J., 2003, "Mud Loss Into a Single Fracture During Drilling of Petroleum Wells: Modeling Approach," *Proc., 6th International Conference on Analysis of Discontinuous Deformation*, Ming Lu, ed., Swets & Zeitlinger, Lisse, pp.189–198.

[5] Lavrov, A., and Tronvoll, J., 2004, "Modeling Mud Loss in Fractured Formations," Paper SPE 88700 to be presented at the 11th Abu Dhabi International Petroleum Exhibition and Conference, Abu Dhabi, U.A.E., 10–13 October, 2004.

[6] Lipscomb, G. G., and Denn, M. M., 1984, "Flow of Bingham Fluids in Complex Geometries," J. Non-Newtonian Fluid Mech., **14**, pp.337–346.

[7] O'Donovan, E. J., and Tanner, R. I., 1984, "Numerical Study of the Bingham Squeeze Film Problem," J. Non-Newtonian Fluid Mech., **15**, pp.75–83.

[8] Carbonell, R., Desroches, J., and Detournay, E., 1999, "A Comparison Between a Semi-Analytical and a Numerical Solution of a Two-Dimensional Hydraulic Fracture", Int. J. Solids Struct., **36**, pp. 4869–4888.

Effective Properties of Nonlinear Laminated Composites With Perfect Adhesion

F. Lebon[1]
Laboratoire de Mécanique de d'Acoustique,
Université Aix-Marseille 1, 31 Chemin Joseph-Aiguier,
13402 Marseille Cedex 20, France
e-mail: lebon@lma.cnrs-mrs.fr

R. Rodríguez-Ramos
e-mail: reinaldo@matcom.uh.cu

J. C. Lopez-Realpozo

J. Bravo-Castillero

R. Guinovart-Diaz

A. Mesejo

Facultad de Matemática y Computación,
Universidad de la Habana, San Lázaro y L, CP. 10400,
Vedado, Habana, Cuba

This paper is devoted to the homogenization of a nonlinear one-dimensional problem as a particular case of laminated composite and its solution by a Wavelet-Galerkin method. This approach is an extension of this method to nonlinear problems. Theoretical results are given and numerical examples are presented.
[DOI: 10.1115/1.2061907]

1 Introduction

Many problems of structural analysis are concerned with heterogeneous media. Theoretical approaches are necessary because of the impossibility to solve numerically real problems, even for a nonlinear behavior. In this paper we are interested in the computation of the effective properties for a periodic heterogeneous media in a special type one-dimensional no-linear elasticity. The following theory can be applied to laminated composites (see Fig. 1) usually used in civil engineering, aircrafts design and for certain applications to ultrasonic transducers. The idea is to consider the material as being a juxtaposition of identical cells, with identical geometrical and mechanical properties. So by multi-scale asymptotic expansion methods it is possible to obtain homogenized equations depending on nonlinear problems on the microstructure and on the global scale. These problems can be solved analytically in one dimension but it is necessary to introduce efficient solvers for two- or three-dimension problems. In the last decades many authors have tried to develop different numerical methods in order to solve the local and global problems, for instance the finite element method [1], Fourier transform [2], and wavelet transform [3]. In this paper a Wavelet-Galerkin method is introduced in order to solve the local and global nonlinear problems in one dimension. The advantages of this method are: (i) there is no creation of mesh contrary to the finite element method, (ii) there is no Gibbs phenomena contrary to the Fourier transform, and (iii) the intrinsic adaptivity of wavelets.

The paper is organized as follows: in Sec. 2, we present the one-dimensional nonlinear elastic problem. Section 3 is devoted to the homogenization of the problem. Section 4 is devoted to the numerical solution by a Wavelet-Galerkin method (Wavelet-Element method). Finally, Sec. 5 contains some numerical examples with two or three types of materials.

2 A One-Dimensional Nonlinear Problem

Let us consider a nonhomogeneous thin bar of length L under the action of volume forces $f(x)$. This bar is supposed to model a laminated composite where the length of each stripe is smaller than the perpendicular direction as shown in Fig. 1. The displacement problem of such a bar is given by the following one-dimensional elliptic equation

$$\frac{d}{dx}\mathcal{F}\left(x,\frac{du}{dx}\right)+f(x)=0 \tag{1}$$

together with the boundary conditions

$$u\Big|_{x=0}=u^0,\quad \mathcal{F}\left(x,\frac{du}{dx}\right)\Big|_{x=L}=S^0 \tag{2}$$

where $\mathcal{F}:[0,L]\times R\to R$, $f:[0,L]\to R$ and $u:[0,L]\to R$.

We assume that the bar is a composite material with periodic structure. For instance, the bar is composed of $p\cdot n$ smaller bars made of p different homogeneous materials (see Fig. 2). The p materials form a periodic cell of length l and it is supposed that $l\ll L$ (equivalent to $n\gg 1$). Under these conditions, the relation between the stress and the strain, given by the map $\mathcal{F}$, is a periodic one in the spatial variable x, then

$$\sigma(x)=\mathcal{F}\left(x,\frac{du}{dx}\right)=\mathcal{F}^{\kappa}\left(x,\frac{du}{dx}\right),\quad \kappa=1,\ldots,p \tag{3}$$

for all x in the κ small bar of the periodic cell. We also suppose that the nonlinear constitutive relation (3) is invertible. Let l_κ, $\kappa=1,\ldots,p$ be the length of the κth bar in the periodic cell, then

$$l=\sum_{\kappa=1}^{p} l_\kappa \tag{4}$$

and together with the boundary conditions (2) we have the continuity conditions $[u]=0$ and $[\sigma]=0$ at the joints of the rods, i.e., at points x_i^κ. Here $x_i^\kappa=(i-1)\cdot l+\sum_{m=1}^{\kappa} l_m$ for $i=1,\ldots,n$, $\kappa=1,\ldots,p$ and $[\cdot]|_{x=x_i^\kappa}$ means the difference between the left and right limits at the point x_i^κ. Equation (1) together with boundary conditions (2), the continuity and conjugation conditions form a typical problem of heterogeneous nonlinear elasticity theory.

3 Homogenization of the Problem

The homogenized equation corresponding to Eq. (1) can be derived by the method of multi-scale asymptotic expansions. In the present problem, there are two natural spatial length scales, one measuring variations within the periodic cell and the other measuring variations within the whole bar. For this reason, we introduce a new variable $\xi=x/\alpha$, where α is a small parameter related to the periodic structure of the material. The variable ξ is called the *fast variable* in relation with x, which is the *slow variable*.

We define now the functions $\mathcal{F}^\alpha(x,\cdot)$, $u^\alpha(x)$, and $\sigma^\alpha(x)$ by

$$\mathcal{F}^\alpha(x,\cdot)=\mathcal{F}\left(\frac{x}{\alpha},\cdot\right)=\mathcal{F}(\xi,\cdot),\quad u^\alpha(x)=u\left(\frac{x}{\alpha}\right)=u(\xi), \tag{5}$$

[1]Corresponding author.

Contributed by the Applied Mechanics Division of ASME for publication in the ASME JOURNAL OF APPLIED MECHANICS. Manuscript received October 29, 2004; final manuscript received March 3, 2005. Review conducted by D. Kouris.

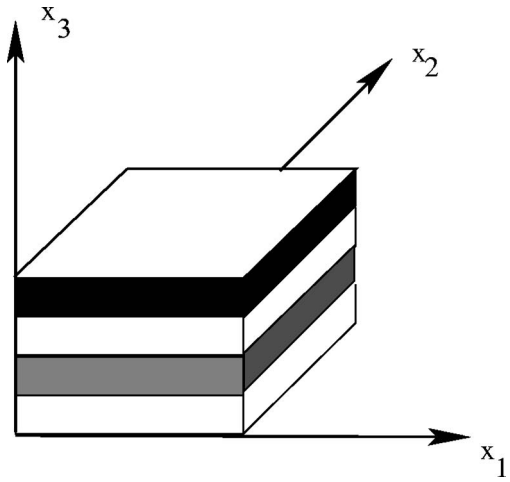

Fig. 1 A laminated composite: the length in directions x_1 and x_2 is small with respect to the length in direction x_3

$$\sigma^\alpha(x) = \mathcal{F}^\alpha\left(x, \frac{du}{dx}\right)$$

and consider the problem

$$\frac{d}{dx}\mathcal{F}^\alpha\left(x, \frac{du^\alpha}{dx}\right) + f^\alpha(x) = 0 \tag{6}$$

$$u^\alpha|_{x=0} = u^0, \quad \mathcal{F}^\alpha\left(x, \frac{du^\alpha}{dx}\right)\Big|_{x=\alpha L} = S^0 \tag{7}$$

$$[u^\alpha]|_{x=\alpha x_i^\kappa} = 0, \quad i = 1,\ldots,n-1, \quad \kappa = 1,\ldots,p,$$
$$[u^\alpha]|_{x=\alpha x_n^\kappa} = 0, \quad \kappa = 1,\ldots,p-1 \tag{8}$$

$$[\sigma^\alpha]|_{x=\alpha x_i^\kappa} = 0, \quad i = 1,\ldots,n-1, \quad \kappa = 1,\ldots,p,$$
$$[\sigma^\alpha]|_{x=\alpha x_n^\kappa} = 0, \quad \kappa = 1,\ldots,p-1 \tag{9}$$

where $f^\alpha(x) = f(x/\alpha)$. The parameter α is properly chosen in order to make the function $\mathcal{F}^\alpha$ 1-periodic in ξ. We search a solution of Eqs. (6)–(9) with the aid of the following two-scale asymptotic expansion of the unknown function u^α

$$u^\alpha(x) = v(x) + \alpha u_1(x,\xi) + \alpha^2 u_2(x,\xi) + \alpha^3 u_3(x,\xi) + \ldots \tag{10}$$

This means that the total dependence on x is obtained directly and through the variable ξ. For an explanation of the physical meaning of the expansion (10) and some other interesting considerations see Ref. [4]. We substitute Eq. (10) into Eq. (6), use the chain rule and make an expansion of $\mathcal{F}^\alpha$ in a Taylor series [4]. After some manipulations equations for orders -1, 0, and 1 are obtained. Finally, we obtain *local problems* [4,5] (LP) for the calculation of the functions $v(x)$ and $u_i(x,\xi)$, $i \geq 1$. For simplicity, we only deal with the problems for the calculation of the functions $v(x)$ and $u_1(x,\xi)$. Suppose there exists a 1-periodic solution $u_1(x,\xi)$ of the following *nonlinear local problem* (LP0) where $v'(x)$ is treated as an independent parameter.

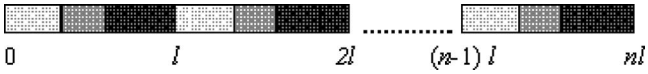

Fig. 2 The periodic structure of the heterogeneous bar for $p=3$

LP0:

$$\frac{\partial}{\partial\xi}\mathcal{F}^\alpha\left(x, v'(x) + \frac{\partial u_1}{\partial\xi}(x,\xi)\right) = 0 \tag{11}$$

$$u_1(x,0) = 0 \tag{12}$$

$$[u_1(x,\xi)]|_{x=x_i^\kappa} = 0, \quad 1 \leq i \leq p-1, \quad 1 \leq \kappa \leq p,$$
$$[u_1(x,\xi)]|_{x=x_n^\kappa} = 0, \quad 1 \leq \kappa \leq p-1 \tag{13}$$

$$\left[\mathcal{F}^\alpha\left(x, v'(x) + \frac{\partial u_1}{\partial\xi}(x,\xi)\right)\right]\Big|_{x=x_i^\kappa} = 0, \quad 1 \leq i \leq p-1, \ 1 \leq \kappa \leq p$$
$$\left[\mathcal{F}^\alpha\left(x, v'(x) + \frac{\partial u_1}{\partial\xi}(x,\xi)\right)\right]\Big|_{x=x_n^\kappa} = 0, \quad 1 \leq \kappa \leq p-1 \tag{14}$$

It follows that u_1 depends on x through $v'(x)$, in other words $u_1 = u_1(v'(x),\xi)$. Once u_1 is known the solution of the recurrent sequence problems are provided $u_2(x,\xi), u_3(x,\xi), \ldots$. Since $u_1 = u_1(v'(x),\xi)$ we can write

$$\frac{d}{dx}\hat{\mathcal{F}}^\alpha(v'(x)) - \hat{f}^\alpha(x) = 0 \tag{15}$$

where

$$\hat{\mathcal{F}}^\alpha(v'(x)) := \left\langle \mathcal{F}^\alpha\left(x, v'(x) + \frac{\partial u_i}{\partial\xi}(x,\xi)\right)\right\rangle,$$
$$\hat{f}^\alpha(x) := \langle f^\alpha(x)\rangle \text{ and } \langle\cdot\rangle := \int_0^1 \cdot \, d\xi \tag{16}$$

The last integral is called the one-dimensional average operator. By definition $v(x)$ is a continuous function, then the continuity conditions are obviously satisfied. The *averaged problem* (AP) of the original problems (1) and (2) is AP

$$\frac{d}{dx}\hat{\mathcal{F}}(v'(x)) - \hat{f}^\alpha(x) = 0 \tag{17}$$

$$v(0) = u^0, \quad \hat{\mathcal{F}}(v'(x))|_{x=L} = S^0 \tag{18}$$

where we define

$$\hat{\mathcal{F}}(y) := \left\langle \mathcal{F}\left(\xi, y + \frac{\partial\theta}{\partial\xi}(\xi,y)\right)\right\rangle \tag{19}$$

As a consequence of LP0 we have

$$\hat{\mathcal{F}}^\alpha(v'(x)) = \mathcal{F}^\alpha\left(x, v'(x) + \frac{\partial u_1}{\partial\xi}(x,\xi)\right) \tag{20}$$

Thus what we need for the construction of the averaged equation (17) is to solve problem LP0 and to use Eq. (20) for stating $\hat{\mathcal{F}}^\alpha(v'(x))$. The normal approach is as follows. We consider the following *parametric problem* (PP) depending on parameter y

PP0(y):

$$\frac{\partial}{\partial\xi}\mathcal{F}\left(\xi, y + \frac{\partial\theta}{\partial\xi}(\xi,y)\right) = 0 \tag{21}$$

$$\theta(0,y) = 0 \tag{22}$$

$$[\theta(\xi,y)]|_{\xi=\xi_i^\kappa} = 0, \quad 1 \leq i \leq p-1, \quad 1 \leq \kappa \leq p,$$
$$[\theta(\xi,y)]|_{\xi=\xi_n^\kappa} = 0, \quad 1 \leq \kappa \leq p-1 \tag{23}$$

$$\left[\mathcal{F}\left(\xi, y+\frac{\partial\theta}{\partial\xi}(\xi,y)\right)\right]\Big|_{\xi=\xi_i^\kappa}=0, \quad 1\leqslant i\leqslant p-1, \quad 1\leqslant\kappa\leqslant p$$

$$\left[\mathcal{F}\left(\xi, y+\frac{\partial\theta}{\partial\xi}(\xi,y)\right)\right]\Big|_{\xi=\xi_n^\kappa}=0, \quad 1\leqslant\kappa\leqslant p-1 \tag{24}$$

From the definitions (5) and from the statement of the problem LP0 it is clear that the solution u_1 of LP0 satisfies

$$u_1(x,\xi)=\theta(\xi,v'(x)) \tag{25}$$

where $\theta(\xi,y)$ is the solution of PP0(y). Therefore, we solve PP0(y) for the construction of the averaged equation and define $\hat{\mathcal{F}}(y)$ from Eq. (19).

4 Numerical Solution by the Wavelet-Element Method

4.1 General Algorithms. As proposed in former papers [3,6], to solve problems PP0 and AP we use the compactly supported wavelets introduced by Daubechies [7] and particularly the Haar basis. These bases are classical bases of $L^2(\mathbb{R})$ and are defined from the data of a function φ called the scaled function and a function ψ, orthogonal to the first one called the associated wavelet. In this paper, we have chosen the classical Haar basis. In the following the unknowns of problems PP0 and AP are approximated in a finite space V_J (J be given). A function f is decomposed in this space on the form

$$f=\sum_{k\in\Lambda_0} f_{0k}\phi_{0k}+\sum_{j=0}^{j=J}\sum_{k\in\Lambda_j} f_{jk}\psi_{jk} \tag{26}$$

where $\Lambda_j=[0,2^j-1]$. The local problem PP0(y) takes on a vectorial form (*discretized nonlinear system*)

NLS0(y): Find $\bar{\theta}_J$ such that $G_y(\bar{\theta}_J)=0$

$\bar{\theta}_J=(\theta_{jk})_{j_0\leqslant j\leqslant J, k\in\Lambda_j}$ is the vector built from the wavelet coefficients of θ. $G_y(\bar{\theta}_J)$ is a nonlinear vectorial function obtained from the discretization of the nonlinear operator $\mathcal{F}^\alpha$. The solution of problem NLS0(y) is obtained using the generalized Newton method (GNM) which is an extension of the classical Newton method to continuous nondifferentiable equations [8]. If $\mathcal{F}^\alpha$ is differentiable this method is reduced to Newton's method.

$$\bar{\theta}_J^0 \text{ given}, \quad \partial G_y(\bar{\theta}_J^i)(\bar{\theta}_J^{i+1}-\bar{\theta}_J^i)=-G_y(\bar{\theta}_J^i) \tag{27}$$

$\partial G_y(\bar{\theta}_J^i)$ is a matrix in the set of the generalized Jacobian of G_y at $\bar{\theta}_J^i$. The initial global problem AP can be written as a problem of minimization under the constraint $v(0)=u_0$ of the potential energy of the system $\phi(w)=\frac{1}{2}\int_0^L\hat{\mathcal{F}}(w'(x))w'(x)dx-\int_0^L fwdx$. In order to solve this problem, we have chosen to use the Lagrangian method. This method consists in introducing a new variable λ, called the Lagrange multiplier, to treat the constraint $v(0)=u_0$. We build a function called Lagrangian $L(w,\mu)=\phi(w)+\mu(w(0)-u_0)$ such that the solution is a saddle point of the Lagrangian (minimum for the displacement, maximum for the multiplier). This method could be improved by the introduction of the augmented Lagrangian method which consists in adding a new term depending on the penalty factor r. The augmented Lagrangian is $L_r(w,\mu)=\phi(w)+\mu(w(0)-u_0)+(r/2)(w(0)-u_0)^2$. To find the saddle point solution, we write that the derivative of the augmented Lagrangian is equal to zero. In other words, we have $\nabla L_r(v,\lambda)(w,\mu)=0$. This problem is first discretized on a wavelet basis in the same way as in the previous part of this section (*nonlinear discretized averaged problem*):

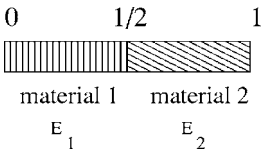

Fig. 3 The first example with two materials on each microstructure

NLAP: Find $(\bar{v},\bar{\lambda}_J)$ such that

$$\hat{G}(\bar{v}_J,\bar{\lambda}_J)=0 \tag{28}$$

This discretized problem is solved by the Generalized Newton method.

4.2 Application to an Illustrating Example. Assume that the function $\mathcal{F}$ is given by

$$\mathcal{F}(x,u'):=\begin{cases}E(x)u' & \text{if } u'<\varepsilon_s(x)\\ \hat{E}(x)u'+(E(x)-\hat{E}(x))\varepsilon_s(x) & \text{if } u'\geqslant\varepsilon_s(x)\end{cases} \tag{29}$$

and that for all x in the interval $[x_i^\kappa,x_i^{\kappa+1}]$ ($1\leqslant i\leqslant N$, $1\leqslant\kappa\leqslant p$, $x_1^1=0$, $x_i^{p+1}=x_{i+1}^1$, $x_N^{p+1}=L$) occupied by the κth small periodic rod, we have $E(x)=E_\kappa$, $\hat{E}(x)=\hat{E}_\kappa$, $\varepsilon_s(x)=\varepsilon_s^\kappa$ ($E_\kappa,\hat{E}_\kappa,\varepsilon_s^\kappa$ be given). In this case, it is possible to compute the elementary terms of the tangent matrix and of the right-hand side necessary for the generalized Newton method

$$[\partial G_y(.)]_{KK'}=\sum_{\kappa=1}^{\kappa=p}E_\kappa^a\int_{\xi^\kappa}^{\xi^{\kappa+1}}\Psi_{jk}\Psi_{j'k'}d\xi$$

$$[G_y(.)]_K=-\sum_{\kappa=1}^{\kappa=p}E_\kappa^a y\int_{\xi^\kappa}^{\xi^{\kappa+1}}\Psi_{jk}d\xi+\sum_{\kappa=1}^{\kappa=p}(E_\kappa^b-E_\kappa^c)\epsilon_\kappa^s\int_{\xi^\kappa}^{\xi^{\kappa+1}}\Psi_{jk}d\xi$$

with $K=k+1+\Sigma_{i=0}^{i=j-1}2^i$, $E_\kappa^a=E_\kappa$ or $\hat{E}_\kappa$. If $E_\kappa^a=E_\kappa$ then $E_\kappa^b=E_\kappa^c=E_\kappa$, and if $E_\kappa^a=\hat{E}_\kappa$ then $E_\kappa^b=\hat{E}_\kappa$ and $E_\kappa^c=E_\kappa$. In the next paragraphs, the deformation is decomposed on the Haar basis. Due to the antiperiodicity of the deformation and to the periodicity of the displacement, we have

$$\frac{\partial\theta}{\partial\xi}(\xi)=\sum_{j=0}^{j=J}\sum_{k\in\Lambda_j}\theta_{jk}\Psi_{jk}, \quad \theta(\xi)=\sum_{j=0}^{j=J}\sum_{k\in\Lambda_j}\theta_{jk}\bar{\Psi}_{jk} \tag{30}$$

where $\bar{\Psi}$ is the primitive of Ψ, i.e., the Schauder basis.

5 Numerical Examples

5.1 First Example (Local Problem). In this first example, we consider a two-phase composite. The elementary cell is split in two equal parts. We denote with indices $i=1$ or 2 the coefficients corresponding to each material (Fig. 3). The first step is to compute the terms of the tangent matrix. $E(y)$ is constant on each compact support of each wavelet Ψ_{jk}. The orthogonality of the Haar basis leads to simple values

$$[\partial G_y(.)]_{11}=\tfrac{1}{2}(E_1^a+E_2^a), \quad [\partial G_y(.)]_{KK}=E_k^a, \quad K\geqslant 2,$$
$$[\partial G_y(.)]_{KK'}=0, \quad K\neq K' \tag{31}$$

The term $[\partial G_y(.)]_{11}$ corresponds to the average of the Young modulus over the cell, i.e., on the compact support of the wavelet. The terms $[\partial G_y(.)]_{KK}$ correspond to the average of the Young modulus on the compact support of each wavelet Ψ_{jk}. The diagonality of the matrix shows the independence between each level. Due to the same arguments in the previous paragraph, only the

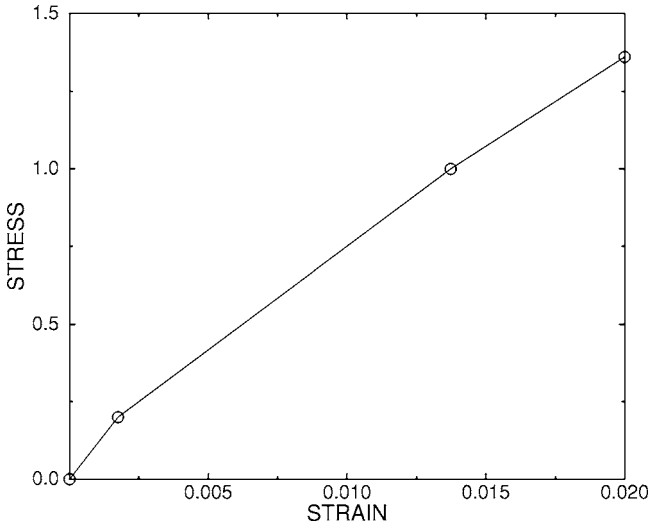

Fig. 4 Macroscopic behavior law (example with two materials)

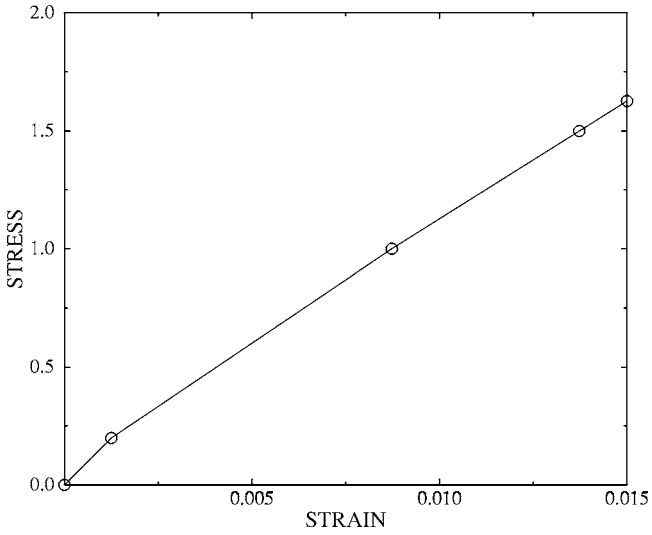

Fig. 6 Macroscopic behavior law (example with three materials)

first component of the right-hand side of (27) has a value not equal to zero. We obtain three different possible values. Thus

$$[G_y(.)]_1 = \tfrac{1}{2}(E_2^a - E_1^a)y + \tfrac{1}{2}(E_1^b - E_1^c)\epsilon_1^s + \tfrac{1}{2}(E_2^b - E_2^c)\epsilon_2^s$$
$$[G_y(.)]_K = 0 \text{ if } K > 1 \tag{32}$$

The global tangent matrix is diagonal and the right-hand side has only its first term which is not equal to zero. We present a numerical application with $E_1 = 80$ GPa, $E_2 = 200$ GPa, $\hat{E}_1 = 40$ GPa, $\hat{E}_2 = 100$ GPa, $\sigma_1^s = 0.2$ GPa, and $\sigma_2^s = 1$ GPa. The macroscopic deformation y increases from 0 to 0.6%. Due to the form of the constitutive equation, the generalized Newton method converges in one or two iterations. At each iteration this method is initialized with the solution at the last step and so, if the solution remains in the same region of linearity, the convergence is obtained in only one iteration. If the region of linearity is changed, due to the evolution of y, the convergence is obtained in two iterations. Figure 4 shows the macroscopic response, i.e., a three phase nonlinear elasticity, these values coincide with the results presented in Refs. [4,5].

5.2 Second Example. The second example concerns a three-phase material. We denote with indices $i = 1, 2, 3$ the coefficients of each material (Fig. 5). Due to the form of the microstructure, the problem is more complex than the former one. The matrix is not a diagonal one. There are interactions between the two first levels of approximation. Thus, using the same notations, we obtain the following tangent matrix

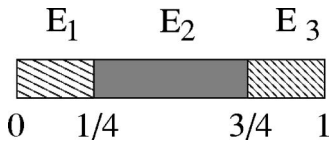

Fig. 5 The second example: a composite with three materials on each microstructure

$$[\partial G_y(.)] = \begin{pmatrix} \frac{1}{4}(E_1^a + 2E_2^a + E_3^a) & \frac{\sqrt{2}}{4}(E_1^a - E_2^a) & \frac{\sqrt{2}}{4}(E_3^a - E_2^a) & 0 & \dots \\ \frac{\sqrt{2}}{4}(E_1^a - E_2^a) & \frac{1}{2}(E_1^a + E_2^a) & 0 & 0 & \dots \\ \frac{\sqrt{2}}{4}(E_3^a - E_2^a) & 0 & \frac{1}{2}(E_2^a + E_3^a) & 0 & \dots \\ 0 & \vdots & & \ddots & \\ \vdots & \vdots & & E_1^a & \\ 0 & \dots & \dots & 0 & E_2^a \end{pmatrix} \tag{33}$$

The right-hand side has only its three first terms which are not equal to zero, thus in this case only three coefficients are not equal to zero θ_{00}, θ_{10}, and θ_{11}. We present a numerical application with $E_1 = 80$ GPa, $E_2 = 200$ GPa, $E_3 = 400$ GPa, $\hat{E}_1 = 40$ GPa, $\hat{E}_2 = 100$ GPa, $\hat{E}_3 = 200$ GPa, $\sigma_1^s = 0.2$ GPa, $\sigma_2^s = 1$ GPa, and $\sigma_3^s = 1.5$ GPa. Figure 6 shows the results obtained for the global response: a nonlinear elasticity law with four phases, these values are the same as those in the analytical approach presented in Refs. [4,5].

6 Conclusion

In this paper, we have presented results concerning the computations of the effective properties of laminated composites. Numerical results show that the wavelet element method is a powerful tool for the characterization of composite materials. In the future, we intend to extend the methods to more general laminated composite (noninvolved behavior, non-perfect interfaces).

Acknowledgment

The work was completed while the author RRR was visiting the Laboratoire de Modélisation en Mécanique from Université Pierre et Marie Curie, Paris supported by the CNRS. The support of project PNCB IBMFQ 09-2004 is also acknowledged. The authors thank Professor G.A. Maugin for his helpful comments.

References

[1] Léné, F., 1984, "Contribution L'étude des Matériaux Composites et a leur Endommagement," Ph.D. thesis, Pierre et Marie Curie University.

[2] Moulinec, H., and Suquet, P., 1994, "A Fast Numerical Method for Computing the Linear and Non Linear Mechanical Properties of Composites," C. R. Acad. Sci. III, **318**, pp. 1417–1423.

[3] Dumont, S., and Lebon, F., 1996, "Representation of Plane Elastostatics Operators in Daubechies Wavelets," Comput. Struct., **60**, pp. 561–569.

[4] Pobedria B. E., 1984, *Mechanics of Composite Materials*, 1st ed., Moscow State University Press, Moscow (in Russian).

[5] Bachvalov, N. S., and Panasenko, G. P., 1989, *Homogenization of Processes in Periodic Media*, Kluwer, Dordrecht.

[6] Dumont, S., and Lebon, F., 1996, "Wavelet-Galerkin Method for Heterogeneous Media," Comput. Struct., **61**, pp. 55–65.

[7] Daubechies, I., 1992, "Orthonormal Bases of Compactly Supported Wavelets," Commun. Pure Appl. Math., **41**, pp. 909–998.

[8] Alart, P., and Lebon, F., 1995, "Solution of Frictional Contact Problems Using ILU and Coarse/Fine Preconditioners," Comput. Mech., **16**, pp. 98–105.

Journal of Applied Mechanics

Announcement

Call for The D'Alembert Award for Multibody System Dynamics and The Lyapunov Award for Nonlinear Dynamics

The *Technical Committee on Multibody Systems and Nonlinear Dynamics* (MSND-TC) of the ASME Design Engineering Division solicits nominations for the *D'Alembert Award* and the *Lyapunov Award*. These awards will be presented at the *6th ASME International Conference on Multibody Systems, Nonlinear Dynamics and Control*, as part of the *ASME 2007 International Design Engineering Technical Conferences* to be held in Las Vegas, Nevada, September, 2007.

The *D'Alembert Award* is established to recognize lifelong contributions to the field of multibody system dynamics.

The *Lyapunov Award* is established to recognize lifelong contributions to the field of nonlinear dynamics.

Selection Criteria and Nomination Materials: These awards recognize lifelong impact of research contributions, education and training of researchers and/or practitioners, and overall leadership in advancing the field. Nominations should include (1) a nomination letter describing the field of, and the impact of, the nominee, (2) a curriculum vitae, and (3) up to five letters of support. All nomination materials must be submitted in electronic (pdf) format.

Submission Instructions: Submit nomination materials before

July 1, 2006

to either one of the Co-Chairs of the Awards Subcommittee.

Professor Olivier A. Bauchau
Co-Chair MSND-TC Awards
School of Aerospace Engineering
Georgia Institute of Technology
270 Ferst Street, SST Building, Rm. 212
Atlanta, GA 30332-0150
Email: olivier.bauchau@ae.gatech.edu
Tel: (404) 894-0042
Fax: (404) 894-2760

Professor Noel C. Perkins
Co-Chair MSND-TC Awards Subcommittee
Mechanical Engineering
University of Michigan
2350 Hayward St.
Ann Arbor, MI 48109-2125
Email: ncp@umich.edu
Tel: (734) 936-0403
Fax: (734) 615-6647

